Development of Time-Domain Green's Functions and Boundary Element Techniques for Transient Elastodynamics of Multi-layered Media

by

Xiaoyong Bai

M.S., China Academy of Engineering Physics, 2010

B.S., Shanghai Jiao Tong University, 2007

A thesis submitted to the

Faculty of the Graduate School of the

University of Colorado in partial fulfillment

of the requirement for the degree of

Doctor of Philosophy

Department of Civil, Environmental, and Architectural Engineering

2018

This thesis entitled:
Development of Time-Domain Green's functions and Boundary Element Techniques for Transient Elastodynamics of Multi-Layered Media

written by Xiaoyong Bai
has been approved for the Department of Civil, Environmental, and Architectural Engineering

____
Ronald Y.S. Pak

____
Richard A. Regueiro

Date_______________

The final copy of this thesis has been examined by the signatories, and we find that both the content and the form meet acceptable presentation standards of scholarly work in the above mentioned discipline.

Xiaoyong Bai (Ph.D., Civil Engineering)

Development of Time-Domain Green’s Functions and Boundary Element Techniques for Transient Elastodynamics of Multi-layered Media

Thesis directed by Professor Ronald Y.S. Pak

Time-domain boundary element method (TD-BEM) is a powerful tool for transient elastodynamic modeling of soil and structures especially for unbounded domain problems. Aimed to add to the advancement of this class of methods and facilitate its coupling with other numerical approaches, a number of new analytical and computational formulations are developed and explored in this study. The work includes the development of a regularized convolution-type boundary integral equation in the time domain for 3-D elastodynamics, the formulation of a rigorous stability analysis via a hybrid amplification matrix of direct TD-BEMs, an extension of a displacement potential-integral transform method from the frequency- to the time-domain, a generalization of the classical Cagniard-de Hoop method in wave propagation theory for Laplace transform's inversion, and the derivation of exact as well as asymptotic forms of the time-domain point-load Green's functions for a homogeneous and a multi-layered half-space. The theoretical developments are employed to develop new computational algorithms such as the new variable-weight multi-step collocation TD-BEM scheme with higher-order time projections and a new numerical contour integration method to compute the fundamental integrals in exact half-space time-domain Green's functions. The efficacy and performance of these developments are evaluated with respect to benchmark elastodynamic problems for both bounded and unbounded domains. The formulation and effectiveness of coupling the proposed TD-BEM approach with a local finite element zone for dynamic soil-structure interaction problems as a rigorous form of wave-absorbing boundary are also investigated.

Dedication

To my wife Xia and my family.

Acknowledgements

I would like to express my sincerest gratitude to my advisor, Professor Ronald Y. S. Pak for the continuous support of my PhD study, for his guidance, motivation, wisdom and immense knowledge. The enriching relationship between mechanics, applied mathematics and numerics that he demonstrated to me through various examples has greatly broadened my horizon. The determination and analytical foresights that he has in dealing with challenging problems has particularly been inspirational to me. Through him, I have found doors to a level of research that I did not know before.

The study is financially supported by the Office of Naval Research (ONR) through Grant N00014-11-1-0691 and the Department of Civil, Environmental and Architectural Engineering through a doctoral dissertation award, both of which I greatly appreciated.

I would also like to thank Professors Richard A. Regueiro, Harihar Rajaram, Jeong-Hoon Song, Yida Zhang and Alireza Doostan for serving on my doctoral thesis committee. I am grateful to Professor Franck Vernerey for serving on the committee of my comprehensive examination as well.

I have benefitted greatly from the work of Professor Pak's former students F. Ji, B. B. Guzina and J. C. Ashlock on the development of frequency-domain boundary element methods. Their high standard and rigor have been awesome examples to me.

Most of all, I wish to thank my wife Xia for her unconditional love and my son Jonathan for the endless happiness he brings to me.

Contents

Tables

Figures

Chapter 1

Introduction

Three-dimensional elastodynamic problems with unbounded domain are fundamental in theoretical and applied mechanics because of their relevance to a wide range of applications in geotechnical and earthquake engineering, dynamic soil-structure interaction, and geophysics. In geotechnical and earthquake engineering, the phenomenon of the wave propagation in a half-space plays a vital role in the investigation of foundation vibration, dynamic bearing capacity of foundation and many modern in-situ test methods (Chopra 2001, Kramer 1996, Das 2016). In dynamic soil-structure interaction, the fundamental challenge is to model the unbounded foundation medium so that the effective reaction of the structure as a result of the wave radiation and scattering upon seismic wave incidence can be comprehensively determined (Wolf 1985, Enrique Luco 1998, Stewart 2012). In seismology, a cornerstone is the theory of wave propagation which underlies the modeling of the earth as a three-dimensional body with complex depthwise and laterally isotropic or anisotropic media (Aki and Richards 2002, Cerveny 2005, Shearer 2009).

By common domain-type numerical methods (for example, the Finite Element Method, Finite Difference Method and Meshless methods) for this class of problems, the discretization of an infinite region has to be limited to a finite region. Besides the needs to have many degrees of freedoms to cover a sufficiently large domain, the artificial boundaries rising from the spatial truncation in dynamic and wave propagation problems can generate spurious reflections and distortions that can contaminate the solution. Boundary Element Methods (BEM) that are formulated for exterior region using appropriate Green’s functions can bypass such issues as they can satisfy rigorously the far-field radiation condition at infinity while needing only to discretize the near-field boundary surfaces (Karabalis 1984, Brebbia, et al. 1984, Dominguez 1993). With the enabling possibility of coupling it with finite element and other numerical methods as well, further development of boundary element methods is believed to be warranted from the viewpoint of theoretical and applied mechanics as well as general engineering modeling of physical problems.

In past developments of BEMs for elastodynamics, they were commonly formulated and used in the frequency domain, with the time-domain responses being synthesized by means of Fourier transforms (Rizzo 1985, Karabalis 1987, Pak and Guzina 1999). For fast loading resulting from transient events like blast loading, however, the use of the frequency-domain BEM approach will necessitate the evaluation of dynamic Green's functions at not only numerous but ultra-high frequencies. For such problems, a time-domain BEM formulation would likely be considered as more attractive and logical. To facilitate the development of hybrid numerical methods such as FEM, FDM and meshless methods to tackle complicated geometric or material problems, the availability of an effective BEM approach in the time-domain should also be more helpful. For example, in the modeling of dynamic soil-structure interaction or a buried blast problem, the BEM can be employed for the far-field domain while the local region can be handled by finite element, meshless or even discrete element methods (Rizos and Wang 2002, Bode et al. 2002, Regueiro 2014, Galvín and Romero 2014).

On TD-BEMs, the most commonly-used approach is to apply a step-by-step direct time integration method with a collocation scheme to the fundamental boundary integral equation that involves multiple convolution integrals. To date, a number of such TD-BEM formulations have been proposed for 2-D (e.g., Mansur 1983, Antes 1985, Coda and Venturini 1995, Carrer et al. 2012) and 3-D problems (e.g., Karabalis and Beskos 1985, Banerjee et al. 1986, Rizos and Karabalis 1994, Rizos and Zhou 2006, Galvín and Romero 2014) **)**. While various advances have been made in recent years, there are still basic theoretical and numerical issues that can use better resolutions. For example, one common feature among many time-domain BEM formulations is the presence of Cauchy principal values (CPV) of integrals and the jump term as a result of the strong singularity of the point-load traction Green's functions. Although there are schemes for their computation using special quadrature weights, the method of finite part integration (Coda and Venturini 1995, Kutt 1975) or the indirect rigid-body motion technique (Banerjee et al. 1986), they are generally sensitive numerically or limited to specific load and geometric configurations.

Most critically, the numerical instability and accuracy issue of TD-BEM in the execution of the time integration has remained a fundamental challenge to be fully resolved as they tend to be problem- and mesh-specific in time-domain boundary element treatments (Cole et al. 1978, Dominguez 1993, Peirce and Siebrits 1997). Aimed to mitigate the stability problem, a number of TD-BEM schemes have been proposed. As direct time integration strategies, there are for example the half-step and ϵ-methods (Peirce and Siebrits 1997), the linear-θ method (Araujo et al. 1999, Yu 1998), the time-weighting method (Marrero and Dominguez 2003, Soares and Mansur 2007, Yazdi et al. 2011, Yu et al. 1998), and the Galerkin procedure (Frangi and Novati 1999, Yu et al. 2000). In most past studies, however, the stability of an algorithm was often proclaimed by executing only a finite number of steps that was deemed sufficiently large in lieu of a rigorous analytical assessment. Such a choice unfortunately runs the risk of misjudgment since a scheme that looks stable over N steps may still eventually see instability emerging at $N+k$ steps or upon the imposition of an alternative set of loading-boundary conditions. To date, the most rigorous approach to BEM's stability question is by Peirce and Siebrits (1997). Utilizing the method of amplification polynomial (Strikwerda 2004), they proposed the use of a discrete z-transform to the time-marching algorithm to develop an approximate characteristic polynomial equation whose roots can be used as direct indicators of the scheme's stability for their half-step and ϵ-methods.

As one can easily deduce, the most important element in BEMs or boundary integral equation methods (BIEMs) is the kernel of the integral equation, i.e., the Green's function. Unfortunately, time-domain Green's function for elastodynamics is very limited and the classical Stokes' solution (Stokes 1849) remains the prevalent one used in most implementations. For problems involving semi-infinite media typically found in geotechnical engineering, geophysics and seismology problems, the use of full-space Green's functions in a BEM will require a discretization of the free-surface with truncation (Padrón et al. 2011, Von Estorff and Hagen 2006). This increases not only the size of the matrix system but also limit the time interval of a solution's validity. Should the half-space Green's functions be available that can satisfy the conditions of infinite free-surface fully, the accuracy of many TD-BEMs should be improved fundamentally upon their incorporation.

To obtain elastodynamic half-space Green's functions in 3D, a powerful method of solution is the methods of displacement potentials (Lamb 1904, Gurtin and Sternberg 1962, Pak 1987). By means of the analytical decompositions, they enable the conversion of the coupled Navier's equations of motion to a set of uncoupled wave equations. To obtain rigorous mathematical solutions, techniques such as Fourier transform method can be used to convert the problem to one in the frequency domain or the partial differential equations to the elliptic type. Through an inverse Fourier transform, the time-domain response can then be theoretically recovered. To achieve it analytically and numerically, however, the time-function of the imposed loading or excitation needs to be reasonably smooth so that it does not contain any very high frequency components. Otherwise, it will require a frequency-domain characterization over a large or infinite range which is unwieldy numerically. An analytical alternative for developing time-domain Green's functions is the use of Laplace transform together with the ingenious inversion technique conceived by Cagniard (1962) and modified by de Hoop (1960). As the most rigorous theoretical platform for wave propagation problem in solid mechanics (Miklowitz 1978), acoustics (Brekhovskikh 2012), seismology (Aki and Richards 2002) as well as electromagnetics (de Hoop 1988), the key idea of Cagniard entails finding a special integration path in the complex plane and manipulating the variables so that the transformed solution can be re-cast in a canonical format. A number of basic wave propagation problems in 2-D (Dix 1954, Pekeris 1955a, Pekeris 1955b) were solved analytically by the Cagniard-de Hoop method but the method's application to general three-dimensional elastodynamic source-response problems has been limited owing to the complexity of the mathematics involved except for special cases such as the surface response due to a buried source or the interior response due to surface loading (see Chao 1960, Verweij and de Hoop 1990). For example, Chao (1960) considered the response of an elastic half-space to a tangential surface load. A review of past solutions for the case of surface source and response can be found in Kausel (2012) which included some simplified formulas. As to the case of a general buried source and a general observer location on or in a homogeneous half-space, the main solution is that of Johnson (1974) who obtained a solution of the 3-D Navier's equations in terms of Laplace and Fourier transforms, and adapted Cagniard-de Hoop's method for his choice of a rectangular coordinate system. The resulting mathematical derivation and operations involved are, however, lengthy and complicated, with multiple variable transformations and analytical manipulations and the suggested numerical implementation had some basic issues (Galvín and Romero 2014).

For the more complicated scenario of a *multi-layered* half-space which is essential for representing common in-situ soil's properties' variations in nature, past advances were mostly achieved in the frequency domain as in Thomson (1950), Haskell (1953), Knopoff (1964), Gilbert and Backus (1966), Kennett (1979), Aspel (1979), and Pak and Guzina (2002) where the Green's functions were developed by means of Hankel transfroms with respect to the radial coordinate, Fourier decompositions with respect to the angular coordinate, and the method of "propagator matrices" that allow for the determination of integration coefficients by means of boundary and interfacical conditions. In the work by Ma and Lee (2006), a method to computing the time-domain Green's function was developed to invert the Laplace transform solution via Cagniard's method but there remain important analytical issues such as a proper treatment of various singularities, to be resolved.

Intended to be a rigorous effort to extend the analytical and computational foundations for BEMs for general 3-D elastodynamic problems especially for unbounded 3-D multi-layered media, the following developments were pursued and presented in this dissertation:

1. Regularized Time-Domain Boundary Element Method (BEM) formulation

With the recognition of the analytical and numerical issues that have plagued TD-BEMs for elastodynamics, an effort was made to develop a compact but rigorous mathematical foundation for BEMs for the time domain that may help to ease some of the numerical issues in a direct time-integration solution scheme. Owing to the strong singularity of some of the Green's functions in elastodynamics, the classical BEM formulation requires the computation of Cauchy Principal Values (CPV) which is often sensitive and tricky. To this end, by means of a general decomposition of time-dependent point-load Green’s functions into a singular and regular part, it is shown that a regularized boundary integral equation for the time domain can be formulated. Its numerical implementation via a variable-weight multi-step collocation scheme that allows for different orders of time projection for the boundary displacements and tractions is also accomplished and evaluated.

2. Stability analysis of direct time-integration schemes in boundary element methods

As noted earlier, the numerical instability of TD-BEM schemes has been a critical issue in direct time-domain boundary element methods (TD-BEM) especially for elastodynamics. While there are some schemes that appear to be stable for a finite number of time steps, few have offered a mathematical proof that they actually are because of the absence of a rigorous assessment formalism. In this study, a compact analytical framework for evaluating the issue is presented. By finding a way to cast the convolution integral-based TD-BEM algorithm in the form of a linear multi-step method with a hybrid amplification matrix and the incorporation of some fundamental characteristics of commonly used transient Green’s functions, the assessment problem is shown to be reducible to a standard spectral analysis in matrix theory by which the stability threshold can be clearly defined. Apt to be applicable for the evaluation of a wide class of TD-BEMs, the approach is applied to the proposed regularized time-domain direct boundary element method with optional collocation weights and orders of solution variable projections as illustration. With the aid of the rigorous stability analysis and a systematic parametric study, an analytical resolution of some critical aspects in some past schemes as well as the versatility of the generalized TD-BEM algorithm as they pertain to the benchmark finite-domain square-bar and the infinite-domain cavity elastodynamic problems are given as examples.

3. Indirect Time-domain elastodynamic Green's functions for homogeneous and multi-layered half-space for “B-Spline" time function and frequency-domain formulation

Intended as a benchmark solution for assessing the TD-BEM to be developed for half-space problems, a time-domain Green's function of homogeneous half-space subjected to arbitrarily-located point-load with a cubic B-spline time function is implemented using a Fourier synthesis of the frequency-domain half-space Green's function presented in Pak and Guzina (2002). The adoption of a smoothened impulse-type time history such as a cubic B-spline function for the fundamental solution is shown to be useful in nullifying the need to computing the frequency-domain Greens function at excessively high frequency.

4. Direct Time-domain Green’s function for a homogeneous half-space by an extended displacement potential-Laplace-Hankel-Cagniard transform method

With aid of Laplace and Hankel transforms with respect to time and space, a method of displacement potentials is extended to obtain time-domain dynamic response of an elastic half-space resulting from an arbitrary, finite, buried source is presented. To recover the time dependence of the Green’s functions, a novel approach in extending Cagniard’s idea to the derived analytical transformed solution is realized. By virtue of a generalized presentation of Bessel functions in the Hankel transform, the well-acknowledged difficult task of discovering the inversion path is replaced by a simplified analytical procedure in finding an effective replacement Cagniard contour that has fewer integration issues. The new solution is given compactly in terms of a single integral over a finite interval, and its numerical implementation is tested against known results for accuracy and robustness.

5. Time-domain Green's function for a multilayer half-space

On the basis of the foregoing developments, a rigorous theoretical framework is formulated to analyze the propagation of transient disturbance in a semi-infinite 3-D multilayered solid due to arbitrary asymmetric loadings in this study. Utilizing the new method of solution in terms of displacement potentials, Laplace and Hankel integral transforms, method of propagator matrix and Cagniard method, it is shown that results such as wave arrival time and wave front singularities in the 3-D multi-layered problem that were obtained in the past by separate analyses via generalized ray expansion and geometric methods in geophysics, can be extracted rigorously from the full mathematical solution.

6. TD-BEM with half-space Green's function and its use in finite element-boundary element (FE-BE) coupling for soil-structure interaction (SSI) problems

With the regularized TD-BEM incorporating the multilayer half-space Green's functions, several problems involving homogeneous and multilayer half-space are considered and validated in this study. An analytical framework for direct BEM-FEM coupling so that a common step-by-step integration scheme can be used for dynamic soil-structure interaction analysis is developed and implemented. A number of soil-foundation-structure interaction configurations are also considered to evaluate the effectiveness of the proposed coupling formulation.

In this thesis, the foregoing work is presented in 9 chapters. Chapter 2 presents the derivation of a regularized form of the time-domain boundary integral equation which forms the core foundation of the proposed TD-BEM developments. With the improved analytical format, the derivation of the new TD-BEM solution algorithm on the basis of a variable-weight multi-step collocation scheme with higher orders of time projections for the field variables for better control of the accuracy and stability is given. Chapter 3 contains a number of examples of the numerical performance of the proposed generalized TD-BEM scheme. The formulation of a formal analytical framework for the evaluation of the stability of a general class of TD-BEMs is outlined in Chapter 4. To provide a reference for the development of new time-domain Green's functions, Chapter 5 describes the use of frequency-domain Green's function to generate time-domain response via Fourier transform approach. Chapter 6 outlines the analytical solution formulation of the time-domain Green's function by means of Laplace-Hankel transforms and the proposed inversion approach by analytic function theory. Chapter 7 presents an extension of the techniques in Chapter 5 and 6 to the more complicated case of multilayer media. Partly as a summarial application of all the analytical and computational developments in the study, Chapter 8 gives a number of examples and results from the application of the time-domain BEM formulation for problems using the half-space Green's function as well as a coupled finite elmenet-boundary element algorithm in a dynamic soil-structure interaction problem. A set of conclusions is provided in Chapter 9.

Chapter 2

Regularized Boundary Element Formulation for Time Domain with Weighted-Collocation and Higher-Order Projection for 3-D Time-Domain Elastodynamics

2.1 Introduction

Boundary element method (BEM) is a powerful numerical method for elastodynamics, as an independent candidate or a component in a hybrid procedure (Cole et al. 1978) especially in unbounded domain problems. While the approach is commonly implemented in the frequency domain, a sound time-domain boundary element formulation (TD-BEM) is of equal fundamental importance to both theoretical and computational developments. Apart from its clear analytical appeal in being able to handle directly in the time domain fast transient and shock-like dynamic conditions for which a frequency-domain approach will have to face the challenge of determining the system response at very high frequencies, an effective TD-BEM is essential to allow the method to be coupled with a wide variety of mesh-based or meshless methods to realize the best modeling of complex physical problems. To date, a number of TD-BEM formulations have been proposed for 2-D (e.g., Mansur 1983, Antes 1985, Coda and Venturini 1995, Carrer et al. 2012) and 3-D problems (e.g., Karabalis and Beskos 1985, Banerjee et al. 1986, Rizos and Karabalis 1994, Rizos and Zhou, 2006, Galvín and Romero 2014). While various advances have been found in recent years, there are still basic theoretical and numerical issues that warrant further attention. For example, one common feature among many time-domain BEM formulations is the presence of Cauchy principal values (CPV) of integrals and the jump term as a result of the strong singularity of the point-load traction Green's functions. Although there are schemes for their computation using special quadrature weights, the method of finite part integration (Coda and Venturini 1995, Kutt 1975) or rigid-body motion that combines both evaluations (Banerjee, et al. 1986), they are generally sensitive numerically or limited to specific load and geometric configurations. More fundamentally, numerical instability and accuracy issues in the execution of the time integration have remained the critical challenge to be fully resolved as they tend to be problem- and mesh-specific in time-domain boundary element treatments (Cole et al. 1978, Dominguez 1993, Peirce and Siebrits 1997). Aimed to mitigate the issue, a number of numerical schemes have been proposed. Examples are the averaged collocation method (Marrero and Dominguez 2003), the ϵ method (Peirce and Siebrits 1997), the linear-θ method (Araujo et al. 1999), the time-weighting method (Frangi and Novati 1999, Yazdi et al. 2011, Yu et al. 1998), and the Galerkin method (Yu et al. 2000). While there are alternative avenues to time-domain solution via, for example, the frequency domain through FFT algorithms or the Laplace transform domain with the method of convolution quadrature (CQ) (Schanz and Antes 1997, Schanz et al. 2016), the direct time-integration boundary element approach has the fundamental appeal of conceptual simplicity and ease in implementation. To advance this class of methods, a TD-BEM scheme that can be customized parametrically to achieve a higher level of stability and accuracy control should be valuable.

In this chapter, a generalized weighted-collocation boundary element method for three-dimensional elastodynamics is presented. On the basis of a decomposition of any time-dependent point-load Green's functions into a singular and regular part (Mansur 1983, Sladek 1991), a regularized boundary integral equation for time-domain analysis is formulated and implemented via a variable-weight multi-step collocation scheme with different temporal projections of the displacement and traction variations. The numerical performance of the formulation using different parametric combinations is tested and compared against some basic treatments in the next chapter. The possibility of improved performance by an optimal choice of the collocation weights and the order of variable projection is also be explored via benchmark finite-domain and infinite-domain problems. In what follows, the fundamental boundary integral equation for 3-D is first established, followed by its regularization and numerical implementation in a new generalized time marching scheme.

2.2 Governing equations for Elastodynamics

With reference to a Cartesian frame $\{O;\xi_1,\xi_2,\xi_3\}$ for a three-dimensional solid in motion whose displacement, Cauchy stress tensor, body force, elasticity tensor and mass density are denoted by $\mathbf{u}(\boldsymbol{\xi},t)$, $\boldsymbol{\tau}(\boldsymbol{\xi},t)$, $\mathbf{f}(\boldsymbol{\xi},t)$, $\mathbf{C}$ and ρ respectively in open regular region Ω, the governing equations in the framework of linearized elastodynamics and component form are

$$\tau_{ij,j}+f_i=\rho\ddot{u}_i, \tag{2.1}$$

from the balance of linear momentum and

$$\tau_{ij}=C_{ijkl}u_{k,l}, \tag{2.2}$$

from the constitutive relationship where C_{ijkl} denotes the fourth-order elasticity tensor with major and minor symmetries. The general displacement and traction boundary conditions for $\Gamma=\Gamma_u+\Gamma_t$ as the closed boundary of Ω (see Figure 2.1) can be expressed as

$$\begin{aligned} u_i(\boldsymbol{\xi},t)&=\tilde{u}_i(t),\ \boldsymbol{\xi}\in\Gamma_u,\ t>0,\\ t_i(\boldsymbol{\xi},t;\mathbf{n})=\tau_{ij}n_j&=\tilde{t}_i(\boldsymbol{\xi},t),\ \boldsymbol{\xi}\in\Gamma_t,\ t>0, \end{aligned} \tag{2.3}$$

where n_i is the outward normal, $\tilde{u}_i$ and $\tilde{t}_i$ are the prescribed displacements and tractions, respectively. In transient problems, the general initial conditions

$$\begin{aligned} u_i(\boldsymbol{\xi},0)&=u_i^0(\boldsymbol{\xi}),\ \boldsymbol{\xi}\in\Omega,\\ \dot{u}_i(\boldsymbol{\xi},0)&=v_i^0(\boldsymbol{\xi}),\ \boldsymbol{\xi}\in\Omega \end{aligned} \tag{2.4}$$

should also be specified.

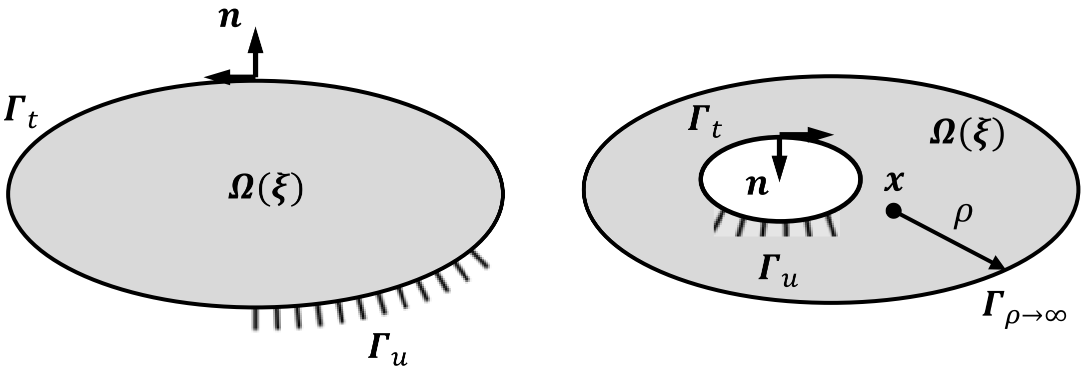

(a)Finite region, interior problem (b)Infinite region, exterior problem

Figure 2.1: Elastodynamic boundary value problem

2.3 Boundary integral representation in time-domain

To establish the boundary integral equation for general initial-boundary value problems in elastodynamics, Graffi's reciprocal theorem (Wheeler and Sternberg 1968) is a useful theoretical platform. In terms of the Riemann convolution of two functions $g(\xi,t)$ and $h(\xi,t)$ defined by

$$[g*h](\xi,t)=\begin{cases} 0, & \xi\in\Omega,\quad t<0 \\ \int_0^t g(\xi,t-s)h(\xi,s)\,ds, & \xi\in\Omega,\quad t>0 \end{cases}, \tag{2.5}$$

the theorem can be stated as

$$\int_\Gamma[\hat{t}_i*u_i]\mathrm{d}\Gamma+\int_\Omega[\hat{f}_i*u_i]\mathrm{d}\Omega-\int_\Omega\rho[\ddot{\hat{u}}_i*u_i]\mathrm{d}\Omega=\int_\Gamma[t_i*\hat{u}_i]\mathrm{d}\Gamma+\int_\Omega[f_i*\hat{u}_i]\mathrm{d}\Omega-\int_\Omega\rho[\ddot{u}_i*\hat{u}_i]\mathrm{d}\Omega \tag{2.6}$$

for any two admissible elastodynamic states $\mathbf{S}=[\mathbf{u},\boldsymbol{\tau};\mathbf{f},\mathbf{C},\rho]$ and $\hat{\mathbf{S}}=[\hat{\mathbf{u}},\hat{\boldsymbol{\tau}};\hat{\mathbf{f}},\mathbf{C},\rho]$ over the same domain, provided that they both satisfy their corresponding momentum balance equations

$$\tau_{ij,j}+f_i-\rho\ddot{u}_i=0,\quad \hat{\tau}_{ij,j}+\hat{f}_i-\rho\ddot{\hat{u}}_i=0, \tag{2.7}$$

the traction formulas

$$t_i = \tau_{ij} n_j , \quad \hat{t}_i = \hat{\tau}_{ij} n_j , \tag{2.8}$$

and the stress-displacement gradient relations

$$\tau_{ij}\left(\xi, t\right) = C_{ijkl} u_{k,l}\left(\xi, t\right), \quad \hat{\tau}_{ij}\left(\xi, t\right) = C_{ijkl} \hat{u}_{k,l}\left(\xi, t\right).$$

By virtue of the commutativity of the Riemann convolution, the major symmetry of C_{ijkl} and the identities

$$\begin{aligned} &\frac{\partial}{\partial t}[\hat{u}_i * u_i] = [\dot{\hat{u}}_i * u_i] + \hat{u}_i^0 u_i , \\ &\frac{\partial^2}{\partial t^2}[\hat{u}_i * u_i] = [\ddot{\hat{u}}_i * u_i] + \dot{\hat{u}}_i^0 u_i + \hat{u}_i^0 \dot{u}_i , \\ &\frac{\partial^2}{\partial t^2}[u_i * \hat{u}_i] = [\ddot{u}_i * \hat{u}_i] + \dot{u}_i^0 \hat{u}_i + u_i^0 \dot{\hat{u}}_i , \end{aligned} \tag{2.9}$$

Eqn. (2.6) can be expressed as

$$\begin{gathered} \int_{\Gamma}[\hat{t}_i * u_i]\mathrm{d}\Gamma + \int_{\Omega}[\hat{f}_i * u_i]\mathrm{d}\Omega + \int_{\Omega}\rho\left(\dot{\hat{u}}_i u_i + \hat{u}_i^0 \dot{u}_i\right)\mathrm{d}\Omega = \\ \int_{\Gamma}[t_i * \hat{u}_i]\mathrm{d}\Gamma + \int_{\Omega}[f_i * \hat{u}_i]\mathrm{d}\Omega + \int_{\Omega}\rho\left(\dot{u}_i^0 \hat{u}_i + u_i^0 \dot{\hat{u}}_i\right)\mathrm{d}\Omega \end{gathered} . \tag{2.10}$$

Focused on the common case of a quiescent past, Eqn. (2.10) can be reduced to

$$\int_{\Gamma}[t_i * \hat{u}_i]\mathrm{d}\Gamma + \int_{\Omega}[f_i * \hat{u}_i]\mathrm{d}\Omega = \int_{\Gamma}[\hat{t}_i * u_i]\mathrm{d}\Gamma + \int_{\Omega}[\hat{f}_i * u_i]\mathrm{d}\Omega . \tag{2.11}$$

To develop the fundamental boundary integral equation in the classical framework of three-dimensional elastodynamics, it is useful to specialize the body force field $\hat{f}_i$ to be $\hat{f}_i^k\left(i = 1, 2, 3\right)$ which corresponds to a time-dependent unit point-load in the k^{th} direction acting at a point $\mathbf{x} \in \Omega$, i.e.,

$$\hat{f}_i^k\left(\xi, t\right) = \delta_{ik}\delta\left(\mathbf{x} - \xi\right) g\left(t\right), \; t > 0, \; k = 1, 2, 3 , \tag{2.12}$$

where δ_{ik} denotes the Kronecker delta and $\delta(\mathbf{x}-\xi)$ the three-dimensional Dirac delta function. The function $g(t)$ is the time variation of the point load that onec an specify, its usual choice being the Dirac delta-function $\delta(t)$ or the Heaviside step-function $H(t)$. Commonly referred to as the displacement, traction and stress Green's functions, respectively, the corresponding elastodynamic solution $\hat{u}_i^k(\xi,\mathbf{x},t)$, $\hat{t}_i^k(\xi,\mathbf{x},t;\mathbf{n})$ and $\hat{\tau}_{ij}^k(\xi,\mathbf{x},t)$ under the point load in (2.12) satisfy the field equations

$$\begin{aligned}
&\hat{\tau}_{ij,j}^k+\delta_{ik}\delta(\xi-\mathbf{x})g(t)=\rho\ddot{\hat{u}}_i^k,\\
&\hat{t}_i^k=\hat{\tau}_{ij}^k n_j,\\
&\hat{\tau}_{ij}^k=C_{ijpq}\hat{u}_{p,q}^k.
\end{aligned}\tag{2.13}$$

with the displacement and traction/stress Green's functions being singular of the order of $O\left(\frac{1}{|\xi-\mathbf{x}|}\right)$ and $O\left(\frac{1}{|\xi-\mathbf{x}|^2}\right)$, respectively as $|\xi-\mathbf{x}|\to 0$.

By virtue of the foregoing characteristics of the Green's functions, an integral representation of the displacement field at a point $\mathbf{x}$ in Ω can be secured from Eqn. (2.11) as

$$\begin{aligned}
D(\mathbf{x})\,[u_k(\mathbf{x},t)*g(t)]&=\int_\Gamma[t_i(\xi,t)*\hat{u}_i^k(\xi,\mathbf{x},t)]\mathrm{d}\Gamma_\xi-\int_\Gamma[\hat{t}_i^k(\xi,\mathbf{x},t;\mathbf{n})*u_i(\xi,t)]\mathrm{d}\Gamma_\xi\\
&\quad+\int_\Omega[f_i(\xi,t)*\hat{u}_i^k(\xi,\mathbf{x},t)]\mathrm{d}\Omega_\xi,\\
D(\mathbf{x})&=\begin{Bmatrix}1, & \mathbf{x}\in\Omega\\ 0, & \mathbf{x}\notin\Omega\end{Bmatrix}
\end{aligned}\tag{2.14}$$

for the interior domain problem depicted in Figure 2.1(a).

For an unbounded domain Ω that is exterior to the boundary surface Γ, the elastodynamic integral representation is identical to Eqn. (2.14), provided that the unit normal on Γ is directed opposite that for the interior case and the solution satisfies the generalized radiation or regularity condition of

$$\lim_{\rho\to\infty}\int_{\Gamma_\rho}\Big([t_i(\boldsymbol{\xi},t)*\hat{u}_i^k(\boldsymbol{\xi},\mathbf{x},t\,|\,g)]-[\hat{t}_i^k(\boldsymbol{\xi},\mathbf{x},t;\mathbf{n}\,|\,g)*u_i(\boldsymbol{\xi},t)]\Big)\mathrm{d}\Gamma_{\boldsymbol{\xi}}=0,\quad\forall\mathbf{x}\in\Omega,\tag{2.15}$$

where Γ_ρ is the spherical outer surface with its radius $\rho\to\infty$ (see Figure 2.1(b)).

2.4 Boundary integral representation in frequency-domain

Letting the upper-case to denote a function's Fourier transform with respect to time, e.g.,

$$G(\xi,\omega)=\mathscr{F}\left[g(\xi,t)\right]=\int_{-\infty}^{\infty}g(\xi,t)e^{-i\omega t}dt\,,\tag{2.16}$$

the boundary integral equation (2.14) can be transformed to a frequency-domain representation as

$$\begin{aligned}D(\mathbf{x})\;U_k(\mathbf{x},\omega)&=\int_{\Gamma}T_i(\boldsymbol{\xi},\omega;\mathbf{n})\hat{U}_i^k(\boldsymbol{\xi},\mathbf{x},\omega)\mathrm{d}\Gamma_{\boldsymbol{\xi}}-\int_{\Gamma}[\hat{T}_i^k(\boldsymbol{\xi},\mathbf{x},\omega;\mathbf{n})U_i(\boldsymbol{\xi},\omega)]\mathrm{d}\Gamma_{\boldsymbol{\xi}}\\&\quad+\int_{\Omega}F_i(\boldsymbol{\xi},\omega)\hat{U}_i^k(\boldsymbol{\xi},\mathbf{x},\omega)]\mathrm{d}\Omega_{\boldsymbol{\xi}},\qquad D(\mathbf{x})=\begin{Bmatrix}1,&\mathbf{x}\in\Omega\\0,&\mathbf{x}\notin\Omega\end{Bmatrix},\end{aligned}\tag{2.17}$$

where $\hat{U}_i^k(\boldsymbol{\xi},\mathbf{x},\omega)$, $\hat{T}_i^k(\boldsymbol{\xi},\mathbf{x},\omega;\mathbf{n})$ are the Fourier-transformed fundamental solution satisfying the field equations

$$\left(C_{ijpq}\hat{U}_{p,q}^k\right)_{,j}+\rho\omega^2\hat{U}_i^k+\delta_{ik}\delta(\mathbf{x}-\boldsymbol{\xi})=0,\;\hat{T}_i^k=\hat{\mathscr{T}}_{ij}^k n_j,\;\hat{\mathscr{T}}_{ij}^k=C_{ijpq}\hat{U}_{p,q}^k\,.\tag{2.18}$$

In frequency domain, the general radiation condition Eqn. (2.15) becomes

$$\lim_{\rho\to\infty}\int_{\Gamma_\rho}\Big(T_i(\boldsymbol{\xi},\omega;\mathbf{n})\hat{U}_i^k(\boldsymbol{\xi},\mathbf{x},\omega)-\hat{T}_i^k(\boldsymbol{\xi},\mathbf{x},\omega;\mathbf{n})U_i(\boldsymbol{\xi},\omega)]\Big)\mathrm{d}\Gamma_{\boldsymbol{\xi}}=0,\;\;\forall\mathbf{x}\in\Omega\,.\tag{2.19}$$

Comparing the two boundary integral representations, i.e., Eqn. (2.14) for time-domain and Eqn. (2.17) for frequency-domain, one may find that the time-domain equation is considerably more complicated because it involves a convolution integration over time besides the spatial integration. As the frequency domain approach has been generally well developed in past decades, e.g., (Pak and Guzina 1999), the focus of this chapter is on the fundamental aspects of time-domain

BEMs and how further theoretical and computational developments can be a meaningful step towards an improved analytical foundation.

2.5 Time-domain boundary integral equation and its regularization

Taking into account the different orders of singularity of the displacement and traction Green's functions $\hat{U}_i^k$ and $\hat{T}_i^k$, the limiting form of Eqn. (2.14) as $\mathbf{x} \to \mathbf{y} \in \Gamma$ can be stated explicitly as

$$\begin{aligned} &\int_0^t c_{ik}(\mathbf{y},t-\tau)u_i(\mathbf{y},\tau)d\tau + \int_0^t \fint_\Gamma \hat{T}_i^k(\boldsymbol{\xi},\mathbf{y},t-\tau;\mathbf{n})u_i(\boldsymbol{\xi};\tau)d\Gamma_\xi d\tau \\ &= \int_0^t \int_\Gamma \hat{U}_i^k(\boldsymbol{\xi},\mathbf{y},t-\tau)t_i(\boldsymbol{\xi},\tau)d\Gamma_\xi d\tau + \int_0^t \int_\Omega \hat{U}_i^k(\boldsymbol{\xi},\mathbf{y},t-\tau) f_i(\boldsymbol{\xi},t)\mathrm{d}\Omega_{\boldsymbol{\xi}} d\tau, \quad \forall \mathbf{y} \in \Gamma \end{aligned} \tag{2.20}$$

where $\fint_\Gamma$ stands for the Cauchy principal value of the surface integral and

$$c_{ik}\left(\mathbf{y},t\right) = \delta_{ik} g(t) + \lim_{\varepsilon \to 0} \int_{\hat{\Gamma}_\varepsilon} \hat{T}_i^k\left(\boldsymbol{\xi},\mathbf{y},t;\mathbf{n}\right) d\Gamma_\xi, \ \mathbf{y} \in \Gamma, \tag{2.21}$$

with $\hat{\Gamma}_\varepsilon$ denoting the small hemispherical surface with a dimension defined by ϵ and centered at $\mathbf{y}$ (see Figure 2.2) so that $\hat{T}_i^k\left(\boldsymbol{\xi},\mathbf{y},t,\mathbf{n}\right)$ is theoretically non-singular in the limit process.

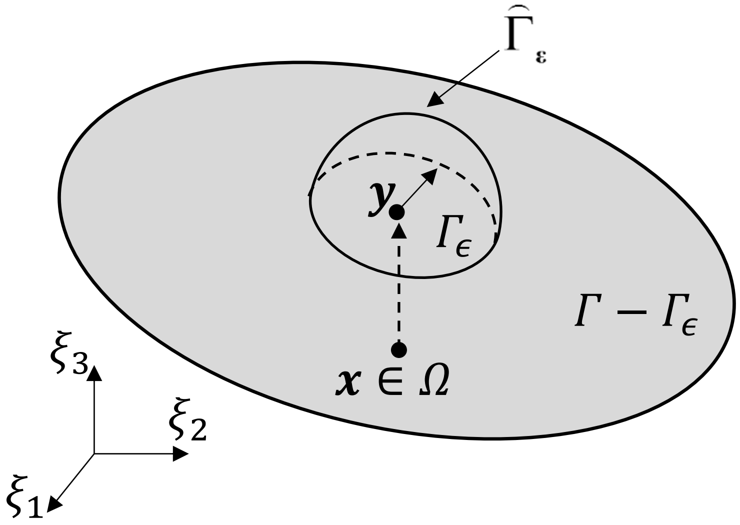

Figure 2.2: Formal domain of definition for the jump term c_{ik}

Despite its classical appeal and adoption, the boundary integral formulation by Eqn. (2.20) and (2.21) is not without some common objections. For one, the second integral of Eqn. (2.20) is in terms of its Cauchy principal value whose numerical evaluation is often sensitive as discussed in the Introduction. For non-homogeneous media and non-smooth boundary geometries, a direct evaluation of the jump term c_{ik} in Eqn. (2.21) is also non-trivial generally. To avoid these obtuse computational challenges while dealing with a complex problem, an alternative boundary integral equation format which can bypass these issues has proven to be an asset as in Pak and Guzina (1999) and Sladek (1991). For this purpose, it is useful to note that dynamic point-load stress Green's function corresponding to Eqn. (2.13) can be decomposed, as a generalization of Pak & Guzina (1999) from the frequency- to the time-domain, into a singular part $[\hat{\Gamma}_{ij}^k(\boldsymbol{\xi},\mathbf{x},t)]_1$ and a regular part $[\hat{\Gamma}_{ij}^k(\boldsymbol{\xi},\mathbf{x},t)]_2$ such that

$$\hat{\Gamma}_{ij}^k(\boldsymbol{\xi},\mathbf{x},t) \equiv [\hat{\Gamma}_{ij}^k(\boldsymbol{\xi},\mathbf{x},t)]_1 + [\hat{\Gamma}_{ij}^k(\boldsymbol{\xi},\mathbf{x},t)]_2 \,, \tag{2.22}$$

with $[\hat{\Gamma}_{ij}^k]_1$ satisfying

$$[\hat{\Gamma}_{ij,j}^k]_1 + \delta_{ik}\delta(\mathbf{x}-\boldsymbol{\xi})\; g(t) = 0 \;. \tag{2.23}$$

For all possible source and observation points in a piecewise homogeneous, isotropic, multi-layered solid for instance, $[\hat{\Gamma}_{ij}^{k}(\boldsymbol{\xi},\mathbf{x},t)]_1$ at any time t can be demonstrated to be the static bi-material full-space Green's function (Pak and Guzina 1999) that is modified by the strength coefficient $g(t)$ of the imposed point load. In the simplest case of a homogeneous full-space, it degenerates to a time-moderated Kelvin's elastostatic state of

$$[\hat{T}_i^k(\boldsymbol{\xi},\mathbf{x},t;\mathbf{n})]_1 = -\frac{g(t)}{8\pi(1-\nu)r^2}\left\{\left((1-2\nu)\delta_{ik}+3r_{,i}r_{,k}\right)\left(r_{,m}n_{,m}\right)-(1-2\nu)\left(r_{,k}n_i-r_{,i}n_k\right)\right\}, \qquad r=|\boldsymbol{\xi}-\mathbf{x}|. \tag{2.24}$$

By virtue of the decomposition of $\hat{T}_i^k(\boldsymbol{\xi},\mathbf{x},t;\mathbf{n})$ as defined by Eqn. (2.22), one may write Eqn. (2.20) as

$$\begin{aligned}&\int_0^t \delta_{ik}u_i(\mathbf{y},\tau)\,g(t-\tau)d\tau+\int_0^t\int_\Gamma[\hat{T}_i^k(\boldsymbol{\xi},\mathbf{y},t-\tau;\mathbf{n})]_1 u_i(\boldsymbol{\xi},\tau)\,d\Gamma_\xi d\tau\\&+\int_0^t\int_\Gamma[\hat{T}_i^k(\boldsymbol{\xi},\mathbf{y},t-\tau;\mathbf{n})]_2 u_i(\boldsymbol{\xi},\tau)\,d\Gamma_\xi d\tau\\&=\int_0^t\int_\Gamma\hat{U}_i^k(\boldsymbol{\xi},\mathbf{x},t-\tau)\,t_i(\boldsymbol{\xi},\tau)\,d\Gamma_\xi d\tau+\int_0^t\int_\Omega\hat{U}_i^k(\boldsymbol{\xi},\mathbf{x},t-\tau)\,f_i(\boldsymbol{\xi},t)\mathrm{d}\Omega_\xi d\tau,\ \ \forall\mathbf{y}\in\Gamma\end{aligned}\quad, \tag{2.25}$$

and express the second term on the left-hand side as

$$\begin{aligned}\int_0^t\int_\Gamma[\hat{T}_i^k(\boldsymbol{\xi},\mathbf{y},t-\tau;\mathbf{n})]_1 u_i(\boldsymbol{\xi},\tau)\,d\Gamma_\xi d\tau&=\int_0^t\int_\Gamma[\hat{T}_i^k(\boldsymbol{\xi},\mathbf{y},t-\tau;\mathbf{n})]_1\left(u_i(\boldsymbol{\xi},\tau)-u_i(\mathbf{y},\tau)\right)d\Gamma_\xi d\tau\\&+\int_0^t\int_\Gamma[\hat{T}_i^k(\boldsymbol{\xi},\mathbf{y},t-\tau;\mathbf{n})]_1)d\Gamma_\xi u_i(\mathbf{y},\tau)\,d\tau\end{aligned}\quad. \tag{2.26}$$

With the aid of the identity that

$$\int_\Gamma[\hat{T}_i^k(\boldsymbol{\xi},\mathbf{y},t-\tau;\mathbf{n})]_1 d\Gamma_\xi \equiv \left\{\begin{matrix}-\delta_{ik} & \text{Int.Problem}\\ 0 & \text{Ext.Problem}\end{matrix}\right\}g(t-\tau), \tag{2.27}$$

according to Eqn. (2.23), Eqn. (2.26) gives

$$\int_0^t\int_\Gamma [\hat{T}_i^k(\boldsymbol{\xi},\mathbf{y},t-\tau;\mathbf{n})]_1 u_i(\boldsymbol{\xi},\tau)\,d\Gamma_\xi d\tau = \int_0^t\int_\Gamma [\hat{T}_i^k(\boldsymbol{\xi},\mathbf{y},t-\tau;\mathbf{n})]_1 \left(u_i(\boldsymbol{\xi},\tau)-u_i(\mathbf{y},\tau)\right) d\Gamma_\xi d\tau$$
$$+\int_0^t u_i(\mathbf{y},\tau)\,g(t-\tau)d\tau \begin{Bmatrix} -\delta_{ik} & \text{Int.Problem} \\ 0 & \text{Ext.Problem} \end{Bmatrix}. \tag{2.28}$$

Making use of the foregoing results, Eqn. (2.25) can be transformed to the compact format of

$$\int_0^t\int_\Gamma \hat{U}_i^k(\boldsymbol{\xi},\mathbf{y},t-\tau)\,t_i(\boldsymbol{\xi},\tau)\,d\Gamma_\xi d\tau + \int_0^t\int_\Omega \hat{U}_i^k(\boldsymbol{\xi},\mathbf{y},t-\tau)\,f_i(\boldsymbol{\xi},t)\mathrm{d}\Omega_\xi d\tau,$$
$$-\int_0^t\int_\Gamma [\hat{T}_i^k(\boldsymbol{\xi},\mathbf{y},t-\tau;\mathbf{n})]_2 u_i(\boldsymbol{\xi},\tau)\,d\Gamma_\xi d\tau - \int_0^t\int_\Gamma [\hat{T}_i^k(\boldsymbol{\xi},\mathbf{y},t-\tau;\mathbf{n})]_1 \left[u_i(\boldsymbol{\xi},\tau)-u_i(\mathbf{y},\tau)\right] d\Gamma_\xi d\tau\,, \tag{2.29}$$
$$=\int_0^t u_k(\mathbf{y},\tau)\,g(t-\tau)d\tau \begin{Bmatrix} 0 & \text{Int.Problem} \\ 1 & \text{Ext.Problem} \end{Bmatrix}, \qquad \forall \mathbf{y}\in\Gamma$$

which is free of Cauchy principal values and the jump term c_{ik}. Amenable to much simpler numerical implementations, the regularized time-domain boundary integral equation in Eqn. (2.29) for three-dimensional elastodynamics provides an equally rigorous mathematical foundation that can facilitate advanced treatments of complicated time-domain singular mixed boundary value problems such as those involving sharp geometries and material discontinuities commonly encountered in engineering mechanics and analysis.

2.6 Numerical implementation

2.6.1 Time and spatial interpolations

Dividing the time interval of interest into M equal segments and discretizing the boundary Γ by a mesh of quadrilateral elements with N nodes, the time and spatial variations of displacements and tractions can be approximated by

$$\mathbf{u}(\boldsymbol{\xi},t) = \sum_{m=1}^{M}\sum_{n=1}^{N}\psi_m(t)\phi_n(\boldsymbol{\xi})\,\mathbf{u}_n^m,$$
$$\mathbf{t}(\boldsymbol{\xi},t) = \sum_{m=1}^{M}\sum_{n=1}^{N}\psi_m(t)\phi_n(\boldsymbol{\xi})\,\mathbf{t}_n^m, \tag{2.30}$$

where $\mathbf{u}_n^m$ and $\mathbf{t}_n^m$ are the displacement and traction components at the n^{th} node at time t^m, $\psi_m(t)$ the time interpolation function for the m^{th} time interval, and $\phi_n(\xi)$ the spatial shape function corresponding to the n^{th} node. Adopting the collocation approach in this treatment, the boundary integral equation is enforced at each nodal location and direction. While techniques such as polar coordinate transformation (Hayami 2005, Liu 1970), h-adaptive and p-adaptive Gaussian integration strategies (Lachat and Watson 1976) can be used to improve the accuracy of elemental quadrature of weakly singular integrals in BEM, the idea of subdividing any element that has one of its nodes as a collocation point into two or more triangular regions, each being considered as the limiting case of a quadrilateral with 2 of its nodes collapsing into the one that coincides with the collocation node (see Figure 2.3 for the case of a bilinear element as an example) is adopted as in Luchi (1987), Pak and Guzina (1999) . Such a degenerate quadrilateral mapping generates a Jacobian that goes to zero at the collocation point, helps to further weaken of any residual singularities and accelerates the convergence of the numerical integration. More details about such improved treatments of linear and quadratic quadrilateral as well as triangular elements can be found in Ashlock (2006).

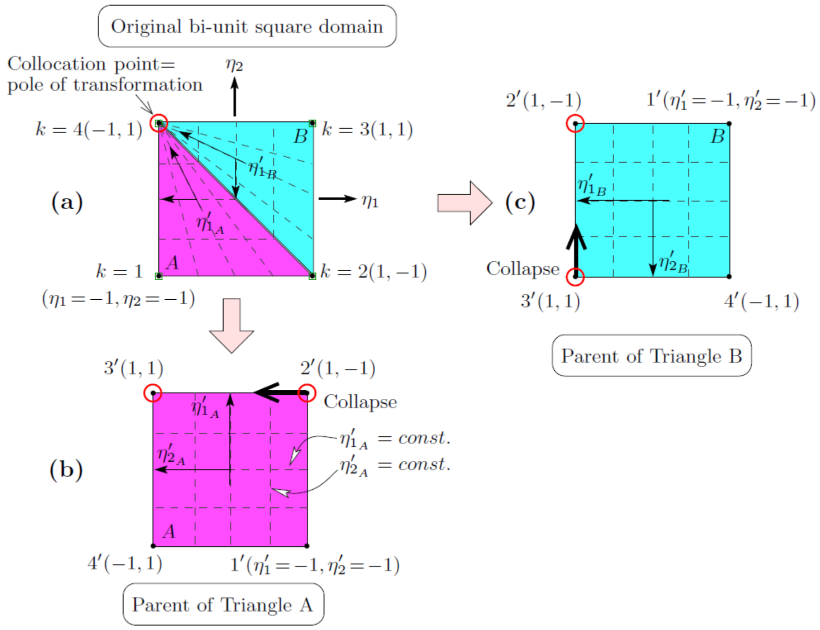

Figure 2.3: Degenerate triangular subdivision and mapping for regularized boundary element integration for a corner node (Ashlock 2006)

Leaving out the forcing term from body-force loading for brevity, the boundary integral equation (2.29) can thus be reduced to the matrix equation

$$\left[\mathbf{H}^{MM}\right]\left\{\mathbf{u}^{M}\right\}=\left[\mathbf{G}^{MM}\right]\left\{\mathbf{t}^{M}\right\}+\sum_{m=0}^{M-1}\left[\mathbf{G}^{Mm}\right]\left\{\mathbf{t}^{m}\right\}-\sum_{m=0}^{M-1}\left[\mathbf{H}^{Mm}\right]\left\{\mathbf{u}^{m}\right\}, M=1,2...,\qquad (2.31)$$

where $\left\{\mathbf{u}^{m}\right\}$ and $\left\{\mathbf{t}^{m}\right\}$ are the assembled global displacement and traction vectors, $[\mathbf{H}^{Mm}]$ and $[\mathbf{G}^{Mm}]$ are $3N\times 3N$ matrices whose component are defined by

$$\begin{aligned}
[H_{AB}^{Mm}] &= \int_{t^{m-1}}^{t^m}\int_{\Gamma}[\hat{T}_i^k(\xi,t^M-\tau;\xi_a^m\,|\,g)]_2\psi_m(\tau)\phi_n(\xi)d\Gamma_{\xi}d\tau \\
&+\int_{t^{m-1}}^{t^m}\int_{\Gamma}[\hat{T}_i^k(\xi,t^M-\tau;\xi_a^m\,|\,g)]_1\psi_m(\tau)\left[\phi_n(\xi)-\delta_{na}\right]d\Gamma_{\xi}d\tau \\
&+\delta_{AB}\left\{\begin{array}{ll} 0 & \text{Int.Problem} \\ 1 & \text{Ext.Problem}\end{array}\right\}\int_{t^{m-1}}^{t^m} g(t-\tau)\psi_m(\tau)d\tau \\
[G_{AB}^{Mm}] &= \int_{t^{m-1}}^{t^m}\int_{\Gamma}\hat{U}_i^k(\xi,t^M-\tau;\xi_a^m\,|\,g)\psi_m(\tau)\phi_n(\xi)d\Gamma_{\xi}d\tau,
\end{aligned}\qquad (2.32)$$

with

$$\begin{aligned}
A&=3(a-1)+k, \quad 1\le a\le N,\ 1\le k\le 3,\ 1\le A\le 3N, \\
B&=3(n-1)+i, \quad 1\le n\le N,\ 1\le i\le 3,\ 1\le B\le 3N.
\end{aligned}\qquad (2.33)$$

2.6.2 Proposed Time marching scheme

Distinguishing the displacement and traction values on the displacement boundary Γ_u and the traction boundary Γ_t respectively, by subscripts "u" and "t", Eqn. (2.31) can be partitioned as

$$\begin{bmatrix}\mathbf{H}_{uu}^{MM} & \mathbf{H}_{ut}^{MM} \\ \mathbf{H}_{tu}^{MM} & \mathbf{H}_{tt}^{MM}\end{bmatrix}\begin{Bmatrix}\mathbf{u}_u^M \\ \mathbf{u}_t^M\end{Bmatrix}=\begin{bmatrix}\mathbf{G}_{uu}^{MM} & \mathbf{G}_{ut}^{MM} \\ \mathbf{G}_{tu}^{MM} & \mathbf{G}_{tt}^{MM}\end{bmatrix}\begin{Bmatrix}\mathbf{t}_u^M \\ \mathbf{t}_t^M\end{Bmatrix}+\sum_{m=0}^{M-1}\left[\mathbf{G}^{Mm}\right]\left\{\mathbf{t}^{m}\right\}-\sum_{m=0}^{M-1}\left[\mathbf{H}^{Mm}\right]\left\{\mathbf{u}^{m}\right\}.\qquad (2.34)$$

For a general mixed boundary value problem, one may rearrange the matrix equation into the form

$$\left\{\mathbf{\Lambda}^{M}\right\}=\left[\tilde{\mathbf{H}}^{MM}\right]\left\{\mathbf{d}^{M}\right\}-\left\{\mathbf{F}^{M}\right\}=\left\{\mathbf{0}\right\},\ M=1,2,... \tag{2.35}$$

where

$$\left[\tilde{\mathbf{H}}^{MM}\right]=\begin{bmatrix}\mathbf{H}_{ut}^{MM} & -\mathbf{G}_{uu}^{MM}\\ \mathbf{H}_{tt}^{MM} & -\mathbf{G}_{tu}^{MM}\end{bmatrix},\qquad \left\{\mathbf{d}^{M}\right\}=\begin{Bmatrix}\mathbf{u}_{t}^{M}\\ \mathbf{t}_{u}^{M}\end{Bmatrix}, \tag{2.36}$$

$$\left\{\mathbf{F}^{M}\right\}=\begin{bmatrix}-\mathbf{H}_{uu}^{MM} & \mathbf{G}_{ut}^{MM}\\ -\mathbf{H}_{tu}^{MM} & \mathbf{G}_{tt}^{MM}\end{bmatrix}\begin{Bmatrix}\mathbf{u}_{u}^{M}\\ \mathbf{t}_{t}^{M}\end{Bmatrix}+\sum_{m=0}^{M-1}\left[\mathbf{G}^{Mm}\right]\left\{\mathbf{t}^{m}\right\}-\sum_{m=0}^{M-1}\left[\mathbf{H}^{Mm}\right]\left\{\mathbf{u}^{m}\right\} \tag{2.37}$$

at each time t^M . To march in time, the elementary single-step approach by means of Eqn. (2.34) for TD-BEM, as noted in many past studies, generally suffers from numerical instability. In what follows, a generalized weighted-collocation scheme for the time marching is thus proposed and implemented. As an extension of Marrero and Dominguez (2003) and Yu et al. (1998), a linear combination of the collocation equations at $t = t^{M-1}, t^M$ and t^{M+1} in the form of

$$\alpha_a\left\{\mathbf{\Lambda}^{M+1}\right\}+\alpha_0\left\{\mathbf{\Lambda}^{M}\right\}+\alpha_b\left\{\mathbf{\Lambda}^{M-1}\right\}=\left\{\mathbf{0}\right\}\ . \tag{2.38}$$

is employed where α_a, α_0, and α_b are three collocation weights that can be chosen to wield a higher level of control of the numerical performance as will be illustrated in the next section. To express $\left\{\mathbf{u}^{M+1}\right\}$ and $\left\{\mathbf{t}^{M+1}\right\}$ in terms of past $\left\{\mathbf{u}^{m}\right\}$ and $\left\{\mathbf{t}^{m}\right\}$, two levels of analytical projection of the temporal variation of $\left\{\mathbf{u}^{m}\right\}$ and $\left\{\mathbf{t}^{m}\right\}$ are also considered in difference form:

(a) First-order projection scheme:

The variation of a function $f(t)$ is taken to be of the first-order. This can be translated to having $\dfrac{\partial^{(2)} f}{\partial t^{(2)}} \approx \dfrac{f^{M-1}-2f^{M}+f^{M+1}}{\Delta t^2}=0$ or

$$\left\{f^{M+1}\right\}=2\left\{f^{M}\right\}-\left\{f^{M-1}\right\}. \tag{2.39}$$

(b) Second-order projection scheme:

The variation is taken to be second-order with respect to time. This is equivalent to having $\frac{\partial^{(3)} f}{\partial t^{(3)}} = 0$ which can be cast as having $\frac{\partial^{(3)} f}{\partial t^{(3)}} \approx \frac{-f^{M-2} + 3f^{M-1} - 3f^{M} + 1f^{M+1}}{\Delta t^{3}}$ =0 or

$$f^{M+1} = f^{M-2} - 3f^{M-1} + 3f^{M} \, . \tag{2.40}$$

The foregoing class of projection relationships for displacement and traction can be compactly expressed in the form of

$$\mathbf{u}^{M+1} = \sum_{j=1}^{\mathcal{O}^{u}+1} \gamma_{j}^{u} \mathbf{u}^{(M+1-j)} \, , \tag{2.41}$$

$$\mathbf{t}^{M+1} = \sum_{j=1}^{\mathcal{O}^{t}+1} \gamma_{j}^{t} \mathbf{t}^{(M+1-j)} \, , \tag{2.42}$$

where the index $\mathcal{O}^{u}$ is the chosen order of projection for the displacement with γ_{j}^{u} being the corresponding coefficients, and $\mathcal{O}^{t}$, γ_{j}^{t} are the corresponding values for the traction. In accordance with Eqns. (2.39) and (2.40), the coefficients for displacement are listed in Table 2.1. It is worth mentioning that $\mathcal{O}^{u}$ and $\mathcal{O}^{t}$ are not necessarily to be equal.

	$\gamma_{1}^{u,t}$	$\gamma_{2}^{u,t}$	$\gamma_{3}^{u,t}$
$\mathcal{O}^{u,t} = 1$	2	-1	0
$\mathcal{O}^{u,t} = 2$	3	-3	1

Table 2.1: Projection coefficients for various order of time variation

By the foregoing definitions, the matrix equations for the time marching can be expressed as

$$
\begin{aligned}
&\left[\alpha_a\gamma_1^u\left[\mathbf{H}^{(M+1)(M+1)}\right]+\alpha_a\left[\mathbf{H}^{(M+1)M}\right]+\alpha_0\left[\mathbf{H}^{MM}\right]\right]\left\{\mathbf{u}^M\right\}\\
&=\left[\alpha_a\gamma_1^t\left[\mathbf{G}^{(M+1)(M+1)}\right]+\alpha_a\left[\mathbf{G}^{(M+1)M}\right]+\alpha_0\left[\mathbf{G}^{MM}\right]\right]\left\{\mathbf{t}^M\right\}\\
&+\alpha_a\left[\mathbf{G}^{(M+1)(M+1)}\right]\sum_{j=2}^{\mathcal{O}^t+1}\gamma_j^t\left\{\mathbf{t}^{M+1-j}\right\}+\sum_{m=0}^{M-1}\left[\alpha_a\left[\mathbf{G}^{(M+1)m}\right]+\alpha_0\left[\mathbf{G}^{Mm}\right]+\alpha_b\left[\mathbf{G}^{(M-1)m}\right]\right]\left\{\mathbf{t}^m\right\}\\
&-\alpha_a\left[\mathbf{H}^{(M+1)(M+1)}\right]\sum_{j=2}^{\mathcal{O}^u+1}\gamma_j^u\left\{\mathbf{u}^{M+1-j}\right\}-\sum_{m=0}^{M-1}\left[\alpha_a\left[\mathbf{H}^{(M+1)m}\right]+\alpha_0\left[\mathbf{H}^{Mm}\right]+\alpha_b\left[\mathbf{H}^{(M-1)m}\right]\right]\left\{\mathbf{u}^m\right\} \qquad (2.43)
\end{aligned}
$$

for the determination of the nodal unknowns at time t^M under arbitrary time-dependent loading. In what follows, $(\alpha_a+\alpha_0+\alpha_b)$ is normalized to be unity with $\alpha_0=1-\alpha_a-\alpha_b$ for clarity. In the next chapter, the numerical performance of the new TD-BEM integration scheme will be explored and illustrated via the benchmark problems.

Chapter 3

3.1 Introduction

To illustrate the boundary element formulation in the previous chapter and its performance characteristics, the basic Stokes dynamic point-load solution with the Heaviside time-function *H(t)* is used as the time-domain Green's function. With its singular part being the corresponding modulated Kelvin's elastostatic state, the resulting time–domain boundary element method is applied to two commonly-used benchmark initial-boundary value problems as illustrations. The first is the 1D wave propagation problem in a square bar, and the second one is a spherical cavity in a full-space under sudden internal pressure.

3.2 1D wave propagation in a prismatic bar

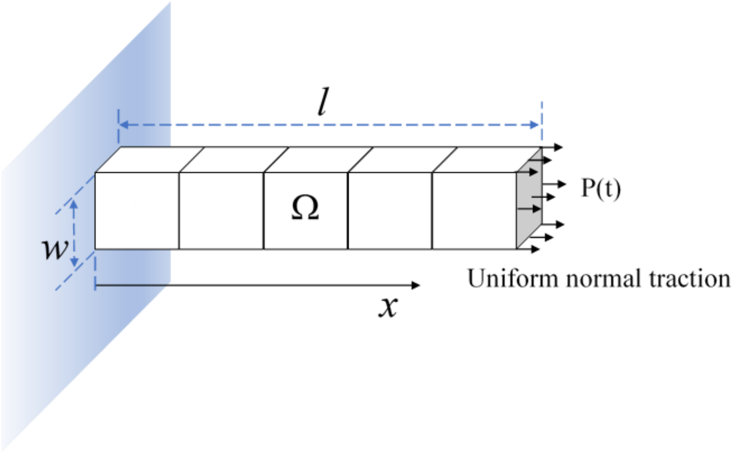

Figure 3.1: A square bar under a step jump in normal end-traction by coarse mesh

Shown in Figure 3.1 is a square, isotropic, linearly elastic bar with zero body-force. It is characterized by a Young's modulus E, a mass density ρ, and Poisson's ratio $\nu = 0$. Its left end is fully fixed at $x = 0$ while a uniform step jump in normal pressure is applied to its right end in the form of

$$P(t) = P_0 H(t). \tag{3.1}$$

Possessing an exact closed-form solution, this 1D wave propagation problem has been used as a benchmark test in many past TD-BEM developments. Using the proposed formulation with several different combinations of displacement and traction projection orders as well as collocation weights, the dynamic solution is computed using the coarse mesh shown in Figure 3.1. The mesh consists of 22 four-node linear surface elements, with double and triple nodes at the edges and corners, respectively to allow for distinct traction vectors at the common location for the adjoining planes (Brebbia et al. 1984, Mitra 1987). Linear time interpolation for the integration is employed for both displacements and tractions. In terms of the dimensionless time-step parameter $\beta = c\,\Delta t / l_e$ where l_e is the minimum dimension of the elements in the direction of wave propagation and c is the relevant wave speed, different time step sizes relative to the time it takes a stress wave to pass through one element were used to examine the performance of the numerical scheme. With $\nu = 0$ in this 1D wave propagation problem, c is equal to $\sqrt{E/\rho}$ which is the bar's longitudinal wave speed.

In the foregoing setting, solutions are computed using 4 different schemes and the resulting time histories of the displacement in the $x-$direction at the loaded end and the normal traction at the fixed end are shown in Figure 3.2 and Figure 3.3, respectively. Unlike the elementary single-step scheme, the 4 time-integration schemes shown in the figures are all stable over many cycles, with computational efficiency. In terms of accuracy, however, one can see from the displays that the scheme with $(\mathcal{O}^u, \mathcal{O}^t) = (2,1)$ and $(\mathcal{O}^u, \mathcal{O}^t) = (2,2)$ gives much better result for the displacement response than the $(\mathcal{O}^u, \mathcal{O}^t) = (1,1)$-scheme for the choice of (α_a, α_b). As to the end-traction solution, one can see from Figure 3.2 and Figure 3.3 that the scheme with $(\mathcal{O}^u, \mathcal{O}^t) = (2,1)$ is the most favorable. Even though all 4 schemes suffer from accuracy because of the coarseness of the mesh and the related causality issue, the scheme with $(\mathcal{O}^u,\mathcal{O}^t;\alpha_a,\alpha_b)=(2,1\,;\,0.2,0.2)$ is the best among them in both displacement and traction aspects. Compared to the scheme of $(\mathcal{O}^u,\mathcal{O}^t;\alpha_a,\alpha_b)=(1,1\,;\,0.25,0.25)$ which corresponds to the algorithm by Marrero & Dominguez (2003), the case of $(\mathcal{O}^u,\mathcal{O}^t;\alpha_a,\alpha_b)=(2,1;0.2,0.2)$ is clearly an improvement.

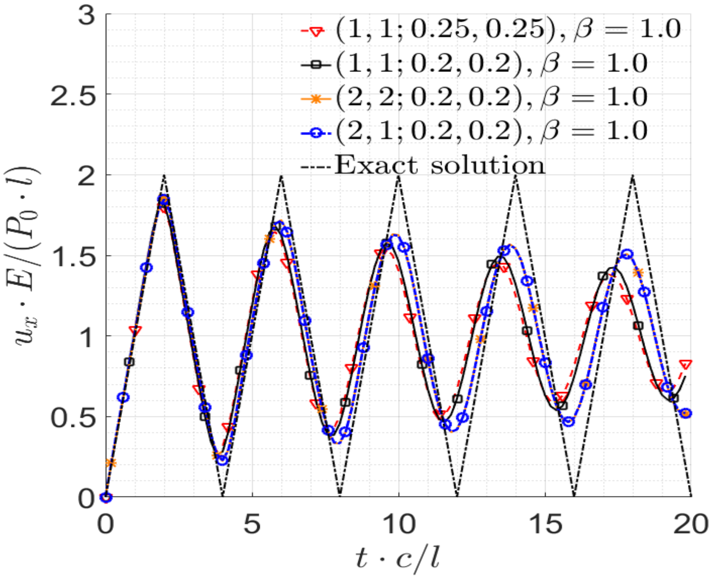

Figure 3.2: Coarse-mesh BEM results for normal displacement time history at loaded end. Row vectors $(\mathcal{O}^u,\mathcal{O}^t;\alpha_a,\alpha_b)$ in the legends labels the parameters for time integration, in which $\mathcal{O}^u$ and $\mathcal{O}^t$ denotes the projection orders for displacement and traction respectively, while α_a and α_b represent the collocation weights.

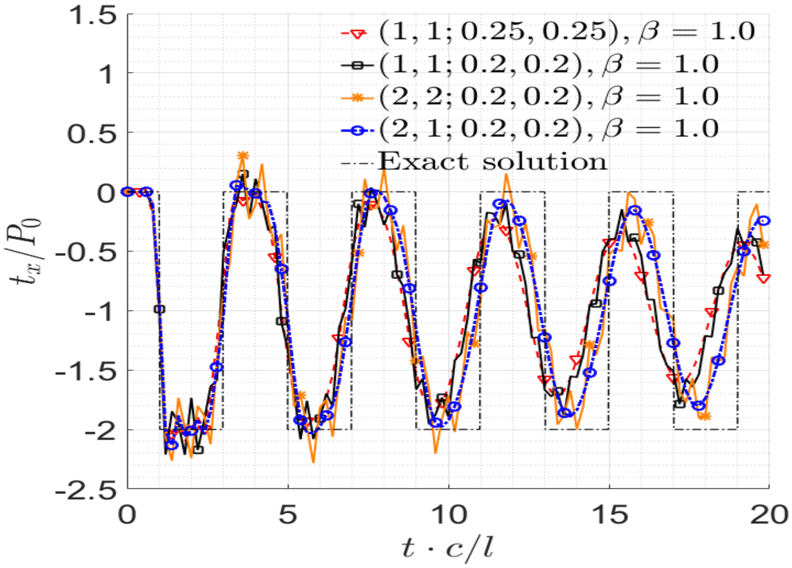

Figure 3.3: Coarse-mesh BEM results for Normal traction time history at fixed end

To confirm the observations, the finer mesh in Figure 3.4 is used for the same bar problem using 3 variations of the generalized schemes. The results are shown in Figure 3.5 and Figure 3.6. Not only do all the 3 schemes remain stable, one can see from the display that they can now deliver much more accurate results relative to the analytical solution except when the exact response has a theoretical discontinuity. As an approximate measure of the solution error, an averaged numerical damping ratio

$$\zeta_{num} = \ln\left(\frac{A(1)}{A(n)}\right) \Big/ 2\pi(n-1), \tag{3.2}$$

over the first n cycles is defined where $A(n)$ is the amplitude of oscillation at n^{th} cycle. Taking $n = 5$ in the determination, one can see from the results in Figure 3.5 with $(\alpha_a, \alpha_b) = (0.2, 0.2)$ that the numerical error in the $(\mathcal{O}^u, \mathcal{O}^t) = (2,1)$ -scheme is less than that of $(\mathcal{O}^u, \mathcal{O}^t) = (1,1)$ -scheme. The same is true for the traction response given by the two schemes, with the former being more accurate and smoother than the latter. Among the 3 choices, the $(\mathcal{O}^u, \mathcal{O}^t; \alpha_a, \alpha_b) = (2,1; 0.2, 0.2)$ case is again the most favorable.

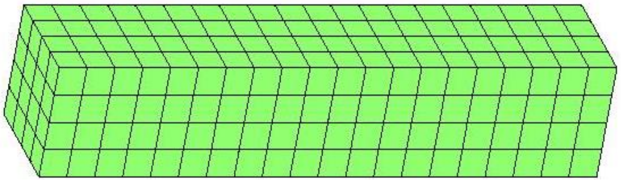

Figure 3.4: A square bar under a step jump in normal end-traction by finer mesh

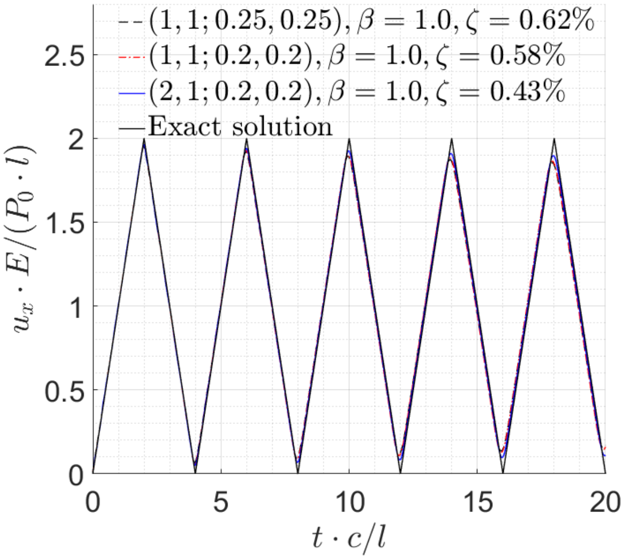

Figure 3.5: Finer-mesh BEM results for normal displacement time history at loaded end of bar. Comparison between $(\mathcal{O}^u,\mathcal{O}^t)=(2,1)$-scheme and $(\mathcal{O}^u,\mathcal{O}^t)=(1,1)$-scheme.

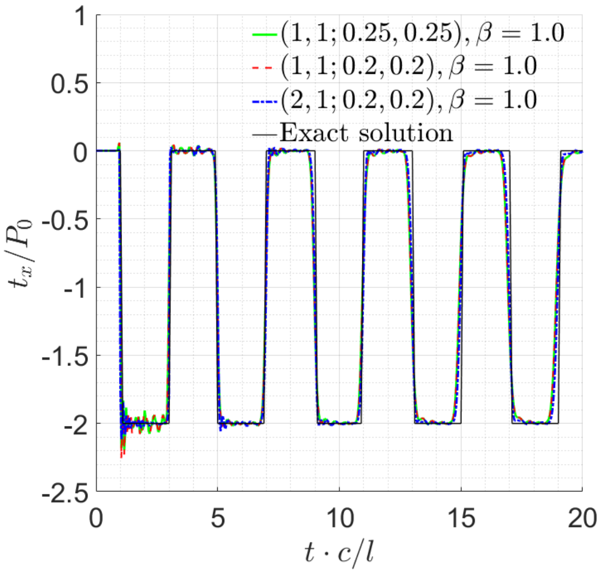

Figure 3.6: Finer-mesh BEM results for normal traction time history at fixed end. Comparison between $(\mathcal{O}^u,\mathcal{O}^t)=(2,1)$-scheme and $(\mathcal{O}^u,\mathcal{O}^t)=(1,1)$-scheme.

To explore more fully the benefits of having variable collocation weights in the formulation, a systematic parametric study is carried out by varying (α_a, α_b) and a summary of the results is given in Table 3.1. One can see from the tabulations that the influence of the collocation weights is significant in both the stability and accuracy of the TD-BEM. Generally, an increasing α_a improves the stability but brings in higher numerical damping, while an increasing α_b reduces the latter. An approximate delineation of the stability region in the parametric space of (α_a, α_b) on the basis of Table 3.1 for the generalized TD-BEM scheme with $(\mathcal{O}^u, \mathcal{O}^t) = (2,1)$ is shown in Figure 3.7.

α_b α_a	0.0	0.1	0.2	0.3	0.4	0.5	0.6	0.7	0.8	0.9
1.0	0.715%	-	-	-	-	-	-	-	-	-
0.9	0.690%	0.690%	-	-	-	-	-	-	-	-
0.8	0.663%	0.663%	0.664%	-	-	-	-	-	-	-
0.7	0.634%	0.635%	0.635%	0.635%	-	-	-	-	-	
0.6	0.605%	0.605%	0.605%	0.604%	0.604%	-	-	-	-	-
0.5	0.574%	0.573%	0.572%	0.571%	0.570%	0.569%	-	-	-	-
0.4	0.540%	0.539%	0.538%	0.537%	0.535%	0.533%	x	-	-	-
0.3	0.442%	0.440%	0.439%	0.437%	0.497%	x	x	x	-	-
0.2	x	0.430%	0.430%	x	x	x	x	x	x	-
0.1	x	x	x	x	x	x	x	x	x	x
0.0	x	x	x	x	x	x	x	x	x	x

Table 3.1: Damping ratio for the displacement Normal displacement time history at loaded end of bar by fine mesh. $(\mathcal{O}^u, \mathcal{O}^t) = (2,1)$ and $\beta = 1.0$. In the table cells, '-' means the combination is not examined, 'x' means the scheme is unstable, and numerical entries are the numerical damping ratios. All schemes are computed with 10,000 steps in the stability assessment.

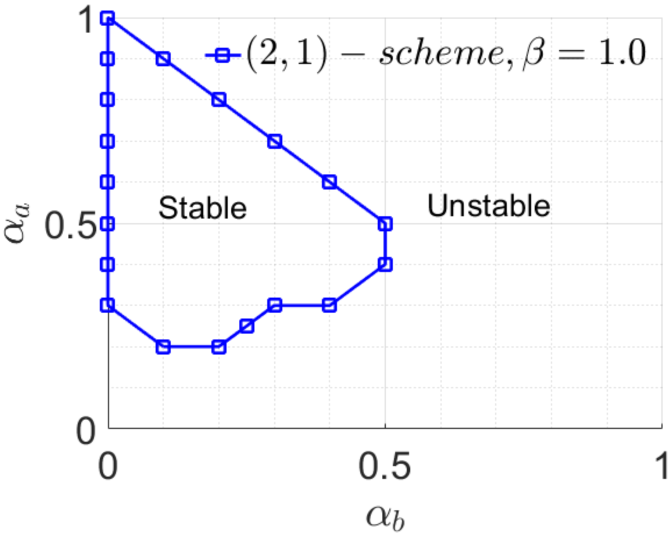

Figure 3.7: Stability zone of the $(\mathcal{O}^u,\mathcal{O}^t)=(2,1)$ -scheme with respect to collocation weights (α_a,α_b)

To explore the influence of time step on the method, Figure 3.8 is a plot of the time histories of the displacement at the loaded end that are computed with four different time step sizes, including $\beta=1.2$, $\beta=1.0$, $\beta=0.8$ and $\beta=0.5$ for the (2,1; 0.4, 0.2) scheme. The comparison shows that the use of a smaller time step size, e.g., with $\beta=0.5$, can give more accurate result despite possibly incurring more causality error. The result for the end-traction in Figure 3.9 shows the same trend.

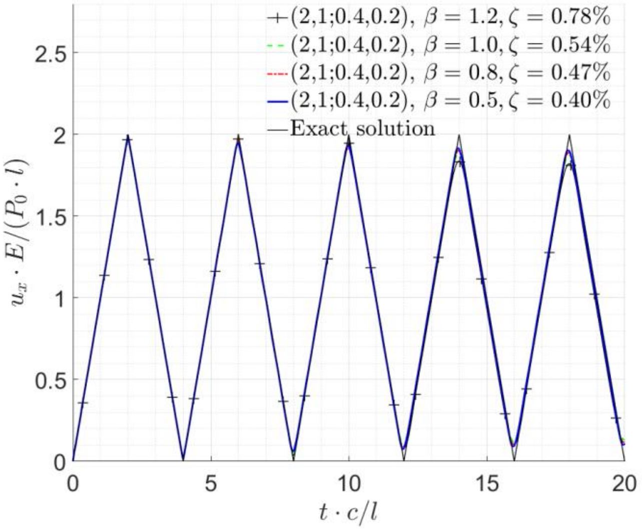

Figure 3.8: Normal displacement time history at loaded end of bar-comparison of different time step sizes.

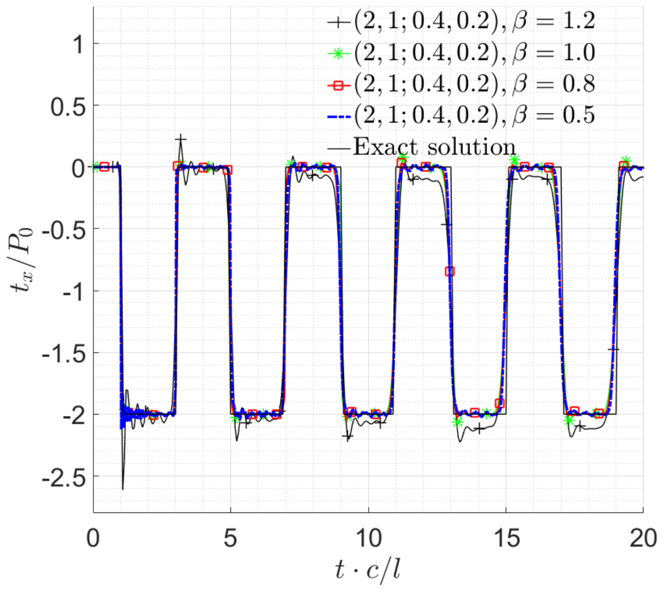

Figure 3.9: Normal traction time history at fixed end of bar-comparison of different time step sizes.

As demonstrated earlier, the collocation weights have significant effect on the stability of the time-marching scheme. To further the insights, the stability regions for both $(\mathcal{O}_u,\mathcal{O}_t)=(2,1)$ and $(\mathcal{O}_u,\mathcal{O}_t)=(1,1)$ schemes in the parametric (α_a,α_b) space are presented in Figure 3.10(a) and (b), respectively as a function of the time-step size. From the displays, one can see that smaller time step size generally reduces the stability zone in the α_a-α_b space, an observation that can be anticipated.

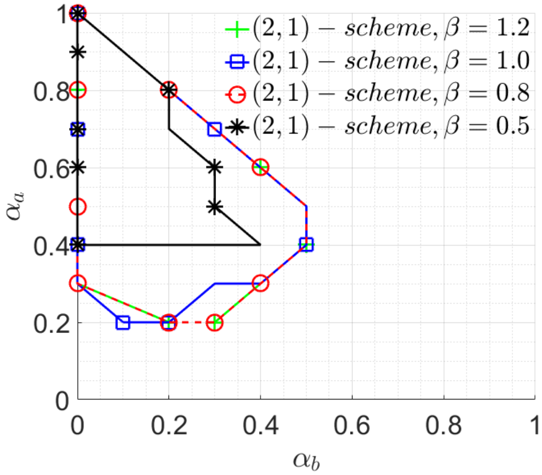

(a) $(\mathcal{O}_u,\mathcal{O}_t)=(2,1)$

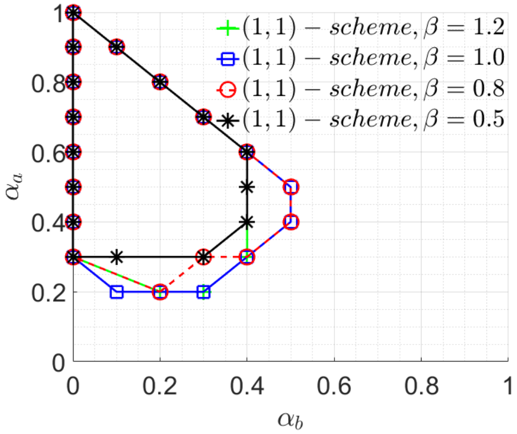

(b) $(\mathcal{O}_u,\mathcal{O}_t)=(1,1)$

Figure 3.10: Stability zones for generalized time-collocation BEM scheme for different time step sizes.

3.3 Sudden pressure in a spherical cavity in a full-space

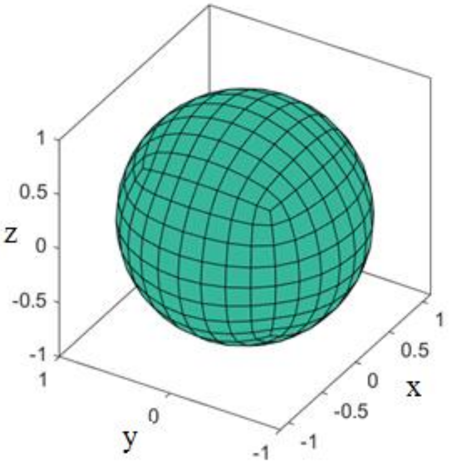

Figure 3.11: Boundary element surface mesh for a spherical cavity in full space

To explore the influence of temporal and spatial interpolation on the TD-BEM formulation in another class of problems, the case of a spherical cavity embedded in a homogeneous isotropic linearly elastic 3-D full-space with a Poisson's ratio $\nu = 0.2$ that is subjected to a step jump in internal pressure as described by Eqn. (3.1) is also considered. Using the mesh shown in Figure 3.11, results computed by the proposed multi-step collocation TD-BEM scheme with different orders of variable projections are shown in Figure 3.12. As can be seen from the illustration, they all show excellent agreement with the analytical solution, with the $(\mathcal{O}^u, \mathcal{O}^t) = (2,1)$-scheme also being the best. To investigate the effect of the time step size on the TD-BEM solution on the problem, the spherical cavity solution is computed with time step sizes of β $=1.0$, 0.8 and 0.5. As illustrated in Figure 3.13, the solutions generated with the 3 time step sizes are found to be all very good and stable, with mean absolute errors relative to the exact solution being 1.20% , 1.18% and 0.59% for β $=1.0$, 0.8 and 0.5, respectively over the time span.

In the numerical examples shown in this section, the computer time it takes using the proposed method are of the order of 10% to 20% more than that from using the elementary single-point collocation method, i.e., it does not incur a significant increase in computing effort to achieve more control of the stability and accuracy by virtue of the generalized collocation and projection TD-BEM scheme.

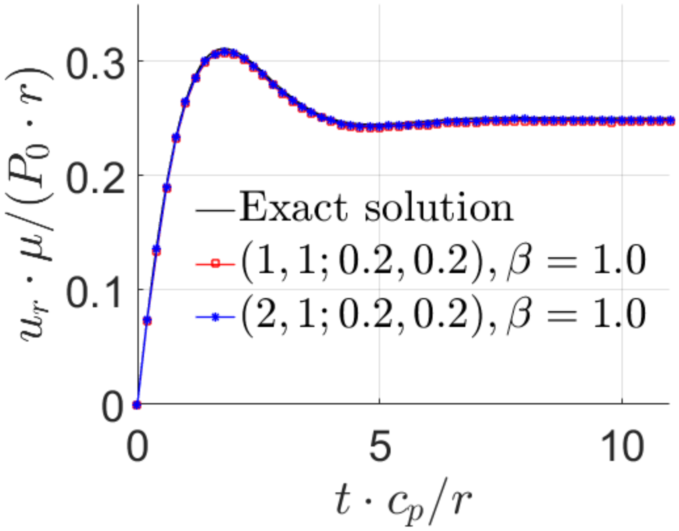

Figure 3.12: Comparison of TD-BEM results for surficial radial displacement of cavity using different orders of variable projection.

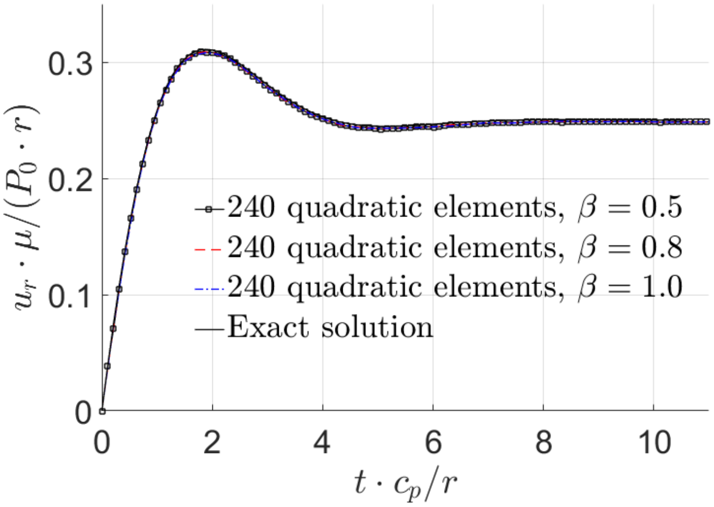

Figure 3.13: Performance of TD-BEM scheme in spherical cavity problem by different time step size with $(\mathcal{O}^u, \mathcal{O}^t) = (2,1)$ and $(\alpha_a, \alpha_b) = (0.2, 0.2)$.

3.4 Summary

In the last chapter, a regularized time-domain boundary integral equation format is presented for three-dimensional elastodynamics. By virtue of a decomposition of the Green's functions into singular and regular parts, all integrals in the proposed boundary element formulation are weakly singular and amenable to standard numerical treatment. Aimed to provide extra control of both the stability and accuracy aspects, the formulation is implemented numerically via a generalized collocation scheme with higher-order projections in a step-by-step time marching scheme. Its performance is illustrated in this chapter via the benchmark tests of a finite 1D-bar and a spherical cavity wave-propagation problem. With its adaptability and efficiency, the proposed TD-BEM scheme is apt to be helpful to a variety of elastodynamic problems.

As shown in some of the numerical examples, numerical instability of the TD-BEM can indeed happen, as has been reported in the literature. In the early stage of the present study, the stability zone in the space of (α_a, α_b) was evaluated by means of long-time simulations, as in most past TD-BEM studies. Recognizing that numerical stability cannot be demonstrated rigorously by mere long-time simulations because a process that looks stable up to a long time may still collapse later, a formal analytical framework for the stability evaluation of TD-BEM schemes is deemed necessary for a solid advance of TD-BEMs. Such a development is the subject of the next chapter.

Chapter 4

Stability Evaluation of Direct Time-Domain Boundary Element Methods for Elastodynamics

4.1 Introduction

In direct time-domain boundary element methods, one of the perennial challenges is their stability in the step-by-step time marching process. The notice of possible instability in a TD-BEM scheme dates back to Cole et al. (1978). It was then found by many that the use of small time steps is prone to more of the problem (Dominguez and Gallego 1991). The fact that instability can manifest itself in the form of early divergence, intermittent instabilities and eventual divergence, and that both too small or too large a time step size can both be the trigger has been noted e.g., see (Frangi and Novati 1999, Pak and Bai 2018, Peirce and Siebrits 1997). Aimed to mitigate the problem, a number of TD-BEM schemes have been proposed. Examples are the half-step and ϵ-methods (Peirce and Siebrits 1997), the linear-θ method (Araujo et al. 1999, Yu et al. 1998), the time-weighting method (Marrero and Dominguez 2003, Soares and Mansur 2007, Yazdi et al. 2011, Yu et al. 1998, Yu et al. 2000), and the method of convolution quadrature (CQ) using Laplace transformed Green's functions (Banjai et al. 2012, Schanz and Antes 1997). As a means to reduce causality errors in modeling wave passage problems, Frangi (2000) proposed a set of causal shape functions for 2-D elasticity problems and tested them in some examples. Panagiotopoulos and Manolis (2011) suggested a TD-BEM formulation that employed velocity and traction as the unknowns to improve the solution performance. The promise of Ha-Duong and Terrasse (2003)'s idea of a space–time Galerkin procedure on the basis of a weak or variational form of the boundary integral equation for acoustics was illustrated in the extension by Aimi (2012) and Aimi et al. (2011) to 3-D elastodynamic problems. While their approach requires another level of integration, it offers a rigorous approximation framework upon which unconditionally stable time integration schemes can be constructed at least theoretically. In the computational implementation of most numerical methods including TD-BEMs, however, different types of approximation errors arising from discretization, as from the choice of mesh, spatial and temporal interpolations, accuracy in elemental integration and the Green's functions, can all affect the actual performance of a scheme. To evaluate the stability of an implemented TD-BEM algorithm, drawing conclusions on the basis of only computed solutions for a finite number of steps that is deemed sufficiently large is a common practice. While expedient, such an empirical approach unfortunately runs a great risk of misjudgment, as a scheme that looks stable over N steps, no matter how large N is, may still eventually become unstable at $N+k$ steps or upon the imposition of an alternative excitation setup or trigger conditions. To date, the most analytical approach to address BEM's stability question for an implemented scheme is perhaps the work of Peirce and Siebrits (1997). Utilizing the method of amplification polynomial (Strikwerda 2004), they employed a discrete z-transform to the time-marching algorithm to develop an approximate characteristic equation whose roots were used as direct indicators of the numerical stability of their half-step and ϵ- TD-BEM schemes.

In this paper, a rigorous analytical framework for the stability evaluation of TD-BEM time integration schemes is proposed. Congruent with the concept of amplification matrix (Gustafsson et al. 1972, Ngo and Erickson 1997), it is shown that direct TD-BEM time-marching algorithms can, with appropriate re-casting, generally be framed as equivalent linear multi-step or higher-order difference schemes similar to those for the numerical solution of initial value problems for a system of differential equations (Richtmyer and Morton 1994, Strikwerda 2004). Should the proposed transformation be accomplished, the stability analysis of a TD-BEM can be formally reduced to the determination of the spectral radius of a hybrid system matrix. As a demonstration, the method is applied to the evaluation of the characteristics of a family of regularized TD-BEMs with variable collocation weights and higher-order projection schemes that includes some past proposals as degenerate cases. Numerical results are included for the canonical finite-domain square-bar and the cavity-in-an-infinite-domain initial boundary value problems as illustrations.

4.2 BEM Formulation for Stability Analysis

Adopting an elastodynamic point-load Green's function in an unbounded full-space or half-space and its associated displacement and traction fields $\hat{U}_i^k$ and $\hat{T}_i^k$ as one of the 2 elastodynamic states in Graffi's reciprocal theorem (Wheeler and Sternberg 1968), a fundamental boundary integral representation of the response at a point $\mathbf{x}$ in an open three-dimensional solid domain $\Omega(\mathbf{x})$ that is bounded by the surface $\Gamma(\mathbf{x})$ with a quiescent past and body force field f_{i} can be stated as

$$\begin{aligned}&\int_0^t \delta_{ik} u_i(\mathbf{x},\tau) g(t-\tau)\, d\tau + \int_0^t \int_\Gamma \hat{T}_i^k(\boldsymbol{\xi},\mathbf{x},\mathbf{n},t-\tau \,|\, g) u_i(\boldsymbol{\xi},\tau)\, d\Gamma_\xi\, d\tau \\ &= \int_0^t \int_\Gamma \hat{U}_i^k(\boldsymbol{\xi},\mathbf{x},t-\tau \,|\, g) t_i(\boldsymbol{\xi},\tau)\, d\Gamma_\xi\, d\tau + \int_0^t \int_\Omega \hat{U}_i^k(\boldsymbol{\xi},\mathbf{x},t-\tau \,|\, g)\, f_i(\boldsymbol{\xi},t) \mathrm{d}\Omega_{\boldsymbol{\xi}}\, d\tau, \forall \mathbf{x} \in \Omega,\ t>0\end{aligned} \tag{4.1}$$

in rectangular coordinates and indicial notation for both interior and exterior problems, where $u_i(\mathbf{x},t)$ and $t_i(\boldsymbol{\xi},t)$ are the displacement and traction fields subject to displacement boundary conditions on Γ_u and traction boundary conditions on Γ_t, and $g(t)$ the arbitrary time-dependent magnitude of the point load at $\boldsymbol{\xi}$ acting in the k^{th}-direction. Equivalent to an extension of the regularization approach in Pak and Guzina (1999) to the time domain, it is useful to decompose $\hat{T}_i^k$ into a singular and regular part in the form of

$$\hat{T}_i^k(\boldsymbol{\xi},\mathbf{x},\mathbf{n},t) \equiv \left[\hat{T}_i^k(\boldsymbol{\xi},\mathbf{x},\mathbf{n},t)\right]_1 + \left[\hat{T}_i^k(\boldsymbol{\xi},\mathbf{x},\mathbf{n},t)\right]_2 \tag{4.2}$$

where

$$\begin{aligned}\left[\hat{T}_i^k(\boldsymbol{\xi},\mathbf{x},\mathbf{n},t)\right]_1 &= g(t) \cdot \bar{T}_i^k(\boldsymbol{\xi},\mathbf{x},\mathbf{n}) \\ \left[\hat{T}_i^k(\boldsymbol{\xi},\mathbf{x},\mathbf{n},t)\right]_2 &= \hat{T}_i^k(\boldsymbol{\xi},\mathbf{x},\mathbf{n},t) - \left[\hat{T}_i^k(\boldsymbol{\xi},\mathbf{x},\mathbf{n},t)\right]_1\end{aligned} \tag{4.3}$$

with $\bar{T}_i^k(\boldsymbol{\xi},\mathbf{x},\mathbf{n})$ being the appropriate static traction Green's function. With the identities that

$$\int_{\Gamma}[\hat{T}_i^k(\xi,\mathbf{y},t-\tau;\mathbf{n})]_1 \, d\Gamma_{\xi} \equiv \left\{\begin{matrix} -\delta_{ik} & \text{Interior problem} \\ 0 & \text{Exterior problem} \end{matrix}\right\} g(t-\tau) \tag{4.4}$$

and

$$\begin{aligned} & \int_0^t \int_{\Gamma} [\hat{T}_i^k(\xi,\mathbf{y},t-\tau;\mathbf{n})]_1 u_i(\xi,\tau) \, d\Gamma_{\xi} d\tau \\ & = \int_0^t \int_{\Gamma} [\hat{T}_i^k(\xi,\mathbf{y},t-\tau;\mathbf{n})]_1 \big(u_i(\xi,\tau)-u_i(\mathbf{y},\tau)\big) \, d\Gamma_{\xi} d\tau \ , \\ & + \int_0^t u_i(\mathbf{y},\tau) g(t-\tau) d\tau \left\{\begin{matrix} -\delta_{ik} & \text{Interior problem} \\ 0 & \text{Exterior problem} \end{matrix}\right\} \end{aligned} \tag{4.5}$$

one may obtain in the limit of $\mathbf{x} \rightarrow \mathbf{y} \in \Gamma$ from Eqn. (4.1) the fundamental boundary integral equation for three-dimensional elastodynamics in the regularized form of

$$\begin{aligned} & \int_0^t \int_{\Gamma} \hat{U}_i^k(\xi,\mathbf{y},t-\tau \,|\, g) t_i(\xi,\tau) \, d\Gamma_{\xi} d\tau - \int_0^t \int_{\Gamma} \Big[\hat{T}_i^k(\xi,\mathbf{y},\mathbf{n},t-\tau \,|\, g)\Big]_2 u_i(\xi,\tau) \, d\Gamma_{\xi} d\tau \\ & - \int_0^t \int_{\Gamma} \Big[\hat{T}_i^k(\xi,\mathbf{y},\mathbf{n},t-\tau \,|\, g)\Big]_1 \big[u_i(\xi,\tau)-u_i(\mathbf{y},\tau)\big] d\Gamma_{\xi} d\tau \\ & = \int_0^t \int_{\Omega} \hat{U}_i^k(\xi,\mathbf{y},t-\tau \,|\, g) f_i(\xi,t) \mathrm{d}\Omega_{\xi} d\tau + \int_0^t \left\{\begin{matrix} 0 & \text{Interior problem} \\ 1 & \text{Exterior problem} \end{matrix}\right\} u_k(\mathbf{y},\tau) g(t-\tau) d\tau, \ \forall \mathbf{y} \in \Gamma \end{aligned} \tag{4.6}$$

as an alternative framework for rigorous numerical developments. For the present development, it is useful to recognize that the function $g(t)$ in commonly adopted full-space or half-space time-domain Green's functions is generally set to be constant, if not zero, beyond a certain time, an example being the Heaviside function *H(t)*. As such, the Green's functions will have the properties that

$$g(t) = \bar{g}, \ \ \hat{U}_i^k(\xi,\mathbf{x},t \,|\, g) = \bar{g} \cdot \bar{U}_i^k(\xi,\mathbf{x}), \ \ \hat{T}_i^k(\xi,\mathbf{x},\mathbf{n},t \,|\, g) = \bar{g} \cdot \bar{T}_i^k(\xi,\mathbf{x},\mathbf{n}), \tag{4.7}$$

between any two points $\mathbf{x}$ and ξ within Ω for $t > T_f$, T_f being the maximum non-steady response period, $\bar{g}$ a constant, and $\bar{U}_i^k(\xi,\mathbf{x})$ and $\bar{T}_i^k(\xi,\mathbf{x},\mathbf{n})$ the corresponding eventual time-independent or static Green's functions, respectively. In the case of using Stokes' full-space solution with a Heaviside load time history for an isotropic linearly elastic full-space characterized by a shear modulus, Poisson's ratio and density as μ, ν and ρ , respectively, one finds that

$$\bar{g}=1,\ \ \bar{T}_i^k(\boldsymbol{\xi},\mathbf{x},\mathbf{n})=\hat{\hat{T}}_i^k\left(\boldsymbol{\xi},\mathbf{x},\mathbf{n}\right),\ \bar{U}_i^k(\boldsymbol{\xi},\mathbf{x})=\hat{\hat{U}}_i^k\left(\boldsymbol{\xi},\mathbf{x}\right),\ \ T_f=\frac{\left|\boldsymbol{\xi}-\mathbf{x}\right|_{max}}{c_2}\ , \tag{4.8}$$

where $\left|\boldsymbol{\xi}-\mathbf{x}\right|_{max}$ denotes the maximum distance between any 2 points for $\mathbf{x},\boldsymbol{\xi}\in\Omega\bigcup\Gamma$, c_2 stands for the shear wave speed of $\sqrt{\mu/\rho}$, $\hat{\hat{U}}_i^k\left(\boldsymbol{\xi},\mathbf{x}\right)$ and $\hat{\hat{T}}_i^k\left(\boldsymbol{\xi},\mathbf{x},\mathbf{n}\right)$ are Kelvin's unit point-load displacement and traction fields, respectively. By virtue of the analytical characteristics of the Green's functions in (4.7), the time interval of the convolution integrals in Eqn. (4.6) can be meaningfully divided into two at T_f , leading to

$$\begin{aligned}
&\int_{t-T_f}^{t}\int_{\Gamma}\hat{U}_i^k(\boldsymbol{\xi},\mathbf{y},t-\tau\,|\,g)t_i\left(\boldsymbol{\xi},\tau\right)d\Gamma_{\xi}d\tau+\bar{g}\int_0^{t-T_f}\int_{\Gamma}\bar{U}_i^k\left(\boldsymbol{\xi},\mathbf{x}\right)t_i\left(\boldsymbol{\xi},\tau\right)d\Gamma_{\xi}d\tau\\
&-\int_{t-T_f}^{t}\int_{\Gamma}\left[\hat{T}_i^k\left(\boldsymbol{\xi},\mathbf{y},\mathbf{n},t-\tau\,|\,g\right)\right]_1\left[u_i\left(\boldsymbol{\xi},\tau\right)-u_i\left(\mathbf{y},\tau\right)\right]d\Gamma_{\xi}d\tau\\
&-\bar{g}\int_0^{t-T_f}\int_{\Gamma}\bar{T}_i^k\left(\boldsymbol{\xi},\mathbf{x},\mathbf{n}\right)\left[u_i\left(\boldsymbol{\xi},\tau\right)-u_i\left(\mathbf{y},\tau\right)\right]d\Gamma_{\xi}d\tau-\int_{t-T_f}^{t}\int_{\Gamma}\left[\hat{T}_i^k(\boldsymbol{\xi},\mathbf{y},\mathbf{n},t-\tau\,|\,g)\right]_2u_i\left(\boldsymbol{\xi},\tau\right)d\Gamma_{\xi}d\tau\\
&=\int_{t-T_f}^{t}\int_{\Omega}\hat{U}_i^k(\boldsymbol{\xi},\mathbf{y},t-\tau\,|\,g)\,f_i(\boldsymbol{\xi},t)\mathrm{d}\Omega_{\boldsymbol{\xi}}d\tau+\bar{g}\int_0^{t-T_f}\int_{\Omega}\bar{U}_i^k\left(\boldsymbol{\xi},\mathbf{x}\right)\,f_i(\boldsymbol{\xi},t)\mathrm{d}\Omega_{\boldsymbol{\xi}}d\tau\\
&+\int_{t-T_f}^{t}\left\{\begin{matrix}0 & \text{Int.Problem}\\ 1 & \text{Ext.Problem}\end{matrix}\right\}u_k\left(\mathbf{y},\tau\right)g(t-\tau)d\tau\\
&+\bar{g}\int_0^{t-T_f}\left\{\begin{matrix}0 & \text{Int.Problem}\\ 1 & \text{Ext.Problem}\end{matrix}\right\}u_k\left(\mathbf{y},\tau\right)d\tau,\ \ \forall\mathbf{y}\in\Gamma,\ \ \forall t>T_f
\end{aligned} \tag{4.9}$$

For a rigorous stability analysis, it is useful to consider the difference of Eqn. (4.9) at time $t+T_0$ and t for any $T_0>0$. By a change of variables and some analytical reductions, it can be shown that

$$\begin{aligned}
&\int_{t-\hat{T}_f}^{t}\int_{\Gamma}\hat{U}_i^k(\boldsymbol{\xi},\mathbf{y},t-\tau\,|\,g_0)t_i\left(\boldsymbol{\xi},\tau\right)d\Gamma_{\xi}d\tau-\int_{t-\hat{T}_f}^{t}\int_{\Gamma}\left[\hat{T}_i^k(\boldsymbol{\xi},\mathbf{y},\mathbf{n},t-\tau\,|\,g_0)\right]_2u_i\left(\boldsymbol{\xi},\tau\right)d\Gamma_{\xi}d\tau\\
&-\int_{t-\hat{T}_f}^{t}\int_{\Gamma}\left[\hat{T}_i^k\left(\boldsymbol{\xi},\mathbf{y},\mathbf{n},t-\tau\,|\,g_0\right)\right]_1\left[u_i\left(\boldsymbol{\xi},\tau\right)-u_i\left(\mathbf{y},\tau\right)\right]d\Gamma_{\xi}d\tau\\
&=\int_{t-\hat{T}_f}^{t}\int_{\Omega}\hat{U}_i^k(\boldsymbol{\xi},\mathbf{y},t-\tau\,|\,g_0)\,f_i(\boldsymbol{\xi},t)\mathrm{d}\Omega_{\boldsymbol{\xi}}d\tau\\
&+\int_{t-\hat{T}_f}^{t}\left\{\begin{matrix}0 & \text{Int.Problem}\\ 1 & \text{Ext.Problem}\end{matrix}\right\}u_k\left(\mathbf{y},\tau\right)g_0(t-\tau)d\tau,\ \ \forall\mathbf{y}\in\Gamma,\ \ \forall t>\hat{T}_f=T_f+T_0
\end{aligned} \tag{4.10}$$

where

$$g_o(t)=\begin{cases} g(t), & for\, t\le T_o \\ g(t)-g(t-T_o), & for\, t>T_o \end{cases}$$
$$\hat{U}_i^k(\xi,\mathbf{y},t\,|\,g_o)=\begin{cases} \hat{U}_i^k(\xi,\mathbf{y},t\,|\,g), & t\le T_o \\ \hat{U}_i^k(\xi,\mathbf{y},t\,|\,g)-\hat{U}_i^k(\xi,\mathbf{y},t-T_o\,|\,g), & t>T_o \end{cases}, \qquad (4.11)$$
$$\hat{T}_i^k(\xi,\mathbf{y},\mathbf{n},t\,|\,g_o)=\begin{cases} \hat{T}_i^k(\xi,\mathbf{y},\mathbf{n},t\,|\,g), & t\le T_o \\ \hat{T}_i^k(\xi,\mathbf{y},\mathbf{n},t\,|\,g)-\hat{T}_i^k(\xi,\mathbf{y},\mathbf{n},t-T_o\,|\,g), & t>T_o \end{cases}$$

Notice that $g_o(t)$ in Eqn. (4.11), defined in terms of $g(t)$ that possesses the properties in (4.7), is identically zero after a finite duration $T_d \ge T_o$. Accordingly, $\hat{U}_i^k(\xi,\mathbf{y},t\,|\,g_o)$ and $\hat{T}_i^k(\xi,\mathbf{y},t\,|\,g_o)$ are effectively the time-domain displacement and traction Green's functions that correspond to a concentrated force pulse of finite duration, with $\hat{T}_f$ being the effective non-steady response period of the finite-pulse Green's functions. For its simplicity in illustrating the ensuing analytical and computational development, Stokes's solution with a Heaviside time function $g(t)=H(t)$ will be employed, with

$$g_0(t)=H(t)-H(t-T_0)\ ,\ T_d=T_0, \qquad (4.12)$$

being the forcing function of a square-pulse full-space point-load Green's function as in (Coda, H. B.; Venturini, W. S., 1995), with the analytical features of

$$T_f=T_0+|\xi-\mathbf{x}|_{max}/c_2\ ,\ \ \bar{T}_i^k(\xi,\mathbf{x},\mathbf{n})=0,\quad \bar{U}_i^k(\xi,\mathbf{x})=0,\quad \forall t>T_f\ . \qquad (4.13)$$

4.3 Square-Pulse Green's function by Stokes' Elastodynamic Solution

For a square-pulse point-load Green's function in a full-space with $g_0(t)=H(t)-H(t-T_0)$, the requisite displacement and traction Green's functions can be composed analytically from Stokes' general solution (Wheeler and Sternberg 1968) with $g(t)=H(t)$, for which the closed form results are

$$
\begin{aligned}
4\pi\rho \hat{U}_i^k(\boldsymbol{\xi},\mathbf{x},t\,|\,H) &= \left[\frac{3r_i r_k}{r^3}-\frac{\delta_{ik}}{r}\right]A_1(t)+\frac{r_i r_k}{r^3}\left[\frac{1}{c_1^2}A_2(t)\text{-}\frac{1}{c_2^2}A_3(t)\right]+\frac{\delta_{ik}}{rc_2^2}A_3(t),\\
4\pi\rho \hat{T}_i^k(\boldsymbol{\xi},\mathbf{x},\mathbf{n},t\,|\,H) &= -6c_2^2\left[\frac{5r_i r_j \mathbf{r}\cdot\mathbf{n}}{r^5}-\frac{n_i r_k+\delta_{ik}\mathbf{r}\cdot\mathbf{n}+n_k r_i}{r^3}\right]A_1(t)\\
&\quad +2\left[\frac{6r_i r_k \mathbf{r}\cdot\mathbf{n}}{r^5}-\frac{n_i r_k+\delta_{ik}\mathbf{r}\cdot\mathbf{n}+n_k r_i}{r^3}\right]\left[A_3(t)-\left(\frac{c_2}{c_1}\right)^2A_2(t)\right]\\
&\quad +\frac{2r_i r_k \mathbf{r}\cdot\mathbf{n}}{r^4 c_2}\left[A_5(t)-\left(\frac{c_2}{c_1}\right)^3A_4(t)\right]-\frac{n_i r_k}{r^3}\left[1-2\left(\frac{c_2}{c_1}\right)^2\right]\left[A_2(t)+\frac{r}{c_1}A_4(t)\right]\\
&\quad -\frac{\delta_{ik}\mathbf{r}\cdot\mathbf{n}+n_k r_i}{r^3}\left[A_4(t)+\frac{r}{c_2}A_5(t)\right],
\end{aligned}
\tag{4.14}
$$

where $r=|\mathbf{x}-\boldsymbol{\xi}|$ is the distance between the load point $\mathbf{x}$ and the field point $\boldsymbol{\xi}$, $\mathbf{n}$ is the outward normal of the surface, $c_1=\sqrt{\dfrac{2(1-\nu)\mu}{(1-2\nu)\rho}}$ and $c_2=\sqrt{\dfrac{\mu}{\rho}}$ are the primary and secondary wave speed, and

$$
\begin{aligned}
A_1(t) &= \left(\frac{t^2}{r^2}-\frac{1}{c_1^2}\right)H(t-r/c_1)-\left(\frac{t^2}{r^2}-\frac{1}{c_2^2}\right)H(t-r/c_2)\\
&\quad -\left(\frac{(t-T_d)^2}{r^2}-\frac{1}{c_1^2}\right)H(t-T_d-r/c_1)+\left(\frac{(t-T_d)^2}{r^2}-\frac{1}{c_2^2}\right)H(t-T_d-r/c_2)\\
A_2(t) &= H(t)-H(t-r/c_1)\\
A_3(t) &= H(t)-H(t-r/c_2)\\
A_4(t) &= \delta(t)-\delta(t-r/c_1)\\
A_5(t) &= \delta(t)-\delta(t-r/c_2)
\end{aligned}
\quad . \tag{4.15}
$$

It is evident from Eqn. (4.14) and (4.15) that

$$
\hat{U}_i^k(\boldsymbol{\xi},\mathbf{x},t\,|\,g_0)=0,\ \hat{T}_i^k(\boldsymbol{\xi},\mathbf{x},\mathbf{n},t\,|\,g_0)=0,\ \forall t>T_o+r/c_2 \tag{4.16}
$$

as noted earlier.

4.4 Discretization and Matrix System

To implement a TD-BEM scheme, the first step is a discretization of the time-domain boundary integral equation. Following the normal procedure in this study, the time interval is divided into M equal segments, and the boundary Γ of Ω by a mesh of quadrilateral elements with N nodes, while the time and spatial variations of displacements and tractions are interpolated by

$$\begin{aligned} \mathbf{u}(\xi,t) &= \sum_{m=1}^{M}\sum_{n=1}^{N}\psi_m(t)\phi_n(\xi)\mathbf{u}_n^m, \\ \mathbf{t}(\xi,t) &= \sum_{m=1}^{M}\sum_{n=1}^{N}\theta_m(t)\phi_n(\xi)\mathbf{t}_n^m, \end{aligned} \tag{4.17}$$

where $\mathbf{u}_n^m$ and $\mathbf{t}_n^m$ are the displacement and traction components at the n^{th} node at time with $\psi_m(t)$, $\theta_m(t)$ being time interpolation functions at m^{th} time interval, and $\phi_n(\xi)$ the spatial shape function corresponding to the n^{th} node. Adopting the collocation approach in what follows, the discretized boundary integral equation is enforced at each nodal location, direction and time. For numerical robustness, an element that has a corner node as the collocation point is subdivided into two triangular regions in the spatial integration, with each triangle taken to be the limiting case of a quadrilateral with 2 nodes collapsing into the one that coincides with the collocation node as in Brebbia et al. (1984), Lachat and Watson (1976) and Pak and Guzina (1999). This results in the Jacobian of the degenerate triangular mapping going to zero at the collocation point that can further weaken any residual singularities while adding to the accuracy of the numerical quadrature. Details about similar treatments of linear, quadratic quadrilaterals and triangular elements can be found in Ashlock (2006).

By the foregoing numerical formulation, the fundamental regularized time-domain boundary integral equation (4.6) at time t^M can be converted to the matrix equations

$$\sum_{m=1}^{M}\left[\mathbf{H}^{Mm}\right]\left\{\mathbf{u}^m\right\} = \sum_{m=1}^{M}\left[\mathbf{G}^{Mm}\right]\left\{\mathbf{t}^m\right\} + \left\{\mathbf{F}^M\right\}, \ \text{for } 1 \le M \le \kappa_f, \tag{4.18}$$

and

$$\sum_{m=M-\kappa}^{M}\left[\mathbf{H}^{Mm}\right]\left\{\mathbf{u}^m\right\} + \left[\bar{\mathbf{H}}\right]\sum_{m=1}^{M-\kappa-1}\left\{\mathbf{u}^m\right\} = \sum_{m=M-\kappa}^{M}\left[\mathbf{G}^{Mm}\right]\left\{\mathbf{t}^m\right\} + \left[\bar{\mathbf{G}}\right]\sum_{m=1}^{M-\kappa-1}\left\{\mathbf{t}^m\right\} + \left\{\mathbf{F}^M\right\}, \ \text{for } M > \kappa_f \tag{4.19}$$

where $\{\mathbf{u}^m\}$ and $\{\mathbf{t}^m\}$ are the displacement and traction of nodes on the boundary surface at time t^m, $\kappa_f \geq T_f / \Delta t$ to the nearest round-up integers. The matrices in (4.18) and (4.19) are defined by

$$\begin{aligned}
[H_{AB}^{Mm}] = & \int_{t^{m-1}}^{t^m} \int_{\Gamma} [\hat{T}_i^k(\xi, \xi_a, t^M - \tau \mid g)]_2 \psi_m(\tau) \phi_n(\xi) d\Gamma_\xi d\tau \\
& + \int_{t^{m-1}}^{t^m} \int_{\Gamma} [\hat{T}_i^k(\xi, \xi_a, t^M - \tau \mid g)]_1 \psi_m(\tau) \left[\phi_n(\xi) - \delta_{na}\right] d\Gamma_\xi d\tau \\
& + \delta_{AB} \begin{Bmatrix} 0 & \text{Int.Problem} \\ 1 & \text{Ext.Problem} \end{Bmatrix} \int_{t^{m-1}}^{t^m} g_0(t^M - \tau) \psi_m(\tau) d\tau
\end{aligned} \tag{4.20}$$

$$[G_{AB}^{Mm}] = \int_{t^{m-1}}^{t^m} \int_{\Gamma} \hat{U}_i^k(\xi, \xi_a, t^M - \tau \mid g) \theta_m(\tau) \phi_n(\xi) d\Gamma_\xi d\tau,$$

$$\begin{aligned}
[\bar{H}_{AB}] = & \bar{g} \int_{t^{m-1}}^{t^m} \theta_m(\tau) \int_{\Gamma} \bar{T}_i^k(\xi, \xi_a, \mathbf{n}) \left[\phi_n(\xi) - \delta_{na}\right] d\Gamma_\xi d\tau \\
& + \delta_{AB} \begin{Bmatrix} 0 & \text{Int.Problem} \\ 1 & \text{Ext.Problem} \end{Bmatrix} \bar{g} \int_{t^{m-1}}^{t^m} \theta_m(\tau) d\tau
\end{aligned} \tag{4.21}$$

$$[\bar{G}_{AB}] = \int_{t^0}^{t^1} \psi_m(\tau) \int_{\Gamma} \bar{U}_i^k(\xi, \xi_a) \phi_n(\xi) d\Gamma_\xi d\tau,$$

$$\left\{\mathbf{F}_A^M\right\} = \int_{t-T_f}^{t} \int_{\Omega} \hat{U}_i^k(\xi, \xi_a, t - \tau \mid g) f_i(\xi, t) \mathrm{d}\Omega_\xi d\tau + \bar{g} \int_0^{t-T_f} \int_{\Omega} \bar{U}_i^k(\xi, \xi_a) f_i(\xi, t) \mathrm{d}\Omega_\xi d\tau \tag{4.22}$$

with indices

$$\begin{aligned}
A &= 3(a-1) + k, \quad 1 \leq a \leq N, \; 1 \leq k \leq 3, \; 1 \leq A \leq 3N, \\
B &= 3(n-1) + i, \quad 1 \leq n \leq N, \; 1 \leq i \leq 3, \; 1 \leq B \leq 3N.
\end{aligned} \tag{4.23}$$

To realize a discretized form for the time-shifted boundary integral equation in Eqn. (4.10) which is equivalent to Eqn. (4.6) with a finite-pulse Green's function as discussed earlier, one may employ the collocation equations in (4.18) and (4.19) that correspond to the latter directly. To this end, one may note that the matrix system of Eqn. (4.19) for $t^{M-\kappa_d}$ can be stated as

$$\begin{aligned}&\sum_{m=M-\kappa_d-\kappa_f}^{M-\kappa_d}\left[\mathbf{H}^{(M-\kappa_d)m}\right]\left\{\mathbf{u}^m\right\}+\left[\bar{\mathbf{H}}\right]\sum_{m=1}^{M-\kappa_d-\kappa_f-1}\left\{\mathbf{u}^m\right\}=\\&\qquad\sum_{m=M-\kappa_d-\kappa_f}^{M-\kappa_d}\left[\mathbf{G}^{(M-\kappa_d)m}\right]\left\{\mathbf{t}^m\right\}+\left[\bar{\mathbf{G}}\right]\sum_{m=1}^{M-\kappa_d-\kappa_f-1}\left\{\mathbf{t}^m\right\}+\left\{\mathbf{F}^{M-\kappa_d}\right\},\ \text{for } M>\kappa_d+\kappa_f\end{aligned} \tag{4.24}$$

whose difference with Eqn. (4.19) is

$$\sum_{m=M-\kappa_d-\kappa_f}^{M}\left[\hat{\mathbf{H}}^{Mm}\right]\left\{\mathbf{u}^m\right\}=\sum_{m=M-\kappa_d-\kappa_f}^{M}\left[\hat{\mathbf{G}}^{Mm}\right]\left\{\mathbf{t}^m\right\}+\left\{\hat{\mathbf{F}}^M\right\}, \tag{4.25}$$

with

$$\begin{aligned}&\left[\hat{\mathbf{H}}^{Mm}\right]=\left[\mathbf{H}^{Mm}\right],\ \left[\hat{\mathbf{G}}^{Mm}\right]=\left[\mathbf{G}^{Mm}\right],\ \text{for } M-\kappa_d<m\le M\\&\left[\hat{\mathbf{H}}^{Mm}\right]=\left[\mathbf{H}^{Mm}\right]-\left[\mathbf{H}^{(M-\kappa_d)m}\right],\ \forall M-\kappa_d-\kappa_f\le m\le M-\kappa_d,\\&\left[\hat{\mathbf{G}}^{Mm}\right]=\left[\mathbf{G}^{Mm}\right]-\left[\mathbf{G}^{(M-\kappa_d)m}\right],\ \forall M-\kappa_d-\kappa_f\le m\le M-\kappa_d,\\&\left\{\hat{\mathbf{F}}^{M}\right\}=\left\{\mathbf{F}^{M}\right\}-\left\{\mathbf{F}^{M-\kappa_d}\right\},\\&\kappa_f\ge T_f/\Delta t,\\&\kappa_d\ge T_d/\Delta t.\end{aligned} \tag{4.26}$$

Upon collecting the nodal boundary unknowns at time t^M into a single vector $\left\{\mathbf{d}^m\right\}$, the final matrix system of equation in (4.25) for the solution of the nodal unknowns can be written compactly as

$$\sum_{m=M-\kappa_d-\kappa_f}^{M}\left[\tilde{\mathbf{H}}^{Mm}\right]\left\{\mathbf{d}^m\right\}=\sum_{m=M-\kappa_d-\kappa_f}^{M}\left[\tilde{\mathbf{G}}^{Mm}\right]\left\{\mathbf{h}^m\right\}+\left\{\hat{\mathbf{F}}^m\right\},\ \text{for } M>\kappa_d+\kappa_f, \tag{4.27}$$

where

$$\left[\tilde{\mathbf{H}}^{Mm}\right]=\begin{bmatrix}\hat{\mathbf{H}}_{ut}^{Mm} & -\hat{\mathbf{G}}_{uu}^{Mm}\\ \hat{\mathbf{H}}_{tt}^{Mm} & -\hat{\mathbf{G}}_{tu}^{MM}\end{bmatrix},\qquad\left\{\mathbf{d}^m\right\}=\begin{Bmatrix}\mathbf{u}_t^m\\ \mathbf{t}_u^m\end{Bmatrix},$$

$$\left[\tilde{\mathbf{G}}^{Mm}\right]=\begin{bmatrix}-\hat{\mathbf{H}}_{uu}^{Mm} & \hat{\mathbf{G}}_{ut}^{Mm}\\ -\hat{\mathbf{H}}_{tu}^{MM} & \hat{\mathbf{G}}_{tt}^{Mm}\end{bmatrix},\qquad\left\{\mathbf{h}^m\right\}=\begin{Bmatrix}\mathbf{u}_u^m\\ \mathbf{t}_t^m\end{Bmatrix},$$

with $\left\{\mathbf{h}^m\right\}$ denoting the nodal boundary values that are imposed and $\left\{\mathbf{d}^m\right\}$ the boundary reactions to be determined at the m^{th} step.

4.5 Stability analysis

To render a rigorous determination of the stability of numerical schemes for time-dependent problems, their performance in the associated free-vibration or homogeneous equation system is the key (Bathe and Wilson 1976, Hilderbrand 1965, Hughes 2012, Peirce and Siebrits 1997). With zero traction on Γ_t, zero displacement on Γ_u and zero body force beyond a time T^*, one may set $\left\{\mathbf{h}^m\right\} = \begin{Bmatrix} \mathbf{u}_u^m \\ \mathbf{t}_t^m \end{Bmatrix}$ and $\left\{\mathbf{F}^m\right\}$ to be $\{\mathbf{0}\}$ on the right-hand side of Eqn. (4.27), reducing it to

$$\sum_{m=M-\kappa_d-\kappa_f}^{M} \left[\tilde{\mathbf{H}}^{Mm}\right]\left\{\mathbf{d}^m\right\} = \{\mathbf{0}\}, \text{ for } t_M > T^* + T_d + T_f \,. \tag{4.28}$$

As a result of the time-translational property of the Green's function and its finite period of non-steady response, the matrices in (4.27) for a fixed mesh and time step size have the property that

$$\left[\tilde{\mathbf{H}}^{M_1 m_1}\right] = \left[\tilde{\mathbf{H}}^{M_2 m_2}\right], \text{ for } M_1 - m_1 = M_2 - m_2 \,, \tag{4.29}$$

i.e., the coefficient matrices in Eqn. (4.28) remains unchanged from step to step (Mansur 1983).

4.5.1 A Hybrid Amplification Matrix for TD-BEM Formulations

Moving the known response quantities up to t^{M-1} in Eqn. (4.28) to the right-hand side, one can express the nodal unknowns in a vector form at time t^M as

$$\left\{\mathbf{d}^M\right\} = -\left[\tilde{\mathbf{H}}^{Mm}\right]^{-1}\left(\sum_{m=M-\kappa_d-\kappa_f}^{M-1} \left[\tilde{\mathbf{H}}^{Mm}\right]\left\{\mathbf{d}^m\right\}\right) \tag{4.30}$$

or

$$\left\{\hat{\mathbf{d}}^{M}\right\}=\left[\mathbf{A}\right]\left\{\hat{\mathbf{d}}^{M-1}\right\}, \tag{4.31}$$

where

$$\left[\mathbf{A}\right]=\begin{bmatrix} -\left[\tilde{\mathbf{H}}^{Mm}\right]^{-1}\left[\tilde{\mathbf{H}}^{M(M-1)}\right] & -\left[\tilde{\mathbf{H}}^{Mm}\right]^{-1}\left[\tilde{\mathbf{H}}^{M(M-2)}\right] & \cdots & -\left[\tilde{\mathbf{H}}^{Mm}\right]^{-1}\left[\tilde{\mathbf{H}}^{M(M-\kappa_d-\kappa_f)}\right] \\ \mathbf{I} & \mathbf{0} & \cdots & \mathbf{0} \\ \mathbf{0} & \mathbf{I} & \cdots & \mathbf{0} \\ \vdots & \vdots & \vdots & \mathbf{0} \\ \mathbf{0} & \mathbf{0} & \mathbf{I} & \mathbf{0} \end{bmatrix} \tag{4.32}$$

and

$$\left\{\hat{\mathbf{d}}^{M}\right\}=\left\{\left\{\mathbf{d}^{M}\right\}^{T},\left\{\mathbf{d}^{M-1}\right\}^{T},\ldots\left\{\mathbf{d}^{M+1-\kappa_d-\kappa_f}\right\}^{T}\right\}^{T} . \tag{4.33}$$

The matrix $\left[\mathbf{A}\right]$ can be termed a *Hybrid Amplification Matrix* for the TD-BEM scheme and $\left\{\hat{\mathbf{d}}^{M}\right\}$ an *extended solution vector* whose components, with the exception of $\left\{\mathbf{d}^{M}\right\}^{T}$, are known from previous steps. With the spectral radius of $\left[\mathbf{A}\right]$ denoted by

$$\rho\left(\mathbf{A}\right)=\max_{i}\left|\lambda_i\left(\mathbf{A}\right)\right|,$$

where $\lambda_i(\mathbf{A})$ is i^{th} eigenvalue of $\left[\mathbf{A}\right]$, the numerical stability of (4.28), and thus (4.25), can be assured by requiring that $\rho\left(\mathbf{A}\right)<1$ by virtue of the theory of Jordan form (Horn & Johnson, 2012). One may note that Eqn. (4.31) is similar in form to a linear multistep vector difference scheme (Gustafsson et al. 1972, Hughes 2012) whose stability is governed by the same criterion.

4.5.2 Stability Evaluation of a TD-BEM Family with Weighted-Collocation and Higher-Order Projections

To demonstrate the steps of the proposed stability evaluation procedure, the regularized direct TD-BEM scheme with optional collocation weights and higher-order projections in chapter 2 is used as an example. Expressed in a compact form, the generalized TD-BEM algorithm involves solving for the vector of unknowns at t^{M} via

$$
\begin{aligned}
&\left[\alpha_a\gamma_1^u\left[\hat{\mathbf{H}}^{(M+1)(M+1)}\right]+\alpha_a\left[\hat{\mathbf{H}}^{(M+1)M}\right]+\alpha_0\left[\hat{\mathbf{H}}^{MM}\right]\right]\left\{\mathbf{u}^M\right\} \\
&=\left[\alpha_a\gamma_1^t\left[\hat{\mathbf{G}}^{(M+1)(M+1)}\right]+\alpha_a\left[\hat{\mathbf{G}}^{(M+1)M}\right]+\alpha_0\left[\hat{\mathbf{G}}^{MM}\right]\right]\left\{\mathbf{t}^M\right\} \\
&+\alpha_a\left[\hat{\mathbf{G}}^{(M+1)(M+1)}\right]\sum_{j=2}^{\mathcal{O}^t+1}\gamma_j^t\left\{\mathbf{t}^{M+1-j}\right\}-\alpha_a\left[\hat{\mathbf{H}}^{(M+1)(M+1)}\right]\sum_{j=2}^{\mathcal{O}^u+1}\gamma_j^u\left\{\mathbf{u}^{M+1-j}\right\} \\
&+\sum_{m=M+1-\kappa_d-\kappa_f}^{M-1}\alpha_a\left[\hat{\mathbf{G}}^{(M+1)m}\right]\left\{\mathbf{t}^m\right\}+\sum_{m=M-\kappa_d-\kappa_f}^{M-1}\alpha_0\left[\hat{\mathbf{G}}^{Mm}\right]\left\{\mathbf{t}^m\right\}+\sum_{m=M-1-\kappa_d-\kappa_f}^{M-1}\alpha_b\left[\hat{\mathbf{G}}^{(M-1)m}\right]\left\{\mathbf{t}^m\right\} \\
&-\sum_{m=M+1-\kappa_d-\kappa_f}^{M-1}\alpha_a\left[\hat{\mathbf{H}}^{(M+1)m}\right]\left\{\mathbf{u}^m\right\}-\sum_{m=M-\kappa_d-\kappa_f}^{M-1}\alpha_0\left[\hat{\mathbf{H}}^{Mm}\right]\left\{\mathbf{u}^m\right\}-\sum_{m=M-1-\kappa_d-\kappa_f}^{M-1}\alpha_b\left[\hat{\mathbf{H}}^{(M-1)m}\right]\left\{\mathbf{u}^m\right\}, \\
&\qquad \mathit{for}\ M>\kappa_f+\kappa_d+1
\end{aligned}
\tag{4.34}
$$

where the matrices $\hat{\mathbf{H}}$ and $\hat{\mathbf{G}}$ are defined in Eqn. (4.26), α_a and α_b are two collocation weights that can be varied to obtain the third as $\alpha_0=1-\alpha_a-\alpha_b$. The indices $\mathcal{O}^u$ and $\mathcal{O}^t$ in the equation denote the order of projection (0 =constant, 1 =linear, 2=quadratic variation) employed in

$$
\mathbf{u}^{M+1}=\sum_{j=1}^{\mathcal{O}^u+1}\gamma_j^u\mathbf{u}^{(M+1-j)}, \tag{4.35}
$$

$$
\mathbf{t}^{M+1}=\sum_{j=1}^{\mathcal{O}^t+1}\gamma_j^t\mathbf{t}^{(M+1-j)}, \tag{4.36}
$$

for the displacement and traction, respectively with the coefficients γ_j^u and γ_j^t given in Table 1.

	γ_1^u, γ_1^t	γ_2^u, γ_2^t	γ_3^u, γ_3^t
$\mathcal{O}^u$ or $\mathcal{O}^t=0$	1	0	0
$\mathcal{O}^u$ or $\mathcal{O}^t=1$	2	-1	0
$\mathcal{O}^u$ or $\mathcal{O}^t=2$	3	-3	1

Table 4.1: Projection coefficients for various order of time variation

Taking the case of $\mathcal{O}^u$ and $\mathcal{O}^t$ both being 1 and the time interpolation being linear and constant for the displacements and tractions respectively, for example, Eqn. (4.34) degenerates to Marrero and Dominguez (2003)'s average-velocity projection scheme, with

$$
\sum_{m=M-\kappa_d-\kappa_f}^{M}\left[\tilde{\mathbf{H}}^{Mm}\right]\left\{\mathbf{d}^m\right\}=\sum_{m=M-\kappa_d-\kappa_f}^{M}\left[\tilde{\mathbf{G}}^{Mm}\right]\left\{\mathbf{h}^m\right\} \tag{4.37}
$$

where

$$\begin{aligned}
\left[\tilde{\mathbf{H}}^{MM}\right] &\equiv \alpha_a\left[\hat{\mathbf{H}}^{M(M-1)}\right]+(2\alpha_a+\alpha_0)\left[\hat{\mathbf{H}}^{MM}\right],\\
\left[\tilde{\mathbf{H}}^{M(M-1)}\right] &\equiv \alpha_a\left[\hat{\mathbf{H}}^{M(M-2)}\right]+\alpha_0\left[\hat{\mathbf{H}}^{M(M-1)}\right]+(\alpha_b-\alpha_a)\left[\hat{\mathbf{H}}^{MM}\right],\\
\left[\tilde{\mathbf{H}}^{Mm}\right] &\equiv \alpha_a\left[\hat{\mathbf{H}}^{M(m-1)}\right]+\alpha_0\left[\hat{\mathbf{H}}^{Mm}\right]+\alpha_b\left[\hat{\mathbf{H}}^{M(m+1)}\right],\ \text{for } M+1-\kappa_d-\kappa_f\le j\le M-2,\\
\left[\tilde{\mathbf{H}}^{M(M-\kappa_d-\kappa_f)}\right] &\equiv \alpha_0\left[\hat{\mathbf{H}}^{M(M-\kappa_d-\kappa_f)}\right]+\alpha_b\left[\hat{\mathbf{H}}^{M(M+1-\kappa_d-\kappa_f)}\right],\\
\left[\tilde{\mathbf{H}}^{M(M-1-\kappa_d-\kappa_f)}\right] &\equiv \alpha_b\left[\hat{\mathbf{H}}^{M(M-\kappa_d-\kappa_f)}\right]
\end{aligned}\tag{4.38}$$

and

$$\begin{aligned}
\left[\tilde{\mathbf{G}}^{MM}\right] &\equiv \alpha_a\left[\hat{\mathbf{G}}^{M(M-1)}\right]+(2\alpha_a+\alpha_0)\left[\hat{\mathbf{G}}^{MM}\right],\\
\left[\tilde{\mathbf{G}}^{M(M-1)}\right] &\equiv \alpha_a\left[\hat{\mathbf{G}}^{M(M-2)}\right]+\alpha_0\left[\hat{\mathbf{G}}^{M(M-1)}\right]+(\alpha_b-\alpha_a)\left[\hat{\mathbf{G}}^{MM}\right],\\
\left[\tilde{\mathbf{G}}^{Mm}\right] &\equiv \alpha_a\left[\hat{\mathbf{G}}^{M(m-1)}\right]+\alpha_0\left[\hat{\mathbf{G}}^{Mm}\right]+\alpha_b\left[\hat{\mathbf{G}}^{M(m+1)}\right],\ \text{for } M+1-\kappa_d-\kappa_f\le j\le M-2,\\
\left[\tilde{\mathbf{G}}^{M(M-\kappa_d-\kappa_f)}\right] &\equiv \alpha_0\left[\hat{\mathbf{G}}^{M(M-\kappa_d-\kappa_f)}\right]+\alpha_b\left[\hat{\mathbf{G}}^{M(M+1-\kappa_d-\kappa_f)}\right],\\
\left[\tilde{\mathbf{G}}^{M(M-1-\kappa_d-\kappa_f)}\right] &\equiv \alpha_b\left[\hat{\mathbf{G}}^{M(M-\kappa_d-\kappa_f)}\right]
\end{aligned}\tag{4.39}$$

With $(\alpha_a, \alpha_b) = (0.25, 0.25)$. By virtue of the proposed formulation, the stability of the time-marching process can be evaluated in a straightforward manner by determining the spectral radius of the hybrid amplification matrix $[\mathbf{A}]$ as defined by Eqn. (4.32).

4.6 Numerical examples

As an illustration of the proposed formulation for the stability analysis, Stokes' solution for a square-impulse with $g_0(t)=H(t)-H(t-\Delta t)$ as discussed in Section 2 is used as the Green's function in the generalized TD-BEM and the eigenvalue solver in SLEPc (Hernandez et al. 2005) is employed in the ensuing spectral radius computations:

4.6.1 Example 1: Axial wave propagation in a square rod

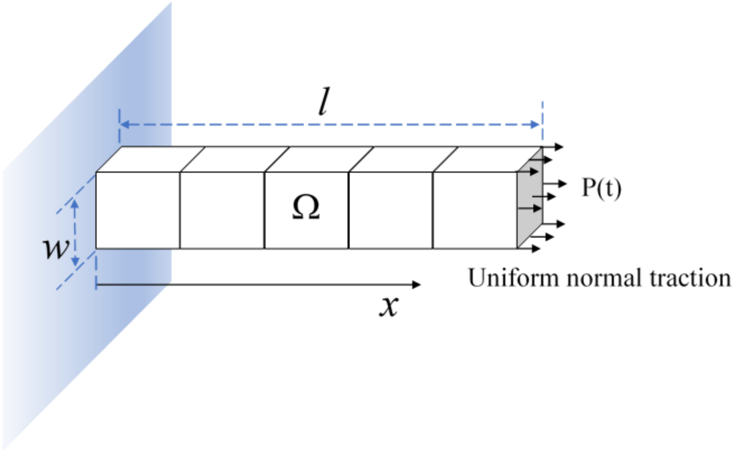

Figure 4.1 : Mesh A for a square bar under a step jump in normal end-traction by coarse mesh

Shown in Figure 4.1 is an isotropic, linearly elastic square bar with zero body-force, characterized by a Young's modulus E , a mass density ρ , Poisson's ratio $\nu = 0$ and a length-to-width ratio of $l/w = 5$. Its left end is fully fixed at $x = 0$ while a uniform step-jump in normal traction is applied to its right end in the form of

$$P(t) = P_0 \; H(t) . \tag{4.40}$$

With a zero Poisson's ratio, the 3-D elastodynamic problem is essentially a 1-D wave propagation one whose exact solution is available in closed form. As was used in many past studies as a demonstrative case, (e.g., Coda and Venturini 1995, Marrero and Dominguez, 2003), a coarse Mesh A is set up as indicated in Figure 4.1. It consists of 22 four-node linear elements with double or triple nodes for the edges and corners. Constant or linear time interpolation for the integration is employed for both displacements and tractions where appropriate, with a dimensionless time-step size denoted by $\beta = c \, \Delta t / l_e$ where l_e is the minimum dimension of the elements in the direction of wave propagation and c the relevant wave speed. The maximum distance between any two points on the boundary in this case is $R_\Gamma = l^e \sqrt{5^2 + 2}$. With $T_f = R_\Gamma / c_2 \simeq 7.4 \Delta t$ and $T_d = \Delta t$ in this case, it is taken that $\kappa_f = 8$, $\kappa_d = 1$. In the case of the elementary 1-step integration scheme which corresponds to the generalized scheme with $(\alpha_a, \alpha_b) = (0,0)$ and linear time interpolation for both displacement and traction, the spectral radius of the corresponding $[\mathbf{A}]$ matrix for the numerical scheme is found to be 4.072. As illustrated in Figure 4.2, such a large deviation of $\rho(\mathbf{A})$ from unity renders the scheme quickly unstable (see also Marrero and Dominguez 2003, Yu et al. 1998). For a 1-step scheme with linear time interpolation for displacements but constant for tractions, the spectral radius of the corresponding $[\mathbf{A}]$ matrix has a value of 2.757, i.e., it is also unstable.

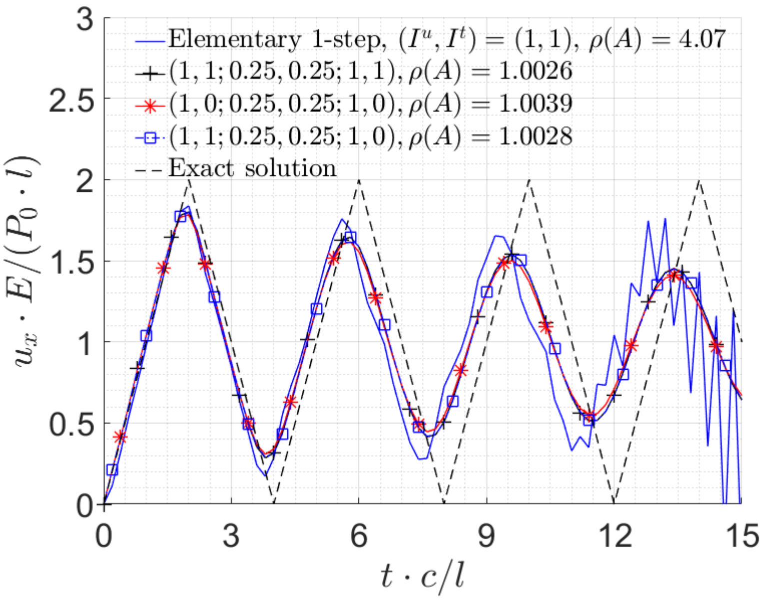

Figure 4.2: TD-BEM results by Mesh A for normal displacement time history at loaded end of square bar in the first several cycles with $\beta = 1$

Figure 4.2 also includes the results from using $(\mathcal{O}^u, \mathcal{O}^t; \alpha_a, \alpha_b; I^u, I^t) = (1, 1; 0.25, 0.25; 1, 0)$ which corresponds to the averaged velocity scheme of Marrero and Dominguez (2003), the $(1,0; 0.25,0.25; 1,0)$ and the $(1,1; 0.25,0.25; 1,0)$ case, with I^u and I^t denoting respectively the order of the time interpolation for displacements and tractions. From the displays, one can see that the 3 weighted collocation schemes show considerable improvement in the time history of the axial displacement response in terms of smoothness and appears stable over the cycles shown. However, the spectral radii $\rho(\mathbf{A})s$ of the corresponding hybrid amplification matrices are found to be all larger than 1, i.e., violating the stability criterion. As a demonstration of the correctness and reliability of the stability criterion, the computations are continued with more steps for two of the schemes, and the results are shown in Figure 4.3. While both solutions look stable in the early going, they are actually unstable and diverge badly at a later stage as predicted. It illustrates well the danger of judging a TD-BEM algorithm's stability by means of only finite-time simulations, and the importance of having a more rigorous approach to the problem as mentioned earlier.

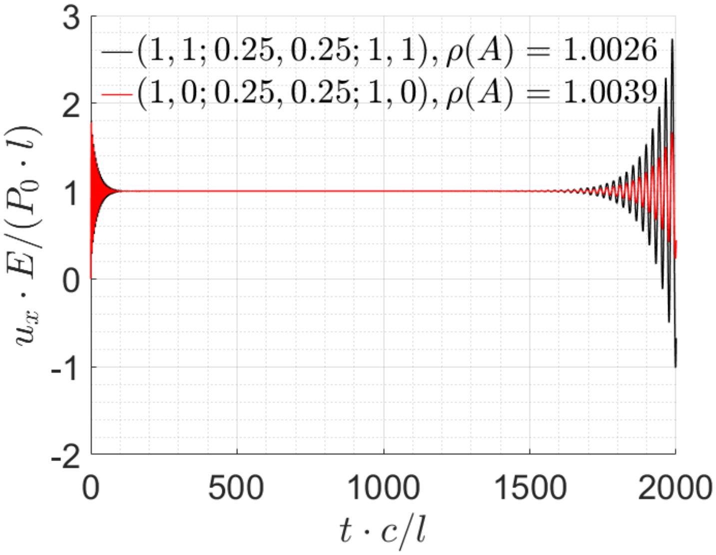

Figure 4.3: TD-BEM results by Mesh A for normal displacement time history at loaded end of square bar in the long run with $\beta = 1$

α_b α_a	0.0	0.1	0.2	0.3	0.4	0.5	0.6	0.7	0.8	0.9
1.0	1.00223	-	-	-	-	-	-	-	-	-
0.9	1.00227	1.00227	-	-	-	-	-	-	-	-
0.8	1.00231	1.00231	1.00231	-	-	-	-	-	-	-
0.7	1.00236	1.00236	1.00236	1.00236	-	-	-	-	-	
0.6	1.00240	1.00240	1.00240	1.00240	1.00240	-	-	-	-	-
0.5	1.00244	1.00244	1.00244	1.00244	1.00244	1.00244	-	-	-	-
0.4	1.00248	1.00248	1.00248	1.00248	1.00248	1.02337	1.2716	-	-	-
0.3	1.00253	1.00253	1.00253	1.00253	1.04498	1.1293	1.3281	2.0764	-	-
0.2	1.09887	1.05150	1.05038	1.10177	1.18413	1.28323	1.3922	2.1593	3.6290	-
0.1	1.62442	1.43247	1.34919	1.34267	1.41671	1.54315	1.6999	2.2448	3.8192	8.324
0.0	4.07158	4.07158	4.07158	4.07158	4.07158	4.07158	4.0715	4.0715	4.0715	9.000

Table 4.2: Spectral radii for generalized TD-BEM scheme with Mesh A with $(\mathcal{O}^u,\mathcal{O}^t)=(2,1)$, $(I^u,I^t)=(1,1)$ and $\beta=1$

To explore how the stability of the TD-BEM time-marching scheme can be changed by having different collocation weights in α_a and α_b, the spectral radius of [A] for the generalized TD-BEM scheme with $(\mathcal{O}^u,\mathcal{O}^t)=(2,1)$ is evaluated for a number of combinations of (α_a,α_b) as shown in Table 4.2. One can see that there are (α_a,α_b) combinations that can lead to substantially smaller $\rho(\mathbf{A})$ with $\alpha_a > 0$ for the TD-BEM setup even though they all remain larger than unity, i.e., all are still unstable for the crude mesh employed.

To demonstrate how the coarseness of the discretization can affect not only the accuracy (as one might expect) but also stability of the scheme as mentioned in the Introduction, results from using the finer Mesh B in Figure 4.4 for the square bar problem are also generated. The mesh comprises 352 linear elements with double or triple nodes at edges and corners as before and a 20x20 Gaussian quadrature rule. With $T_f = R_\Gamma/c_2 \simeq 29.6\Delta T$ for the case, κ_f is set to be 30 and κ_d in the computations. Shown in Figure 4.5 are the computed solutions from using 3 projection schemes with $(\mathcal{O}^u,\mathcal{O}^t)$ = (1,0), (1,1) and (2,1) , the same collocation weights of (0.2,0.2) and (I^u,I^t) =(1,0) or (1,1). From the displays, one can see that their $\rho(\mathbf{A})$s are now all less than 1, i.e., all 3 schemes are numerically stable. In terms of accuracy, however, one can see that $(\mathcal{O}^u,\mathcal{O}^t)$ = (1,1) and (2,1) solutions are generally closer to the exact solution of the problem than the (1,0)'s case.

Focused on the (1,1) and (2,1) schemes' stability with respect to the collocation weights, the spectral radii of their resulting [A] matrices for a large range of different α_a and α_b are computed and shown respectively in Table 4.3 and Table 4.4, as well as the 3-D column plots in Figure 4.6 and Figure 4.7. From the tabulations, the benefits from having optional collocation weights should be evident in regard to stability control. With the plane of $\rho(\mathbf{A})=1$ shown in green color in Figure 4.6 and Figure 4.7 and each column's height representing the magnitude of the spectral radius above 1, one can see that an approximate triangular region exists in the parametric space of (α_a, α_b) over which the weighted-collocation TD-BEM scheme for $(\mathcal{O}^u, \mathcal{O}^t) = (1,1)$ and $(2,1)$ are both stable. Guided by the stability results in Table 4.3 and Table 4.4, the time histories by the generalized TD-BEM with $(\mathcal{O}^u, \mathcal{O}^t)$ = (1,0), (1,1), (2,1) and $\beta = 1$ for three variations of the collocation weights are plotted in Figure 4.8, Figure 4.9 and Figure 4.10 for more detailed comparison of their performance. To provide an idea how the stability of the TD-BEM can be affected by the time step size, $\rho(\mathbf{A})$ is also computed for a few βs for the scheme of (2,1; 0.4,0.0; 1,1) and some results are shown in Table 4.5. As can be seen from the tabulations, the range of stable βs is centered around 1 as expected, and a large deviation from it is not advisable for the case. With the variety of options available via $\mathcal{O}^u, \mathcal{O}^t, \alpha_a, \alpha_b, I^u$ and I^t in the generalized TD-BEM scheme, however, a larger range of β can probably be found for the problem with a suitable parametric set for the algorithm or other methodological improvements.

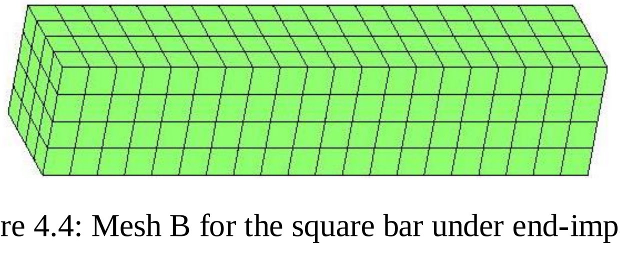

Figure 4.4: Mesh B for the square bar under end-impact

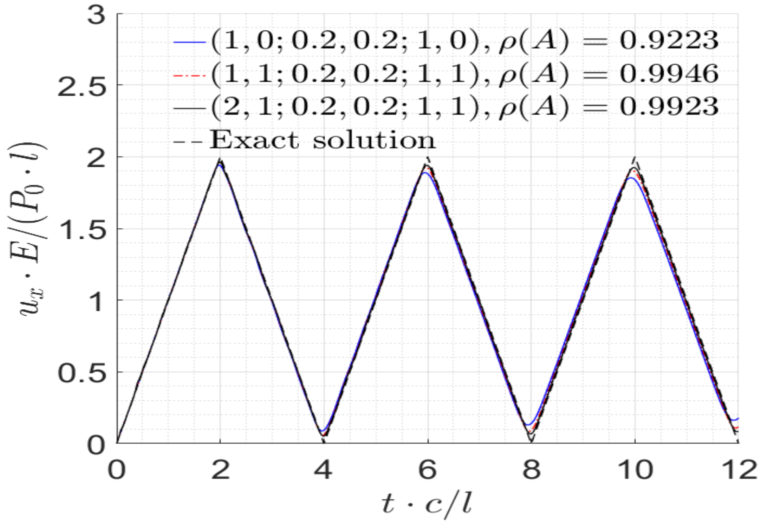

(a) loaded-end displacement

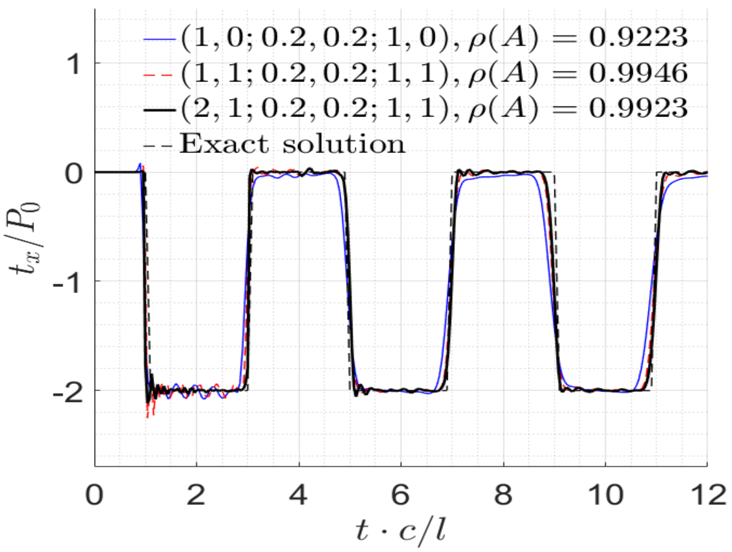

(b) fixed-end traction at x=0

Figure 4.5: Influence of $(\mathcal{O}^u, \mathcal{O}^t)$ on TD-BEM scheme's stability and accuracy: Mesh B, $\beta = 1$

α_b α_a	0	0.1	0.2	0.3	0.4	0.5	0.6	0.7	0.8	0.9
1.0	0.9944	-	-	-	-	-	-	-	-	-
0.9	0.9971	0.9982	-	-	-	-	-	-	-	-
0.8	0.9885	0.9963	0.9999	-	-	-	-	-	-	-
0.7	0.9992	0.9832	0.9997	0.9999	-	-	-	-	-	-
0.6	0.9820	0.9835	0.9837	0.9979	0.9646	-	-	-	-	-
0.5	0.9742	0.9705	0.9986	0.9965	0.9629	0.9614	-	-	-	-
0.4	0.9998	0.9754	0.9973	0.9682	0.9963	0.9996	1.0687	-	-	-
0.3	0.9840	0.9837	0.9814	0.9792	0.9937	1.0811	1.1749	1.2741	-	-
0.2	1.2232	1.0240	0.9946	1.0220	1.1062	1.2111	1.3249	1.4742	1.63	-
0.1	1.8226	1.6823	1.4943	1.1716	1.2810	1.4323	1.6081	1.8208	2.08	2.41
0.0	3.7861	3.7861	3.7861	3.7861	3.7861	3.7861	3.7861	3.7861	4.00	8.99

Table 4.3: Spectral radii for generalized TD-BEM scheme with Mesh B:
$(\mathcal{O}^u,\mathcal{O}^t)=(1,1)$, $(I^u,I^t)=(1,1)$, $\beta=1$

α_b α_a	0.0	0.1	0.2	0.3	0.4	0.5	0.6	0.7	0.8	0.9
1.0	0.9993	-	-	-	-	-	-	-	-	-
0.9	0.9989	0.9966	-	-	-	-	-	-	-	-
0.8	0.9990	0.9990	0.9990	-	-	-	-	-	-	-
0.7	0.9981	0.9857	0.9944	0.9989	-	-	-	-	-	
0.6	0.9974	0.9974	0.9976	0.9992	0.9992	-	-	-	-	-
0.5	0.9981	0.9981	0.9979	0.9963	0.9944	0.9744	-	-	-	-
0.4	0.9982	0.9982	0.9982	0.9983	0.9983	0.9989	1.0599	-	-	-
0.3	0.9985	0.9985	0.9985	0.9982	1.0646	1.1409	1.2208	1.3035	-	-
0.2	1.0142	1.0046	0.9923	1.1011	1.1720	1.2539	1.3621	1.44875	1.60	-
0.1	1.5460	1.3597	1.1883	1.2354	1.3382	1.4928	1.6324	1.8106	2.03	2.33
0.0	3.7861	3.7861	3.7861	3.7861	3.7861	3.7861	3.7861	3.7861	4.00	8.99

Table 4.4: Spectral radii for generalized TD-BEM scheme with Mesh B
with $(\mathcal{O}^u,\mathcal{O}^t)=(2,1)$, $(I^u,I^t)=(1,1)$, $\beta=1$

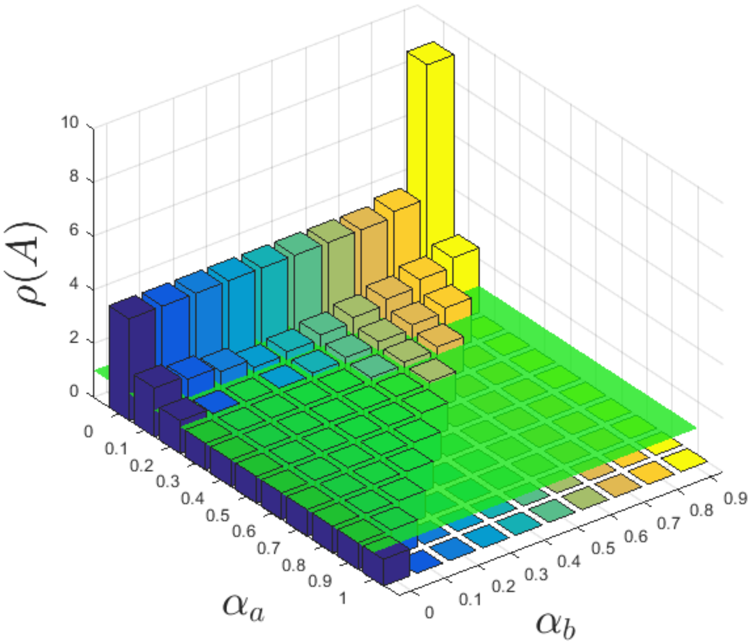

Figure 4.6: Spectral radii and stability region with respect to (α_a, α_b) for generalized TD-BEM scheme with Mesh B: $(\mathcal{O}^u, \mathcal{O}^t) = (1, 1)$, $(I^u, I^t) = (1,1)$, $\beta = 1$

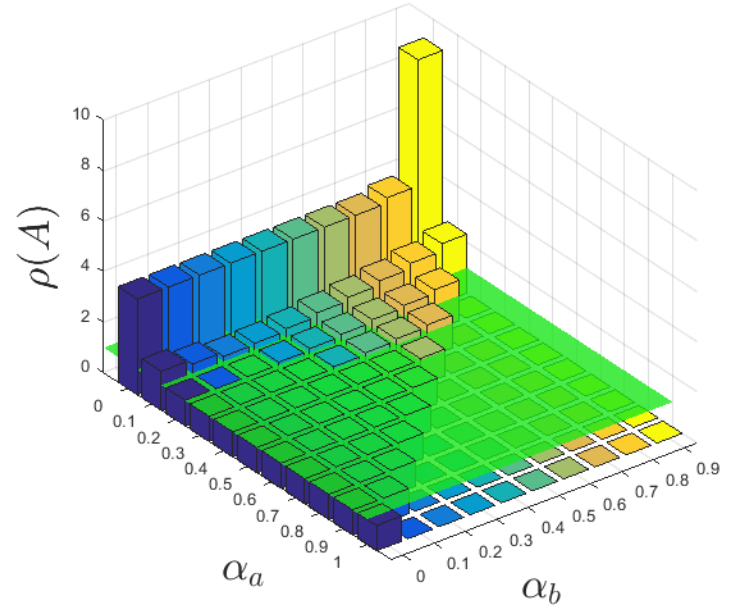

Figure 4.7: Spectral radii and stability region with respect to (α_a, α_b) for generalized TD-BEM scheme with Mesh B: $(\mathcal{O}^u, \mathcal{O}^t) = (2, 1)$, $(I^u, I^t) = (1,1)$, $\beta = 1$

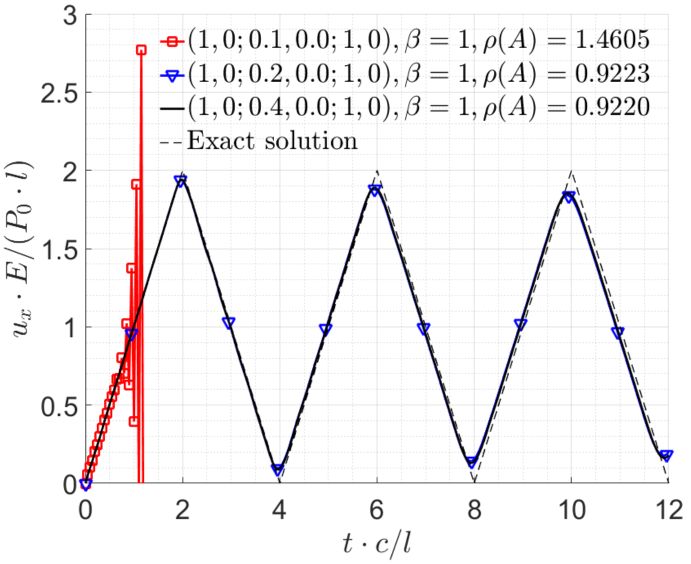

(a) loaded-end displacement

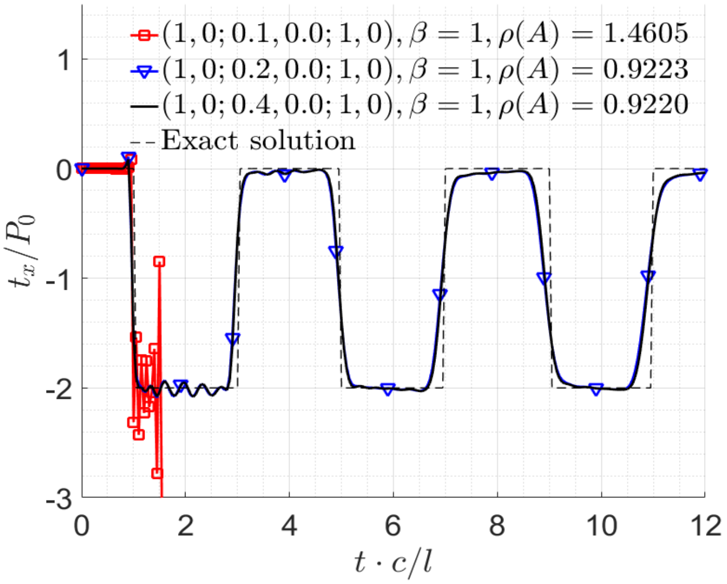

3

(b) fixed-end traction

Figure 4.8: Mesh B results for loaded-end displacement and fixed-end traction time histories of square bar with $(\mathcal{O}^u, \mathcal{O}^t) = (1, 0)$, $\beta = 1$

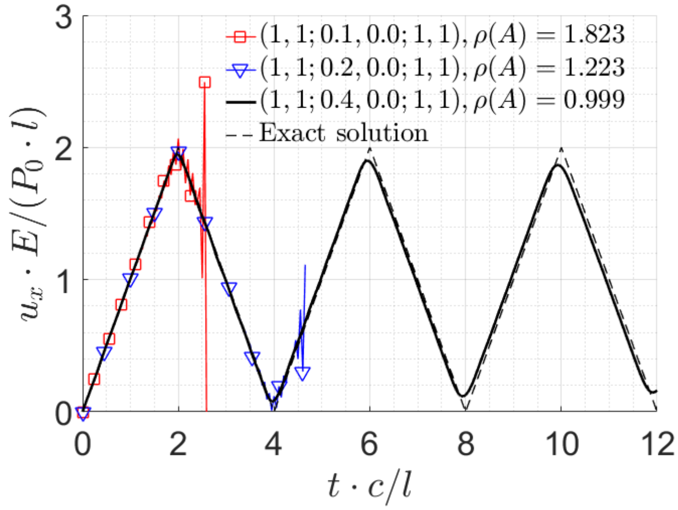

(a) loaded-end displacement

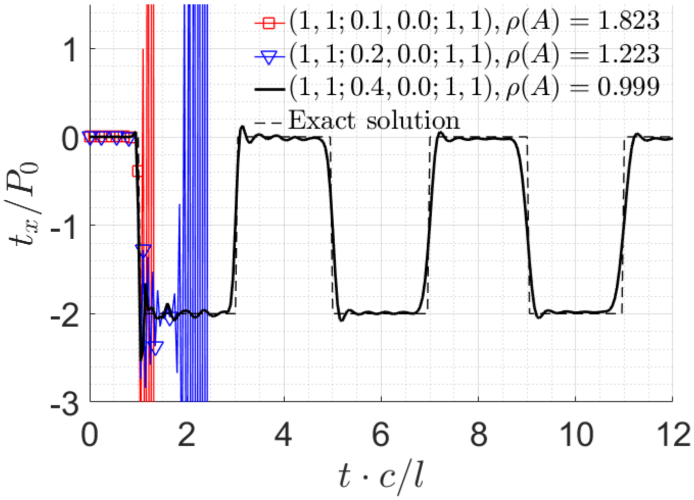

(b) fixed-end traction

Figure 4.9: Mesh B results for loaded-end displacement and fixed-end traction time histories of square bar with $(\mathcal{O}^u, \mathcal{O}^t) = (1,1)$, $\beta = 1$

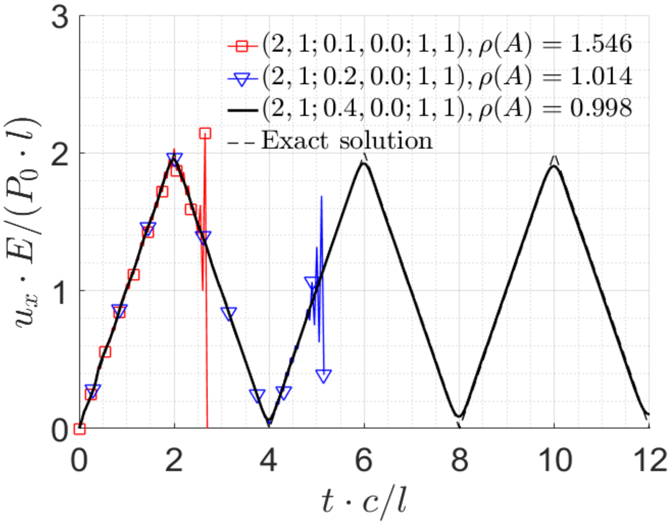

(a) loaded-end displacement

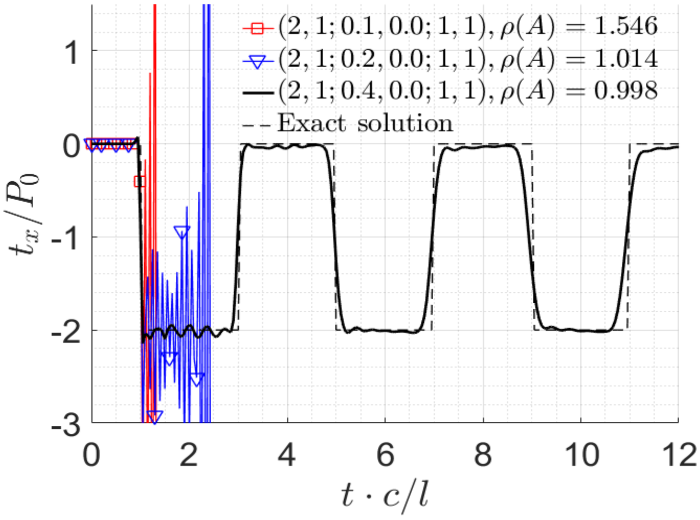

(b) fixed-end traction

Figure 4.10: Mesh B results for loaded-end displacement and fixed-end traction time histories of square bar with $(\mathcal{O}^u, \mathcal{O}^t) = (2,1)$, $\beta = 1$

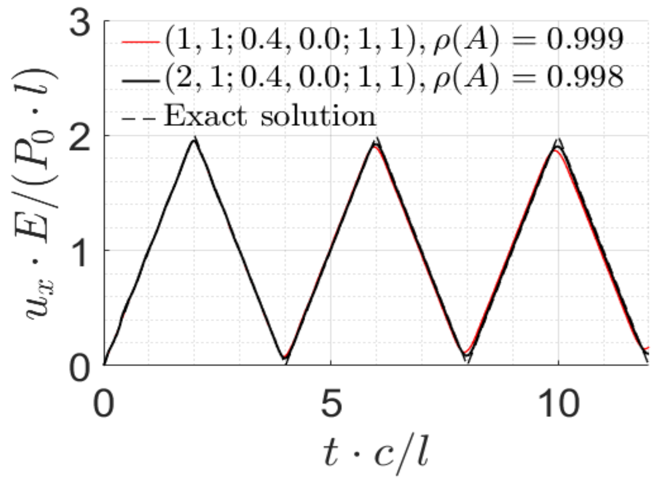

(a) loaded-end displacement

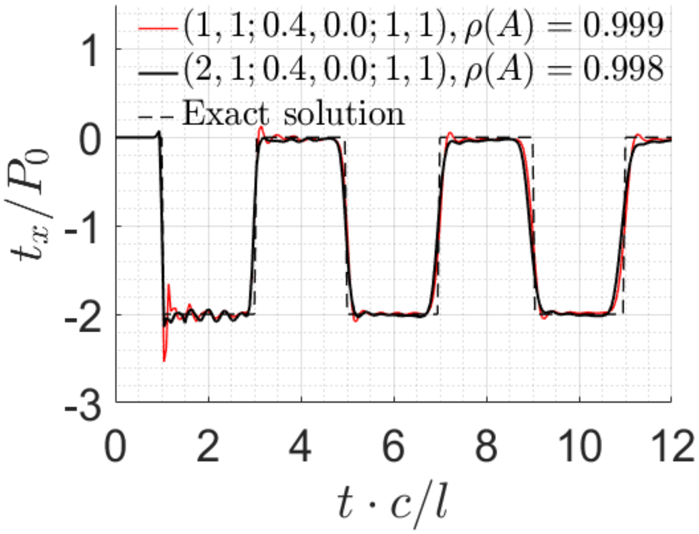

(b) fixed-end traction

Figure 4.11: Comparison of (1,1; 0.4,0.0; 1,1) and (2,1; 0.4,0.0; 1,1) TD-BEM schemes in displacement and traction solutions for square-bar: $\beta = 1$

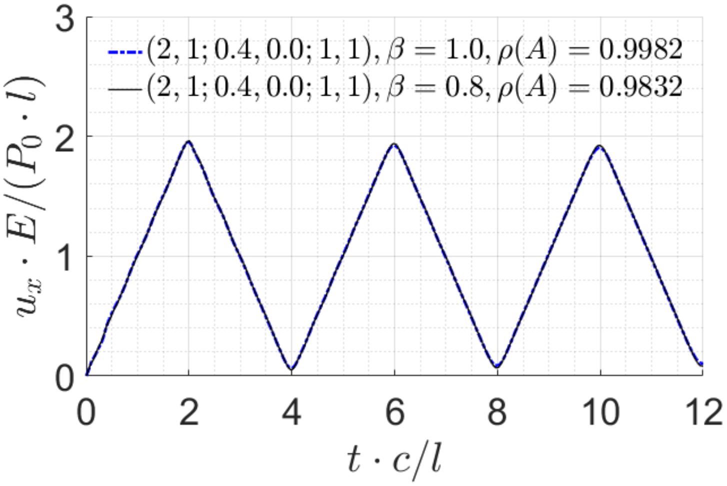

(a) loaded-end displacement

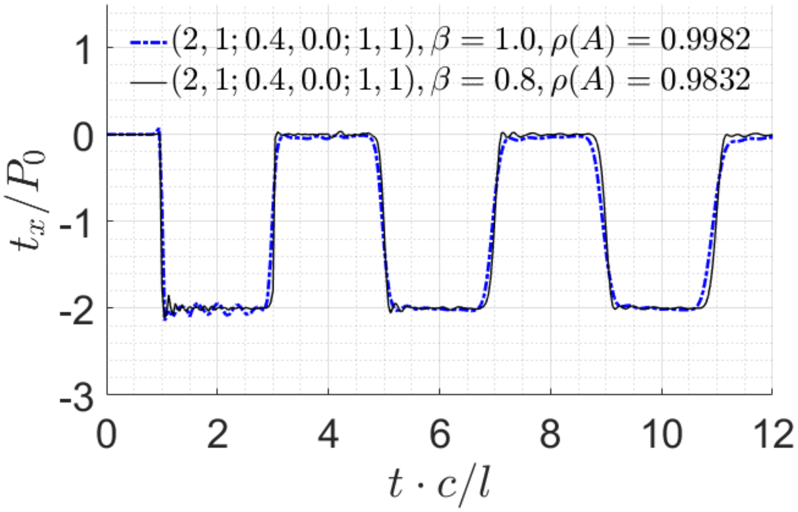

(b) fixed-end traction

Figure 4.12: Comparison of (2,1; 0.4,0.0; 1,1) TD-BEM scheme in displacement and traction solutions for square-bar with $\beta = 1$ and 0.8

$(\mathcal{O}^u,\mathcal{O}^t;\alpha_a,\alpha_b;I^u,I^t)$	(2,1; 0.4,0.0; 1,1)
$\beta = 1.3$	1.0364
$\beta = 1.2$	1.0387
$\beta = 1.1$	0.9884
$\beta = 1.0$	0.9982
$\beta = 0.9$	0.9805
$\beta = 0.8$	0.9832
$\beta = 0.7$	1.03721
$\beta = 0.6$	1.02824

Table 4.5: Spectral radius for a range of βs in generalized TD-BEM scheme with $(\mathcal{O}^u,\mathcal{O}^t;\alpha_a,\alpha_b;I^u,I^t)=(2,1;0.4,0.0;1,1)$

To provide some insights on the influence of the projection orders for the displacement and traction solutions in regard to accuracy, the response time histories for the square-bar problem by the (1,0; 0.4,0; 1,0), (1,1; 0.4,0; 1,1) and (2,1; 0.4,0; 1,1) schemes are plotted together in Figure 4.11. From the display, one can see that while the displacement amplitudes are comparable, the $(2,1;0.4,0.0;1,1)$ solution is more in-phase with the exact solution than the (1,0; 0.4,0; 1,0) and (1,1; 0.4,0; 1,1) solutions. The traction response by the (1,0; 0.4,0; 1,0) and (1,1; 0.4,0; 1,1) schemes also exhibit a bit more distortion or spurious oscillations than the (2,1; 0.4,0;1,1) scheme. Such deviations from a discontinuous solution are however, not unexpected. As a sounder basis of comparison, the response to a smoother half-sine pressure pulse defined by

$$P(t)=\begin{Bmatrix} P_0\cdot\sin\left(\dfrac{c_1\pi t}{2l}\right), & \text{for } t\le 2l/c_1 \\ 0 & \text{for } t>2l/c_1 \end{Bmatrix},$$

in place of the Heaviside load in Eqn. (4.40) as the boundary loading is also computed using the same mesh and the result is shown in Figure 4.13 together with its exact solution. As one can see from the displays, the numerical solution is now considerably smoother and closer to the continuous analytic solution in both displacement and traction responses, with the (2,1; 0.4,0.0;

1,1) scheme still doing somewhat better than the (1,1; 0.4,0.0; 1,1) and (1,0; 0.4, 0.0; 1,0) TD-BEM schemes.

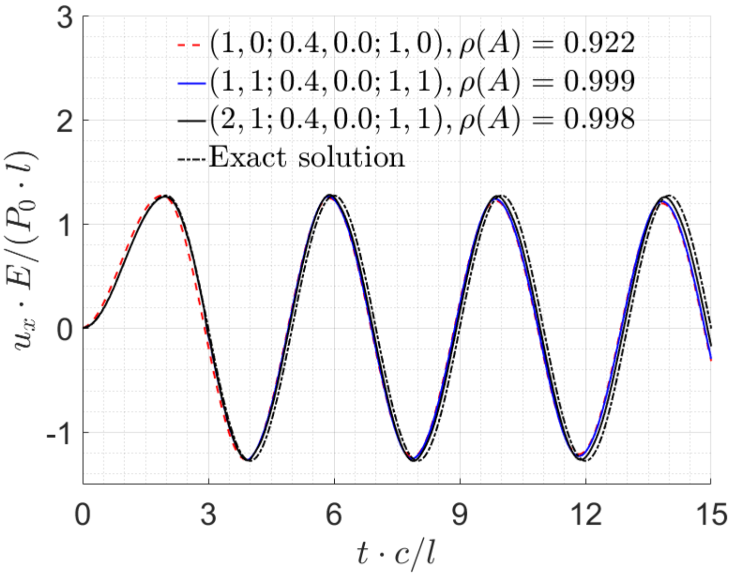

(a) Load-end displacement history

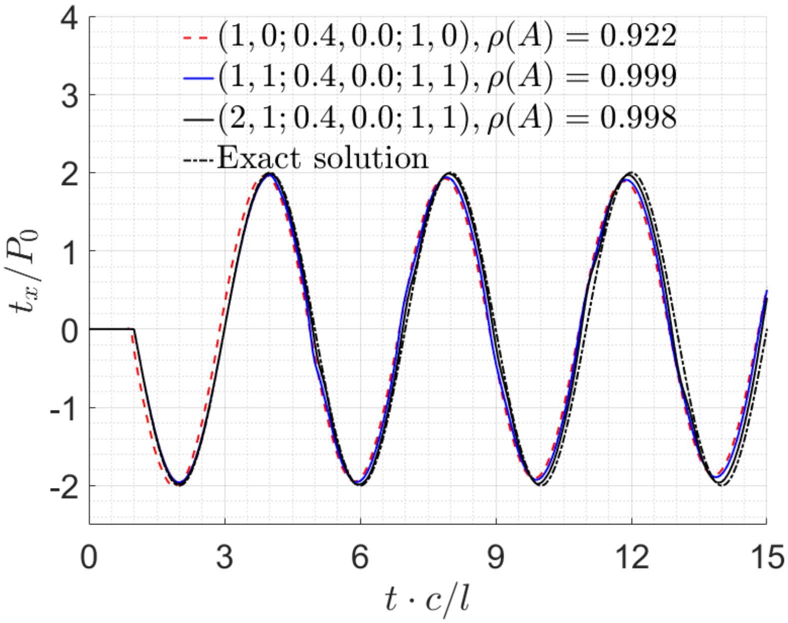

(b) Fixed-end traction history

Figure 4.13: Square-bar response due to a half-sine end impulse by generalized TD-BEM scheme: $\beta=1$

4.6.2 Example 2: Spherical Cavity under step pressure in a full-space

To illustrate the application of the TD-BEM stability assessment method to unbounded domain problems, the case of a spherical cavity embedded in a homogeneous isotropic linearly elastic 3-D full-space with a Poisson's ratio $\nu = 0.2$ and subjected to a step jump in internal pressure is considered. Using the mesh for the spherical surface shown in Figure 4.14 the solution is computed using the single-step scheme. The time history of the radial displacement generated with the elementary single- step time integration and $\beta = 1.0$ is depicted in Figure 4.15. With the spectral radius $\rho(A)$ of its hybrid amplification matrix being 0.997, the TD-BEM scheme is stable and, in fact, very close to the exact solution for this problem. When the time-step size is reduced to $\beta = 0.8$, however, the spectral radius increases to 1.002 indicating instability. As can be seen from the figure, while the solution appears to be stable over a large number of steps, it would eventually explode, illustrating once more the importance of an analytically rigorous stability assessment.

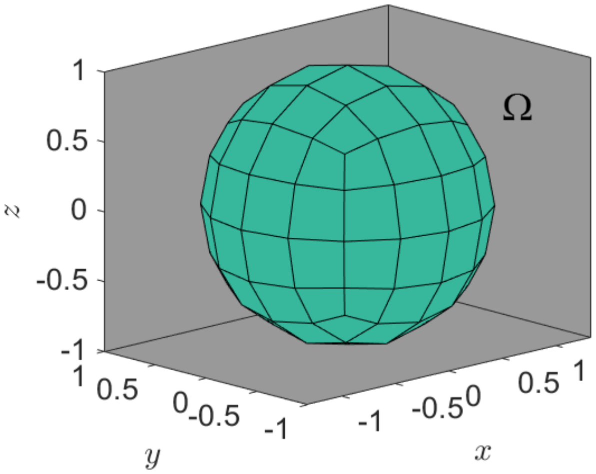

Figure 4.14: Mesh for a full-space with a spherical cavity under sudden internal pressure

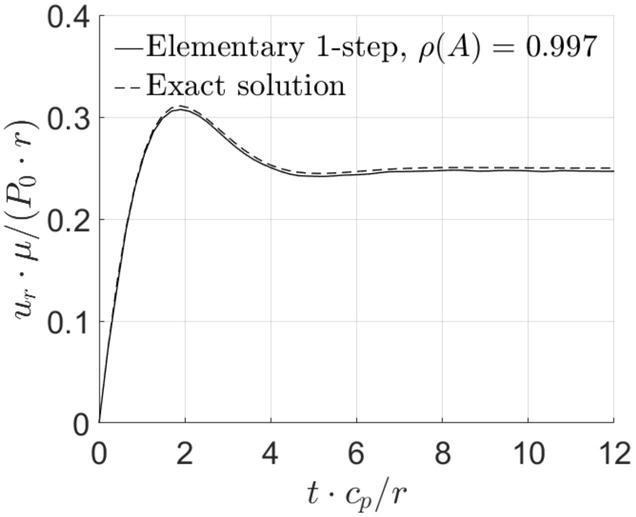

Figure 4.15: Stability of TD-BEM for spherical cavity problem with single step time integration: $(I^u, I^t) = (1,1)$ and $\beta = 1.0$

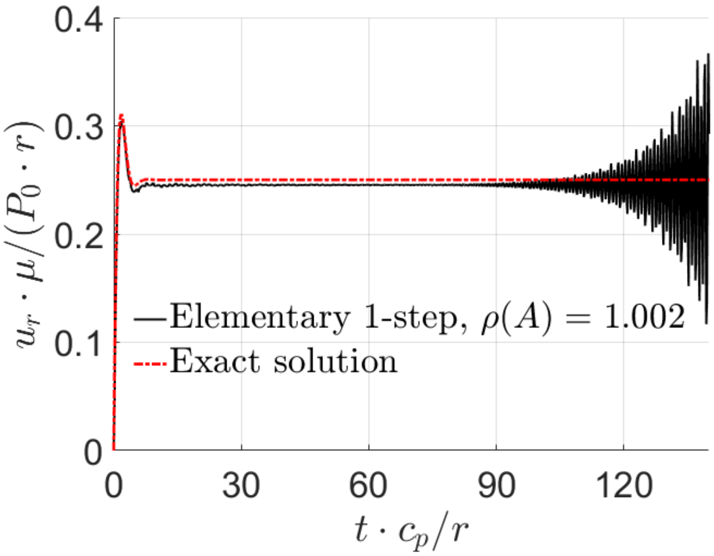

Figure 4.16: Stability of TD-BEM for spherical cavity problem with 1-step time integration: $(I^u, I^t) = (1,1)$, $\beta = 0.8$

Provided as a comparison to the elementary scheme, the results obtained from using the generalized TD-BEM scheme with $(\mathcal{O}^u, \mathcal{O}^t; \alpha_a, \alpha_b; I^u, I^t) = (2, 1; 0.2, 0.2; 1, 1)$ and $(1, 1; 0.2, 0.2; 1, 1)$ are shown in Figure 4.17 and Figure 4.18 for the same two β values. With their spectral radii both being less than 1 as indicated in the figure, they both satisfy the stability requirement, allowing one's focus to be placed on other aspects such as accuracy and efficiency of the method with confidence.

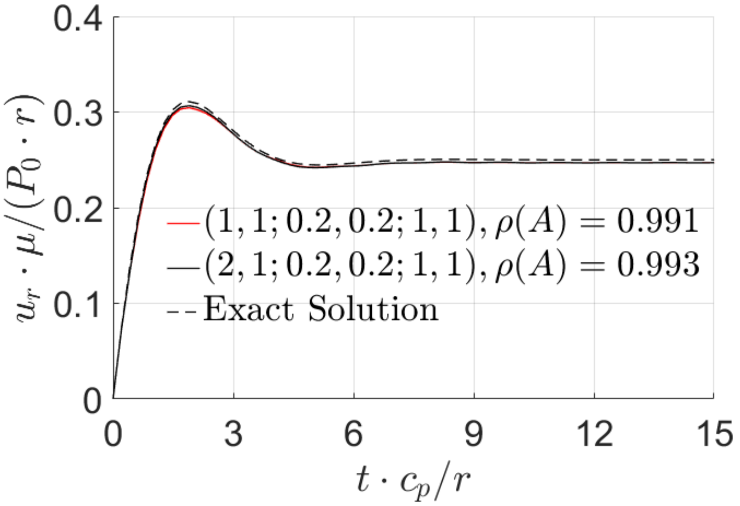

Figure 4.17: Stability of generalized TD-BEM for spherical cavity problem: $\beta = 1.0$

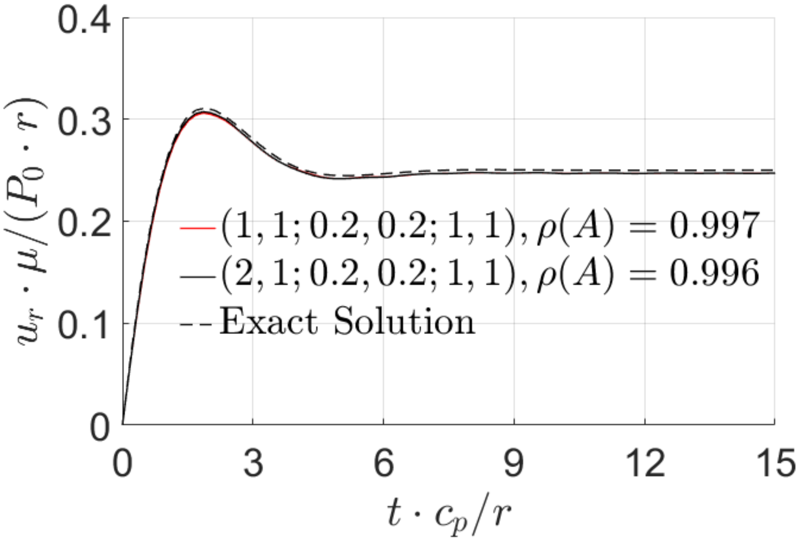

Figure 4.18: Stability of generalized TD-BEM for spherical cavity problem: $\beta = 0.8$

4.7 Conclusions

In this paper, a rigorous analytical formulation that can be used to assess reliably the stability of time-domain boundary element methods for 3-D elastodynamics is presented. By casting a step-by-step time-domain boundary element algorithm in the form of a linear multi-step method with a hybrid amplification matrix and using the fundamental characteristics of commonly-used dynamic Green's functions, a formal stability evaluation is shown to be possible and the resultant procedure is equivalent to a standard spectral analysis in numerical methods. As an illustration, the approach is applied to a regularized time-domain direct boundary element formulation with multiple collocation weights and optional solution projections in the solution of the benchmark finite-domain square bar and the infinite-domain step-pressure cavity problems. Through the use of some of its parametric options, a group of stable time-marching schemes within the realm of the generalized TD-BEM is identified and their performance illustrated. With suitable adaptations and translations, the proposed approach for determining TD-BEM's stability should be helpful in a thorough evaluation and development of more robust time-domain boundary integral-element methods for engineering and applied sciences.

Chapter 5

Synthesis of TD-elastodynamic Green's function for homogeneous and multi-layered half-space by frequency-domain solutions

5.1 Introduction

The dynamics of an elastic half-space under external or internal loads has long been a subject of great interest because of its fundamental importance in earthquake engineering and seismology and geophysical applications. Following Lamb's study on waves produced by a line source (Lamb 1904), the early investigations focused on either line-source, axisymmetric pulse, vertical or surficial load (Cagniard 1962, de Hoop 1960, Pekeris and Lifson 1957). The time-harmonic response to an arbitrarily distributed buried load, with point-load solutions as degenerate cases, was developed by Pak (1987) for a homogeneous isotropic elastic half-space. For a piecewise homogeneous horizontally multi-layered half-space, there were the works by Kennett (2013**)**, Kennett and Kerry (1979), Luco and Apsel (1983), Apsel and Luco (1983), Hisada (1994), Hisada (1995) and Pak and Guzina (2002) . In particular, Pak and Guzina (2002) showed through a local analysis that the singular parts of the multi-layer Green's function coincide with the corresponding static bi-material Green's functions (Guzina and Pak 1999) with appropriate material parameters.

To employ time-domain boundary element methods for dynamic soil-structure interaction analysis (Galvín and Romero 2014, Doménech et al. 2016, Romero and Galvín 2015), the availability of effective time-domain half-space Green's function is essential. This can be achieved by means of a Fourier synthesis of frequency-domain Green's functions. With a true Heaviside step function or the Dirac delta function as the time function *g(t)* in Eqn. (2.12), however, numerical reliability and accuracy will inherently be a problem because they both correspond to a white frequency spectrum. To avoid such practical difficulties, it is logical to employ a smoother time variation such as B-spline functions for *g(t)* in a BEM (e.g., see Rizos and Karabalis 1994, Rizos and Zhou 2006). The improved smoothness of the point load Green's function brings some advantages in the numerics. For one, Fourier transforms of B-spline functions can be evaluated in close form. Secondly, their frequency spectrum decays strongly, reducing the need to compute the frequency-domain Green's functions at very high frequencies, the task of which is daunting. There are more frequency-domain than time-domain Green's functions available in the literature as well. In this chapter, the development of a 3-D time-domain BEM via a frequency-domain approach is described as an approach in its own right as well as a useful basis to validate the development of a direct time-domain Green's functions in the research program

5.2 Statement of the problem

5.2.1 Elastodynamic Green's function for a Homogeneous half-space

For a homogeneous, isotropic, and linearly elastic half-space (see Figure 5.1 for the dual rectangular and cylindrical coordinate systems), Navier's equation of motion can be written as

$$(\lambda+2\mu)\nabla\left(\nabla\cdot\mathbf{u}(\mathbf{x},t)\right)-\mu\nabla\times\nabla\times\mathbf{u}(\mathbf{x},t)+\mathbf{f}(\mathbf{x},t)=\rho\frac{\partial^2\mathbf{u}(\mathbf{x},t)}{\partial t^2}, \tag{5.1}$$

where ρ stands for the density, λ and μ stand for the Lamé constants of the classical theory of elasticity, while t is the time, $\mathbf{x}$ is the coordinate vector, $\mathbf{u}$ is the displacement, and $\mathbf{f}$ is the body force respectively. The boundary conditions for the free surface at $z = 0$ are

$$\tau_{13}(\mathbf{x},t)=\tau_{23}(\mathbf{x},t)=\tau_{33}(\mathbf{x},t)=0. \tag{5.2}$$

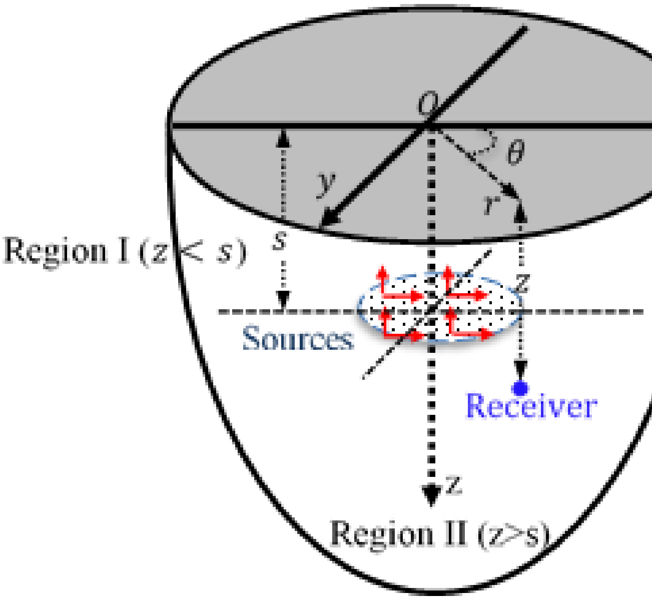

Figure 5.1: Homogeneous half-space under internal point load

A point load applied on the free surface or in the interior of the half-space can be specified by

$$\mathbf{f}(\mathbf{x},t)=\mathcal{F}\cdot B(t)\delta(\mathbf{x}-\mathbf{y})\mathbf{e}\,, \tag{5.3}$$

where $\mathcal{F}$ is the magnitude of the force, $\mathbf{e}$ is a unit vector in the direction of the force $\mathbf{f}$, and $B(t)$ is the cubic B-Spline basis function, defined as

$$B(t)=\begin{cases} \dfrac{32}{3}\dfrac{t^3}{\Delta T^3}, & 0\le t<\Delta T/4, \\ -32\dfrac{t^3}{\Delta T^3}+32\dfrac{t^2}{\Delta T^2}-8\dfrac{t}{\Delta T}+\dfrac{2}{3}, & \Delta T/4\le t<2\Delta T/4, \\ 32\dfrac{t^3}{\Delta T^3}-64\dfrac{t^2}{\Delta T^2}+40\dfrac{t}{\Delta T}-\dfrac{22}{3}, & 2\Delta T/4\le t<3\Delta T/4, \\ -\dfrac{32}{3}\dfrac{t^3}{\Delta T^3}+32\dfrac{t^2}{\Delta T^2}-32\dfrac{t}{\Delta T}+\dfrac{32}{3}, & 3\Delta T/4\le t\le \Delta T, \\ 0, & \text{elsewhere}, \end{cases} \tag{5.4}$$

where ΔT is the width of B-Spline function that can be chosen to suit a particular problem.

For comparison, the linear, quadratic and cubic B-Spline basis functions in time-domain are plotted in Figure 5.2 and their corresoponding Fourier transforms are depicted in Figure 5.3. From the plots, one can see that frequency spectrum of higher-order B-Spline functions are generally smoother and narrower than those of lower-order B-Spline functions. In this implementation, the cubic B-Spline is adopted for *g(t)*.

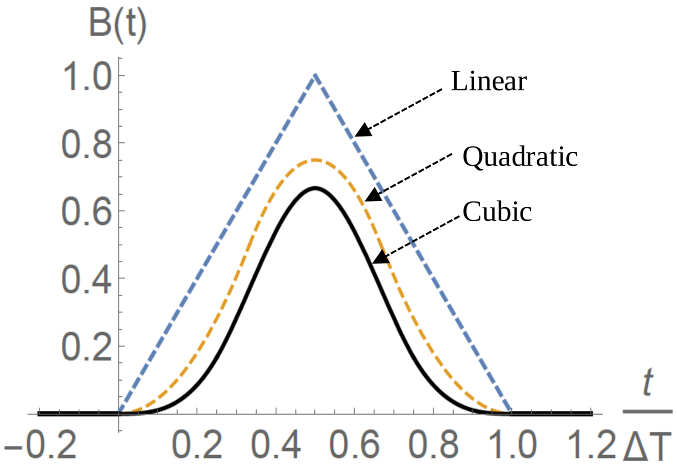

Figure 5.2: The linear, quadratic and cubic order B-Spline basis functions

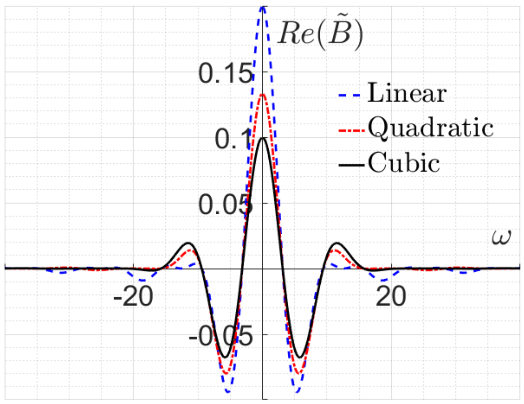

(a) Real part of the Fourier transforms

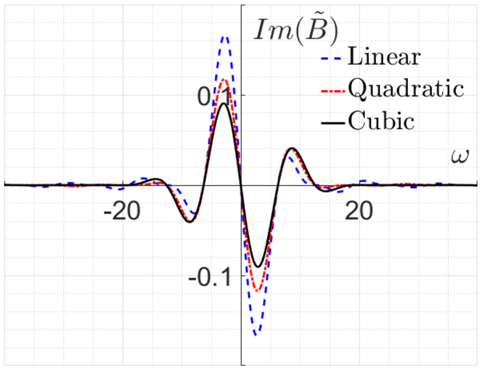

(b) Imaginary part of the Fourier transforms

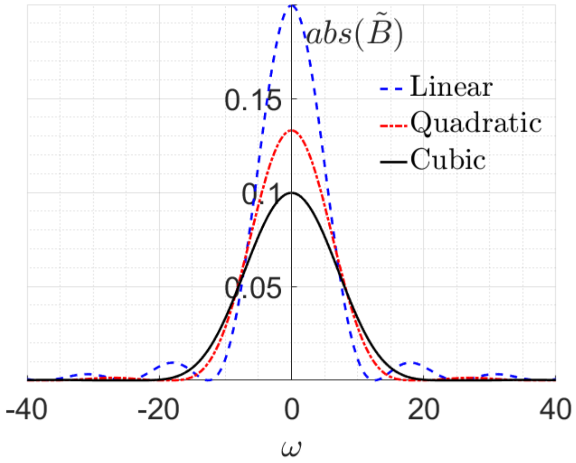

(c) Magnitude of the Fourier transforms

Figure 5.3: Fourier transforms of the linear, quadratic and cubic B-Spline basis functions

5.2.2 A horizontally multi-layered half-space

Depicted in Figure 5.4 is a homogeneous elastic half-space overlaid by n parallel piecewise-homogeneous elastic layers. A coordinate system is ataached to the half-space with the origin located at the top free-surface and the positive $z-$direction pointing downward. Bounded by the upper and lower interfaces located at depths z_{j-1} and z_j respectively, the domain of the j^{th} layer is denoted by $\mathcal{L}_j$ and characterized by the material parameters ρ_j, ν_j, μ_j, thickness $h_j = z_j - z_{j-1}$, which can be formally written as

$$\begin{aligned} \mathcal{L}_j = \{(r,\theta,z;\rho,\nu,\mu) \,|\, 0 \le r < \infty, 0 \le \theta < 2\pi, z_{j-1} < z < z_j, \\ \mu = \mu_j, \lambda = \lambda_j, \rho = \rho_j\}, \quad j = 1,2,\ldots,n \end{aligned}. \tag{5.5}$$

Likewise, the domain of the underlying half-space is denoted by

$$\begin{aligned} \mathcal{L}_{n+1} = \{(r,\theta,z;\rho,\nu,\mu) \,|\, 0 \le r < \infty, 0 \le \theta < 2\pi, z_n < z < z_\infty, \\ \mu = \mu_{n+1}, \lambda = \lambda_{n+1}, \rho = \rho_{n+1}\} \end{aligned}. \tag{5.6}$$

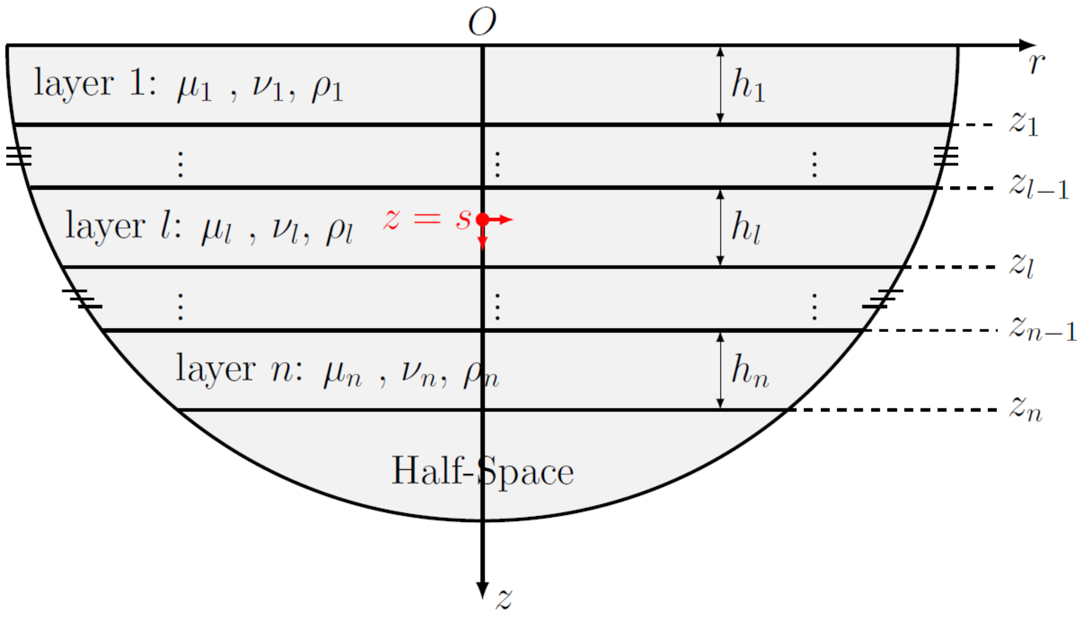

Figure 5.4: A piecewise homogeneous horizontally multi-layered half-space

Of interest is the time-domain response of the layered half-space due to an arbitrarily located point load with a time variation of $B(t)$ by a frequency-domain synthesis.

5.3 From frequency domain to time domain

To derive the time-domain fundamental solutions, existing Green's functions in the frequency domain is a natural point of departure. With the Green's function of displacement $\mathbf{U}(r,\theta,z;s;\omega)$ corresponding to a time harmonic load with a time factor of $e^{i\omega t}$ in Pak (1987), the time-domain Green's function corresponding to the concentrated cubic B-spline loading defined by Eqn. (5.3) can be obtained by an inverse Fourier transform in the form of

$$\mathbf{u}(r,\theta,z;s;t)=\frac{1}{2\pi}\int_{-\infty}^{\infty}\tilde{B}(\omega)\mathbf{U}(r,\theta,z;s;\omega)e^{i\omega t}d\omega, \tag{5.7}$$

where $\tilde{B}(\omega)$ is the Fourier transform of the cubic B-Spline function whose the exact form is

$$\tilde{B}(\omega)=\frac{1}{\sqrt{2\pi}}\int_{-\infty}^{\infty}B(t)e^{-i\omega t}dt=32\sqrt{\frac{2}{\pi}}\frac{e^{-i\Delta T\omega}\left(e^{i\Delta T\omega/4}-1\right)^{4}}{\Delta T^{3}\omega^{4}}. \tag{5.8}$$

The numerical evaluation of the improper Fourier integral over the infinite interval in Eqn. (5.7) is obviously difficult. Numerical integrations of it can be carried out only if it is analytically justifiable to truncate the lower and/or upper limits to a reasonable value. For such a purpose, it is observed from Eqn. (5.8) that $\tilde{B}(\omega)$ decays strongly with increasing ω at the rate of

$$\tilde{B}(\omega)\sim O\left(\frac{1}{\omega^{4}}\right).$$

With such a characteristics, even though $\mathbf{U}$ and $e^{i\omega t}$ do not decay with increasing ω, the whole integrand $\tilde{B}(\omega)\mathbf{U}(r,\theta,z;s;\omega)e^{i\omega t}$ in Eqn. (5.7) will decay quickly to 0 because of the strong decaying rate of $\tilde{B}(\omega)$. Accordingly, one may reduce Eqn. (5.7) computationally to

$$\mathbf{u}(r,\theta,z;s;t) \simeq \frac{1}{2\pi}\int_{-\omega_{trunc}}^{\omega_{trunc}} \tilde{B}(\omega)\mathbf{U}(r,\theta,z;s;\omega)e^{i\omega t}d\omega, \tag{5.9}$$

with a sufficiently large enough limit of ω_{trunc}.

5.3.1 Choice of $\boldsymbol{\omega_{trunc}}$

To ensure a high degree of accuracy in the evaluation of $\mathbf{u}(r,\theta,z;s;t)$, a sufficiently large ω_{trunc} should be taken but not to the extent that is computationally unnecesary. With the closed-form expression of $\tilde{B}(\omega)$, ω_{trunc} in this study is chosen such that

$$\left|\tilde{B}(\omega)\right| \le \alpha\tilde{B}(\omega)|_{\omega=0}, \ \forall|\omega| \ge \omega_{trunc}, \tag{5.10}$$

where α is a small value that specifies the degree of accuracy. It can be deduced from Eqn. (5.8) that the crtiterion can be given analytically as

$$\left|\tilde{B}(\omega)\right| \le \sqrt{\frac{2}{\pi}}\frac{32\times1\times2^4}{\Delta T^3\omega^4}, \ \tilde{B}(0) = \frac{\Delta T}{4\sqrt{2\pi}}. \tag{5.11}$$

Combining with Eqn. (5.10), it yields

$$\omega_{trunc} \equiv \frac{1}{\Delta T}\frac{8}{\alpha^{1/4}}. \tag{5.12}$$

In dimensionless form, one can define the frequency truncation limit as

$$\bar{\omega}_{trunc} \equiv \omega_{trunc}\frac{a}{c_s} = \frac{8}{\alpha^{1/4}}\frac{a}{\Delta T\cdot c_s} \tag{5.13}$$

where a is a basic reference length and c_s is the reference shear wave speed. For example, if one chooses $\alpha = 1e^{-4}$, then $\bar{\omega}_{trunc} = 80\frac{a}{\Delta T\cdot c_s}$.

5.3.2 Numerical Examples

To illustrate the idea of Fourier synthesis in this section, an example is presented in Figure 5.5 of the response computation for a point source and observation point both in the interior of a half-space that is described in the caption of Figure 5.5. In this example, loading point is put at $\mathbf{y}=(0,0,1)$, and the observation point at $\mathbf{x}=(10,0,4)$ in meters. The elastic parameters of the material are: $\mu=4Mpa$, $\rho=2000Kg/m^3$, and $\nu=0.25$. The width of the B-Spline pulse is $T=0.02\sec$, while the observation time is $t=0.05\sec$. The displacment Green's function $\mathbf{U}_1^1$ in the frequency-domain are shown in Figure 5.5(a) and (b) in complex notation. One can see that the magnitude of $\mathbf{U}_1^1$ doesn't decay as the frequency ω increases. A plot of Fourier transform of B(t) is shown in Figure 5.6. Notice that $\tilde{B}$ decays quickly to 0 with increasing ω, as discussed earlier in Eqn. (5.8). Accordingly, the whole integrand in Eqn. (5.9) which is the product of $\mathbf{U}$, $\tilde{B}$ and $e^{i\omega t}$ will decay quickly as ω increases for any *t* as illustrated in Figure 5.7.

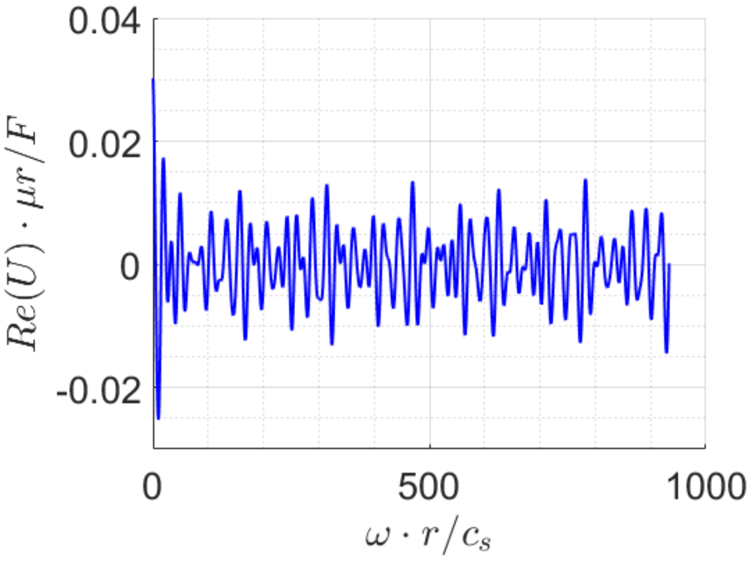

(a) Real part

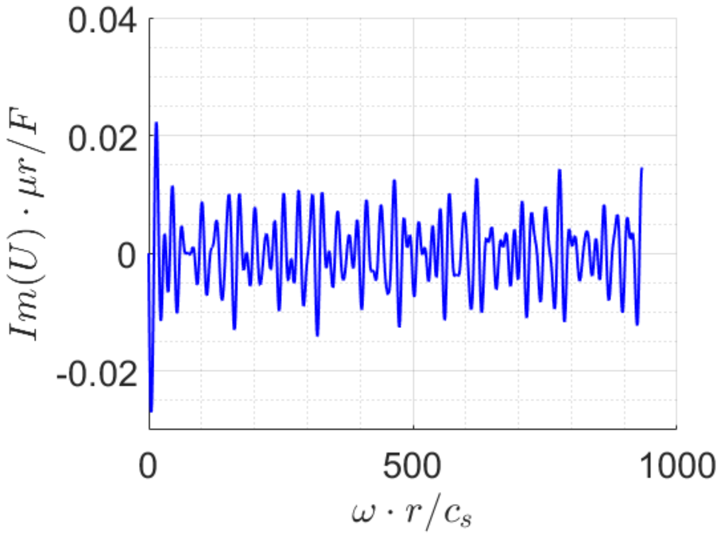

(b) Imaginary part

Figure 5.5: Green's function of displacement

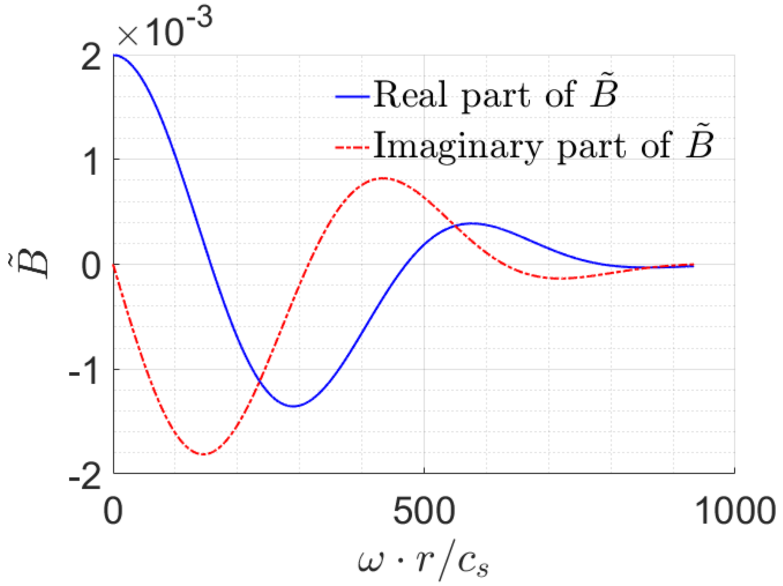

Figure 5.6: Cubic B-Spline basis function in frequency-domain

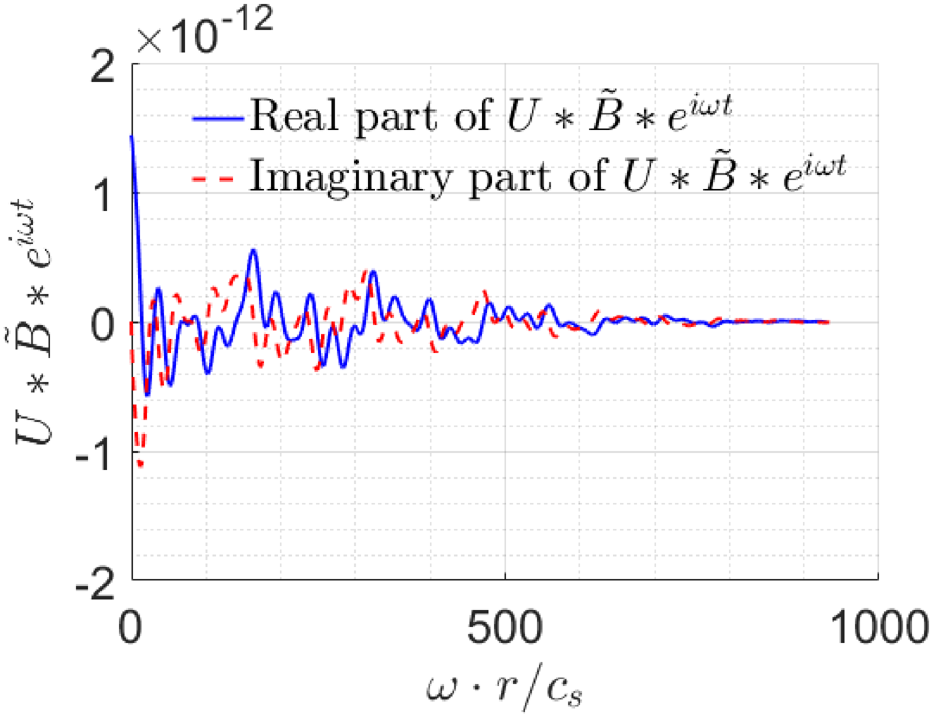

Figure 5.7: Behavior of the integrand as a function of frequency

5.4 Numerical aspects related to frequency-domain Green's function computations

The general point-load elastodynamic Green's function in the frequency domin for a homogeneous half-space can be found in Pak (1987). With a being a characteristic length, and the dimensionless parameters

$$\begin{aligned}
&\bar{r} = \frac{r}{a},\ \bar{z} = \frac{z}{a},\ \bar{s} = \frac{s}{a},\ \bar{\omega} = \frac{\omega}{\omega_0} = \frac{\omega a}{c_s},\\
&\bar{\xi} = \frac{\xi}{k_s},\ \bar{\alpha} = (\bar{\xi}^2 - c_s^2 / c_d^2)^{\frac{1}{2}},\ \bar{\beta} = (\bar{\xi}^2 - 1)^{\frac{1}{2}},\\
&\bar{R}^{\pm}\left(\bar{\xi}\right) = (2\bar{\xi}^2 - \bar{k}_s^2)^2 \pm 4\bar{\xi}^2\bar{\alpha}\bar{\beta},
\end{aligned} \tag{5.14}$$

one may cast the displacement and stress Green's functions due to a point load of magnitude $\mathcal{F}$ at a depth s in a homogeneous half-space in frequency domain can be cast in the form of

$$\begin{aligned}
\mathbf{U}\left(r,\theta,z;s;\omega\right) &= \frac{\mathcal{F}}{a\mu}\bar{\mathbf{U}}\left(\bar{r},\theta,\bar{z};\bar{s};\bar{\omega}\right),\\
\boldsymbol{\tau}\left(r,\theta,z;s;\omega\right) &= \frac{\mathcal{F}}{a^2}\bar{\boldsymbol{\tau}}\left(\bar{r},\theta,\bar{z};\bar{s};\bar{\omega}\right),
\end{aligned} \tag{5.15}$$

where the dimensionless displacements $\bar{\mathbf{U}}$ and stresses $\bar{\boldsymbol{\tau}}$ are defined as follows.

1) **For horizontal loading in $\boldsymbol{\theta = \theta_0}$ direction**

$$\begin{aligned}
\bar{U}_r^h\left(\bar{r},\theta,\bar{z};\bar{s};\bar{\omega}\right) &= \frac{\cos\left(\theta-\theta_0\right)\bar{\omega}}{4\pi}\int_0^\infty \left\{\begin{array}{l} \bar{\gamma}_1\left(\bar{z},\bar{s};\bar{\omega};\bar{\xi}\right)\bar{\xi}\left[J_0\left(\bar{\xi}\bar{\omega}\bar{r}\right) - J_2\left(\bar{\xi}\bar{\omega}\bar{r}\right)\right] \\ +\bar{\gamma}_2\left(\bar{z},\bar{s};\bar{\omega};\bar{\xi}\right)\bar{\xi}\left[J_0\left(\bar{\xi}\bar{\omega}\bar{r}\right) + J_2\left(\bar{\xi}\bar{\omega}\bar{r}\right)\right] \end{array}\right\} d\bar{\xi}\\
\bar{U}_\theta^h\left(\bar{r},\theta,\bar{z};\bar{s};\bar{\omega}\right) &= \frac{-\sin\left(\theta-\theta_0\right)\bar{\omega}}{4\pi}\int_0^\infty \left\{\begin{array}{l} \bar{\gamma}_1\left(\bar{z},\bar{s};\bar{\omega};\bar{\xi}\right)\bar{\xi}\left[J_0\left(\bar{\xi}\bar{\omega}\bar{r}\right) + J_2\left(\bar{\xi}\bar{\omega}\bar{r}\right)\right] \\ +\bar{\gamma}_2\left(\bar{z},\bar{s};\bar{\omega};\bar{\xi}\right)\bar{\xi}\left[J_0\left(\bar{\xi}\bar{\omega}\bar{r}\right) - J_2\left(\bar{\xi}\bar{\omega}\bar{r}\right)\right] \end{array}\right\} d\bar{\xi}\ ,\\
\bar{U}_z^h\left(\bar{r},\theta,\bar{z};\bar{s};\bar{\omega}\right) &= \frac{\cos\left(\theta-\theta_0\right)\bar{\omega}}{2\pi}\int_0^\infty \bar{\Omega}_1\left(\bar{z},\bar{s};\bar{\omega};\bar{\xi}\right)\bar{\xi}J_1\left(\bar{\xi}\bar{\omega}\bar{r}\right)d\bar{\xi}
\end{aligned} \tag{5.16}$$

2) For vertical loading in $z-$ direction

$$\begin{array}{l}
\bar{U}_r^v\left(\bar{r},\theta,\bar{z};\bar{s};\bar{\omega}\right)=-\dfrac{\bar{\omega}}{2\pi}\displaystyle\int_0^\infty\bar{\gamma}_3\left(\bar{z},\bar{s};\bar{\omega};\bar{\xi}\right)\bar{\xi}\,J_1\left(\bar{\xi}\bar{\omega}\bar{r}\right)d\bar{\xi}\\
\bar{U}_\theta^v\left(\bar{r},\theta,\bar{z};\bar{s};\bar{\omega}\right)=0 \qquad\qquad ,\\
\bar{U}_z^v\left(\bar{r},\theta,\bar{z};\bar{s};\bar{\omega}\right)=\dfrac{\bar{\omega}}{2\pi}\displaystyle\int_0^\infty\bar{\Omega}_2\left(\bar{z},\bar{s};\bar{\omega};\bar{\xi}\right)\bar{\xi}\,J_0\left(\bar{\xi}\bar{\omega}\bar{r}\right)d\bar{\xi}
\end{array} \tag{5.17}$$

with

$$\bar{\gamma}_1\left(\bar{z},\bar{s};\bar{\omega};\bar{\xi}\right)=\left\{\begin{array}{l}
\dfrac{1}{2}\{\dfrac{\bar{\xi}^2}{\bar{\alpha}}e^{-\bar{\alpha}\bar{\omega}|\bar{z}-\bar{s}|}-\bar{\beta}e^{-\bar{\beta}\bar{\omega}|\bar{z}-\bar{s}|}\\
-\dfrac{\bar{R}^+\left(\bar{\xi}\right)}{\bar{R}^-\left(\bar{\xi}\right)}\left(\dfrac{\bar{\xi}^2}{\bar{\alpha}}e^{-\bar{\alpha}\bar{\omega}\left(\bar{z}+\bar{s}\right)}+\bar{\beta}e^{-\bar{\beta}\bar{\omega}\left(\bar{z}+\bar{s}\right)}\right)\\
+\dfrac{4\bar{\xi}^2\bar{\beta}\left(2\bar{\xi}^2-1\right)}{\bar{R}^-\left(\bar{\xi}\right)}\left(e^{-\bar{\omega}\left(\bar{\beta}\bar{z}+\bar{\alpha}\bar{s}\right)}+e^{-\bar{\omega}\left(\bar{\beta}\bar{s}+\bar{\alpha}\bar{z}\right)}\right)
\end{array}\right\}, \tag{5.18a}$$

$$\bar{\gamma}_2\left(\bar{z},s;\bar{\omega};\bar{\xi}\right)=\frac{1}{2\bar{\beta}}\left(e^{-\bar{\beta}\bar{\omega}|\bar{z}-\bar{s}|}+e^{-\bar{\beta}\bar{\omega}\left(\bar{z}+\bar{s}\right)}\right)\ , \tag{5.18b}$$

$$\bar{\gamma}_3\left(\bar{z},\bar{s};\bar{\omega};\bar{\xi}\right)=\left\{\begin{array}{l}
sgn\left(\bar{z}-\bar{s}\right)\dfrac{\bar{\xi}}{2}\left(e^{-\bar{\alpha}\bar{\omega}|\bar{z}-\bar{s}|}-e^{-\bar{\beta}\bar{\omega}|\bar{z}-\bar{s}|}\right)\\
+\dfrac{\bar{\xi}}{2}\dfrac{\bar{R}^+\left(\bar{\xi}\right)}{\bar{R}^-\left(\bar{\xi}\right)}\left(e^{-\bar{\alpha}\bar{\omega}\left(\bar{z}+\bar{s}\right)}+e^{-\bar{\beta}\bar{\omega}\left(\bar{z}+\bar{s}\right)}\right)\\
-\dfrac{2\bar{\xi}\left(2\bar{\xi}^2-1\right)}{\bar{R}^-\left(\bar{\xi}\right)}\left(\bar{\alpha}\bar{\beta}e^{-\bar{\omega}\left(\bar{\beta}\bar{z}+\bar{\alpha}\bar{s}\right)}+\bar{\xi}^2e^{-\bar{\omega}\left(\bar{\beta}\bar{s}+\bar{\alpha}\bar{z}\right)}\right)
\end{array}\right\}, \tag{5.18c}$$

$$\bar{\Omega}_1\left(\bar{z},\bar{s};\bar{\omega};\bar{\xi}\right)=\left\{\begin{array}{l}
-sgn\left(\bar{z}-\bar{s}\right)\dfrac{\bar{\xi}}{2}\left(e^{-\left(\bar{\alpha}\bar{\omega}|\bar{z}-\bar{s}|\right)}-e^{-\left(\bar{\beta}\bar{\omega}|\bar{z}-\bar{s}|\right)}\right)\\
+\dfrac{\bar{\xi}}{2}\dfrac{\bar{R}^+\left(\bar{\xi}\right)}{\bar{R}^-\left(\bar{\xi}\right)}\left(e^{-\bar{\alpha}\bar{\omega}\left(\bar{z}+\bar{s}\right)}+e^{-\bar{\beta}\bar{\omega}\left(\bar{z}+\bar{s}\right)}\right)\\
-\dfrac{2\bar{\xi}\left(2\bar{\xi}^2-1\right)}{\bar{R}^-\left(\bar{\xi}\right)}\left(\bar{\xi}^2e^{-\bar{\omega}\left(\bar{\beta}\bar{z}+\bar{\alpha}\bar{s}\right)}+\bar{\alpha}\bar{\beta}e^{-\bar{\omega}\left(\bar{\beta}\bar{s}+\bar{\alpha}\bar{z}\right)}\right)
\end{array}\right\}, \tag{5.18d}$$

$$\bar{\Omega}_2\left(\bar{z},\bar{s};\bar{\omega};\bar{\xi}\right)=\left\{\begin{matrix} -\dfrac{\bar{\alpha}}{2}e^{-\bar{\alpha}\bar{\omega}\left|\bar{z}-\bar{s}\right|}+\dfrac{\bar{\xi}^2}{2\bar{\beta}}e^{-\bar{\beta}\bar{\omega}\left|\bar{z}-\bar{s}\right|} \\ -\dfrac{1}{2}\dfrac{\bar{R}^+\left(\bar{\xi}\right)}{\bar{R}^-\left(\bar{\xi}\right)}\left(\bar{\alpha}e^{-\bar{\alpha}\bar{\omega}\left(\bar{z}+\bar{s}\right)}+\dfrac{\bar{\xi}^2}{\bar{\beta}}e^{-\bar{\beta}\bar{\omega}\left(\bar{z}+\bar{s}\right)}\right) \\ +\dfrac{2\bar{\xi}^2\bar{\alpha}\left(2\bar{\xi}^2-1\right)}{\bar{R}^-\left(\bar{\xi}\right)}\left(e^{-\bar{\omega}\left(\bar{\beta}\bar{z}+\bar{\alpha}\bar{s}\right)}+e^{-\bar{\omega}\left(\bar{\beta}\bar{s}+\bar{\alpha}\bar{z}\right)}\right)\end{matrix}\right\}. \qquad (5.19e)$$

5.4.1 Evaluation by asymptotic decomposition

Owing to the complex behavior of the integrands involved, a direct evaluation of the improper integrals in Eqn. (5.16) and (5.17) is difficult both analytically and numerically. The situation is further complicated by the intrinsic singular behavior of the Green's functions in case of observation point approaching loading point. One can however use the method of asymptotic decomposition of Pak (1987) to extract analytically from the integral form of the Green's function the singular component so that the residual part of the integral can be evaluated numerically in a robust manner. Taking $\bar{U}_z^v$ in equation (5.17) as an example, one may write,

$$\bar{U}_z^v=\left[\bar{U}_z^v\right]_1+\left[\bar{U}_z^v\right]_2,$$

where the subscripts "1" and "2" denote the analytically- and numerically-evaluated parts of the Green's function respectively. They are defined respectively by

$$[\bar{U}_i^k]_1=\frac{\bar{\omega}}{2\pi}\int_0^\infty \bar{\Upsilon}^{\text{asym}}\left(\bar{z},\bar{s};\bar{\omega};\bar{\xi}\right)\bar{\xi}J_n\left(\bar{\xi}\bar{\omega}\bar{r}\right)d\bar{\xi},\ i=r,\theta,z,\ k=v,h,\ n=0,1,2 \qquad (5.20a)$$

$$\left[\bar{U}_i^k\right]_2=\frac{\bar{\omega}}{2\pi}\int_0^\infty\left(\bar{\Upsilon}\left(\bar{z},\bar{s};\bar{\omega};\bar{\xi}\right)-\bar{\Upsilon}^{\text{asym}}\left(\bar{z},\bar{s};\bar{\omega};\bar{\xi}\right)\right)\bar{\xi}J_n\left(\bar{\xi}\bar{\omega}\bar{r}\right)d\bar{\xi}, \qquad (5.20b)$$

where $\bar{\Upsilon}$ can be $\bar{\gamma}_1$, $\bar{\gamma}_2$, $\bar{\gamma}_3$, $\bar{\Omega}_1$ and $\bar{\Omega}_2$ with $\bar{\Upsilon}^{\text{asym}}\left(\bar{z},\bar{s};\bar{\omega};\bar{\xi}\right)=\underset{\bar{\xi}\to\infty}{\text{Asym}}\left\{\bar{\Upsilon}\left(\bar{z},\bar{s};\bar{\omega};\bar{\xi}\right)\right\}$.

Specifically, the asymptotic kernels are

$$\bar{\gamma}_1^{asym}\left(\bar{z},\bar{s};\bar{\varpi};\bar{\xi}\right)=\frac{1}{8\left(1-\nu\right)\bar{\xi}}\left\{\begin{array}{l}e^{-\bar{\xi}\bar{\varpi}\bar{d}_1}\left(-\bar{d}_1\bar{\varpi}\bar{\xi}+3-4\nu\right)\\+e^{-\bar{\xi}\bar{\varpi}\bar{d}_2}\left(\begin{array}{l}2\overline{zs}\,\bar{\varpi}^2\bar{\xi}^2-\left(3-4\nu\right)\bar{d}_2\bar{\varpi}\bar{\xi}\\+\left(5-12\nu+8\nu^2\right)\end{array}\right)\end{array}\right\}, \tag{5.21a}$$

$$\bar{\gamma}_2^{asym}\left(\bar{z},\bar{s};\bar{\varpi};\bar{\xi}\right)=\frac{1}{2\bar{\xi}}\left\{e^{-\bar{\xi}\bar{\varpi}\bar{d}_1}+e^{-\bar{\xi}\bar{\varpi}\bar{d}_2}\right\}, \tag{5.21b}$$

$$\bar{\gamma}_3^{asym}\left(\bar{z},\bar{s};\bar{\varpi};\bar{\xi}\right)=\frac{1}{8\left(1-\nu\right)\bar{\xi}}\left\{\begin{array}{l}-e^{-\bar{\xi}\bar{\varpi}\bar{d}_1}\left(\bar{d}_3\bar{\varpi}\bar{\xi}\right)\\+e^{-\bar{\xi}\bar{\varpi}\bar{d}_2}\left(\begin{array}{l}-2\overline{zs}\,\bar{\varpi}^2\bar{\xi}^2-\left(3-4\nu\right)\bar{d}_3\bar{\varpi}\bar{\xi}\\+\left(4-4\nu\right)\left(1-2\nu\right)\end{array}\right)\end{array}\right\}, \tag{5.21c}$$

$$\bar{\Omega}_1^{asym}\left(\bar{z},\bar{s};\bar{\varpi};\bar{\xi}\right)=\frac{1}{8\left(1-\nu\right)\bar{\xi}}\left\{\begin{array}{l}e^{-\bar{\xi}\bar{\varpi}\bar{d}_1}\left(\bar{d}_3\bar{\varpi}\bar{\xi}\right)\\+e^{-\bar{\xi}\bar{\varpi}\bar{d}_2}\left(\begin{array}{l}-2\overline{zs}\,\bar{\varpi}^2\bar{\xi}^2+\left(3-4\nu\right)\bar{d}_3\bar{\varpi}\bar{\xi}\\+\left(4-4\nu\right)\left(1-2\nu\right)\end{array}\right)\end{array}\right\}, \tag{5.21d}$$

$$\bar{\Omega}_2^{asym}\left(\bar{z},\bar{s};\bar{\varpi};\bar{\xi}\right)=\frac{1}{8\left(1-\nu\right)\bar{\xi}}\left\{\begin{array}{l}e^{-\bar{\xi}\bar{\varpi}\bar{d}_1}\left(\bar{d}_3\bar{\varpi}\bar{\xi}+3-4\nu\right)\\+e^{-\bar{\xi}\bar{\varpi}\bar{d}_2}\left(\begin{array}{l}2\overline{zs}\,\bar{\varpi}^2\bar{\xi}^2+\left(3-4\nu\right)\bar{d}_2\bar{\varpi}\bar{\xi}\\+\left(5-12\nu+8\nu^2\right)\end{array}\right)\end{array}\right\}, \tag{5.21e}$$

As pointed out by Pak and Guzina (2001), the analytically-evaluated parts of the Green's functions are identical to Mindlin (1936)'s static point-load solution for a homogeneous half-space which is a special case of the bi-material Green's function in Guzina and Pak (1999).

5.4.2 Numerical integration of residual integrals

As mentioned earlier, the residual integrands after the asymptotic or singularity extraction are designed to be decaying quickly with increasing $\bar{\xi}$ so that the semi-infinite integrals of the type of Eqn. (5.20b) can be evaluated numerically with a suitable truncation of the upper limit. It's should be noted, however, that the integrands generally have three singularities along the formal path of inversion integration along the real axis in the complex dimensionless $\bar{\xi}-$ plane at the branch points of $\bar{\alpha}$ and $\bar{\beta}$ at $\frac{c_s}{c_d}$ and 1, and the Rayleigh pole at $\frac{c_s}{c_R}$ where c_R denotes the Rayleigh wave speed. By virtue of the analyticity of the integrands, on the other hand, the path of integration can be deformed suitably to avoid these singularities. In this study, the simple triangular path depicted in Figure 5.8 and chosen by Pak (1987) is adopted. The height h of the triangular path can be adjusted to be tangent to the formal steepest decent path as shown in the figure) near the origin for any of the specific exponential kermels in the Green's function if desired.

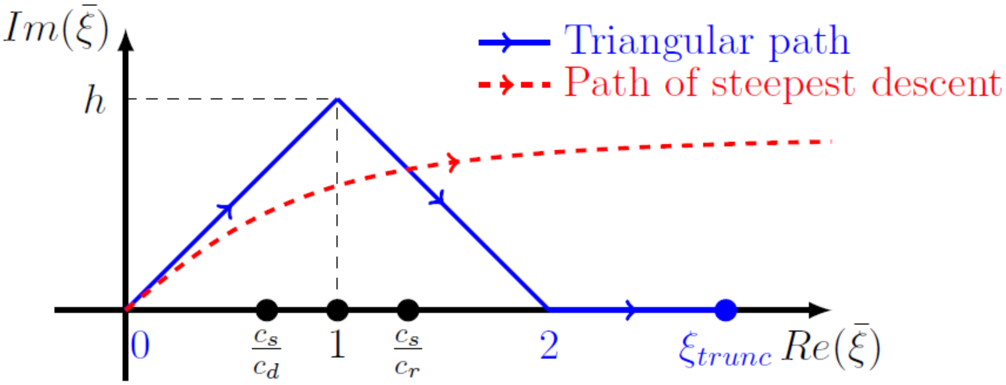

Figure 5.8: Deformed path of integration.

One of the advantages in using the triangular path is that the integrands are smoother and nonsingular along it. As an illustration, the variation of the term $\frac{\bar{\xi}^3}{\bar{\beta}} e^{-\bar{\beta}\bar{\omega}\bar{d}_1} J_0\left(\bar{\xi}\bar{\omega}\bar{r}\right)$ in Eqn. (5.17) is plotted in Figure 5.9. From the figure, it can be seen that both the real and imaginary part of the term oscillate rapidly along the real axis (i.e., the formal path) while it's much smoother along Pak's triangular path as well as the formal path of steepest descent.

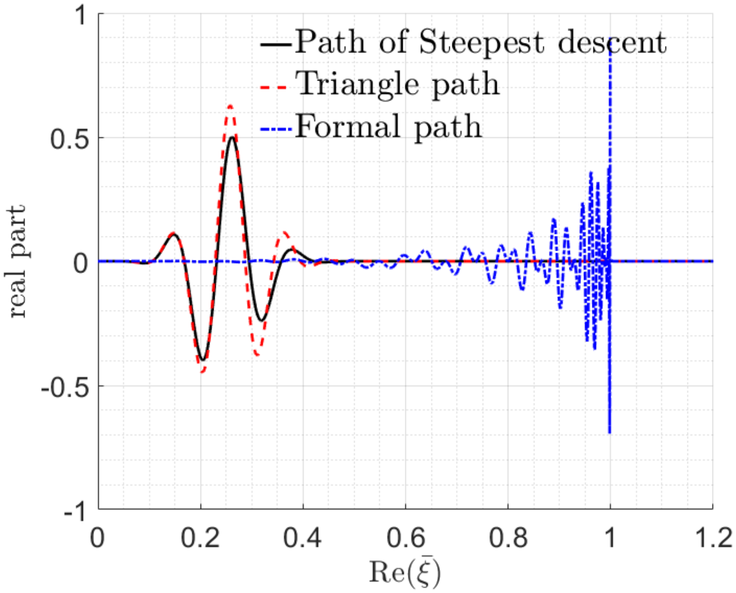

(a) Real part

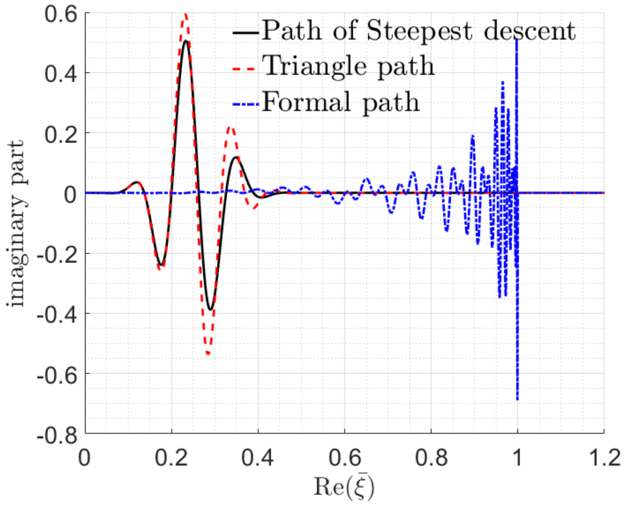

(b) Imaginary part

Figure 5.9: Variation of $\frac{\bar{\xi}^3}{\bar{\beta}} e^{-\bar{\beta}\bar{\varpi}\bar{d}_1} J_0\left(\bar{\xi}\bar{\varpi}\bar{r}\right)$ along the different paths for $\bar{d}_1 = 1, \bar{r} = 0.5, \bar{\varpi} = 100$ and triangular height $h = 1$. The steepest descent path is defined by $\bar{\xi} = a + ib$ with $b = \sqrt{a^2 / \left(1 + a^2\right)}$, for $a \geq 0$.

The triangular path has a further advantage than the steepest decent path in that the whole integrand generally decays more rapidly along the former than the latter for large $\bar{\xi}$ (see Figure 5.10). This is because the Bessel function decays more rapidly along the real axis than on the steepest descent path. In this study, numerical integrations for all terms were conducted along the same triangular path for computational efficiency with the height h= 1.

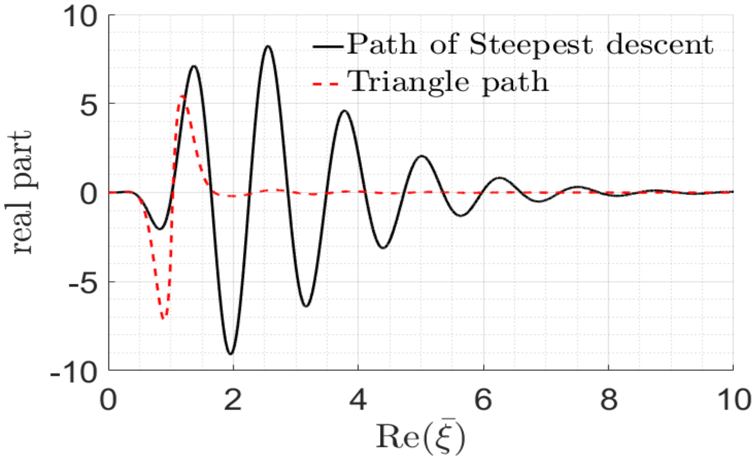

(a) Real part

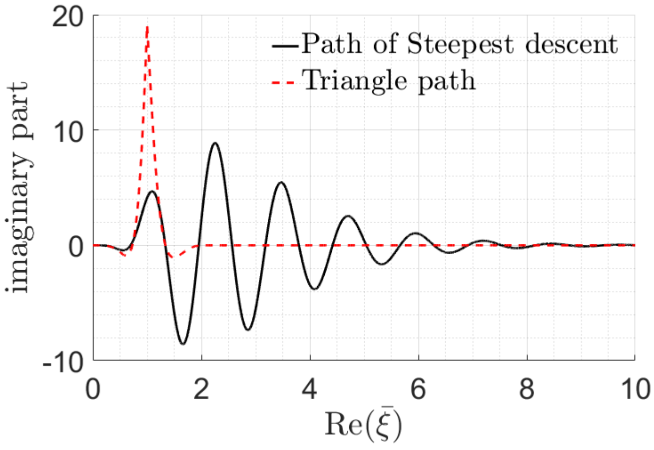

(b) Imaginary part

Figure 5.10: Variation of $\frac{\bar{\xi}^3}{\bar{\beta}} e^{-\bar{\beta}\bar{\varpi}\bar{d}_1} J_0\left(\bar{\xi}\bar{\varpi}\bar{r}\right)$ with $\bar{d}_1 = 0.2, \bar{r} = 1, \bar{\varpi} = 5$ along the paths in Figure 5.8.

In the examples shown in Figure 5.9 and Figure 5.10, the integrand decays rapidly due to the exponential term $e^{-\bar{\beta}\bar{\varpi}\bar{d}_1}$ and the Bessel function $J_0\left(\bar{\xi}\bar{\varpi}\bar{r}\right)$, thus the upper limit of the integration can be truncated. When $\bar{d}_1=0$, i.e. source point and observation point are in the same depth, however, the exponential term degenerates to 1 and the decay provided by the Bessel function is insufficient in the original integrand for a legitmate truncation of the integration limit. This is another reason behind the method of asymptotic decomposition of Pak (1987). Consider the example shown in Figure 5.11, one can see that the original integrand $F\left(\bar{\xi}\right)$ with a zero exponent (i.e., d_1=0) in the exponential term actually grows rather than decays with increasing $\bar{\xi}$. On the other hand, the residual integrand that is left behind after $F^{asym}\left(\bar{\xi}\right)$ is extracted decays strongly to 0 (see Figure 5.11(b)).

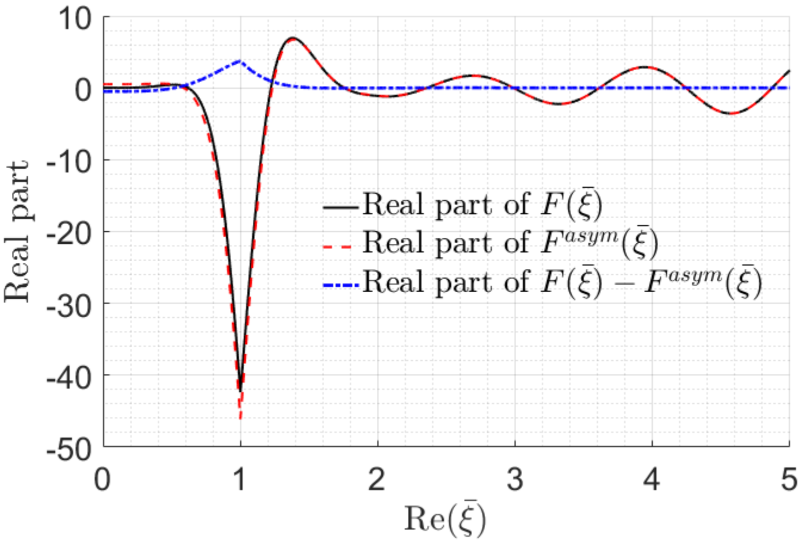

(a) Real part

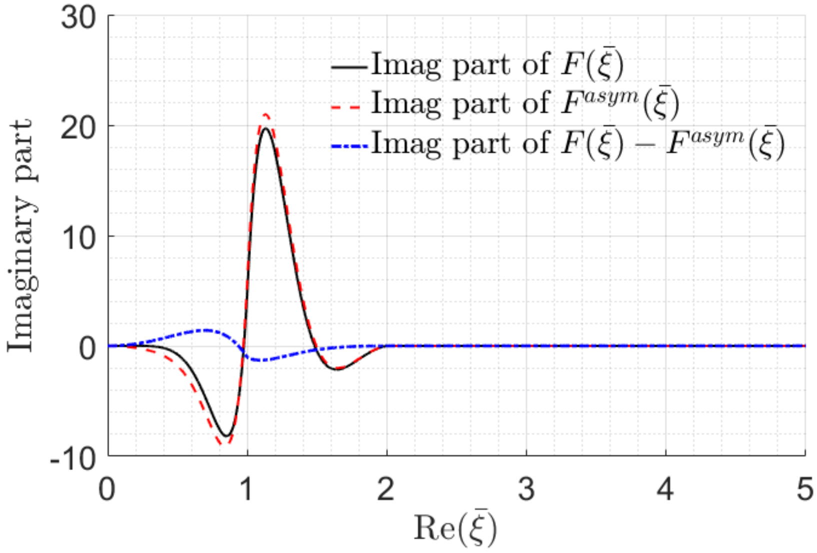

(b) Imaginary part

Figure 5.11: Asymptotic decomposition. $F\left(\bar\xi\right) = \frac{\bar\xi^{3}}{\bar\beta} e^{-\bar\beta\bar\varpi\bar d_1} J_0\left(\bar\xi\bar\varpi\bar r\right)$, $F^{asym}\left(\bar\xi\right) = \bar\xi\left(\bar\xi + \frac{1}{2\bar\xi} + \frac{\bar\varpi\bar d_1}{2}\right) e^{-\bar\xi\bar\varpi\bar d_1} J_0\left(\bar\xi\bar\varpi\bar r\right)$, with $\bar d_1 = 0, \bar r = 1, \bar\varpi = 5$. Variation is plotted along triangle path.

5.5 Numerical results

5.5.1 Verification with full-space Green's function

For verification, the proposed solution is checked against the Stokes' exact solution for a full-space. In this example, the source point in the full-space is taken to be $\mathbf{y} = \left(0,0,0\right)$, and the observation at $\mathbf{x} = \left(1,0,4\right)$ in meters. The material parameters for the homogeneous full-space are $\mu = 20MPa$, $\rho = 1730Kg/m^3$, $\nu = 0.25$ and the non-zero duration of the B-Spline loading function is set to be $\Delta T = 0.01\sec$. The time histories of the four non-zero components of the displacement are plotted in Figure 5.12, with the Fourier synthesized solution agreeing very well with Stokes' solution. In the display, $u_i^j(\mathbf{x};\mathbf{y};t)$ stands for the i th displacement component under a unit point load at j th direction.

.

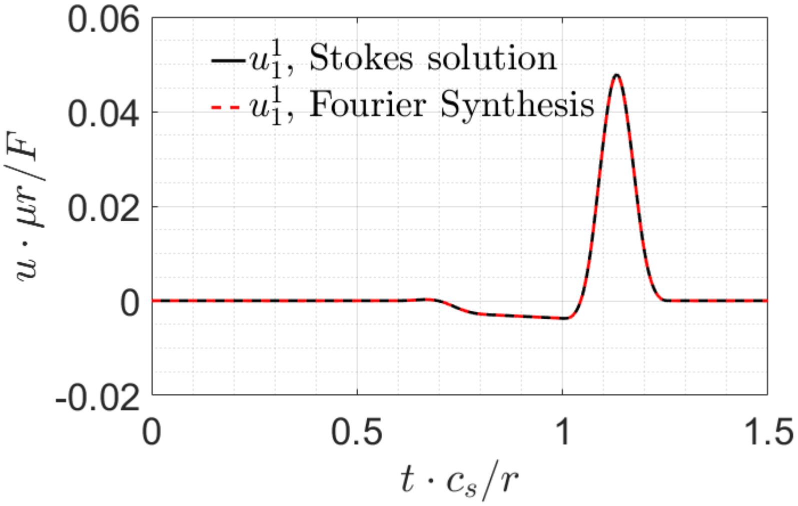

(a) u_1^1

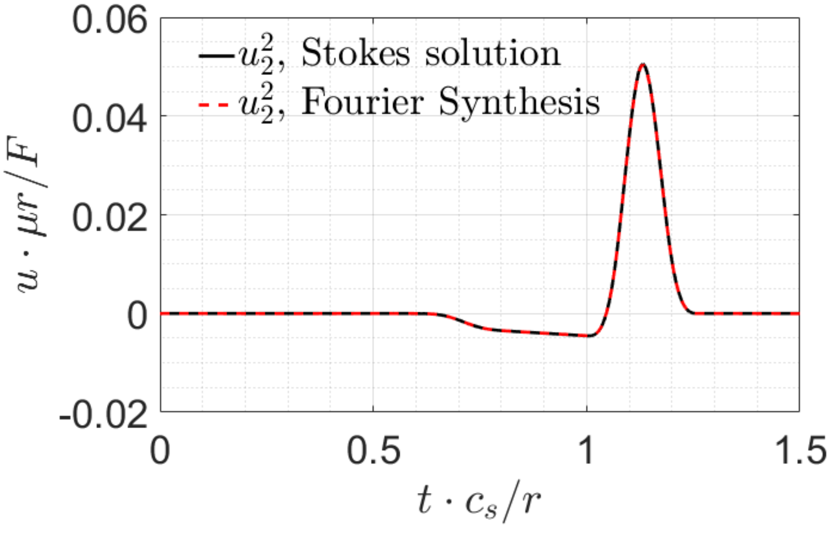

(b) u_2^2

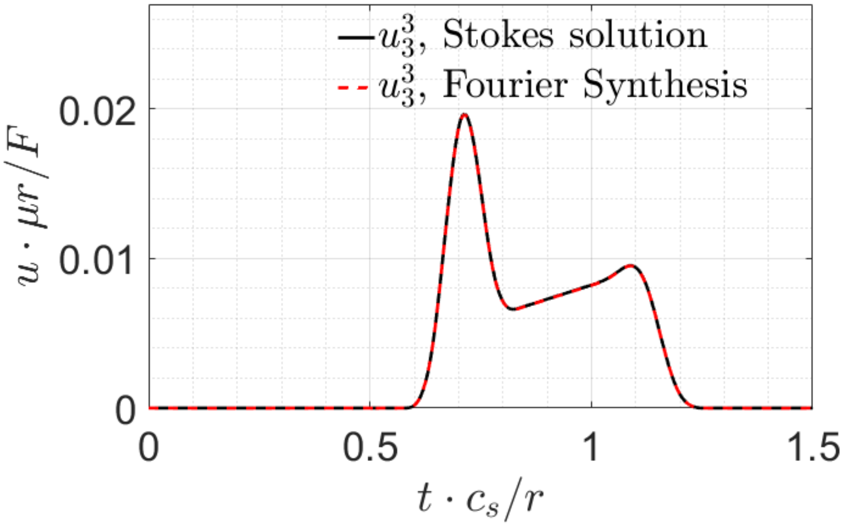

(c) u_3^3

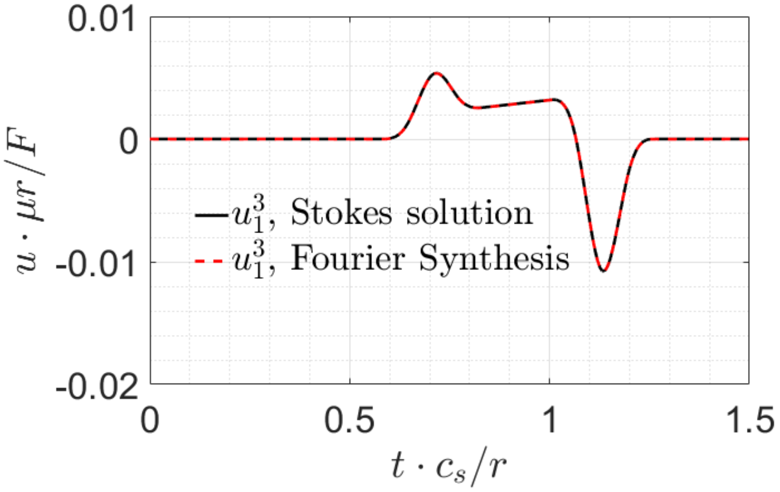

(d) u_1^3

Figure 5.12: Displacement histories for the case where both the source and observation point in a full-space.

5.5.2 Case of source and observation points both on surface of half-space

There is special interest in the case of having both the source and observation points located on the surface of a homogenous half-space and far apart (e.g. Lamb 1904) so that P-, S- and Rayleigh- wave generated by the source point will arrive at the observation point distinctly. To illustrate an example of such a case, the source point is taken at $\mathbf{y}=(0,0,0)$ and the observation point at $\mathbf{x}=(20,0,0)$, while the time function of the unit point load is taken to be cubic B-Spline function with a width of $\Delta T=0.02sec$. The displacement Green's function obtained by Fourier transform as described in this paper is compared with the results of Kausel (2012) in Figure 5.13. It is evident that the solutions agrees very well. On can notice that most of displacement response components have 3 identifiable moments of arrivial corresponding to P-, S- and Rayleigh-wave, although some are clearer than others.

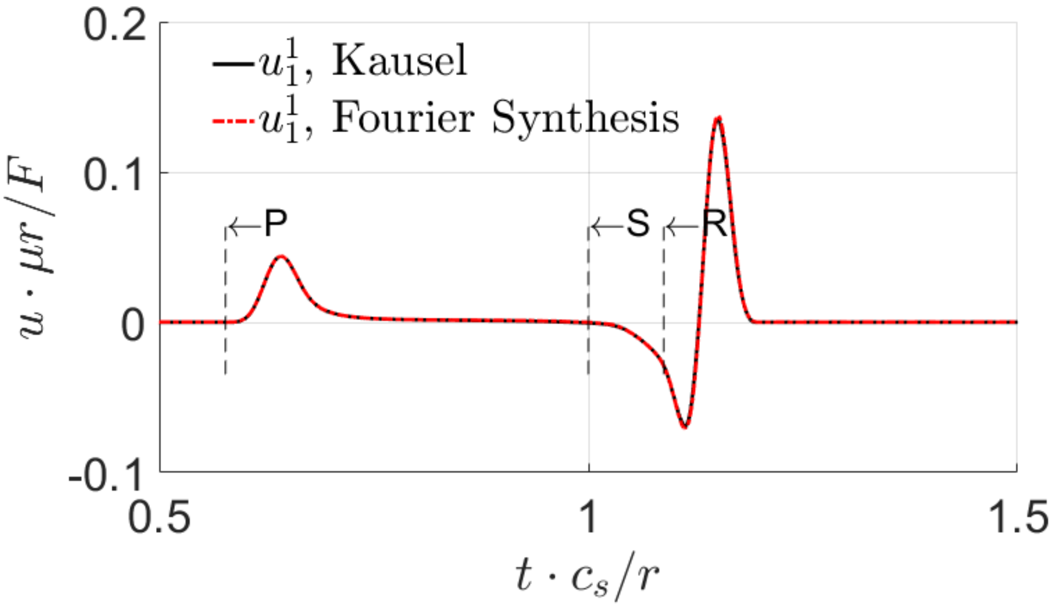

(a) u_1^1

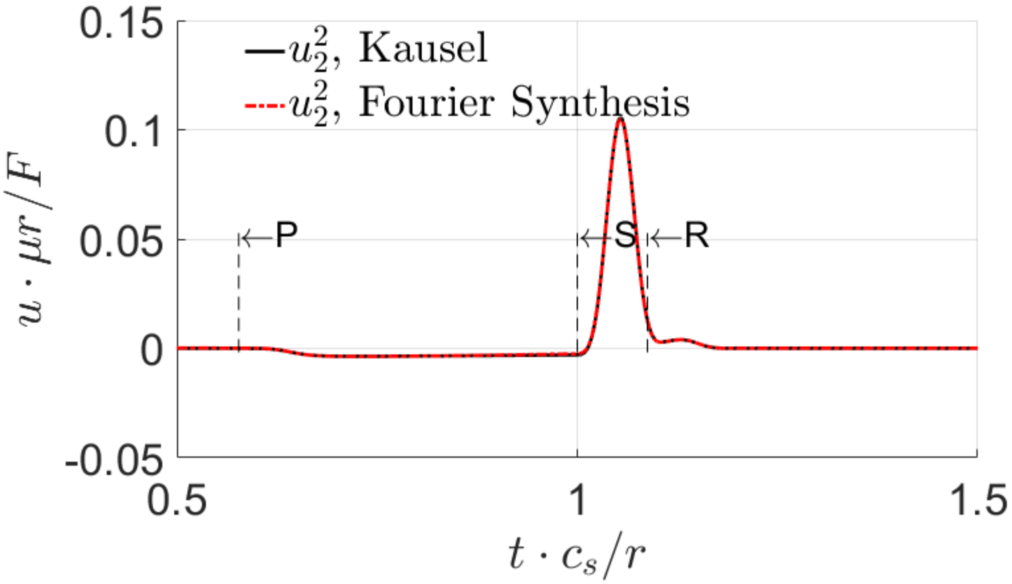
0.15
0.1
0.05
0
-0.05
0.5
1
1.5
u_2^2, Kausel
u_2^2, Fourier Synthesis
P
S
R
$u \cdot \mu r / F$
$t \cdot c_s / r$

(b) u_2^2

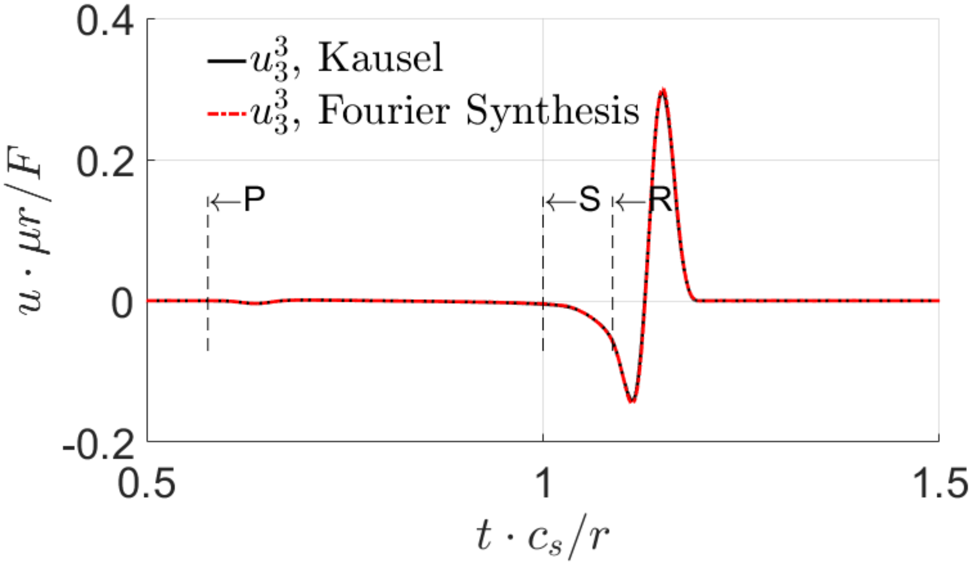
0.4
0.2
0
-0.2
0.5
1
1.5
u_3^3, Kausel
u_3^3, Fourier Synthesis
P
S
R
$u \cdot \mu r / F$
$t \cdot c_s / r$

(c) u_3^3

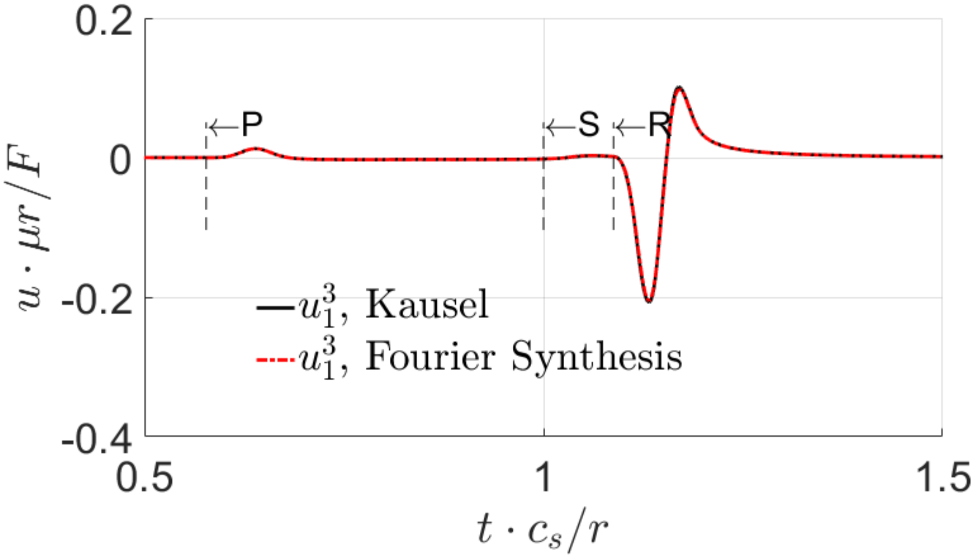

(d) u_1^3

Figure 5.13: Displacement response $u_i^j(\mathbf{x};\mathbf{y};t)$ in a half-space at $\mathbf{x}=(20,0,0)$ and $\mathbf{y}=(0,0,0)$ with $\mu=20Mpa$, $\rho=1730Kg/m^3$, $\nu = 0.25$ for a cubic B-Spline loading with $\Delta T=0.02sec$.

5.5.3 Buried source and observation points

Shown in Figure 5.14 is an example where both source and observation points are buried in a homogenous half-space with $\mu=20Mpa$, $\rho=1730Kg/m^3$, $\nu = 0.25$, at a finite depth with the source point at $\mathbf{y}=(0,0,2)$ and the observation point at $\mathbf{x}=(10,0,4)$. The cubic B-Spline impulse again has $\Delta T=0.02sec$. In the display, $u_i^j(\mathbf{x};\mathbf{y};t)$ stands for the i th displacement component under a unit point load in the j th direction. This is a case where the reflected waves from the free surface has a significant influence on the response at the observation point. The time-domain results computed via the present synthesis of the frequency-domain Green's function are compared with those in Johnson (1974). One can see again that the results show excellent agreement.

The more complex wave form occurs in this case because the waves traveling from the source point to the observation point can arrive at a location along multiple paths through reflection, mode conversion and grazing incidence. The result is that the travelling wave motion can be regarded as composed of 6 groups that can be named as the direct P-, S-wave and the reflected PP-, PS-, SS-, SP-wave trains in the half-space problem (see Graff 1975). Their sequential arrival times can be derived from the Green's function's contour integrals and are denoted in Figure 5.14 by the vertical dashed lines.

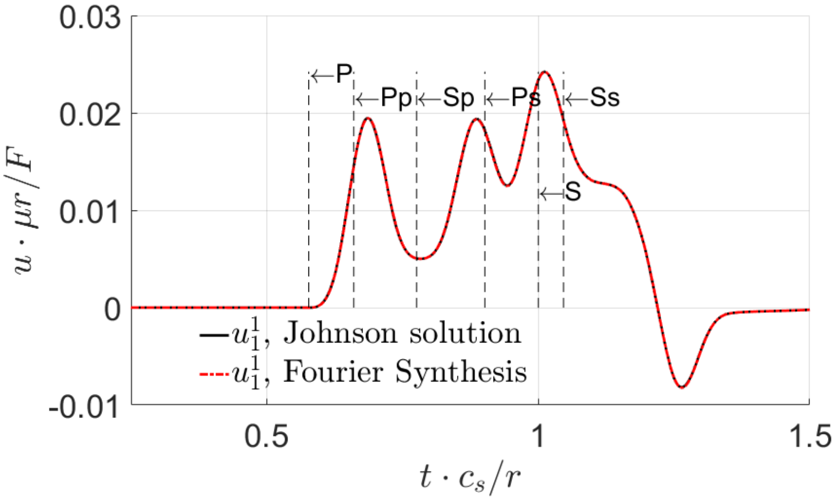

(a) u_1^1

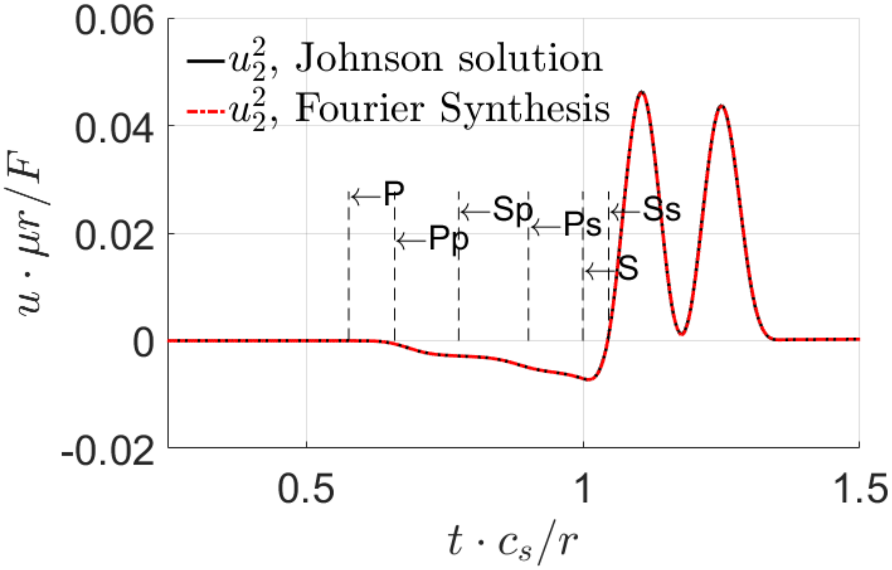

(b) u_2^2

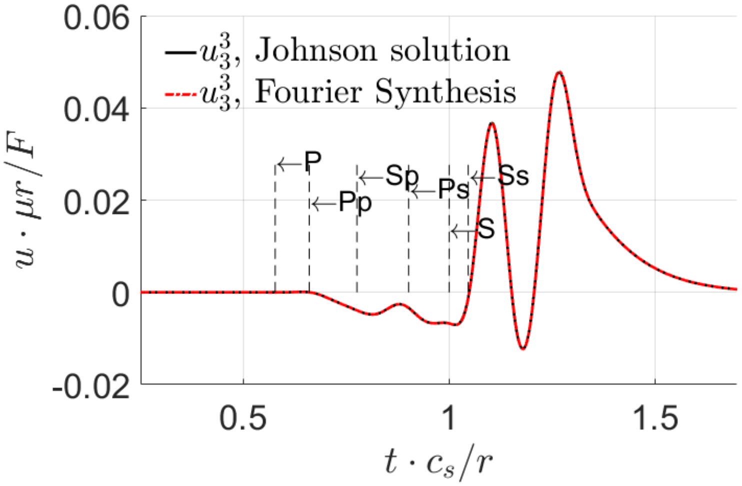

(c) u_3^3

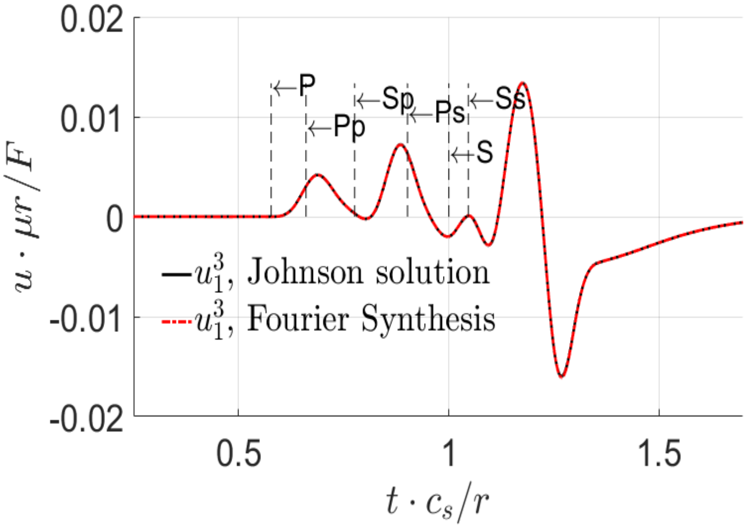

(d) u_1^3

Figure 5.14: Displacement response $u_i^j(\mathbf{x};\mathbf{y};t)$ at $\mathbf{x}=(10,0,4)$ and $\mathbf{y}=(0,0,2)$ with $\mu=20Mpa$, $\rho=1730Kg/m^3$, $\nu = 0.25$ for a B-Spline loading with $\Delta T=0.02sec$

5.5.4 Hysteretic damping

The frequency-domain approach for an elastic medium can be extended to viscoelastic media by means of the correspondence principle (see e.g., Christensen 2012). To model materials that incur energy loss in cyclic loading that is insensitive to frequency (Newmark and Rosenblueth

1971) as in soils and rocks, one can use a hysteretic damping model for which the stress-strain relationship in the frequency domain can be expressed as

$$\tilde{\mu}(\omega) = \mu(1 + i\zeta_{hy}) \, , \tag{1.1}$$

with ζ_{hy} being a constant damping ratio. From the displacement time histories corresponding to various ζ_{hy} shown in Figure 5.15, one can see that the arrival time is not very sensitive to the damping ratio, while the amplitude of the displacement generally decreases with increasing hysteretical damping ratio.

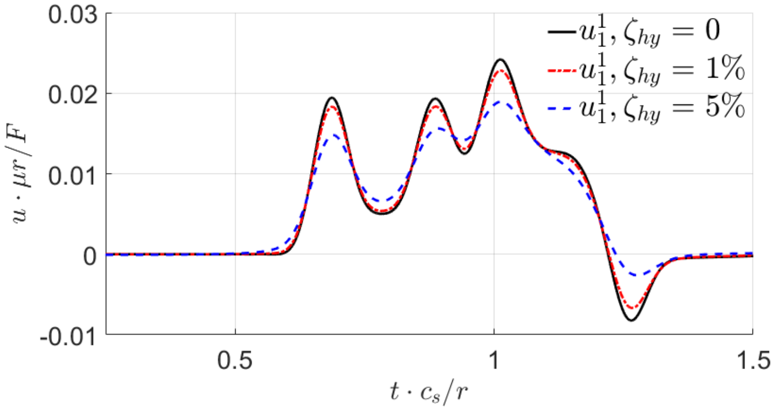

(a) u_1^1

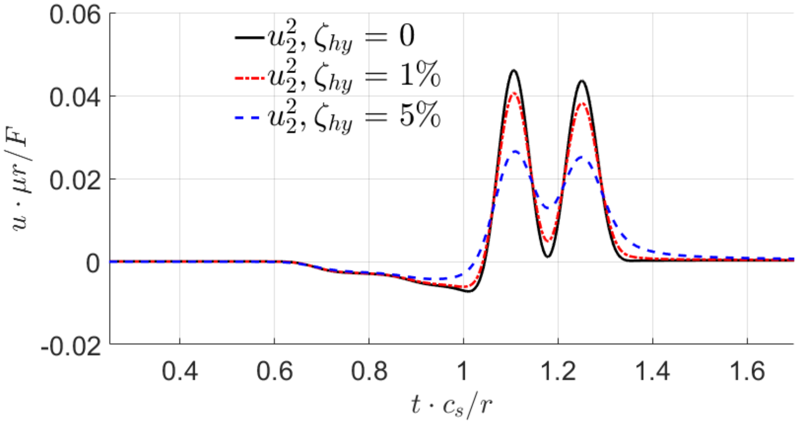

(b) u_2^2

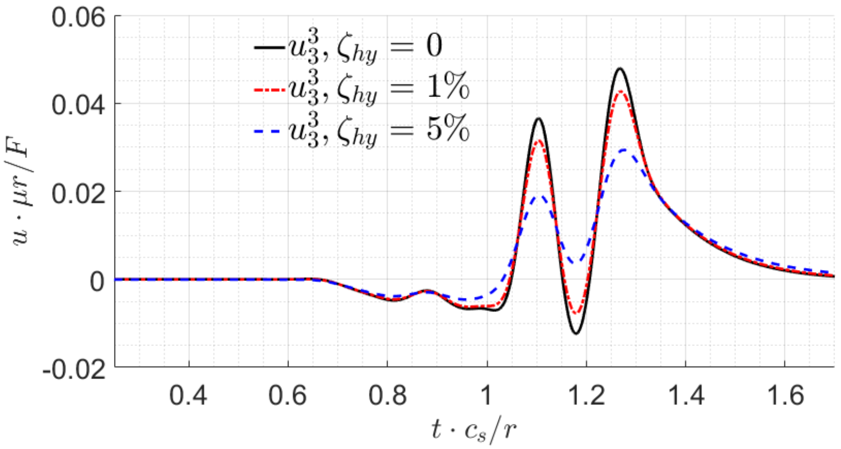

(c) u_3^3

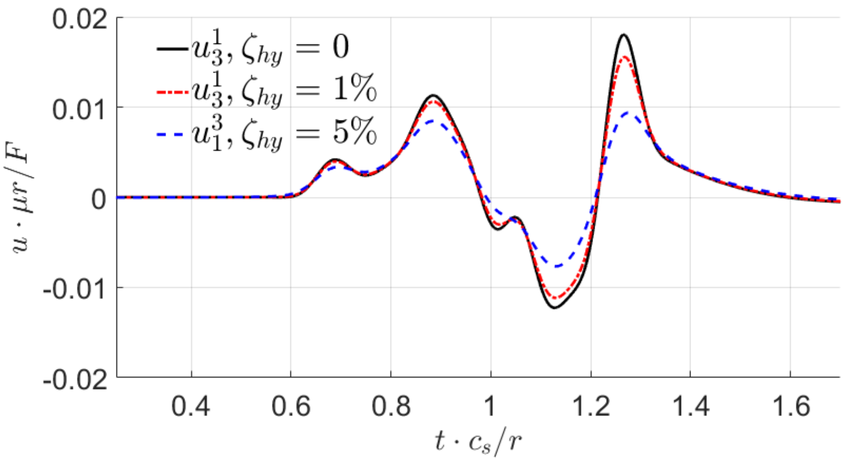

(d) u_1^3

Figure 5.15: Displacement response $u_i^j(\mathbf{x};\mathbf{y};t)$ at $\mathbf{x}=(10,0,4)$ and $\mathbf{y}=(0,0,2)$ in a viscoelastic half-space.

5.5.5 Response of a single layer bonded to a half-space

In this example, the case of a homogenous layer boneded to the top of a homogenous half-space is considered. The thickness of the top layer is taken to be $h=10m$. As a reference, the elastic material parameters of the top layer are $\mu_1 = 20$MPa, $\rho_1 = 1730kg/m^3$, $\nu_1 = 0.25$. The mass densities and the Poisson's ratios of the layer and the half-space are taken to be the same, i.e., $\rho_2 = \rho_1$, $\nu_2 = \nu_2$, but the shear modului μ_2 of the halfspace is taken to be twice or half of μ_1. The results are shown in Figure 5.16 (a)-(c). With the observer point $\mathbf{x} = (10, 0, 4)$ and source point $\mathbf{y} = (0, 0, 2)$, i.e., both are in the top layer, one can see that the responses for the 2 cases are the same before waves are reflected by the layer interface or the free-surface to the observation point, and differ afterwards.

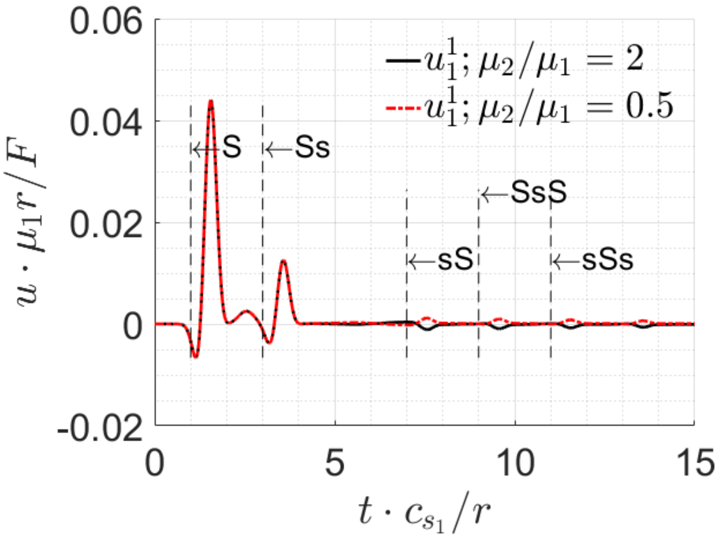

(a) u_1^1

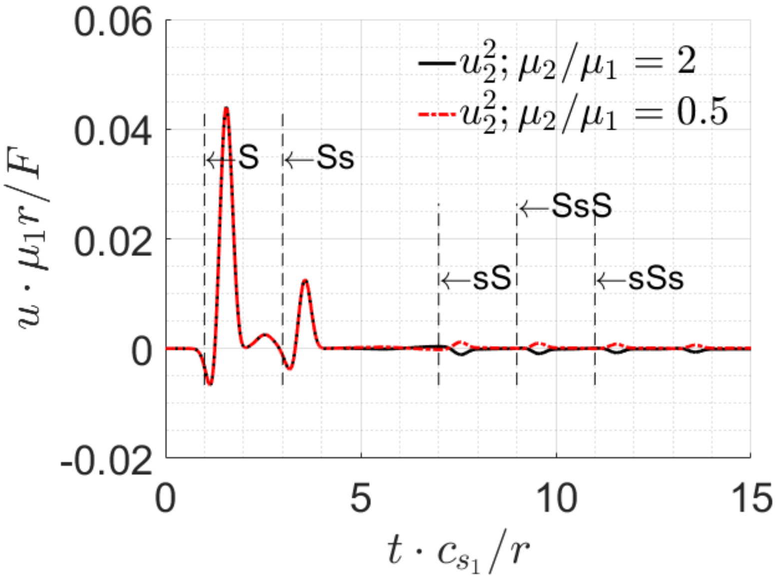

(b) u_2^2

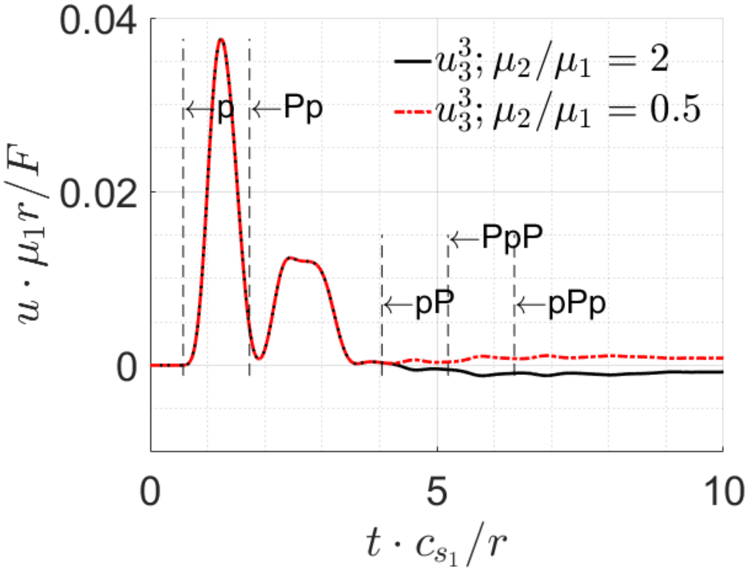

(c) u_3^3

Figure 5.16: Displacement response $u_i^j(\mathbf{x};\mathbf{y};t)$ at $\mathbf{x}=(10,0,4)$ and $\mathbf{y}=(0,0,2)$ in a layer overlying a half-space.

5.6 Summary

This chapter describes the Fourier synthesis approach using frequency-domain Green's functions method to obtain time-domain elastodynamic Green's function. In using this method, a necessary theoretical accommodation is to limit the time function (for the load) to ones whose Fourier transforms decay sufficiently strongly at high frequency so that the Green's function integral kernel as a whole in the inverse Fourier transform format also decay sufficiently strongly to allow a legitimate truncation of the infinite integration interval. The success of the approach in obtaining the time-domain response for cubic B-Spline loading time histories is demonstrated by several examples.

Chapter 6

Direct Time-Domain Green's functions for a Homogeneous Half-Space

6.1 Introduction

Since the classic work of Lamb (1904), an effective solution for the time-domain elastodynamic Green's function pertaining to a homogeneous, isotropic, linearly elastic half-space has been sought for over a century because of its fundamental importance in seismology, earthquake engineering, dynamic stress analysis and boundary integral equation-type methods. The approach to solve the underlying wave propagation problems generally falls into the four categories: (a) Numerical methods with high performance computing (Reshef 1988), (b) Semi-analytical (hybrid) methods, which is based on numerical solution in the direction of layering and integral transforms in the other directions (Desceliers 2008), (c) Geometric ray theory which yields the asymptotic approximations for the waves (Verweij and de Hoop 1990, Aki and Richards 2002), and (d) Analytical methods seeking for exact solutions (Pekeris 1955a, Pekeris 1955b, Pekeris and Hanna 1957, Chao 1960, Kausel 2012).

Generally speaking, exact analytical approaches are the most attractive ones. In seeking rigorous solutions, powerful analytical techniques and formulations such as the method of potentials, method of separation of variables, integral transforms and complex variables are available. While integral transforms are often straightforward to carry out and solutions in the transformed domain can be derived without excessive difficulties, their inversion back to the physical time and spatial domains is usally the most challenging aspect except in simple problems. In developing the 2-D theory of the propagation of seismic pulses in two homogeneous media separated by a plane non-slipping boundary using Laplace transform for the time variable, Cagniard suggested an ingenious method to obtain the inverse transform (Cagniard 1962). His list of change of variables and transformations was later simplified by de Hoop (1960) and the reduced method has been commonly referred to as the Cagniard-de Hoop method (e.g., Miklowitz 1978, Ben-Menahem and Vered 1973). Partly to explore the mathematical transformations in Cagniard (1962), Dix (1954) determined the axisymmetric seismic pulse motion generated by an impulsive point pressure source located in a homogeneous, isotropic, infinite medium. By virtue of Cagniard's procedure, the axisymmetric motion of the surface of a homogeneous half-space produced by the point pressure pulse on the surface and buried in the half-space were investigated in Pekeris (1955a) and Pekeris (1955b), respectively. The method was also applied to explore the surface motion of a homogeneous half-space under the excitation of a buried vertical point force (Pekeris and Hanna 1957). The investigation in Pekeris & Hanna (1957) was however limited to the case of Poisson's ratio is $\nu = 0.25$. Mooney (1974) later generalized it for an arbitrary Poisson's ratio and presented solutions of the velocity, acceleration, strain and displacement.

Owing to the axisymmetric nature of point pressure/dilatational source and vertical point force, the equations involving these loadings are considerably simpler than those in the general case where there is no inherent symmetry. As one of the few examples of the latter, Chao (1960) considered the response of an elastic half-space to a tangential surface point force. Making use of the method of mirror image, he constructed a formal solution of the problem in the Laplace-transform domain and inverted it back to the time domain by Cagniard's method. Because performing Cagniard's inverse Laplace transform of the solutions for an arbitrary observer location is much more complicated, only the surface displacement and the displacements along the z-axis directly below the applied surficial tangential force were reported. A collection of a number of past analytical results for the surface displacements of a homogeneous half-space under the vertical and horizontal points loads on the surface with certain simplifications was given in Kausel (2012).

As indicated in the preceding discussion, most of the past solutions were confined to either an axisymmetric load or special geometrical placements of the source and observation points.

While they have fundamental scientific values, they have limited use as Green's functions for general boundary value problems in three-dimensional elastodynamics via boundary integral equation or boundary element formulations. For the case that allows a pair of general source and observer locations and asymmetric loading in a 3-D half-space, the main contribution to date remains that of Johnson (1974) . Using the Cartesian coordinate system so that de Hoop (1960)'s transformations could be applied in the Laplace transform's time-inversion, he employed Laplace transforms with respect to the spatial coordinates as well as the time variable. Despite the complicated expressions and some basic issues, the resulting Green's function is fundamental in studying wave propagation in seismology while forming a useful basis in boundary element methods as in Triantafyllids (1991) and Galvín and Romero (2014) for dynamic soil-structure interaction problems.

In this chapter, a new compact analytical solution procedure is presented for the three-dimensional time-domain elastodynamic response at the general point on or in a homogeneous half-space under an arbitrary point load on its surface or interior. While the problem has been studied by Johnson (1974) as discussed earlier, the present treatment has the advantages of (a) a simpler and more systematic mathematical derivation of the transformed solution by virtue of the use of displacement potentials in lieu of dealing with the complicated Navier's equation of motion, (b) using cylindrical coordinates and Hankel transforms which are physically more natural and allows the avoidance of dealing with nested infinite integrals from using Fourier transforms and (c) an improvement in the analytical and numerical efficiency and robustness.

6.2 A Method of Displacement Potentials

For a homogeneous linear elastic solid, Navier's equation of motion with zero body force can be written as

$$(\lambda+2\mu)\nabla(\nabla\cdot\mathbf{u}(\mathbf{x},t))-\mu\nabla\times\nabla\times\mathbf{u}(\mathbf{x},t)=\rho\frac{\partial^2\mathbf{u}(\mathbf{x},t)}{\partial t^2}, \tag{6.1}$$

where ρ stands for the density, λ and μ denote the Lamé constants of the classical theory of elasticity, while t is the time, $\mathbf{x}$ is the position vector, and $\mathbf{u}$ is the displacement. The half space under consideration is depicted in Figure 6.1. In cylindrical coordinates (r,θ,z), the free surface of the half space is defined by $z=0$ and positive z points into the half space.

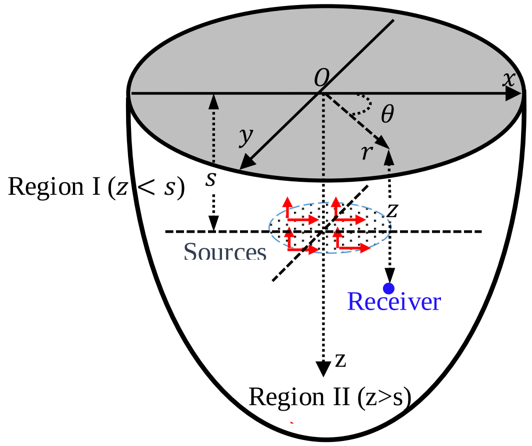

Figure 6.1: A distributed time-dependent buried source in a half-space

In classical elastodynamics, a powerful method for solution is by displacement potentials together with integral transforms. As shown in (Pak 1987), a suitably regular displacement vector field $\mathbf{u}$ in a half-space can be decomposed in terms of three scalar fields ϕ_i, $i=1,2,3$ as

$$\mathbf{u}(r,\theta,z,t)=\nabla\phi_1(r,\theta,z,t)+\nabla\times\phi_2(r,\theta,z,t)\mathbf{e}_z+\nabla\times\nabla\times\phi_3(r,\theta,z,t)\mathbf{e}_z \tag{6.2}$$

with $\mathbf{e}_z$ being the unit vector for a cylindrical coordinate system and ϕ_i satisfying the wave equations

$$\nabla^2\phi_q(r,\theta,z,t)=\frac{1}{c_q^2}\frac{\partial^2\phi_q(r,\theta,z,t)}{\partial t^2},\ \ q=1,2,3 \tag{6.3}$$

Respectively (see also Pak and Morteza 2007). In the above, $c_1 = c_d = \sqrt{(\lambda + 2\mu)/\rho}$ and $c_2 = c_3 = c_s = \sqrt{\mu/\rho}$ are respectively the compressional and shear wave speed, and $\frac{c_d}{c_s} = \sqrt{\frac{2(1-\nu)}{1-2\nu}}$ with the Poisson's ratio $\nu = \frac{(c_d/c_s)^2 - 2}{2\left((c_d/c_s)^2 - 1\right)}$. With the definition of Laplace transform as

$$\hat{f}\left(r,\theta,z,p\right) = \int_0^\infty f\left(r,\theta,z,t\right) e^{-pt} dt \tag{6.4}$$

and its Bromwich inversion integral (Churchill 1972)

$$f\left(r,\theta,z,t\right) = \frac{1}{2\pi i} \int_{\gamma - i\infty}^{\gamma + i\infty} \widehat{f}\left(r,\theta,z,p\right) e^{tp} dp \tag{6.5}$$

with respect to time for an arbitrary function $\hat{f}\left(r,\theta,z,p\right)$ with a quiescent past, the 3 wave equations in (6.3) are equivalent to the Helmholtz equations

$$\nabla^2 \widehat{\phi}_i - k_i^2 \widehat{\phi}_i = 0,\ i = 1,2,3, \tag{6.6}$$

where

$$\widehat{\phi}_i\left(r,\theta,z,p\right) = \int_0^\infty \phi_i\left(r,\theta,z,t\right) e^{-pt} dt \tag{6.7}$$

with $k_1 = k_d \equiv \frac{p}{c_d}$ and $k_2 = k_3 = k_s \equiv \frac{p}{c_s}$. With the completeness of the eigenfunctions $\left\{e^{im\theta}\right\}$ with respect to the azimuthal coordinates, the potentials and the response of the half-space can be further decomposed as

$$\begin{aligned} \widehat{\phi}\left(r,\theta,z,p\right) &= \sum_{m=-\infty}^{\infty} \widehat{\phi}_{q_m}\left(r,z,p\right) e^{im\theta},\ q = 1,2,3 \\ \widehat{\mathbf{u}}\left(r,\theta,z,p\right) &= \sum_{m=-\infty}^{\infty} \widehat{\mathbf{u}}_m\left(r,z,p\right) e^{im\theta},\ e.t.c. \end{aligned} \tag{6.8}$$

Upon the application of the m^{th} order Hankel transform with respect to the radial coordinate via

$$\tilde{f}^m\left(\xi\right) = \int_0^\infty f\left(r\right) r J_m\left(r\xi\right) dr,$$

whose inverse is

$$f(r) = \int_0^\infty \tilde{f}^m(\xi)\xi J_m(r\xi)\,d\xi$$

where $J_m(r)$ is the Bessel function of the first kind of order *m*, the Helmholtz equations in Equation (6.6) can be reduced in the Laplace-Hankel transform domain to

$$\frac{d^2}{dz^2}\hat{\tilde{\phi}}^m_{q_m} - \left(\xi^2 + k_q^2(p)\right)\hat{\tilde{\phi}}^m_{q_m} = 0, \quad q = 1,2,3, \quad m = 0,\pm1,\pm2,.... \tag{6.9}$$

whose general solution can be written as

$$\begin{aligned} \hat{\tilde{\phi}}^m_{1_m}(\xi,z,p) &= A^I_{1_m}(\xi,p)e^{\alpha z} + B^I_{1_m}(\xi,p)e^{-\alpha z}, \\ \hat{\tilde{\phi}}^m_{q_m}(\xi,z,p) &= A^I_{q_m}(\xi,p)e^{\beta z} + B^I_{q_m}(\xi,p)e^{-\beta z}, \ \text{q=2,3, for z<s} \end{aligned} \tag{6.10}$$

and

$$\begin{aligned} \hat{\tilde{\phi}}^m_{1_m}(\xi,z,p) &= B^I_{1_m}(\xi,p)e^{-\alpha z}, \\ \hat{\tilde{\phi}}^m_{q_m}(\xi,z,p) &= B^I_{q_m}(\xi,p)e^{-\beta z}, \ \text{q=2,3, for z>s} \end{aligned} \tag{6.11}$$

where $\alpha = (\xi^2 + k_d^2(p))^{1/2}$, $\beta = (\xi^2 + k_s^2(p))^{1/2}$ and $A^I_{q_m}$, $B^I_{q_m}$, $B^{II}_{q_m}$, $q = 1,2,3$ are constants of integration to be determined from the boundary and interfacial conditions. The branches cuts of α and β are chosen as shown in Figure 6.2 such that the real parts of α and β are always non-negative with their branch points on the imaginary axis. They, in turn render the $e^{\alpha z}$ and $e^{\beta z}$ terms in Region II inadmissible owing to the radiation condition of the z-direction and are thus omitted in Eqn. (6.11).

On the free surface of z=0, it is required that

$$\tau_{zr}(\mathbf{x},t) = \tau_{z\theta}(\mathbf{x},t) = \tau_{zz}(\mathbf{x},t) = 0, \ \text{for } z = 0\,. \tag{6.12}$$

For an arbitrarily distributed time-dependent body-force field over an open disc Π_s at a depth s, it is convenient to view the half-space as being composed of an upper and a lower region of the same material (Regions I and II in Figure 6.1) divided by the plane $z = s$ and regard the imposed loading as a general discontinuity in stresses across Π_s that is defined by

$$\begin{aligned}
\tau_{zr}(r,\theta,s^-,t)-\tau_{zr}(r,\theta,s^+,t) &= \begin{cases} P(r,\theta,t), & (r,\theta,s)\in\Pi_s \\ 0, & (r,\theta,s)\notin\Pi_s \end{cases} \\
\tau_{z\theta}(r,\theta,s^-,t)-\tau_{z\theta}(r,\theta,s^+,t) &= \begin{cases} Q(r,\theta,t), & (r,\theta,s)\in\Pi_s \\ 0, & (r,\theta,s)\notin\Pi_s \end{cases} \\
\tau_{zz}(r,\theta,s^-,t)-\tau_{zz}(r,\theta,s^+,t) &= \begin{cases} R(r,\theta,t), & (r,\theta,s)\in\Pi_s \\ 0, & (r,\theta,s)\notin\Pi_s \end{cases}
\end{aligned} \tag{6.13}$$

where $P(r,\theta,t)$, $Q(r,\theta,t)$, and $R(r,\theta,t)$ represent the body-force distributions in the radial, angular and axial directions, respectively. For the horizontal and vertical concentrated point loads located at the point $(0,0,s)$ of the form

$$\begin{aligned}
\mathbf{f}^h(r,\theta,z) &= \mathcal{F}\frac{\delta(r)}{2\pi r}\delta(z-s)\mathbf{e}_h, \\
\mathbf{f}^v(r,\theta,z) &= \mathcal{F}\frac{\delta(r)}{2\pi r}\delta(z-s)\mathbf{e}_z,
\end{aligned} \tag{6.14}$$

the body-force distribution can be specified as

$$\begin{cases}
P(r,\theta,t) = \mathcal{F}\dfrac{\delta(r)}{2\pi r}\cos(\theta-\theta_0)g(t), \\
Q(r,\theta,t) = -\mathcal{F}\dfrac{\delta(r)}{2\pi r}\sin(\theta-\theta_0)g(t), \quad \text{Horizontal loading,} \\
R(r,\theta,t) = 0,
\end{cases}$$
$$\begin{cases}
P(r,\theta,t) = 0, \\
Q(r,\theta,t) = 0, \qquad \text{Vertical loading,} \\
R(r,\theta,t) = \mathcal{F}\dfrac{\delta(r)}{2\pi r}g(t),
\end{cases} \tag{6.15}$$

respectively, where $\delta(r)$ is the Dirac-Delta function, and $g(t)$ is any specific time variation of the point load, $\mathbf{e}_h = \mathbf{e}_r \cos(\theta-\theta_0) - \mathbf{e}_\theta \sin(\theta-\theta_0)$ is the unit horizontal vector in the $\theta = \theta_0$ direction. In this study, the transient solution of displacements and stresses, which are commonly referred to as Green's functions, for the impulsive case where $g(t)=H(t)$ is a step impulse is considered.

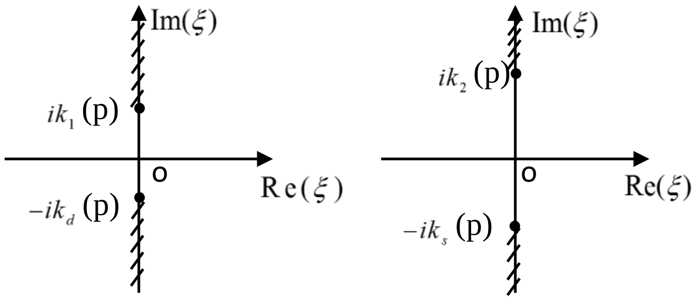

(b) Branch cut of α (a) Branch cut of β

Figure 6.2: Branch cuts of α and β

6.3 Solution in Laplace transform domain

The 9 coefficients $A^{I}_{q_m}$, $B^{I}_{q_m}$, $B^{II}_{q_m}$, $q=1,2,3$ in (6.10) and (6.11) corresponding to an arbitrarily distributed force-force field concentrated on the plane at a depth $z=s$ can be obtained by imposing the traction-free boundary conditions at z=0, the displacement continuity and the induced stress-jump condition at z=s , with the aid of the compact transformed displacement- and stress-potential relations analogous to those derived in (Pak 1987). For a concentrated point loads with a resultant of $\mathcal{F}$ with $g(t)=H(t)$, the transformed displacement response or Green's function can be expressed as

$$\hat{\mathbf{u}}(r,\theta,z;s;p)=\frac{\mathcal{F}}{\mu c_s}\bar{\mathbf{U}}(\bar{r},\theta,\bar{z};\bar{s};\bar{p}), \tag{6.16}$$

where $\bar{\mathbf{U}}(\bar{r},\theta,\bar{z};\bar{s};\bar{p})$ is in a dimensionless form in terms of the normalized parameters and functions

$$\bar{r}=\frac{r}{a},\ \bar{z}=\frac{z}{a},\ \bar{s}=\frac{s}{a},\ \bar{d}_1=|\bar{z}-\bar{s}|,\ \bar{d}_2=\bar{z}+\bar{s},\ \bar{p}=\frac{pa}{c_s},\bar{\xi}=\frac{\xi}{k_2(p)},$$
$$\bar{\alpha}=(\bar{\xi}^2+K^2)^{\frac{1}{2}},\ \bar{\beta}=(\bar{\xi}^2+1)^{\frac{1}{2}},\bar{R}^{\pm}\left(\bar{\xi}\right)=(2\bar{\xi}^2+1)^2\pm 4\bar{\xi}^2\bar{\alpha}\bar{\beta},\ \ K=c_s\,/\,c_d \tag{6.17}$$

with reference to (6.10), (6.11) and a is a chosen characteristic length for the problem.

With the superscripts $\gamma=h,\ \mathrm{z}$ denoting the horizontal and vertical unit load directions and subscripts $i=r,\theta,z$ denoting the displacement response directions, respectively, the following Green's function cases are considered:

6.3.1 Horizontal loading in $\theta=\theta_0$ direction

$$\bar{U}_r^h\left(\bar{r},\theta,\bar{z};\bar{s};\bar{p}\right)=\frac{\cos\left(\theta-\theta_0\right)}{4\pi}I_r^h\left(\bar{r},\bar{z};\bar{s};\bar{p}\right), \tag{6.18}$$

$$\bar{U}_\theta^h\left(\bar{r},\theta,\bar{z};\bar{s};\bar{p}\right)=\frac{-\sin\left(\theta-\theta_0\right)}{4\pi}I_\theta^h\left(\bar{r},\bar{z};\bar{s};\bar{p}\right), \tag{6.19}$$

$$\bar{U}_z^h\left(\bar{r},\theta,\bar{z};\bar{s};\bar{p}\right)=\frac{\cos\left(\theta-\theta_0\right)}{2\pi}I_z^h\left(\bar{r},\bar{z};\bar{s};\bar{p}\right), \tag{6.20}$$

6.3.2 Vertical loading in z-direction

$$\bar{U}_r^z\left(\bar{r},\theta,\bar{z};\bar{s};\bar{p}\right)=-\frac{1}{2\pi}I_r^z\left(\bar{r},\bar{z};\bar{s};\bar{p}\right), \tag{6.21}$$

$$\bar{U}_\theta^z\left(\bar{r},\theta,\bar{z};\bar{s};\bar{p}\right)=0, \tag{6.22}$$

$$\bar{U}_z^z\left(\bar{r},\theta,\bar{z};\bar{s};\bar{p}\right)=\frac{1}{2\pi}I_z^z\left(\bar{r},\bar{z};\bar{s};\bar{p}\right), \tag{6.23}$$

where

$$I_r^h\left(\bar{r},\bar{z};\bar{s};\bar{p}\right)=\int_0^\infty\left\{\begin{array}{l}\bar{\gamma}_1\left(\bar{z},\bar{s};\bar{p};\bar{\xi}\right)\bar{\xi}\left[J_0\left(\bar{p}\bar{\xi}\bar{r}\right)-J_2\left(\bar{p}\bar{\xi}\bar{r}\right)\right]\\+\bar{\gamma}_2\left(\bar{z},\bar{s};\bar{p};\bar{\xi}\right)\bar{\xi}\left[J_0\left(\bar{p}\bar{\xi}\bar{r}\right)+J_2\left(\bar{p}\bar{\xi}\bar{r}\right)\right]\end{array}\right\}d\bar{\xi}, \tag{6.24}$$

$$I_\theta^h\left(\bar r,\bar z;\bar s;\bar p\right)=\int_0^\infty\left\{\begin{matrix}\bar\gamma_1\left(\bar z,\bar s;\bar p;\bar\xi\right)\bar\xi\left[J_0\left(\bar p\bar\xi\bar r\right)+J_2\left(\bar p\bar\xi\bar r\right)\right]\\+\bar\gamma_2\left(\bar z,\bar s;\bar p;\bar\xi\right)\bar\xi\left[J_0\left(\bar p\bar\xi\bar r\right)-J_2\left(\bar p\bar\xi\bar r\right)\right]\end{matrix}\right\}d\bar\xi, \tag{6.25}$$

$$I_z^h\left(\bar r,\bar z;\bar s;\bar p\right)=\int_0^\infty\bar\Omega_1\left(\bar z,\bar s;\bar p;\bar\xi\right)\bar\xi J_1\left(\bar p\bar\xi\bar r\right)d\bar\xi, \tag{6.26}$$

$$I_r^z\left(\bar r,\bar z;\bar s;\bar p\right)=\int_0^\infty\bar\gamma_3\left(\bar z,\bar s;\bar p;\bar\xi\right)\bar\xi J_1\left(\bar p\bar\xi\bar r\right)d\bar\xi, \tag{6.27}$$

$$I_z^z\left(\bar r,\bar z;\bar s;\bar p\right)=\int_0^\infty\bar\Omega_2\left(\bar z,\bar s;\bar p;\bar\xi\right)\bar\xi J_0\left(\bar p\bar\xi\bar r\right)d\bar\xi. \tag{6.28}$$

and

$$\bar\gamma_1(\bar z,\bar s;\bar p;\bar\xi)=\frac{1}{2}\begin{pmatrix}\dfrac{-\bar\xi^2}{\bar\alpha}e^{-\bar p\bar\alpha|\bar z-\bar s|}+\bar\beta e^{-\bar p\bar\beta|\bar z-\bar s|}+\dfrac{\bar R^+(\bar\xi)}{\bar R^-(\bar\xi)}(\dfrac{\bar\xi^2}{\bar\alpha}e^{-\bar p\bar\alpha(\bar z+\bar s)}+\bar\beta e^{-\bar p\bar\beta(\bar z+\bar s)})\\-\dfrac{4\bar\xi^2\bar\beta(2\bar\xi^2+1)}{\bar R^-(\bar\xi)}(e^{-\bar p(\bar\beta\bar z+\bar\alpha\bar s)}+e^{-\bar p(\bar\beta\bar s+\bar\alpha\bar z)})\end{pmatrix},$$

$$\bar\gamma_2(\bar z,\bar s;\bar p;\bar\xi)=\frac{1}{2\bar\beta}\left(e^{-\bar p\bar\beta|\bar z-\bar s|}+e^{-\bar p\bar\beta(\bar z+\bar s)}\right), \tag{6.29}$$

$$\bar\gamma_3(\bar z,\bar s;\bar p;\bar\xi)=\begin{pmatrix}-sgn\left(\bar z-\bar s\right)\dfrac{\bar\xi}{2}\left(e^{-\bar p\bar\alpha|\bar z-\bar s|}-e^{-\bar p\bar\beta|\bar z-\bar s\|}\right)-\dfrac{\bar\xi}{2}\dfrac{\bar R^+(\bar\xi)}{\bar R^-(\bar\xi)}\left(e^{-\bar p\bar\alpha\left(\bar z+\bar s\right)}+e^{-\bar p\bar\beta\left(\bar z+\bar s\right)}\right)\\+\dfrac{2\bar\xi\left(2\bar\xi^2+1\right)}{\bar R^-(\bar\xi)}\left(\bar\alpha\bar\beta e^{-\bar p\left(\bar\beta\bar z+\bar\alpha\bar s\right)}+\bar\xi^2e^{-\bar p\left(\bar\beta\bar s+\bar\alpha\bar z\right)}\right)\end{pmatrix},$$

$$\bar\Omega_1(\bar z,\bar s;\bar p;\bar\xi)=\begin{pmatrix}sgn\left(\bar z-\bar s\right)\dfrac{\bar\xi}{2}\left(e^{-\bar p\bar\alpha|\bar z-\bar s|}-e^{-\bar p\bar\beta|\bar z-\bar s|}\right)-\dfrac{\bar\xi}{2}\dfrac{\bar R^+(\bar\xi)}{\bar R^-(\bar\xi)}\left(e^{-\bar p\bar\alpha\left(\bar z+\bar s\right)}+e^{-\bar p\bar\beta\left(\bar z+\bar s\right)}\right)\\+\dfrac{2\bar\xi\left(2\bar\xi^2+1\right)}{\bar R^-(\bar\xi)}\left(\bar\xi^2e^{-\bar p\left(\bar\beta\bar z+\bar\alpha\bar s\right)}+\bar\alpha\bar\beta e^{-\bar p\left(\bar\beta\bar s+\bar\alpha\bar z\right)}\right)\end{pmatrix},$$

$$\bar\Omega_2\left(\bar z,\bar s;\bar p;\bar\xi\right)=\begin{pmatrix}\dfrac{\bar\alpha}{2}e^{-\bar p\alpha|\bar z-\bar s|}-\dfrac{\bar\xi^2}{2\bar\beta}e^{-\bar p\bar\beta|\bar z-\bar s|}+\dfrac{1}{2}\dfrac{\bar R^+\left(\bar\xi\right)}{\bar R^-\left(\bar\xi\right)}\left(\bar\alpha e^{-\bar p\alpha\left(\bar z+\bar s\right)}+\dfrac{\bar\xi^2}{\bar\beta}e^{-\bar p\bar\beta\left(\bar z+\bar s\right)}\right)\\-\dfrac{2\bar\xi^2\bar\alpha\left(2\bar\xi^2+1\right)}{\bar R^-\left(\bar\xi\right)}\left(e^{-\bar p\left(\bar\beta\bar z+\bar\alpha\bar s\right)}+e^{-\bar p\left(\bar\beta\bar s+\bar\alpha\bar z\right)}\right)\end{pmatrix}, \tag{6.30}$$

6.4 Inversion of Laplace-Hankel transformed Green's functions by Cagniard's idea

As a simple but ingenious observation by Cagniard (1939, 1962), a powerful and effective way for the inversion of a Laplace transform is to analytically re-cast it in its defining integral form with an explicit kernel e^{-pt} as a factor in the integrand so that residual factor is by definition the sought-after time function. Owing to the use of Cartesian coordinate system in Cagniard and de-Hoop and many studies that followed it (setting things up in a Cartesian coordinate system), past approaches typically involved a sequence of mystic analytic transformations and change of variables (whose design, while functional, might be less than obvious) to find a contour in a complex-plane for its realization. For its use of the approach in the more natural setting of a cylindrical coordinate system for a general point-load in a 3-D half-space, there was the concern of added difficulties owing to the need to deal with transcendental special functions such as Bessel functions (see Verweij and de Hoop 1990). As a result, the formulation proposed by Johnson (1974) employed a double Laplace transform for the horizontal coordinates in a Cartesian system so that Cagniard-de Hoop transformations in Cartesian coordinates can be applied. The steps that are involved are however mathematically complicated as a result of having to deal with two spatial or transformed coordinates. As will be illustrated in the following sections, the proposed method of potentials and Laplace-Hankel transforms in cylindrical coordinates can lend itself to a much more straightforward and systematic derivation in their inversion back to the physical time and spatial domains for this class of fundamental elastodynamic problems.

6.5 Application of Cagniard inversion approach - basic rendition

As a simple but ingenious observation by Cagniard (1962), an effective way for the inversion of Laplace transforms is to find a way to cast them in the defining integral form of a Laplace transform with an explicit kernel e^{-pt} as a factor in the integrand so that the integral residual kernel is by definition the sought-after time function. By means of some special analytic transformations from Cartesian to polar coordinates in 2-D problems, Cagniard, de Hoop and others were able to find a complex contour to transform the p-variable integration. To apply the inversion approach effectively to the present transformed 3-D Green's function in Eqns. (6.18)-(6.23), however, it is relevant to note that they all involve Bessel functions. In this treatment, it will be shown that fundamental integral representations

$$\begin{aligned} J_0(z) &= \frac{1}{\pi}\int_0^{\pi} e^{\mathrm{iz}\cos\phi}\,d\phi, \\ J_1(z) &= \frac{-i}{\pi}\int_0^{\pi} e^{\mathrm{iz}\cos\phi}\cos(\phi)\,d\phi, \\ J_2(z) &= \frac{-1}{\pi}\int_0^{\pi} e^{\mathrm{iz}\cos\phi}\cos(2\phi)\,d\phi. \end{aligned} \tag{6.31}$$

are particularly helpful in the analytical reduction.

6.5.1 Inverse Laplace transform by Cagniard's idea

I_r^h, I_θ^h, I_z^h and $I_r^{\mathrm{v}}, I_z^{\mathrm{v}}$ in Eqns. (6.24)–(6.28) can be expressed as

$$\begin{Bmatrix} I_r^h(\bar{r},\bar{z};\bar{s};\bar{p}) \\ I_\theta^h(\bar{r},\bar{z};\bar{s};\bar{p}) \\ I_z^h(\bar{r},\bar{z};\bar{s};\bar{p}) \end{Bmatrix} = \int_0^{\infty} \begin{Bmatrix} \mathcal{I}_r^h(\bar{r},\bar{z};\bar{s};\bar{t}) \\ \mathcal{I}_\theta^h(\bar{r},\bar{z};\bar{s};\bar{t}) \\ \mathcal{I}_z^h(\bar{r},\bar{z};\bar{s};\bar{t}) \end{Bmatrix} e^{-\bar{p}\bar{t}}\,d\bar{t}, \tag{6.32}$$

as well as

$$\begin{Bmatrix} I_r^{\mathrm{v}}(\bar{r},\bar{z};\bar{s};\bar{p}) \\ I_z^{\mathrm{v}}(\bar{r},\bar{z};\bar{s};\bar{p}) \end{Bmatrix} = \int_0^{\infty} \begin{Bmatrix} \mathcal{I}_r^{\mathrm{v}}(\bar{r},\bar{z};\bar{s};\bar{t}) \\ \mathcal{I}_z^{\mathrm{v}}(\bar{r},\bar{z};\bar{s};\bar{p}) \end{Bmatrix} e^{-\bar{p}\bar{t}}\,d\bar{t}, \tag{6.33}$$

where $\mathcal{I}_r^h, \mathcal{I}_\theta^h, \mathcal{I}_z^h$ and $\mathcal{I}_r^{\mathrm{v}}, \mathcal{I}_z^{\mathrm{v}}$ are the targeted the time-domain Green's functions. Arranging the 5 integrals in equation (6.32) and (6.33) as the column vector

$$\{I(\bar{r},\bar{z};\bar{s};\bar{p})\} = \{I_r^h, I_\theta^h, I_z^h, I_r^{\mathrm{v}}, I_z^{\mathrm{v}}\}^T, \tag{6.34}$$

and collecting together the terms those involves the same exponential terms, $\{I(\bar{r},\bar{z};\bar{s};\bar{p})\}$ can be expressed as

$$\left\{I\left(\bar{r},\bar{z};\bar{s};\bar{p}\right)\right\}=\begin{matrix}\{I\}^{p}\left(\bar{r},\bar{z};\bar{s};\bar{p}\right)+\{I\}^{s}\left(\bar{r},\bar{z};\bar{s};\bar{p}\right)+\{I\}^{pp}\left(\bar{r},\bar{z};\bar{s};\bar{p}\right)\\+\{I\}^{ss}\left(\bar{r},\bar{z};\bar{s};\bar{p}\right)+\{I\}^{ps}\left(\bar{r},\bar{z};\bar{s};\bar{p}\right)+\{I\}^{sp}\left(\bar{r},\bar{z};\bar{s};\bar{p}\right)\end{matrix}, \tag{6.35}$$

where

$$\begin{aligned}
\{I\}^{p}\left(\bar{r},\bar{z};\bar{s};\bar{p}\right)&=\frac{1}{\pi}\int_{0}^{\infty}\int_{0}^{\pi}\{M\}^{p}\left(\bar{\xi},\phi\right)e^{-\bar{p}\,\left(\bar{\alpha}\bar{d}_1-i\bar{\xi}\bar{r}\cos\phi\right)}d\phi d\bar{\xi},\\
\{I\}^{s}\left(\bar{r},\bar{z};\bar{s};\bar{p}\right)&=\frac{1}{\pi}\int_{0}^{\infty}\int_{0}^{\pi}\{M\}^{s}\left(\bar{\xi},\phi\right)e^{-\bar{p}\,\left(\bar{\beta}\bar{d}_1-i\bar{\xi}\bar{r}\cos\phi\right)}d\phi d\bar{\xi},\\
\{I\}^{pp}\left(\bar{r},\bar{z};\bar{s};\bar{p}\right)&=\frac{1}{\pi}\int_{0}^{\infty}\int_{0}^{\pi}\{M\}^{pp}\left(\bar{\xi},\phi\right)e^{-\bar{p}\,\left(\bar{\alpha}\bar{d}_2-i\bar{\xi}\bar{r}\cos\phi\right)}d\phi d\bar{\xi},\\
\{I\}^{ss}\left(\bar{r},\bar{z};\bar{s};\bar{p}\right)&=\frac{1}{\pi}\int_{0}^{\infty}\int_{0}^{\pi}\{M\}^{ss}\left(\bar{\xi},\phi\right)e^{-\bar{p}\,\left(\bar{\beta}\bar{d}_2-i\bar{\xi}\bar{r}\cos\phi\right)}d\phi d\bar{\xi},\\
\{I\}^{ps}\left(\bar{r},\bar{z};\bar{s};\bar{p}\right)&=\frac{1}{\pi}\int_{0}^{\infty}\int_{0}^{\pi}\{M\}^{ps}\left(\bar{\xi},\phi\right)e^{-\bar{p}\,\left(\bar{\beta}\bar{d}+\bar{\alpha}\bar{s}-i\bar{\xi}\bar{r}\cos\phi\right)}d\phi d\bar{\xi},\\
\{I\}^{sp}\left(\bar{r},\bar{z};\bar{s};\bar{p}\right)&=\frac{1}{\pi}\int_{0}^{\infty}\int_{0}^{\pi}\{M\}^{sp}\left(\bar{\xi},\phi\right)e^{-\bar{p}\,\left(\bar{\alpha}\bar{d}+\bar{\beta}\bar{s}-i\bar{\xi}\bar{r}\cos\phi\right)}d\phi d\bar{\xi},
\end{aligned} \tag{6.36}$$

with $\bar{d}_1=|\bar{d}-\bar{s}|$, $\bar{d}_2=\bar{d}+\bar{s}$, and

$$\{M\}^{p}\left(\bar{\xi},\phi\right)=\begin{Bmatrix}-\dfrac{\bar{\xi}^{3}}{2\bar{\alpha}}\left(1+\cos\left(2\phi\right)\right)\\-\dfrac{\bar{\xi}^{3}}{2\bar{\alpha}}\left(1-\cos\left(2\phi\right)\right)\\-sgn\left(\bar{z}-\bar{s}\right)\dfrac{i}{2}\bar{\xi}^{2}\cos\phi\\sgn\left(\bar{z}-\bar{s}\right)\dfrac{i}{2}\bar{\xi}^{2}\cos\phi\\\dfrac{\bar{\xi}\bar{\alpha}}{2}\end{Bmatrix}, \tag{6.37}$$

$$\{M\}^{s}\left(\bar{\xi},\phi\right)=\left\{\begin{array}{l}\dfrac{\bar{\xi}}{2}\left[\left(1+\cos\left(2\phi\right)\right)\bar{\beta}+\left(1-\cos\left(2\phi\right)\right)\dfrac{1}{\bar{\beta}}\right]\\ \dfrac{\bar{\xi}}{2}\left[\left(1-\cos\left(2\phi\right)\right)\bar{\beta}+\left(1+\cos\left(2\phi\right)\right)\dfrac{1}{\bar{\beta}}\right]\\ sgn\left(\bar{z}-\bar{s}\right)\dfrac{i}{2}\bar{\xi}^{2}\cos\phi\\ -sgn\left(\bar{z}-\bar{s}\right)\dfrac{i}{2}\bar{\xi}^{2}\cos\phi\\ -\dfrac{\bar{\xi}^{3}}{2\bar{\beta}}\end{array}\right\}, \tag{6.38}$$

$$\{M\}^{pp}\left(\bar{\xi},\phi\right)=\left\{\begin{array}{l}\dfrac{1}{2}\left(1+\cos\left(2\phi\right)\right)\dfrac{R^{+}\left(\bar{\xi}\right)}{R^{-}\left(\bar{\xi}\right)}\dfrac{\bar{\xi}^{3}}{\bar{\alpha}}\\ \dfrac{1}{2}\left(1-\cos\left(2\phi\right)\right)\dfrac{R^{+}\left(\bar{\xi}\right)}{R^{-}\left(\bar{\xi}\right)}\dfrac{\bar{\xi}^{3}}{\bar{\alpha}}\\ \dfrac{i}{2}\cos\phi\dfrac{R^{+}\left(\bar{\xi}\right)}{R^{-}\left(\bar{\xi}\right)}\bar{\xi}^{2}\\ \dfrac{i}{2}\cos\phi\dfrac{R^{+}\left(\bar{\xi}\right)}{R^{-}\left(\bar{\xi}\right)}\bar{\xi}^{2}\\ \dfrac{i}{2}\bar{\xi}\bar{\alpha}\dfrac{R^{+}\left(\bar{\xi}\right)}{R^{-}\left(\bar{\xi}\right)}\end{array}\right\}, \tag{6.39}$$

$$\{M\}^{ss}\left(\bar{\xi},\phi\right)=\left\{\begin{matrix}\dfrac{\bar{\xi}}{2}\left[\left(1+\cos\left(2\phi\right)\right)\dfrac{R^{+}\left(\bar{\xi}\right)}{R^{-}\left(\bar{\xi}\right)}\bar{\beta}+\left(1-\cos\left(2\phi\right)\right)\dfrac{1}{\bar{\beta}}\right] \\ \dfrac{\bar{\xi}}{2}\left[\left(1-\cos\left(2\phi\right)\right)\dfrac{R^{+}\left(\bar{\xi}\right)}{R^{-}\left(\bar{\xi}\right)}\bar{\beta}+\left(1+\cos\left(2\phi\right)\right)\dfrac{1}{\bar{\beta}}\right] \\ \dfrac{i}{2}\cos\phi\dfrac{R^{+}\left(\bar{\xi}\right)}{R^{-}\left(\bar{\xi}\right)}\bar{\xi}^{2} \\ \dfrac{i}{2}\cos\phi\dfrac{R^{+}\left(\bar{\xi}\right)}{R^{-}\left(\bar{\xi}\right)}\bar{\xi}^{2} \\ \dfrac{i}{2}\dfrac{\bar{\xi}^{3}}{\bar{\beta}}\dfrac{R^{+}\left(\bar{\xi}\right)}{R^{-}\left(\bar{\xi}\right)}\end{matrix}\right\}, \tag{6.40}$$

$$\{M\}^{ps}\left(\bar{\xi},\phi\right)=\left\{\begin{matrix}\dfrac{-2\bar{\xi}^{3}\bar{\beta}\left(2\bar{\xi}^{2}+1\right)}{\bar{R}^{-}\left(\bar{\xi}\right)}\left(1+\cos\left(2\phi\right)\right) \\ \dfrac{-2\bar{\xi}^{3}\bar{\beta}\left(2\bar{\xi}^{2}+1\right)}{\bar{R}^{-}\left(\bar{\xi}\right)}\left(1-\cos\left(2\phi\right)\right) \\ -2i\cos\phi\dfrac{\bar{\xi}^{4}\left(2\bar{\xi}^{2}+1\right)}{\bar{R}^{-}\left(\bar{\xi}\right)} \\ -2i\cos\phi\dfrac{\bar{\xi}^{2}\left(2\bar{\xi}^{2}+1\right)\bar{\alpha}\bar{\beta}}{\bar{R}^{-}\left(\bar{\xi}\right)} \\ \dfrac{-2\bar{\xi}^{3}\bar{\alpha}\left(2\bar{\xi}^{2}+1\right)}{\bar{R}^{-}\left(\bar{\xi}\right)}\end{matrix}\right\}, \tag{6.41}$$

$$\{M\}^{sp}\left(\bar{\xi},\phi\right)=\left\{\begin{array}{l} \dfrac{-2\bar{\xi}^{3}\bar{\beta}\left(2\bar{\xi}^{2}+1\right)}{\bar{R}^{-}\left(\bar{\xi}\right)}\left(1+\cos\left(2\phi\right)\right) \\ \dfrac{-2\bar{\xi}^{3}\bar{\beta}\left(2\bar{\xi}^{2}+1\right)}{\bar{R}^{-}\left(\bar{\xi}\right)}\left(1-\cos\left(2\phi\right)\right) \\ -2i\cos\phi\dfrac{\bar{\xi}^{2}\left(2\bar{\xi}^{2}+1\right)\bar{\alpha}\bar{\beta}}{\bar{R}^{-}\left(\bar{\xi}\right)} \\ -2i\cos\phi\dfrac{\bar{\xi}^{4}\left(2\bar{\xi}^{2}+1\right)}{\bar{R}^{-}\left(\bar{\xi}\right)} \\ \dfrac{-2\bar{\xi}^{3}\bar{\alpha}\left(2\bar{\xi}^{2}+1\right)}{\bar{R}^{-}\left(\bar{\xi}\right)} \end{array}\right\}. \tag{6.42}$$

The six terms in Eqn. (6.35) correspond to the six physical waves as shown in Figure 6.3, namely, the direct P-, and S-waves, and the reflected PP-, SS-, PS- and SP-waves, as will be. They can also be in turn transformed inversely to the time domain by the Cagniard's idea as to be demonstrated in the next section.

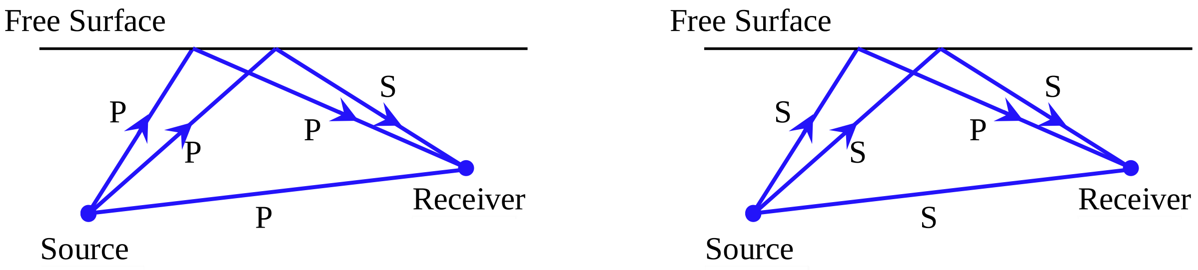

Figure 6.3: The six waves emanating from source to receiver.

(1) Direct P-wave term

Consider the term associated with the direct P-wave in Eqn. (6.36), i.e.,

$$[I]^p\left(\bar{r},\bar{z};\bar{s};\bar{p}\right)=\frac{1}{\pi}\int_0^{\infty}\int_0^{\pi}[M]^p\left(\bar{\xi},\phi\right)e^{-\bar{p}\left(\bar{\alpha}\bar{d}_1-i\bar{\xi}\bar{r}\cos\phi\right)}d\phi d\bar{\xi}. \tag{6.43}$$

By the analyticity of the integrand $[M]^p$, the order of integration with respect to ϕ and $\bar{\xi}$ is interchanged in (6.43) allowing it to be written as

$$[I]^p\left(\bar{r},\bar{z};\bar{s};\bar{p}\right)=\frac{1}{\pi}\int_0^{\pi}\int_0^{\infty}[M]^p\left(\bar{\xi},\phi\right)e^{-\bar{p}\left(\bar{\alpha}\bar{d}_1-i\bar{\xi}\bar{r}\cos\phi\right)}d\bar{\xi}d\phi. \tag{6.44}$$

The goal of Cagniard's idea is to cast the inner integral on the right-hand side in such a form that its time domain counterpart, $[\mathcal{I}]^p\left(\bar{r},\bar{z};\bar{s};\bar{t}\right)$ becomes obvious. To achieve the goal, the improper inner integral is first extended to the complex $\bar{\xi}-$ plane and a path is sought such that its exponential kernel is identical to the standard Laplace transform kernel of $e^{-\bar{p}t}$, where $\bar{t}$ is real and ≥ 0. Demanding that

$$\bar{\tau}_p=(\bar{\xi}^2+K^2)^{1/2}\bar{d}_1-i\bar{\xi}\bar{r}\cos\phi \tag{6.45}$$

is real and positive, and rearranging $\bar{\xi}$ as a function of $\bar{\tau}_p$, one finds two possible roots as

$$\bar{\xi}_{1,2}(\bar{r},\bar{d}_1,K;\bar{\tau}_p,\phi)=\frac{i\bar{\tau}_p\bar{r}\cos\phi\pm\bar{d}_1\sqrt{\bar{\tau}_p^2-K^2\left(\bar{d}_1^2+\bar{r}^2\cos^2\phi\right)}}{\bar{d}_1^2+\bar{r}^2\cos^2\phi}, \tag{6.46}$$

whose derivative with respect to $\bar{\tau}_p$ are respectively

$$\frac{d\bar{\xi}_{1,2}}{d\bar{\tau}_p}(\bar{r},\bar{d}_1,K;\bar{\tau}_p,\phi)=\frac{i\bar{r}\cos\phi\pm\bar{d}_1\bar{\tau}_p/\sqrt{\bar{\tau}_p^2-K^2\left(\bar{d}_1^2+\bar{r}^2\cos^2\phi\right)}}{\bar{d}_1^2+\bar{r}^2\cos^2\phi}. \tag{6.47}$$

Here, $K=c_s/c_d$ is introduced for the brevity of notation.

Evidently, the path under seeking is composed of the two roots. Next, consideration is given to the character of the roots. For the expected real value of $\bar{r},\bar{d}_1,K$, and $0\leq\phi<\pi/2$, the contour on the complex $\bar{\xi}-$ plane defined by Eqn. (6.46), i.e., Root 1, for $0\leq\bar{\tau}_p<\infty$ is depicted in Figure 6.4(a). Generally, the contour starts at point A (see Figure 6.4) for $\bar{\tau}_p = 0$ and then pass through points B, C and D, coordinates of which are respectively

$$\begin{aligned} A &= \left(0, K\bar{d}_1 \Big/ \sqrt{\bar{d}_1^2 + \bar{r}^2 \cos^2\phi}\right) \text{ at } \bar{\tau}_p = 0, \\ B &= (0, K) \text{ at } \bar{\tau}_p = K\bar{r}\cos\phi, \\ C &= \left(0, K\bar{r}\cos\phi \Big/ \sqrt{\bar{d}_1^2 + \bar{r}^2 \cos^2\phi}\right) \text{ at } \bar{\tau}_p = K\sqrt{\bar{d}_1^2 + \bar{r}^2 \cos^2\phi}. \end{aligned} \tag{6.48}$$

It is noted that $\dfrac{d\bar{\xi}_1}{d\bar{\tau}_p} = 0$ at point B, where the contour begins to turn downwardly. Also, Note $\dfrac{d\bar{\xi}_1}{d\bar{\tau}_p} \to \infty$ at point C, indicating that the contour has a kink there.

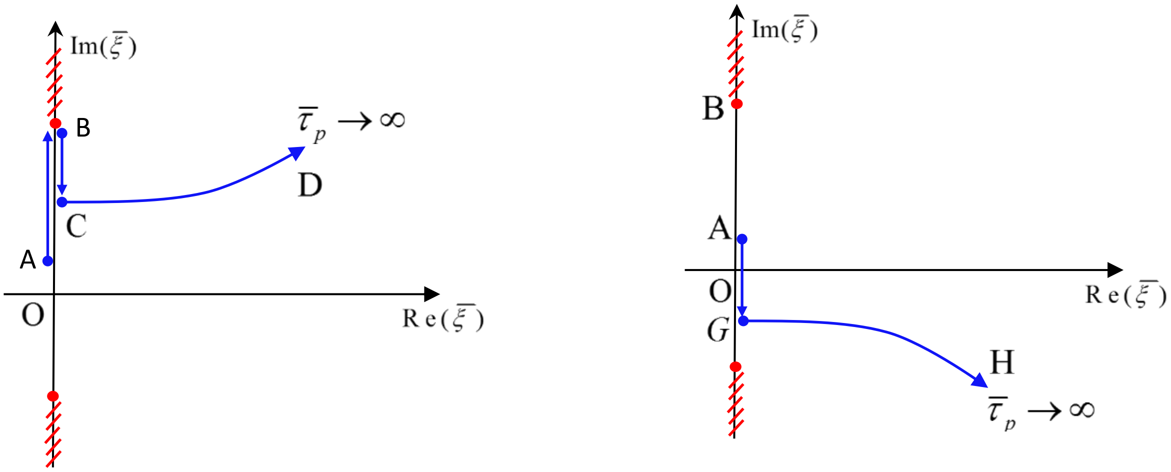

(a) $0 \le \phi < \pi/2, \ \cos\phi > 0$ (b) $\pi/2 < \phi \le \pi, \ \cos\phi < 0$

Figure 6.4: Path of Root 1 in Eqn. (6.46) in $\bar{\xi}$ – plane as $\bar{\tau}_p$ increases.

Under the same condition, the contour defined by Eqn. (6.46), i.e., Root 2, for $0 \le \bar{\tau}_p < \infty$ is depicted in Figure 6.5(a). As $\bar{\tau}_p$ increases from 0 to ∞, the contour starts at point E, and then passes through point C and F. The point C is identical to the one defined in Eqn. (6.46), while coordinate of point E is

$$E = \left(0, -K\bar{d}_1 \Big/ \sqrt{\bar{d}_1^2 + \bar{r}^2 \cos^2\phi}\right) \text{ at } \bar{\tau}_p = 0. \tag{6.49}$$

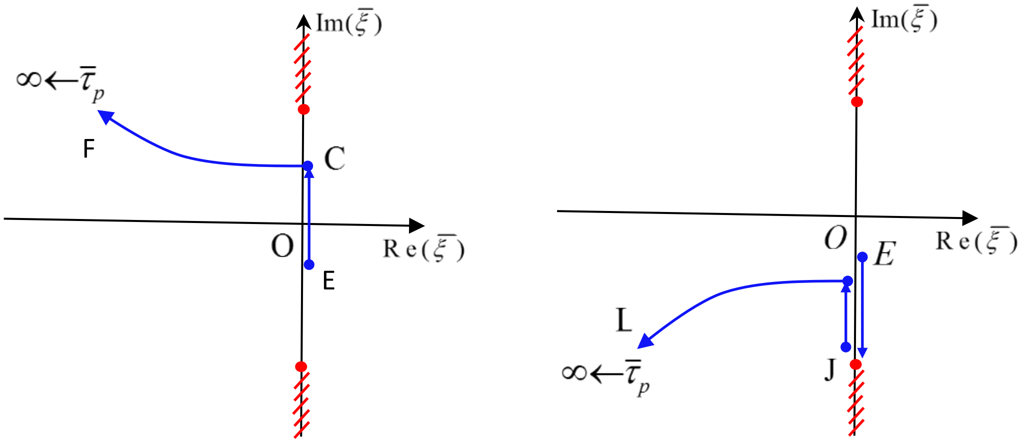

(a) $0 \le \phi < \pi/2,\ \cos\phi > 0$ (b) $\pi/2 < \phi \le \pi,\ \cos\phi < 0$

Figure 6.5: Path of Root 2 in Eqn. (6.46) in $\bar{\xi}$ – plane as $\bar{\tau}_p$ increases.

By Cauchy's theorem and Jordan's Lemma (see e.g., Ablowitz and Fokas 2003), and in view of the branch cut for α , the formal integration path of the interior integral in Eqn. (6.44) can be deformed to $C_1 + C_2$ at the case where $0 \le \phi < \pi/2$, as shown in Figure 6.6(a). Here, C_1 is the segment from the point O to C in Figure 6.5(a), and C_2 is the segment between the point C and D in Figure 6.4(a).

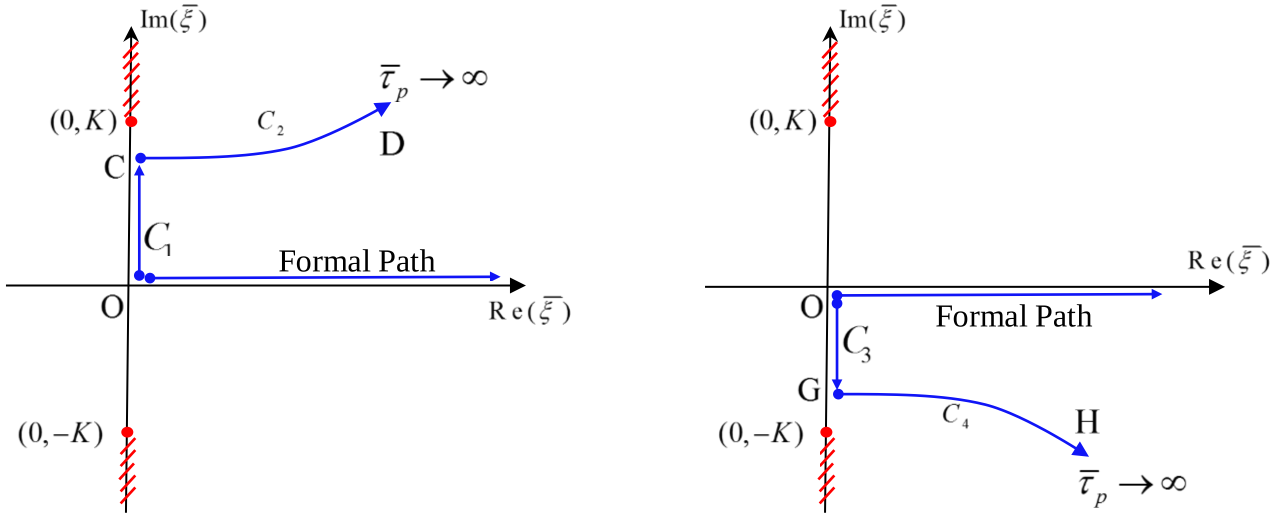

(a) $0 \le \phi < \pi/2,\ \cos\phi > 0$ (b) $\pi/2 < \phi \le \pi,\ \cos\phi < 0$

Figure 6.6: Chosen Cagniard path for direct P-wave.

Similarly, for $\pi/2 < \phi \le \pi$, Eqn. (6.46) defines for $0 \le \bar{\tau}_p < \infty$ the contour showed in Figure 6.4(b). The contour starts at point A, and then passes point G and H. Point A is the point that is defined in Eqn. (6.48), while the coordinate of G and H are

$$\begin{aligned} G &= \left(0, -K\bar{r}\cos\phi \Big/ \sqrt{\bar{d}_1^2 + \bar{r}^2\cos^2\phi}\right) \text{ at } \bar{\tau}_p = K\sqrt{\bar{d}_1^2 + \bar{r}^2\cos^2\phi}, \\ H &= \left(\bar{d}_1, -\bar{r}\cos\phi\right)\cdot\infty / (\bar{d}_1^2 + \bar{r}^2\cos^2\phi) \text{ at } \bar{\tau}_p = +\infty. \end{aligned} \tag{6.50}$$

In this case, the formal path of integration can be deformed to $C_3 + C_4$ as shown in Figure 6.6(b), where C_3 is the segment from point O to G, and C_4 is from point G to H.

After deforming the path of integration, one can have

$$\begin{aligned} \{I\}^p\left(\bar{r},\bar{z};\bar{s};\bar{p}\right) = {} & \frac{1}{\pi}\int_0^{\pi/2}\left\{\begin{aligned} & \int_{C_1(\bar{\xi};\phi)} \{M\}^p\left(\bar{\xi}(\bar{r},\bar{d}_1,K;\bar{\tau}_p,\phi),\phi\right)e^{-\bar{p}\left(\bar{\alpha}\bar{d}_1 - i\bar{\xi}\bar{r}\cos\phi\right)}d\bar{\xi} \\ & + \int_{C_2(\bar{\xi};\phi)} \{M\}^p\left(\bar{\xi}(\bar{r},\bar{d}_1,K;\bar{\tau}_p,\phi),\phi\right)e^{-\bar{p}\left(\bar{\alpha}\bar{d}_1 - i\bar{\xi}\bar{r}\cos\phi\right)}d\bar{\xi} \end{aligned}\right\}d\phi \\ & + \frac{1}{\pi}\int_{\pi/2}^{\pi}\left\{\begin{aligned} & \int_{C_3(\bar{\xi};\phi)} \{M\}^p\left(\bar{\xi}(\bar{r},\bar{d}_1,K;\bar{\tau}_p,\phi),\phi\right)e^{-\bar{p}\left(\bar{\alpha}\bar{d}_1 - i\bar{\xi}\bar{r}\cos\phi\right)}d\bar{\xi} \\ & + \int_{C_4(\bar{\xi};\phi)} \{M\}^p\left(\bar{\xi}(\bar{r},\bar{d}_1,K;\bar{\tau}_p,\phi),\phi\right)e^{-\bar{p}\left(\bar{\alpha}\bar{d}_1 - i\bar{\xi}\bar{r}\cos\phi\right)}d\bar{\xi} \end{aligned}\right\}d\phi. \end{aligned} \tag{6.51}$$

Then by changing the variable of integration from $\bar{\xi}$ to $\bar{\tau}_p$, one obtains from Equation (6.51) that

$$\begin{aligned} \{I\}^p\left(\bar{r},\bar{z};\bar{s};\bar{p}\right) = {} & \frac{1}{\pi}\int_0^{\pi/2}\left\{\begin{aligned} & \int_{K\bar{d}_1}^{K\sqrt{\bar{d}_1^2+\bar{r}^2\cos^2\phi}} \{M\}^p\left(\bar{\xi}_2(\bar{\tau}_p,\phi),\phi\right)e^{-\bar{p}\bar{\tau}_p}\frac{d\bar{\xi}_2}{d\bar{\tau}_p}d\bar{\tau}_p \\ & + \int_{K\sqrt{\bar{d}_1^2+\bar{r}^2\cos^2\phi}}^{\infty} \{M\}^p\left(\bar{\xi}_1(\bar{\tau}_p,\phi),\phi\right)e^{-\bar{p}\bar{\tau}_p}\frac{d\bar{\xi}_1}{d\bar{\tau}_p}d\bar{\tau}_p \end{aligned}\right\}d\phi \\ & + \frac{1}{\pi}\int_{\pi/2}^{\pi}\left\{\begin{aligned} & \int_{K\bar{d}_1}^{K\sqrt{\bar{d}_1^2+\bar{r}^2\cos^2\phi}} \{M\}^p\left(\bar{\xi}_1(\bar{\tau}_p,\phi),\phi\right)e^{-\bar{p}\bar{\tau}_p}\frac{d\bar{\xi}_1}{d\bar{\tau}_p}d\bar{\tau}_p \\ & + \int_{K\sqrt{\bar{d}_1^2+\bar{r}^2\cos^2\phi}}^{\infty} \{M\}^p\left(\bar{\xi}_1(\bar{\tau}_p,\phi),\phi\right)e^{-\bar{p}\bar{\tau}_p}\frac{d\bar{\xi}_1}{d\bar{\tau}_p}d\bar{\tau}_p \end{aligned}\right\}d\phi, \end{aligned} \tag{6.52}$$

where $\bar{\xi}_1$ and $\bar{\xi}_2$ are the two roots defined in Eqn. (6.46).

To show that the two integrals in Eqn. (6.52) are complex conjugate to each other, it is useful to introduce a change of variable to the second integral as

$$\psi = \pi - \phi , \tag{6.53}$$

such that

$$\begin{aligned}\{I\}^p\left(\bar{r},\bar{z};\bar{s};\bar{p}\right) = {} & \frac{1}{\pi}\int_0^{\pi/2}\left\{\begin{array}{l}\displaystyle\int_{K\bar{d}_1}^{K\sqrt{\bar{d}_1^2+\bar{r}^2\cos^2\phi}} \{M\}^p\left(\bar{\xi}_2(\bar{\tau}_p,\phi),\phi\right)e^{-\bar{p}\bar{\tau}_p}\frac{d\bar{\xi}_2}{d\bar{\tau}_p}d\bar{\tau}_p \\ \displaystyle + \int_{K\sqrt{\bar{d}_1^2+\bar{r}^2\cos^2\phi}}^{\infty} \{M\}^p\left(\bar{\xi}_1(\bar{\tau}_p,\phi),\phi\right)e^{-\bar{p}\bar{\tau}_p}\frac{d\bar{\xi}_1}{d\bar{\tau}_p}d\bar{\tau}_p\end{array}\right\}d\phi \\ & + \frac{1}{\pi}\int_0^{\pi/2}\left\{\begin{array}{l}\displaystyle\int_{K\bar{d}_1}^{K\sqrt{\bar{d}_1^2+\bar{r}^2\cos^2\phi}} \{M\}^p\left(\bar{\xi}_1(\bar{\tau}_p,\pi-\psi),\pi-\psi\right)e^{-\bar{p}\bar{\tau}_p}\frac{d\bar{\xi}_1}{d\bar{\tau}_p}d\bar{\tau}_p \\ \displaystyle + \int_{K\sqrt{\bar{d}_1^2+\bar{r}^2\cos^2\phi}}^{\infty} \{M\}^p\left(\bar{\xi}_1(\bar{\tau}_p,\pi-\psi),\pi-\psi\right)e^{-\bar{p}\bar{\tau}_p}\frac{d\bar{\xi}_1}{d\bar{\tau}_p}d\bar{\tau}_p\end{array}\right\}d\psi ,\end{aligned} \tag{6.54}$$

which is also

$$\{I\}^p\left(\bar{r},\bar{z};\bar{s};\bar{p}\right) = \frac{1}{\pi}\int_0^{\pi/2}\left\{\begin{array}{l}\displaystyle\int_{K\bar{d}_1}^{K\sqrt{\bar{d}_1^2+\bar{r}^2\cos^2\phi}}\left(\begin{array}{l}\{M\}^p\left(\bar{\xi}_2(\bar{\tau}_p,\phi),\phi\right)\dfrac{d\bar{\xi}_2}{d\bar{\tau}_p}+ \\ \{M\}^p\left(\bar{\xi}_1(\bar{\tau}_p,\pi-\phi),\pi-\phi\right)\dfrac{d\bar{\xi}_1}{d\bar{\tau}_p}\end{array}\right)e^{-\bar{p}\bar{\tau}_p}d\bar{\tau}_p \\ \displaystyle + \int_{K\sqrt{\bar{d}_1^2+\bar{r}^2\cos^2\phi}}^{\infty}\left(\begin{array}{l}\{M\}^p\left(\bar{\xi}_1(\bar{\tau}_p,\phi),\phi\right)\dfrac{d\bar{\xi}_1}{d\bar{\tau}_p}+ \\ \{M\}^p\left(\bar{\xi}_1(\bar{\tau}_p,\pi-\phi),\pi-\psi\right)\dfrac{d\bar{\xi}_1}{d\bar{\tau}_p}\end{array}\right)e^{-\bar{p}\bar{\tau}_p}d\bar{\tau}_p\end{array}\right\}d\phi . \tag{6.55}$$

From Eqn. (6.46) and (6.47), one can have for $0 \le \phi \le \pi/2$ and $K\bar{d} \le \bar{\tau}_p \le K\sqrt{\bar{d}_1^2+\bar{r}^2\cos^2\phi}$

$$\bar{\xi}_2(\bar{\tau}_p,\phi) = \left(\bar{\xi}_1(\bar{\tau}_p,\pi-\phi)\right)^*, \quad \frac{d\bar{\xi}_2}{d\bar{\tau}_p}(\bar{\tau}_p,\phi) = \left(\frac{d\bar{\xi}_1}{d\bar{\tau}_p}(\bar{\tau}_p,\pi-\phi)\right)^*, \tag{6.56}$$

while for $0 \le \phi \le \pi/2$ and $\bar{\tau}_p > K\sqrt{\bar{d}_1^2 + \bar{r}^2\cos^2\phi}$

$$\bar{\xi}_1(\bar{\tau}_p,\phi) = \left(\bar{\xi}_1(\bar{\tau}_p,\pi-\phi)\right)^*,\ \frac{d\bar{\xi}_1}{d\bar{\tau}_p}(\bar{\tau}_p,\phi) = \left(\frac{d\bar{\xi}_1}{d\bar{\tau}_p}(\bar{\tau}_p,\pi-\phi)\right)^*, \tag{6.57}$$

wherein * stands for complex conjugation. Recall Schwarz's reflection principle (Ahlfors 1953): *If a function* $f(z)$ *is (1) analytic over some region including the real axis and (2) real when z is real, then*

$$f^*(z) = f(z^*). \tag{6.58}$$

As defined in Eqn. (6.37), $\{M\}^p\left(\bar{\xi},\phi\right)$ is an analytic function of $\bar{\xi}$, and is real when both $\bar{\xi}$ and ϕ are real. Thus, based on Eqn. (6.58), one has

$$\{M\}^p\left(\bar{\xi}_2(\bar{\tau}_p,\phi),\phi\right) = \left(\{M\}^p\left(\bar{\xi}_1(\bar{\tau}_p,\pi-\phi),\pi-\phi\right)\right)^* \tag{6.59}$$

for $0 \le \phi \le \pi/2$ and $K\bar{d} \le \bar{\tau}_p \le K\sqrt{\bar{d}_1^2 + \bar{r}^2\cos^2\phi}$, and

$$\{M\}^p\left(\bar{\xi}_1(\bar{\tau}_p,\phi),\phi\right) = \left(\{M\}^p\left(\bar{\xi}_1(\bar{\tau}_p,\pi-\phi),\pi-\psi\right)\right)^* \tag{6.60}$$

for $0 \le \phi \le \pi/2$ and $\bar{\tau}_p > K\sqrt{\bar{d}_1^2 + \bar{r}^2\cos^2\phi}$.

Since the integrands in Eqn. (6.55) form a pair of complex conjugate, imaginary part of which will cancels each other out, it can be reduced to

$$\{I\}^p\left(\bar{r},\bar{z};\bar{s};\bar{p}\right) = \frac{2}{\pi}\int_0^{\pi/2} \mathrm{Re}\left\{ \begin{array}{l} \displaystyle\int_{K\bar{d}_1}^{K\sqrt{\bar{d}_1^2+\bar{r}^2\cos^2\phi}} \{M\}^p\left(\bar{\xi}_2(\bar{\tau}_p,\phi),\phi\right)e^{-\bar{p}\bar{\tau}_p}\frac{d\bar{\xi}_2}{d\bar{\tau}_p}d\bar{\tau}_p \\ \displaystyle +\int_{K\sqrt{\bar{d}_1^2+\bar{r}^2\cos^2\phi}}^{\infty} \{M\}^p\left(\bar{\xi}_1(\bar{\tau}_p,\phi),\phi\right)e^{-\bar{p}\bar{\tau}_p}\frac{d\bar{\xi}_1}{d\bar{\tau}_p}d\bar{\tau}_p \end{array} \right\} d\phi. \tag{6.61}$$

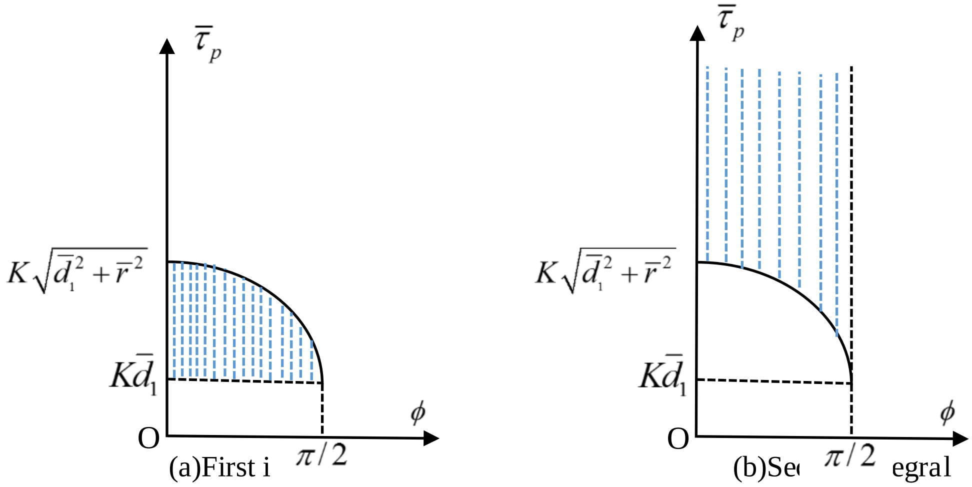

(a)First i (b)Se egral

Figure 6.7: Integration range marked as the shaded area.

Next, one may interchange the order of integration to obtain

$$\{I\}^p\left(\bar{r},\bar{z};\bar{s};\bar{p}\right)=\frac{2}{\pi}\int_{K\bar{d}_1}^{K\sqrt{\bar{d}_1^2+\bar{r}^2}}\mathrm{Re}\left\{\begin{array}{l}\displaystyle\int_0^{\phi^*}\{M\}^p\left(\bar{\xi}_2(\bar{\tau}_p,\phi),\phi\right)\frac{d\bar{\xi}_2}{d\bar{\tau}_p}d\phi\\ \displaystyle+\int_{\phi^*}^{\frac{\pi}{2}}\{M\}^p\left(\bar{\xi}_1(\bar{\tau}_p,\phi),\phi\right)\frac{d\bar{\xi}_1}{d\bar{\tau}_p}d\phi\end{array}\right\}e^{-\bar{p}\bar{\tau}_p}d\bar{\tau}_p \tag{6.62}$$

$$+\frac{2}{\pi}\int_{K\sqrt{\bar{d}_1^2+\bar{r}^2}}^{\infty}\mathrm{Re}\left\{\int_0^{\frac{\pi}{2}}\{M\}^p\left(\bar{\xi}_1(\bar{\tau}_p,\phi),\phi\right)\frac{d\bar{\xi}_1}{d\bar{\tau}_p}d\phi\right\}e^{-\bar{p}\bar{\tau}_p}d\bar{\tau}_p,$$

where $\phi^*=\cos^{-1}\sqrt{\dfrac{\bar{\tau}_p-K^2\bar{d}_1^2}{K^2\bar{r}^2}}$. It should be pointed out that, for $0<\phi<\phi^*$, $\bar{\xi}(\bar{\tau}_p,\phi)$ takes the value of Root 2 in the first integral of Eqn. (6.46), while for $0<\phi<\phi^*$, $\bar{\xi}(\bar{\tau}_p,\phi)$ takes the value of Root 1.

Through many numerical tests, it is confirmed that

$$\int_0^{\phi^*}\{M\}^p\left(\bar{\xi}(\bar{\tau}_p,\phi),\phi\right)\frac{d\bar{\xi}}{d\bar{\tau}_p}d\phi+\int_{\phi^*}^{\frac{\pi}{2}}\{M\}^p\left(\bar{\xi}(\bar{\tau}_p,\phi),\phi\right)\frac{d\bar{\xi}}{d\bar{\tau}_p}d\phi=0, \tag{6.63}$$

hence

$$[I]^p\left(\bar r,\bar z;\bar s;\bar p\right)=\frac{2}{\pi}\int_{K\sqrt{\bar d_1^2+\bar r^2}}^{\infty}\mathrm{Re}\left\{\int_0^{\frac{\pi}{2}}\{M\}^p\left(\bar\xi(\bar\tau_p,\phi),\phi\right)\frac{d\bar\xi}{d\bar\tau_p}d\phi\right\}e^{-\bar p\bar\tau_p}d\bar\tau_p. \tag{6.64}$$

Finally, Eqn. (6.64) can be written in the general form of Laplace transform

$$\{I\}^p\left(\bar r,\bar z;\bar s;\bar p\right)=\int_0^{\infty}\{\mathcal{I}\}^p\left(\bar r,\bar z;\bar s;\bar t\right)e^{-\bar p\bar t}d\bar t, \tag{6.65}$$

where in this case,

$$\{\mathcal{I}\}^p\left(\bar r,\bar z;\bar s;\bar t\right)=\frac{2}{\pi}H\left(\bar t-K\sqrt{\bar d_1^2+\bar r^2}\right)\mathrm{Re}\left\{\int_0^{\frac{\pi}{2}}\{M\}^p\left(\bar\xi\left(\bar r,\bar d_1,\bar t,\phi\right),\phi\right)\frac{d\bar\xi}{d\bar t}d\phi\right\}, \tag{6.66}$$

with

$$\begin{aligned}\bar\xi\left(\bar r,\bar d_1,\bar t,\phi\right)&=\frac{i\bar t\bar r\cos\phi+\bar d_1\sqrt{\bar t^2-K^2\left(\bar d_1^2+\bar r^2\cos^2\phi\right)}}{\bar d_1^2+\bar r^2\cos^2\phi},\\ \frac{d\bar\xi}{d\bar t}\left(\bar r,\bar d_1,\bar t,\phi\right)&=\frac{i\bar r\cos\phi+\bar d_1\bar t\,/\sqrt{\bar t^2-K^2\left(\bar d_1^2+\bar r^2\cos^2\phi\right)}}{\bar d_1^2+\bar r^2\cos^2\phi}.\end{aligned} \tag{6.67}$$

By similar analyses, the time inversion of the other 5 terms can be accomplished. They are given as follows.

(2) The direct S-wave term

$$\{I\}^s\left(\bar r,\bar z;\bar s;\bar p\right)=\int_0^{\infty}\{\mathcal{I}\}^s\left(\bar r,\bar z;\bar s;\bar t\right)e^{-\bar p\bar t}d\bar t, \tag{6.68}$$

where

$$\{\mathcal{I}\}^s\left(\bar r,\bar z;\bar s;\bar t\right)=\frac{2}{\pi}H\left(\bar t-\sqrt{\bar d_1^2+\bar r^2}\right)\mathrm{Re}\left\{\int_0^{\frac{\pi}{2}}\{M\}^s\left(\bar\xi,\phi\right)\frac{d\bar\xi}{d\bar\tau_p}d\phi\right\}, \tag{6.69}$$

with

$$\begin{aligned} \bar{\xi}(\bar{t},\phi) &= \frac{i\bar{t}\bar{r}\cos\phi + \bar{d}_1\sqrt{\bar{t}^2 - \left(\bar{d}_1^2 + \bar{r}^2\cos^2\phi\right)}}{\bar{d}_1^2 + \bar{r}^2\cos^2\phi}, \\ \frac{d\bar{\xi}}{d\bar{t}}(\bar{t},\phi) &= \frac{i\bar{r}\cos\phi + \bar{d}_1\bar{t} \,/\, \sqrt{\bar{t}^2 - \left(\bar{d}_1^2 + \bar{r}^2\cos^2\phi\right)}}{\bar{d}_1^2 + \bar{r}^2\cos^2\phi}. \end{aligned} \tag{6.70}$$

(3) The reflected PP-wave

$$\{I\}^{pp}\left(\bar{r},\bar{z};\bar{s};\bar{p}\right) = \int_0^\infty \{\mathcal{I}\}^{pp}\left(\bar{r},\bar{z};\bar{s};\bar{t}\right) e^{-\bar{p}\bar{t}}\, d\bar{t}, \tag{6.71}$$

where

$$\{\mathcal{I}\}^{pp}\left(\bar{r},\bar{z};\bar{s};\bar{t}\right) = \frac{2}{\pi} H\left(\bar{t} - K\sqrt{\bar{d}_2^2 + \bar{r}^2}\right) \mathrm{Re}\left\{ \int_0^{\frac{\pi}{2}} \{M\}^{pp}\left(\bar{\xi},\phi\right) \frac{d\bar{\xi}}{d\bar{t}}\, d\phi \right\}, \tag{6.72}$$

with

$$\begin{aligned} \bar{\xi}(\bar{t},\phi) &= \frac{i\bar{t}\bar{r}\cos\phi + \bar{d}_2\sqrt{\bar{t}^2 - K^2\left(\bar{d}_2^2 + \bar{r}^2\cos^2\phi\right)}}{\bar{d}_2^2 + \bar{r}^2\cos^2\phi}, \\ \frac{d\bar{\xi}}{d\bar{t}}(\bar{t},\phi) &= \frac{i\bar{r}\cos\phi + \bar{d}_2\bar{t} \,/\, \sqrt{\bar{t}^2 - K^2\left(\bar{d}_2^2 + \bar{r}^2\cos^2\phi\right)}}{\bar{d}_2^2 + \bar{r}^2\cos^2\phi}. \end{aligned} \tag{6.73}$$

(4) The reflected SS-wave

$$\{I\}^{ss}\left(\bar{r},\bar{z};\bar{s};\bar{p}\right) = \int_0^\infty \{\mathcal{I}\}^{ss}\left(\bar{r},\bar{z};\bar{s};\bar{t}\right) e^{-\bar{p}\bar{t}}\, d\bar{t}, \tag{6.74}$$

where

$$\{\mathcal{I}\}^{ss}\left(\bar{r},\bar{z};\bar{s};\bar{t}\right) = \frac{2}{\pi} H\left(\bar{t} - \bar{t}_{ss}\right) \mathrm{Re}\left\{ \int_0^{\frac{\pi}{2}} \{M\}^{ss}\left(\bar{\xi},\phi\right) \frac{d\bar{\xi}}{d\bar{t}}\, d\phi \right\}, \tag{6.75}$$

with $\bar{t}_{ss}$ be the arrival time of the reflected SS-wave, and

$$
\begin{cases}
\bar{\xi}(\bar{t},\phi)=\dfrac{i\bar{t}\bar{r}\cos\phi+\bar{d}_2\sqrt{\bar{t}^2-\left(\bar{d}_2^2+\bar{r}^2\cos^2\phi\right)}}{\bar{d}_2^2+\bar{r}^2\cos^2\phi}, \\
\dfrac{d\bar{\xi}}{d\bar{t}}(\bar{t},\phi)=\dfrac{i\bar{r}\cos\phi+\bar{d}_2\bar{t}\,/\sqrt{\bar{t}^2-\left(\bar{d}_2^2+\bar{r}^2\cos^2\phi\right)}}{\bar{d}_2^2+\bar{r}^2\cos^2\phi},
\end{cases}
\quad for\ \bar{t}\geq\left(\bar{d}_2^2+\bar{r}^2\cos^2\phi\right),
$$

$$
\begin{cases}
\bar{\xi}(\bar{t},\phi)=\dfrac{i\bar{t}\bar{r}\cos\phi-\bar{d}_2\sqrt{\bar{t}^2-\left(\bar{d}_2^2+\bar{r}^2\cos^2\phi\right)}}{\bar{d}_2^2+\bar{r}^2\cos^2\phi}, \\
\dfrac{d\bar{\xi}}{d\bar{t}}(\bar{t},\phi)=\dfrac{i\bar{r}\cos\phi-\bar{d}_2\bar{t}\,/\sqrt{\bar{t}^2-\left(\bar{d}_2^2+\bar{r}^2\cos^2\phi\right)}}{\bar{d}_2^2+\bar{r}^2\cos^2\phi},
\end{cases}
\quad for\ \bar{t}<\left(\bar{d}_2^2+\bar{r}^2\cos^2\phi\right). \tag{6.76}
$$

(5) The reflected PS-wave

$$
\{I\}^{ps}\left(\bar{r},\bar{z};\bar{s};\bar{p}\right)=\int_0^{\infty}\{\mathcal{I}\}^{ps}\left(\bar{r},\bar{z};\bar{s};\bar{t}\right)e^{-\bar{p}\bar{t}}\,d\bar{t}, \tag{6.77}
$$

where

$$
\{\mathcal{I}\}^{ps}\left(\bar{r},\bar{z};\bar{s};\bar{t}\right)=\frac{2}{\pi}H\left(\bar{t}-\bar{t}_{ps}\right)\mathrm{Re}\left\{\int_0^{\frac{\pi}{2}}\{M\}^{ps}\left(\bar{\xi}(\bar{t},\phi),\phi\right)\frac{d\bar{\xi}}{d\bar{t}}\,d\phi\right\}, \tag{6.78}
$$

with $\bar{t}_{ps}$ be the arriving time of the reflected PS-wave, and $\bar{\xi}$ is determined by solving the following quartic equation

$$
\bar{t}=(\bar{\xi}^2+1)^{1/2}\bar{d}+(\bar{\xi}^2+K^2)^{1/2}\bar{s}-i\bar{\xi}\bar{r}\cos\phi \tag{6.79}
$$

(6) The reflected SP-wave

$$
\{I\}^{sp}\left(\bar{r},\bar{z};\bar{s};\bar{p}\right)=\int_0^{\infty}\{\mathcal{I}\}^{sp}\left(\bar{r},\bar{z};\bar{s};\bar{t}\right)e^{-\bar{p}\bar{t}}\,d\bar{t}, \tag{6.80}
$$

with

$$
\{\mathcal{I}\}^{sp}\left(\bar{r},\bar{z};\bar{s};\bar{t}\right)=\frac{2}{\pi}H\left(\bar{t}-\bar{t}_{sp}\right)\mathrm{Re}\left\{\int_0^{\frac{\pi}{2}}\{M\}^{sp}\left(\bar{\xi}(\bar{t},\phi),\phi\right)\frac{d\bar{\xi}}{d\bar{t}}\,d\phi\right\}, \tag{6.81}
$$

where $\overline{t}_{sp}$ is the arriving time of the reflected PS-wave, and $\overline{\xi}(\overline{t},\phi)$ is determined by solving the following quartic equation

$$\overline{t} = (\overline{\xi}^2 + K^2)^{1/2}\overline{d} + (\overline{\xi}^2 + 1)^{1/2}\overline{s} - i\overline{\xi}\overline{r}\cos\phi. \tag{6.82}$$

The time domain solutions derived here are all presented as integrals with respect to θ on the interval of 0 to 2 π and can be evaluated numerically with appropriate attentions as will be discussed in the next section.

6.5.2 Numerical Implemenation

(1) Integration of weakly singular function

Looking at Eqn. (6.75) which represents the displacement related to the reflected SS-wave, one can find that the integrand contains a singular point at $\phi^* = \text{Arccos}\sqrt{(\overline{t}^2 - \overline{d}_2^2)/\overline{r}^2}$ where $\frac{d\overline{\xi}}{d\overline{t}} \to \infty$. To avoid this problem, a transformation of the variable of integration is introduced as below

$$\phi = \phi^* + \psi^2,\ d\phi = 2\psi d\psi \tag{6.83}$$

where ψ is the newly introduced variable of integration. It is noted here that such a transformation is only needed for $\overline{t} < \sqrt{\overline{d}_2^2 + \overline{r}^2}$.

(2) Integration around Rayleigh pole

When both the source and receiver points are located on the free surface, one may encounter another numerical challenge associated with the Rayleigh pole, which is the root of $\overline{R}^-\left(\overline{\xi}\right) = 0$ and occupies a position on the imaginary axis of the complex $\overline{\xi}-$ plane.

To illustrate, take the result for the reflected PP-wave as an example which has the representation of

$$\{\mathcal{I}\}^{pp}\left(\bar{r},\bar{z};\bar{s};\bar{t}\right)=\frac{2}{\pi}H\left(\bar{t}-K\sqrt{\bar{d}_2^2+\bar{r}^2}\right)\mathrm{Re}\left\{\int_0^{\frac{\pi}{2}}\{M\}^{pp}\left(\bar{\xi},\phi\right)\frac{d\bar{\xi}}{d\bar{t}}d\phi\right\}, \tag{6.84}$$

with

$$\bar{\xi}(\bar{t},\phi)=\frac{i\bar{t}\bar{r}\cos\phi+\bar{d}_2\sqrt{\bar{t}^2-K^2\left(\bar{d}_2^2+\bar{r}^2\cos^2\phi\right)}}{\bar{d}_2^2+\bar{r}^2\cos^2\phi}. \tag{6.85}$$

With condition of $s=z=0$, i.e., $d_2=0$, Eqn. (6.73) is reduced to

$$\bar{\xi}(\bar{t},\phi)=i\cdot\bar{t}\,/\,(\bar{r}\cos\phi)\ . \tag{6.86}$$

It's known that the integrand $\{M\}^{pp}$ has a pole at point $\bar{\xi}=i\ (c_s/c_R)$, (C_R is the Rayleigh wave speed), which corresponds to $\phi=\cos^{-1}(c_s\bar{r}\,/\,c_R\bar{t}\,)$. If such a pole lies within the interval $[0,\pi/2]$, then the integration path of the integral stated in Eqn. (6.72) needs to be deformed in the complex $\phi-$ plane to avoid the pole.

One should also note from Eqn. (6.86) that $\bar{\xi}(\bar{t},\phi=\pi/2)=i\infty$. It is useful to retrieve the integration range in Eqn. (6.84) from $[0,\pi/2]$ to $[0,\pi]$, so that

$$\{\mathcal{I}\}^{pp}\left(\bar{r},\bar{z};\bar{s};\bar{t}\right)=\frac{1}{\pi}H\left(\bar{t}-K\sqrt{\bar{d}_2^2+\bar{r}^2}\right)\mathrm{Re}\left\{\int_0^{\pi}\{M\}^{pp}\left(\bar{\xi},\phi\right)\frac{d\bar{\xi}}{d\bar{t}}d\phi\right\}. \tag{6.87}$$

Then the integration path on the real axis of $\phi-$ plane is deformed to a triangle path as shown in Figure 6.8.

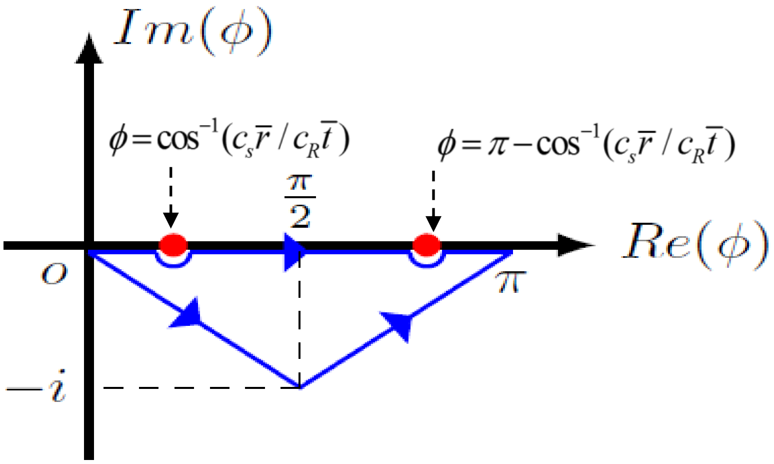

Figure 6.8: Contour path in complex $\phi-$ plane.

6.6 Application of Cagniard inversion approach – 2nd rendition

As one may notice, the Cagniard approach presented in Section 6.5 requires some careful choices of the Cagniard contour paths where branch lines, branch points and poles can be encountered. To execute the inversion approach in a simpler manner, reference is made to the fact that an alternative path of integration is permissible for (6.31) in lieu of going from 0 to π along the real axis owing to the analyticity of the integrands. For the present treatment, it is found to be most advantageous to take

$$J_n(\xi r)=\frac{2}{\pi}\mathrm{Re}\left((-i)^n(1-i\zeta)\int_0^{\pi/2} e^{i\xi r\cos[(1-i\zeta)\phi]}\cos[n(1-i\zeta)\phi]d\phi\right),\quad n=0,1,2;\ \zeta\ge 0 \tag{6.88}$$

or

$$J_0(r)=\frac{2}{\pi}\mathrm{Re}\left((1-i\zeta)\int_0^{\pi/2} e^{ir\cos[(1-i\zeta)\phi]}d\phi\right). \tag{6.89a}$$

$$J_1(r)=-\frac{2}{\pi}\mathrm{Re}\left(i(1-i\zeta)\int_0^{\pi/2} e^{ir\cos[(1-i\zeta)\phi]}\cos[(1-i\zeta)\phi]d\phi\right), \tag{6.89b}$$

$$J_2(z)=-\frac{2}{\pi}\mathrm{Re}\left((1-i\zeta)\int_0^{\pi/2} e^{iz\cos[(1-i\zeta)\phi]}\cos[2(1-i\zeta)\phi]d\phi\right). \tag{6.89c}$$

As will be shown in what follows, (6.88) is an effective decomposition of the Bessel functions in terms of elementary functions that can lead to considerable ease in reducing the Green's functions to a single line-integral representation for the half-space time-domain Green's functions. To this end, it is useful to first group the 5 fundamental integrals in Eqns. (6.24)-(6.28) for the Green's functions in the column vector form of

$$\left\{I_i^{\gamma}\left(\bar{r},\bar{z};\bar{s};\bar{p}\right)\right\}=\left\{I_r^x,I_\theta^x,I_z^x,I_r^z,I_z^z\right\}^T \tag{6.90}$$

where the superscripts $\gamma=\mathrm{h},\mathrm{v}$ denoting the horizontal and vertical t load directions and $i=r,\theta,z$ denoting the displacement response directions, respectively. Upon replacing their Bessel functions $J_0(\bar{p}\bar{\xi}\bar{r})$, $J_1(\bar{p}\bar{\xi}\bar{r})$, $J_2(\bar{p}\bar{\xi}\bar{r})$ by their integral representation in Eqn. (6.88), $\left\{I_i^{\gamma}\left(\bar{r},\bar{z};\bar{s};\bar{p}\right)\right\}$ can be expressed as

$$\{I_i^{\gamma}\left(\bar{r},\bar{z};\bar{s};\bar{p}\right)\}=\begin{matrix}\{I_i^{\gamma}\}^{P}\left(\bar{r},\bar{z};\bar{s};\bar{p}\right)+\{I_i^{\gamma}\}^{S}\left(\bar{r},\bar{z};\bar{s};\bar{p}\right)+\{I_i^{\gamma}\}^{PP}\left(\bar{r},\bar{z};\bar{s};\bar{p}\right)\\+\{I_i^{\gamma}\}^{SS}\left(\bar{r},\bar{z};\bar{s};\bar{p}\right)+\{I_i^{\gamma}\}^{PS}\left(\bar{r},\bar{z};\bar{s};\bar{p}\right)+\{I_i^{\gamma}\}^{SP}\left(\bar{r},\bar{z};\bar{s};\bar{p}\right)\end{matrix} \tag{6.91}$$

where

$$\{I_i^{\gamma}\}^{P}\left(\bar{r},\bar{z};\bar{s};\bar{p}\right)=\frac{2}{\pi}\mathrm{Re}\left((1-i\zeta)\int_0^{\pi/2}\int_0^{\infty}\left\{M_i^{\gamma}\right\}^{P}\left(\bar{\xi},\phi\right)e^{-\bar{p}\,\left(\bar{\alpha}\bar{d}_1-i\bar{\xi}\bar{r}\cos[(1-i\zeta)\phi]\right)}d\bar{\xi}\,d\phi\right), \tag{6.92a}$$

$$\{I_i^{\gamma}\}^{S}\left(\bar{r},\bar{z};\bar{s};\bar{p}\right)=\frac{2}{\pi}\mathrm{Re}\left((1-i\zeta)\int_0^{\pi/2}\int_0^{\infty}\{M_i^{\gamma}\}^{S}\left(\bar{\xi},\phi\right)e^{-\bar{p}\,\left(\bar{\beta}\bar{d}_1-i\bar{\xi}\bar{r}\cos[(1-i\zeta)\phi]\right)}d\bar{\xi}\,d\phi\right), \tag{6.92b}$$

$$\left\{I_i^{\gamma}\right\}^{PP}\left(\bar{r},\bar{z};\bar{s};\bar{p}\right)=\frac{2}{\pi}\mathrm{Re}\left((1-i\zeta)\int_0^{\pi/2}\int_0^{\infty}\{M_i^{\gamma}\}^{PP}\left(\bar{\xi},\phi\right)e^{-\bar{p}\,\left(\bar{\alpha}\bar{d}_2-i\bar{\xi}\bar{r}\,\cos[(1-i\zeta)\phi]\right)}d\bar{\xi}\,d\phi\right), \tag{6.92c}$$

$$\left\{I_i^{\gamma}\right\}^{SS}\left(\bar{r},\bar{z};\bar{s};\bar{p}\right)=\frac{2}{\pi}\mathrm{Re}\left((1-i\zeta)\int_0^{\pi/2}\int_0^{\infty}\left\{M_i^{\gamma}\right\}^{SS}\left(\bar{\xi},\phi\right)e^{-\bar{p}\,\left(\bar{\beta}\bar{d}_2-i\bar{\xi}\bar{r}\,\cos[(1-i\zeta)\phi]\right)}d\bar{\xi}\,d\phi\right), \tag{6.92d}$$

$$\left\{I_i^{\gamma}\right\}^{PS}\left(\bar{r},\bar{z};\bar{s};\bar{p}\right)=\frac{2}{\pi}\mathrm{Re}\left((1-i\zeta)\int_0^{\pi/2}\int_0^{\infty}\left\{M_i^{\gamma}\right\}^{PS}\left(\bar{\xi},\phi\right)e^{-\bar{p}\,\left(\bar{\beta}\bar{d}+\bar{\alpha}\bar{s}-i\bar{\xi}\bar{r}\,\cos[(1-i\zeta)\phi]\right)}d\bar{\xi}\,d\phi\right), \tag{6.92e}$$

$$\left\{I_i^{\gamma}\right\}^{SP}\left(\bar{r},\bar{z};\bar{s};\bar{p}\right)=\frac{2}{\pi}\mathrm{Re}\left((1-i\zeta)\int_0^{\pi/2}\int_0^{\infty}\left\{M_i^{\gamma}\right\}^{SP}\left(\bar{\xi},\phi\right)e^{-\bar{p}\,\left(\bar{\alpha}\bar{d}+\bar{\beta}\bar{s}-i\bar{\xi}\bar{r}\,\cos[(1-i\zeta)\phi]\right)}d\bar{\xi}\,d\phi\right), \tag{6.92f}$$

with $\left\{M_i^{\gamma}\left(\bar{\xi},\phi\right)\right\}=\left\{M_r^x,M_\theta^x,M_z^x,M_r^z,M_z^z\right\}^T$ where

$$\left\{M_i^{\gamma}\right\}^{P}\left(\bar{\xi},\phi\right)=\left\{-\frac{\bar{\xi}^{3}}{2\bar{\alpha}}\left(1+\cos\left(2\eta\right)\right),-\frac{\bar{\xi}^{3}}{2\bar{\alpha}}\left(1-\cos\left(2\eta\right)\right),\right.$$
$$\left.-sgn\left(\bar{z}-\bar{s}\right)\frac{i}{2}\bar{\xi}^{2}\cos\eta,\ sgn\left(\bar{z}-\bar{s}\right)\frac{i}{2}\bar{\xi}^{2}\cos\eta,\ \frac{\bar{\xi}\bar{\alpha}}{2}\right\}^{T},\tag{6.93a}$$

$$\left\{M_i^{\gamma}\right\}^{S}\left(\bar{\xi},\phi\right)=\left\{\frac{\bar{\xi}}{2}\left(\left(1+\cos\left(2\eta\right)\right)\bar{\beta}+\left(1-\cos\left(2\eta\right)\right)\frac{1}{\bar{\beta}}\right),\right.$$
$$\frac{\bar{\xi}}{2}\left(\left(1-\cos\left(2\eta\right)\right)\bar{\beta}+\left(1+\cos\left(2\eta\right)\right)\frac{1}{\bar{\beta}}\right),\qquad,\tag{6.93b}$$
$$\left.sgn\left(\bar{z}-\bar{s}\right)\frac{i}{2}\bar{\xi}^{2}\cos\eta,-sgn\left(\bar{z}-\bar{s}\right)\frac{i}{2}\bar{\xi}^{2}\cos\eta,-\frac{\bar{\xi}^{3}}{2\bar{\beta}}\right\}^{T}$$

$$\left\{M_i^{\gamma}\right\}^{PP}\left(\bar{\xi},\phi\right)=\left\{\frac{1}{2}\left(1+\cos\left(2\eta\right)\right)\frac{R^{+}\left(\bar{\xi}\right)}{R^{-}\left(\bar{\xi}\right)}\frac{\bar{\xi}^{3}}{\bar{\alpha}},\frac{1}{2}\left(1-\cos\left(2\eta\right)\right)\frac{R^{+}\left(\bar{\xi}\right)}{R^{-}\left(\bar{\xi}\right)}\frac{\bar{\xi}^{3}}{\bar{\alpha}},\right.$$
$$\left.\frac{i}{2}\cos\eta\frac{R^{+}\left(\bar{\xi}\right)}{R^{-}\left(\bar{\xi}\right)}\bar{\xi}^{2},\frac{i}{2}\cos\eta\frac{R^{+}\left(\bar{\xi}\right)}{R^{-}\left(\bar{\xi}\right)}\bar{\xi}^{2},\frac{\bar{\xi}\bar{\alpha}}{2}\frac{R^{+}\left(\bar{\xi}\right)}{R^{-}\left(\bar{\xi}\right)}\right\}^{T},\tag{6.93c}$$

$$\{M_i^{\gamma}\}^{SS}\left(\bar{\xi},\phi\right)=\left\{\frac{\bar{\xi}}{2}\left(\left(1+\cos\left(2\eta\right)\right)\frac{R^{+}\left(\bar{\xi}\right)}{R^{-}\left(\bar{\xi}\right)}\bar{\beta}+\left(1-\cos\left(2\eta\right)\right)\frac{1}{\bar{\beta}}\right),\right.$$
$$\frac{\bar{\xi}}{2}\left(\left(1-\cos\left(2\eta\right)\right)\frac{R^{+}\left(\bar{\xi}\right)}{R^{-}\left(\bar{\xi}\right)}\bar{\beta}+\left(1+\cos\left(2\eta\right)\right)\frac{1}{\bar{\beta}}\right),\qquad,\tag{6.93d}$$
$$\left.\frac{i}{2}\cos\eta\frac{R^{+}\left(\bar{\xi}\right)}{R^{-}\left(\bar{\xi}\right)}\bar{\xi}^{2},\frac{i}{2}\cos\eta\frac{R^{+}\left(\bar{\xi}\right)}{R^{-}\left(\bar{\xi}\right)}\bar{\xi}^{2},\frac{\bar{\xi}^{3}}{2\bar{\beta}}\frac{R^{+}\left(\bar{\xi}\right)}{R^{-}\left(\bar{\xi}\right)}\right\}^{T}$$

$$\left\{M_i^{\gamma}\right\}^{PS}\left(\bar{\xi},\phi\right)=\left\{\frac{-2\bar{\xi}^{3}\bar{\beta}\left(2\bar{\xi}^{2}+1\right)}{\bar{R}^{-}\left(\bar{\xi}\right)}\left(1+\cos\left(2\eta\right)\right),\frac{-2\bar{\xi}^{3}\bar{\beta}\left(2\bar{\xi}^{2}+1\right)}{\bar{R}^{-}\left(\bar{\xi}\right)}\left(1-\cos\left(2\eta\right)\right),\right.$$
$$\left.-2i\cos\eta\frac{\bar{\xi}^{4}\left(2\bar{\xi}^{2}+1\right)}{\bar{R}^{-}\left(\bar{\xi}\right)},-2i\cos\eta\frac{\bar{\xi}^{2}\left(2\bar{\xi}^{2}+1\right)\bar{\alpha}\bar{\beta}}{\bar{R}^{-}\left(\bar{\xi}\right)},\frac{-2\bar{\xi}^{3}\bar{\alpha}\left(2\bar{\xi}^{2}+1\right)}{\bar{R}^{-}\left(\bar{\xi}\right)}\right\}^{T},\tag{6.93e}$$

$$\left\{M_i^{\gamma}\right\}^{SP}\left(\bar{\xi},\phi\right)=\left\{\frac{-2\bar{\xi}^3\bar{\beta}\left(2\bar{\xi}^2+1\right)}{\bar{R}^-\left(\bar{\xi}\right)}\left(1+\cos\left(2\eta\right)\right),\frac{-2\bar{\xi}^3\bar{\beta}\left(2\bar{\xi}^2+1\right)}{\bar{R}^-\left(\bar{\xi}\right)}\left(1-\cos\left(2\eta\right)\right),\right.$$
$$\left.-2i\cos\eta\frac{\bar{\xi}^2\left(2\bar{\xi}^2+1\right)\bar{\alpha}\bar{\beta}}{\bar{R}^-\left(\bar{\xi}\right)},-2i\cos\eta\frac{\bar{\xi}^4\left(2\bar{\xi}^2+1\right)}{\bar{R}^-\left(\bar{\xi}\right)},\frac{-2\bar{\xi}^3\bar{\alpha}\left(2\bar{\xi}^2+1\right)}{\bar{R}^-\left(\bar{\xi}\right)}\right\}^T, \quad (6.93f)$$

with $\eta=(1-i\zeta)\phi$. Note that all the functions in the 5x1 column arrays of $\{M_i^{\gamma}\}$'s in Eqns. (6.93a) to (6.93f) are analytic in the first quadrant of the complex $\bar{\xi}-$ plane, except at the branch points and branch lines of $\bar{\alpha}$, $\bar{\beta}$ and the simple pole associated with the Rayleigh wave function $\bar{R}^-\left(\bar{\xi}\right)$, all on the imaginary axis. As will be clarified in later reduction and inversion to the time domain in the following sections, the six integral terms in Eqn. (6.91) correspond to six physical wave groups that can be termed as the direct P-, and S-waves, and the reflected PP-, SS-, PS- and SP-wave groups, as previously done in Graff (1975), Johnson (1974) and others, for an arbitrary pair of surface or buried source-receiver locations and expressed single finite-line integrals.

6.6.1 Inverse Laplace transform by Cagniard approach

(1) Direct P-wave integral

Consider first the wave-group integral

$$\{I_i^{\gamma}\}^P\left(\bar{r},\bar{z};\bar{s};\bar{p}\right)=\frac{2}{\pi}\mathrm{Re}\left((1-i\zeta)\int_0^{\pi/2}\int_0^{\infty}\{M_i^{\gamma}\}^P\left(\bar{\xi},\phi;\bar{r},\bar{z},\bar{s}\right)e^{-\bar{p}\left(\bar{\alpha}\bar{d}_1-i\bar{\xi}\bar{r}\cos[(1-i\zeta)\phi]\right)}d\bar{\xi}\,d\phi\right). \quad (6.94)$$

in Eqn. (6.93) and extend the integration variable $\bar{\xi}$ of the inner semi-infinite integral onto the complex plane. In seeking an integration path with respect to $\bar{\xi}$ such that the exponential kernel is identical to the standard Laplace transform kernel of $e^{-\bar{p}\bar{t}}$ where $\bar{t}$ is real and ≥ 0 as suggested by Cagniard (1939) for an exact Laplace transform inversion, it is natural to define

$$\bar{t}(\bar{\xi},\phi)=\bar{\alpha}\bar{d}_1-i\bar{\xi}\bar{r}\cos[(1-i\zeta)\phi]=\sqrt{\left(\bar{\xi}^2+K^2\right)}\bar{d}_1-i\bar{\xi}\bar{r}\cos[(1-i\zeta)\phi]. \quad (6.95)$$

Equation (6.95) has an inverse one-to-one mapping of $\bar{t}$ to $\bar{\xi}$ in

$$\bar{\xi}\ (\bar{t},\phi) = \frac{i\bar{t}\bar{r}\cos[(1-i\zeta)\phi] + \bar{d}_1\sqrt{\bar{t}^2 - K^2\left(\bar{d}_1^2 + \bar{r}^2\cos^2[(1-i\zeta)\phi]\right)}}{\bar{d}_1^2 + \bar{r}^2\cos^2[(1-i\zeta)\phi]}, \tag{6.96}$$

with the square root function $\sqrt{Z}$ in (6.96) taken with $-\pi \le \arg Z < \pi$.

For any chosen set of source and receiver locations and ϕ in the integration range, Eqn. (6.96) represents an alternate contour to the real axis in the complex $\bar{\xi}-$plane, going from the origin *0* to ∞ in the first quadrant as a function of $\bar{t}$ monotonically by virtue of the simple non-singular nature of the integrand of (6.94). For any pair of source and receiver locations with a specific time $\bar{t}$ of interest, on the other hand, the variation of ϕ from 0 to $\pi/2$ for the integration in (6.94) traces a finite curvilinear arc that begins at a point on either the imaginary axis or in the first quadrant of the complex $\bar{\xi}-$ plane and ends on the real axis. Denoting the former path as C $(\bar{t};\phi)$ and the latter contour as $D\ (\phi;\bar{t})$, a family of them are shown in Figure 6.9. They illustrate a number of interesting and important analytical features that lead to a set of appealing consequences and are shared by the other wave integrals. From the display, for instance, one can see that the contours are generally smooth curves and away from the imaginary axis where the branch point for α and the Rayleigh pole of $\bar{R}^-$ lie. Furthermore, the mappings defined in (6.95) and (6.96) have the features of

(a) $\bar{\xi}(K\bar{d}_1,\phi) = 0$, (6.97)

(b) $\bar{\xi}(\bar{t},0) = i\left(\dfrac{\bar{t}\bar{r} - \bar{d}_1\sqrt{K^2\left(\bar{d}_1^2+\bar{r}^2\right)-\bar{t}^2}}{\bar{d}_1^2+\bar{r}^2}\right)$ for $0 \le \bar{t} \le K\sqrt{\left(\bar{d}_1^2+\bar{r}^2\right)}$, (6.98)

(c) $\bar{t}(\bar{\xi},\pi/2) = (\bar{\xi}^2+K^2)^{\frac{1}{2}}\bar{d}_1 + \sinh\left(\zeta\pi/2\right)\bar{\xi}\bar{r}$. (6.99)

By these analytical features, Cauchy's theorem and Jordan's Lemma, (6.94) can be written as

$$\left\{I_i^\gamma\right\}^P\left(\bar{r},\bar{z};\bar{s};\bar{p}\right)=\frac{2}{\pi}\mathrm{Re}\left((1-i\zeta)\int_0^{\pi/2}\int_{C(\bar{\xi})}\left\{M_i^\gamma\right\}^p\left(\bar{\xi},\phi;\bar{r},d_1\right)e^{-\bar{p}\,\left(\bar{\alpha}\bar{d}_1-i\bar{\xi}\bar{r}\cos[(1-i\zeta)\phi]\right)}d\bar{\xi}\;d\phi\right) \tag{6.100}$$

by the theory of contour integration. Through the use of (6.96) in the reversal of the order of integration, (6.100) can be written as

$$\begin{aligned}\{I_i^\gamma\}^P\left(\bar{r},\bar{z};\bar{s};\bar{p}\right)&=\frac{2}{\pi}\mathrm{Re}\left((1-i\zeta)\int_0^{\pi/2}\int_{C(\bar{t}:[Kd_1,\infty);\phi)}\{M_i^\gamma\}^P(\bar{\xi}(\bar{t},\phi),\phi;\bar{r},\bar{z};\bar{s})\frac{\partial\,\bar{\xi}}{\partial\,\bar{t}}(\bar{t},\phi)e^{-\bar{p}\,\bar{t}}d\bar{t}\;d\phi\right)\\&=\int_{Kd_1}^{\infty}\frac{2}{\pi}\mathrm{Re}\left\{(1-i\zeta)\int_{D(\phi:(0,\pi/2);\bar{t})}\{M_i^\gamma\}^P(\bar{\xi}(\bar{t},\phi),\phi;\bar{r},\bar{z};\bar{s})\frac{\partial\,\bar{\xi}}{\partial\,t}(\bar{t},\phi)d\phi\right\}e^{-\bar{p}\,\bar{t}}d\bar{t}\\&=\int_0^{\infty}\left\{H(\bar{t}-Kd_1)\frac{2}{\pi}\mathrm{Re}\left\{(1-i\zeta)\int_{D(\phi:(0,\pi/2);\bar{t})}\{M_i^\gamma\}^P(\bar{\xi}(\bar{t},\phi),\phi;\bar{r},\bar{z};\bar{s})\frac{\partial\,\bar{\xi}}{\partial\,t}(\bar{t},\phi)d\phi\right\}\right\}e^{-\bar{p}\,\bar{t}}d\bar{t}\end{aligned} \tag{6.101}$$

where *H(t)* is the Heaviside function. For further reduction, it is useful to note that on the occasion that the point $\bar{\xi}(\bar{t},0)=\bar{\xi}_0$ (point A) is on the imaginary axis but at or below the lowest singular point (in this case, the branch point of α at *iK)*, it can be shown by the virtue of the analytical characteristics of the integrand $\{M\}^p\left(\bar{\xi},\phi;\bar{r},\bar{z},\bar{s}\right)$ in (6.93a) that the integral

$$\mathrm{Re}\left\{(1-i\zeta)\int_0^{\pi/2}\left\{M_i^\gamma\right\}^P\left(\bar{\xi}(\bar{t},\phi),\phi;\bar{r},\bar{z},\bar{s}\right)\frac{\partial\bar{\xi}}{\partial\bar{t}}(\bar{t},\phi)d\phi\right\}=0 \tag{6.102}$$

by contour integration. Together with the observation of the (6.102), $I^P(\bar{t};\bar{r},\bar{z};\bar{s})$ can thus be proved to be identically zero for $0\le\bar{t}\le K\sqrt{\bar{d}_1^2+\bar{r}^2}$, allowing (6.101) to be reduced to the compact form of

$$\{I_i^\gamma\}^P\left(\bar{r},\bar{z};\bar{s};\bar{p}\right)=\int_0^{\infty}\{\mathcal{I}_i^\gamma\}^P\left(\bar{r},\bar{z};\bar{s};\bar{t}\right)\;e^{-\bar{p}\,\bar{t}}d\bar{t} \tag{6.103}$$

where

$$\{\mathcal{I}_i^\gamma\}^P\left(\bar{r},\bar{z};\bar{s};\bar{t}\right)=H(\bar{t}-\bar{t}^{\,P}\;)\;\frac{2}{\pi}\mathrm{Re}\left\{(1-i\zeta)\int_0^{\pi/2}\{M_i^\gamma\}^P(\bar{\xi}(\bar{t}),\phi;\bar{r},\bar{z};\bar{s})\frac{\partial\,\bar{\xi}}{\partial\,t}(\bar{t},\phi)d\phi\right\} \tag{6.104}$$

is the requisite time-domain solution with

$$\bar{t}^{\,p} = K\sqrt{\bar{d}_1^{2} + \bar{r}^{2}} \tag{6.105}$$

representing the direct P-wave group's arrival time that is well known in seismology and geophysics.

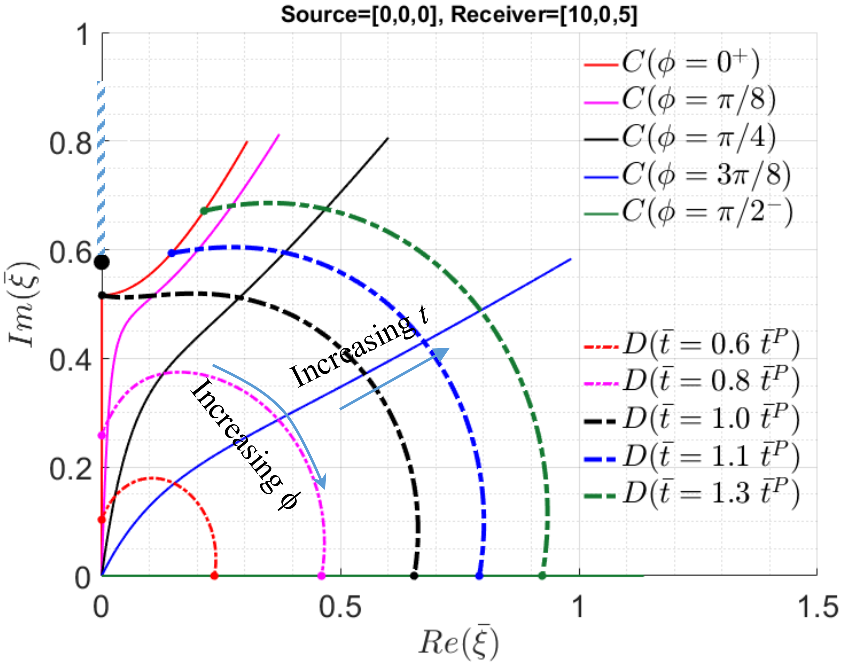

Figure 6.9: A family of Cagniard and ϕ-integration (C-P) contours for $(r, z; s) = (10, 5; 0)$, $\nu = 0.25$, $K = 0.577$, ζ=0.2

It is relevant to note that Bessel contour parameter ζ can be any positive real number. Its influence on the variation of the integrand and its helpfulness as a means to improve the efficiency in numerical quadrature over the integration range is illustrated in Figure 6.10.

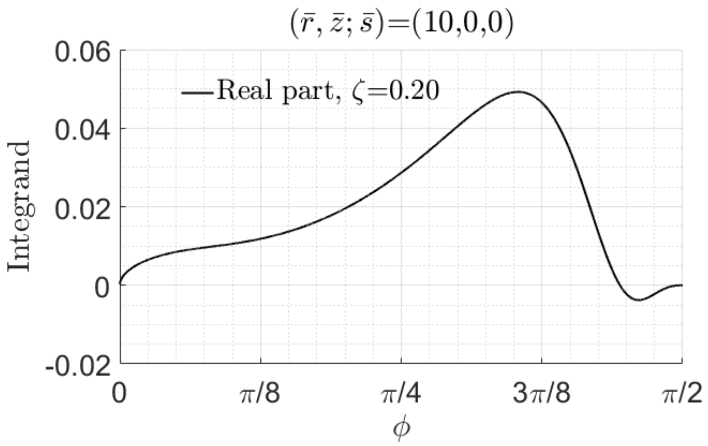

Figure 6.10: Variations of $\left(I_r^x\right)^P$ integrand along D contours over ϕ from 0 to $\pi/2$ for $\zeta=0.2$($\bar{s}=0$, $\bar{z}=0$, $\bar{r}=10$, $\bar{t}=1.1K\sqrt{\bar{d}_1^2+\bar{r}^2}$).

The time domain results for the other 5 wave-group integrals can be obtained in a similar manner as outlined below:

(2) Direct S-wave integral

$$\left\{I_i^\gamma\right\}^S\left(\bar{r},\bar{z};\bar{s};\bar{p}\right)=\int_0^\infty\left\{\mathcal{I}_i^\gamma\right\}^S\left(\bar{r},\bar{z};\bar{s};\bar{t}\right)e^{-\bar{p}\bar{t}}d\bar{t}\ , \tag{6.106}$$

where

$$\left\{\mathcal{I}_i^\gamma\right\}^S\left(\bar{r},\bar{z};\bar{s};\bar{t}\right)=\frac{2}{\pi}H\left(\bar{t}-\bar{t}^S\right)\mathrm{Re}\left\{(1-i\zeta)\int_0^{\frac{\pi}{2}}\left\{M_i^\gamma\right\}^S\left(\bar{\xi}(\bar{t},\phi;\bar{r},\bar{z};\bar{s}),\phi\right)\frac{\partial\bar{\xi}}{\partial\bar{t}}(\bar{t},\phi)d\phi\right\}, \tag{6.107}$$

with

$$\bar{\xi}(\bar{t},\phi)=\frac{i\bar{t}\bar{r}\cos[(1-i\zeta)\phi]+\bar{d}_1\sqrt{\bar{t}^2-\left(\bar{d}_1^2+\bar{r}^2\cos^2[(1-i\zeta)\phi]\right)}}{\bar{d}_1^2+\bar{r}^2\cos^2[(1-i\zeta)\phi]}\,. \tag{6.108}$$

and

$$\bar{t}^S=\sqrt{\bar{d}_1^2+\bar{r}^2} \tag{6.109}$$

as the arrival time of the S-wave group at the receiver location.

(3) Reflected PP-wave integral

$$\left\{I_i^{\gamma}\right\}^{PP}\left(\bar{r},\bar{z};\bar{s};\bar{p}\right)=\int_0^{\infty}\left\{\mathcal{I}_i^{\gamma}\right\}^{PP}\left(\bar{r},\bar{z};\bar{s};\bar{t}\right)e^{-\bar{p}\bar{t}}\,d\bar{t}, \tag{6.110}$$

where

$$\left\{\mathcal{I}_i^{\gamma}\right\}^{PP}\left(\bar{r},\bar{z};\bar{s};\bar{t}\right)=\frac{2}{\pi}H\left(\bar{t}-\bar{t}^{PP}\right)\mathrm{Re}\left\{(1-i\zeta)\int_0^{\frac{\pi}{2}}\left\{M_i^{\gamma}\right\}^{PP}\left(\bar{\xi}(\bar{t},\phi;\bar{r},d_2),\phi\right)\frac{\partial\bar{\xi}}{\partial\bar{t}}\,d\phi\right\}, \tag{6.111}$$

with

$$\bar{\xi}(\bar{t},\phi;\bar{r},d_2)=\frac{i\bar{t}\bar{r}\cos[(1-i\zeta)\phi]+\bar{d}_2\sqrt{\bar{t}^2-K^2\left(\bar{d}_2^2+\bar{r}^2\cos^2[(1-i\zeta)\phi]\right)}}{\bar{d}_2^2+\bar{r}^2\cos^2[(1-i\zeta)\phi]}. \tag{6.112}$$

and

$$\bar{t}^{PP}=K\sqrt{\bar{d}_2^2+\bar{r}^2} \tag{6.113}$$

as the arrival time for the PP- wave.

(4) Reflected SS-wave integral

On defining $\bar{t}=\left(\bar{\beta}\bar{d}_2-i\bar{\xi}\bar{r}\ \cos[(1-i\zeta)\phi]\right)=\sqrt{\left(\bar{\xi}^2+1\right)}\bar{d}_2-i\bar{\xi}\bar{r}\cos[(1-i\zeta)\phi]$ which has $\bar{t}=\bar{d}_2$ at $\bar{\xi}=0$, $\left\{I\right\}^{ss}$ can be written as

$$\left\{I_i^{\gamma}\right\}^{ss}\left(\bar{r},\bar{z};\bar{s};\bar{p}\right)=\int_0^{\infty}\left\{\mathcal{I}_i^{\gamma}\right\}^{ss}\left(\bar{r},\bar{z};\bar{s};\bar{t}\right)e^{-\bar{p}\bar{t}}\,d\bar{t}, \tag{6.114}$$

$$\left\{\mathcal{I}_i^{\gamma}\right\}^{ss}\left(\bar{r},\bar{z};\bar{s};\bar{t}\right)=\frac{2}{\pi}H\left(\bar{t}-\bar{t}_{ss}\right)\mathrm{Re}\left\{(1-i\zeta)\int_0^{\frac{\pi}{2}}\left\{M_i^{\gamma}\right\}^{ss}\left(\bar{\xi}(\bar{t},\phi;\bar{r},d_2),\phi\right)\frac{\partial\bar{\xi}}{\partial\bar{t}}\,d\phi\right\}, \tag{6.115}$$

with

$$\bar{\xi}(\bar{t},\phi;\bar{r},d_2)=\frac{i\bar{t}\bar{r}\cos[(1-i\zeta)\phi]+\bar{d}_2\sqrt{\bar{t}^2-\left(\bar{d}_2^2+\bar{r}^2\cos^2[(1-i\zeta)\phi]\right)}}{\bar{d}_2^2+\bar{r}^2\cos^2[(1-i\zeta)\phi]}\ . \qquad (6.116)$$

where $\bar{t}^{SS}$ denotes the arrival time of reflected SS-wave group. In this case, however, the arrival time $\bar{t}^{SS}$ proves to be a function of two criteria. The dual condition arises mathematically because of the possibility that $\bar{\xi}(\bar{t},0)\equiv\bar{\xi}_0^{SS}$ can be located directly below the α-branch point on the positive imaginary axis, along the right α-branch line or off into the first quadrant depending on the relative value of $\bar{r},\bar{d}_2$ and K according to (6.116). For instance, one can see that

(a) $\bar{\xi}_0^{SS}$ is on the positive imaginary axis if $\bar{d}_2 \le \bar{t} < \sqrt{\bar{d}_2^2+\bar{r}^2}$,

(b) $\bar{\xi}_0^{SS}$ has a positive real part if $\bar{t} > \sqrt{\bar{d}_2^2+\bar{r}^2}$,

(c) when $\bar{t}=\sqrt{\bar{d}_2^2+\bar{r}^2}$, $\bar{\xi}=i\left(\dfrac{\bar{r}}{\sqrt{\bar{d}_2^2+\bar{r}^2}}\right)$. In this case, one can easily deduce from Eqn. (6.116) that $\bar{\xi}_0^{SS}$ will be below the P-wave branch point on the positive imaginary axis if $\dfrac{\bar{r}}{\sqrt{\bar{d}_2^2+\bar{r}^2}}<K$ (or $r\le\bar{d}_2\,K\big/\sqrt{1-K^2}$) or above it (i.e., on the branch line) if $r>\bar{d}_2\,K\big/\sqrt{1-K^2}$.

The first scenario is illustrated in Figure 6.11 where the $C\,(\bar{t};\phi)$-$D\,(\phi;\bar{t})$ contour net in the complex $\bar{\xi}-$ plane is plotted for a case whose source-receiver locations satisfy the criterion $\bar{r}<K\bar{d}_2/\sqrt{1-K^2}$. As one can see for the three times that satisfy $\bar{d}_2\le\bar{t}\le\sqrt{\bar{d}_2^2+\bar{r}^2}$, the D-contours all start from some locations on the imaginary axis below the branch point iK for $\bar{t}\le\sqrt{\bar{d}_2^2+\bar{r}^2}$, while the two cases of $\bar{t}>\sqrt{\bar{d}_2^2+\bar{r}^2}$ have their $\bar{\xi}_0$ lying in the first quadrant. Similar to the direct P-wave scenario, it can be shown by the analytical characteristics of the integrand $\left\{M_i^\gamma\right\}^{SS}\left(\bar{\xi},\phi;\bar{r},\bar{z},\bar{s}\right)$and analytic function theory that the integral $\left\{I\right\}^{SS}$ in the former case are identically zero as in the $\left\{I_i^\gamma\right\}^P$ case, giving the arrival time $\bar{t}_1^{SS}=\sqrt{\bar{d}_2^2+\bar{r}^2}$ for the case

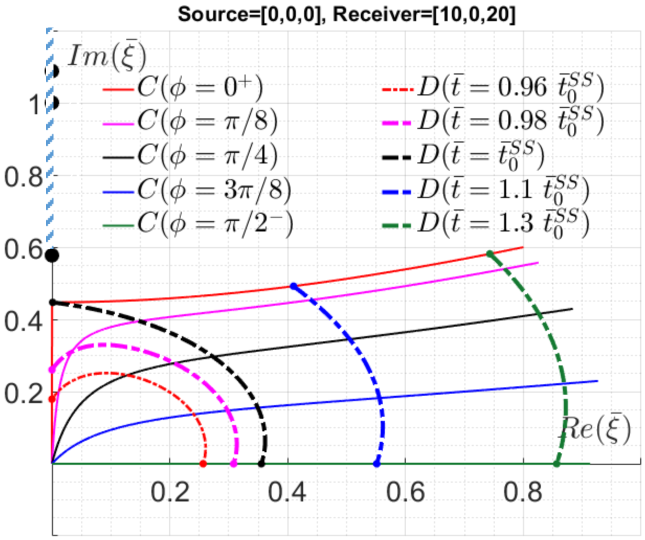

Figure 6.11: A family of (C-P) contours for $[\mathcal{I}]^{SS}$ integral: $(r, z; s) = (10, 20; 0)$, $\nu = 0.25$, $K = 0.577$, ζ=0.2, $\bar{r} = 10$, $\bar{d}_2 = 20$, $\bar{t}_0^{SS} = 22.36$, $\bar{\xi}_0(\bar{t}_0^{SS}) = 0.447i$

An example of the second scenario, i.e., $r > K\bar{d}_2 / \sqrt{1-K^2}$, is shown in Figure 6.12. In this case, the starting point $\bar{\xi}_0$ of the integration contour D that corresponds to $\bar{t} = \sqrt{\bar{d}_2^2 + \bar{r}^2}$ is a point sitting on the P-wave branch line on the boundary of the first quadrant. Owing to the change in character of the radical $\bar{\alpha}(\bar{\xi})$ in $\{M\}^{SS}$, the line integral over D in Eqn. (6.115) is generally be non-zero. In mathematical form, such a requirement is

$$\frac{\bar{\xi}(\bar{t}, \phi = 0; \bar{r}, d_2)}{i} = \frac{\bar{t}\bar{r} - \bar{d}_2\sqrt{\left(\bar{d}_2^2 + \bar{r}^2\right) - \bar{t}^2}}{\bar{d}_2^2 + \bar{r}^2} < K, \tag{6.117}$$

which leads to

$$\bar{t} < K\bar{r} + \bar{d}_2\sqrt{1-K^2}. \tag{6.118}$$

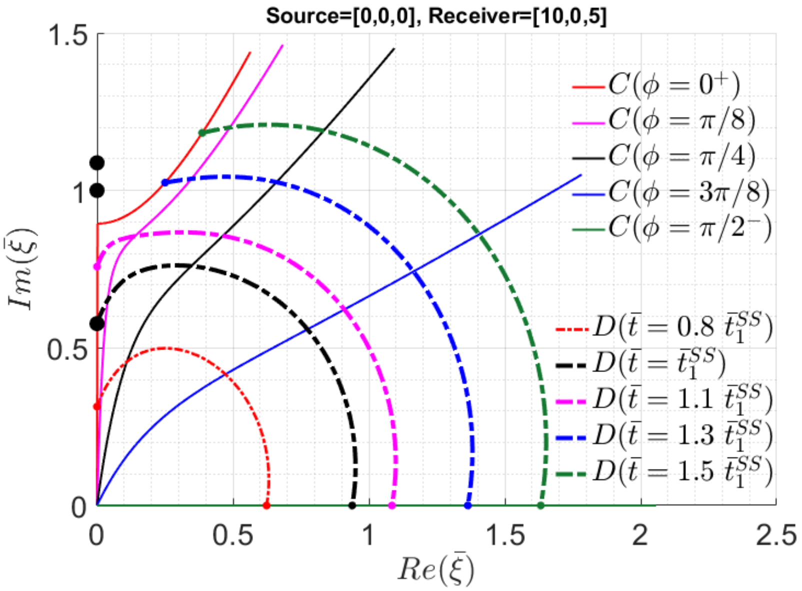

Figure 6.12: A family of (C-P) contours for $[\mathcal{I}]^{SS}$ integral: $(r, z; s) = (10, 5; 0)$, $\nu = 0.25$, $K = 0.577$, ζ=0.2, $\bar{r} = 10$, $\bar{d}_2 = 5$, $\bar{t}_1^{SS} = 9.86$, $\bar{\xi}_0(\bar{t}_1^{SS}) = iK = 0.577\mathrm{i}$

In summary, the arrival time for the SS-wave group can be determined by

$$\bar{t}^{SS} = \left\{ \begin{array}{ll} \bar{t}_1^{SS} \equiv \sqrt{\bar{d}_2^2 + \bar{r}^2}, & for\ \bar{r} \le \bar{d}_2 K \big/ \sqrt{1-K^2} \\ \bar{t}_2^{SS} \equiv K\bar{r} + \bar{d}_2\sqrt{1-K^2}, & for\ \bar{r} > \bar{d}_2 K \big/ \sqrt{1-K^2} \end{array} \right\}. \qquad (6.119)$$

as was previously found by geometric ray theory (Shearer 2009).

(5) Reflected PS-wave integral

On defining

$$\bar{t} = (\bar{\xi}^2 + 1)^{1/2}\bar{z} + (\bar{\xi}^2 + K^2)^{1/2}\bar{s} - i\bar{\xi}\bar{r}\cos[(1 - i\zeta)\phi] \qquad (6.120)$$

which has the value of $\bar{z} + K\bar{s}$ at $\bar{\xi} = 0$, $\{I\}^{PS}$ in Eqn. (6.93e) can be written as

$$\left\{I_i^{\gamma}\right\}^{PS}\left(\bar{r},\bar{z};\bar{s};\bar{p}\right)=\int_0^{\infty}\left\{\mathcal{I}_i^{\gamma}\right\}^{PS}\left(\bar{r},\bar{z};\bar{s};\bar{t}\right)e^{-\bar{p}\bar{t}}d\bar{t} \tag{6.121}$$

with

$$\left\{\mathcal{I}_i^{\gamma}\right\}^{PS}\left(\bar{r},\bar{z};\bar{s};\bar{t}\right)=\frac{2}{\pi}H\left(\bar{t}-\bar{t}^{PS}\right)\mathrm{Re}\left\{(1-i\zeta)\int_0^{\frac{\pi}{2}}\left\{M_i^{\gamma}\right\}^{PS}\left(\bar{\xi}(\bar{t},\phi;\bar{r},\bar{z}),\phi\right)\frac{d\bar{\xi}}{d\bar{t}}d\phi\right\}, \tag{6.122}$$

where $\bar{t}^{PS}$ denotes the arrival time of the reflected PS-wave. At $\phi=0$, $\bar{\xi}_0$ of the D-contour for $\bar{t}\geq\bar{z}+K\bar{s}$ is determined through Eqn. (6.120) by

$$\bar{t}=(\bar{\xi}_0^2+1)^{1/2}\bar{z}+(\bar{\xi}_0^2+K^2)^{1/2}\bar{s}-i\bar{\xi}_0\bar{r}\ . \tag{6.123}$$

Similar to the SS-wave integral, the arrival time $\bar{t}^{PS}$ is also a function of two criteria because $\bar{\xi}(\bar{t},0)\equiv\bar{\xi}_0^{PS}$ can be located directly below the α-branch point on the imaginary axis, along the right α-branch line or off into the first quadrant depending on the relative value of $\bar{r}$, $\bar{z}$, $\bar{s}$ and K according to Eqn. (6.123). For instance, one can see that

- For $\bar{s}>0$, the point $\bar{\xi}_0$ cannot locate above the branch point $(0,iK)$ when it is on the imaginary axis for a real $\bar{t}$. This is because for points on the imaginary axis above the branch point, the term $(\bar{\xi}_0^2+K^2)^{1/2}$ is purely $(+)$ imaginary, and there is no solution of Eqn. (6.123) for a real $\bar{t}$.

In this scenario to find the largest time or the highest coordinate $\bar{\xi}_0$ on the imaginary axis, one can set

$$\frac{d\bar{t}}{d\bar{\xi}}=\frac{\bar{\xi}\bar{z}}{(\bar{\xi}^2+1)^{1/2}}+\frac{\bar{\xi}\bar{s}}{(\bar{\xi}^2+K^2)^{1/2}}-i\bar{r}=0\ . \tag{6.124}$$

and replace $\bar{\xi}=ia$ where a is real. The equation then becomes

$$\frac{a\bar{z}}{(1-a^2)^{1/2}}+\frac{a\bar{s}}{(K^2-a^2)^{1/2}}=\bar{r},\quad a\leq K\,, \tag{6.125}$$

Denoting its solution as a_{ps}, the arrival time can then be expressed as

$$\bar{t}^{PS} = (1-a_{ps}^2)^{1/2}\bar{z} + (K^2 - a_{ps}^2)^{1/2}\bar{s} + a_{ps}\bar{r} \tag{6.126}$$

Upon replacing $\bar{r}$ by $\dfrac{a\bar{z}}{(1-a^2)^{1/2}} + \dfrac{a\bar{s}}{(K^2-a^2)^{1/2}}$ as noted in Eqn. (6.126), (6.126) can be reduced to

$$\bar{t}_0^{PS} = \frac{K^2\bar{s}}{\sqrt{K^2 - a_{ps}^2}} + \frac{\bar{z}}{\sqrt{1-a_{ps}^2}}, \quad \bar{s} > 0. \tag{6.127}$$

Such a scenario is illustrated in Figure 6.13.

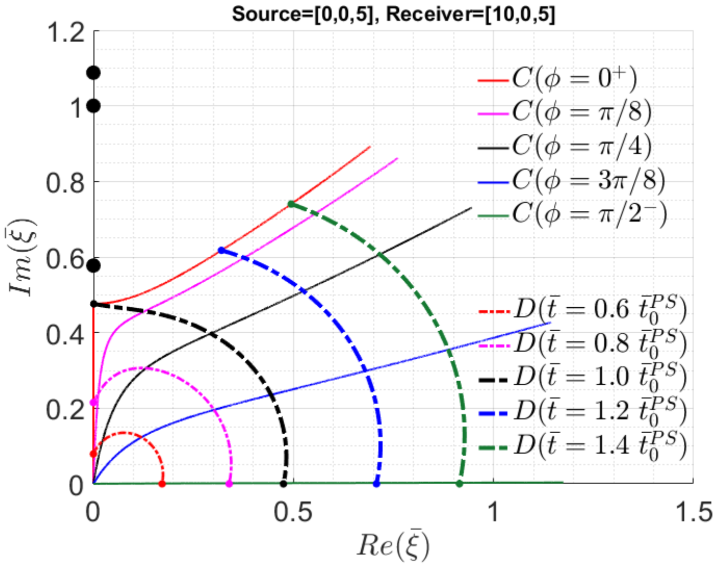

Figure 6.13: A family of (C-P) contours for $[\mathcal{I}]^{PS}$ integral: (r, z; s) = (10, 5; 5), ν = 0.25, K = 0.577, ζ=0.2, $\bar{t}_0^{PS} = 10.79$, $\bar{\xi}_0(\bar{t}_0^{PS}) = 0.476i$

- For $\bar{s} = 0$, Eqn. (6.123) reduces to $\bar{t} = (\bar{\xi}_0^2 + 1)^{1/2}\bar{z} - i\bar{\xi}_0\bar{r}$, from which one obtains that

$$\bar{\xi}_0^{PS}(\bar{t}) = \frac{i\bar{t}\bar{r} + \bar{d}_2\sqrt{\bar{t}^2 - \left(\bar{z}^2 + \bar{r}^2\right)}}{\bar{z}^2 + \bar{r}^2}. \tag{6.128}$$

When $\bar{t} = \sqrt{\bar{z}^2 + \bar{r}^2}$, $\bar{\xi}_0^{PS} = i\left(\frac{\bar{r}}{\sqrt{\bar{z}^2 + \bar{r}^2}}\right)$ and one can easily deduce that $\bar{\xi}_0^{PS}$ will be below the P-wave branch point on the positive imaginary axis if $\frac{\bar{r}}{\sqrt{\bar{z}^2 + \bar{r}^2}} < K$ (or $r \le \bar{z}\,K\big/\sqrt{1-K^2}$) or above it (i.e., on the branch line) if $r > \bar{z}\,K\big/\sqrt{1-K^2}$.

Following a similar analysis for the SS-wave integral, one concludes that

$$\bar{t}_1^{PS} = \sqrt{\bar{z}^2 + \bar{r}^2} \quad for \quad \frac{\bar{r}}{\sqrt{\bar{r}^2 + \bar{z}^2}} \le K. \tag{6.129}$$

and

$$\bar{t}_2^{PS} = \bar{z}\sqrt{1-K^2} + K\bar{r}, \quad for \quad \frac{\bar{r}}{\sqrt{\bar{r}^2 + \bar{z}^2}} > K. \tag{6.130}$$

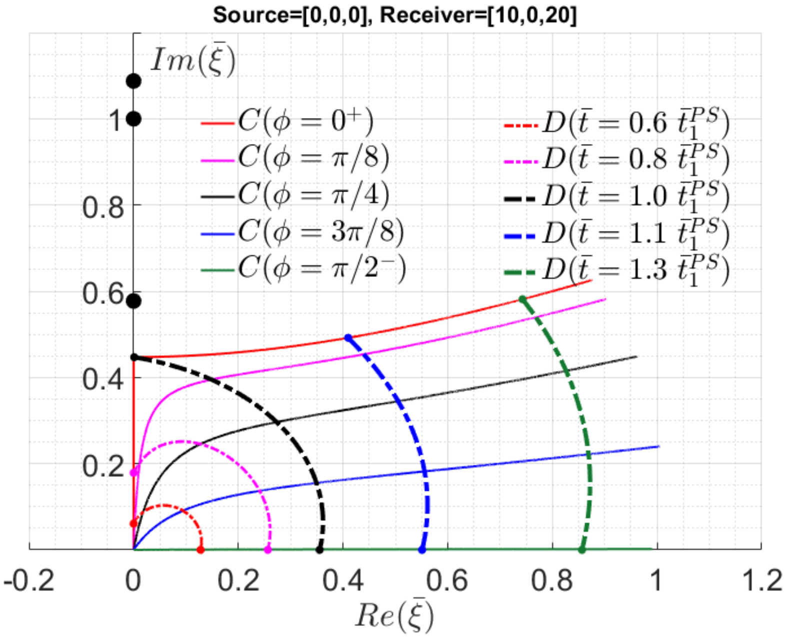

Figure 6.14: A family of (C-P) contours for $[\mathcal{I}]^{PS}$ integral: $(r, z; s) = (10, 20; 0)$, $\nu = 0.25$, $K = 0.577$, ζ=0.2, $\bar{t}_1^{PS} = 22.36$, $\bar{\xi}_0(\bar{t}_1^{PS}) = 0.447i$

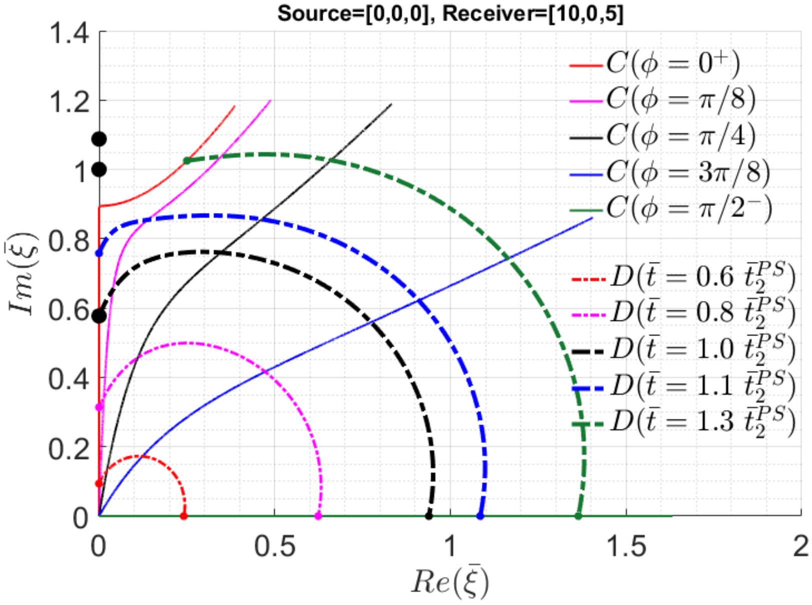

Figure 6.15: A family of (C-P) contours for $[\mathcal{I}]^{PS}$ integral: $(r, z; s) = (10, 20; 0)$, $\nu = 0.25$, $K = 0.577$, ζ=0.2, $\bar{t}_2^{PS} = 9.86$, $\bar{\xi}_0(\bar{t}_2^{PS}) = 0.577\mathrm{i}$

For the PS-wave integral, the arrival time can thus be summarized as

$$\begin{cases} \textit{for}\ \bar{s} > 0, & \begin{cases} \bar{t}_0^{PS} = (1-a^2)^{1/2}\bar{z} + (K^2-a^2)^{1/2}\bar{s} + a\bar{r} \\ \text{where}\ \dfrac{a\bar{z}}{(1-a^2)^{1/2}} + \dfrac{a\bar{s}}{(K^2-a^2)^{1/2}} - \bar{r} = 0 \end{cases} \\ \textit{for}\ \bar{s} = 0, & \begin{cases} \bar{t}_1^{PS} = \sqrt{\bar{z}^2+\bar{r}^2}, & \text{for}\ \dfrac{\bar{r}}{\sqrt{\bar{r}^2+\bar{z}^2}} \le K \\ \bar{t}_2^{PS} = \bar{z}\sqrt{1-K^2} + K\bar{r}, & \text{for}\ \dfrac{\bar{r}}{\sqrt{\bar{r}^2+\bar{z}^2}} > K \end{cases} \end{cases} \tag{6.131}$$

Now, look at the end point $\bar{\xi}_{\pi/2}$ (or point B) which is determined by

$$\bar{t} = (\bar{\xi}_{\pi/2}{}^2 + 1)^{1/2}\bar{z} + (\bar{\xi}_{\pi/2}{}^2 + K^2)^{1/2}\bar{s} - i\bar{\xi}_{\pi/2}\bar{r}\cos[(1-i\varsigma)\pi/2] \tag{6.132}$$

Noting that $\cos[(1-ib)\pi/2] = i\cdot\sinh(b\pi/2)$, Eqn. (6.132) becomes

$$\bar{t} = \bar{z}(\bar{\xi}_{\pi/2}{}^2 + 1)^{1/2} + \bar{s}(\bar{\xi}_{\pi/2}{}^2 + K^2)^{1/2} + \bar{\xi}_{\pi/2}\bar{r}\sinh(\varsigma\pi/2) \tag{6.133}$$

Then any $\bar{t} \geq \bar{z} + K\bar{s}$, Eqn. (6.133) has a positive real root, indicating that the $D(\bar{\xi}(\phi), \bar{t})$-contour will always end on the positive real axis.

(6) Reflected SP-wave integral

$$[I]^{sp}\left(\bar{r},\bar{z};\bar{s};\bar{p}\right) = \int_0^\infty [\mathcal{I}]^{sp}\left(\bar{r},\bar{z};\bar{s};\bar{t}\right) e^{-\bar{p}\bar{t}} d\bar{t}, \tag{6.134}$$

with

$$[\mathcal{I}]^{SP}\left(\bar{r},\bar{z};\bar{s};\bar{t}\right) = \frac{2}{\pi} H\left(\bar{t} - \bar{t}^{SP}\right) \mathrm{Re}\left\{ (1-i\zeta) \int_0^{\frac{\pi}{2}} [M]^{SP}\left(\bar{\xi}(\bar{t},\phi;\bar{r},\bar{z}),\phi\right) \frac{\partial\bar{\xi}}{\partial\bar{t}} d\phi \right\}, \tag{6.135}$$

where $\bar{\xi}(\bar{t},\phi)$ is determined by the solution of

$$\bar{t} = (\bar{\xi}^2 + K^2)^{1/2}\bar{z} + (\bar{\xi}^2 + 1)^{1/2}\bar{s} - i\bar{\xi}\bar{r}\cos[(1-i\zeta)\phi], \tag{6.136}$$

and $\bar{t}^{SP}$ is the arrival time of the reflected SP-wave. By means of a similar complex-plane and contour analysis as for the PS-wave group, $\bar{t}^{SP}$ can be summarized as

$$\begin{cases} \text{if } \bar{z} > 0 & \begin{cases} \bar{t}_0^{SP} = (1-a_{sp}^2)^{1/2}\bar{s} + (K^2 - a_{sp}^2)^{1/2}\bar{z} + a_{sp}\bar{r} \\ \text{with } \dfrac{a\bar{s}}{(1-a^2)^{1/2}} + \dfrac{a\bar{z}}{(K^2-a^2)^{1/2}} - \bar{r} = 0 \end{cases} \\ \text{if } \bar{z} = 0 & \begin{cases} \bar{t}_1^{SP} = \sqrt{\bar{s}^2 + \bar{r}^2}, & \text{for } \dfrac{\bar{r}}{\sqrt{\bar{r}^2 + \bar{s}^2}} \leq K \\ \bar{t}_2^{SP} = \bar{s}\sqrt{1-K^2} + K\bar{r}, & \text{for } \dfrac{\bar{r}}{\sqrt{\bar{r}^2 + \bar{s}^2}} > K \end{cases} \end{cases}. \tag{6.137}$$

6.6.2 Wave front characteristics extraction for $\bar{s} = \bar{z} = 0$

With a non-zero ζ, the integrands in Eqns. (6.104, 6.107, 6.111, 6.115, 6.122, 6.135) are finite and smooth, except in the case where $\bar{s} \to 0,\ \bar{z} \to 0,\ \bar{t} \to \bar{r}/\bar{c}_R$, i.e., both the source and receiver points are on or near the free surface and the time is close to the Rayleigh wave arrival. Here, $\bar{c}_R$ is the normalized Rayleigh wave speed. In such a case, the path of integration at complex

$\bar{\xi}$ −plane starts from a point that touches or is close to the Rayleigh pole (see Figure 6.16), and thus the integrands can be singular or nearly-singular at $\phi = 0$. To deal with such scenarios in the numerical integration, a singularity extraction technique is adopted here.

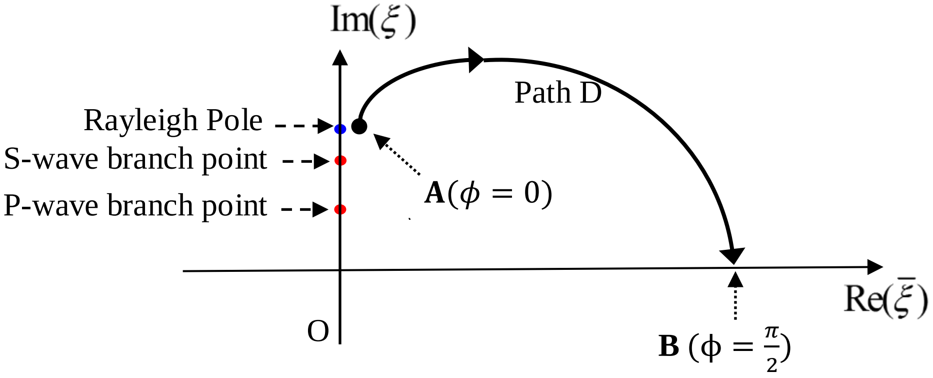

Figure 6.16: Integration path at $\bar{s} \to 0,\ \bar{z} \to 0,\ \bar{t} \to \bar{r}/\bar{c}_R$.

Next, the singularity extraction technique will be presented for the case of $\bar{s} = 0,\ \bar{z} = 0$ and $\bar{t} \to \bar{r}/\bar{c}_R$. Recalling Eqn. (6.91) that

$$\{\boldsymbol{\mathcal{I}}_i^{\gamma}(\bar{r},\bar{z};\bar{s};\bar{p})\} = \begin{array}{l} \{I_i^{\gamma}\}^{P}(\bar{r},\bar{z};\bar{s};\bar{p}) + \{I_i^{\gamma}\}^{S}(\bar{r},\bar{z};\bar{s};\bar{p}) + \{I_i^{\gamma}\}^{PP}(\bar{r},\bar{z};\bar{s};\bar{p}) \\ +\{I_i^{\gamma}\}^{SS}(\bar{r},\bar{z};\bar{s};\bar{p}) + \{I_i^{\gamma}\}^{PS}(\bar{r},\bar{z};\bar{s};\bar{p}) + \{I_i^{\gamma}\}^{SP}(\bar{r},\bar{z};\bar{s};\bar{p}) \end{array},$$

one can collect Eqns. (6.92a)-(6.92f) to get that

$$\{I_i^{\gamma}(\bar{r},\bar{z};\bar{s};\bar{p})\} = \int_0^{\infty} \left\{\mathcal{I}_i^{\gamma}\right\}(\bar{r},\bar{z};\bar{s};\bar{t})\, e^{-\bar{p}\bar{t}}\, d\bar{t}, \tag{6.138}$$

where

$$\begin{aligned} \{\boldsymbol{\mathcal{I}}_i^{\gamma}\}(\bar{r},\bar{z};\bar{s};\bar{t}) = {} & \{\mathcal{I}_i^{\gamma}\}^{P}(\bar{r},\bar{z};\bar{s};\bar{t}) + \{\mathcal{I}_i^{\gamma}\}^{S}(\bar{r},\bar{z};\bar{s};\bar{t}) + \{\mathcal{I}_i^{\gamma}\}^{PP}(\bar{r},\bar{z};\bar{s};\bar{t}) \\ & +\{\mathcal{I}_i^{\gamma}\}^{SS}(\bar{r},\bar{z};\bar{s};\bar{t}) + \{\mathcal{I}_i^{\gamma}\}^{PS}(\bar{r},\bar{z};\bar{s};\bar{t}) + \{\mathcal{I}_i^{\gamma}\}^{SP}(\bar{r},\bar{z};\bar{s};\bar{t}) \end{aligned}. \tag{6.139}$$

For the case of $\bar{s} = 0$ and $\bar{z} = 0$, Eqn. (6.139) can be simplified to

$$\{\mathcal{I}_i^{\alpha}\}\left(\overline{r},\overline{z};\overline{s};\overline{t}\right)=\frac{2}{\pi}H\left(\overline{t}-K\overline{r}\right)\mathrm{Re}\left\{(1-i\zeta)\int_0^{\frac{\pi}{2}}\left(\{M_i^{\gamma}\}^{P}+\{M_i^{\gamma}\}^{S}+\{M_i^{\gamma}\}^{PP}+\{M_i^{\gamma}\}^{SS}+\{M_i^{\gamma}\}^{PS}+\{M_i^{\gamma}\}^{SP}\right)\frac{\partial\overline{\xi}}{\partial\overline{t}}\,d\phi\right\}$$

(6.140)

with

$$\overline{\xi}=\frac{i\overline{t}}{\overline{r}\cos[(1-i\zeta)\phi]},\ \frac{d\overline{\xi}}{d\overline{t}}=\frac{i}{\overline{r}\cos[(1-i\zeta)\phi]}\,. \tag{6.141}$$

Recall components of $[\mathcal{I}_i^{\gamma}]\left(\overline{r},\overline{z};\overline{s};\overline{t}\right)$ as

$$[\mathcal{I}]\left(\overline{r},\overline{z};\overline{s};\overline{t}\right)=\begin{bmatrix}\mathcal{I}_r^h\left(\overline{r},\overline{z};\overline{s};\overline{t}\right)\\ \mathcal{I}_\theta^h\left(\overline{r},\overline{z};\overline{s};\overline{t}\right)\\ \mathcal{I}_z^h\left(\overline{r},\overline{z};\overline{s};\overline{t}\right)\\ \mathcal{I}_r^{\mathrm{v}}\left(\overline{r},\overline{z};\overline{s};\overline{t}\right)\\ \mathcal{I}_z^{\mathrm{v}}\left(\overline{r},\overline{z};\overline{s};\overline{t}\right)\end{bmatrix}. \tag{6.142}$$

Each component can be derived from Eqn. (6.140).

(1) $\mathcal{I}_r^h(\overline{r},\overline{t})$ - Radial displacement due to unit horizontal load with $\overline{s}=0$ and $\overline{z}=0$

From Eqn. (6.140), $\mathcal{I}_r^h(\overline{r},\overline{t})$ can be simplified to

$$\mathcal{I}_r^h(\bar{r},\bar{t})=\frac{2}{\pi}H\left(\bar{t}-K\bar{r}\right)\mathrm{Re}\left\{(1-i\zeta)\int_0^{\frac{\pi}{2}}\left(\begin{array}{l} -\frac{\bar{\xi}^3}{2\bar{\alpha}}\left(1+\cos\left(2\eta\right)\right) \\ +\frac{\bar{\xi}}{2}\left(\left(1+\cos\left(2\eta\right)\right)\bar{\beta}+\left(1-\cos\left(2\eta\right)\right)\frac{1}{\bar{\beta}}\right) \\ +\frac{1}{2}\left(1+\cos\left(2\eta\right)\right)\frac{R^+\left(\bar{\xi}\right)}{R^-\left(\bar{\xi}\right)}\frac{\bar{\xi}^3}{\bar{\alpha}} \\ +\frac{\bar{\xi}}{2}\left(\left(1+\cos\left(2\eta\right)\right)\frac{R^+\left(\bar{\xi}\right)}{R^-\left(\bar{\xi}\right)}\bar{\beta}+\left(1-\cos\left(2\eta\right)\right)\frac{1}{\bar{\beta}}\right) \\ +\frac{-2\bar{\xi}^3\bar{\beta}\left(2\bar{\xi}^2+1\right)}{\bar{R}^-\left(\bar{\xi}\right)}\left(1+\cos\left(2\eta\right)\right) \\ +\frac{-2\bar{\xi}^3\bar{\beta}\left(2\bar{\xi}^2+1\right)}{\bar{R}^-\left(\bar{\xi}\right)}\left(1+\cos\left(2\eta\right)\right) \end{array}\right)\frac{d\bar{\xi}}{d\bar{t}}\,d\phi\right\}.$$

(6.143)

where $\bar{\xi}=\frac{i\bar{t}}{\bar{r}\cos[(1-i\zeta)\phi]}=\frac{i\bar{t}}{\bar{r}}\sec[(1-i\zeta)\phi$ and $\eta=(1-i\zeta)\phi$. In terms of the reference time variable $\tau=\bar{t}\,/\,\bar{r}$, Eqn. (6.143) can be condensed to the form of

$$\mathcal{I}_r^h(\bar{r},\bar{t})=\frac{2}{\pi}H\left(\bar{t}-K\bar{r}\right)\mathrm{Re}\left\{(1-i\zeta)\int_0^{\frac{\pi}{2}}\frac{\Xi(\bar{r},\bar{t},\phi)}{\vartheta(\bar{r},\bar{t},\phi)}\,d\phi\right\} \tag{6.144}$$

where

$$\Xi(\bar{r},\bar{t},\phi)=2\tau\sec^2\eta\left(\begin{array}{l} -1-4\tau^4\sec^2\eta+4\tau^2\sec^2\eta\left(1+\tau^2-\sqrt{1-\tau^2\sec^2\eta}\sqrt{K^2-\tau^2\sec^2\eta}\right) \\ +\tau^2\left(-3+4\sqrt{1-\tau^2\sec^2\eta}\sqrt{K^2-\tau^2\sec^2\eta}\right) \end{array}\right), \tag{6.145}$$

and

$$\vartheta(\bar{r},\bar{t},\phi)=\sqrt{1-\tau^2\sec^2\eta}\left(1+4\tau^2\sec^2\eta\left(-1+\tau^2\sec^2\eta+\sqrt{1-\tau^2\sec^2\eta}\sqrt{K^2-\tau^2\sec^2\eta}\right)\right). \tag{6.146}$$

To determine the general analytical characteristics of the integral in Eqn. (6.144) around the lower limit of $\phi = 0$, it is useful to note that $\Xi(\bar{r},\bar{t},\phi)$ and $\vartheta(\bar{r},\bar{t},\phi)$ admit the power series representations

$$\Xi(\bar{r},\bar{t},\phi) \approx \left(-2\tau + 2\tau^3\right) + \left(-2\tau + 10\tau^3 - 8\tau^5 - 8\tau^3\sqrt{1-\tau^2}\sqrt{K^2-\tau^2}\right)\phi^2 + O\left[\phi\right]^3, \ \phi \to 0^+, \tag{6.147}$$

and

$$\begin{aligned}\vartheta(\bar{r},\bar{t},\phi) \approx \sqrt{1-\tau^2}\,\widehat{R}^-(\tau) + \Bigg(4(1-i\zeta)^2\tau^2\sqrt{1-\tau^2}\,\Bigg(&-1+2\tau^2+\sqrt{1-\tau^2}\sqrt{K^2-\tau^2} \\ &+\frac{\tau^2\left(-1-K^2+2\tau^2\right)}{2\sqrt{1-\tau^2}\sqrt{K^2-\tau^2}}\Bigg) - \frac{\tau^2\widehat{R}^-(\tau)}{2\sqrt{1-\tau^2}}\Bigg)\phi^2 + O\left[\phi\right]^3\end{aligned} \qquad \phi \to 0^+, \tag{6.148}$$

around $\phi = 0$ with $\widehat{R}^-(\tau) = 1 + 4\tau^2\left(-1+\tau^2+\sqrt{1-\tau^2}\sqrt{K^2-\tau^2}\right)$.

By virtue of (6.147) and (6.148), one may define

$$\left[\mathcal{I}_r^h(\bar{r},\bar{t})\right]_{analytic} = \frac{2}{\pi}H\left(\bar{t}-K\bar{r}\right)\mathrm{Re}\left\{\int_0^{\frac{\pi}{2}}\frac{\kappa_1(\tau)}{\kappa_2(\tau)+\kappa_3(\tau)\phi^2}\,d\phi\right\}, \tag{6.149}$$

which can be evaluated in closed-form as

$$\left[\mathcal{I}_r^h(\bar{r},\bar{t})\right]_{analytic} = \frac{2\kappa_1(\tau)}{\pi\sqrt{\kappa_3(\tau)}}H\left(\bar{t}-K\bar{r}\right)\,\tan^{-1}\left(\frac{\pi\sqrt{\kappa_3(\tau)}}{2\sqrt{\kappa_2(\tau)}}\right)\frac{1}{\sqrt{\kappa_2(\tau)}} \tag{6.150}$$

with

$$\begin{aligned}&\tau = \bar{t}\,/\,\bar{r}, \\ &\kappa_1(\tau) = 2\tau(\tau^2-1), \\ &\kappa_2(\tau) = \sqrt{1-\tau^2}\,\widehat{R}^-(\tau), \\ &\kappa_3(\tau) = 4(1-i\zeta)^2\tau^2\sqrt{1-\tau^2}\left(-1+2\tau^2+\sqrt{1-\tau^2}\sqrt{K^2-\tau^2}+\frac{\tau^2\left(-1-K^2+2\tau^2\right)}{2\sqrt{1-\tau^2}\sqrt{K^2-\tau^2}}\right)-\frac{\tau^2\widehat{R}^-(\tau)}{2\sqrt{1-\tau^2}}.\end{aligned} \tag{6.151}$$

Note that the only source of 'strong' singularity of (6.150) stems from $\kappa_2(\bar{r},\bar{t})$, with
$$\frac{1}{\kappa_2(\bar{r},\bar{t})}=\frac{1}{\sqrt{1-\left(\frac{\bar{t}}{\bar{r}}\right)^2}\left(1+4\left(\frac{\bar{t}}{\bar{r}}\right)^2\left(-1+\left(\frac{\bar{t}}{\bar{r}}\right)^2+\sqrt{1-\left(\frac{\bar{t}}{\bar{r}}\right)^2}\sqrt{K^2-\left(\frac{\bar{t}}{\bar{r}}\right)^2}\right)\right)}$$
is singular at the time $\bar{t}=\bar{t}^R=\bar{r}c_s/c_r$. Decomposing $\mathcal{I}_r^h(\bar{r},\bar{t})$ as

$$\mathcal{I}_r^h(\bar{r},\bar{t})=\left[\mathcal{I}_r^h(\bar{r},\bar{t})\right]_{analytic}+\left[\mathcal{I}_r^h(\bar{r},\bar{t})\right]_{residual}, \tag{6.152}$$

it can be shown that $\left[\mathcal{I}_r^h(\bar{r},\bar{t})\right]_{residual}=\mathcal{I}_r^h(\bar{r},\bar{t})-\left[\mathcal{I}_r^h(\bar{r},\bar{t})\right]_{analytic}$ is regular over requisite range of integration of [0, π/2] and thus is amenable to normal numerical quadrature even at $\bar{t}=\bar{t}^R=\bar{r}c_s/c_R$ or when ξ_o is at the Rayleigh pole. As an illustration, $\mathcal{I}_r^h(\bar{r},\bar{t})$ and $\left[\mathcal{I}_r^h(\bar{r},\bar{t})\right]_{asym}$ are plotted as function of ϕ in Figure 6.17 for the case of $c_s/c_r=1.0876$, $\bar{s}=\bar{z}=0,\ \bar{r}=1,\ \bar{t}=0.9999\bar{t}_R$, $\nu=0.25$, while $\left[\mathcal{I}_r^h(\bar{r},\bar{t})\right]_{numerical}$ is plotted in Figure 6.18. One can see that the integrand of $\bar{u}_r^h(\bar{r},\bar{t})$ is nearly-singular at this case, and its evaluation cannot be done accurately with numerical integration. In contrast, $\left[\mathcal{I}_r^h(\bar{r},\bar{t})\right]_{residual}$ is finite (small) and smooth as discussed earlier.

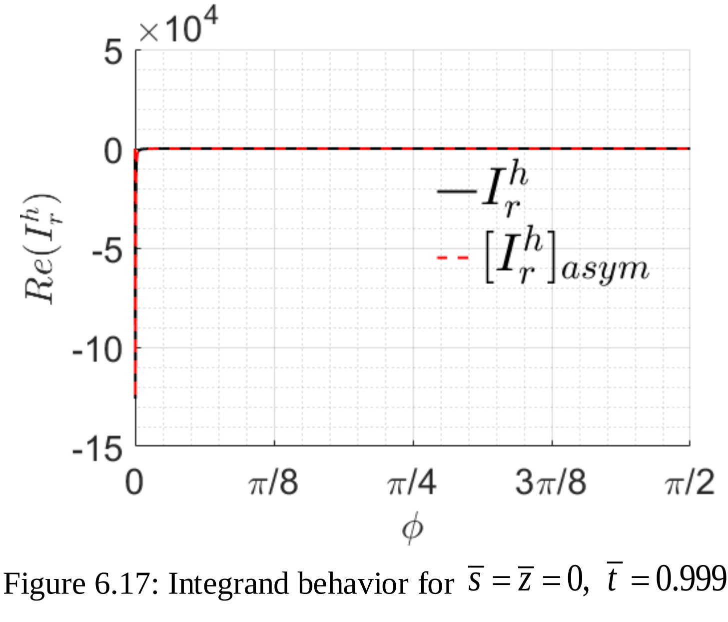

Figure 6.17: Integrand behavior for $\bar{s}=\bar{z}=0,\ \bar{t}=0.9999\bar{t}_R$.

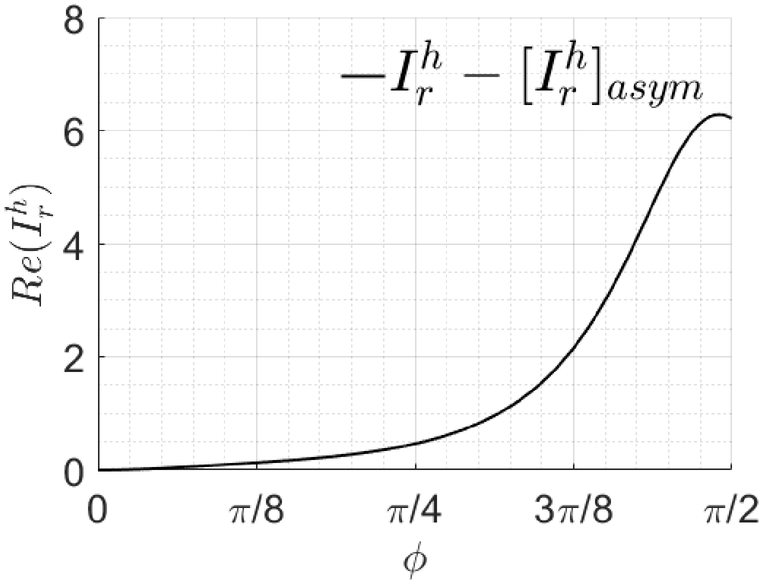

Figure 6.18: Extracted Integrand for $\bar{s}=\bar{z}=0,\ \bar{t}=0.9999\bar{t}_R$.

(2) $\mathcal{I}_\theta^h(\bar{r},\bar{t})$**. Tangential displacement due to horizontal load with** $\bar{s}=0$ **and** $\bar{z}=0$

$$\begin{aligned}\left[\mathcal{I}_\theta^h(\bar{r},\bar{t})\right]_{analytic} &= \frac{2}{\pi}H\left(\bar{t}-K\bar{r}\right)\mathrm{Re}\left\{\int_0^{\frac{\pi}{2}}\frac{\kappa_1(\tau)}{\kappa_2(\tau)+\kappa_3(\tau)\phi^2}\,d\phi\right\} \\ &= \frac{2\kappa_1(\tau)}{\pi\sqrt{\kappa_3(\tau)}}H\left(\bar{t}-K\bar{r}\right)\mathrm{Tan}^{-1}\left(\frac{\pi\sqrt{\kappa_3(\tau)}}{2\sqrt{\kappa_2(\tau)}}\right)\frac{1}{\sqrt{\kappa_2(\tau)}}\end{aligned} \tag{6.153}$$

where $\tau=\bar{t}\,/\,\bar{r}$,

$$\begin{aligned}\kappa_1(\tau) &= -2\tau\widehat{R}^-(\tau) \\ \kappa_2(\tau) &= \sqrt{1-\tau^2}\,\widehat{R}^-(\tau) \\ \kappa_3(\tau) &= 4(1-i\zeta)^2\tau^2\sqrt{1-\tau^2}\left(-1+2\tau^2+\sqrt{1-\tau^2}\sqrt{K^2-\tau^2}+\frac{\tau^2\left(-1-K^2+2\tau^2\right)}{2\sqrt{1-\tau^2}\sqrt{K^2-\tau^2}}\right)-\frac{\tau^2\widehat{R}^-(\tau)}{2\sqrt{1-\tau^2}}\end{aligned}\ . \tag{6.154}$$

(3) $\mathcal{I}_z^x(\bar{r},\bar{t})$. Vertical displacement due to horizontal load with $\bar{s}=0$ and $\bar{z}=0$

$$\begin{aligned}\left[\mathcal{I}_z^h(\bar{r},\bar{t})\right]_{analytic} &= \frac{2}{\pi} H\left(\bar{t}-K\bar{r}\right)\mathrm{Re}\left\{\int_0^{\frac{\pi}{2}} \frac{\kappa_1(\tau)}{\kappa_2(\tau)+\kappa_3(\tau)\phi^2}\,d\phi\right\} \\ &= \frac{2\kappa_1(\tau)}{\pi\sqrt{\kappa_3(\tau)}} H\left(\bar{t}-K\bar{r}\right)\mathrm{Tan}^{-1}\left(\frac{\pi\sqrt{\kappa_3(\tau)}}{2\sqrt{\kappa_2(\tau)}}\right)\frac{1}{\sqrt{\kappa_2(\tau)}}\end{aligned} \tag{6.155}$$

where $\tau=\bar{t}\,/\,\bar{r}$,

$$\begin{aligned}\kappa_1(\tau) &= \tau^2\left(1-2\tau^2-2\sqrt{1-\tau^2}\sqrt{K^2-\tau^2}\right) \\ \kappa_2(\tau) &= -\widehat{R}^-(\tau) \\ \kappa_3(\tau) &= 4(1-i\zeta)^2\tau^2\left(-1+2\tau^2+\sqrt{1-\tau^2}\sqrt{K^2-\tau^2}+\frac{\tau^2\left(-1-K^2+2\tau^2\right)}{2\sqrt{1-\tau^2}\sqrt{K^2-\tau^2}}\right)\end{aligned} \tag{6.156}$$

(4) Term $\mathcal{I}_r^z(\bar{r},\bar{t})$. Vertical displacement due to vertical load with $\bar{s}=0$ and $\bar{z}=0$

$\mathcal{I}_r^z(\bar{r},\bar{t})$ is identical to $\mathcal{I}_z^{r\ or\ x}(\bar{r},\bar{t})$.

(5) Term $\mathcal{I}_z^z(\bar{r},\bar{t})$. Vertical displacement due to vertical load with $\bar{s}=0$ and $\bar{z}=0$

$$\begin{aligned}\left[\mathcal{I}_z^z(\bar{r},\bar{t})\right]_{analytic} &= \frac{2}{\pi} H\left(\bar{t}-K\bar{r}\right)\mathrm{Re}\left\{\int_0^{\frac{\pi}{2}} \frac{\kappa_1(\tau)}{\kappa_2(\tau)+\kappa_3(\tau)\phi^2}\,d\phi\right\} \\ &= \frac{2\kappa_1(\tau)}{\pi\sqrt{\kappa_3(\tau)}} H\left(\bar{t}-K\bar{r}\right)\mathrm{Tan}^{-1}\left(\frac{\pi\sqrt{\kappa_3(\tau)}}{2\sqrt{\kappa_2(\tau)}}\right)\frac{1}{\sqrt{\kappa_2(\tau)}}\end{aligned} \tag{6.157}$$

where $\tau=\bar{t}\,/\,\bar{r}$,

$$\begin{aligned}\kappa_1(\tau) &= -\tau\sqrt{K^2-\tau^2} \\ \kappa_2(\tau) &= \widehat{R}^-(\tau) \\ \kappa_3(\tau) &= 4(1-i\zeta)^2\tau^2\left(-1+2\tau^2+\sqrt{1-\tau^2}\sqrt{K^2-\tau^2}+\frac{\tau^2\left(-1-K^2+2\tau^2\right)}{2\sqrt{1-\tau^2}\sqrt{K^2-\tau^2}}\right)\end{aligned} \tag{6.158}$$

(6) Verification of analytical decomposition

As explored in Chao (1960) and Pekeris and Hanna (1957, the Rayleigh wave front behaves as $1/\sqrt{\bar{t}-\bar{t}_R}$. To verify the validity of the proposed analytical decomposition technique, the displacements at the Rayleigh wave front is compared with existed solution in Chao (1960) and Kausel (2012). As can be seen in Figure 6.19, for $\nu \in [0, 0.49]$, the strength of singularity at $t = t^R$ obtained by analytical decomposition agrees well with the existed solution.

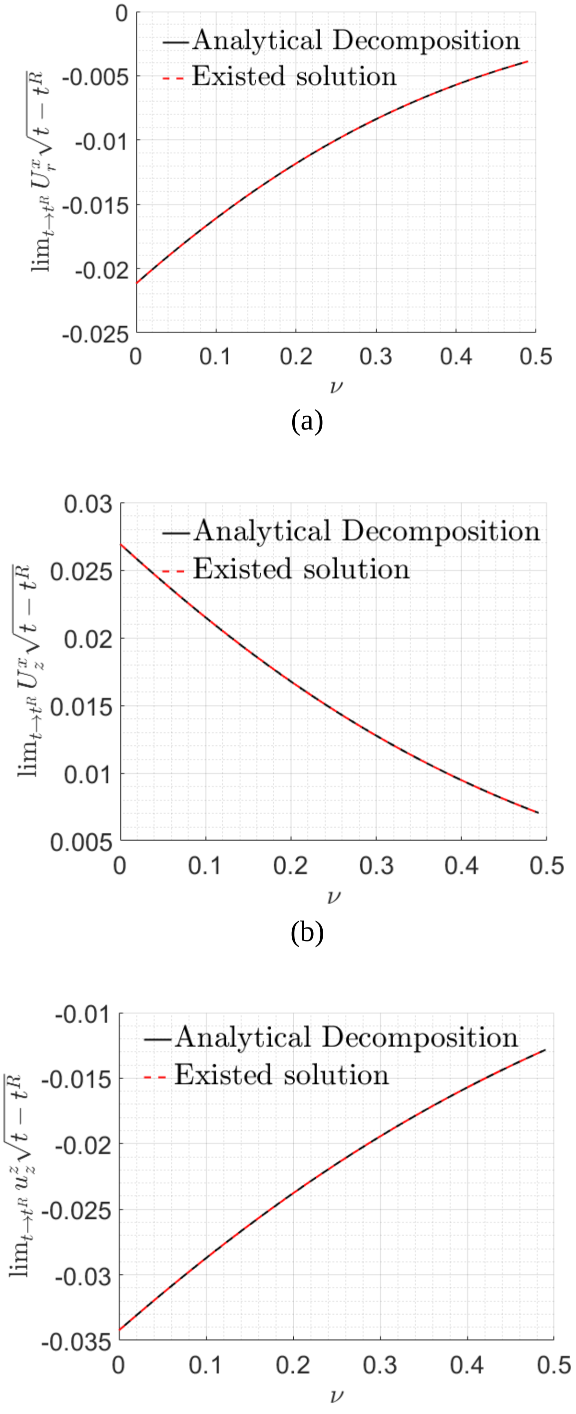

(a)

(b)

(c)

Figure 6.19: Displacements at Rayleigh wave front.

6.7 Green’s function for stresses

In the Laplace transform domain, the stress response due ot point load with magnitude $\mathcal{F}$ is given as

$$\boldsymbol{\tau}\left(r,\theta,z;s;p\right)=\frac{\mathcal{F}\cdot p}{c_s^2}\bar{\boldsymbol{\tau}}\left(\bar{r},\theta,\bar{z};\bar{s};\bar{p}\right), \tag{6.159}$$

where the components of the dimensionless tensorial stress Green’s function $\bar{\boldsymbol{\tau}}$ are defined as follows.

6.7.1 horizontal loading in $\boldsymbol{\theta=\theta_0}$ direction

$$\bar{\tau}_{rr}\left(\bar{r},\theta,\bar{z};\bar{s};\bar{p}\right)+\frac{1}{\bar{p}}\frac{2}{\bar{r}}\left\{\bar{U}_r+i\left(\bar{U}_{\theta_1}e^{i\theta}-\bar{U}_{\theta_{-1}}e^{-i\theta}\right)\right\}=\frac{\cos\left(\theta-\theta_0\right)}{2\pi}T_{rr}^{h}(\bar{r},\bar{z};\bar{s};\bar{p}), \tag{6.160}$$

$$\bar{\tau}_{\theta\theta}\left(\bar{r},\theta,\bar{z};\bar{s};\bar{p}\right)-\frac{1}{\bar{p}}\frac{2}{\bar{r}}\left\{\bar{U}_r+i\left(\bar{U}_{\theta_1}e^{i\theta}-\bar{U}_{\theta_{-1}}e^{-i\theta}\right)\right\}=\frac{\cos\left(\theta-\theta_0\right)}{2\pi}T_{\theta\theta}^{h}(\bar{r},\bar{z};\bar{s};\bar{p}), \tag{6.161}$$

$$\bar{\tau}_{r\theta}\left(\bar{r},\theta,\bar{z};\bar{s};\bar{p}\right)+\frac{1}{\bar{p}}\frac{2}{\bar{r}}\left\{\bar{U}_\theta-i\left(\bar{U}_{r_1}e^{i\theta}-\bar{U}_{r_{-1}}e^{-i\theta}\right)\right\}=\frac{\sin\left(\theta-\theta_0\right)}{2\pi}T_{r\theta}^{h}(\bar{r},\bar{z};\bar{s};\bar{p}), \tag{6.162}$$

$$\bar{\tau}_{zz}\left(\bar{r},\theta,\bar{z};\bar{s};\bar{p}\right)=\frac{\cos\left(\theta-\theta_0\right)}{2\pi}T_{zz}^{h}(\bar{r},\bar{z};\bar{s};\bar{p}), \tag{6.163}$$

$$\bar{\tau}_{zr}\left(\bar{r},\theta,\bar{z};\bar{s};\bar{p}\right)=\frac{\cos\left(\theta-\theta_0\right)}{4\pi}T_{zr}^{h}(\bar{r},\bar{z};\bar{s};\bar{p}), \tag{6.164}$$

$$\bar{\tau}_{z\theta}\left(\bar{r},\theta,\bar{z};\bar{s};\bar{p}\right)=\frac{-\sin\left(\theta-\theta_0\right)}{4\pi}T_{z\theta}^{h}(\bar{r},\bar{z};\bar{s};\bar{p}), \tag{6.165}$$

where

$$\bar{U}_{r_1}e^{i\theta}-\bar{U}_{r_{-1}}e^{-i\theta}=\frac{i\cdot\sin\left(\theta-\theta_0\right)}{4\pi}I_r^{h}(\bar{r},\bar{z};\bar{s};\bar{p}), \tag{6.166}$$

$$\bar{U}_{\theta_1}e^{i\theta}-\bar{U}_{\theta_{-1}}e^{-i\theta}=\frac{i\cdot\cos\left(\theta-\theta_0\right)}{4\pi}I_\theta^{h}(\bar{r},\bar{z};\bar{s};\bar{p}). \tag{6.167}$$

6.7.2 vertical loading in $z-$ direction

$$\bar{\tau}_{rr}\left(\bar{r},\theta,\bar{z};\bar{s};\bar{p}\right)+\frac{1}{\bar{p}}\frac{2}{\bar{r}}\bar{U}_r=\frac{1}{2\pi}T_{rr}^{v}\left(\bar{r},\bar{z};\bar{s};\bar{p}\right), \tag{6.168}$$

$$\bar{\tau}_{\theta\theta}\left(\bar{r},\theta,\bar{z};\bar{s};\bar{p}\right)-\frac{1}{\bar{p}}\frac{2}{\bar{r}}\bar{U}_r=\frac{1}{2\pi}T_{\theta\theta}^{v}\left(\bar{r},\bar{z};\bar{s};\bar{p}\right), \tag{6.169}$$

$$\bar{\tau}_{r\theta}\left(\bar{r},\theta,\bar{z};\bar{s};\bar{p}\right)=0, \tag{6.170}$$

$$\bar{\tau}_{zz}\left(\bar{r},\theta,\bar{z};\bar{s};\bar{p}\right)=\frac{1}{2\pi}T_{zz}^{v}\left(\bar{r},\bar{z};\bar{s};\bar{p}\right), \tag{6.171}$$

$$\bar{\tau}_{zr}\left(\bar{r},\theta,\bar{z};\bar{s};\bar{p}\right)=\frac{-1}{2\pi}T_{zr}^{v}\left(\bar{r},\bar{z};\bar{s};\bar{p}\right), \tag{6.172}$$

$$\bar{\tau}_{z\theta}\left(\bar{r},\theta,\bar{z};\bar{s};\bar{p}\right)=0, \tag{6.173}$$

where $I_r^h(\bar{r},\bar{z};\bar{s};\bar{p})$, $I_\theta^h(\bar{r},\bar{z};\bar{s};\bar{p})$ are defined by Eqn. (6.24-6.25), and

$$T_{rr}^{h}(\bar{r},\bar{z};\bar{s};\bar{p})=\int_0^\infty\left(\bar{\lambda}\frac{\overline{d\Omega_1}}{dz}-\left(\bar{\lambda}+2\right)\bar{\xi}\bar{\gamma}_1\right)\bar{\xi}\,J_1\left(\bar{\xi}\,\overline{pr}\right)d\bar{\xi}, \tag{6.174}$$

$$T_{\theta\theta}^{h}(\bar{r},\bar{z};\bar{s};\bar{p})=\int_0^\infty\bar{\lambda}\left(\frac{\overline{d\Omega_1}}{dz}-\bar{\xi}\bar{\gamma}_1\right)\bar{\xi}\,J_1\left(\bar{p}\bar{\xi}\bar{r}\right)d\bar{\xi}, \tag{6.175}$$

$$T_{r\theta}^{h}(\bar{r},\bar{z};\bar{s};\bar{p})=\int_0^\infty\bar{\gamma}_2\bar{\xi}^2J_1\left(\bar{p}\bar{\xi}\bar{r}\right)d\bar{\xi}, \tag{6.176}$$

$$T_{zz}^{h}(\bar{r},\bar{z};\bar{s};\bar{p})=\int_0^\infty\left(\left(\bar{\lambda}+2\right)\frac{\overline{d\Omega_1}}{dz}-\bar{\lambda}\bar{\xi}\bar{\gamma}_1\right)\bar{\xi}\,J_1\left(\bar{p}\bar{\xi}\bar{r}\right)d\bar{\xi}, \tag{6.177}$$

$$T_{zr}^{h}(\bar{r},\bar{z};\bar{s};\bar{p})=\int_0^\infty\left(\frac{\overline{d\gamma_2}}{dz}+\frac{\overline{d\gamma_1}}{dz}+\bar{\xi}\bar{\Omega}_1\right)\bar{\xi}\,J_0\left(\bar{p}\bar{\xi}\bar{r}\right)d\bar{\xi}+\int_0^\infty\left(\frac{\overline{d\gamma_2}}{dz}-\frac{\overline{d\gamma_1}}{dz}-\bar{\xi}\bar{\Omega}_1\right)\bar{\xi}\,J_2\left(\bar{p}\bar{\xi}\bar{r}\right)d\bar{\xi}, \tag{6.178}$$

$$T_{z\theta}^{h}(\bar{r},\bar{z};\bar{s};\bar{p})=\int_0^\infty\left(\frac{\overline{d\gamma_2}}{dz}+\frac{\overline{d\gamma_1}}{dz}+\bar{\xi}\bar{\Omega}_1\right)\bar{\xi}\,J_0\left(\bar{p}\bar{\xi}\bar{r}\right)d\bar{\xi}-\int_0^\infty\left(\frac{\overline{d\gamma_2}}{dz}-\frac{\overline{d\gamma_1}}{dz}-\bar{\xi}\bar{\Omega}_1\right)\bar{\xi}\,J_2\left(\bar{p}\bar{\xi}\bar{r}\right)d\bar{\xi}, \tag{6.179}$$

$$T_{rr}^{v}\left(\bar{r},\bar{z};\bar{s};\bar{p}\right)=\int_0^\infty\left(\bar{\lambda}\frac{\overline{d\Omega_2}}{dz}-\left(\bar{\lambda}+2\right)\bar{\xi}\bar{\gamma}_3\right)\bar{\xi}\,J_0\left(\bar{p}\bar{\xi}\bar{r}\right)d\bar{\xi}, \tag{6.180}$$

$$T_{\theta\theta}^{v}\left(\bar{r},\bar{z};\bar{s};\bar{p}\right)=\int_0^\infty\bar{\lambda}\left(\frac{\overline{d\Omega_2}}{dz}-\bar{\xi}\bar{\gamma}_3\right)\bar{\xi}\,J_0\left(\bar{\xi}\bar{\varpi}\bar{r}\right)d\bar{\xi}, \tag{6.181}$$

$$T_{zz}^{v}\left(\bar{r},\bar{z};\bar{s};\bar{p}\right)=\int_{0}^{\infty}\left(\left(\bar{\lambda}+2\right)\frac{\overline{d\Omega_2}}{dz}-\bar{\lambda}\bar{\xi}\bar{\gamma}_3\right)\bar{\xi}\,J_0\left(\bar{\xi}\bar{\varpi}\bar{r}\right)d\bar{\xi}\ , \tag{6.182}$$

$$T_{zr}^{v}\left(\bar{r},\bar{z};\bar{s};\bar{p}\right)=\int_{0}^{\infty}\left(\frac{\overline{d\gamma_3}}{dz}+\overline{\xi\Omega}_2\right)\bar{\xi}\,J_1\left(\bar{\xi}\bar{\varpi}\bar{r}\right)d\bar{\xi}\ . \tag{6.183}$$

Similar analytical and numerical treatments can be applied as in the case of the displacement Green's functions.

6.7.3 Time domain solution of stresses

Putting the 10 integrals in (6.174-6.183) into one column array as

$$\left\{T_{ij}^{\gamma}\left(\bar{r},\bar{z};\bar{s};\bar{p}\right)\right\}=\left\{T_{rr}^{h},T_{\theta\theta}^{h},T_{r\theta}^{h},T_{zz}^{h},T_{zr}^{h},T_{z\theta}^{h},T_{rr}^{\mathrm{v}},T_{\theta\theta}^{\mathrm{v}},T_{zz}^{\mathrm{v}},T_{zr}^{\mathrm{v}}\right\}^{T}\ , \tag{6.184}$$

and collect together the terms those involve the same exponential terms, $\left\{T_{ij}^{\gamma}\left(\bar{r},\bar{z};\bar{s};\bar{p}\right)\right\}$ can be expressed as

$$\left\{T_{ij}^{\gamma}\left(\bar{r},\bar{z};\bar{s};\bar{p}\right)\right\}=\begin{array}{c}\left\{T_{ij}^{\gamma}\right\}^{P}\left(\bar{r},\bar{z};\bar{s};\bar{p}\right)+\left\{T_{ij}^{\gamma}\right\}^{S}\left(\bar{r},\bar{z};\bar{s};\bar{p}\right)+\left\{T_{ij}^{\gamma}\right\}^{PP}\left(\bar{r},\bar{z};\bar{s};\bar{p}\right)\\+\left\{T_{ij}^{\gamma}\right\}^{SS}\left(\bar{r},\bar{z};\bar{s};\bar{p}\right)+\left\{T_{ij}^{\gamma}\right\}^{PS}\left(\bar{r},\bar{z};\bar{s};\bar{p}\right)+\left\{T_{ij}^{\gamma}\right\}^{SP}\left(\bar{r},\bar{z};\bar{s};\bar{p}\right)\end{array}, \tag{6.185}$$

where

$$\begin{aligned}
\left\{T_{ij}^{\gamma}\right\}^{P}\left(\bar{r},\bar{z};\bar{s};\bar{p}\right)&=\frac{1}{\pi}\int_{0}^{\infty}\int_{0}^{\pi}\left\{N_{ij}^{\gamma}\right\}^{P}\left(\bar{\xi},\phi\right)e^{-\bar{p}\,\left(\bar{\alpha}\bar{d}_1-i\bar{\xi}\bar{r}\cos[(1-i\zeta)\phi]\right)}d\phi d\bar{\xi},\\
\left\{T_{ij}^{\gamma}\right\}^{S}\left(\bar{r},\bar{z};\bar{s};\bar{p}\right)&=\frac{1}{\pi}\int_{0}^{\infty}\int_{0}^{\pi}\left\{N_{ij}^{\gamma}\right\}^{S}\left(\bar{\xi},\phi\right)e^{-\bar{p}\,\left(\bar{\beta}\bar{d}_1-i\bar{\xi}\bar{r}\cos[(1-i\zeta)\phi]\right)}d\phi d\bar{\xi},\\
\left\{T_{ij}^{\gamma}\right\}^{PP}\left(\bar{r},\bar{z};\bar{s};\bar{p}\right)&=\frac{1}{\pi}\int_{0}^{\infty}\int_{0}^{\pi}\left\{N_{ij}^{\gamma}\right\}^{PP}\left(\bar{\xi},\phi\right)e^{-\bar{p}\,\left(\bar{\alpha}\bar{d}_2-i\bar{\xi}\bar{r}\cos[(1-i\zeta)\phi]\right)}d\phi d\bar{\xi},\\
\left\{T_{ij}^{\gamma}\right\}^{SS}\left(\bar{r},\bar{z};\bar{s};\bar{p}\right)&=\frac{1}{\pi}\int_{0}^{\infty}\int_{0}^{\pi}\left\{N_{ij}^{\gamma}\right\}^{SS}\left(\bar{\xi},\phi\right)e^{-\bar{p}\,\left(\bar{\beta}\bar{d}_2-i\bar{\xi}\bar{r}\cos[(1-i\zeta)\phi]\right)}d\phi d\bar{\xi},\\
\left\{T_{ij}^{\gamma}\right\}^{PS}\left(\bar{r},\bar{z};\bar{s};\bar{p}\right)&=\frac{1}{\pi}\int_{0}^{\infty}\int_{0}^{\pi}\left\{N_{ij}^{\gamma}\right\}^{PS}\left(\bar{\xi},\phi\right)e^{-\bar{p}\,\left(\bar{\beta}\bar{d}+\bar{\alpha}\bar{s}-i\bar{\xi}\bar{r}\cos[(1-i\zeta)\phi]\right)}d\phi d\bar{\xi},\\
\left\{T_{ij}^{\gamma}\right\}^{SP}\left(\bar{r},\bar{z};\bar{s};\bar{p}\right)&=\frac{1}{\pi}\int_{0}^{\infty}\int_{0}^{\pi}\left\{N_{ij}^{\gamma}\right\}^{SP}\left(\bar{\xi},\phi\right)e^{-\bar{p}\,\left(\bar{\alpha}\bar{d}+\bar{\beta}\bar{s}-i\bar{\xi}\bar{r}\cos[(1-i\zeta)\phi]\right)}d\phi d\bar{\xi},
\end{aligned} \tag{6.186}$$

with $\bar{d}_1 = |\bar{z} - \bar{s}|$, $\bar{d}_2 = \bar{z} + \bar{s}$ and

$$\begin{aligned}
\left\{N_{ij}^{\gamma}\right\}^{P}(\bar{\xi},\phi) = \Bigg\{ & \frac{i\cos\eta\,\bar{\xi}^2(\bar{\lambda}\bar{\alpha}^2-(\bar{\lambda}+2)\bar{\xi}^2)}{2\bar{\alpha}}, \frac{i\bar{\lambda}\cos\eta\,\bar{\xi}^2(\bar{\alpha}^2-\bar{\xi}^2)}{2\bar{\alpha}}, \\
& \frac{i\cos\eta\,\bar{\xi}^2((\bar{\lambda}+2)\bar{\alpha}^2-\bar{\lambda}\bar{\xi}^2)}{2\bar{\alpha}},\ 0,\ \operatorname{sgn}(\bar{z}-\bar{s})\left(1+\cos\left(2\eta\right)\right)\bar{\xi}^3, \\
& \operatorname{sgn}(\bar{z}-\bar{s})\left(1-\cos\left(2\eta\right)\right)\bar{\xi}^3, \frac{\operatorname{sgn}(\bar{z}-\bar{s})}{2}\bar{\xi}\left(\left(2+\bar{\lambda}\right)\bar{\xi}^2-\bar{\lambda}\bar{\alpha}^2\right), \\
& \frac{\operatorname{sgn}(\bar{z}-\bar{s})}{2}\bar{\lambda}\bar{\xi}\left(\bar{\xi}^2-\bar{\alpha}^2\right), \frac{\operatorname{sgn}(\bar{z}-\bar{s})}{2}\bar{\xi}\left(\bar{\lambda}\bar{\xi}^2-\bar{\alpha}^2\left(2+\bar{\lambda}\right)\right),\ -i\cos\eta\,\bar{\alpha}\bar{\xi}^2\Bigg\}^{T}
\end{aligned} \tag{6.187}$$

$$\begin{aligned}
\left\{N_{ij}^{\gamma}\right\}^{S}(\bar{\xi},\phi) = \Bigg\{ & i\cos\eta\,\bar{\beta}\bar{\xi}^2,\ 0,\ -i\cos\eta\,\bar{\beta}\bar{\xi}^2, -\frac{i\cos\eta\,\bar{\xi}^2}{2\bar{\beta}}, \\
& -\frac{\operatorname{sgn}(\bar{z}-\bar{s})}{2}\bar{\xi}\left(1+\bar{\beta}^2+\bar{\xi}^2+\cos\left(2\eta\right)\left(\bar{\beta}^2+\bar{\xi}^2-1\right)\right), \\
& \frac{\operatorname{sgn}(\bar{z}-\bar{s})}{2}\bar{\xi}\left(-1-\bar{\beta}^2-\bar{\xi}^2+\cos\left(2\eta\right)\left(\bar{\beta}^2+\bar{\xi}^2-1\right)\right), \\
& -\operatorname{sgn}(\bar{z}-\bar{s})\bar{\xi}^3, 0, \operatorname{sgn}(\bar{z}-\bar{s})\bar{\xi}^3, \frac{i\cos\eta\,\bar{\xi}^2\left(\bar{\beta}^2+\bar{\xi}^2\right)}{2\bar{\beta}}\Bigg\}^{T}
\end{aligned} \tag{6.188}$$

$$\begin{aligned}
\left\{N_{ij}^{\gamma}\right\}^{PP}(\bar{\xi},\phi) = \Bigg\{ & \frac{i\cos\eta\,\bar{\xi}^2((\bar{\lambda}+2)\bar{\xi}^2-\bar{\lambda}\bar{\alpha}^2)}{2\bar{\alpha}}\frac{\bar{R}^+}{\bar{R}^-}, \frac{i\cos\eta\,\bar{\xi}^2\bar{\lambda}(\bar{\xi}^2-\bar{\alpha}^2)}{2\bar{\alpha}}\frac{\bar{R}^+}{\bar{R}^-}, \\
& \frac{i\cos\eta\,\bar{\xi}^2(\bar{\lambda}\bar{\xi}^2-(\bar{\lambda}+2)\bar{\alpha}^2)}{2\bar{\alpha}}\frac{\bar{R}^+}{\bar{R}^-}, 0, -(1+\cos(2\eta))\bar{\xi}^3\frac{\bar{R}^+}{\bar{R}^-}, \\
& (\cos(2\eta)-1)\bar{\xi}^3\frac{\bar{R}^+}{\bar{R}^-}, \frac{((\bar{\lambda}+2)\bar{\xi}^2-\bar{\lambda}\bar{\alpha}^2)\bar{\xi}}{2}\frac{\bar{R}^+}{\bar{R}^-}, \\
& \frac{\bar{\lambda}\bar{\xi}(\bar{\xi}^2-\bar{\alpha}^2)}{2}\frac{\bar{R}^+}{\bar{R}^-}, \frac{\bar{\xi}(\bar{\lambda}\bar{\xi}^2-(\bar{\lambda}+2)\bar{\alpha}^2)}{2}\frac{\bar{R}^+}{\bar{R}^-}, -i\cos\eta\,\bar{\alpha}\bar{\xi}^2\frac{\bar{R}^+}{\bar{R}^-}\Bigg\}^{T}
\end{aligned} \tag{6.189}$$

$$
\begin{aligned}
\left\{N_{ij}^{\gamma}\right\}^{SS}(\overline{\xi},\phi) = \Bigg\{ & i\cos\eta\ \overline{\beta}\overline{\xi}^{2}\frac{\overline{R}^{+}}{\overline{R}^{-}}, 0, -i\cos\eta\ \overline{\beta}\overline{\xi}^{2}\frac{\overline{R}^{+}}{\overline{R}^{-}}, \frac{-i\cos\eta\ \overline{\xi}^{2}}{2\overline{\beta}}, \\
& -\frac{\overline{\xi}\left((1-\cos(2\eta))\overline{R}^{-}+\left(1+\cos\left(2\eta\right)\right)\left(\overline{\beta}^{2}+\overline{\xi}^{2}\right)\overline{R}^{+}\right)}{2\overline{R}^{-}}, \\
& \frac{\overline{\xi}\left(\left(\cos(2\eta)-1\right)\left(\overline{\beta}^{2}+\overline{\xi}^{2}\right)\overline{R}^{+}-\left(1+\cos\left(2\eta\right)\right)\overline{R}^{-}\right)}{2\overline{R}^{-}}, \\
& \overline{\xi}^{3}\frac{\overline{R}^{+}}{\overline{R}^{-}}, 0, -\overline{\xi}^{3}\frac{\overline{R}^{+}}{\overline{R}^{-}}, -\frac{i\cos\eta\ \overline{\xi}^{2}\left(\overline{\beta}^{2}+\overline{\xi}^{2}\right)}{2\overline{\beta}}\frac{\overline{R}^{+}}{\overline{R}^{-}}\Bigg\}^{T}
\end{aligned}
\tag{6.190}
$$

$$
\begin{aligned}
\left\{N_{ij}^{\gamma}\right\}^{PS}(\overline{\xi},\phi) = \Big\{ & -4i\cos\eta\ \overline{\xi}^{4}\overline{\beta}(1+2\overline{\xi}^{2})/\overline{R}^{-}, 0, 4i\cos\eta\ \overline{\xi}^{4}\overline{\beta}(1+2\xi^{2})/\overline{R}^{-}, \\
& 0,\ 2(1+\cos(2\eta))\overline{\xi}^{3}(\overline{\beta}^{2}+\overline{\xi}^{2})(1+2\overline{\xi}^{2})/\overline{R}^{-}, \\
& 2(1-\cos(2\eta))\overline{\xi}^{3}(\overline{\beta}^{2}+\overline{\xi}^{2})(1+2\overline{\xi}^{2})/\overline{R}^{-}, \\
& -4\overline{\alpha}\overline{\beta}\overline{\xi}^{3}(1+2\overline{\xi}^{2})/\overline{R}^{-}, 0, 4\overline{\alpha}\overline{\beta}\overline{\xi}^{3}(1+2\overline{\xi}^{2})/\overline{R}^{-}, \\
& 2i\cos\eta\ \overline{\alpha}\overline{\xi}^{2}(\overline{\beta}^{2}+\overline{\xi}^{2})(1+2\overline{\xi}^{2})/\overline{R}^{-}\Big\}^{T}
\end{aligned}
\tag{6.191}
$$

$$
\begin{aligned}
\left\{N_{ij}^{\gamma}\right\}^{SP}(\overline{\xi},\phi) = \Big\{ & 2i\cos\eta\ \overline{\beta}\overline{\xi}^{2}\left(1+2\overline{\xi}^{2}\right)\left(\overline{\lambda}\overline{\alpha}^{2}-\left(\overline{\lambda}+2\right)\overline{\xi}^{2}\right)/\overline{R}^{-}, \\
& 2i\cos\eta\ \overline{\beta}\overline{\xi}^{2}\overline{\lambda}\left(\overline{\alpha}^{2}-\overline{\xi}^{2}\right)\left(1+2\overline{\xi}^{2}\right)/\overline{R}^{-}, \\
& 2i\cos\eta\ \overline{\beta}\overline{\xi}^{2}\left(1+2\overline{\xi}^{2}\right)\left(\left(\overline{\lambda}+2\right)\overline{\alpha}^{2}-\overline{\lambda}\overline{\xi}^{2}\right)/\overline{R}^{-}, 0, \\
& 4\left(1+\cos(2\eta)\right)\overline{\alpha}\overline{\beta}\overline{\xi}^{3}\left(1+2\overline{\xi}^{2}\right)/\overline{R}^{-}, 4\left(1-\cos(2\eta)\right)\overline{\alpha}\overline{\beta}\overline{\xi}^{3}\left(1+2\overline{\xi}^{2}\right)/\overline{R}^{-}, \\
& 2\overline{\xi}^{3}\left(1+2\overline{\xi}^{2}\right)\left(\overline{\lambda}\overline{\alpha}^{2}-\left(\overline{\lambda}+2\right)\overline{\xi}^{2}\right)/\overline{R}^{-}, 2\overline{\lambda}\overline{\xi}^{3}\left(\overline{\alpha}^{2}-\overline{\xi}^{2}\right)\left(1+2\overline{\xi}^{2}\right)/\overline{R}^{-}, \\
& 2\overline{\xi}^{3}\left(1+2\overline{\xi}^{2}\right)\left(\overline{\alpha}^{2}\left(\overline{\lambda}+2\right)-\overline{\lambda}\overline{\xi}^{2}\right)/\overline{R}^{-}, 4i\cos\eta\ \overline{\xi}^{4}\overline{\alpha}\left(1+2\overline{\xi}^{2}\right)/\overline{R}^{-}\Big\}^{T}
\end{aligned}
\tag{6.192}
$$

Through the same analysis and disposition as those for the displacements, the 6 integrals in Eqn. (6.185) can be inverted by the proposed rendition of Cagniard’s idea, .e., by writing

$$
\{T_{ii}^{\gamma}\}^{P,S,PP,SS,PS,SP}\left(\overline{r},\overline{z};\overline{s};\overline{p}\right)=\int_{0}^{\infty}\{\mathcal{T}_{ij}^{\gamma}\}^{P,S,PP,SS,PS,SP}\left(\overline{r},\overline{z};\overline{s};\overline{t}\right)\ e^{-\overline{p}\,\overline{t}}d\overline{t}
\tag{6.193}
$$

where

$$\{\mathcal{T}_{ij}^{\gamma}\}^{P,S,PP,SS,PS,SP}\left(\bar{r},\bar{z};\bar{s};\bar{t}\right)=H(\bar{t}-\bar{t}^{P,S,PP,SS,PS,SP}\ ) \\ \frac{2}{\pi}\mathrm{Re}\left\{(1-i\zeta)\int_{0}^{\pi/2}\{N_{ij}^{\gamma}\}^{P,S,PP,SS,PS,SP}(\bar{\xi}(\bar{t}),\phi;\bar{r},\bar{z};\bar{s})\frac{\partial\,\bar{\xi}}{\partial\,t}(\bar{t},\phi)d\phi\right\}, \tag{6.194}$$

where the arrival times and D-paths for various wave integrals are identical to those of displacements.

6.8 Numerical Illustrations

6.8.1 Example 1

As an example, Figure 6.20 shows the components of the displacement Green's function for the classical Pekeris-Chao case of $\nu = 0.3, \mu = c_s = 1,$, where source point is put at $(0,0,0)$, receiver point is put at $(-0.7,0.5,0)$ in meters, and the point load is specified to be a Heaviside step load. For this case, the Rayleigh wave speed is $c_R = 0.9274\, c_s$. The results obtained by the presented method are compared with those in Kausel (2012) for the simplest case where both source and receiver points are on the free surface. The comparison shows that they are identical. In this example, the direct P-, reflected PP-, SS-, PS- and SP-waves arrive the receiver point at the same time, then arrives the direct S- wave and the Rayleigh wave. Each time when a wave arrives, the displacements have some abrupt changes. In this case the Rayleigh wave component dominates the other waves.

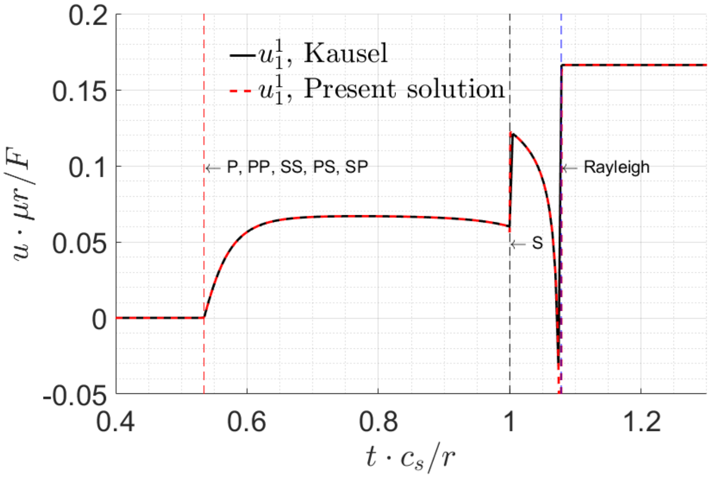
u_1^1, Kausel
u_1^1, Present solution
P, PP, SS, PS, SP
S
Rayleigh
0.2
0.15
0.1
0.05
0
-0.05
0.4
0.6
0.8
1
1.2
$u \cdot \mu r/F$
$t \cdot c_s/r$

(a)

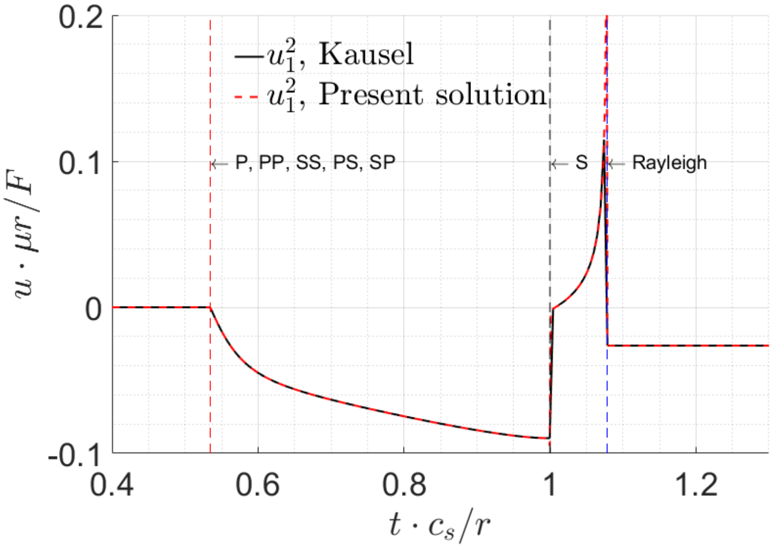
u_1^2, Kausel
u_1^2, Present solution
P, PP, SS, PS, SP
S
Rayleigh
0.2
0.1
0
-0.1
0.4
0.6
0.8
1
1.2
$u \cdot \mu r/F$
$t \cdot c_s/r$

(b)

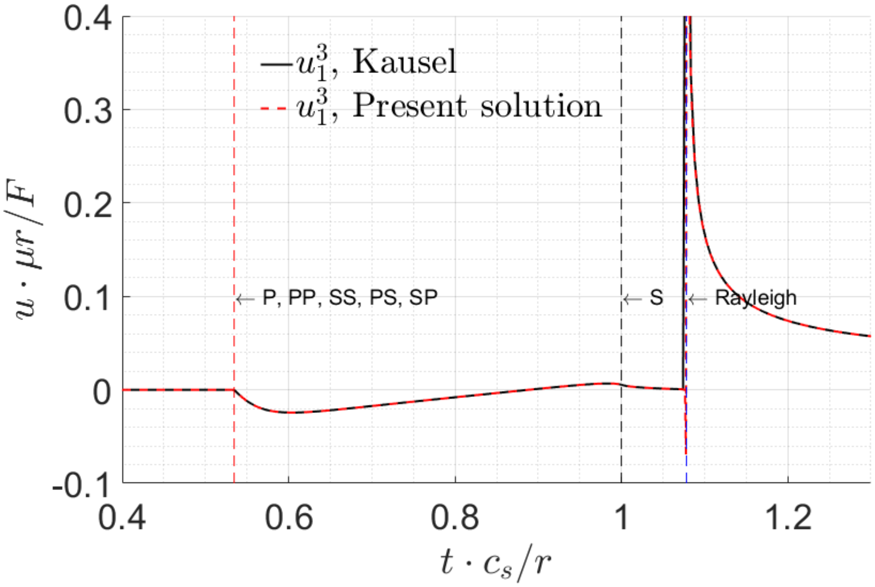
u_1^3, Kausel
u_1^3, Present solution
P, PP, SS, PS, SP
S
Rayleigh
$u \cdot \mu r / F$
$t \cdot c_s / r$
0.4
0.3
0.2
0.1
0
-0.1
0.4
0.6
0.8
1
1.2

(c)

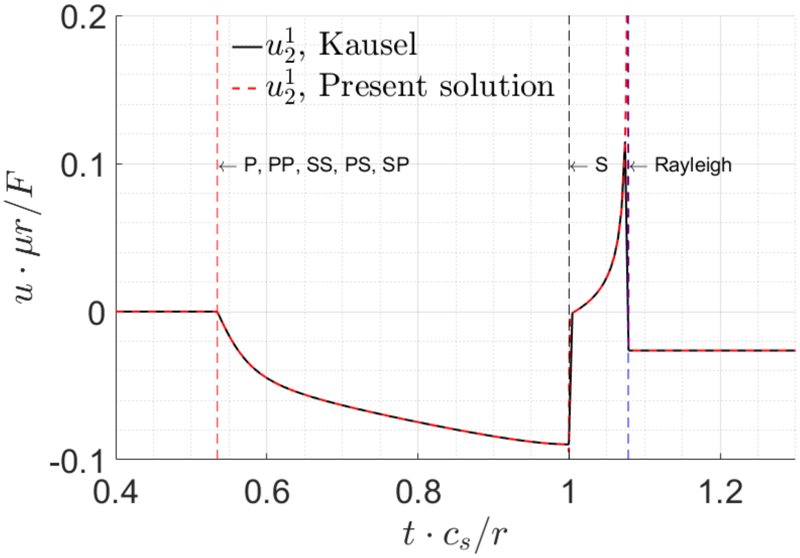
u_2^1, Kausel
u_2^1, Present solution
P, PP, SS, PS, SP
S
Rayleigh
$u \cdot \mu r / F$
$t \cdot c_s / r$
0.2
0.1
0
-0.1
0.4
0.6
0.8
1
1.2

(d)

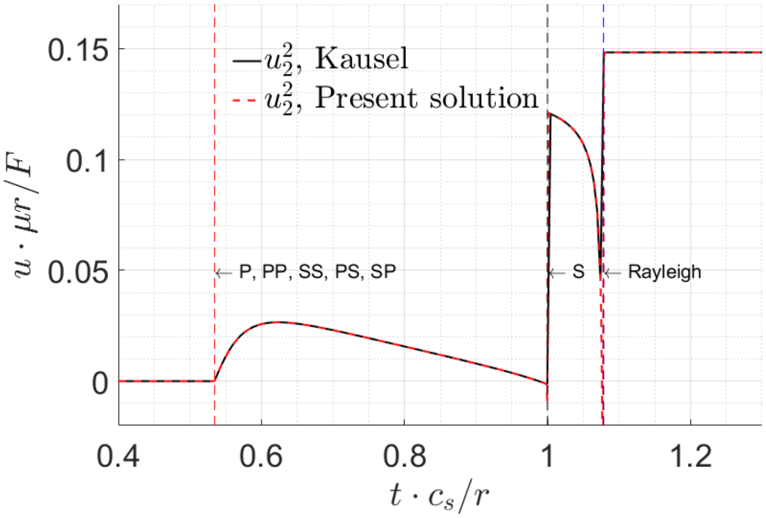

u_2^2, Kausel
u_2^2, Present solution
P, PP, SS, PS, SP
S
Rayleigh
$u \cdot \mu r / F$
0.15
0.1
0.05
0
0.4
0.6
0.8
1
1.2
$t \cdot c_s / r$

(e)

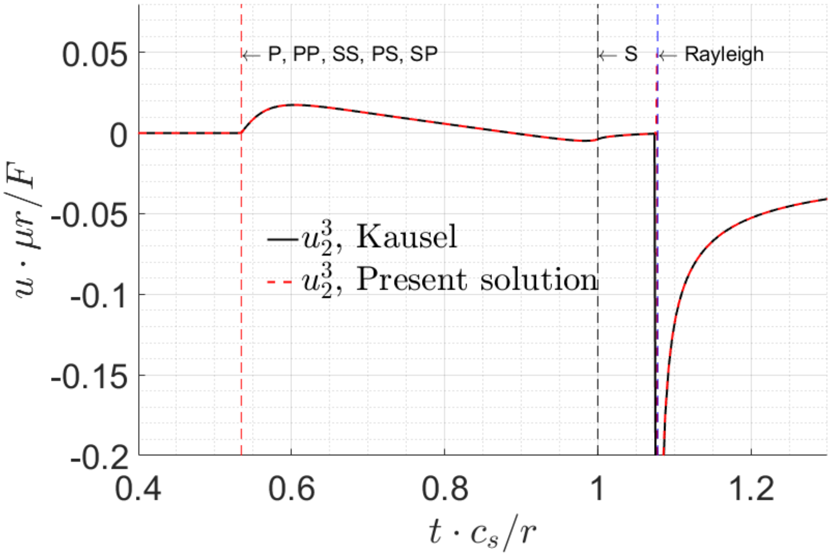

P, PP, SS, PS, SP
S
Rayleigh
u_2^3, Kausel
u_2^3, Present solution
$u \cdot \mu r / F$
0.05
0
-0.05
-0.1
-0.15
-0.2
0.4
0.6
0.8
1
1.2
$t \cdot c_s / r$

(f)

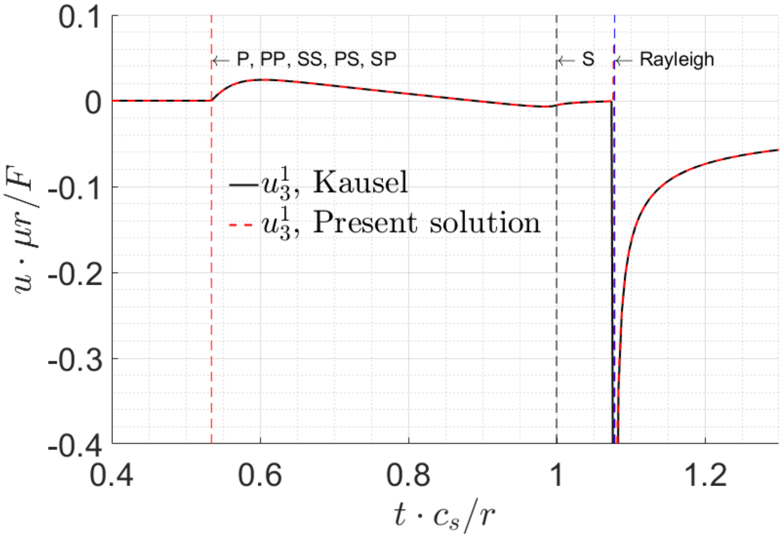
0.1
0
-0.1
-0.2
-0.3
-0.4
0.4
0.6
0.8
1
1.2
$t \cdot c_s/r$
$u \cdot \mu r/F$
P, PP, SS, PS, SP
S
Rayleigh
u_3^1, Kausel
u_3^1, Present solution

(g)

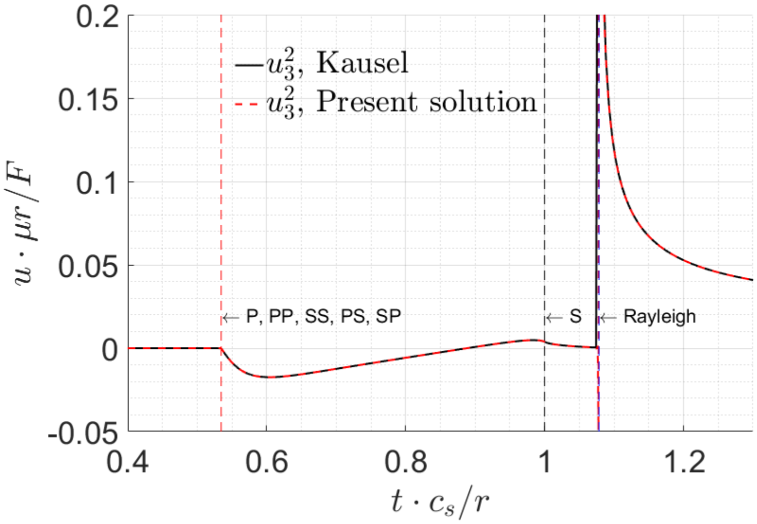
0.2
0.15
0.1
0.05
0
-0.05
0.4
0.6
0.8
1
1.2
$t \cdot c_s/r$
$u \cdot \mu r/F$
u_3^2, Kausel
u_3^2, Present solution
P, PP, SS, PS, SP
S
Rayleigh

(h)

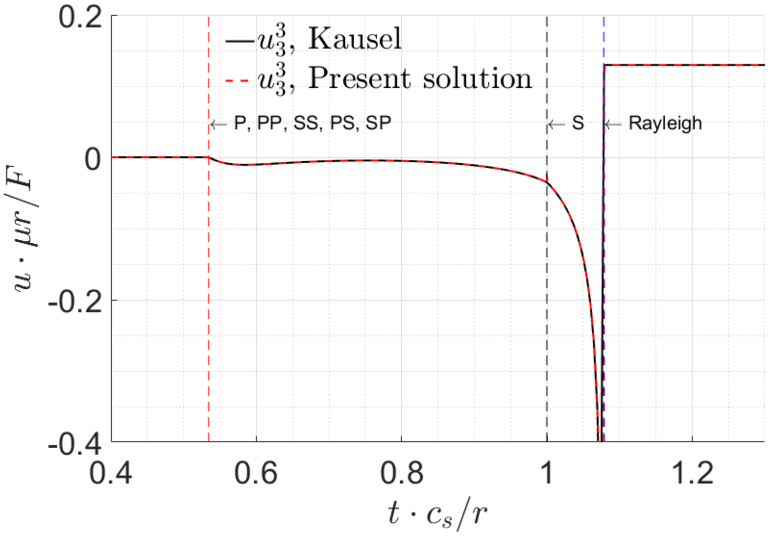

(i)

Figure 6.20: Result of displacements for Example 1.

6.8.2 Example 2

Another case to test the solution format in this chapter was the one that was investigated in Johnson (1974). In this example, the elastic half-space has material parameters as $c_s = 4.62\text{km}/\text{s}$, $c_d = 8.00km/s$, $\rho = 3.3g/cm^3$, while the source point is embedded at (0,0,2) and the observation point at (10,0,4). The corresponding Possion's ratio is $\nu = 0.25$, and Rayleigh wave speed is $c_R = 0.9194\, c_s = 4.25km/s$.

Consider a Heaviside-type point force with magnitude of F is applied at the source point. Time history of displacement components at the observation point are shown in Figure 6.21, where the arrival of the direct and reflected waves, as well as the head wave are marked on the displacement curves. The solutions obtained by the present method are in very good agreement with Johnson's plotted solution, except for the displacement between the arrival of the reflected SP- and PS-waves. At the arrival time of these two waves, the present result by the propsed method exhibits a jump, which Johnson's plotted solution apparently missed it (see also Eatwell et al. 1982).

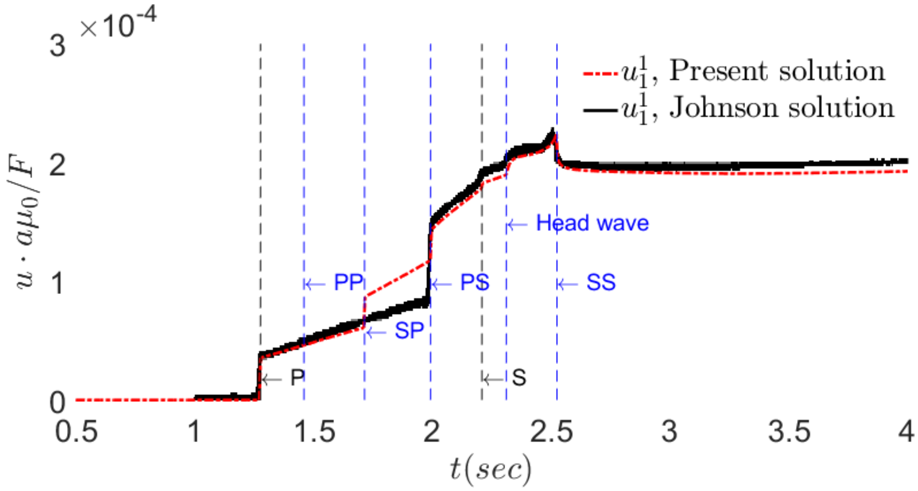

(a)

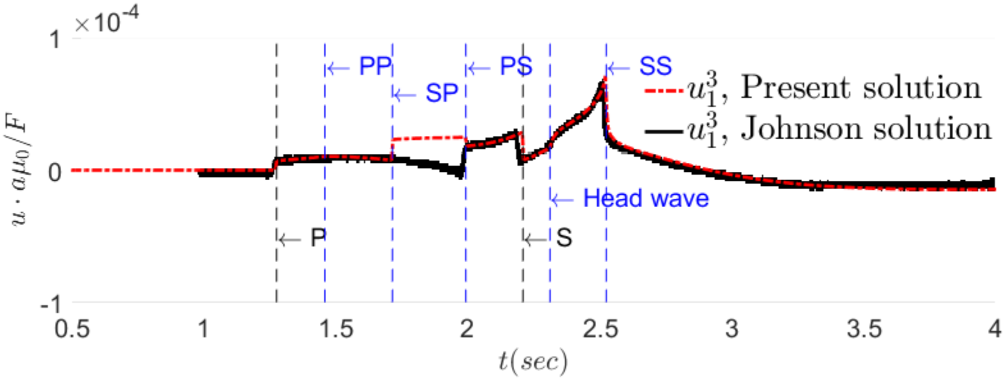

(b)

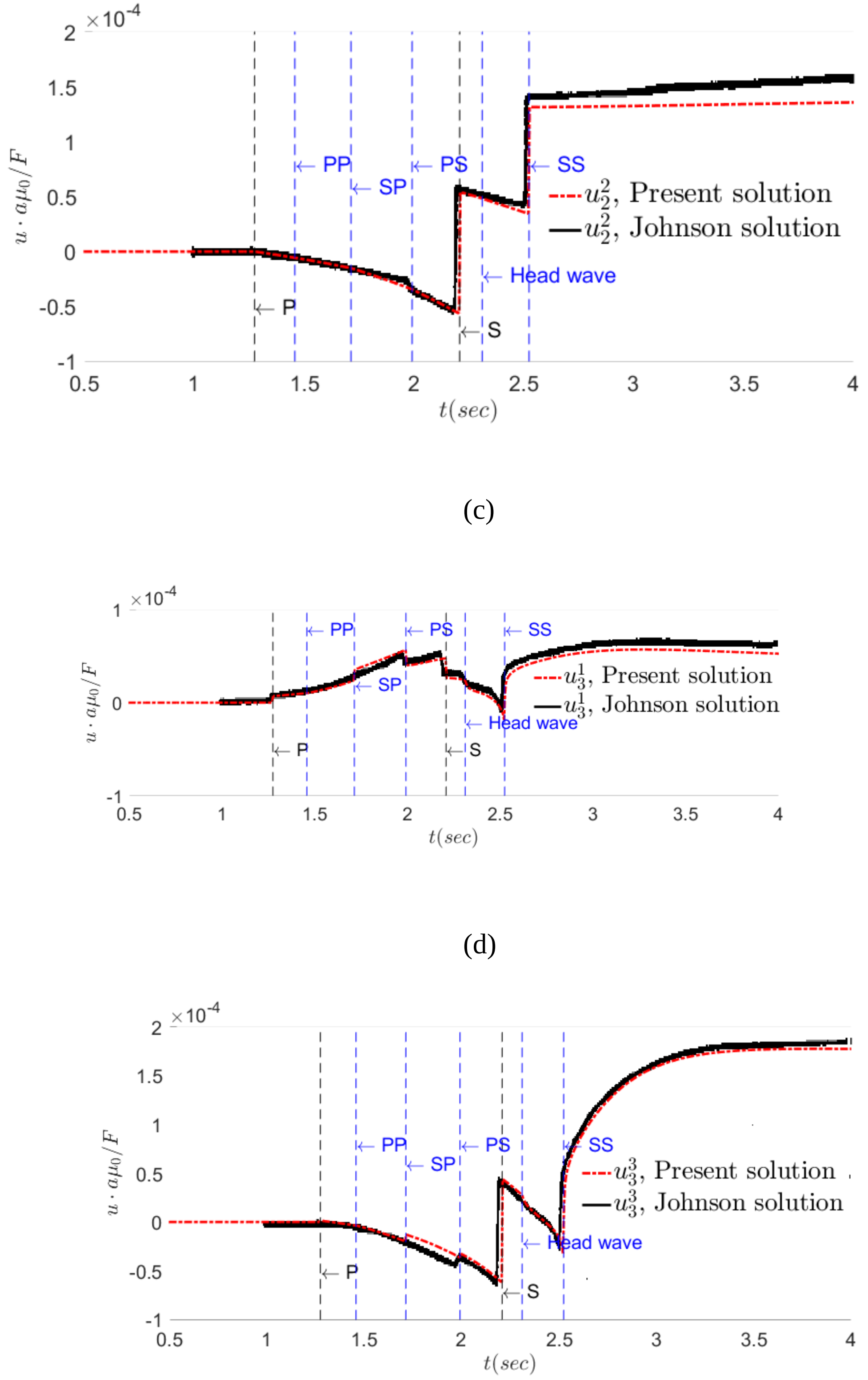

(c)

(d)

(e)

Figure 6.21: Result of displacements for Example 2.

6.8.3 Example 3

By virtue of a time convolution, one can compute the Green's function for a load with a cubic B-Spline time function that is defined by

$$B(t)=\begin{cases} \dfrac{32}{3}\dfrac{t^3}{\Delta T^3}, & 0\le t<\Delta T/4, \\ -32\dfrac{t^3}{\Delta T^3}+32\dfrac{t^2}{\Delta T^2}-8\dfrac{t}{\Delta T}+\dfrac{2}{3}, & \Delta T/4\le t<2\Delta T/4, \\ 32\dfrac{t^3}{\Delta T^3}-64\dfrac{t^2}{\Delta T^2}+40\dfrac{t}{\Delta T}-\dfrac{22}{3}, & 2\Delta T/4\le t<3\Delta T/4, \\ -\dfrac{32}{3}\dfrac{t^3}{\Delta T^3}+32\dfrac{t^2}{\Delta T^2}-32\dfrac{t}{\Delta T}+\dfrac{32}{3}, & 3\Delta T/4\le t\le \Delta T, \\ 0, & \text{elsewhere}, \end{cases} \tag{6.195}$$

with ΔT being the width of the B-Spline load. In this example, it was set to be $\Delta T = 0.3\text{sec}$. The result can be compared with the one by the inverse Fourier transform method as presented in Chapter 5.

For the same half-space, source and receiver point in Example 6.10.2, the response curves of displacements and stresses to the cubic B-Spline load are obtained by these two methods and plotted for comparison in Figure 6.22 - Figure 6.25. Figure 6.22 presents the non-zero components of displacement due to load in all three directions, while Figure 6.23 - Figure 6.25 display the non-zeros components of stress caused by load in $x, y, z-$ direction correspondingly. As expected, the response curves corresponding to this smooth loading are continuous and smooth. The comparisons show that the two results match each other quite well.

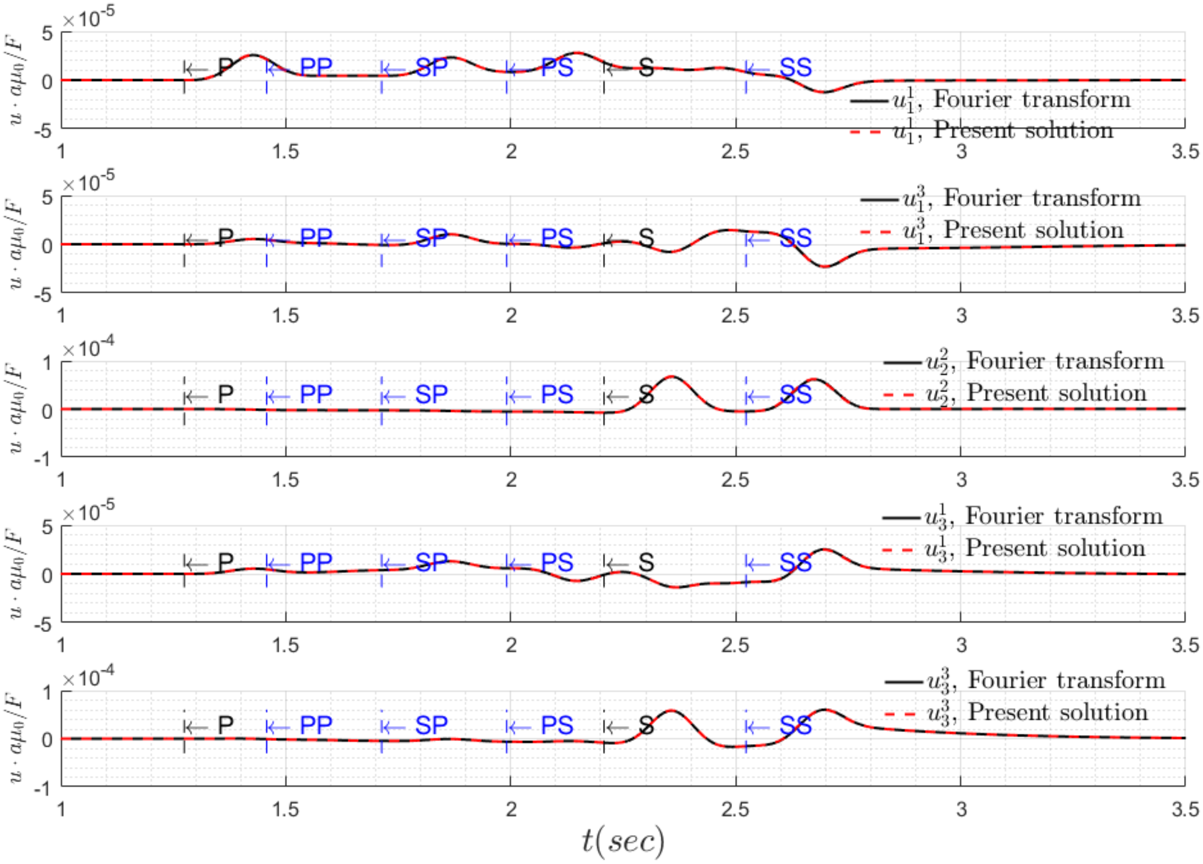

Figure 6.22: Green's function of displacement for Example 3. For U_i^k, i stands for the displacement component, while k stands for the loading direction.

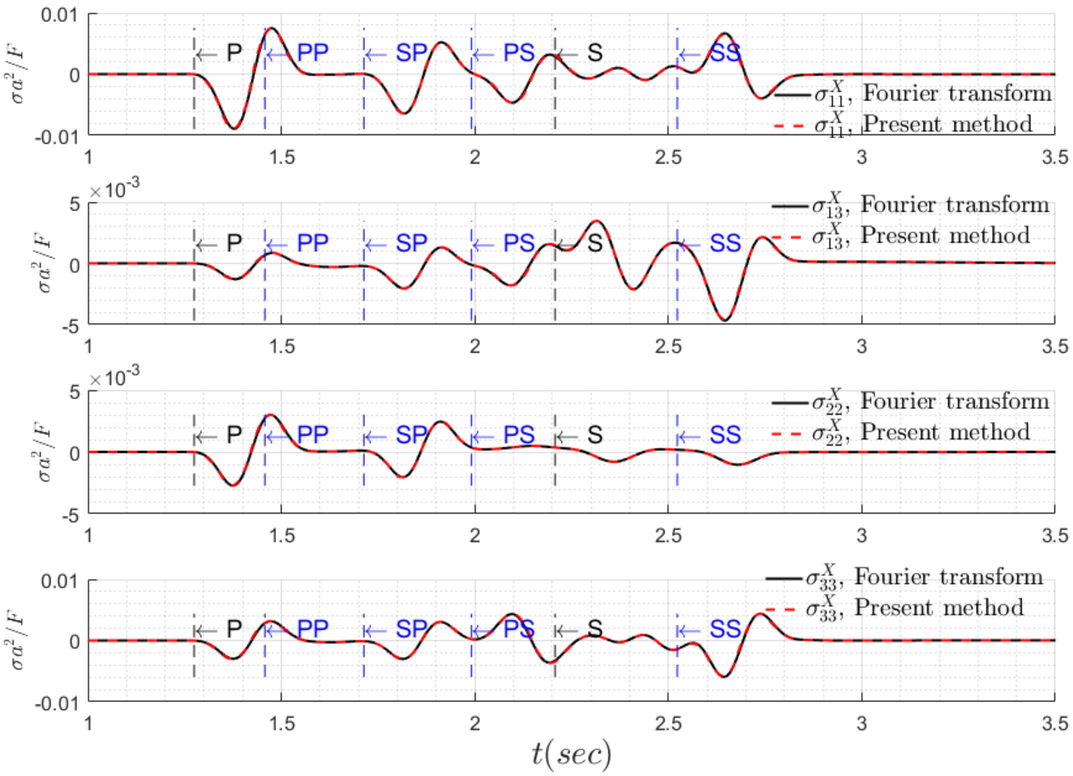

Figure 6.23: Green’s function of stresses for Example 3. Point load is in $x-$ direction.

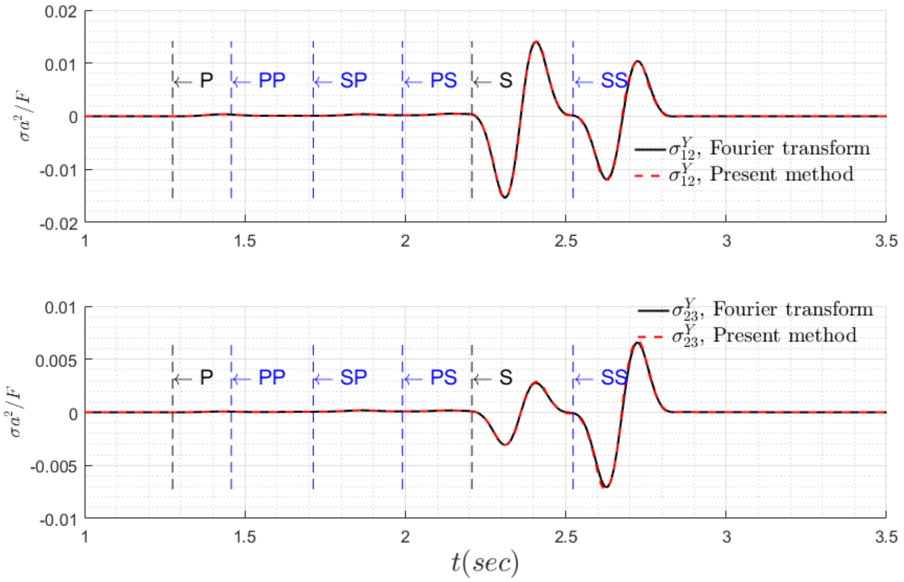

Figure 6.24: Green’s function of stresses for Example 3. Point load is in $y-$direction.

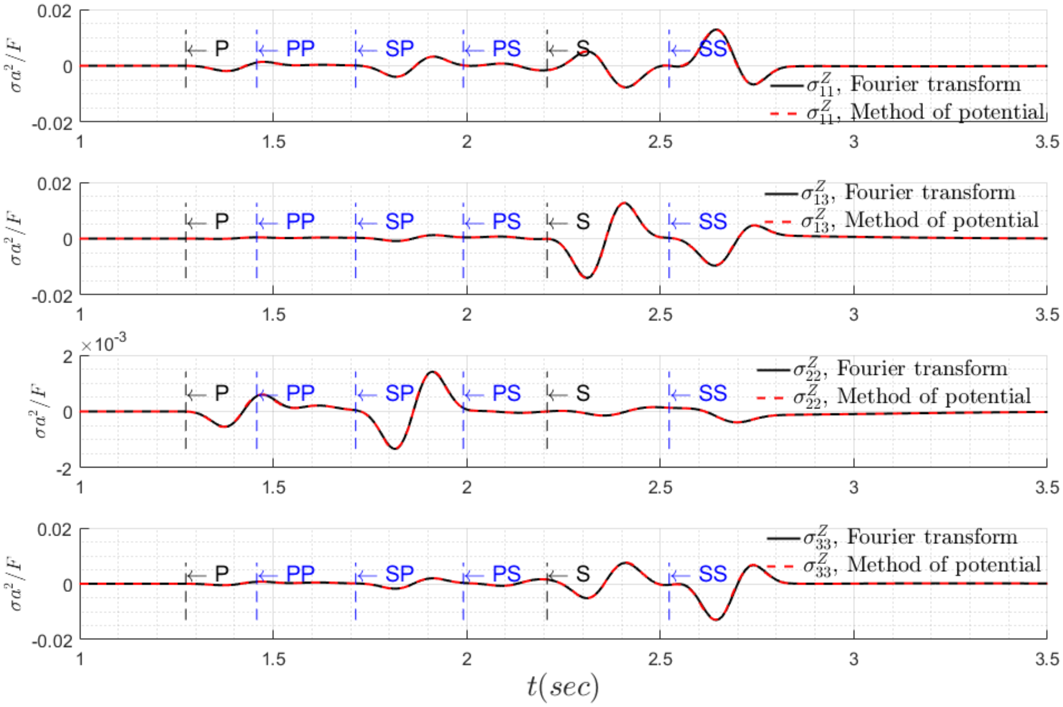

Figure 6.25: Green's function of stresses for Example 3. Point load is in z −direction.

6.8.4 Example 4

Another example investigated here is the problem described in Figure 5 of Johnson (1974), where the half-space has properties of $c_s = 4.62\text{km}/s$, $c_d = 8.00km/s$, $\rho = 3.3g/cm^3$. The source point is put at $(0,0,2)m$, while and observation is taken at (10,0,4)m. Figure 6.26 includes the non-zero components of the Green's function of displacement. Each component produced by the proposed method is compared with the solution present in Johnson (1974).

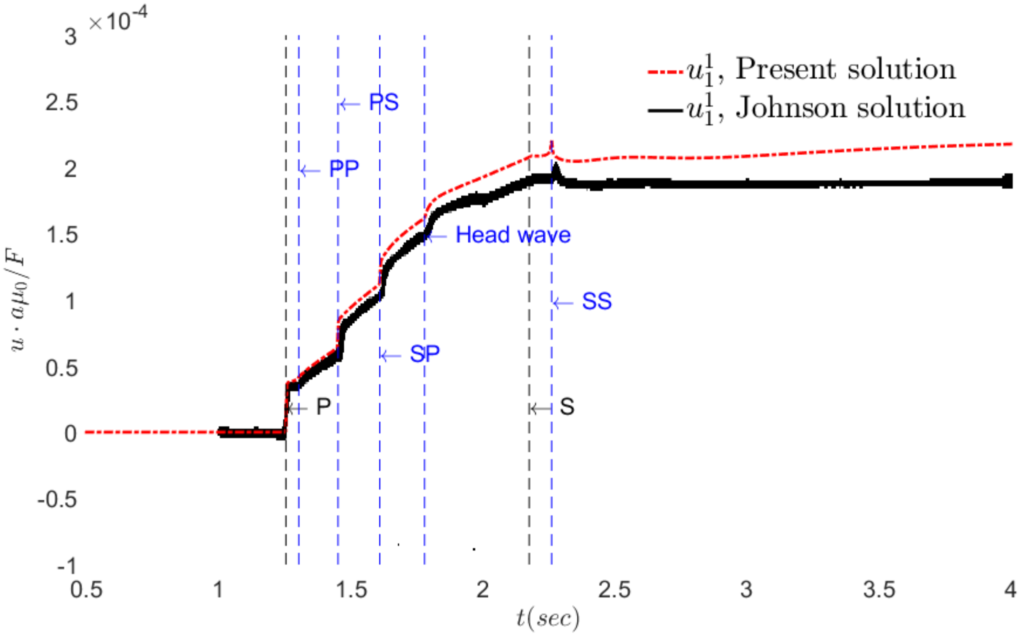
$\times 10^{-4}$
3
2.5
2
1.5
1
0.5
0
-0.5
-1
$u \cdot a\mu_0/F$
0.5
1
1.5
2
2.5
3
3.5
4
$t(sec)$
P
PP
PS
SP
Head wave
S
SS
u_1^1, Present solution
u_1^1, Johnson solution

(a)

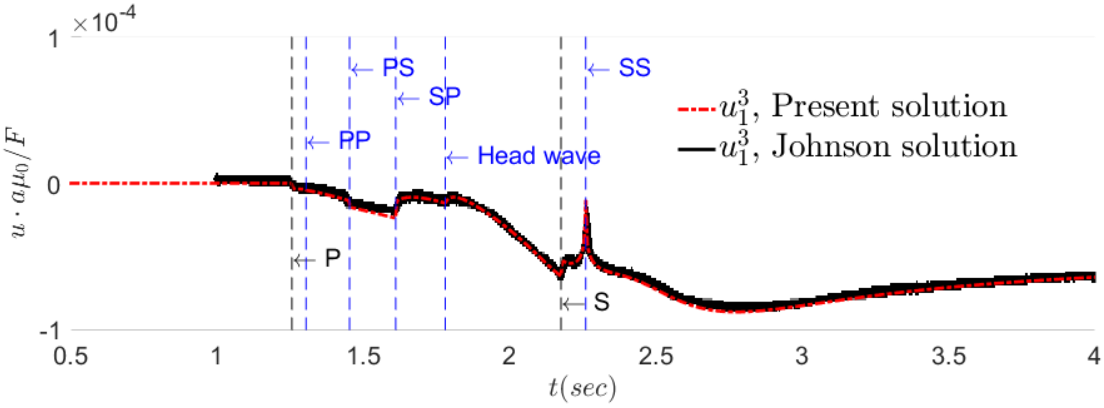
$\times 10^{-4}$
1
0
-1
$u \cdot a\mu_0/F$
0.5
1
1.5
2
2.5
3
3.5
4
$t(sec)$
P
PP
PS
SP
Head wave
S
SS
u_1^3, Present solution
u_1^3, Johnson solution

(b)

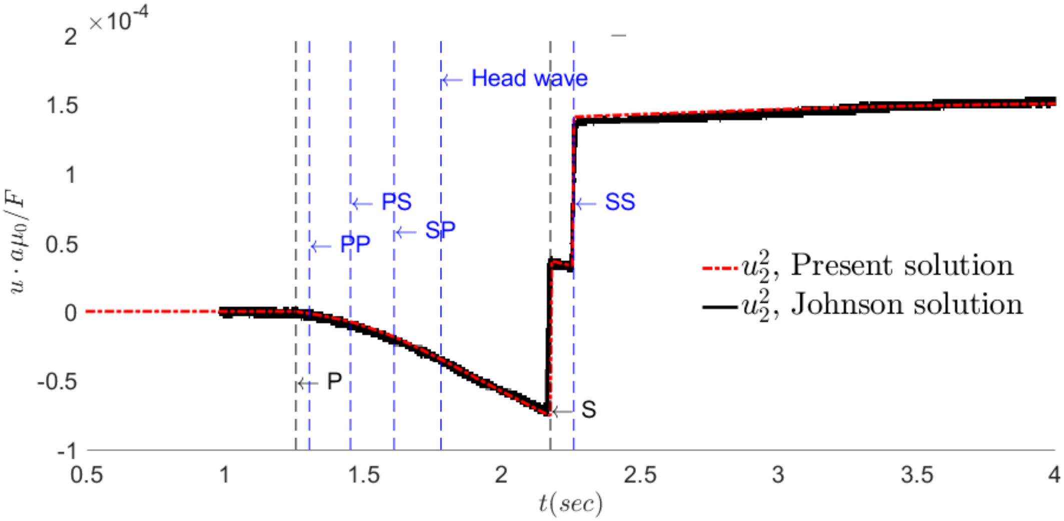
$\times 10^{-4}$
2
1.5
1
0.5
0
-0.5
-1
$u \cdot a\mu_0/F$
0.5
1
1.5
2
2.5
3
3.5
4
$t(sec)$
← Head wave
← PS
← PP
← SP
← SS
← P
← S
u_2^2, Present solution
u_2^2, Johnson solution

(c)

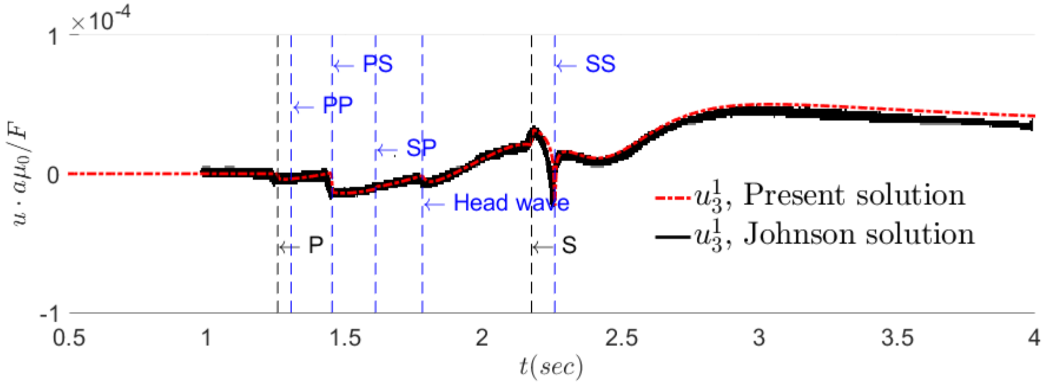
$\times 10^{-4}$
1
0
-1
$u \cdot a\mu_0/F$
0.5
1
1.5
2
2.5
3
3.5
4
$t(sec)$
← PS
← SS
← PP
← SP
← Head wave
← P
← S
u_3^1, Present solution
u_3^1, Johnson solution

(d)

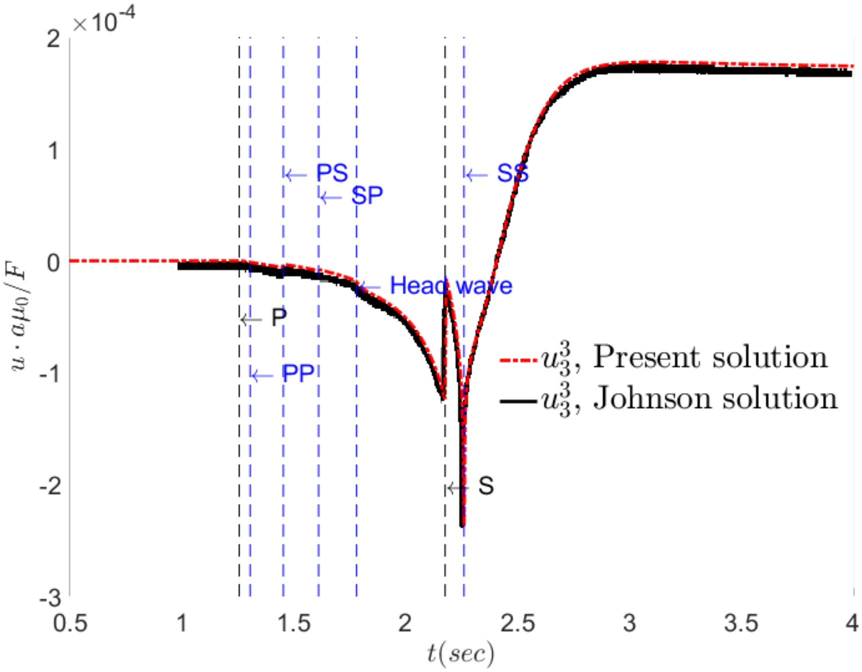

(e)

Figure 6.26: Response curve of displacements for Example 4.

6.8.5 Example 5

For the same half-space, source and receiver point in Example 4, the response curves of displacements and stresses to a B-Spline load are obtained by the presented method and the inverse Fourier transform method. The width of the cubic B-Spline load is again taken to be $\Delta T = 0.3\text{sec}$. The results by the direct time-domain and frequency domain methods are plotted together for comparison. It can be seen that they again agree very well with each other.

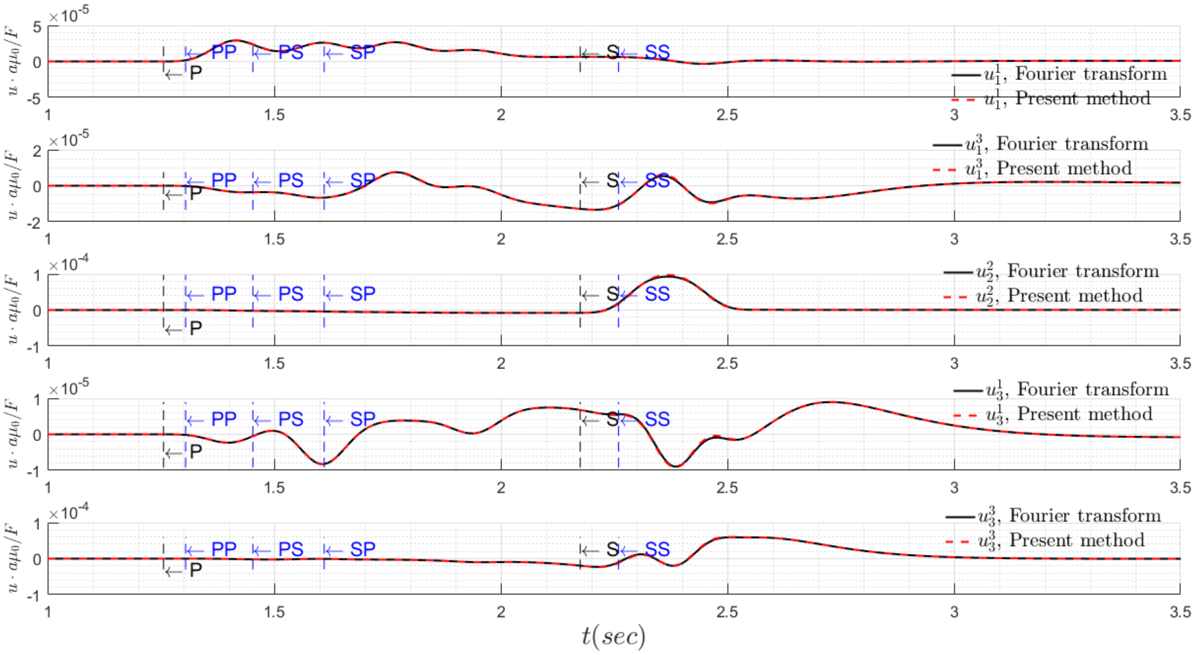

Figure 6.27: Response of displacement for Example 5. For U_i^k, i stands for the displacement component, while k stands for the loading direction.

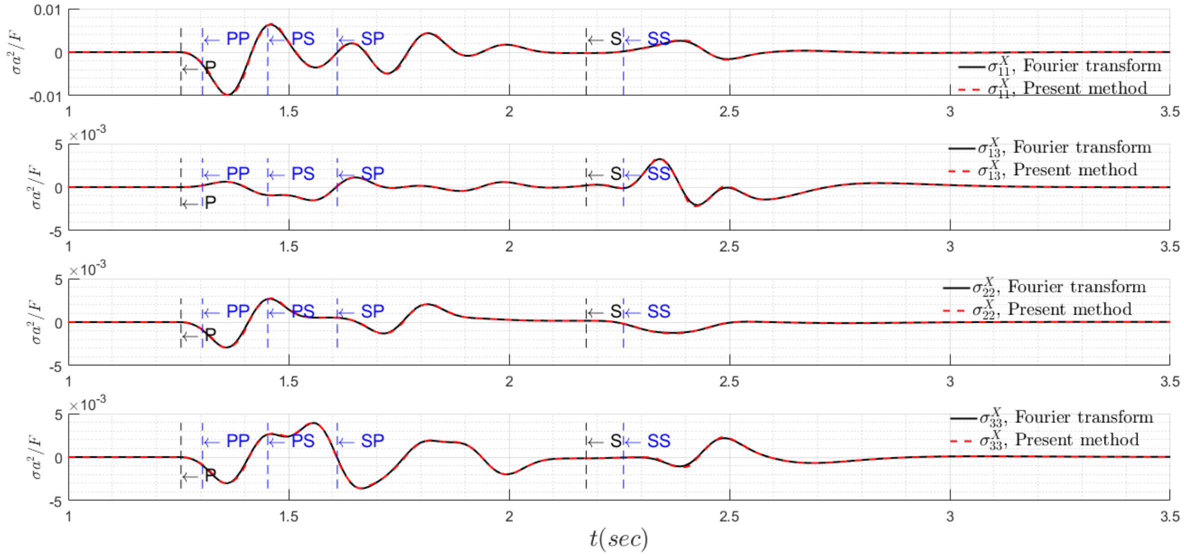

Figure 6.28: Green's function of stresses for Example 5. Load is in $x-$ direction.

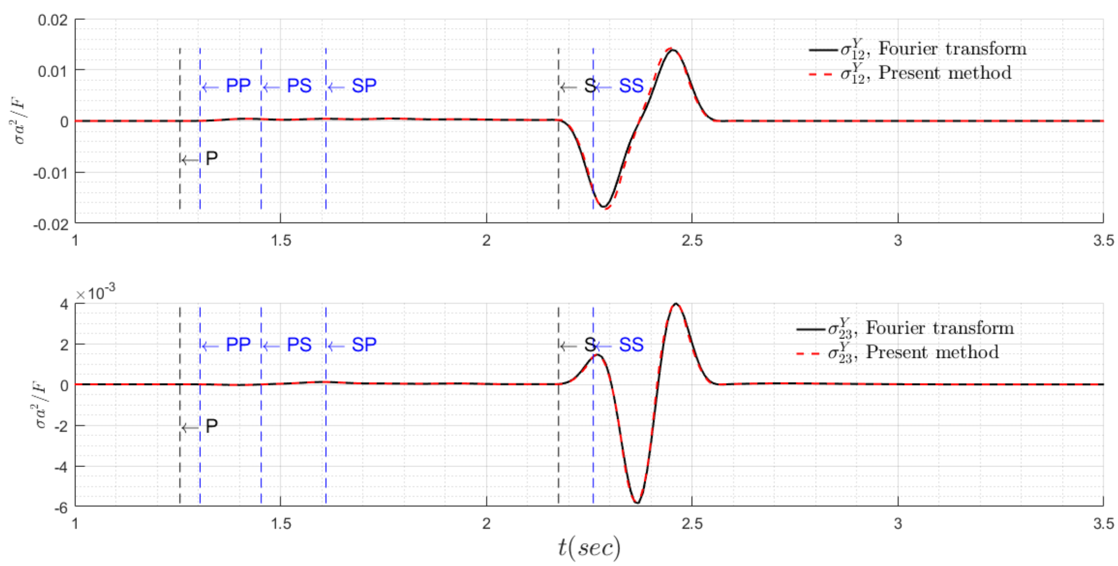

Figure 6.29: Green's function of stresses for Example 5. Load is in $y-$direction.

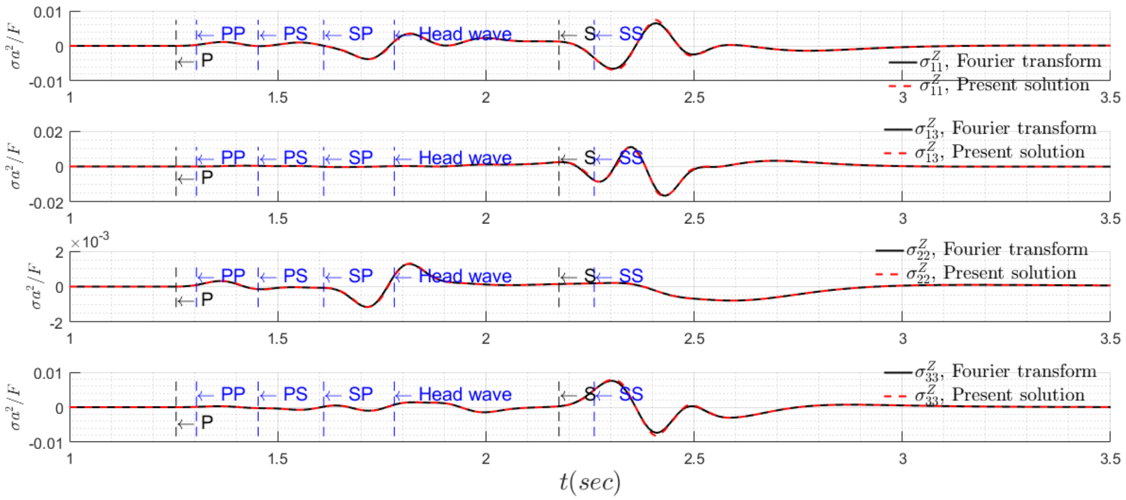

Figure 6.30: Green's function of stresses for Example 5. Load is in $z-$ direction.

6.9 Summary

In this chapter, a method of potentials with Laplace and Hankel transforms to investigate the transient wave propagation in homogeneous half-space due to an arbitrary point load is presented. The time-domain solution is obtained by adapting Cagniard's inversion approach to the use of Hankel transforms and Bessel integrals with which past researchers had tried to avoid. A singularity extraction technique that allows an explicit analytical characterization of the Rayleigh wave front singularity is also employed to ensure a rigorous and complete solution. To confirm the reliability of the proposed method, multiple examples are considered with successful numerical checks against past solutions in the literature.

As will be shown in Chapter 8, the Green's functions developed here have been incorporated into a 3-D boundary element method for the analysis of transient dynamic problems related to a half-space.

Chapter 7

Time-domain Green's function for multi-layer half-space by a method of potentials

7.1 Introduction

The analysis of elastic wave propagation in a multilayered half-space is of fundamental importance in civil engineering, mechanical engineering and geophysics due to its applications in dynamic soil-structure interaction, geotechnical earthquake engineering, foundation vibration and quantitative seismology method where the medium's material properties cannot be considered as spatially homogeneous but vary with depth or thickness.

For a piecewise homogeneous but horizontally multilayered solid medium, the equations of motion differ in parameters from layer to layer and form a set of equations that are related by boundary and interfacial conditions. The solution of such a dynamical system is generally complicated before the development of the propagator matrix method. The method of propagator matrix was first proposed by Thomson (1950) to investigate the transmission of a plane elastic wave at oblique incidence through a stratified solid, where the relationship between wave quantities in two adjoining layers is established in matrix form using interfacial conditions. As noted in Haskell (1953), "although the method may be regarded as no more than a change in notation, the matrix notation itself suggests a systematic computational procedure that makes it possible to handle at least a three-layer case on an ordinary desk calculator without an unreasonable expenditure of time." The formalism was later used by Haskell (1953) to obtain the phase velocity's dispersion equation for surface waves of Rayleigh and Love types. In parallel to the formulation in Thomson (1950) who adopted a potential representation of the displacements, an alternative method of propagator matrix using directly displacements as the unknowns was devised by Knopoff (1964) to investigate the plane harmonic waves in multilayer half-space. In terms of Fourier transforms with repect to both time and spatial coordinate for a plane time harmonic SH-wave field, a systematically transfer matrix for stress and displacements in the frequency domain between two adjacent layers in the multilayer media were developed (Gilbert and Backus 1966) .

By establishing the connection between the method of propagator matrix and the reflection/transmission properties of a single layer, i.e., expressing the stress-displacement vectors in terms of the local upgoing/downgoing P- and S- waves and building their connections between the upgoing/downgoing waves on the two sides of the layer interfaces, an iterative approach to the calculation of reflection and transmission coefficients for plane waves in a two-dimensional multilayer media was set up in Kennett (1974). The response of a multilayered half-space to a buried point source was then constructed in terms of reflection and transmission coefficients (Kennett and Kerry 1979). With a factorization of the overall reflection and transmission matrices into generalized transmission and reflection matrices at individual interfaces, Apsel and Luco (1983), Luco and Apsel (1983) obtained the complete three-dimensional dynamic response of a multilayered half-space in a simpler form. By virtue of a method of displacement potentials (Pak, 1987), Pak and Guzina (2002) presented a more compact mathematical development for the three-dimensional elastodynamic problem, with a rigorous attendance to the singular response in the interior of a layer or at the bi-material interfaces and the elimination of past growing exponential terms.

In seismology, a common method to investigate wave propagation in multilayer media is the generalized ray theory (Spencer, 1960). Instead of dealing with the full definition of the boundary value problem analytically, the generalized ray theory constructs the responses directly using geometric and Snell’s law type arguments in terms of an infinite series of Laplace transforms of the response (displacement, stress, etc.) of the wave components from a source in a multilayered medium. Each term in the series describes the wave motion that traverses a corresponding generalized ray path between the source and receiver, and each term is inverted by Cagniard’s idea to get a time-domain response. The method was used to investigate, for example, the surface response of a stratified half space to the radiation from an axisymmetric load in Spencer (1960). Helmberger (1968) determined the pressure response in a fluid half-space overlying a stratified solid half-space using the generalized ray theory and Cagniard-de Hoop method to obtain the transient responses. Wigginst and Helmberger (1974) presented an efficient computational implementation and the elaboration of such a method can be found in Kennett (2013).

The success of generalized ray theory approach relies on the correct choice of the generalized rays from the infinite series. For half-space configurations with layers more than just two or three and when long-time response is of interest, the problem is cumbersome as it involves checking and developing many generalized rays and one's intuition. The generalized ray theory is thus generally not used for complicated 3-D mechanics boundary value problems. As pointed out in Kennett (1974), the Taylor series expansion of some particular terms in the integral representations obtained via the method of propagator matrix can be expanded into an infinite series, each term of which can be related to a group of geometric rays. As a problem that involves complicated reflections, transmissions and conversions, Lee and Ma (2000) studied the propagation of elastic transient waves in a two-dimensional multi-layered media subjected to in-plane loadings by a matrix method. In their development, Helmholtz displacement potentials in Cartesian coordinates were used together with one-sided Laplace transform for time and double-sided Laplace transform for the horizontal spatial coordinates. The equation system in the triple transformed domain constructed from the boundary conditions were then solved by a matrix formulation and the solution was expanded into a power series of phase-related reflection and transmission matrices. They applied the same method to investigate the dynamic response of a layered media subjected to anti-plane loadings in Ma et al. (2001). Exetending the method developed in Lee and Ma (2000) for the 2-D case, Ma and Lee (2006) also considered the propagation of transient elastic waves in a three-dimensional multilayered half-space to point loads by means of (*i*) the standard Lame's representation with 4 potential functions, (*ii*) triple Fourier transform over time and horizontal spatial coordinates (*iii*) decomposition of motion into two groups of P-SV and SH-waves, (*iv*) method of propagator matrices to determine the field unknowns in the transformed domain, (*v*) power series expansion of coefficient matrices, (*vi*) Cagniard's method to obtain time-domain responses. Using the method of reverberation-ray matrix (Pao 2000), the propagation of elastic waves in a layered solid due to an axisymmetric point source and/or a line source was considered by Su et al. (2002). In the reverberation matrix method, the approximate time-domain solution was obtained numerically by fast inverse Laplace transform and fast Fourier transform. Tian and Xie, Z. (2009) presented a hybrid approach for the evaluation of transient elastic-wave propagation in a multilayered solid, integrating reverberation matrix method with Cagniard-de Hoop's method.

Built on the analytical and computational developments in earlier chapters, a rigorous and systematic method will be presented in this chapter for tackling the time-domain multi-layered half-space Green's function problem. Highlights of the development include:

(a) In contrast to most past studies, the proposed formulation adopts the more natural cylindrical coordinate system for this class of problems. Similar to what is shown in the last chapter, the time domain displacements and stresses in a multi-layer half-space can be reduced to a single interal over a fixed finite interval.

(b) Instead of using Helmholtz-Lame's potential presentation which involves 4 unknown potentials and thus requiring an additional constraint, Pak's method of displacement potentials with 3 scalar unknowns is employed leading to considerable analytical compactness.

(c) Ray expansion results in an infinite series of integrals, which must be truncated to a finite number of terms in practice. To get the exact response at the receiver point for a specified time interval of interest, all terms associated with the rays arriving ahead of that time should be included in the truncated series. In the present development, a new analytical method to extract the arrival times for all the wave group terms in the exact potential solution is developed by means of branch-cut and integral contour analysis.

(d) In the case where both source and receiver points are on free surface or the same layer interface, the formal integration path for the integral representation of response functions will run into Rayleigh and/or Stoneley poles whose analytical contributions to the integrals are difficult to evaluate by pure numerics, even if one can formally write the integral as the sum of the principal value of an integral over the real axis plus a contribution due to a small semicircular detour above the pole. In this study, the complex function theory and contour integration method employed by Pak (1987) is extended to facilitate the treatment of the time-domain Laplace-Hankel transform inversion problem, leading to not only a reduction in the mathematical complexities but also an improvement in the computational efficiency.

7.2 Statement of the problem

Consider n bonded parallel homogeneous, isotropic, linearly elastic layers overlying and adhering fully to a homogeneous elastic half-space (see Figure 7.1). A cylindrical coordinate system is employed with its origin on the top free-surface and the positive $z-$direction pointing downwardly into the half-space. Bounded by the upper and lower interfaces located at depths z_{j-1} and z_j respectively, the domain of the j^{th} layer is denoted by $\mathcal{L}_j$ and characterized by the material parameters μ_j, ν_j, ρ_j , a thickness $h_j = z_j - z_{j-1}$, with the notation of

$$\begin{aligned}\mathcal{L}_j = \{(r,\theta,z;\rho,\nu,\mu) \,|\, 0 \le r < \infty, 0 \le \theta < 2\pi, z_{j-1} < z < z_j,\\ \mu = \mu_j, \lambda = \lambda_j, \rho = \rho_j\},\quad j = 1,2,...,n\end{aligned}. \tag{7.1}$$

Likewise, the domain of the underlying half-space is denoted as

$$\begin{aligned}\mathcal{L}_{n+1} = \{(r,\theta,z;\rho,\nu,\mu) \,|\, 0 \le r < \infty, 0 \le \theta < 2\pi, z_n < z < z_\infty,\\ \mu = \mu_{n+1}, \lambda = \lambda_{n+1}, \rho = \rho_{n+1}\}\end{aligned}. \tag{7.2}$$

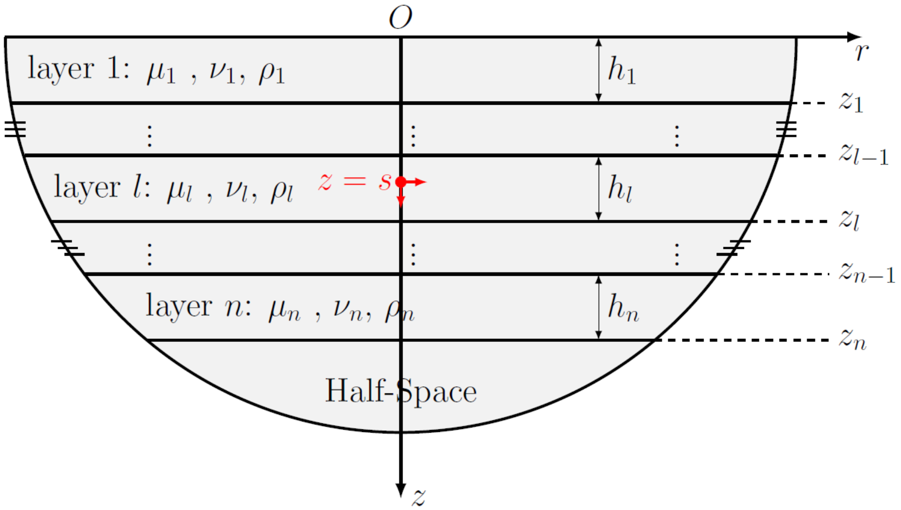

Figure 7.1: Multi-layered half-space.

In view of the elastodynamic solution for a homogeneous medium in absence of body force as outlined in Chapter 6, the displacement and stress fields in each layer not containing the source $(1 \le (j \ne l) \le n+1$ can be completely described by six coefficients of integration $A_m^j(\xi, p)$, $B_m^j(\xi, p)$, ..., $F_m^j(\xi, p)$ of the potential for the j^th^ layer. Labelling the layer that contains a source within as the l^{th} layer, one can view it as composed of Region I $\{z_{l-1} < z < s\}$ and Region II $\{s < z < z_l\}$. Denoting $A_{m1}^l(\xi, p)$, $B_{m1}^l(\xi, p)$, ..., $F_{m1}^l(\xi, p)$ and $A_{m2}^l(\xi, p)$, $B_{m2}^l(\xi, p)$, ..., $F_{m2}^l(\xi, p)$ to be the integration coefficients associated with Region I and II respectively, the depth-dependent coefficients for the l^{th} layer can be expressed as

$$
\begin{aligned}
A_m^l(\xi, z, p) &= A_{m2}^l(\xi, p) + H(s-z)\left(A_{m1}^l(\xi, p) - A_{m2}^l(\xi, p)\right), \\
B_m^l(\xi, z, p) &= B_{m1}^l(\xi, p) + H(z-s)\left(B_{m2}^l(\xi, p) - B_{m1}^l(\xi, p)\right), \\
C_m^l(\xi, z, p) &= C_{m2}^l(\xi, p) + H(s-z)\left(C_{m1}^l(\xi, p) - C_{m2}^l(\xi, p)\right), \\
\\
D_m^l(\xi, z, p) &= D_{m1}^l(\xi, p) + H(z-s)\left(D_{m2}^l(\xi, p) - D_{m1}^l(\xi, p)\right), \\
E_m^l(\xi, z, p) &= E_{m2}^l(\xi, p) + H(s-z)\left(E_{m1}^l(\xi, p) - E_{m2}^l(\xi, p)\right), \\
F_m^l(\xi, z, p) &= F_{m1}^l(\xi, p) + H(z-s)\left(F_{m2}^l(\xi, p) - F_{m1}^l(\xi, p)\right),
\end{aligned}
\tag{7.3}
$$

where H is the Heaviside function. The next step is to determine the $6(n+2)$ unknown coefficients of integration from the boundary, interfacial and jump conditions.

7.3 Problem decomposition

For the ease of referencing and general usage, it is useful to define the following dimensionless parameters:

$$\begin{array}{lll} \bar{r} = r/a, & \bar{z} = z/a, & \bar{z}_j = z_j/a, \\ \bar{s} = s/a, & \bar{h}_j = \left(\bar{z}_j - \bar{z}_{j-1}\right), & \bar{p} = pa/c_{s_0}, \\ \bar{\xi} = \xi c_{s_0}/p, & \bar{c}_{s_j} = c_{s_j}/c_{s_0}, & \bar{c}_{d_j} = c_{d_j}/c_{s_0}, \\ \bar{\alpha}_j = \left(\bar{\xi}^2 + 1/\bar{c}_{d_j}^2\right)^{1/2}, & \bar{\beta}_j = \left(\bar{\xi}^2 + 1/\bar{c}_{s_j}^2\right)^{1/2}, & \bar{\mu}_j = \mu_j/\mu_0, \\ \bar{\lambda} = \lambda_j/\mu_0, & \bar{\rho}_j = \rho_j/\rho_0, & \end{array} \tag{7.4}$$

where a , μ_0 , ρ_0 represent a chosen “reference” length, shear modulus and mass density respectively, and $c_{s_0} = \sqrt{\mu_0/\rho_0}$ is the reference wave speed. In terms of Eqn. (7.4), one may also define a set of dimensionless integration coefficients

$$a_m^j\left(\bar{\xi}, \bar{z}, \bar{p}\right) \equiv a_m^j\left(\bar{\xi}, \bar{p}\right) = \frac{\mu_0 p^2}{\mathcal{F}_m c_{s_0}^2} A_m^j\left(\xi, p\right) e^{\bar{p}\bar{\alpha}_j \bar{z}_j} \tag{7.5}$$

$$b_m^j\left(\bar{\xi}, \bar{z}, \bar{p}\right) \equiv b_m^j\left(\bar{\xi}, \bar{p}\right) = \frac{\mu_0 p^2}{\mathcal{F}_m c_{s_0}^2} B_m^j\left(\xi, p\right) e^{-\bar{p}\bar{\alpha}_j \bar{z}_{j-1}} \tag{7.6}$$

$$c_m^j\left(\bar{\xi}, \bar{z}, \bar{p}\right) \equiv c_m^j\left(\bar{\xi}, \bar{p}\right) = \frac{\mu_0 p^2}{\mathcal{F}_m c_{s_0}^2} C_m^j\left(\xi, p\right) e^{\bar{p}\bar{\beta}_j \bar{z}_j} \tag{7.7}$$

$$d_m^j\left(\bar{\xi}, \bar{z}, \bar{p}\right) \equiv d_m^j\left(\bar{\xi}, \bar{p}\right) = \frac{\mu_0 p^2}{\mathcal{F}_m c_{s_0}^2} D_m^j\left(\xi, p\right) e^{-\bar{p}\bar{\beta}_j \bar{z}_{j-1}} \tag{7.8}$$

$$e_m^j\left(\bar{\xi}, \bar{z}, \bar{p}\right) \equiv e_m^j\left(\bar{\xi}, \bar{p}\right) = \frac{\mu_0 p^3}{\mathcal{F}_m c_{s_0}^3} E_m^j\left(\xi, p\right) \bar{\xi} e^{\bar{p}\bar{\beta}_j \bar{z}_j} \tag{7.9}$$

$$f_m^j\left(\bar{\xi},\bar{z},\bar{p}\right)\equiv f_m^j\left(\bar{\xi},\bar{p}\right)=\frac{\mu_0 p^3}{\mathcal{F}_m c_{s_0}^3}F_m^j\left(\xi,p\right)e^{-\bar{p}\bar{\beta}_j\bar{z}_{j-1}} \tag{7.10}$$

for layers not containing the source, and

$$a_m^l\left(\bar{\xi},\bar{z},\bar{p}\right)\equiv a_{m_1}^l\left(\bar{\xi},\bar{p}\right)+H\left(\bar{s}-\bar{z}\right)a_{m_2}^l\left(\bar{\xi},\bar{p}\right)=\frac{\mu_0 p^2}{\mathcal{F}_m c_{s_0}^2}A_m^l\left(\xi,z,p\right)e^{\bar{p}\bar{\alpha}_l\bar{z}_l}, \tag{7.11}$$

$$b_m^l\left(\bar{\xi},\bar{z},\bar{p}\right)\equiv b_{m_1}^l\left(\bar{\xi},\bar{p}\right)+H\left(\bar{z}-\bar{s}\right)b_{m_2}^l\left(\bar{\xi},\bar{p}\right)=\frac{\mu_0 p^2}{\mathcal{F}_m c_{s_0}^2}B_m^l\left(\xi,z,p\right)e^{-\bar{p}\bar{\alpha}_l\bar{z}_{l-1}}, \tag{7.12}$$

$$c_m^l\left(\bar{\xi},\bar{z},\bar{p}\right)\equiv c_{m_1}^l\left(\bar{\xi},\bar{p}\right)+H\left(\bar{s}-\bar{z}\right)c_{m_2}^l\left(\bar{\xi},\bar{p}\right)=\frac{\mu_0 p^2}{\mathcal{F}_m c_{s_0}^2}C_m^l\left(\xi,z,p\right)e^{\bar{p}\bar{\beta}_l\bar{z}_l}, \tag{7.13}$$

$$d_m^l\left(\bar{\xi},\bar{z},\bar{p}\right)\equiv d_{m_1}^l\left(\bar{\xi},\bar{p}\right)+H\left(\bar{z}-\bar{s}\right)d_{m_2}^l\left(\bar{\xi},\bar{p}\right)=\frac{\mu_0 p^2}{\mathcal{F}_m c_{s_0}^2}D_m^l\left(\xi,z,p\right)e^{-\bar{p}\bar{\beta}_l\bar{z}_{l-1}}, \tag{7.14}$$

$$e_m^l\left(\bar{\xi},\bar{z},\bar{p}\right)\equiv e_{m_1}^l\left(\bar{\xi},\bar{p}\right)+H\left(\bar{s}-\bar{z}\right)e_{m_2}^l\left(\bar{\xi},\bar{p}\right)=\frac{\mu_0 p^3}{\mathcal{F}_m c_{s_0}^3}E_m^l\left(\xi,z,p\right)\bar{\xi}e^{\bar{p}\bar{\beta}_l\bar{z}_l}, \tag{7.15}$$

$$f_m^l\left(\bar{\xi},\bar{z},\bar{p}\right)\equiv f_{m_1}^l\left(\bar{\xi},\bar{p}\right)+H\left(\bar{z}-\bar{s}\right)f_{m_2}^l\left(\bar{\xi},\bar{p}\right)=\frac{\mu_0 p^3}{\mathcal{F}_m c_{s_0}^3}F_m^l\left(\xi,z,p\right)\bar{\xi}e^{-\bar{p}\bar{\beta}_l\bar{z}_{l-1}}, \tag{7.16}$$

for the loaded layer.

Transformed variables such as the displacements and stresses for the multilayered medium can likewise be expressed in terms of the dimensionless transformed displacement kernels as

$$\begin{aligned}
v_{1_m}^j\left(\bar{\xi},\bar{z};\bar{s};\bar{p}\right)&=\frac{\mu_0 p}{2\mathcal{F}_m c_{s_0}}\left\{\left(\tilde{u}_{r_m}^{m+1}+i\tilde{u}_{\theta_m}^{m+1}\right)-\left(\tilde{u}_{r_m}^{m-1}-i\tilde{u}_{\theta_m}^{m-1}\right)\right\}^j,\\
v_{2_m}^j\left(\bar{\xi},\bar{z};\bar{s};\bar{p}\right)&=\frac{\mu_0 p}{2\mathcal{F}_m c_{s_0}}\left\{\tilde{u}_{z_m}^m\right\}^j,\\
v_{3_m}^j\left(\bar{\xi},\bar{z};\bar{s};\bar{p}\right)&=\frac{\mu_0 p}{2\mathcal{F}_m c_{s_0}}\left\{\left(\tilde{u}_{r_m}^{m+1}+i\tilde{u}_{\theta_m}^{m+1}\right)+\left(\tilde{u}_{r_m}^{m-1}-i\tilde{u}_{\theta_m}^{m-1}\right)\right\}^j,
\end{aligned} \tag{7.17}$$

and dimensionless stress kernels as

$$\begin{aligned}
\sigma^{j}_{21_m}\left(\bar{\xi},\bar{z};\bar{s};\bar{p}\right) &= \frac{1}{2\mathcal{F}_m}\left\{\left(\tilde{\tau}^{m+1}_{zr_m}+i\tilde{\tau}^{m+1}_{z\theta_m}\right)-\left(\tilde{\tau}^{m-1}_{zr_m}-i\tilde{\tau}^{m-1}_{z\theta_m}\right)\right\}^{j}, \\
\sigma^{j}_{22_m}\left(\bar{\xi},\bar{z};\bar{s};\bar{p}\right) &= \frac{1}{2\mathcal{F}_m}\left\{\tilde{\tau}^{m}_{zz_m}\right\}^{j}, \\
\sigma^{j}_{23_m}\left(\bar{\xi},\bar{z};\bar{s};\bar{p}\right) &= \frac{1}{2\mathcal{F}_m}\left\{\left(\tilde{\tau}^{m+1}_{zr_m}+i\tilde{\tau}^{m+1}_{z\theta_m}\right)+\left(\tilde{\tau}^{m-1}_{zr_m}-i\tilde{\tau}^{m-1}_{z\theta_m}\right)\right\}^{j},
\end{aligned} \tag{7.18}$$

$$\begin{aligned}
\sigma^{j}_{11_m}\left(\bar{\xi},\bar{z};\bar{s};\bar{p}\right) &= \frac{1}{\mathcal{F}_m}\left\{\tilde{\tau}^{m}_{rr_m}+2\mu\widetilde{\left(\frac{u_{r_m}}{r}+im\frac{u_{\theta_m}}{r}\right)}^{m}\right\}^{j}, \\
\sigma^{j}_{33_m}\left(\bar{\xi},\bar{z};\bar{s};\bar{p}\right) &= \frac{1}{\mathcal{F}_m}\left\{\tilde{\tau}^{m}_{\theta\theta_m}-2\mu\widetilde{\left(\frac{u_{r_m}}{r}+im\frac{u_{\theta_m}}{r}\right)}^{m}\right\}^{j}, \\
\sigma^{j}_{13_m}\left(\bar{\xi},\bar{z};\bar{s};\bar{p}\right) &= \frac{1}{\mathcal{F}_m}\left\{\tilde{\tau}^{m}_{r\theta_m}+2\mu\widetilde{\left(\frac{u_{\theta_m}}{r}-im\frac{u_{r_m}}{r}\right)}^{m}\right\}^{j}.
\end{aligned} \tag{7.19}$$

By means of the Eqns. (7.5) to (7.16), the transformed stress and displacement components in Eqns. (7.17) to (7.19) within the j^{th} layer can be expressed in terms of the unknown potential coefficients as

$$\begin{Bmatrix} v^{j}_{1_m} \\ v^{j}_{2_m} \\ \sigma^{j}_{21_m} \\ \sigma^{j}_{22_m} \\ \sigma^{j}_{33_m} \\ \sigma^{j}_{11_m} \end{Bmatrix} = \begin{bmatrix} -\bar{\xi} & \bar{\beta}_j & -\bar{\xi} & -\bar{\beta}_j \\ -\bar{\alpha}_j & \bar{\xi} & \bar{\alpha}_j & \bar{\xi} \\ 2\bar{\mu}_j\bar{\xi}\bar{\alpha}_j & -\bar{\mu}_j\left(\bar{\beta}^2_j+\bar{\xi}^2\right) & -2\bar{\mu}_j\bar{\xi}\bar{\alpha}_j & -\bar{\mu}_j\left(\bar{\beta}^2+\bar{\xi}^2\right) \\ \bar{\mu}_j\left(\bar{\beta}^2_j+\bar{\xi}^2\right) & -2\bar{\mu}_j\overline{\xi\beta}_j & \bar{\mu}_j\left(\bar{\beta}^2_j+\bar{\xi}^2\right) & 2\bar{\mu}_j\overline{\xi\beta}_j \\ \bar{\lambda}_j\left(\bar{\alpha}^2_j-\bar{\xi}^2\right) & 0 & \bar{\lambda}_j\left(\bar{\alpha}^2_j-\bar{\xi}^2\right) & 0 \\ \bar{\lambda}_j\bar{\alpha}^2_j-\left(\bar{\lambda}+2\bar{\mu}_j\right)\bar{\xi}^2 & 2\bar{\mu}\xi\bar{\beta}_j & \bar{\lambda}_j\bar{\alpha}^2_j-\left(\bar{\lambda}_j+2\bar{\mu}_j\right)\bar{\xi}^2-2\bar{\mu}_j\overline{\xi\beta}_j & -2\bar{\mu}\xi\bar{\beta}_j \end{bmatrix} \times \begin{Bmatrix} b^{j}_{m}e^{-\bar{p}\bar{\alpha}_j\left(\bar{z}-\bar{z}_{j-1}\right)} \\ f^{j}_{m}e^{-\bar{p}\bar{\beta}_j\left(\bar{z}-\bar{z}_{j-1}\right)} \\ a^{j}_{m}e^{\bar{p}\bar{\alpha}_j\left(\bar{z}-\bar{z}_{j}\right)} \\ e^{j}_{m}e^{\bar{p}\bar{\beta}_j\left(\bar{z}-\bar{z}_{j}\right)} \end{Bmatrix}, \tag{7.20}$$

and

$$\begin{Bmatrix} v^{j}_{3_m} \\ \sigma^{j}_{23_m} \\ \sigma^{j}_{13_m} \end{Bmatrix} = \begin{bmatrix} i\bar{\xi} & i\bar{\xi} \\ -i\bar{\mu}_j\overline{\xi\beta}_j & i\bar{\mu}_j\overline{\xi\beta}_j \\ \bar{\mu}\bar{\xi}^2 & \bar{\mu}\bar{\xi}^2 \end{bmatrix} \times \begin{Bmatrix} d^{j}_{m}e^{-\bar{p}\bar{\beta}_j\left(\bar{z}-\bar{z}_{j-1}\right)} \\ c^{j}_{m}e^{\bar{p}\bar{\beta}_j\left(\bar{z}-\bar{z}_{j}\right)} \end{Bmatrix}. \tag{7.21}$$

7.4 Propagation of vertically-polarized waves

In this section, the unknown integration coefficients $a_m^j,\ b_m^j,\ e_m^j,\ f_m^j,\ j=1,\ldots n$ associated with P-SV waves will be solved from the boundary and interfacial conditions. The corresponding mathematical expression for the boundary, interfacial conditions are listed as follows.

7.4.1 Boundary and interfacial conditions

(1) Free-surface condition

$$\sigma_{21_m}^1\left(\bar{\xi},\bar{z}_0;\bar{s};\bar{p}\right)=\sigma_{22_m}^1\left(\bar{\xi},\bar{z}_0;\bar{s};\bar{p}\right)=0\,. \tag{7.22}$$

(2) Continuity of displacements and tractions across all layer interfaces

$$\begin{aligned}
&v_{1_m}^j\left(\bar{\xi},\bar{z}_j;\bar{s};\bar{p}\right)=v_{1_m}^{j+1}\left(\bar{\xi},\bar{z}_j;\bar{s};\bar{p}\right),\\
&v_{2_m}^j\left(\bar{\xi},\bar{z}_j;\bar{s};\bar{p}\right)=v_{2_m}^{j+1}\left(\bar{\xi},\bar{z}_j;\bar{s};\bar{p}\right),\\
&\sigma_{21_m}^j\left(\bar{\xi},\bar{z}_j;\bar{s};\bar{p}\right)=\sigma_{21_m}^{j+1}\left(\bar{\xi},\bar{z}_j;\bar{s};\bar{p}\right),\quad j=1,\ldots n.\\
&\sigma_{22_m}^j\left(\bar{\xi},\bar{z}_j;\bar{s};\bar{p}\right)=\sigma_{22_m}^{j+1}\left(\bar{\xi},\bar{z}_j;\bar{s};\bar{p}\right).
\end{aligned} \tag{7.23}$$

(3) Jump condition across the loaded plane $\bar{z}=\bar{s}$

$$\begin{aligned}
&v_{1_m}^l\left(\bar{\xi},\bar{s}^-;\bar{s};\bar{p}\right)-v_{1_m}^l\left(\bar{\xi},\bar{s}^+;\bar{s};\bar{p}\right)=0,\\
&v_{2_m}^l\left(\bar{\xi},\bar{s}^-;\bar{s};\bar{p}\right)-v_{2_m}^l\left(\bar{\xi},\bar{s}^+;\bar{s};\bar{p}\right)=0,\\
&\sigma_{21_m}^l\left(\bar{\xi},\bar{s}^-;\bar{s};\bar{p}\right)-\sigma_{21_m}^l\left(\bar{\xi},\bar{s}^+;\bar{s};\bar{p}\right)=\frac{Y_m(\bar{\xi},\bar{p})-X_m(\bar{\xi},\bar{p})}{2\mathcal{F}},\\
&\sigma_{22_m}^l\left(\bar{\xi},\bar{s}^-;\bar{s};\bar{p}\right)-\sigma_{22_m}^l\left(\bar{\xi},\bar{s}^+;\bar{s};\bar{p}\right)=\frac{Z_m(\bar{\xi},\bar{p})}{2\mathcal{F}}.
\end{aligned} \tag{7.24}$$

with

$$\begin{aligned}
&X_m(\bar{\xi},\bar{p})=\tilde{P}_m^{m-1}(\bar{\xi},\bar{p})-i\tilde{Q}_m^{m-1}(\bar{\xi},\bar{p}),\\
&Y_m(\bar{\xi},\bar{p})=\tilde{P}_m^{m+1}(\bar{\xi},\bar{p})+i\tilde{Q}_m^{m+1}(\bar{\xi},\bar{p}),\\
&Z_m(\bar{\xi},\bar{p})=\tilde{R}_m^{m}(\bar{\xi},\bar{p}).
\end{aligned} \tag{7.25}$$

(4) Regularity condition

$$\lim_{\bar{z}\to\infty}v_{1_m}^{n+1}\left(\bar{\xi},\bar{z}_j;\bar{s};\bar{p}\right)=\lim_{\bar{z}\to\infty}v_{2_m}^{n+1}\left(\bar{\xi},\bar{z}_j;\bar{s};\bar{p}\right)=0\,. \tag{7.26}$$

To solve for the unknown integration coefficients $a_m^j,\ b_m^j,\ e_m^j,\ f_m^j,\ j=1,\ldots n$, one must express all boundary and interfacial conditions as equations for these coefficients, i.e.,

1) Free surface condition

In terms of $a_m^1,\ b_m^1,\ e_m^1,\ f_m^1$, Eqn. (7.22) can be expressed as

$$\begin{aligned}&\begin{bmatrix} 2\bar{\mu}_1\bar{\xi}\bar{\alpha}_1 & -\bar{\mu}_1\left(\bar{\beta}_1^2+\bar{\xi}^2\right) \\ \bar{\mu}_1\left(\bar{\beta}_1^2+\bar{\xi}^2\right) & -2\bar{\mu}_1\bar{\xi}\bar{\beta}_1 \end{bmatrix} \begin{Bmatrix} b_m^1\left(\bar{\xi},0,\bar{p}\right) \\ f_m^1\left(\bar{\xi},0,\bar{p}\right) \end{Bmatrix} \\ &\quad = \begin{bmatrix} 2\bar{\mu}_1\bar{\xi}\bar{\alpha}_1 & \bar{\mu}_1\left(\bar{\beta}_1^2+\bar{\xi}^2\right) \\ -\bar{\mu}_1\left(\bar{\beta}_1^2+\bar{\xi}^2\right) & -2\bar{\mu}_1\bar{\xi}\bar{\beta}_1 \end{bmatrix} \begin{Bmatrix} a_m^1\left(\bar{\xi},0,\bar{p}\right)e^{-\bar{p}\bar{\alpha}_1\bar{h}_1} \\ e_m^1\left(\bar{\xi},0,\bar{p}\right)e^{-\bar{p}\bar{\beta}_1\bar{h}_1} \end{Bmatrix},\end{aligned} \tag{7.27}$$

which can be written as

$$\begin{Bmatrix} b_m^1\left(\bar{\xi},0,\bar{p}\right) \\ f_m^1\left(\bar{\xi},0,\bar{p}\right) \end{Bmatrix} = \mathbf{R}_0^u\left(\bar{\xi},\bar{p}\right) \begin{Bmatrix} a_m^1\left(\bar{\xi},0,\bar{p}\right) \\ e_m^1\left(\bar{\xi},0,\bar{p}\right) \end{Bmatrix} \tag{7.28}$$

where

$$\mathbf{R}_0^u\left(\bar{\xi},\bar{p}\right) = \mathbf{R}_0^{u\mathcal{N}}\left(\bar{\xi}\right) \begin{bmatrix} e^{-\bar{p}\bar{\alpha}_1\bar{h}_1} & 0 \\ 0 & e^{-\bar{p}\bar{\beta}_1\bar{h}_1} \end{bmatrix}, \tag{7.29}$$

with

$$\begin{aligned} R_{0_{pp}}^{u\mathcal{N}}\left(\bar{\xi}\right) &\equiv R_{0_{11}}^{u\mathcal{N}}\left(\bar{\xi}\right) = \frac{-1}{R_1^-\left(\bar{\xi}\right)}\left\{(\bar{\beta}_1^2+\bar{\xi}^2)^2+4\bar{\xi}^2\bar{\alpha}_1\bar{\beta}_1\right\} \\ R_{0_{ps}}^{u\mathcal{N}}\left(\bar{\xi}\right) &\equiv R_{0_{12}}^{u\mathcal{N}}\left(\bar{\xi}\right) = \frac{-1}{R_1^-\left(\bar{\xi}\right)}\left\{4\bar{\xi}\bar{\beta}_1\left(\bar{\beta}_1^2+\bar{\xi}^2\right)\right\} \\ R_{0_{sp}}^{u\mathcal{N}}\left(\bar{\xi}\right) &\equiv R_{0_{21}}^{u\mathcal{N}}\left(\bar{\xi}\right) = \frac{-1}{R_1^-\left(\bar{\xi}\right)}\left\{4\bar{\xi}\bar{\alpha}_1\left(\bar{\beta}_1^2+\bar{\xi}^2\right)\right\} \\ R_{0_{ss}}^{u\mathcal{N}}\left(\bar{\xi}\right) &\equiv R_{0_{22}}^{u\mathcal{N}}\left(\bar{\xi}\right) = \frac{-1}{R_1^-\left(\bar{\xi}\right)}\left\{(\bar{\beta}_1^2+\bar{\xi}^2)^2+4\bar{\xi}^2\bar{\alpha}_1\bar{\beta}_1\right\} \end{aligned}, \tag{7.30}$$

and

$$R_1^-\left(\bar{\xi}\right)=(\bar{\beta}_1^2+\bar{\xi}^2)^2-4\bar{\xi}^2\bar{\alpha}_1\bar{\beta}_1. \tag{7.31}$$

2) Continuity of displacements and tractions across all layer interfaces

Also, expressing Eqn. (7.23) in terms of $a_m^j,\ b_m^j,\ e_m^j,\ f_m^j,\ j=1,\ldots n$ leads to

$$\begin{bmatrix} \bar{\xi} & \bar{\beta}_{j+1} & -\bar{\xi} & -\bar{\beta}_j \\ \bar{\alpha}_{j+1} & -\bar{\xi} & \bar{\alpha}_j & \bar{\xi} \\ -2\bar{\mu}_{j+1}\bar{\xi}\bar{\alpha}_{j+1} & \bar{\mu}_{j+1}\left(\bar{\beta}_{j+1}^2+\bar{\xi}^2\right) & -2\bar{\mu}_j\bar{\xi}\bar{\alpha}_j & -\bar{\mu}_j\left(\bar{\beta}_j^2+\bar{\xi}^2\right) \\ -\bar{\mu}_{j+1}\left(\bar{\beta}_{j+1}+\bar{\xi}^2\right) & 2\bar{\mu}_{j+1}\overline{\xi\beta}_{j+1} & \bar{\mu}_j\left(\bar{\beta}_j^2+\bar{\xi}^2\right) & 2\bar{\mu}_j\overline{\xi\beta}_j \end{bmatrix}\begin{Bmatrix} b_m^{j+1} \\ f_m^{j+1} \\ a_m^j \\ e_m^j \end{Bmatrix}=$$
$$\begin{bmatrix} \bar{\xi} & \bar{\beta}_j & -\bar{\xi} & -\bar{\beta}_{j+1} \\ \bar{\alpha}_j & -\bar{\xi} & \bar{\alpha}_{j+1} & \bar{\xi} \\ -2\bar{\mu}_j\bar{\xi}\bar{\alpha}_j & \bar{\mu}_j\left(\bar{\beta}_j^2+\bar{\xi}^2\right) & -2\bar{\mu}_{j+1}\bar{\xi}\bar{\alpha}_{j+1} & -\bar{\mu}_{j+1}\left(\bar{\beta}_{j+1}^2+\bar{\xi}^2\right) \\ -\bar{\mu}_j\left(\bar{\beta}_j+\bar{\xi}^2\right) & 2\bar{\mu}_j\overline{\xi\beta}_j & \bar{\mu}_{j+1}\left(\bar{\beta}_{j+1}^2+\bar{\xi}^2\right) & 2\bar{\mu}_{j+1}\overline{\xi\beta}_{j+1} \end{bmatrix}\begin{Bmatrix} b_m^j e^{-\bar{p}\bar{\alpha}_j\bar{h}_j} \\ f_m^j e^{-\bar{p}\bar{\beta}_j\bar{h}_j} \\ a_m^{j+1} e^{-\bar{p}\bar{\alpha}_{j+1}\bar{h}_{j+1}} \\ e_m^{j+1} e^{-\bar{p}\bar{\beta}_{j+1}\bar{h}_{j+1}} \end{Bmatrix} \tag{7.32}$$

which can be condensed to

$$\begin{Bmatrix} b_m^{j+1}\left(\bar{\xi},\bar{z}_j,\bar{p}\right) \\ f_m^{j+1}\left(\bar{\xi},\bar{z}_j,\bar{p}\right) \\ a_m^j\left(\bar{\xi},\bar{z}_j,\bar{p}\right) \\ e_m^j\left(\bar{\xi},\bar{z}_j,\bar{p}\right) \end{Bmatrix}=\begin{bmatrix} \mathbf{T}_j^d\left(\bar{\xi},\bar{p}\right) & \mathbf{R}_j^u\left(\bar{\xi},\bar{p}\right) \\ \mathbf{R}_j^d\left(\bar{\xi},\bar{p}\right) & \mathbf{T}_j^u\left(\bar{\xi},\bar{p}\right) \end{bmatrix}\begin{Bmatrix} b_m^j\left(\bar{\xi},\bar{z}_j,\bar{p}\right) \\ f_m^j\left(\bar{\xi},\bar{z}_j,\bar{p}\right) \\ a_m^{j+1}\left(\bar{\xi},\bar{z}_j,\bar{p}\right) \\ e_m^{j+1}\left(\bar{\xi},\bar{z}_j,\bar{p}\right) \end{Bmatrix}, \tag{7.33}$$

where

$$\begin{bmatrix} \mathbf{T}_j^d\left(\bar{\xi},\bar{p}\right) & \mathbf{R}_j^u\left(\bar{\xi},\bar{p}\right) \\ \mathbf{R}_j^d\left(\bar{\xi},\bar{p}\right) & \mathbf{T}_j^u\left(\bar{\xi},\bar{p}\right) \end{bmatrix}=\begin{bmatrix} \mathbf{T}_j^{d\mathcal{N}}\left(\bar{\xi}\right) & \mathbf{R}_j^{u\mathcal{N}}\left(\bar{\xi}\right) \\ \mathbf{R}_j^{d\mathcal{N}}\left(\bar{\xi}\right) & \mathbf{T}_j^{u\mathcal{N}}\left(\bar{\xi}\right) \end{bmatrix}\begin{bmatrix} e^{-\bar{p}\bar{\alpha}_j\bar{h}_j} & 0 & 0 & 0 \\ 0 & e^{-\bar{p}\bar{\beta}_j\bar{h}_j} & 0 & 0 \\ 0 & 0 & e^{-\bar{p}\bar{\alpha}_{j+1}\bar{h}_{j+1}} & 0 \\ 0 & 0 & 0 & e^{-\bar{p}\bar{\beta}_{j+1}\bar{h}_{j+1}} \end{bmatrix} \tag{7.34}$$

with the coefficients of the “normalized” transmission and reflection matrices which are now independent of $\bar{p}$ to be given by

$$T_{j_{pp}}^{d\mathcal{N}}\left(\bar{\xi}\right)\equiv T_{j_{11}}^{d\mathcal{N}}\left(\bar{\xi}\right)=\frac{-2\bar{\rho}_j\bar{\alpha}_j}{S_{j+1}^j\left(\bar{\xi}\right)}\left\{2\bar{\xi}^2\left(\bar{\mu}_{j+1}-\bar{\mu}_j\right)\left(\bar{\beta}_{j+1}-\bar{\beta}_j\right)-\left(\bar{\rho}_j\bar{\beta}_{j+1}+\bar{\rho}_{j+1}\bar{\beta}_j\right)\right\}, \tag{7.35}$$

$$T_{j_{ps}}^{d\mathcal{N}}\left(\bar{\xi}\right)\equiv T_{j_{12}}^{d\mathcal{N}}\left(\bar{\xi}\right)=\frac{-2\bar{\rho}_j\bar{\beta}_j}{S_{j+1}^{j}\left(\bar{\xi}\right)}\left\{2\bar{\xi}\left(\bar{\mu}_{j+1}-\bar{\mu}_j\right)\left(\bar{\xi}^2-\bar{\alpha}_j\bar{\beta}_{j+1}\right)+\bar{\xi}\left(\bar{\rho}_{j+1}-\bar{\rho}_j\right)\right\}, \quad (7.36)$$

$$T_{j_{sp}}^{d\mathcal{N}}\left(\bar{\xi}\right)\equiv T_{j_{21}}^{d\mathcal{N}}\left(\bar{\xi}\right)=\frac{-2\bar{\rho}_j\bar{\alpha}_j}{S_{j+1}^{j}\left(\bar{\xi}\right)}\left\{2\bar{\xi}\left(\bar{\mu}_{j+1}-\bar{\mu}_j\right)\left(\bar{\xi}^2-\bar{\alpha}_{j+1}\bar{\beta}_j\right)+\bar{\xi}\left(\bar{\rho}_{j+1}-\bar{\rho}_j\right)\right\}, \quad (7.37)$$

$$T_{j_{ss}}^{d\mathcal{N}}\left(\bar{\xi}\right)\equiv T_{j_{22}}^{d\mathcal{N}}\left(\bar{\xi}\right)=\frac{-2\bar{\rho}_j\bar{\beta}_j}{S_{j+1}^{j}\left(\bar{\xi}\right)}\left\{2\bar{\xi}^2\left(\bar{\mu}_{j+1}-\bar{\mu}_j\right)\left(\bar{\alpha}_{j+1}-\bar{\alpha}_j\right)-\left(\bar{\rho}_j\bar{\alpha}_{j+1}+\bar{\rho}_{j+1}\bar{\alpha}_j\right)\right\}, \quad (7.38)$$

$$T_{j_{pp}}^{u\mathcal{N}}\left(\bar{\xi}\right)\equiv T_{j_{11}}^{u\mathcal{N}}\left(\bar{\xi}\right)=\frac{-2\bar{\rho}_{j+1}\bar{\alpha}_{j+1}}{S_{j+1}^{j}\left(\bar{\xi}\right)}\left\{2\bar{\xi}^2\left(\bar{\mu}_{j+1}-\bar{\mu}_j\right)\left(\bar{\beta}_{j+1}-\bar{\beta}_j\right)-\left(\bar{\rho}_j\bar{\beta}_{j+1}+\bar{\rho}_{j+1}\bar{\beta}_j\right)\right\}, \quad (7.39)$$

$$T_{j_{ps}}^{u\mathcal{N}}\left(\bar{\xi}\right)\equiv T_{j_{12}}^{u\mathcal{N}}\left(\bar{\xi}\right)=\frac{-2\bar{\rho}_{j+1}\bar{\beta}_{j+1}}{S_{j+1}^{j}\left(\bar{\xi}\right)}\left\{2\bar{\xi}\left(\bar{\mu}_{j+1}-\bar{\mu}_j\right)\left(\bar{\xi}^2-\bar{\alpha}_{j+1}\bar{\beta}_j\right)+\bar{\xi}\left(\bar{\rho}_{j+1}-\bar{\rho}_j\right)\right\}, \quad (7.40)$$

$$T_{j_{sp}}^{u\mathcal{N}}\left(\bar{\xi}\right)\equiv T_{j_{21}}^{u\mathcal{N}}\left(\bar{\xi}\right)=\frac{-2\bar{\rho}_{j+1}\bar{\alpha}_{j+1}}{S_{j+1}^{j}\left(\bar{\xi}\right)}\left\{2\bar{\xi}\left(\bar{\mu}_{j+1}-\bar{\mu}_j\right)\left(\bar{\xi}^2-\bar{\alpha}_j\bar{\beta}_{j+1}\right)+\bar{\xi}\left(\bar{\rho}_{j+1}-\bar{\rho}_j\right)\right\}, \quad (7.41)$$

$$T_{j_{ss}}^{u\mathcal{N}}\left(\bar{\xi}\right)\equiv T_{j_{22}}^{u\mathcal{N}}\left(\bar{\xi}\right)=\frac{-2\bar{\rho}_{j+1}\bar{\beta}_{j+1}}{S_{j+1}^{j}\left(\bar{\xi}\right)}\left\{2\bar{\xi}^2\left(\bar{\mu}_{j+1}-\bar{\mu}_j\right)\left(\bar{\alpha}_{j+1}-\bar{\alpha}_j\right)-\left(\bar{\rho}_j\bar{\alpha}_{j+1}+\bar{\rho}_{j+1}\bar{\alpha}_j\right)\right\}, \quad (7.42)$$

$$R_{j_{pp}}^{u\mathcal{N}}\left(\bar{\xi}\right)\equiv R_{j_{11}}^{u\mathcal{N}}\left(\bar{\xi}\right)=\frac{1}{S_{j+1}^{j}\left(\bar{\xi}\right)}\left\{\begin{array}{l}4\bar{\xi}^2(\bar{\mu}_{j+1}-\bar{\mu}_j)^2\left(\bar{\xi}^2-\bar{\alpha}_j\bar{\beta}_j\right)\left(\bar{\xi}^2+\bar{\alpha}_{j+1}\bar{\beta}_{j+1}\right)\\ -4\bar{\xi}^2\left(\bar{\mu}_{j+1}-\bar{\mu}_j\right)\left(\bar{\rho}_j\left(\bar{\xi}^2+\bar{\alpha}_{j+1}\bar{\beta}_{j+1}\right)-\bar{\rho}_{j+1}\left(\bar{\xi}^2-\bar{\alpha}_j\bar{\beta}_j\right)\right)\\ +\bar{\xi}^2(\bar{\rho}_{j+1}-\bar{\rho}_j)^2+\left(\bar{\rho}_j\bar{\beta}_{j+1}+\bar{\rho}_{j+1}\bar{\beta}_j\right)\left(\bar{\rho}_j\bar{\alpha}_{j+1}-\bar{\rho}_{j+1}\bar{\alpha}_j\right)\}\end{array}\right\}, \quad (7.43)$$

$$R_{j_{ps}}^{u\mathcal{N}}\left(\bar{\xi}\right)\equiv R_{j_{12}}^{u\mathcal{N}}\left(\bar{\xi}\right)=\frac{2\overline{\xi\beta}_{j+1}}{S_{j+1}^{j}\left(\bar{\xi}\right)}\left\{\begin{array}{l}4\bar{\xi}^2(\bar{\mu}_{j+1}-\bar{\mu}_j)^2\left(\bar{\xi}^2-\overline{\alpha_j}\bar{\beta}_j\right)\\ -2\left(\bar{\mu}_{j+1}-\bar{\mu}_j\right)\left(2\bar{\rho}_j\bar{\xi}^2-\bar{\rho}_{j+1}\left(\bar{\xi}^2-\bar{\alpha}_j\bar{\beta}_j\right)\right)-\bar{\rho}_j\left(\bar{\rho}_{j+1}-\bar{\rho}_j\right)\end{array}\right\}, \quad (7.44)$$

$$R_{j_{sp}}^{u\mathcal{N}}\left(\bar{\xi}\right)\equiv R_{j_{21}}^{u\mathcal{N}}\left(\bar{\xi}\right)=\frac{2\bar{\xi}\bar{\alpha}_{j+1}}{S_{j+1}^{j}\left(\bar{\xi}\right)}\left\{\begin{array}{l}4\bar{\xi}^2(\bar{\mu}_{j+1}-\bar{\mu}_j)^2\left(\bar{\xi}^2-\overline{\alpha_j}\bar{\beta}_j\right)\\ -2\left(\bar{\mu}_{j+1}-\bar{\mu}_j\right)\left(2\bar{\rho}_j\bar{\xi}^2-\bar{\rho}_{j+1}\left(\bar{\xi}^2-\bar{\alpha}_j\bar{\beta}_j\right)\right)-\bar{\rho}_j\left(\bar{\rho}_{j+1}-\bar{\rho}_j\right)\end{array}\right\}, \quad (7.45)$$

$$R_{j_{ss}}^{u\mathcal{N}}\left(\bar{\xi}\right)\equiv R_{j_{22}}^{u\mathcal{N}}\left(\bar{\xi}\right)=\frac{1}{S_{j+1}^{j}\left(\bar{\xi}\right)}\left\{\begin{array}{l}4\bar{\xi}^2(\bar{\mu}_{j+1}-\bar{\mu}_j)^2\left(\bar{\xi}^2-\bar{\alpha}_j\bar{\beta}_j\right)\left(\bar{\xi}^2+\bar{\alpha}_{j+1}\bar{\beta}_{j+1}\right)\\ -4\bar{\xi}^2\left(\bar{\mu}_{j+1}-\bar{\mu}_j\right)\left(\bar{\rho}_j\left(\bar{\xi}^2+\bar{\alpha}_{j+1}\bar{\beta}_{j+1}\right)-\bar{\rho}_{j+1}\left(\bar{\xi}^2-\bar{\alpha}_j\bar{\beta}_j\right)\right)\\ +\bar{\xi}^2(\bar{\rho}_{j+1}-\bar{\rho}_j)^2+\left(\bar{\rho}_j\bar{\beta}_{j+1}-\bar{\rho}_{j+1}\bar{\beta}_j\right)\left(\bar{\rho}_j\bar{\alpha}_{j+1}+\bar{\rho}_{j+1}\bar{\alpha}_j\right)\}\end{array}\right\}, \quad (7.46)$$

and

$$R_{d_{pp}}^{u\mathcal{N}}\left(\bar{\xi}\right)\equiv R_{d_{11}}^{d\mathcal{N}}\left(\bar{\xi}\right)=\frac{1}{S_{j+1}^{j}\left(\bar{\xi}\right)}\left\{\begin{array}{l}4\bar{\xi}^{2}(\bar{\mu}_{j+1}-\bar{\mu}_{j})^{2}\left(\bar{\xi}^{2}+\bar{\alpha}_{j}\bar{\beta}_{j}\right)\left(\bar{\xi}^{2}-\bar{\alpha}_{j+1}\bar{\beta}_{j+1}\right)\\-4\bar{\xi}^{2}\left(\bar{\mu}_{j+1}-\bar{\mu}_{j}\right)\left(\bar{\rho}_{j}\left(\bar{\xi}^{2}-\bar{\alpha}_{j+1}\bar{\beta}_{j+1}\right)-\bar{\rho}_{j+1}\left(\bar{\xi}^{2}+\bar{\alpha}_{j}\bar{\beta}_{j}\right)\right)\\+\bar{\xi}^{2}(\bar{\rho}_{j+1}-\bar{\rho}_{j})^{2}-\left(\bar{\rho}_{j}\bar{\beta}_{j+1}+\bar{\rho}_{j+1}\bar{\beta}_{j}\right)\left(\bar{\rho}_{j}\bar{\alpha}_{j+1}-\bar{\rho}_{j+1}\bar{\alpha}_{j}\right)\}\end{array}\right\},\tag{7.47}$$

$$R_{j_{ps}}^{d\mathcal{N}}\left(\bar{\xi}\right)\equiv R_{j_{12}}^{d\mathcal{N}}\left(\bar{\xi}\right)=\frac{2\overline{\xi\beta}_{j}}{S_{j+1}^{j}\left(\bar{\xi}\right)}\left\{\begin{array}{l}-4\bar{\xi}^{2}(\bar{\mu}_{j+1}-\bar{\mu}_{j})^{2}\left(\bar{\xi}^{2}-\overline{\alpha_{j+1}}\bar{\beta}_{j+1}\right)\\-2\left(\bar{\mu}_{j+1}-\bar{\mu}_{j}\right)\left(2\bar{\rho}_{j+1}\bar{\xi}^{2}-\bar{\rho}_{j}\left(\bar{\xi}^{2}-\bar{\alpha}_{j+1}\bar{\beta}_{j+1}\right)\right)-\bar{\rho}_{j+1}\left(\bar{\rho}_{j+1}-\bar{\rho}_{j}\right)\end{array}\right\},\tag{7.48}$$

$$R_{j_{sp}}^{d\mathcal{N}}\left(\bar{\xi}\right)\equiv R_{j_{21}}^{d\mathcal{N}}\left(\bar{\xi}\right)=\frac{2\bar{\xi}\bar{\alpha}_{j}}{S_{j+1}^{j}\left(\bar{\xi}\right)}\left\{\begin{array}{l}-4\bar{\xi}^{2}(\bar{\mu}_{j+1}-\bar{\mu}_{j})^{2}\left(\bar{\xi}^{2}-\overline{\alpha_{j+1}}\bar{\beta}_{j+1}\right)\\-2\left(\bar{\mu}_{j+1}-\bar{\mu}_{j}\right)\left(2\bar{\rho}_{j+1}\bar{\xi}^{2}-\bar{\rho}_{j}\left(\bar{\xi}^{2}-\bar{\alpha}_{j+1}\bar{\beta}_{j+1}\right)\right)-\bar{\rho}_{j+1}\left(\bar{\rho}_{j+1}-\bar{\rho}_{j}\right)\end{array}\right\},\tag{7.49}$$

$$R_{j_{ss}}^{d\mathcal{N}}\left(\bar{\xi}\right)\equiv R_{j_{22}}^{d\mathcal{N}}\left(\bar{\xi}\right)=\frac{1}{S_{j+1}^{j}\left(\bar{\xi}\right)}\left\{\begin{array}{l}4\bar{\xi}^{2}(\bar{\mu}_{j+1}-\bar{\mu}_{j})^{2}\left(\bar{\xi}^{2}+\bar{\alpha}_{j}\bar{\beta}_{j}\right)\left(\bar{\xi}^{2}-\bar{\alpha}_{j+1}\bar{\beta}_{j+1}\right)\\-4\bar{\xi}^{2}\left(\bar{\mu}_{j+1}-\bar{\mu}_{j}\right)\left(\bar{\rho}_{j}\left(\bar{\xi}^{2}-\bar{\alpha}_{j+1}\bar{\beta}_{j+1}\right)-\bar{\rho}_{j+1}\left(\bar{\xi}^{2}+\bar{\alpha}_{j}\bar{\beta}_{j}\right)\right)\\+\bar{\xi}^{2}(\bar{\rho}_{j+1}-\bar{\rho}_{j})^{2}-\left(\bar{\rho}_{j}\bar{\beta}_{j+1}-\bar{\rho}_{j+1}\bar{\beta}_{j}\right)\left(\bar{\rho}_{j}\bar{\alpha}_{j+1}+\bar{\rho}_{j+1}\bar{\alpha}_{j}\right)\end{array}\right\}.\tag{7.50}$$

similar to Pak and Guzina (2002) for the frequency-domain. Here, $S_{j+1}^{j}\left(\bar{\xi}\right)$ denotes the Stoneley wave function corresponding to the interface between the layers $\mathcal{L}_j$ and $\mathcal{L}_{j+1}$, i.e.

$$S_{j+1}^{j}\left(\bar{\xi}\right)=-\left\{\begin{array}{l}4\bar{\xi}^{2}(\bar{\mu}_{j+1}-\bar{\mu}_{j})^{2}\left(\bar{\xi}^{2}-\bar{\alpha}_{j}\bar{\beta}_{j}\right)\left(\bar{\xi}^{2}-\bar{\alpha}_{j+1}\bar{\beta}_{j+1}\right)\\-4\bar{\xi}^{2}\left(\bar{\mu}_{j+1}-\bar{\mu}_{j}\right)\left(\bar{\rho}_{j}\left(\bar{\xi}^{2}-\bar{\alpha}_{j+1}\bar{\beta}_{j+1}\right)-\bar{\rho}_{j+1}\left(\bar{\xi}^{2}-\bar{\alpha}_{j}\bar{\beta}_{j}\right)\right)\\+\bar{\xi}^{2}(\bar{\rho}_{j+1}-\bar{\rho}_{j})^{2}-\left(\bar{\rho}_{j}\bar{\beta}_{j+1}+\bar{\rho}_{j+1}\bar{\beta}_{j}\right)\left(\bar{\rho}_{j}\bar{\alpha}_{j+1}+\bar{\rho}_{j+1}\bar{\alpha}_{j}\right)\end{array}\right\}.\tag{7.51}$$

3) Traction jump condition and displacement continuity conditions across the loaded plane $\bar{z}=\bar{s}$ within the l^{th} layer

Similarly, Eqn. (7.24) can be rewritten as

$$\begin{bmatrix}-\bar{\xi} & \bar{\beta}_l & -\bar{\xi} & -\bar{\beta}_l\\-\bar{\alpha}_l & \bar{\xi} & \bar{\alpha}_l & \bar{\xi}\\2\bar{\mu}_l\bar{\xi}\bar{\alpha}_l & -\bar{\mu}_l\left(\bar{\beta}_l^2+\bar{\xi}^2\right) & -2\bar{\mu}_l\bar{\xi}\bar{\alpha}_l & -\bar{\mu}_l\left(\bar{\beta}_l^2+\bar{\xi}^2\right)\\\bar{\mu}_l\left(\bar{\beta}_l^2+\bar{\xi}^2\right) & -2\bar{\mu}_l\bar{\xi}\bar{\alpha}_l & \bar{\mu}_l\left(\bar{\beta}_l^2+\bar{\xi}^2\right) & 2\bar{\mu}_l\bar{\xi}\bar{\alpha}_l\end{bmatrix}\times\left\{\begin{array}{c}-b_{m_2}^{l}e^{-\bar{p}\bar{\alpha}_l\left(\bar{s}-\bar{z}_{l-1}\right)}\\-f_{m_2}^{l}e^{-\bar{p}\bar{\beta}_l\left(\bar{s}-\bar{z}_{l-1}\right)}\\a_{m_2}^{l}e^{\bar{p}\bar{\alpha}_l\left(\bar{s}-\bar{z}_l\right)}\\e_{m_2}^{l}e^{\bar{p}\bar{\beta}_l\left(\bar{s}-\bar{z}_l\right)}\end{array}\right\}=\left\{\begin{array}{c}0\\0\\\dfrac{Y_m-X_m}{2\mathcal{F}_m}\\\dfrac{Z_m}{\mathcal{F}_m}\end{array}\right\}.\tag{7.52}$$

It can be deduced then

$$a_{m_2}^{l}\left(\bar{\xi},\bar{p}\right)=\frac{1}{2\bar{\rho}_l\mathcal{F}_m}\left\{Z_m-\frac{\bar{\xi}}{2\bar{\alpha}_l}\left(X_m-Y_m\right)\right\}e^{-\bar{p}\bar{\alpha}_l\left(\bar{s}-\bar{z}_l\right)}, \tag{7.53}$$

$$b_{m_2}^{l}\left(\bar{\xi},\bar{p}\right)=\frac{-1}{2\bar{\rho}_l\mathcal{F}_m}\left\{Z_m+\frac{\bar{\xi}}{2\bar{\alpha}_l}\left(X_m-Y_m\right)\right\}e^{\bar{p}\bar{\alpha}_l\left(\bar{s}-\bar{z}_{l-1}\right)}, \tag{7.54}$$

$$e_{m_2}^{l}\left(\bar{\xi},\bar{p}\right)=\frac{1}{2\bar{\rho}_l\mathcal{F}_m}\left\{\frac{-\bar{\xi}}{\bar{\beta}_l}Z_m+\frac{1}{2}\left(X_m-Y_m\right)\right\}e^{-\bar{p}\bar{\beta}_l\left(\bar{s}-\bar{z}_l\right)}, \tag{7.55}$$

$$f_{m_2}^{l}\left(\bar{\xi},\bar{p}\right)=\frac{-1}{2\bar{\rho}_l\mathcal{F}_m}\left\{\frac{\bar{\xi}}{\bar{\beta}_l}Z_m+\frac{1}{2}\left(X_m-Y_m\right)\right\}e^{\bar{p}\bar{\beta}_l\left(\bar{s}-\bar{z}_{l-1}\right)}. \tag{7.56}$$

4) Regularity condition

Eqn. (7.26) furnishes that

$$a_m^{n+1}\left(\bar{\xi},\bar{z},\bar{p}\right)=e_m^{n+1}\left(\bar{\xi},\bar{z},\bar{p}\right)=0. \tag{7.57}$$

7.4.2 Formulation of solution by "Propagator Matrices"

As shown in Guzina and Pak (1996), Guzina and Pak (2001), the equation system represented by Eqn. (7.28), (7.33), (7.52) and (7.57) can be solved by the method of propagator matrices. To this end, one should first group the unknown coefficients $a_m^j,\dots,f_m^j$ into two arrays ro vectors:

$$\mathbf{w}_{d_m}^{j}\left(\bar{\xi},\bar{z},\bar{p}\right)=\begin{Bmatrix} wp_{d_m}^{j}\left(\bar{\xi},\bar{z},\bar{p}\right)\\ ws_{d_m}^{j}\left(\bar{\xi},\bar{z},\bar{p}\right)\end{Bmatrix}\equiv\begin{Bmatrix} b_m^{j}\left(\bar{\xi},\bar{z},\bar{p}\right)\\ f_m^{j}\left(\bar{\xi},\bar{z},\bar{p}\right)\end{Bmatrix},\quad j=1,\dots,n+1, \tag{7.58}$$

and

$$\mathbf{w}_{u_m}^{j}\left(\bar{\xi},\bar{z},\bar{p}\right)=\begin{Bmatrix} wp_{u_m}^{j}\left(\bar{\xi},\bar{z},\bar{p}\right)\\ ws_{u_m}^{j}\left(\bar{\xi},\bar{z},\bar{p}\right)\end{Bmatrix}\equiv\begin{Bmatrix} a_m^{j}\left(\bar{\xi},\bar{z},\bar{p}\right)\\ e_m^{j}\left(\bar{\xi},\bar{z},\bar{p}\right)\end{Bmatrix},\quad j=1,\dots,n+1. \tag{7.59}$$

In Eqn. (7.58) and (7.59), $\mathbf{w}^j_{d_m}\left(\bar\xi,\bar z,\bar p\right)$ can be termed the *downwardly propagating waves* in the j^{th} layer, while $\mathbf{w}^j_{u_m}\left(\bar\xi,\bar z,\bar p\right)$ stands for the correspond *upwardly propagating wave* components. As noted in Guzina and Pak (1996), Guzina and Pak (2001), the solutions of $\mathbf{w}^j_{d_m}\left(\bar\xi,\bar z,\bar p\right)$ and $\mathbf{w}^j_{u_m}\left(\bar\xi,\bar z,\bar p\right)$ can be obtained as follows:

- **Solution in the loaded l^{th} layer**

$$\begin{aligned}\mathbf{w}^l_{d_m}\left(\bar\xi,\bar z,\bar p\right)&=\left[\mathbf{I}-\hat{\mathbf{R}}^u_{l-1}\hat{\mathbf{R}}^d_l\right]^{-1}\hat{\mathbf{R}}^u_{l-1}\left(\mathbf{s}^l_{u_m}+\hat{\mathbf{R}}^d_l\mathbf{s}^l_{d_m}\right)+\mathbf{H}\left(\bar z-\bar s\right)\mathbf{s}^l_{d_m},\\ \mathbf{w}^l_{u_m}\left(\bar\xi,\bar z,\bar p\right)&=\left[\mathbf{I}-\hat{\mathbf{R}}^d_l\hat{\mathbf{R}}^u_{l-1}\right]^{-1}\hat{\mathbf{R}}^d_l\left(\mathbf{s}^l_{d_m}+\hat{\mathbf{R}}^u_{l-1}\mathbf{s}^l_{u_m}\right)+\mathbf{H}\left(\bar s-\bar z\right)\mathbf{s}^l_{u_m}.\end{aligned}\tag{7.60}$$

where

$$\mathbf{s}^l_{d_m}\left(\bar\xi,\bar p\right)=\begin{Bmatrix}b^l_{m_2}\left(\bar\xi\right)\\ f^l_{m_2}\left(\bar\xi\right)\end{Bmatrix}=\frac{-1}{2\bar\rho_l\mathcal{F}_m}\begin{bmatrix}e^{\bar p\bar\alpha_l\left(\bar s-\bar z_{l-1}\right)} & 0\\ 0 & e^{\bar p\bar\beta_l\left(\bar s-\bar z_{l-1}\right)}\end{bmatrix}\begin{Bmatrix}Z_m+\dfrac{\bar\xi}{2\bar\alpha_l}\left(X_m-Y_m\right)\\ \dfrac{\bar\xi}{\bar\beta_l}Z_m+\dfrac{1}{2}\left(X_m-Y_m\right)\end{Bmatrix},\tag{7.61}$$

$$\mathbf{s}^l_{u_m}\left(\bar\xi,\bar p\right)=\begin{Bmatrix}a^l_{m_2}\left(\bar\xi\right)\\ e^l_{m_2}\left(\bar\xi\right)\end{Bmatrix}=\frac{1}{2\bar\rho_l\mathcal{F}_m}\begin{bmatrix}e^{-\bar p\bar\alpha_l\left(\bar s-\bar z_l\right)} & \\ & e^{-\bar p\bar\beta_l\left(\bar s-\bar z_l\right)}\end{bmatrix}\begin{Bmatrix}Z_m-\dfrac{\bar\xi}{2\bar\alpha_l}\left(X_m-Y_m\right)\\ -\dfrac{\bar\xi}{\bar\beta_l}Z_m+\dfrac{1}{2}\left(X_m-Y_m\right)\end{Bmatrix}.\tag{7.62}$$

- **Solution in the layers above the source**

$$\begin{aligned}\mathbf{w}^j_{u_m}\left(\bar\xi,\bar p\right)&=\hat{\mathbf{T}}^u_j\hat{\mathbf{T}}^u_{j+1}...\hat{\mathbf{T}}^u_{l-1}\mathbf{w}^l_{u_m}\left(\bar\xi,\bar z_{l-1}\right),\ \ j=1,...,l-1,\\ \mathbf{w}^j_{d_m}\left(\bar\xi,\bar p\right)&=\hat{\mathbf{R}}^u_{j-1}\mathbf{w}^j_{u_m}\left(\bar\xi,\bar p\right),\ \ j=1,...,l-1,\end{aligned}\tag{7.63}$$

where

$$\begin{aligned}\hat{\mathbf{R}}^u_0&=\mathbf{R}^u_0,\\ \hat{\mathbf{T}}^u_j&=\left[\mathbf{I}-\mathbf{R}^d_j\hat{\mathbf{R}}^u_{j-1}\right]^{-1}\mathbf{T}^u_j,\ 1\le j\le l-1\ .\\ \hat{\mathbf{R}}^u_j&=\mathbf{R}^u_j+\mathbf{T}^d_j\hat{\mathbf{R}}^u_{j-1}\hat{\mathbf{T}}^u_j,\ 1\le j\le l-1\end{aligned}\tag{7.64}$$

- **Solution in the layers below the source**

$$\begin{aligned}&\mathbf{w}_{d_m}^{j}\left(\bar{\xi},\bar{p}\right)=\hat{\mathbf{T}}_{j-1}^{d}\hat{\mathbf{T}}_{j-2}^{d}\ldots\hat{\mathbf{T}}_{l}^{d}\mathbf{w}_{d_m}^{l}\left(\bar{\xi},\bar{z}_l\right),\quad j=l+1,\ldots,n+1,\\&\mathbf{w}_{u_m}^{j}\left(\bar{\xi},\bar{p}\right)=\hat{\mathbf{R}}_{j}^{d}\mathbf{w}_{d_m}^{j}\left(\bar{\xi},\bar{p}\right),\quad j=l+1,\ldots,n+1,\end{aligned}\tag{7.65}$$

where

$$\begin{aligned}&\hat{\mathbf{R}}_{n+1}^{d}=0,\\&\hat{\mathbf{T}}_{j}^{d}=\left[\mathbf{I}-\mathbf{R}_{j}^{u}\hat{\mathbf{R}}_{j+1}^{d}\right]^{-1}\mathbf{T}_{j}^{d},\ l\leq j\leq n,\\&\hat{\mathbf{R}}_{j}^{d}=\mathbf{R}_{j}^{d}+\mathbf{T}_{j}^{u}\hat{\mathbf{R}}_{j+1}^{d}\hat{\mathbf{T}}_{j}^{d},\ l\leq j\leq n.\end{aligned}\tag{7.66}$$

7.5 Propagation of horizontally-polarized waves

In analogy to the investigation in the last section, the unknown integration coefficients $c_m^j,\ d_m^j,\ j=1,\ldots n$ associated with P-SV waves can be derived from the boundary and interfacial conditions. The corresponding mathematical expression for the boundary, interfacial conditions are listed as follows.

7.5.1 Boundary and interfacial conditions

(1) Free-surface condition

$$\sigma_{23_m}^{1}\left(\bar{\xi},\bar{z}_0;\bar{s};\bar{p}\right)=0.\tag{7.67}$$

(2) Continuity of displacement and traction across all layer interfaces

$$\begin{aligned}&v_{3_m}^{j}\left(\bar{\xi},\bar{z}_j;\bar{s};\bar{p}\right)=v_{3_m}^{j+1}\left(\bar{\xi},\bar{z}_j;\bar{s};\bar{p}\right),\\&\sigma_{23_m}^{j}\left(\bar{\xi},\bar{z}_j;\bar{s};\bar{p}\right)=\sigma_{23_m}^{j+1}\left(\bar{\xi},\bar{z}_j;\bar{s};\bar{p}\right),\quad j=1,\ldots,n.\end{aligned}\tag{7.68}$$

(3) Traction jump and displacement continuity conditions across the loaded plane $z=s$

$$\begin{aligned}&v_{3_m}^{l}\left(\bar{\xi},\bar{s}^{-};\bar{s};\bar{p}\right)-v_{3_m}^{l}\left(\bar{\xi},\bar{s}^{+};\bar{s};\bar{p}\right)=0,\\&\sigma_{23_m}^{l}\left(\bar{\xi},\bar{s}^{-};\bar{s};\bar{p}\right)-\sigma_{23_m}^{j+1}\left(\bar{\xi},\bar{s}^{+};\bar{s};\bar{p}\right)=\frac{X_m+Y_m}{2\mathcal{F}_m}.\end{aligned}\tag{7.69}$$

(4) Regularity condition

$$\lim_{\bar{z}\to\infty} v_{3_m}^{n+1}\left(\bar{\xi},\bar{z};\bar{s};\bar{p}\right)=0. \tag{7.70}$$

Analogous to the approach for vertically polarized waves, one can express all these conditions in terms of the unknown constants of integration $c_m^j\left(\bar{\xi},\bar{z},\bar{p}\right)$, $d_m^j\left(\bar{\xi},\bar{z},\bar{p}\right)$, $j=1,\ldots n$, i.e.,

(5) Free surface condition

$$d_m^1\left(\bar{\xi},\bar{z},\bar{p}\right)=\mathcal{R}_0^u\left(\bar{\xi},\bar{p}\right)c_m^1\left(\bar{\xi},\bar{z},\bar{p}\right), \tag{7.71}$$

where

$$\mathcal{R}_0^u\left(\bar{\xi},\bar{p}\right)\equiv\mathcal{R}_0^{u\mathcal{N}}\left(\bar{\xi}\right)e^{-\bar{p}\bar{\beta}_1\bar{h}_1}=e^{-\bar{p}\bar{\beta}_1\bar{h}_1}. \tag{7.72}$$

(6) Continuity of displacement and traction across all layer

$$\begin{bmatrix}-i\bar{\xi} & i\bar{\xi}\\ i\bar{\mu}_{j+1}\overline{\xi\beta}_{j+1} & i\bar{\mu}_j\overline{\xi\beta}_j\end{bmatrix}\begin{Bmatrix}d_m^{j+1}\\ c_m^j\end{Bmatrix}=\begin{bmatrix}-i\bar{\xi} & i\bar{\xi}\\ i\bar{\mu}_j\overline{\xi\beta}_j & i\bar{\mu}_{j+1}\overline{\xi\beta}_{j+1}\end{bmatrix}\begin{Bmatrix}d_m^j e^{-\bar{p}\bar{\beta}_j\bar{h}_j}\\ c_m^{j+1}e^{-\bar{p}\bar{\beta}_{j+1}\bar{h}_{j+1}}\end{Bmatrix}. \tag{7.73}$$

This condition can be rearranged to

$$\begin{aligned}d_m^{j+1}\left(\bar{\xi},\bar{z},\bar{p}\right)&=\mathcal{T}_j^d\left(\bar{\xi},\bar{p}\right)d_m^j\left(\bar{\xi},\bar{z},\bar{p}\right)+\mathcal{R}_j^u\left(\bar{\xi},\bar{p}\right)c_m^{j+1}\left(\bar{\xi},\bar{z},\bar{p}\right),\\ c_m^j\left(\bar{\xi},\bar{z},\bar{p}\right)&=\mathcal{R}_j^d\left(\bar{\xi},\bar{p}\right)d_m^j\left(\bar{\xi},\bar{z},\bar{p}\right)+\mathcal{T}_j^u\left(\bar{\xi},\bar{p}\right)c_m^{j+1}\left(\bar{\xi},\bar{z},\bar{p}\right),\quad j=1,\ldots n.\end{aligned} \tag{7.74}$$

where

$$\mathcal{T}_j^d\left(\bar{\xi},\bar{p}\right)=\mathcal{T}_j^{d\mathcal{N}}\left(\bar{\xi}\right)e^{-\bar{p}\bar{\beta}_j\bar{h}_j}=\frac{2\bar{\mu}_j\bar{\beta}_j}{\bar{\mu}_j\bar{\beta}_j+\bar{\mu}_{j+1}\bar{\beta}_{j+1}}e^{-\bar{p}\bar{\beta}_j\bar{h}_j}, \tag{7.75}$$

$$\mathcal{R}_j^d\left(\bar{\xi},\bar{p}\right)=\mathcal{R}_j^{d\mathcal{N}}\left(\bar{\xi}\right)e^{-\bar{p}\bar{\beta}_j\bar{h}_j}=\frac{\bar{\mu}_j\bar{\beta}_j-\bar{\mu}_{j+1}\bar{\beta}_{j+1}}{\bar{\mu}_j\bar{\beta}_j+\bar{\mu}_{j+1}\bar{\beta}_{j+1}}e^{-\bar{p}\bar{\beta}_j\bar{h}_j}, \tag{7.76}$$

$$\mathcal{R}_j^u\left(\bar{\xi},\bar{p}\right)=\mathcal{R}_j^{u\mathcal{N}}\left(\bar{\xi}\right)e^{-\bar{p}\bar{\beta}_{j+1}\bar{h}_{j+1}}=\frac{\bar{\mu}_j\bar{\beta}_j-\bar{\mu}_{j+1}\bar{\beta}_{j+1}}{\bar{\mu}_j\bar{\beta}_j+\bar{\mu}_{j+1}\bar{\beta}_{j+1}}e^{-\bar{p}\bar{\beta}_{j+1}\bar{h}_{j+1}}, \tag{7.77}$$

$$\mathcal{T}_j^u\left(\bar{\xi},\bar{p}\right)=\mathcal{T}_j^{u\mathcal{N}}\left(\bar{\xi}\right)e^{-\bar{p}\bar{\beta}_{j+1}\bar{h}_{j+1}}=\frac{2\bar{\mu}_{j+1}\bar{\beta}_{j+1}}{\bar{\mu}_j\bar{\beta}_j+\bar{\mu}_{j+1}\bar{\beta}_{j+1}}e^{-\bar{p}\bar{\beta}_{j+1}\bar{h}_{j+1}},\quad j=1,\ldots n. \tag{7.78}$$

(7) Traction jump and displacement continuity conditions across the loaded plane $z = s$

$$\begin{bmatrix} i\overline{\xi} & i\overline{\xi} \\ -i\overline{\mu}_l\overline{\xi\beta_l} & i\overline{\mu}_l\overline{\xi\beta_l} \end{bmatrix} \begin{Bmatrix} -d_{m_2}^{l} e^{-\overline{p}\overline{\beta}_l\left(\overline{s}-\overline{z}_{l-1}\right)} \\ c_{m_2}^{l} e^{\overline{p}\overline{\beta}_l\left(\overline{s}-\overline{z}_l\right)} \end{Bmatrix} = \begin{Bmatrix} 0 \\ \dfrac{X_m+Y_m}{2\mathcal{F}_m} \end{Bmatrix} \tag{7.79}$$

which gives that

$$\begin{aligned} c_{m_2}^{l}\left(\overline{\xi},\overline{p}\right) &= \frac{-i}{2\mathcal{F}_m}\left\{\frac{1}{2\overline{\mu}\overline{\xi\beta_l}}\left(X_m+Y_m\right)\right\}e^{-\overline{p}\overline{\beta}_l\left(\overline{s}-\overline{z}_l\right)}, \\ d_{m_2}^{l}\left(\overline{\xi},\overline{p}\right) &= \frac{-i}{2\mathcal{F}_m}\left\{\frac{1}{2\overline{\mu}\overline{\xi\beta_l}}\left(X_m+Y_m\right)\right\}e^{\overline{p}\overline{\beta}_l\left(\overline{s}-\overline{z}_{l-1}\right)}. \end{aligned} \tag{7.80}$$

(8) Regularity condition

$$c_m^{n+1}\left(\overline{\xi},\overline{z},\overline{p}\right) = 0. \tag{7.81}$$

7.5.2 Formulation of solution by method of "Propagator Matrices"

For the convenience of applying the method of "propagator matrices", one may define

$$w_{d_m}^{j}\left(\overline{\xi},\overline{z},\overline{p}\right) \equiv d_m^{j}\left(\overline{\xi},\overline{z},\overline{p}\right),\ \ w_{u_m}^{j}\left(\overline{\xi},\overline{z},\overline{p}\right) \equiv c_m^{j}\left(\overline{\xi},\overline{z},\overline{p}\right),\ \ j = 1,\ldots n., \tag{7.82}$$

similar to Guzina (1996) and Pak and Guzina (2002):

a) Solution in the loaded l^{th} layer

$$\begin{aligned} w_{d_m}^{l}\left(\overline{\xi},\overline{z},\overline{p}\right) &= (1-\hat{\mathcal{R}}_{l-1}^{u}\hat{\mathcal{R}}_{l}^{d})^{-1}\hat{\mathcal{R}}_{l-1}^{u}\left(s_{u_m}^{l}+\hat{\mathcal{R}}_{l}^{d}s_{d_m}^{l}\right)+H\left(\overline{z}-\overline{s}\right)s_{d_m}^{l}, \\ w_{u_m}^{l}\left(\overline{\xi},\overline{z},\overline{p}\right) &= (1-\hat{\mathcal{R}}_{l}^{d}\hat{\mathcal{R}}_{l-1}^{u})^{-1}\hat{\mathcal{R}}_{l}^{d}\left(s_{d_m}^{l}+\hat{\mathcal{R}}_{l-1}^{u}s_{u_m}^{l}\right)+H\left(\overline{s}-\overline{z}\right)s_{u_m}^{l}, \end{aligned} \tag{7.83}$$

where

$$s_{d_m}^{l}\left(\overline{\xi},\overline{p}\right) = d_{m_2}^{l}\left(\overline{\xi}\right) = \frac{-i}{2\mathcal{F}_m}\left\{\frac{1}{2\overline{\mu}\overline{\xi\beta_l}}\left(X_m+Y_m\right)\right\}e^{\overline{p}\overline{\beta}_l\left(\overline{s}-\overline{z}_{l-1}\right)}, \tag{7.84}$$

$$s_{u_m}^{l}\left(\overline{\xi},\overline{p}\right) = c_{m_2}^{l}\left(\overline{\xi}\right) = \frac{-i}{2\mathcal{F}_m}\left\{\frac{1}{2\overline{\mu}\overline{\xi\beta_l}}\left(X_m+Y_m\right)\right\}e^{-\overline{p}\overline{\beta}_l\left(\overline{s}-\overline{z}_l\right)}. \tag{7.85}$$

b) Solution in the layers above the source

$$\begin{aligned} w^j_{u_m}\left(\bar{\xi},\bar{p}\right) &= \hat{\mathcal{T}}^u_j \hat{\mathcal{T}}^u_{j+1} \ldots \hat{\mathcal{T}}^u_{l-1} w^l_{u_m}\left(\bar{\xi},\bar{z}_{l-1}\right), \;\; j=1,\ldots,l-1, \\ w^j_{d_m}\left(\bar{\xi},\bar{p}\right) &= \hat{\mathcal{R}}^u_{j-1} w^j_{u_m}\left(\bar{\xi},\bar{p}\right), \;\; j=1,\ldots,l-1, \end{aligned} \tag{7.86}$$

where

$$\begin{aligned} \hat{\mathcal{R}}^u_0 &= \mathcal{R}^u_0, \\ \hat{\mathcal{T}}^u_j &= \left(1-\mathcal{R}^d_j \hat{\mathcal{R}}^u_{j-1}\right)^{-1} \mathcal{T}^u_j, \;\; 1 \le j \le l-1, \\ \hat{\mathcal{R}}^u_j &= \mathcal{R}^u_j + \mathcal{T}^d_j \hat{\mathcal{R}}^u_{j-1} \hat{\mathcal{T}}^u_j, \;\; 1 \le j \le l-1. \end{aligned} \tag{7.87}$$

c) Solution in the layers below the source

$$\begin{aligned} w^j_{d_m}\left(\bar{\xi},\bar{p}\right) &= \hat{\mathcal{T}}^d_{j-1} \hat{\mathcal{T}}^d_{j-2} \ldots \hat{\mathcal{T}}^d_{l} w^l_{d_m}\left(\bar{\xi},\bar{z}_{l}\right), \;\; j=l+1,\ldots,n+1, \\ w^j_{u_m}\left(\bar{\xi},\bar{p}\right) &= \hat{\mathcal{R}}^d_{j} w^j_{d_m}\left(\bar{\xi},\bar{p}\right), \;\; j=l+1,\ldots,n+1, \end{aligned} \tag{7.88}$$

where

$$\begin{aligned} \hat{\mathcal{R}}^d_{n+1} &= 0, \\ \hat{\mathcal{T}}^d_j &= \left(1-\mathcal{R}^u_j \hat{\mathcal{R}}^d_{j+1}\right)^{-1} \mathcal{T}^d_j, \;\; l \le j \le n, \\ \hat{\mathcal{R}}^d_j &= \mathcal{R}^d_j + \mathcal{T}^u_j \hat{\mathcal{R}}^d_{j+1} \hat{\mathcal{T}}^d_j, \;\; l \le j \le n. \end{aligned} \tag{7.89}$$

7.6 Laplace transform inversion of multi-layer Green's function to time domain

Inversion of the multi-layer Green's function in the Laplace-Hankel transform domain to the time domain for the arbitrary time and loading has always been an analytical challenge in theoretical mechanics and applied mathematics. For slow dynamic loading, the frequency-domain approach developed by Pak and Guzina (2001, 2002) is a natural approach. For very fast loading such as shocks and blasts, however, such an approach will require the computation of the Green's function response at not only many but also high frequencies whose numerics is not trivial. Furthermore, for many practical engineering problems, the critical cases are concerned with the response over only a finite time interval right after the loading. To serve such needs, an effective approach to obtain the desired time-domain Green's function's response exactly up to a specific time interval will be helpful and described in this section.

7.6.1 Ray expansion through Neumann series of matrix

To obtain a rigorous finite time representation of the Green's function, it is useful to recognize that one of the key complexities in the integration kernel in Laplace domain Green's functions (Eqns. (7.60), (7.63), (7.65) for P-SV waves, and Eqns. (7.83), (7.86), (7.88) for SH waves) stems from the presence of terms of the form

$$\left[\mathbf{I}-\mathbf{R}\right]^{-1}, \tag{7.90}$$

where $\mathbf{R}$ is typically the products of 2 generalized reflection matrices in Eqns. (7.60), (7.64), (7.66), or scalar function in Eqns. (7.83), (7879), (7.89). For the case where the moduli of the eigenvalues of $\mathbf{R}$ are all sufficiently smaller than 1 which will be the case for sufficiently large Laplace transform parameter $\overline{p}$ in the negative exponent of the exponential functions in the matrix elements, it is legitmate to expand $\left[\mathbf{I}-\mathbf{R}\right]^{-1}$ into a *Neumann series of the form*

$$\left[\mathbf{I}-\mathbf{R}\right]^{-1}=\mathbf{I}+\sum_{n=1}^{\infty}\mathbf{R}^{n}. \tag{7.91}$$

By virtue of the foregoing approach, the expressions of the integrands $\mathbf{w}_{d_m}^{j}\left(\overline{\xi},\overline{p}\right)$, $\mathbf{w}_{u_m}^{j}\left(\overline{\xi},\overline{p}\right)$ in Eqns. (7.60), (7.63), (7.65) and $w_{d_m}^{j}\left(\overline{\xi},\overline{p}\right)$, $w_{u_m}^{j}\left(\overline{\xi},\overline{p}\right)$ in Eqns. (7.83), (7.86), (7.88) are expanded into infinite series, each term of which is a product from a sequence of multiplication of coefficients of transmission and reflection matrices and source vector. For example, the equations in (7.60) for the kernels of the solutions in the loaded l^{th} layer corresponding to P-SV waves become

$$\begin{aligned}
\mathbf{w}_{d_m}^{l}\left(\overline{\xi},\overline{z},\overline{p}\right)&=\left[\mathbf{I}+\sum_{n=1}^{\infty}\left(\hat{\mathbf{R}}_{l-1}^{u}\hat{\mathbf{R}}_{l}^{d}\right)^{n}\right]\hat{\mathbf{R}}_{l-1}^{u}\left(\mathbf{s}_{u_m}^{l}+\hat{\mathbf{R}}_{l}^{d}\mathbf{s}_{d_m}^{l}\right)+\mathbf{H}\left(\overline{z}-\overline{s}\right)\mathbf{s}_{d_m}^{l}\\
\mathbf{w}_{u_m}^{l}\left(\overline{\xi},\overline{z},\overline{p}\right)&=\left[\mathbf{I}+\sum_{n=1}^{\infty}\left(\hat{\mathbf{R}}_{l}^{d}\hat{\mathbf{R}}_{l-1}^{u}\right)^{n}\right]\hat{\mathbf{R}}_{l}^{d}\left(\mathbf{s}_{d_m}^{l}+\hat{\mathbf{R}}_{l-1}^{u}\mathbf{s}_{u_m}^{l}\right)+\mathbf{H}\left(\overline{s}-\overline{z}\right)\mathbf{s}_{u_m}^{l}
\end{aligned}, \tag{7.92}$$

while for SH waves, Eqn. (7.83) become

$$\begin{aligned} w^l_{d_m}\left(\bar{\xi},\bar{z},\bar{p}\right) &= \left[1+\sum_{n=1}^{\infty}\left(\hat{\mathcal{R}}^u_{l-1}\hat{\mathcal{R}}^d_l\right)^n\right]\hat{\mathcal{R}}^u_{l-1}\left(s^l_{u_m}+\hat{\mathcal{R}}^d_l s^l_{d_m}\right)+H\left(\bar{z}-\bar{s}\right)s^l_{d_m} \\ w^l_{u_m}\left(\bar{\xi},\bar{z},\bar{p}\right) &= \left[1+\sum_{n=1}^{\infty}\left(\hat{\mathcal{R}}^d_l\hat{\mathcal{R}}^u_{l-1}\right)^n\right]\hat{\mathcal{R}}^d_l\left(s^l_{d_m}+\hat{\mathcal{R}}^u_{l-1}s^l_{u_m}\right)+H\left(\bar{s}-\bar{z}\right)s^l_{u_m} \end{aligned}. \tag{7.93}$$

Likewise, the kernels of the solutions in the layers above the source in Eqn. (7.63) become

$$\begin{aligned} \mathbf{w}^j_{u_m}\left(\bar{\xi},\bar{p}\right) &= \hat{\mathbf{T}}^u_j\hat{\mathbf{T}}^u_{j+1}\ldots\hat{\mathbf{T}}^u_{l-1}\mathbf{w}^l_{u_m}\left(\bar{\xi},\bar{z}_{l-1}\right),\ \ j=1,\ldots,l-1, \\ \mathbf{w}^j_{d_m}\left(\bar{\xi},\bar{p}\right) &= \hat{\mathbf{R}}^u_{j-1}\mathbf{w}^j_{u_m}\left(\bar{\xi},\bar{p}\right),\ \ j=1,\ldots,l-1, \end{aligned} \tag{7.94}$$

with

$$\begin{aligned} \hat{\mathbf{R}}^u_0 &= \mathbf{R}^u_0, \\ \hat{\mathbf{T}}^u_j &= \left[\mathbf{I}+\sum_{n=1}^{\infty}\left(\mathbf{R}^d_j\hat{\mathbf{R}}^u_{j-1}\right)^n\right]\mathbf{T}^u_j,\ 1\le j\le l-1. \\ \hat{\mathbf{R}}^u_j &= \mathbf{R}^u_j+\mathbf{T}^d_j\hat{\mathbf{R}}^u_{j-1}\hat{\mathbf{T}}^u_j,\ 1\le j\le l-1 \end{aligned} \tag{7.95}$$

For SH-waves, the integrands in Eqn. (7.86) are

$$\begin{aligned} w^j_{u_m}\left(\bar{\xi},\bar{p}\right) &= \hat{\mathcal{T}}^u_j\hat{\mathcal{T}}^u_{j+1}\ldots\hat{\mathcal{T}}^u_{l-1}w^l_{u_m}\left(\bar{\xi},\bar{z}_{l-1}\right),\ \ j=1,\ldots,l-1, \\ w^j_{d_m}\left(\bar{\xi},\bar{p}\right) &= \hat{\mathcal{R}}^u_{j-1}w^j_{u_m}\left(\bar{\xi},\bar{p}\right),\ \ j=1,\ldots,l-1, \end{aligned} \tag{7.96}$$

where

$$\begin{aligned} \hat{\mathcal{R}}^u_0 &= \mathcal{R}^u_0, \\ \hat{\mathcal{T}}^u_j &= \left[1+\sum_{n=1}^{\infty}\left(\mathcal{R}^d_j\hat{\mathcal{R}}^u_{j-1}\right)^n\right]\mathcal{T}^u_j,\ 1\le j\le l-1, \\ \hat{\mathcal{R}}^u_j &= \mathcal{R}^u_j+\mathcal{T}^d_j\hat{\mathcal{R}}^u_{j-1}\hat{\mathcal{T}}^u_j,\ 1\le j\le l-1. \end{aligned} \tag{7.97}$$

Similarly, kernels of the solutions in the layers below the source in Eqn. (7.65) for P-SV waves become

$$\begin{aligned} \mathbf{w}_{d_m}^{j}\left(\bar{\xi},\bar{p}\right) &= \hat{\mathbf{T}}_{j-1}^{d}\hat{\mathbf{T}}_{j-2}^{d}\ldots\hat{\mathbf{T}}_{l}^{d}\mathbf{w}_{d_m}^{l}\left(\bar{\xi},\bar{z}_l\right), \quad j=l+1,\ldots,n+1, \\ \mathbf{w}_{u_m}^{j}\left(\bar{\xi},\bar{p}\right) &= \hat{\mathbf{R}}_{j}^{d}\mathbf{w}_{d_m}^{j}\left(\bar{\xi},\bar{p}\right), \quad j=l+1,\ldots,n+1, \end{aligned} \tag{7.98}$$

with

$$\begin{aligned} \hat{\mathbf{R}}_{n+1}^{d} &= 0, \\ \hat{\mathbf{T}}_{j}^{d} &= \left[\mathbf{I}+\sum_{n=1}^{\infty}\left(\mathbf{R}_{j}^{u}\hat{\mathbf{R}}_{j+1}^{d}\right)^{n}\right]\mathbf{T}_{j}^{d}, \ l \le j \le n, \\ \hat{\mathbf{R}}_{j}^{d} &= \mathbf{R}_{j}^{d}+\mathbf{T}_{j}^{u}\hat{\mathbf{R}}_{j+1}^{d}\hat{\mathbf{T}}_{j}^{d}, \ l \le j \le n. \end{aligned} \tag{7.99}$$

For SH waves, the kernels in Eqn. (7.88) become

$$\begin{aligned} w_{d_m}^{j}\left(\bar{\xi},\bar{p}\right) &= \hat{\mathcal{T}}_{j-1}^{d}\hat{\mathcal{T}}_{j-2}^{d}\ldots\hat{\mathcal{T}}_{l}^{d}w_{d_m}^{l}\left(\bar{\xi},\bar{z}_l\right), \quad j=l+1,\ldots,n+1, \\ w_{u_m}^{j}\left(\bar{\xi},\bar{p}\right) &= \hat{\mathcal{R}}_{j}^{d}w_{d_m}^{j}\left(\bar{\xi},\bar{p}\right), \quad j=l+1,\ldots,n+1, \end{aligned} \tag{7.100}$$

where

$$\begin{aligned} \hat{\mathcal{R}}_{n+1}^{d} &= 0, \\ \hat{\mathcal{T}}_{j}^{d} &= \left[1+\sum_{n=1}^{\infty}\left(\mathcal{R}_{j}^{u}\hat{\mathcal{R}}_{j+1}^{d}\right)^{n}\right]\mathcal{T}_{j}^{d}, \ l \le j \le n, \\ \hat{\mathcal{R}}_{j}^{d} &= \mathcal{R}_{j}^{d}+\mathcal{T}_{j}^{u}\hat{\mathcal{R}}_{j+1}^{d}\hat{\mathcal{T}}_{j}^{d}, \ l \le j \le n. \end{aligned} \tag{7.101}$$

To provide more insights, consider the simple configuration where a layer is bonded to the top of a homogenous half-space. For such a configuration, one has from Eqn. (7.93) that

$$w_{d_m}^{1}\left(\bar{\xi},\bar{z},\bar{p}\right) = \left[1+\sum_{n=1}^{\infty}\left(\mathcal{R}_{0}^{u}\mathcal{R}_{1}^{d}\right)^{n}\right]\mathcal{R}_{0}^{u}\left(s_{u_m}^{1}+\mathcal{R}_{1}^{d}s_{d_m}^{1}\right), \tag{7.102}$$

for $\bar{z} < \bar{s}$ as the second term in (7.93) is zero. Recalling that

$$\begin{aligned} \mathcal{R}_{0}^{u}\left(\bar{\xi},\bar{p}\right) &= e^{-\bar{p}\bar{\beta}_1\bar{h}_1} \\ \mathcal{R}_{1}^{d}\left(\bar{\xi},\bar{p}\right) &= \mathcal{R}_{1}^{d\mathcal{N}}\left(\bar{\xi}\right)e^{-\bar{p}\bar{\beta}_1\bar{h}_1} \\ s_{d_m}^{1}\left(\bar{\xi},\bar{p}\right) &= s_{d_m}^{1\mathcal{N}}\left(\bar{\xi}\right)e^{\bar{p}\bar{\beta}_1\left(\bar{s}-\bar{z}_0\right)} \ , \\ s_{u_m}^{1}\left(\bar{\xi},\bar{p}\right) &= s_{d_m}^{1\mathcal{N}}\left(\bar{\xi}\right)e^{-\bar{p}\bar{\beta}_1\left(\bar{s}-\bar{z}_1\right)} \end{aligned} \tag{7.103}$$

Eqn. (7.102) leads to an explicit expression for the infinite series of $w_{d_m}^{1}\left(\bar{\xi},\bar{z},\bar{p}\right)$ which is

$$w_{d_m}^{1}\left(\bar{\xi},\bar{z},\bar{p}\right)=\left[1+\sum_{n=1}^{\infty}\left(\mathcal{R}_1^{d\mathcal{N}}(\bar{\xi})e^{-\bar{p}\bar{\beta}_1\left(2\bar{h}\right)}\right)^n\right]e^{-\bar{p}\bar{\beta}_1\bar{h}}\left(s_{u_m}^{1\mathcal{N}}(\bar{\xi})e^{\bar{p}\bar{\beta}_1(\bar{s}-\bar{z}_0)}+\mathcal{R}_1^{d\mathcal{N}}(\bar{\xi})s_{d_m}^{1\mathcal{N}}(\bar{\xi})e^{\bar{p}\bar{\beta}_1(\bar{s}-\bar{z}_1-h)}\right). \quad (7.104)$$

whose terms can be organized according to the exponential terms, i.e., the terms with the same exponents are grouped as one term. Accordingly one can write Eqn. (7.104) as

$$\begin{aligned}w_{d_m}^{1}\left(\bar{\xi},\bar{z},\bar{p}\right)&=s_{u_m}^{1\mathcal{N}}(\bar{\xi})e^{\bar{p}\bar{\beta}_1\left(\bar{s}-\bar{z}_0-\bar{h}\right)}+\sum_{n=1}^{\infty}\left(\mathcal{R}_1^{d\mathcal{N}}(\bar{\xi})\right)^n s_{u_m}^{1\mathcal{N}}(\bar{\xi})e^{-\bar{p}\bar{\beta}_1\left(2n\bar{h}-\bar{s}+\bar{h}_0\right)}\\&+\mathcal{R}_1^{d\mathcal{N}}(\bar{\xi})s_{d_m}^{1\mathcal{N}}(\bar{\xi})e^{\bar{p}\bar{\beta}_1(\bar{s}-\bar{z}_1-h)}+\sum_{n=1}^{\infty}\left(\mathcal{R}_1^{d\mathcal{N}}(\bar{\xi})\right)^n\mathcal{R}_1^{d\mathcal{N}}(\bar{\xi})s_{d_m}^{1\mathcal{N}}(\bar{\xi})e^{\bar{p}\bar{\beta}_1(\bar{s}-\bar{z}_1-(2n+1)h)}\end{aligned}. \quad (7.105)$$

As each term of series corresponds to a generalized ray group which has its particular arrival time, it is meaningful to sort these terms in an ascending order on their arrival time as will be discussed later.

By similar algebraic expansions, the components of $\mathbf{w}_{d_m}^{j}\left(\bar{\xi},\bar{p}\right)$, $\mathbf{w}_{u_m}^{j}\left(\bar{\xi},\bar{p}\right)$, $w_{d_m}^{j}\left(\bar{\xi},\bar{p}\right)$ and $w_{u_m}^{j}\left(\bar{\xi},\bar{p}\right)$ namely, $a_m^j\left(\bar{\xi},\bar{z},\bar{p}\right)$, $b_m^j\left(\bar{\xi},\bar{z},\bar{p}\right)$, $c_m^j\left(\bar{\xi},\bar{z},\bar{p}\right)$, $d_m^j\left(\bar{\xi},\bar{z},\bar{p}\right)$, $e_m^j\left(\bar{\xi},\bar{z},\bar{p}\right)$, $f_m^j\left(\bar{\xi},\bar{z},\bar{p}\right)$ can likewise be expressed as infinite series, with each of their terms having a general form of

$$\left(\prod_{i=1}^{n_T}M_i(\bar{\xi},\bar{p})\right)\cdot e^{-\bar{p}\sum_{k=1}^{n_T}d_k\sqrt{\bar{\xi}^2+\frac{1}{\bar{c}_k^2}}}, \quad (7.106)$$

where n_s is an integer, M_i are the coefficients of the general transmission, reflection matrices and source vector, $\bar{c}_k$ are the wave speeds and d_k are vertical distance parameters in the exponents of the grouped exponential terms.

7.6.2 General analytical character of the integrands in multilayer Green's functions

The integrands in Eqns. 7.30, 7.35-7.52, 7.61, 7.62, 7.75, 7.78, 7.84 and 7.85 are generally analytic in the complex plane except for the multiple branch cuts and poles. All poles of the coefficients in the propagator matrices, however, lie on the imaginary axis of the complex $\bar{\xi}-$ plane in the present formulation. For example, as defined in Eqns. (7.30), (7.35)-(7.52), the coefficients in the reflection and transmission matrix can have a simple pole when

$$R_1^-\left(\bar{\xi}\right)=(\bar{\beta}_1^2+\bar{\xi}^2)^2-4\bar{\xi}^2\bar{\alpha}_1\bar{\beta}_1=0\,, \tag{7.107}$$

or

$$S_{j+1}^{j}\left(\bar{\xi}\right)=-\left\{\begin{matrix}4\bar{\xi}^2(\bar{\mu}_{j+1}-\bar{\mu}_j)^2\left(\bar{\xi}^2+\bar{\alpha}_j\bar{\beta}_j\right)\left(\bar{\xi}^2-\bar{\alpha}_{j+1}\bar{\beta}_{j+1}\right)\\ -4\bar{\xi}^2\left(\bar{\mu}_{j+1}-\bar{\mu}_j\right)\left(\bar{\rho}_j\left(\bar{\xi}^2-\bar{\alpha}_{j+1}\bar{\beta}_{j+1}\right)-\bar{\rho}_{j+1}\left(\bar{\xi}^2-\bar{\alpha}_j\bar{\beta}_j\right)\right)\\ +\bar{\xi}^2(\bar{\rho}_{j+1}-\bar{\rho}_j)^2-\left(\bar{\rho}_j\bar{\beta}_{j+1}+\bar{\rho}_{j+1}\bar{\beta}_j\right)\left(\bar{\rho}_j\bar{\alpha}_{j+1}+\bar{\rho}_{j+1}\bar{\alpha}_j\right)\end{matrix}\right\}=0\,. \tag{7.108}$$

The solution of Eqn. (7.107) is $\bar{\xi}=\pm i/\bar{c}_R$, where $\bar{c}_R=c_R/c_{s_0}$ with $\bar{c}_R$ being the Rayleigh wave speed. The solution of Eqn. (7.108) is $\bar{\xi}=\pm i/\bar{c}_s^{j,j+1}$, where $\bar{c}_s^{j,j+1}=c_s^{j,j+1}/c_{s_0}$ with $c_s^{j,j+1}$ denoting the speed of Stoneley waves that can propagate along or near the interface between j^{th} and $\left(j+1\right)^{th}$ layer if it exists (see Miklowitz, 1978).

Since the integrands in form of Eqn. (7.106) are multiplications of coefficients in the propagator matrices, one can see that all poles of the integrands lie on the imaginary axis of the complex $\bar{\xi}-$plane. Using the ζ-contour representation of the Bessel function involved, the integration path will avoid running into these poles as illustrated in Chapter 6.

7.7 Wave front solution to point-loads in transformed domain

7.7.1 Loading coefficients

For a point load, the loading coefficients are:

- Load in x_1- direction

$$\begin{aligned}&X_1(\bar{\xi},\bar{p})=\frac{1}{2\pi}\tilde{g}(\bar{p}),\quad X_m(\bar{\xi},\bar{p})=0,\ m\neq 1,\\ &Y_{-1}(\bar{\xi},\bar{p})=\frac{1}{2\pi}\tilde{g}(\bar{p}),\quad Y_m(\bar{\xi},\bar{p})=0,\ m\neq -1,\\ &Z_m(\bar{\xi},\bar{p})=0,\ \forall m.\end{aligned} \tag{7.109}$$

- Load in $x_2 -$ direction

$$\begin{aligned} &X_1(\bar{\xi},\bar{p}) = -\frac{i}{2\pi}\tilde{g}(\bar{p}), \quad X_m(\bar{\xi},\bar{p}) = 0,\ m \neq 1, \\ &Y_{-1}(\bar{\xi},\bar{p}) = \frac{i}{2\pi}\tilde{g}(\bar{p}), \quad Y_m(\bar{\xi},\bar{p}) = 0,\ m \neq -1, \\ &Z_m(\bar{\xi},\bar{p}) = 0,\ \forall m. \end{aligned} \tag{7.110}$$

- Load in $x_3 -$ direction

$$\begin{aligned} &X_m(\bar{\xi},\bar{p}) = 0,\ \forall m \\ &Y_m(\bar{\xi},\bar{p}) = 0,\ \forall m \\ &Z_0(\bar{\xi},\bar{p}) = \frac{1}{2\pi}\tilde{g}(\bar{p}), \quad Z_m(\bar{\xi},\bar{p}) = 0,\ m \neq 0. \end{aligned} \tag{7.111}$$

7.7.2 Integral representations of displacement and stress fields

Once all the $6(n+2)$ unknown constants, i.e., $a_m^j(\bar{\xi},\bar{z},\bar{p})$, $b_m^j(\bar{\xi},\bar{z},\bar{p})$, $c_m^j(\bar{\xi},\bar{z},\bar{p})$, $d_m^j(\bar{\xi},\bar{z},\bar{p})$, $e_m^j(\bar{\xi},\bar{z},\bar{p})$, $f_m^j(\bar{\xi},\bar{z},\bar{p})$, are determined (see Eqn. (7.106)), applying inverse Hankel transform to the Fourier components of the displacements and stresses, and substituting them into the corresponding Fourier series give that

$$\begin{aligned} \hat{\mathbf{u}}(r,\theta,z;s;p;j) &= \frac{\mathcal{F}\cdot p}{\mu c_s}\bar{\mathbf{u}}(\bar{r},\theta,\bar{z};\bar{s};\bar{p};j), \\ \hat{\boldsymbol{\tau}}(r,\theta,z;s;p;j) &= \frac{\mathcal{F}\cdot p^2}{c_s^2}\bar{\boldsymbol{\tau}}(\bar{r},\theta,\bar{z};\bar{s};\bar{p};j), \end{aligned} \tag{7.112}$$

where $\hat{\mathbf{u}}(r,\theta,z;s;p;j)$ and $\hat{\boldsymbol{\tau}}(r,\theta,z;s;p;j)$ are the Laplace transform of displacement and stress of the j^{th} layer, and $\bar{\mathbf{u}}(\bar{r},\theta,\bar{z};\bar{s};\bar{p};j)$, $\bar{\boldsymbol{\tau}}(\bar{r},\theta,\bar{z};\bar{s};\bar{p};j)$ are their dimensionless form which admit the integral representation

$$\begin{aligned} \bar{u}_r(\bar{r},\theta,\bar{z};\bar{s};\bar{p};j) = \frac{1}{2}\sum_{m=-1}^{1}\Big\{&\int_0^\infty (v_{3_m}^j + v_{1_m}^j)\bar{\xi}J_{m+1}(\bar{p}\bar{\xi}\bar{r})d\bar{\xi} \\ &+\int_0^\infty (v_{3_m}^j - v_{1_m}^j)\bar{\xi}J_{m-1}(\bar{p}\bar{\xi}\bar{r})d\bar{\xi}\Big\}e^{im\theta} \end{aligned} \tag{7.113}$$

$$\bar{u}_\theta\left(\bar{r},\theta,\bar{z};\bar{s};\bar{p};j\right)=\frac{-i}{2}\sum_{m=-1}^{1}\left\{\int_0^\infty (v^j_{3_m}+v^j_{1_m})\bar{\xi}J_{m+1}(\bar{p}\bar{\xi}\bar{r})d\bar{\xi}\right. \\ \left.-\int_0^\infty (v^j_{3_m}-v^j_{1_m})\bar{\xi}J_{m-1}(\bar{p}\bar{\xi}\bar{r})d\bar{\xi}\right\}e^{im\theta} \tag{7.114}$$

$$\bar{u}_z\left(\bar{r},\theta,\bar{z};\bar{s};\bar{p};j\right)=\sum_{m=-1}^{1}\left\{\int_0^\infty v^j_{2_m}\bar{\xi}J_m(\bar{p}\bar{\xi}\bar{r})d\bar{\xi}\right\}e^{im\theta}, \tag{7.115}$$

$$\bar{\tau}_{rr}(\bar{r},\theta,\bar{z};\bar{s};\bar{p};j)+\frac{1}{\bar{p}}\frac{2}{\bar{r}}\sum_{m=-1}^{1}\left\{\bar{u}_{r_m}+im\bar{u}_{\theta_m}\right\}e^{im\theta}=\sum_{m=-1}^{1}\left\{\int_0^\infty\left(\sigma^j_{11_m}\right)\bar{\xi}J_m(\bar{p}\bar{\xi}\bar{r})d\bar{\xi}\right\}e^{im\theta} \tag{7.116}$$

$$\bar{\tau}_{\theta\theta}(\bar{r},\theta,\bar{z};\bar{s};\bar{p};j)-\frac{1}{\bar{p}}\frac{2}{\bar{r}}\sum_{m=-1}^{1}\left\{\bar{u}_{r_m}+im\bar{u}_{\theta_m}\right\}e^{im\theta}=\sum_{m=-1}^{1}\left\{\int_0^\infty\left(\sigma^j_{33_m}\right)\bar{\xi}J_m(\bar{p}\bar{\xi}\bar{r})d\bar{\xi}\right\}e^{im\theta} \tag{7.117}$$

$$\bar{\tau}_{zz}(\bar{r},\theta,\bar{z};\bar{s};\bar{p};j)=\sum_{m=-1}^{1}\left\{\int_0^\infty\left(\sigma^j_{22_m}\right)\bar{\xi}J_m(\bar{p}\bar{\xi}\bar{r})d\bar{\xi}\right\}e^{im\theta} \tag{7.118}$$

$$\bar{\tau}_{r\theta}(\bar{r},\theta,\bar{z};\bar{s};\bar{p};j)+\frac{1}{\bar{p}}\frac{2}{\bar{r}}\sum_{m=-1}^{1}\left\{\bar{u}_{\theta_m}-im\bar{u}_{r_m}\right\}e^{im\theta}=\sum_{m=-1}^{1}\left\{\int_0^\infty\left(\sigma^j_{13_m}\right)\bar{\xi}J_m(\bar{p}\bar{\xi}\bar{r})d\bar{\xi}\right\}e^{im\theta} \tag{7.119}$$

$$\bar{\tau}_{rz}(\bar{r},\theta,\bar{z};\bar{s};\bar{p};j)=\frac{1}{2}\sum_{m=-1}^{1}\left\{\int_0^\infty\left(\sigma^j_{23_m}+\sigma^j_{21_m}\right)\bar{\xi}J_{m+1}(\bar{p}\bar{\xi}\bar{r})d\bar{\xi}\right. \\ \left.+\int_0^\infty\left(\sigma^j_{23_m}-\sigma^j_{21_m}\right)\bar{\xi}J_{m-1}(\bar{p}\bar{\xi}\bar{r})d\bar{\xi}\right\}e^{im\theta} \tag{7.120}$$

$$\bar{\tau}_{\theta z}(\bar{r},\theta,\bar{z};\bar{s};\bar{p};j)=\frac{-i}{2}\sum_{m=-1}^{1}\left\{\int_0^\infty\left(\sigma^j_{23_m}+\sigma^j_{21_m}\right)\bar{\xi}J_{m+1}(\bar{p}\bar{\xi}\bar{r})d\bar{\xi}\right. \\ \left.-\int_0^\infty\left(\sigma^j_{23_m}-\sigma^j_{21_m}\right)\bar{\xi}J_{m-1}(\bar{p}\bar{\xi}\bar{r})d\bar{\xi}\right\}e^{im\theta} \tag{7.121}$$

Here, the dimensionless transformed displacement kernels $v^j_{i_m},\ i=1,2,3$ and stress kernels $\sigma^j_{ik_m},\ i,k=1,2,3$ are obtained via Eqns. (7.20) and (7.21) respectively. For a specified point-load, the integral representations in the above equations can be simplified upon the substitution of the corresponding loading coefficients.

- Unit load in x_1- direction

$$\bar{u}_r\left(\bar{r},\theta,\bar{z};\bar{s};\bar{p};j\right)=\cos(\theta)I^h_r\left(\bar{r},\bar{z};\bar{s};\bar{p};j\right), \tag{7.122}$$

$$\bar{u}_\theta\left(\bar{r},\theta,\bar{z};\bar{s};\bar{p};j\right)=-\sin(\theta)I^h_\theta\left(\bar{r},\bar{z};\bar{s};\bar{p};j\right), \tag{7.123}$$

$$\bar{u}_z\left(\bar{r},\theta,\bar{z};\bar{s};\bar{p};j\right)=2\cos(\theta)I_z^h\left(\bar{r},\bar{z};\bar{s};\bar{p};j\right), \tag{7.124}$$

- Unit load in $x_2 -$ direction

$$\bar{u}_r\left(\bar{r},\theta,\bar{z};\bar{s};\bar{p};j\right)=\sin(\theta)I_r^h\left(\bar{r},\bar{z};\bar{s};\bar{p};j\right), \tag{7.125}$$

$$\bar{u}_\theta\left(\bar{r},\theta,\bar{z};\bar{s};\bar{p};j\right)=\cos(\theta)I_\theta^h\left(\bar{r},\bar{z};\bar{s};\bar{p};j\right), \tag{7.126}$$

$$\bar{u}_z\left(\bar{r},\theta,\bar{z};\bar{s};\bar{p};j\right)=2\sin(\theta)I_z^h\left(\bar{r},\bar{z};\bar{s};\bar{p};j\right), \tag{7.127}$$

- Unit load in $x_3 -$ direction

$$\bar{u}_r\left(\bar{r},\theta,\bar{z};\bar{s};\bar{p};j\right)=I_r^{\mathrm{v}}\left(\bar{r},\bar{z};\bar{s};\bar{p};j\right), \tag{7.128}$$

$$\bar{u}_\theta\left(\bar{r},\theta,\bar{z};\bar{s};\bar{p};j\right)=0, \tag{7.129}$$

$$\bar{u}_z\left(\bar{r},\theta,\bar{z};\bar{s};\bar{p};j\right)=I_z^{\mathrm{v}}\left(\bar{r},\bar{z};\bar{s};\bar{p};j\right), \tag{7.130}$$

where

$$I_r^h\left(\bar{r},\bar{z};\bar{s};\bar{p};j\right)=\int_0^\infty(v^j_{3_{m=1}}-v^j_{1_{m=1}})\bar{\xi}J_0(\bar{p}\bar{\xi}\bar{r})d\bar{\xi}+\int_0^\infty(v^j_{3_{m=1}}+v^j_{1_{m=1}})\bar{\xi}J_2(\bar{p}\bar{\xi}\bar{r})d\bar{\xi}\ , \tag{7.131}$$

$$I_\theta^h\left(\bar{r},\bar{z};\bar{s};\bar{p};j\right)=\int_0^\infty(v^j_{3_{m=1}}-v^j_{1_{m=1}})\bar{\xi}J_0(\bar{p}\bar{\xi}\bar{r})d\bar{\xi}-\int_0^\infty(v^j_{3_{m=1}}+v^j_{1_{m=1}})\bar{\xi}J_2(\bar{p}\bar{\xi}\bar{r})d\bar{\xi}\ , \tag{7.132}$$

$$I_z^h\left(\bar{r},\bar{z};\bar{s};\bar{p};j\right)=\int_0^\infty(v^j_{2_{m=1}})\bar{\xi}J_1(\bar{p}\bar{\xi}\bar{r})d\bar{\xi}\ , \tag{7.133}$$

$$I_r^{\mathrm{v}}\left(\bar{r},\bar{z};\bar{s};\bar{p};j\right)=\int_0^\infty(v^j_{1_{m=0}})\bar{\xi}J_1(\bar{p}\bar{\xi}\bar{r})d\bar{\xi}\ , \tag{7.134}$$

$$I_z^{\mathrm{v}}\left(\bar{r},\bar{z};\bar{s};\bar{p};j\right)=\int_0^\infty(v^j_{2_{m=0}})\bar{\xi}J_0(\bar{p}\bar{\xi}\bar{r})d\bar{\xi}\ . \tag{7.135}$$

It is worth mentioning that the loading coefficients in Eqn. (7.109) are used for I_r^h, I_θ^h and I_z^h, while loading coefficients in Eqn. (7.111) are adopted for I_r^{v} and I_z^{v}. As pointed out in Eqn. (7.106), the integration coefficients $a_m^j\left(\bar{\xi},\bar{z},\bar{p}\right)$, $b_m^j\left(\bar{\xi},\bar{z},\bar{p}\right)$, $c_m^j\left(\bar{\xi},\bar{z},\bar{p}\right)$, $d_m^j\left(\bar{\xi},\bar{z},\bar{p}\right)$, $e_m^j\left(\bar{\xi},\bar{z},\bar{p}\right)$, $f_m^j\left(\bar{\xi},\bar{z},\bar{p}\right)$ are expressed by infinite series, thus as consequences, the integrals I_r^h,

I_θ^h, I_z^h, I_r^{v} and I_z^{v} are all infinite series. Accordingly, the functions I_r^h, I_θ^h, I_z^h, I_r^{v} and I_z^{v} are infinite series of integrals as well.

7.7.3 Inversion to time domain solution by Cagniard's idea

As mentioned above, the multi-layer Green's function solutions in the Laplace transform domain are now in the form of infinite series of integrals. To obtain their time domain counterparts, one may apply the Cagniard-Hankel method developed in Chapter 6 term by term in ascending order of time. The usage of it to invert term corresponding to a generalized ray is presented as follows.

Consider a term with given n_T, M_i, $\overline{c}_k$ and d_k as described in Eqn. (7.106). One can determine the dimensionless displacements and stresses in the transformed domain through Eqns. (7.20) and (7.21). Taking $I_r^h\left(\overline{r},\overline{z};\overline{s};\overline{p};j\right)$ in Eqn. (7.131) as an example, a process utilizing the proposed Cagniard method to -obtain time-domain counterpart will be illustrated.

As explained in Chapter 6, it is useful for the inversion to replace the Bessel functions with their integral representations, i.e.,

$$J_0\left(z\right)=\frac{2}{\pi}\mathrm{Re}\left((1-i\zeta)\int_0^{\pi/2}e^{iz\cos[(1-i\zeta)\Phi]}d\Phi\right) \tag{7.136}$$

$$J_1\left(z\right)=-\frac{2}{\pi}\mathrm{Re}\left(i(1-i\zeta)\int_0^{\pi/2}e^{iz\cos[(1-i\zeta)\Phi]}\cos[(1-i\zeta)\Phi]d\Phi\right), \tag{7.137}$$

$$J_2\left(z\right)=-\frac{2}{\pi}\mathrm{Re}\left((1-i\zeta)\int_0^{\pi}e^{iz\cos[(1-i\zeta)\Phi]}\cos[2(1-i\zeta)\Phi]d\Phi\right), \tag{7.138}$$

where z is an arbitrary complex argument and ζ is an arbitrary non-negative real number, such that Eqn. (7.131) becomes

$$I_r^h\left(\bar{r},\bar{z};\bar{s};\bar{p};j\right)=\frac{2}{\pi}\mathrm{Re}\left\{(1-i\zeta)\int_0^{\pi/2}\int_0^{\infty}N(\bar{\xi},\Phi)e^{-\bar{p}\left[\sum_{k=1}^{n_S}d_k\sqrt{\bar{\xi}^2+\frac{1}{\bar{c}_k^2}}-i\bar{\xi}\bar{r}\cos[(1-i\zeta)\Phi]\right]}d\bar{\xi}\,d\Phi\right\}, \quad (7.139)$$

where

$$N(\bar{\xi},\Phi)=\bar{\xi}\left[v_{3_{m=1}}^{j\mathcal{N}}(\bar{\xi})\left(1-\cos[2(1-i\zeta)\Phi]\right)-v_{1_{m=1}}^{j\mathcal{N}}(\bar{\xi})\left(1+\cos[2(1-i\zeta)\Phi]\right)\right]. \quad (7.140)$$

As noted before, the idea of Cagniard's inversion approach is to extend the inner integrations in Eqn. (7.139) with respect to $\bar{\xi}$ to the complex plane and arrange the integrands into a Laplace transform format so that their time domain counterparts $\mathcal{I}_r^h\left(\bar{r},\bar{z};\bar{s};\bar{t};j\right)$ can be clearly identified. To achieve the goal, the improper inner integral is first extended to the complex $\bar{\xi}$-plane and a path is sought such that its exponential kernel is identical to the standard Laplace transform kernel of $e^{-\bar{p}\bar{t}}$, i.e.,

$$\bar{t}=\sum_{k=1}^{n_T}d_k\sqrt{\bar{\xi}^2+\frac{1}{\bar{c}_k^2}}-i\bar{\xi}\bar{r}\cos[(1-i\zeta)\Phi], \quad (7.141)$$

where $\bar{t}$ is real and ≥ 0. For $\sum_{k=1}^{n_T}\frac{d_k}{c_k}\leq\bar{t}\leq\infty$, Eqn. (7.141) represents a contour in the first quadrant of complex $\bar{\xi}$-plane as shown in Figure 7.2.

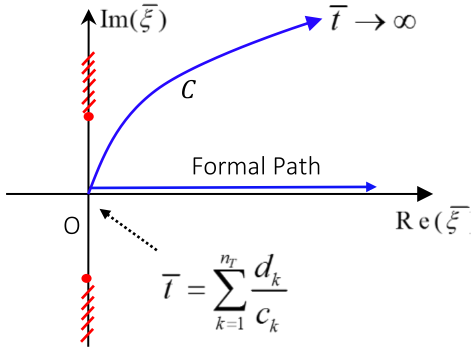

Figure 7.2: *Cagniard path.*

By means of the principle of the argument, it can be checked that the inner integrand in Eqn. (7.139), i.e., $N(\bar{\xi},\Phi)$, has no singularity in the first quadrant. Consequently, by virtue of Cauchy's theorem and Jordan's lemma, the formal integration path of the inner integral in Eqn. (7.139) can be deformed to C, such that it becomes

$$I_r^h\left(\bar{r},\bar{z};\bar{s};\bar{p};j\right)=\frac{2}{\pi}\mathrm{Re}\left\{(1-i\zeta)\int_0^{\pi/2}\int_{C(\Phi)}N(\bar{\xi},\Phi)e^{-\bar{p}\left[\sum_{k=1}^{n_T}d_k\sqrt{\bar{\xi}^2+\frac{1}{\bar{c}_k^2}}-i\bar{\xi}\bar{r}\cos[(1-i\zeta)\Phi]\right]}d\bar{\xi}\,d\Phi\right\}. \quad (7.142)$$

Then, changing the variable of integration from $\bar{\xi}$ to $\bar{t}$, one obtains from Eqn. (7.142) that

$$I_r^h\left(\bar{r},\bar{z};\bar{s};\bar{p};j\right)=\frac{2}{\pi}\mathrm{Re}\left\{(1-i\zeta)\int_0^{\pi/2}\int_{\bar{t}^*}^{\infty}N(\bar{\xi},\Phi)\frac{d\bar{\xi}}{d\bar{t}}e^{-\bar{p}\bar{t}}d\bar{t}\,d\Phi\right\}, \qquad (7.143)$$

where $\bar{\xi}$ is obtained from Eqn. (7.141) using numerical method and

$$\bar{t}^*=\sum_{k=1}^{n_T}\frac{d_k}{c_k}. \qquad (7.144)$$

Interchanging the order of integration between Φ and $\bar{t}$ furnishes that

$$I_r^h\left(\bar{r},\bar{z};\bar{s};\bar{p};j\right)=\frac{2}{\pi}\int_{\bar{t}^*}^{\infty}\mathrm{Re}\left\{(1-i\zeta)\int_0^{\pi/2}N(\bar{\xi},\Phi)\frac{d\bar{\xi}}{d\bar{t}}d\Phi\right\}e^{-\bar{p}\bar{t}}d\bar{t}. \qquad (7.145)$$

Clearly, Eqn. (7.145) bears a general form of Laplace transform

$$I_r^h\left(\bar{r},\bar{z};\bar{s};\bar{p};j\right)=\int_0^\infty \mathcal{I}_r^h\left(\bar{r},\bar{z};\bar{s};\bar{t};j\right)e^{-\bar{p}\bar{t}}d\bar{t}\;, \tag{7.146}$$

with time function being

$$\mathcal{I}_r^h\left(\bar{r},\bar{z};\bar{s};\bar{t};j\right)=\frac{2}{\pi}H\left(\bar{t}-\bar{t}^*\right)\mathrm{Re}\left\{(1-i\zeta)\int_0^{\pi/2}N\left(\bar{\xi},\Phi\right)\frac{d\bar{\xi}}{d\bar{t}}d\Phi\right\}. \tag{7.147}$$

As illustrated in Chapter 6, there exists a finite time $\bar{t}_{\text{arrival}}$ such that

$$\mathcal{I}_r^h\left(\bar{r},\bar{z};\bar{s};\bar{t};j\right)=0,\ \forall\bar{t}<\bar{t}_{\text{arrival}}\,. \tag{7.148}$$

Physically, $\bar{t}_{\text{arrival}}$ is interpreted as the arrival time of this group of waves before which they do not contribute to the response. One way to compute $\bar{t}_{\text{arrival}}$ is by the analytical treatment on Eqn. (7.147), and the other way is by Snell's law as illustrated in the next section. It can be shown in Section 7.7.5 that

$$\bar{t}_{\text{arrival}}\geq\bar{t}^*, \tag{7.149}$$

So that Eqn. (7.147) can be written as

$$\mathcal{I}_r^h\left(\bar{r},\bar{z};\bar{s};\bar{t};j\right)=\frac{2}{\pi}H\left(\bar{t}-\bar{t}_{\text{arrival}}\right)\mathrm{Re}\left\{(1-i\zeta)\int_0^{\pi/2}N\left(\bar{\xi},\Phi\right)\frac{d\bar{\xi}}{d\bar{t}}d\Phi\right\}. \tag{7.150}$$

7.7.4 Computation of time-domain response and characteristics of multi-layer Green's functions

Following the same Laplace transform inversion procedure, one can invert $I_r^h\left(\bar{r},\bar{z};\bar{s};\bar{p};j\right)$, $I_\theta^h\left(\bar{r},\bar{z};\bar{s};\bar{p};j\right)$, $I_z^h\left(\bar{r},\bar{z};\bar{s};\bar{p};j\right)$, $I_r^{\mathrm{v}}\left(\bar{r},\bar{z};\bar{s};\bar{p};j\right)$ and $I_z^{\mathrm{v}}\left(\bar{r},\bar{z};\bar{s};\bar{p};j\right)$ term wisely to time domain and obtain the time domain counterparts as $\mathcal{I}_r^h\left(\bar{r},\bar{z};\bar{s};\bar{t};j\right)$, $\mathcal{I}_\theta^h\left(\bar{r},\bar{z};\bar{s};\bar{t};j\right)$, $\mathcal{I}_z^h\left(\bar{r},\bar{z};\bar{s};\bar{t};j\right)$, $\mathcal{I}_r^v\left(\bar{r},\bar{z};\bar{s};\bar{t};j\right)$, $\mathcal{I}_z^v\left(\bar{r},\bar{z};\bar{s};\bar{t};j\right)$. By virtue of Eqns. (7.122)-(7.130), the displacements in time domain can then be obtained to be

- Unit load in $x_1 -$ direction

$$\bar{u}_r\left(\bar{r},\theta,\bar{z};\bar{s};\bar{t};j\right)=\cos(\theta)\mathcal{I}_r^h\left(\bar{r},\bar{z};\bar{s};\bar{t};j\right), \tag{7.151}$$

$$\bar{u}_\theta\left(\bar{r},\theta,\bar{z};\bar{s};\bar{t};j\right)=-\sin(\theta)\mathcal{I}_\theta^h\left(\bar{r},\bar{z};\bar{s};\bar{t};j\right), \tag{7.152}$$

$$\bar{u}_z\left(\bar{r},\theta,\bar{z};\bar{s};\bar{t};j\right)=2\cos(\theta)\mathcal{I}_z^h\left(\bar{r},\bar{z};\bar{s};\bar{t};j\right), \tag{7.153}$$

- Unit load $x_2 -$ direction

$$\bar{u}_r\left(\bar{r},\theta,\bar{z};\bar{s};\bar{t};j\right)=\sin(\theta)\mathcal{I}_r^h\left(\bar{r},\bar{z};\bar{s};\bar{t};j\right), \tag{7.154}$$

$$\bar{u}_\theta\left(\bar{r},\theta,\bar{z};\bar{s};\bar{t};j\right)=\cos(\theta)\mathcal{I}_\theta^h\left(\bar{r},\bar{z};\bar{s};\bar{t};j\right), \tag{7.155}$$

$$\bar{u}_z\left(\bar{r},\theta,\bar{z};\bar{s};\bar{t};j\right)=2\sin(\theta)\mathcal{I}_z^h\left(\bar{r},\bar{z};\bar{s};\bar{t};j\right), \tag{7.156}$$

- Unit load in $x_3 -$ direction

$$\bar{u}_r\left(\bar{r},\theta,\bar{z};\bar{s};\bar{t};j\right)=\mathcal{I}_r^{\mathrm{v}}\left(\bar{r},\bar{z};\bar{s};\bar{t};j\right), \tag{7.157}$$

$$\bar{u}_\theta\left(\bar{r},\theta,\bar{z};\bar{s};\bar{t};j\right)=0, \tag{7.158}$$

$$\bar{u}_z\left(\bar{r},\theta,\bar{z};\bar{s};\bar{t};j\right)=\mathcal{I}_z^{\mathrm{v}}\left(\bar{r},\bar{z};\bar{s};\bar{t};j\right). \tag{7.159}$$

Viewing that $\mathcal{I}_r^h\left(\bar{r},\bar{z};\bar{s};\bar{t};j\right)$, $\mathcal{I}_\theta^h\left(\bar{r},\bar{z};\bar{s};\bar{t};j\right)$, $\mathcal{I}_z^h\left(\bar{r},\bar{z};\bar{s};\bar{t};j\right)$, $\mathcal{I}_r^v\left(\bar{r},\bar{z};\bar{s};\bar{t};j\right)$, and $\mathcal{I}_z^v\left(\bar{r},\bar{z};\bar{s};\bar{t};j\right)$ are infinite series bearing the form in Eqn. (7.150), the displacements and stresses in time domain can be written as

$$\begin{aligned}\mathbf{u}\left(\bar{r},\theta,\bar{z};\bar{s};\bar{t}\right)&=\sum_{n=1}^{\infty}\left[H(\bar{t}-\bar{t}_{\text{arrival}}^{n})\mathbf{\bar{u}}^{n}\left(\bar{r},\theta,\bar{z};\bar{s};\bar{t}\right)\right]\\ \boldsymbol{\tau}\left(\bar{r},\theta,\bar{z};\bar{s};\bar{t}\right)&=\sum_{n=1}^{\infty}\left[H(\bar{t}-\bar{t}_{\text{arrival}}^{n})\boldsymbol{\tau}^{n}\left(\bar{r},\theta,\bar{z};\bar{s};\bar{t}\right)\right]\end{aligned}, \tag{7.160}$$

where the n^{th} term of the series is zero for $\bar{t}-\bar{t}_{\text{arrival}}^{n}$, i.e., the wave group corresponding to n^{th} term has no contribution to the response before they arrive at the observation point. To exploit such a property, it is proper to order the series by the term's arrival times in ascending order that wave group arriving earlier appears in the series before the later ones. When the series is kept up to n terms, the solution is exact for $\bar{t} \in [0, \bar{t}^{n}_{arrival}]$ and an approximation beyond it. Should one desire the exact solution for an arbitrary $\bar{t}$, one needs to determine analytically and retain only those terms that have $\bar{t}^{n}_{arrival} \geq \bar{t}$.

7.7.5 Arrival times of different wave groups

A general term of the infinite series for $\mathcal{I}^{h}_{r}\left(\bar{r},\bar{z};\bar{s};\bar{t};j\right)$, $\mathcal{I}^{h}_{\theta}\left(\bar{r},\bar{z};\bar{s};\bar{t};j\right)$, $\mathcal{I}^{h}_{z}\left(\bar{r},\bar{z};\bar{s};\bar{t};j\right)$, $\mathcal{I}^{v}_{r}\left(\bar{r},\bar{z};\bar{s};\bar{t};j\right)$, and $\mathcal{I}^{v}_{z}\left(\bar{r},\bar{z};\bar{s};\bar{t};j\right)$ can all be written as

$$\mathcal{I}\left(\bar{r},\bar{z};\bar{s};\bar{t}\right) = \frac{2}{\pi}\mathrm{Re}\left\{(1-i\zeta)\int_{0}^{\pi/2} N(\bar{\xi},\phi)\frac{d\bar{\xi}}{d\bar{t}}\,d\phi\right\} \tag{7.161}$$

where $N(\bar{\xi},\phi)$ is the relevant coefficient in the product of the multi-layer transmission/reflection matrices, and $\bar{\xi}$ is sought from

$$\bar{t} = \sum_{k=1}^{K} d_k \sqrt{\bar{\xi}^2 + \frac{1}{\bar{c}_k^2}} - i\bar{\xi}\bar{r}\cos\left[(1-i\zeta)\phi\right]. \tag{7.162}$$

on the condition that $\bar{t}$ is positive and real. For a chosen contour parameter ζ and a given $\bar{t}$, Eqn. (7.162) translates to a contour path D in the complex $\bar{\xi}$ −plane as ϕ goes from 0 to $\pi/2$ (see Figure 7.3). Following a similar analysis for all 6 wave-integrals for the homogeneous half-space Green's function, it can be shown that then one has $\mathcal{I}\left(\bar{r},\bar{z};\bar{s};\bar{t}\right)=0$, if Point A or $\bar{\xi}_0$ of the path D is located on the imaginary axis but below all the branch points and singularities in $N(\bar{\xi},\phi)$.

Accordingly, one may refer to the time $\bar{t}$ which corresponds to such a position of Point A as the arrival time $\bar{t}_{arrival}$. Should A be at the lowest branch point, the corresponding time $\bar{t}_{arrival}$ is given by

$$\bar{t}_{arrival} = \sum_{k=1}^{K} d_k \sqrt{\frac{1}{\bar{c}_k^2} - \frac{1}{\bar{c}_m^2}} + \frac{\bar{r}}{\bar{c}_m}. \tag{7.163}$$

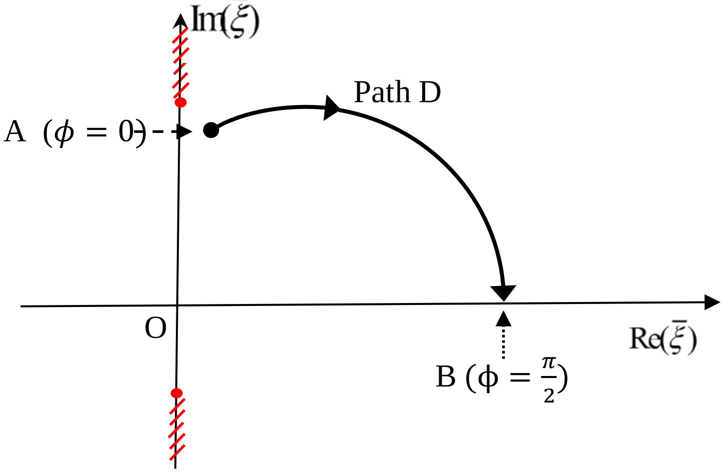

Figure 7.3: Integration path in $\bar{\xi}$ −plane for increasing ϕ from 0 to $\pi/2$.

To seek the highest location of $\bar{\xi}_0$ on the imaginary axis, one may note that the time corresponding to the starting point $\bar{\xi}_0$ at $\phi = 0$ is

$$\bar{t} = \sum_{k=1}^{K} d_k \sqrt{\bar{\xi}^2 + \frac{1}{\bar{c}_k^2}} - i\bar{\xi}\bar{r} \; , \qquad (7.164)$$

according to Eqn. (7.162) and set $\bar{\xi}_0 = ia$ -with a being real. This leads to

$$\bar{t} = \sum_{k=1}^{K} d_k \sqrt{\frac{1}{\bar{c}_k^2} - a^2} + a\bar{r} \; , \qquad (7.165)$$

which will stay real and positive, provided $0 \le a < \left(\frac{1}{\bar{c}_{\max}} \right)$. To find the maximum a and thus $\bar{t}_{max}$, within the range, one may set the derivative of Eqn. (7.177) with respect to a to zero, leading to the condition that

$$\sum_{k=1}^{K} \frac{d_k a_{\mathrm{A}}}{\sqrt{\frac{1}{\bar{c}_k^2} - a_{\mathrm{A}}^2}} = \bar{r} \; , \qquad (7.166)$$

whose solution is straightforward numerically. The true arrival time $\bar{t}$ will thus be the time that corresponds to the smaller a in Eqn. (7.165) and solution of (7.166).

In practice, while the number of terms in the series representation of $\mathbf{w}^{j}_{d_m}\left(\bar{\xi},\bar{p}\right)$, $\mathbf{w}^{j}_{u_m}\left(\bar{\xi},\bar{p}\right)$, $w^{j}_{d_m}\left(\bar{\xi},\bar{p}\right)$, $w^{j}_{u_m}\left(\bar{\xi},\bar{p}\right)$ is infinite, only a finite number of terms will be non-zero during a finite observation time. Accordingly, to get the response at a certain time of interest, only the terms whose corresponding waves arrive before the time are needed to be included.

7.8 Numerical examples

7.8.1 Example 1

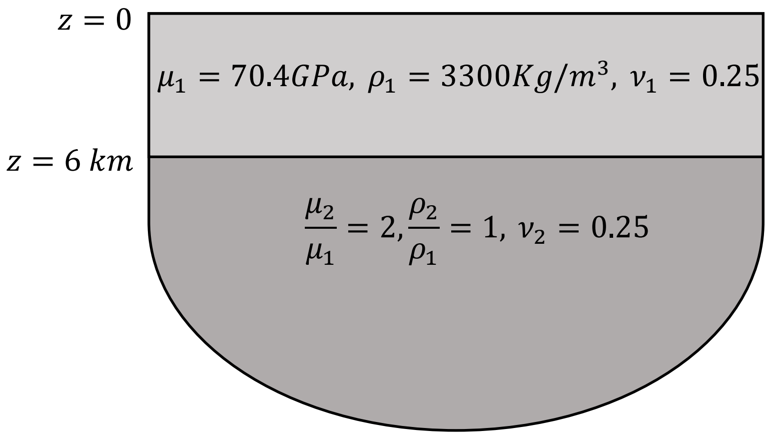

Figure 7.4: A 2-layer half-space

As shown in Figure 7.4, a two-layer half-space (a single layer on top of a homogeneous half-space) is considered. The point-load is put at $(0,0,2)$ and the observation is taken at $(10,0,4)$ in kilometers. To validate the proposed formulation, time function of the point-load is set to be $f(t) = F \cdot B(t)$, where $B(t)$ is the cubic B-Spline function, i.e.,

$$B(t)=\begin{cases} \dfrac{32}{3}\dfrac{t^3}{\Delta T^3}, & 0\le t<\Delta T/4, \\ -32\dfrac{t^3}{\Delta T^3}+32\dfrac{t^2}{\Delta T^2}-8\dfrac{t}{\Delta T}+\dfrac{2}{3}, & \Delta T/4\le t<2\Delta T/4, \\ 32\dfrac{t^3}{\Delta T^3}-64\dfrac{t^2}{\Delta T^2}+40\dfrac{t}{\Delta T}-\dfrac{22}{3}, & 2\Delta T/4\le t<3\Delta T/4, \\ -\dfrac{32}{3}\dfrac{t^3}{\Delta T^3}+32\dfrac{t^2}{\Delta T^2}-32\dfrac{t}{\Delta T}+\dfrac{32}{3}, & 3\Delta T/4\le t\le \Delta T, \\ 0, & \text{elsewhere}, \end{cases} \tag{7.167}$$

with $\Delta T = 0.3\sec$.

As illustrations, the terms of the series in Eqn. (7.160) are sorted in an ascending order by the corresponding arrival times, the first several of which are listed in Table 7.1. To distinguish the terms, upward-going and downward-going longitudinal waves are denoted as P and p respectively, while the upward-going and downward-going shear waves are denoted as S and s respectively. The waves depart from the source point and then arrive at observation point. For example, a pP-wave denotes a P-wave that first departs downward from the source point as a down-going longitudinal wave, then gets reflected back by the interface between the two layers and arrives at the observation point.

Order	Arrival time (sec)	Wave types	Number of d_k terms	Exponent of exponential functions
1	1.2744	p	1	$-\bar{p}\left[(\bar{z}-\bar{s})\bar{\alpha}_1-i\bar{\xi}\bar{r}\cos[(1-i\zeta)\phi]\right]$
2	1.4138	pP	2	$-\bar{p}\left[(\bar{z}_1-\bar{s})\bar{\alpha}_1+(\bar{z}_1-\bar{z})\bar{\alpha}_1-i\bar{\xi}\bar{r}\cos[(1-i\zeta)\phi]\right]$
3	1.4574	Pp	2	$-\bar{p}\left[(\bar{s}-\bar{z}_0)\bar{\alpha}_1+(\bar{z}-\bar{z}_0)\bar{\alpha}_1-i\bar{\xi}\bar{r}\cos[(1-i\zeta)\phi]\right]$
4	1.6323	pS	2	$-\bar{p}\left[(\bar{z}_1-\bar{s})\bar{\alpha}_1+(\bar{z}_1-\bar{z})\bar{\beta}_1-i\bar{\xi}\bar{r}\cos[(1-i\zeta)\phi]\right]$
5	1.7128	Sp	2	$-\bar{p}\left[(\bar{s}-\bar{z}_0)\bar{\beta}_1+(\bar{z}-\bar{z}_0)\bar{\alpha}_1-i\bar{\xi}\bar{r}\cos[(1-i\zeta)\phi]\right]$
6	1.7673	PpP	3	$-\bar{p}\left[(\bar{s}-\bar{z}_0)\bar{\alpha}_1+(\bar{z}_1-\bar{z}_0)\bar{\alpha}_1+(\bar{z}_1-\bar{z})\bar{\alpha}_1-i\bar{\xi}\bar{r}\cos[(1-i\zeta)\phi]\right]$
7	1.8507	sP	2	$-\bar{p}\left[(\bar{z}_1-\bar{s})\bar{\beta}_1+(\bar{z}_1-\bar{z})\bar{\alpha}_1-i\bar{\xi}\bar{r}\cos[(1-i\zeta)\phi]\right]$
8	1.9858	PpS	3	$-\bar{p}\left[(\bar{s}-\bar{z}_0)\bar{\alpha}_1+(\bar{z}_1-\bar{z}_0)\bar{\alpha}_1+(\bar{z}_1-\bar{z})\bar{\beta}_1-i\bar{\xi}\bar{r}\cos[(1-i\zeta)\phi]\right]$
9	1.9858	SpP	3	$-\bar{p}\left[(\bar{s}-\bar{z}_0)\bar{\beta}_1+(\bar{z}_1-\bar{z}_0)\bar{\alpha}_1+(\bar{z}_1-\bar{z})\bar{\alpha}_1-i\bar{\xi}\bar{r}\cos[(1-i\zeta)\phi]\right]$
10	1.9905	Ps	2	$-\bar{p}\left[(\bar{s}-\bar{z}_0)\bar{\alpha}_1+(\bar{z}-\bar{z}_0)\bar{\beta}_1-i\bar{\xi}\bar{r}\cos[(1-i\zeta)\phi]\right]$
11	2.0692	sS	2	$-\bar{p}\left[(\bar{z}_1-\bar{s})\bar{\beta}_1+(\bar{z}_1-\bar{z})\bar{\beta}_1-i\bar{\xi}\bar{r}\cos[(1-i\zeta)\phi]\right]$
12	2.1500	pPp	3	$-\bar{p}\left[(\bar{z}_1-\bar{s})\bar{\alpha}_1+(\bar{z}_1-\bar{z}_0)\bar{\alpha}_1+(\bar{z}-\bar{z}_0)\bar{\alpha}_1-i\bar{\xi}\bar{r}\cos[(1-i\zeta)\phi]\right]$
13	2.2042	SpS	3	$-\bar{p}\left[(\bar{s}-\bar{z}_0)\bar{\beta}_1+(\bar{z}_1-\bar{z}_0)\bar{\alpha}_1+(\bar{z}_1-\bar{z})\bar{\beta}_1-i\bar{\xi}\bar{r}\cos[(1-i\zeta)\phi]\right]$
14	2.2074	s	1	$-\bar{p}\left[(\bar{z}-\bar{s})\bar{\beta}_1-i\bar{\xi}\bar{r}\cos[(1-i\zeta)\phi]\right]$
15	2.3101	Ss	2	$-\bar{p}\left[(\bar{s}-\bar{z}_0)\bar{\beta}_1+(\bar{z}-\bar{z}_0)\bar{\beta}_1-i\bar{\xi}\bar{r}\cos[(1-i\zeta)\phi]\right]$
16	2.4227	PsP	3	$-\bar{p}\left[(\bar{s}-\bar{z}_0)\bar{\alpha}_1+(\bar{z}_1-\bar{z}_0)\bar{\beta}_1+(\bar{z}_1-\bar{z})\bar{\alpha}_1-i\bar{\xi}\bar{r}\cos[(1-i\zeta)\phi]\right]$
17	2.5646	sPp	3	$-\bar{p}\left[(\bar{z}_1-s)\bar{\beta}_1+(\bar{z}_1-\bar{z}_0)\bar{\alpha}_1+(\bar{z}_1-\bar{z})\bar{\alpha}_1-i\bar{\xi}\bar{r}\cos[(1-i\zeta)\phi]\right]$
18	2.5646	pPs	3	$-\bar{p}\left[(\bar{z}_1-s)\bar{\alpha}_1+(\bar{z}_1-\bar{z}_0)\bar{\alpha}_1+(\bar{z}_1-\bar{z})\bar{\beta}_1-i\bar{\xi}\bar{r}\cos[(1-i\zeta)\phi]\right]$
19	2.5732	pPpP	4	$-\bar{p}\left[(\bar{z}_1-s)\bar{\alpha}_1+2(\bar{z}_1-\bar{z}_0)\bar{\alpha}_1+(\bar{z}_1-\bar{z})\bar{\alpha}_1-i\bar{\xi}\bar{r}\cos[(1-i\zeta)\phi]\right]$
20	2.5732	PpPp	4	$-\bar{p}\left[(\bar{s}-\bar{z}_0)\bar{\alpha}_1+2(\bar{z}_1-\bar{z}_0)\bar{\alpha}_1+(\bar{z}-\bar{z}_0)\bar{\alpha}_1-i\bar{\xi}\bar{r}\cos[(1-i\zeta)\phi]\right]$
21	2.6411	PsS	3	$-\bar{p}\left[(\bar{s}-\bar{z}_0)\bar{\alpha}_1+(\bar{z}_1-\bar{z}_0)\bar{\beta}_1+(\bar{z}_1-\bar{z})\bar{\beta}_1-i\bar{\xi}\bar{r}\cos[(1-i\zeta)\phi]\right]$
22	2.6411	SsP	3	$-\bar{p}\left[(\bar{s}-\bar{z}_0)\bar{\beta}+(\bar{z}_1-\bar{z}_0)\bar{\beta}_1+(\bar{z}_1-\bar{z})\bar{\alpha}_1-i\bar{\xi}\bar{r}\cos[(1-i\zeta)\phi]\right]$
23	2.7710	SpPp	4	$-\bar{p}\left[(\bar{s}-\bar{z}_0)\bar{\beta}+2(\bar{z}_1-\bar{z}_0)_1\bar{\alpha}_1+(\bar{z}-\bar{z}_0)\bar{\alpha}_1-i\bar{\xi}\bar{r}\cos[(1-i\zeta)\phi]\right]$
24	2.7710	pPpS	4	$-\bar{p}\left[(\bar{s}-\bar{z}_0)\bar{\alpha}_1+2(\bar{z}_1-\bar{z}_0)\bar{\alpha}_1+(\bar{z}-\bar{z}_0)\bar{\beta}_1-i\bar{\xi}\bar{r}\cos[(1-i\zeta)\phi]\right]$
25	2.7772	pSp	3	$-\bar{p}\left[(\bar{z}_1-s)\bar{\alpha}_1+(\bar{z}_1-\bar{z}_0)\bar{\beta}_1+(\bar{z}_1-\bar{z})\bar{\alpha}_1-i\bar{\xi}\bar{r}\cos[(1-i\zeta)\phi]\right]$
26	2.8569	SsS	3	$-\bar{p}\left[(\bar{s}-\bar{z}_0)\bar{\beta}+(\bar{z}_1-\bar{z}_0)\bar{\beta}_1+(\bar{z}_1-\bar{z})\bar{\beta}-i\bar{\xi}\bar{r}\cos[(1-i\zeta)\phi]\right]$

Table 7.1: Arrival time of waves in Example 1

	Fourier Synthesis	Present method with 5 terms	Present method with 26 terms	Present method with 50 terms
Computing time (percentage)	100%	5.2%	13.8%	39.9%

Table 7.2:Computing time

To provide a basis for assessment for the computational procedure for the multi-layer case, the time-domain response for a cubic B-Spline loading is first computed by the method of Fourier synthesis using the frequency domain Green’s functions by Pak and Guzina (2012) and Guzina and Pak (2011) as presented in Chapter 5. Three responses are then computed by the proposed method with a variable number of terms, namely, 5, 26 and 50 terms. Their time histories of displacements are depicted in Figure 7.5, from which one can see that the present result with 5 terms agree well with the result by Fourier synthesis before the wave corresponding to the 6th term arrives. Similarly, the result with 26 terms is very good until the arrival of the 27th wave group, and the result with 50 terms is good until the arrival of the 51st wave group.

The computing time is given in Table 7.2. When only a small number of terms are included, the present time-domain method for the B-spline loading is much more efficient then the Fourier synthesis method. As the number of terms included increases, the computing time of the present method does grow. For very sudden, fast or discontinuous loading and the case where the time of interest is short in duration, however, the present time-domain approach should have significant advanatges over the Fourier synthesis approach which will require the computation of a frequency domain Green’s function at super-high frequency in such situations.

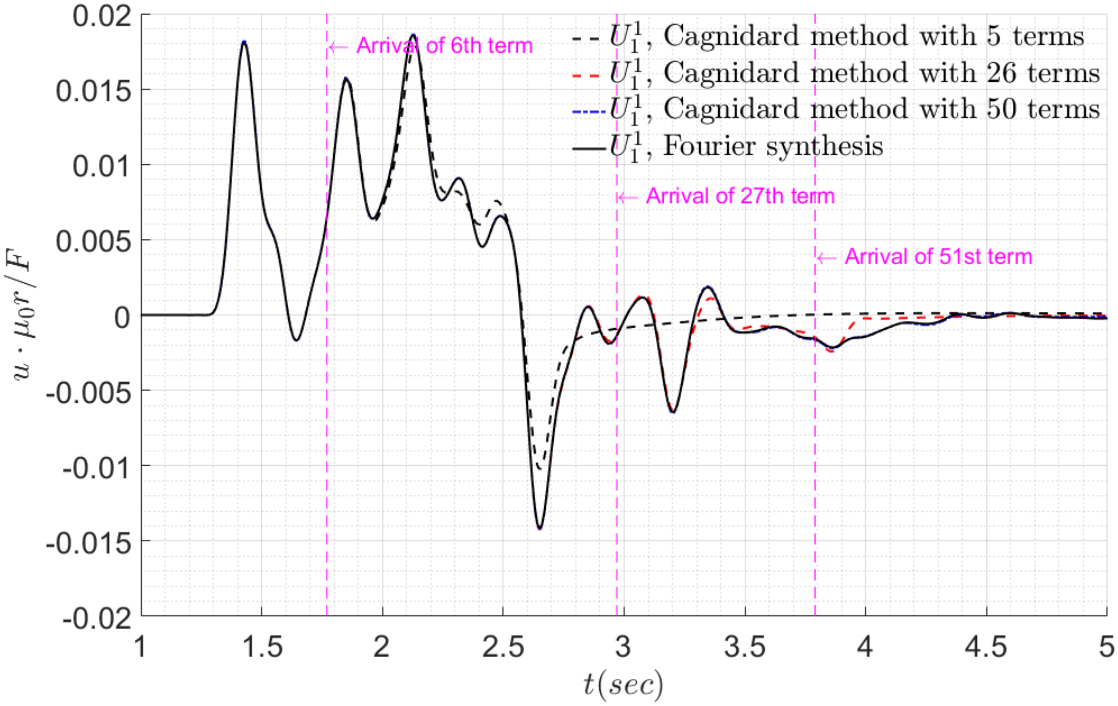

0.02
0.015
0.01
0.005
0
-0.005
-0.01
-0.015
-0.02
1
1.5
2
2.5
3
3.5
4
4.5
5
$u \cdot \mu_0 r / F$
$t(sec)$
Arrival of 6th term
Arrival of 27th term
Arrival of 51st term
U_1^1, Cagnidard method with 5 terms
U_1^1, Cagnidard method with 26 terms
U_1^1, Cagnidard method with 50 terms
U_1^1, Fourier synthesis

(a)

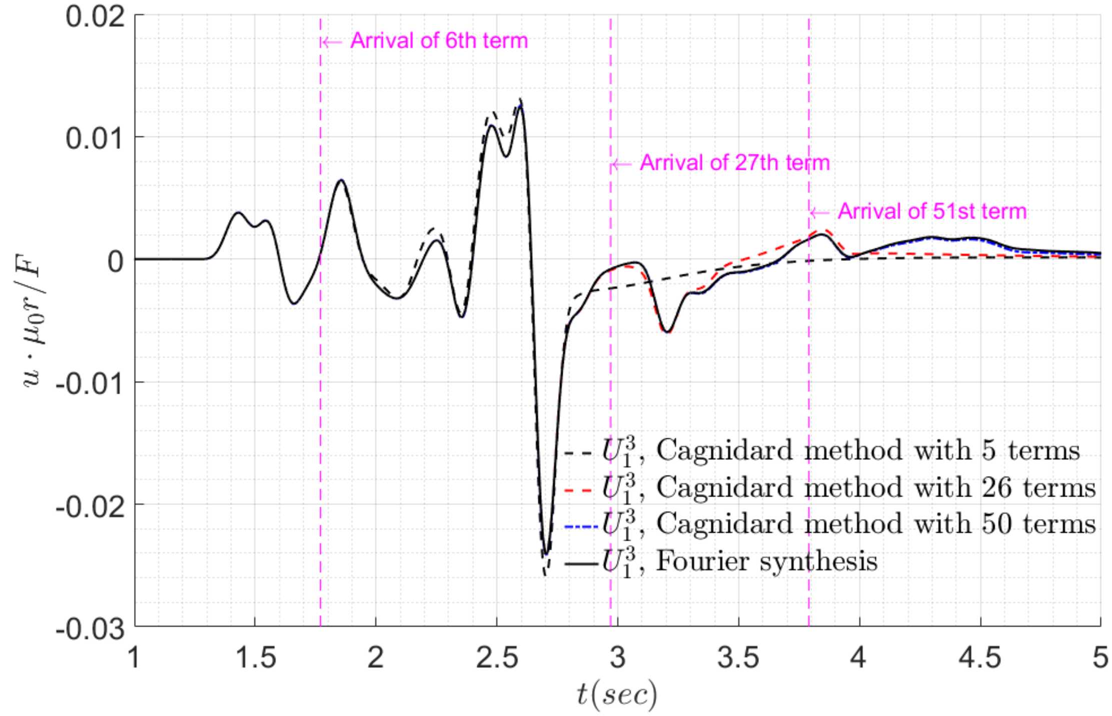

0.02
0.01
0
-0.01
-0.02
-0.03
1
1.5
2
2.5
3
3.5
4
4.5
5
$u \cdot \mu_0 r / F$
$t(sec)$
Arrival of 6th term
Arrival of 27th term
Arrival of 51st term
U_1^3, Cagnidard method with 5 terms
U_1^3, Cagnidard method with 26 terms
U_1^3, Cagnidard method with 50 terms
U_1^3, Fourier synthesis

(b)

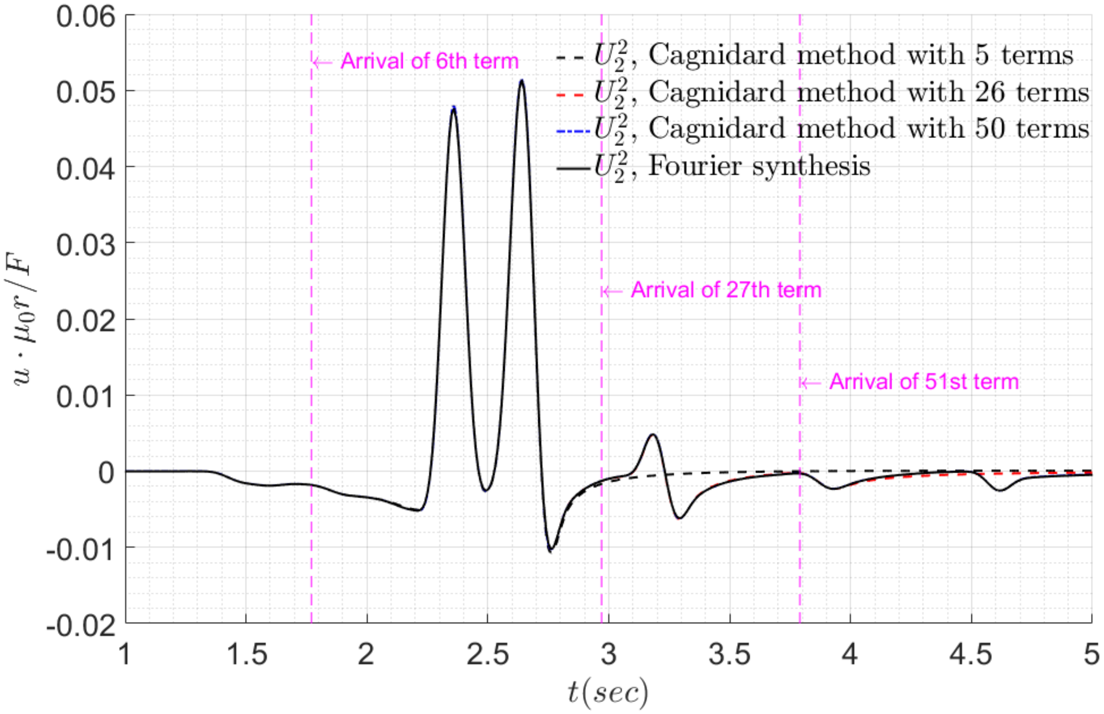
0.06
0.05
0.04
0.03
0.02
0.01
0
-0.01
-0.02
$u \cdot \mu_0 r/F$
1
1.5
2
2.5
3
3.5
4
4.5
5
$t(sec)$
Arrival of 6th term
Arrival of 27th term
Arrival of 51st term
U_2^2, Cagnidard method with 5 terms
U_2^2, Cagnidard method with 26 terms
U_2^2, Cagnidard method with 50 terms
U_2^2, Fourier synthesis

(c)

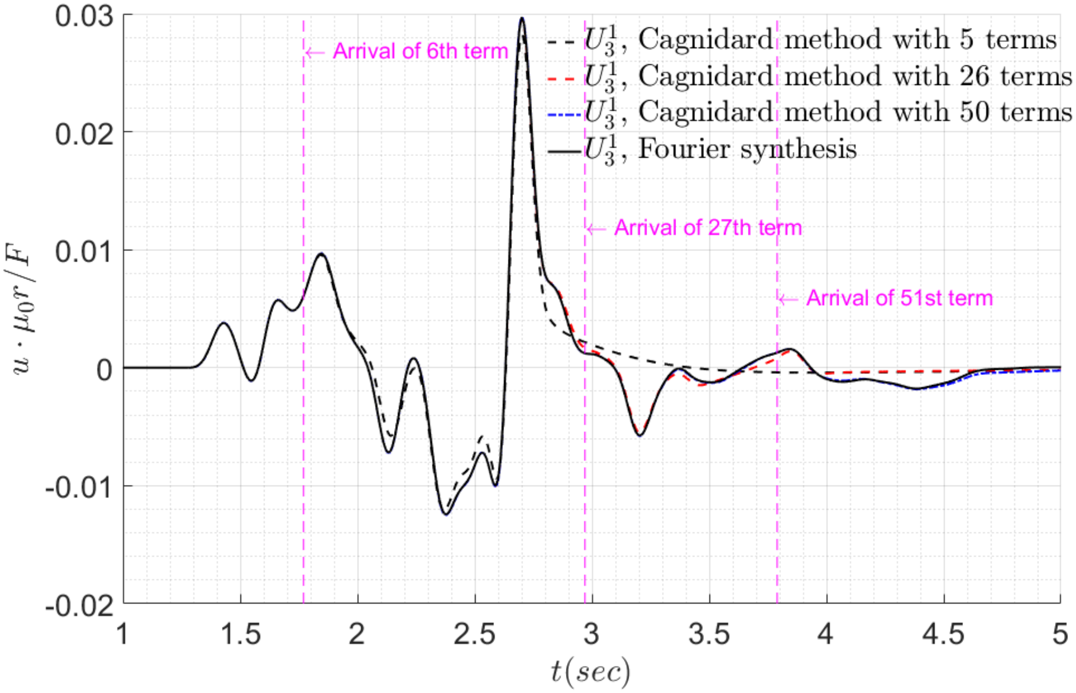
0.03
0.02
0.01
0
-0.01
-0.02
$u \cdot \mu_0 r/F$
1
1.5
2
2.5
3
3.5
4
4.5
5
$t(sec)$
Arrival of 6th term
Arrival of 27th term
Arrival of 51st term
U_3^1, Cagnidard method with 5 terms
U_3^1, Cagnidard method with 26 terms
U_3^1, Cagnidard method with 50 terms
U_3^1, Fourier synthesis

(d)

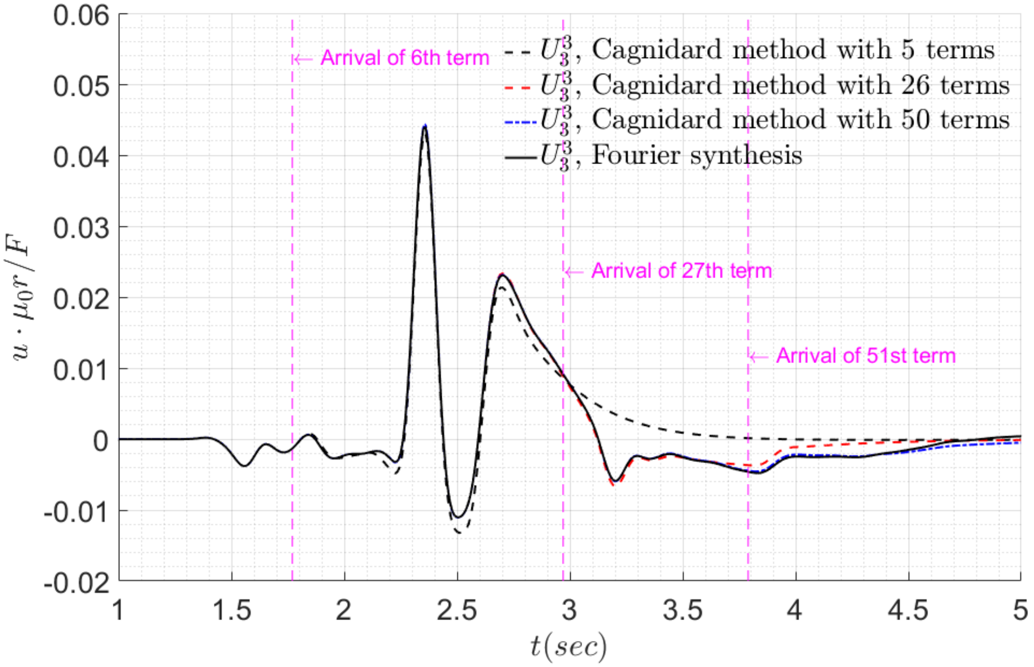

(e)

Figure 7.5: Time history of displacement components for Example 1

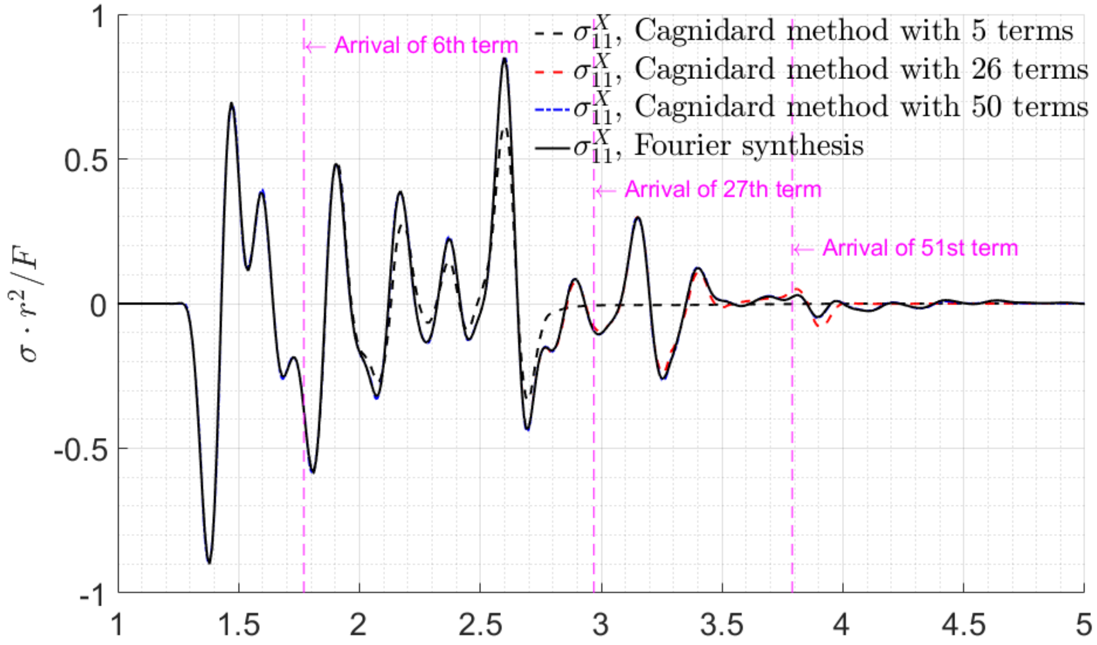
σ_{11}^X, Cagnidard method with 5 terms
σ_{11}^X, Cagnidard method with 26 terms
σ_{11}^X, Cagnidard method with 50 terms
σ_{11}^X, Fourier synthesis
Arrival of 6th term
Arrival of 27th term
Arrival of 51st term
$\sigma \cdot r^2/F$
1
0.5
0
-0.5
-1
1
1.5
2
2.5
3
3.5
4
4.5
5

(a)

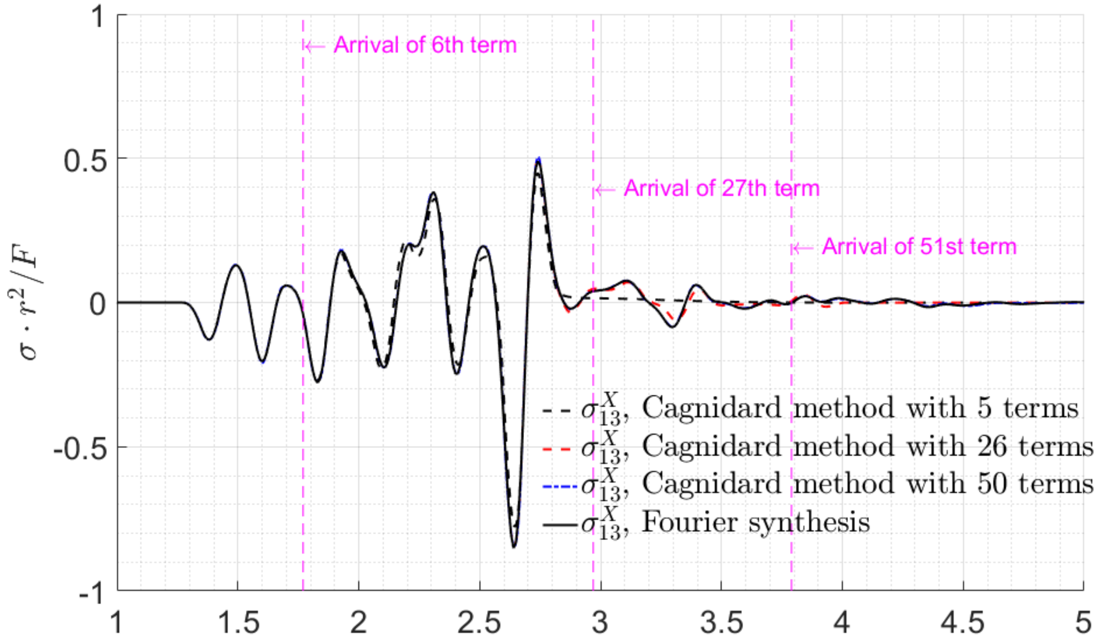
Arrival of 6th term
Arrival of 27th term
Arrival of 51st term
σ_{13}^X, Cagnidard method with 5 terms
σ_{13}^X, Cagnidard method with 26 terms
σ_{13}^X, Cagnidard method with 50 terms
σ_{13}^X, Fourier synthesis
$\sigma \cdot r^2/F$
1
0.5
0
-0.5
-1
1
1.5
2
2.5
3
3.5
4
4.5
5

(b)

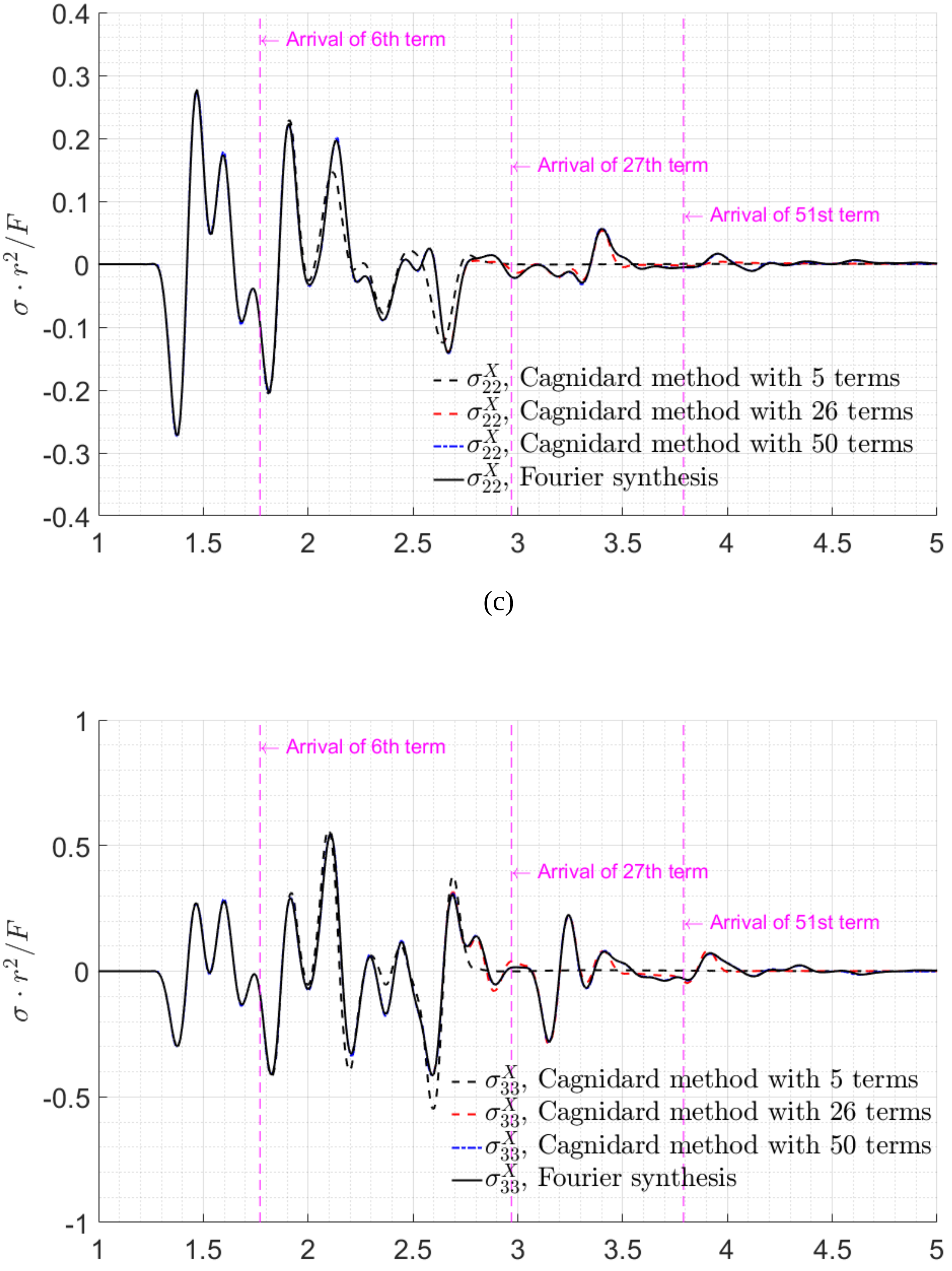

(c)

(d)

Figure 7.6: Time history of stress components for loading in x −direction at Example 1

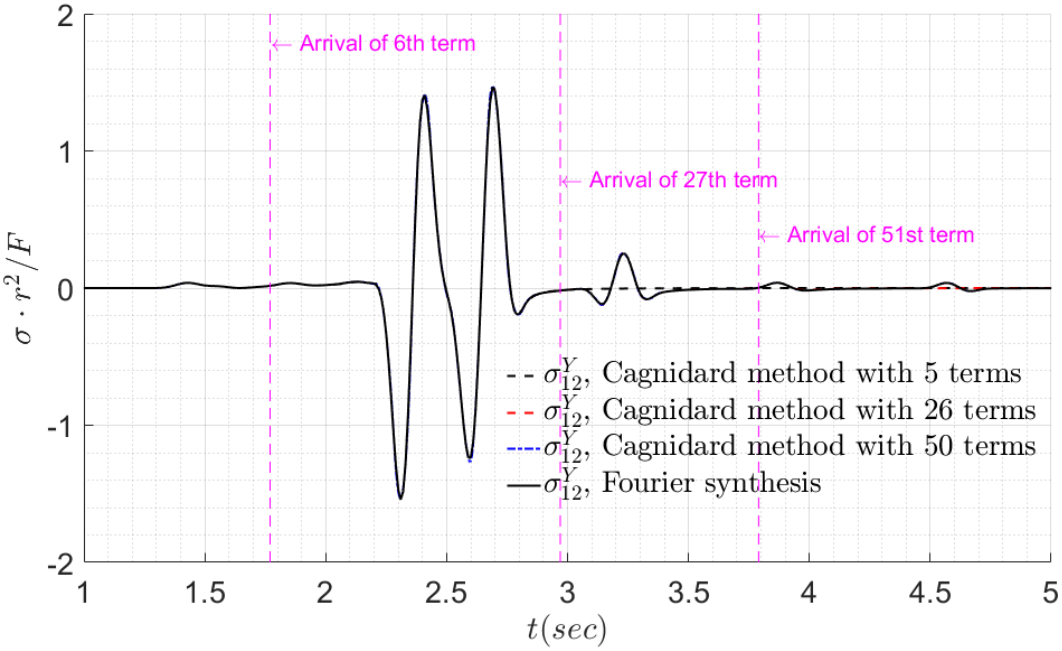

(a)

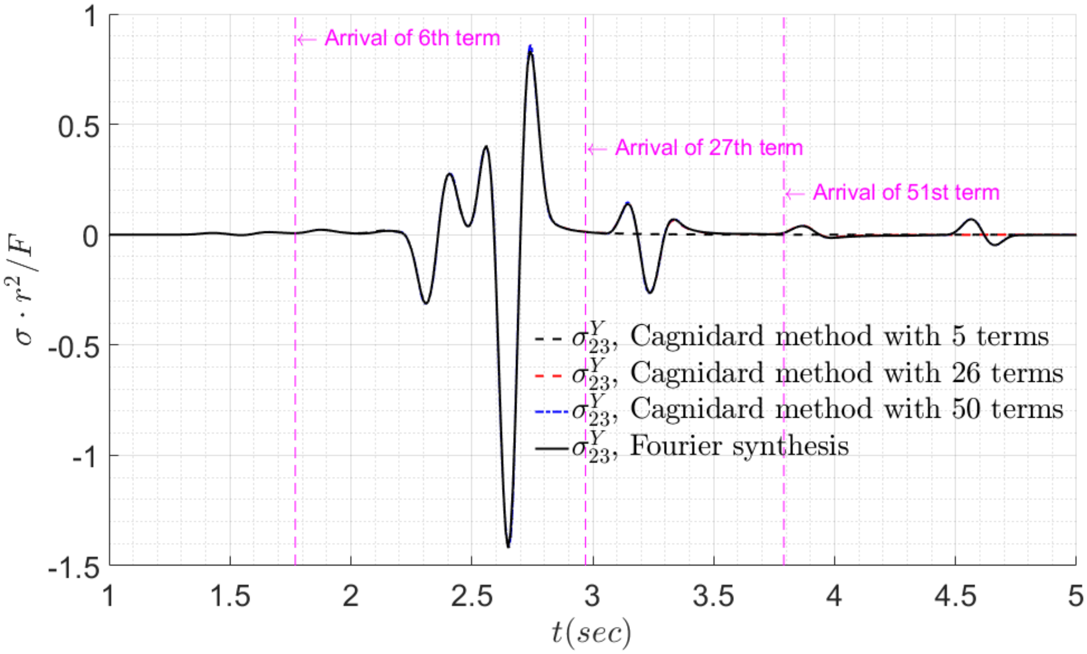

(b)

Figure 7.7: Time history of stress components for loading in y −direction at Example 1

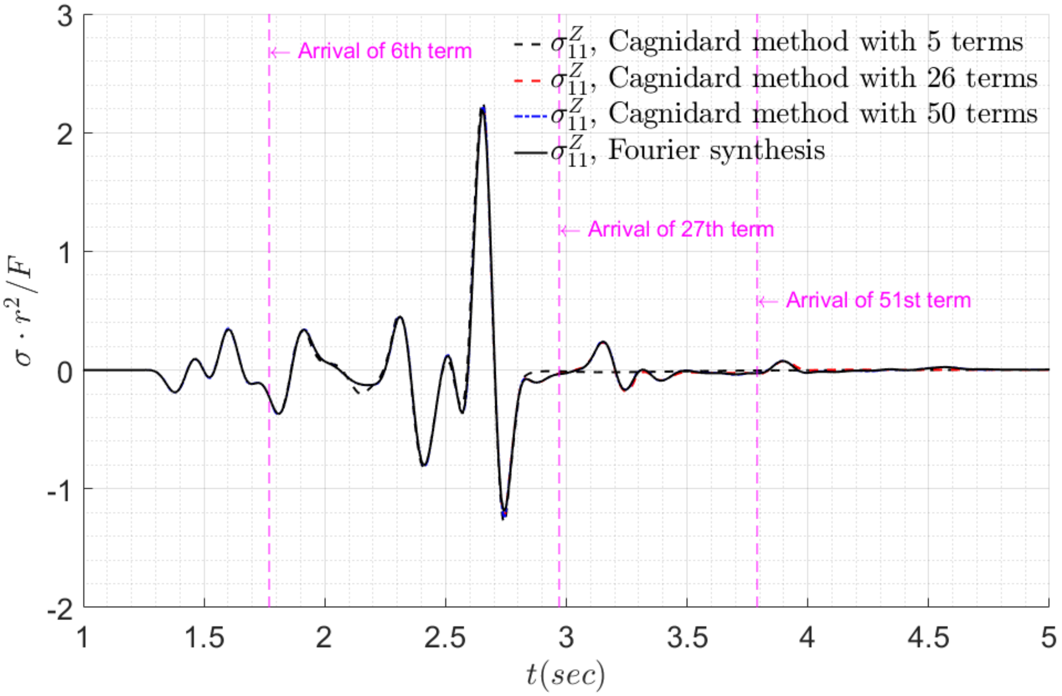

Arrival of 6th term
Arrival of 27th term
Arrival of 51st term
σ_{11}^{Z}, Cagnidard method with 5 terms
σ_{11}^{Z}, Cagnidard method with 26 terms
σ_{11}^{Z}, Cagnidard method with 50 terms
σ_{11}^{Z}, Fourier synthesis
$\sigma \cdot r^2/F$
$t(sec)$
3
2
1
0
-1
-2
1
1.5
2
2.5
3
3.5
4
4.5
5

(a)

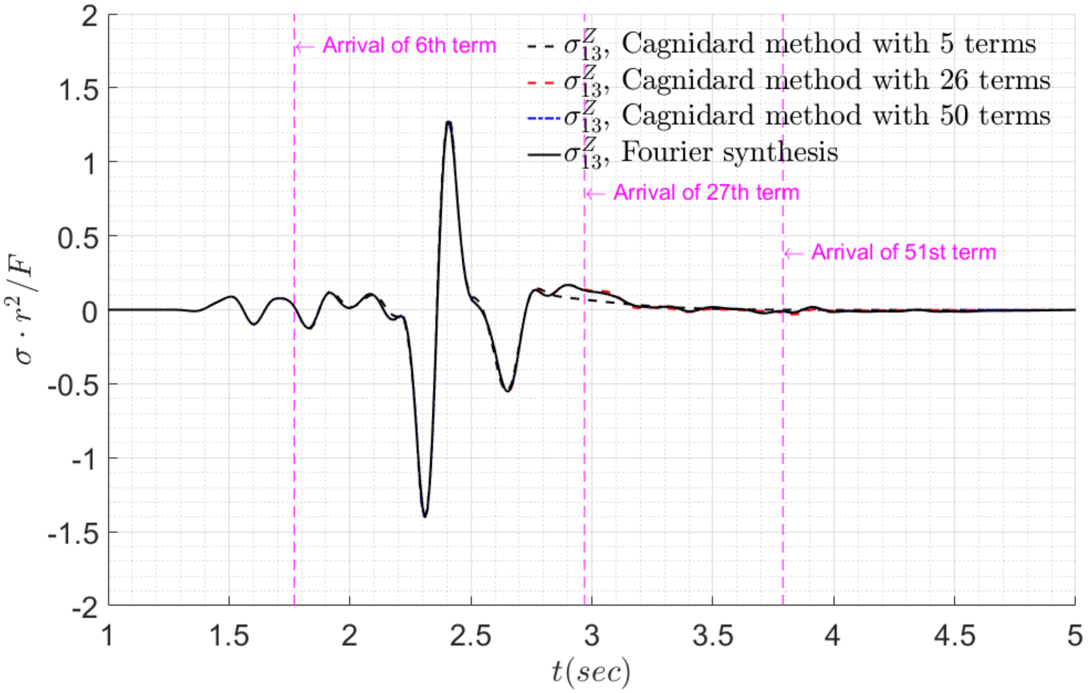

Arrival of 6th term
Arrival of 27th term
Arrival of 51st term
σ_{13}^{Z}, Cagnidard method with 5 terms
σ_{13}^{Z}, Cagnidard method with 26 terms
σ_{13}^{Z}, Cagnidard method with 50 terms
σ_{13}^{Z}, Fourier synthesis
$\sigma \cdot r^2/F$
$t(sec)$
2
1.5
1
0.5
0
-0.5
-1
-1.5
-2
1
1.5
2
2.5
3
3.5
4
4.5
5

(b)

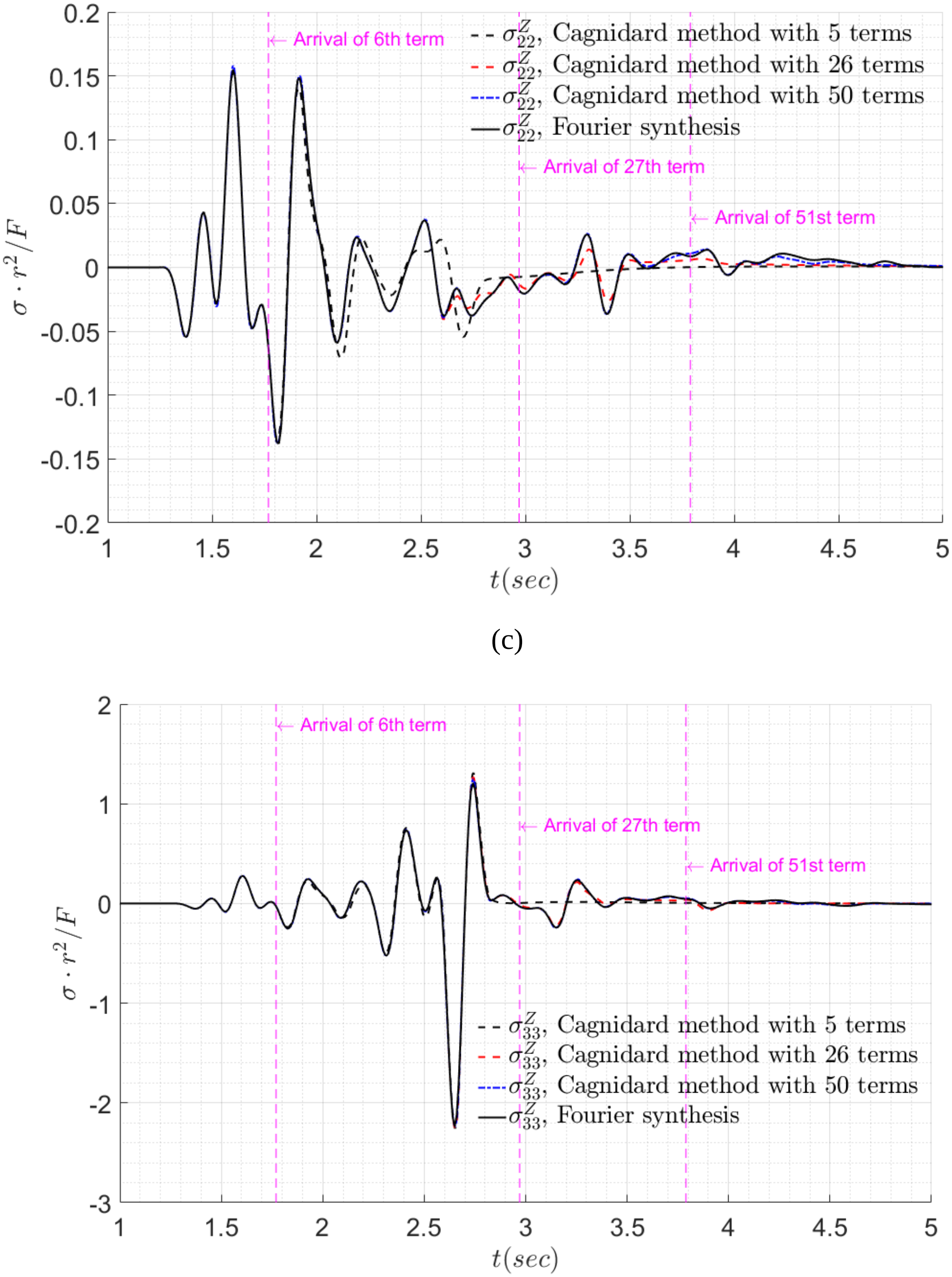

(c)

(d)

Figure 7.8: Time history of stress components for loading in z −direction at Example 1

7.8.2 Example 2

For the same geometrical configuration as in Example 1, now consider a Heaviside time function for the point load, i.e. $f(t) = F \cdot H(t)$, where F is the magnitude of the point force. Time history of displacements are shown in Figure 7.9.

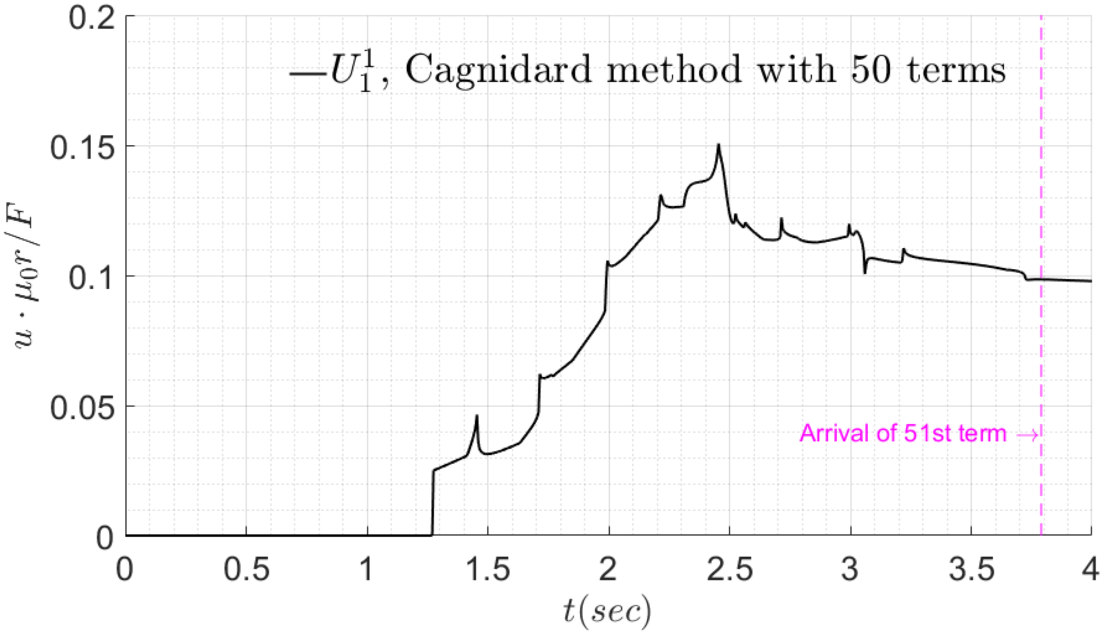

(a)

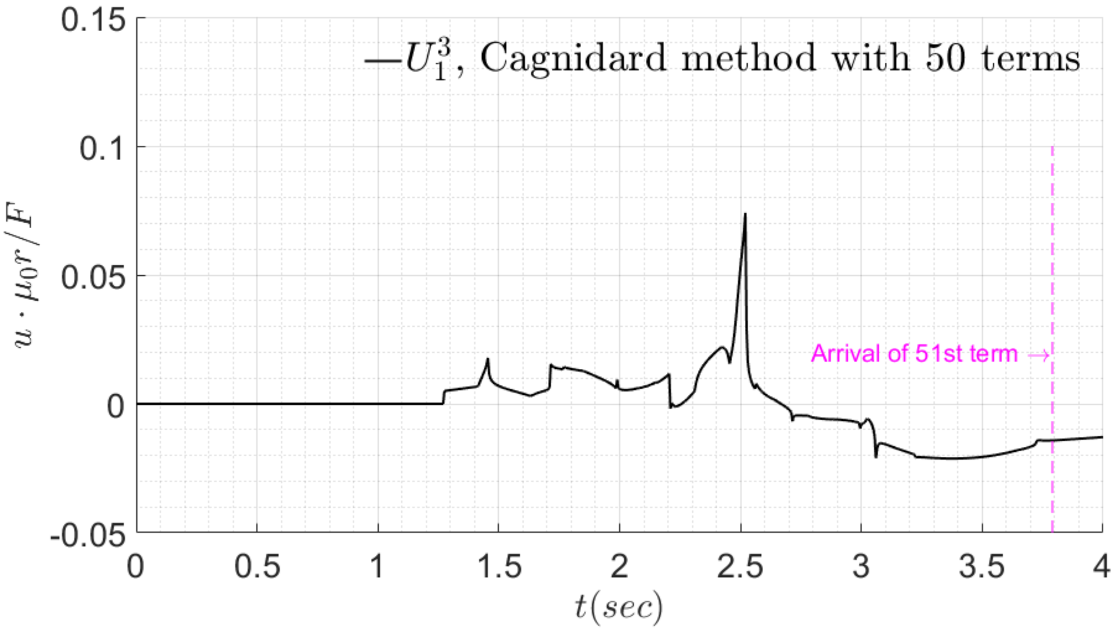

—U_1^3, Cagnidard method with 50 terms
Arrival of 51st term →
$u \cdot \mu_0 r / F$
$t(sec)$
0.15
0.1
0.05
0
-0.05
0
0.5
1
1.5
2
2.5
3
3.5
4

(b)

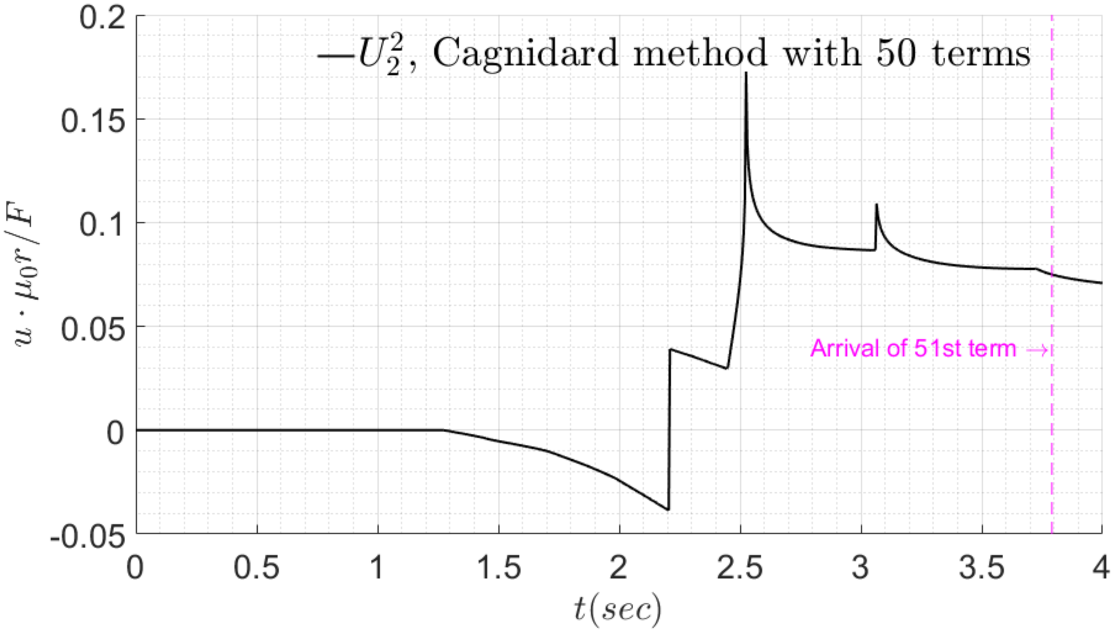

—U_2^2, Cagnidard method with 50 terms
Arrival of 51st term →
$u \cdot \mu_0 r / F$
$t(sec)$
0.2
0.15
0.1
0.05
0
-0.05
0
0.5
1
1.5
2
2.5
3
3.5
4

(c)

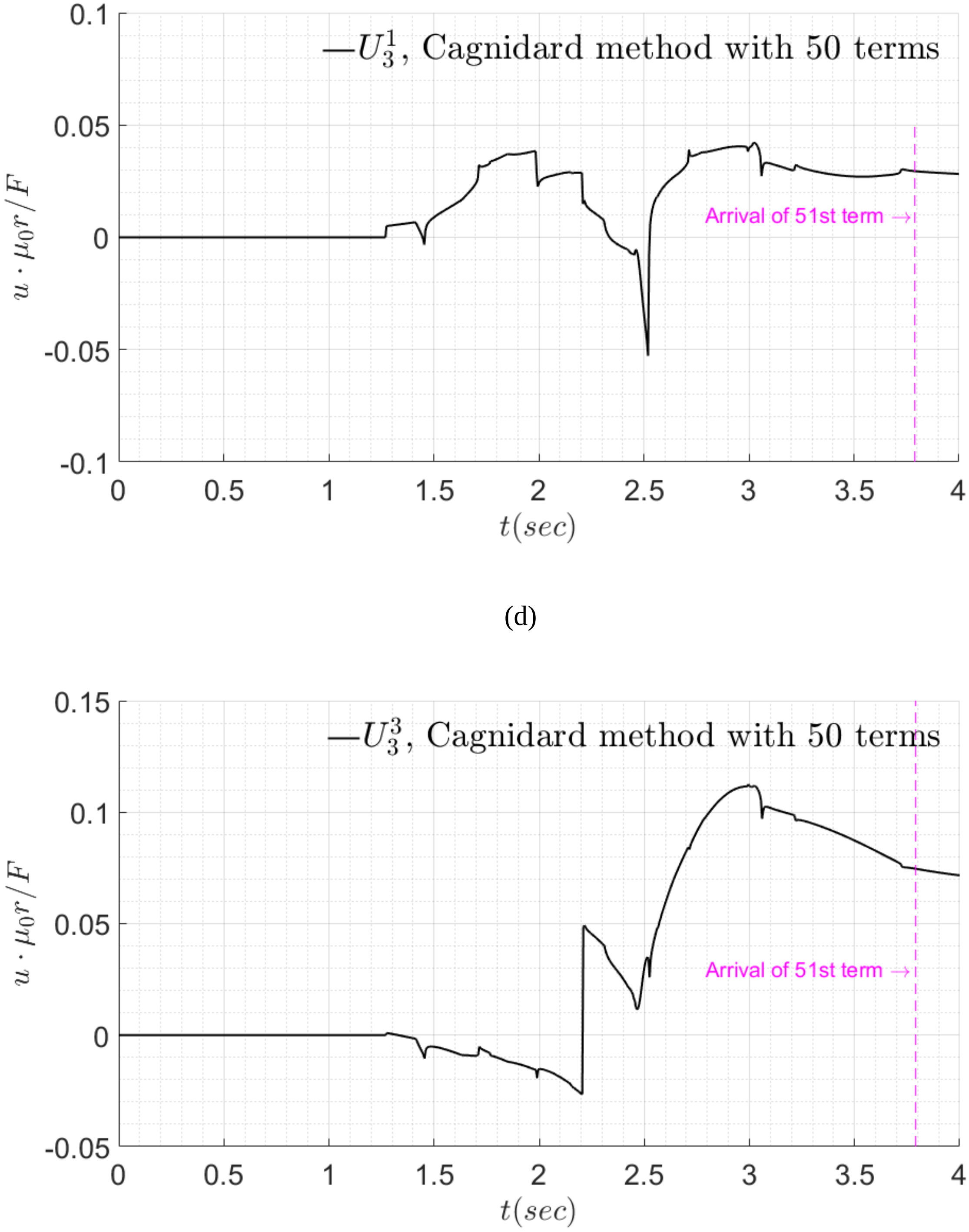

(d)

(e)

Figure 7.9: Time history of displacement components for Example 2

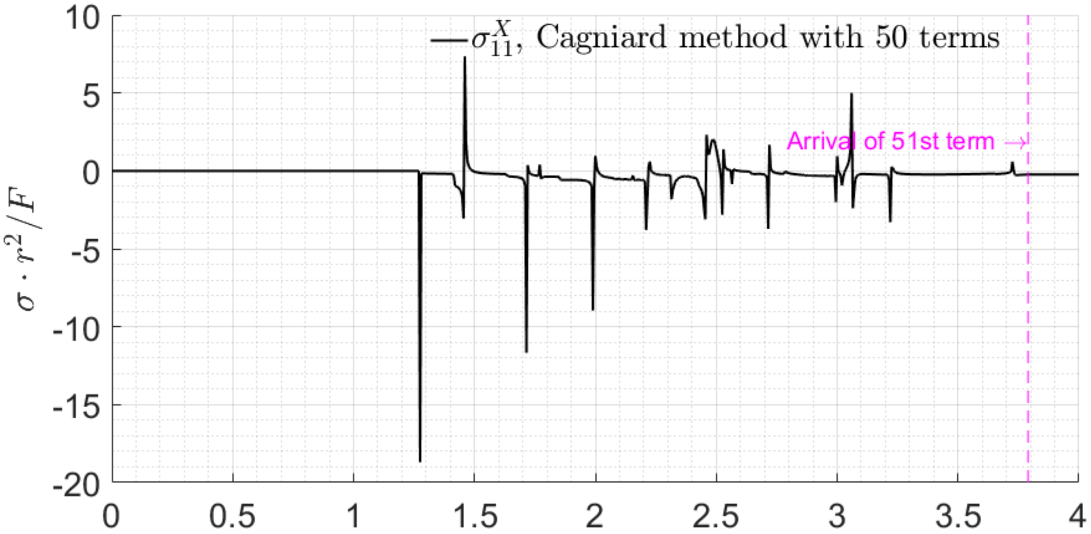
σ_{11}^{X}, Cagniard method with 50 terms
Arrival of 51st term →
$\sigma \cdot r^2/F$
10
5
0
-5
-10
-15
-20
0
0.5
1
1.5
2
2.5
3
3.5
4

(a)

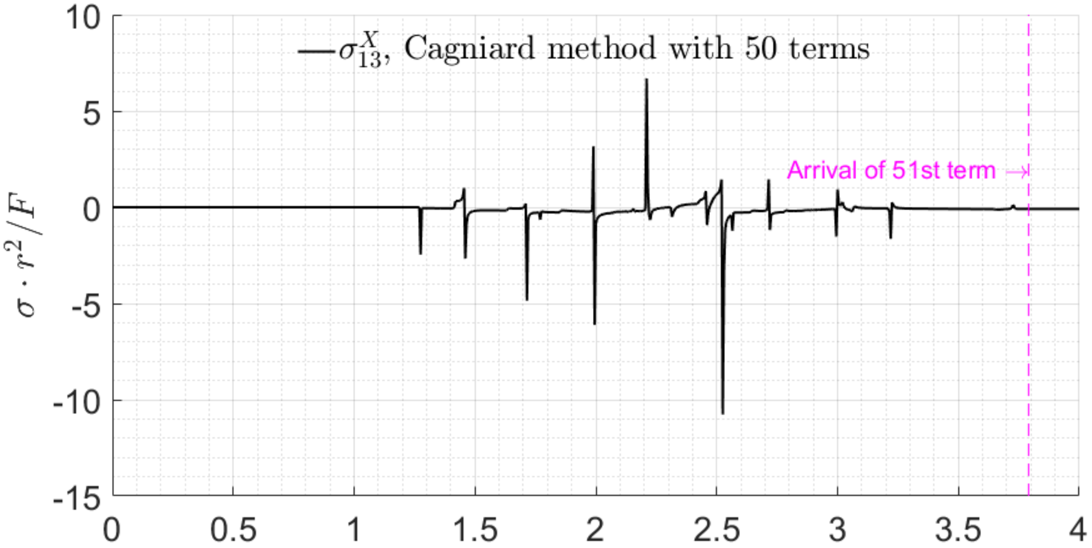
σ_{13}^{X}, Cagniard method with 50 terms
Arrival of 51st term →
$\sigma \cdot r^2/F$
10
5
0
-5
-10
-15
0
0.5
1
1.5
2
2.5
3
3.5
4

(b)

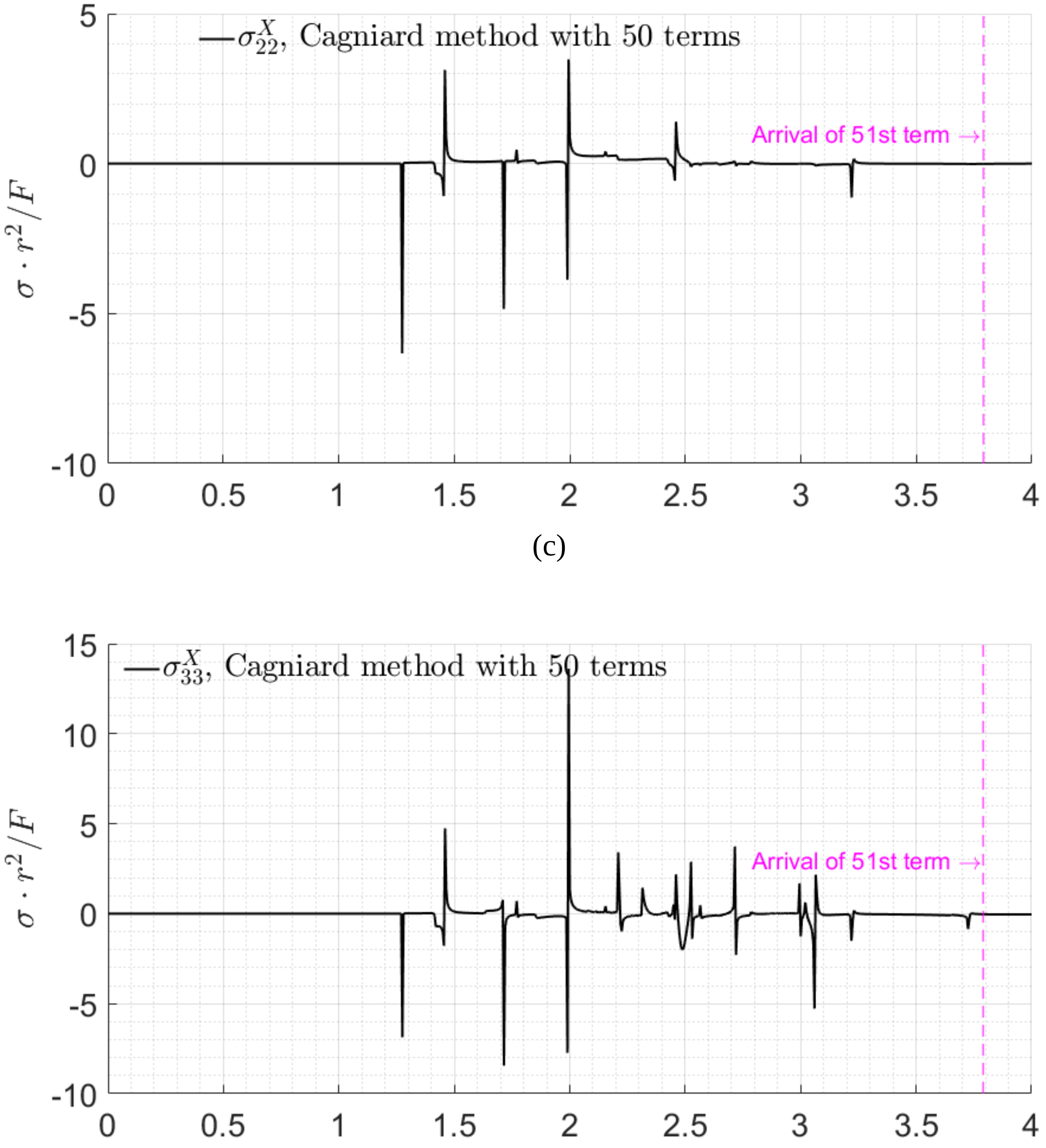

(c)

(d)

Figure 7.10: Time history of stress components for loading in x −direction at Example 2

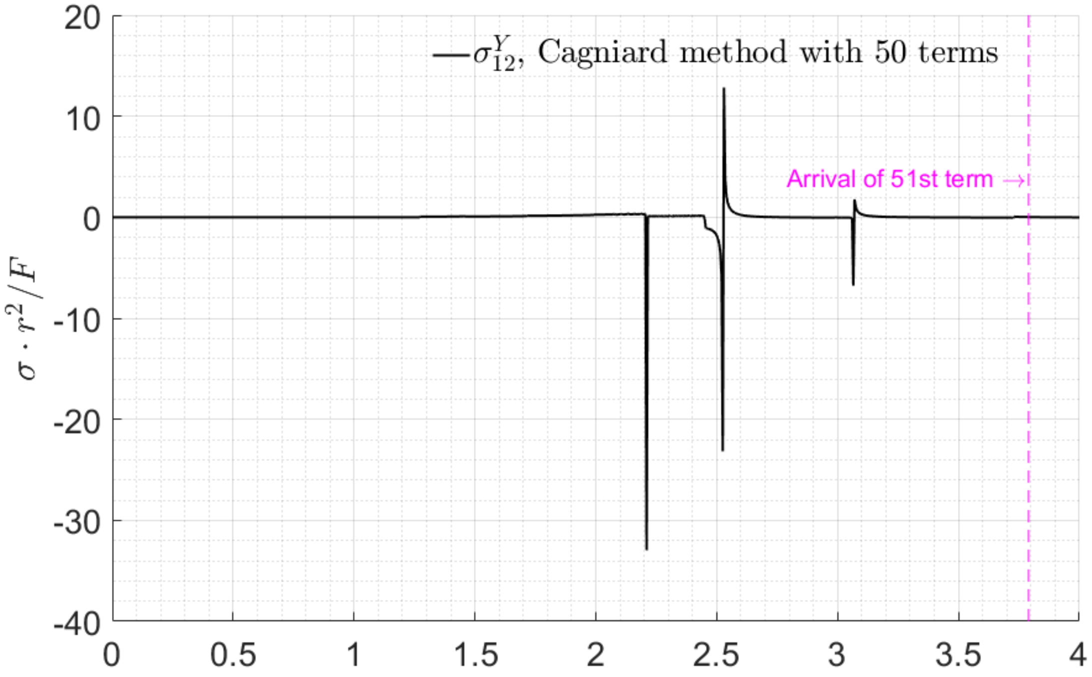

(a)

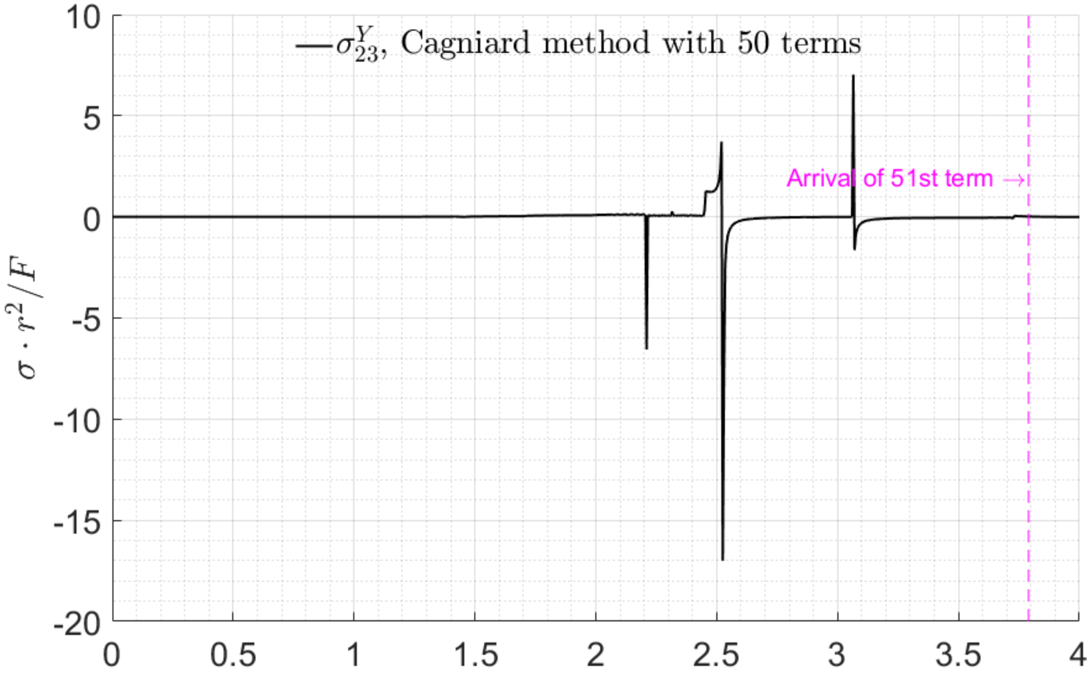

(b)

Figure 7.11: Time history of stress components for loading in y −direction at Example 2

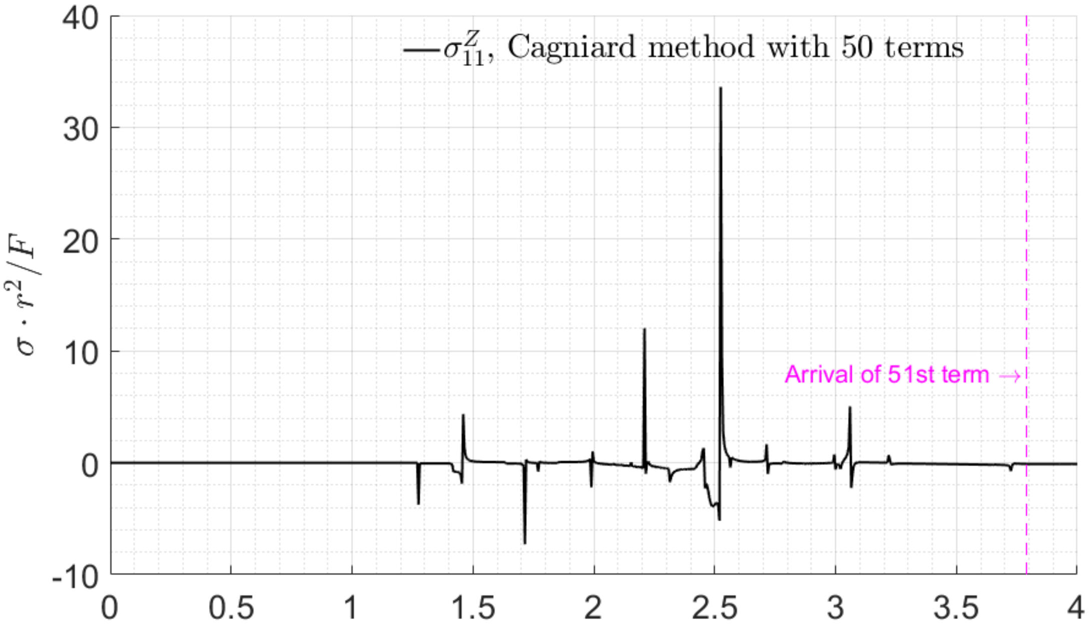
σ_{11}^{Z}, Cagniard method with 50 terms
Arrival of 51st term →
$\sigma \cdot r^2/F$
40
30
20
10
0
-10
0
0.5
1
1.5
2
2.5
3
3.5
4

(a)

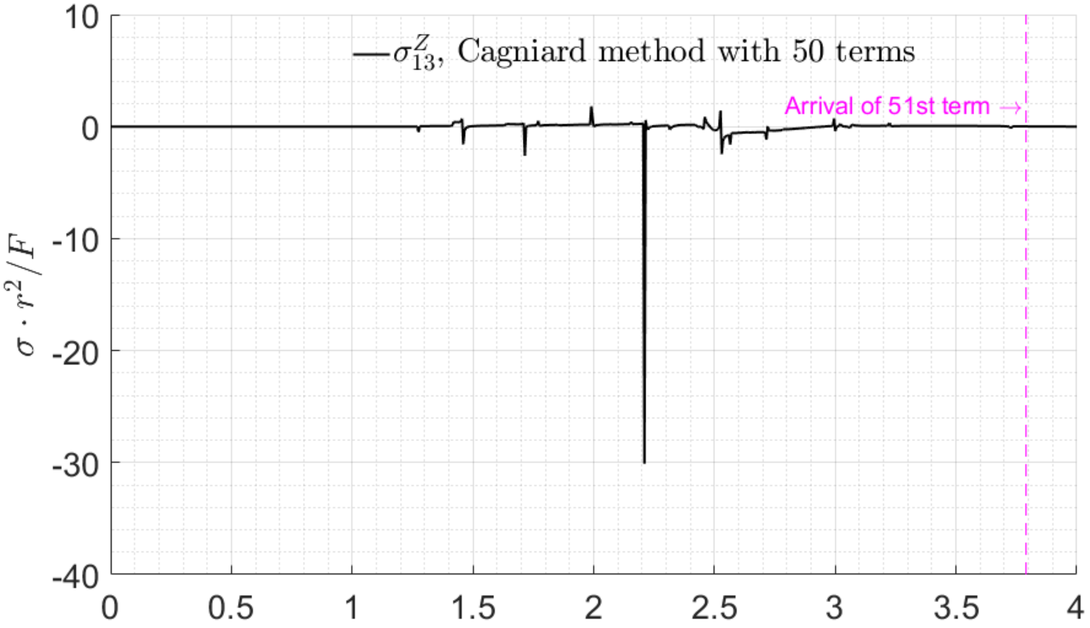
σ_{13}^{Z}, Cagniard method with 50 terms
Arrival of 51st term →
$\sigma \cdot r^2/F$
10
0
-10
-20
-30
-40
0
0.5
1
1.5
2
2.5
3
3.5
4

(b)

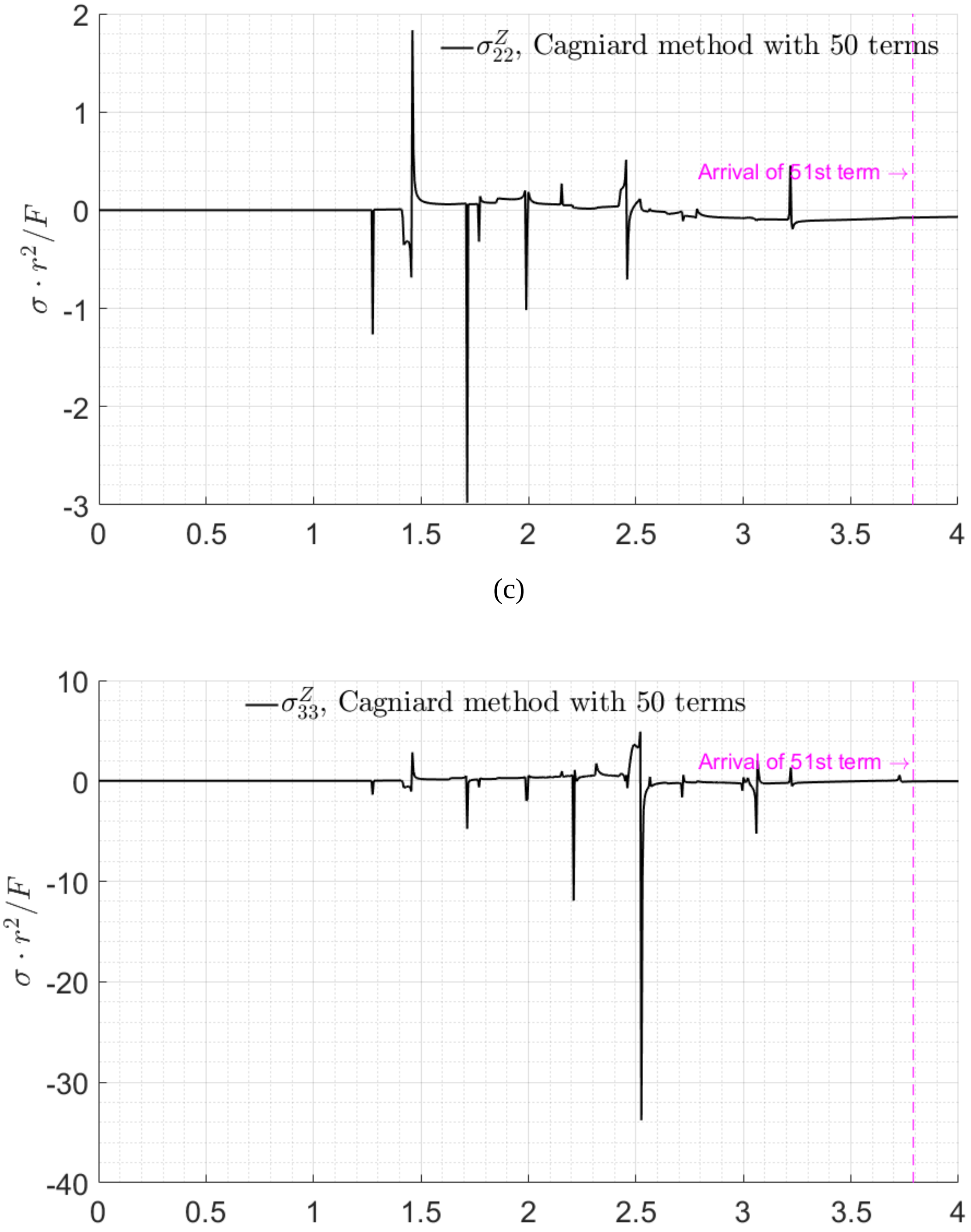

(c)

(d)

Figure 7.12: Time history of stress components for loading in z −direction at Example 2

7.8.3 Example 3

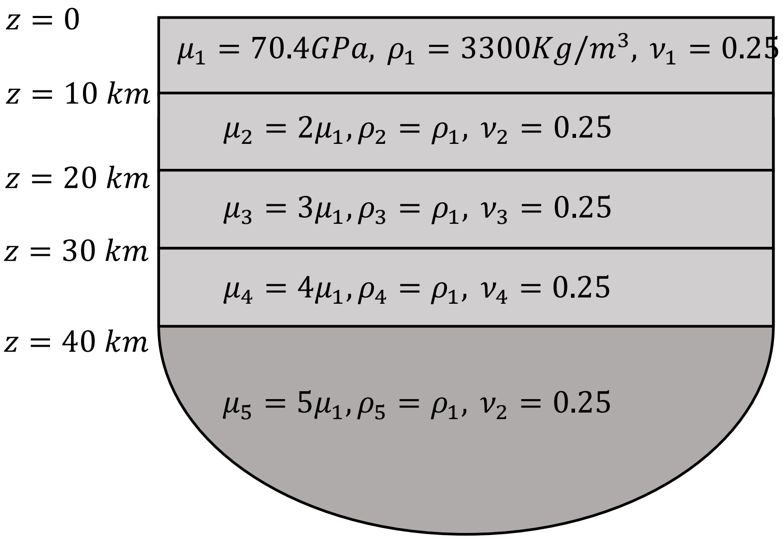

Figure 7.13: A 5-layer half-space

As shown in Figure 7.13 is a 5-layer half-space, each layer of which is homogeneous and has material parameters as indicated in the figure. The point-load is put at $(0,0,10)$ with a B-Spline time function specified in Eqn. (7.167) and the observation is taken at $(20,0,10)$. Time history of the displacement components at the observation point are shown in Figure 7.14. The solutions obtained by the current method has very good agreement with the solutions produced by the Fourier synthesis.

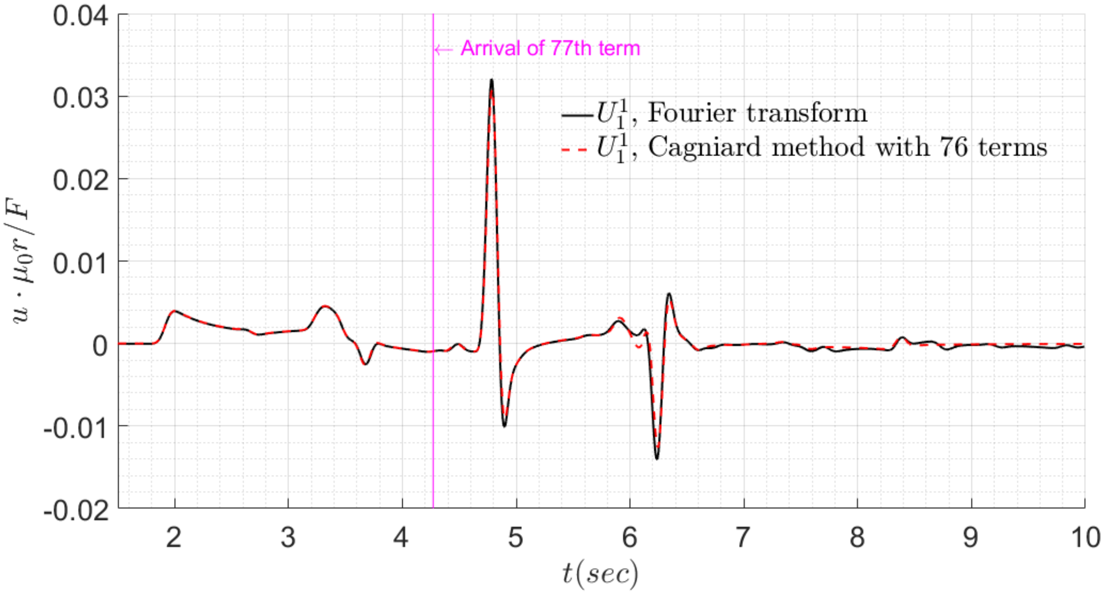
Arrival of 77th term
U_1^1, Fourier transform
U_1^1, Cagniard method with 76 terms
$u \cdot \mu_0 r/F$
0.04
0.03
0.02
0.01
0
-0.01
-0.02
2
3
4
5
6
7
8
9
10
$t(sec)$

(a)

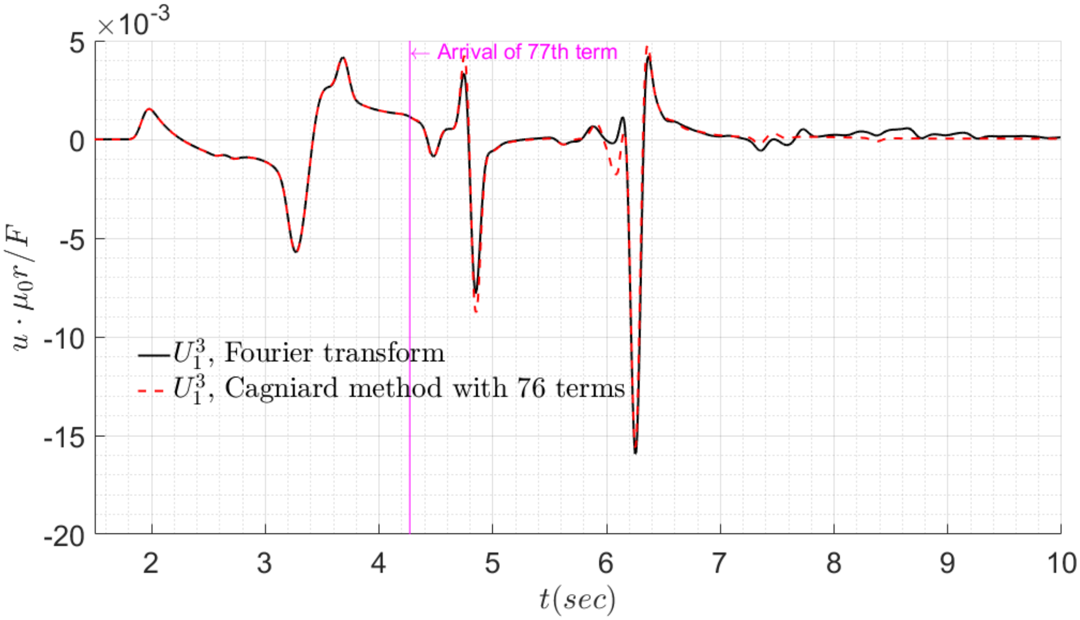
$\times 10^{-3}$
Arrival of 77th term
U_1^3, Fourier transform
U_1^3, Cagniard method with 76 terms
$u \cdot \mu_0 r/F$
5
0
-5
-10
-15
-20
2
3
4
5
6
7
8
9
10
$t(sec)$

(b)

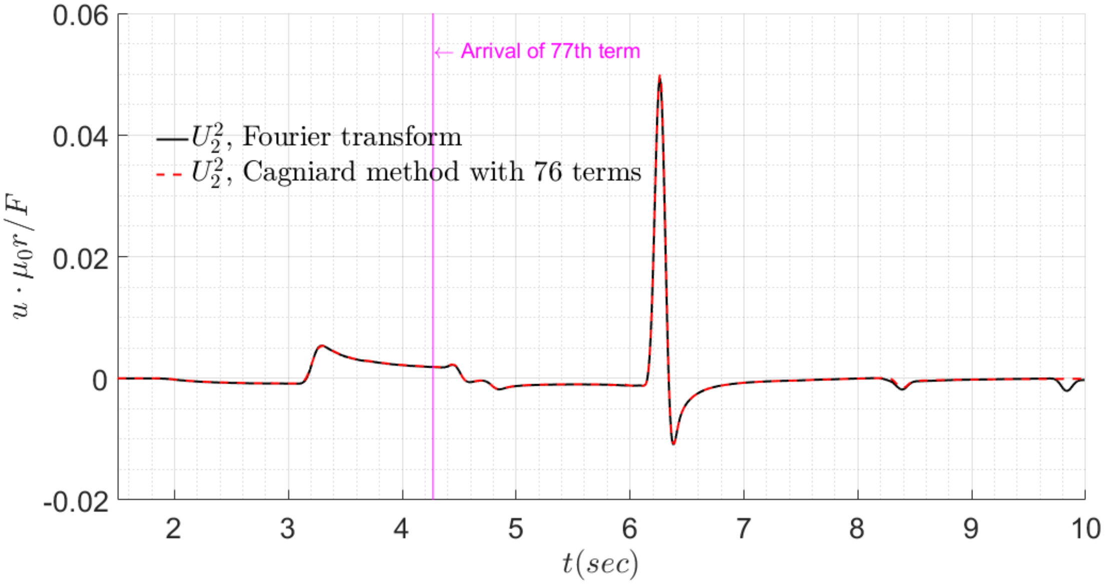

Arrival of 77th term
U_2^2, Fourier transform
U_2^2, Cagniard method with 76 terms
$u \cdot \mu_0 r/F$
0.06
0.04
0.02
0
-0.02
2
3
4
5
6
7
8
9
10
$t(sec)$

(c)

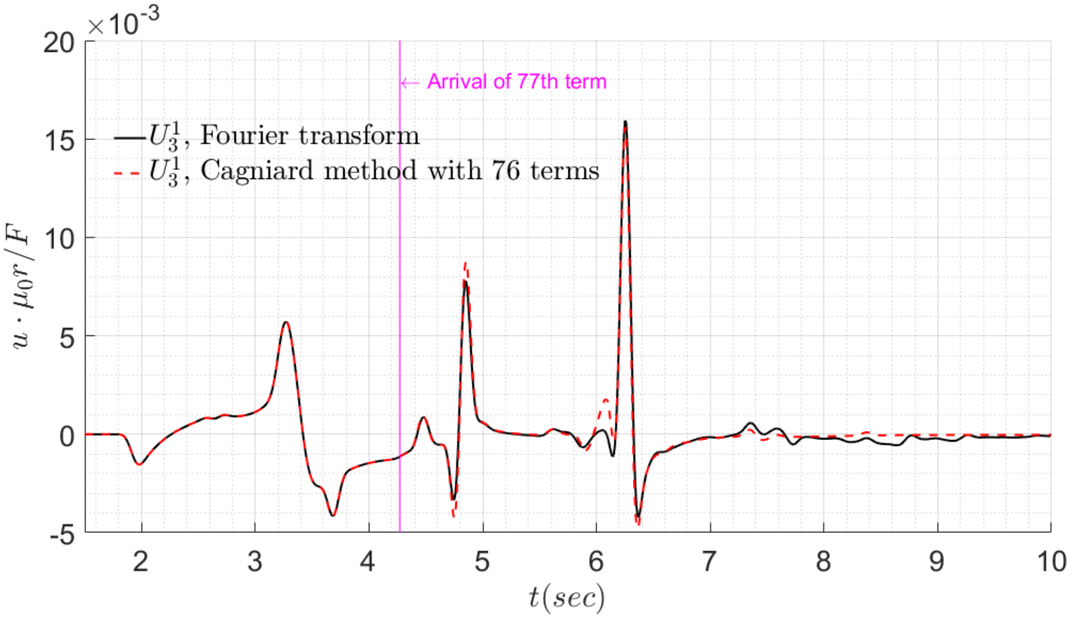

×10-3
Arrival of 77th term
U_3^1, Fourier transform
U_3^1, Cagniard method with 76 terms
$u \cdot \mu_0 r/F$
20
15
10
5
0
-5
2
3
4
5
6
7
8
9
10
$t(sec)$

(d)

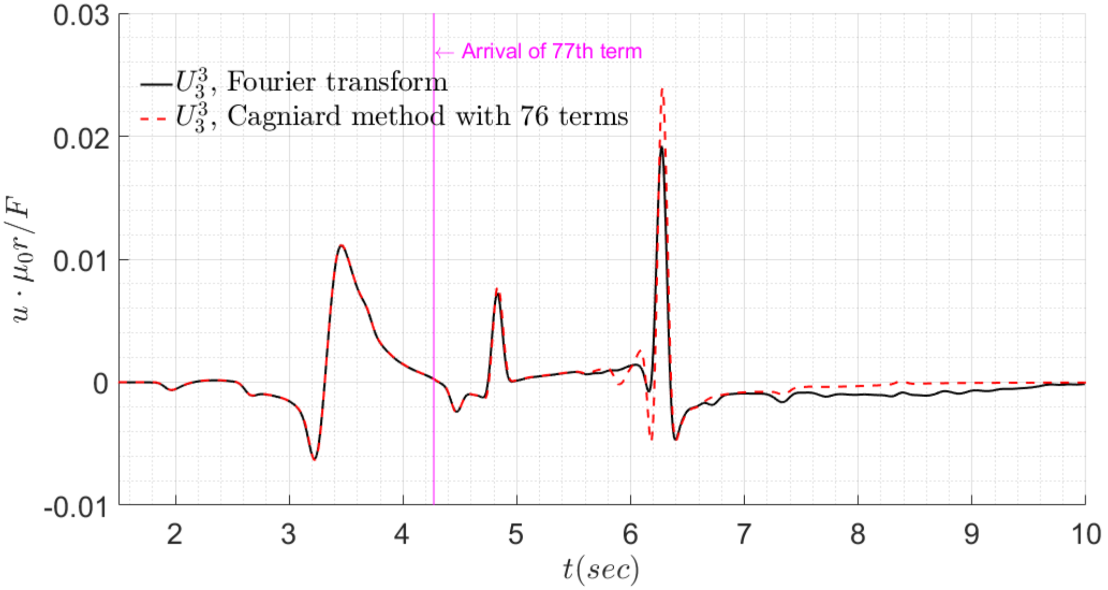

(e)

Figure 7.14: Time history of displacement components with cubic B-Spline load for Example 3

7.8.4 Example 4

For the same 5-layer half-space, source and observation points, now consider a Heaviside function as the time variation for the point load. The time history of displacement components is illustrated in Figure 7.15.

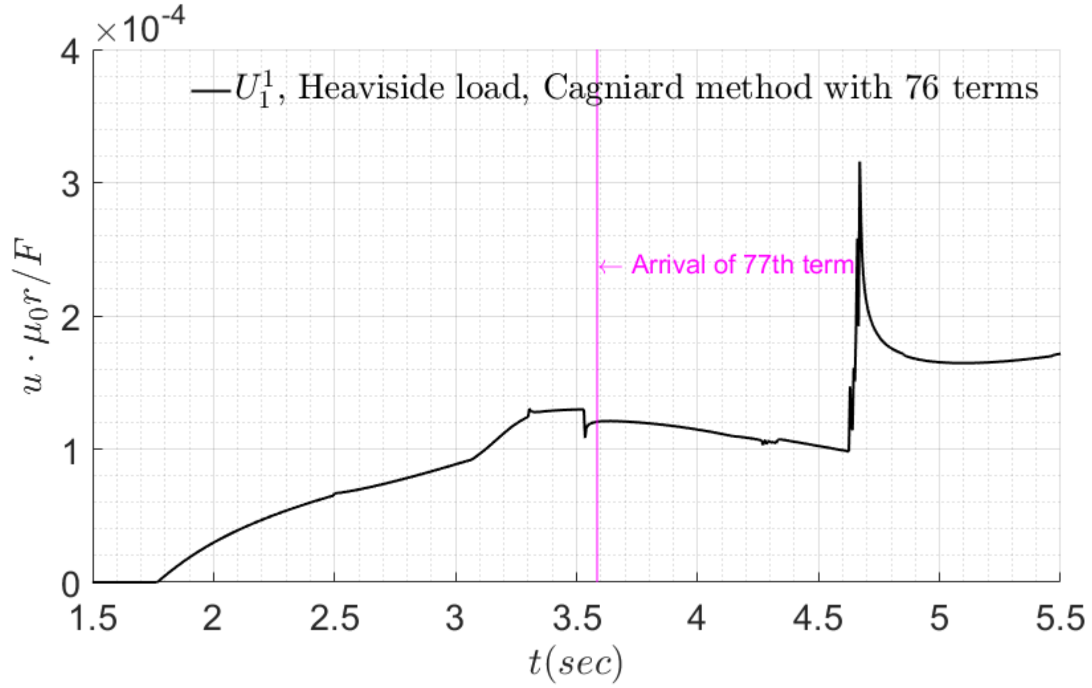
$\times 10^{-4}$
4
3
2
1
0
$u \cdot \mu_0 r / F$
1.5
2
2.5
3
3.5
4
4.5
5
5.5
$t(sec)$
U_1^1, Heaviside load, Cagniard method with 76 terms
← Arrival of 77th term

(a)

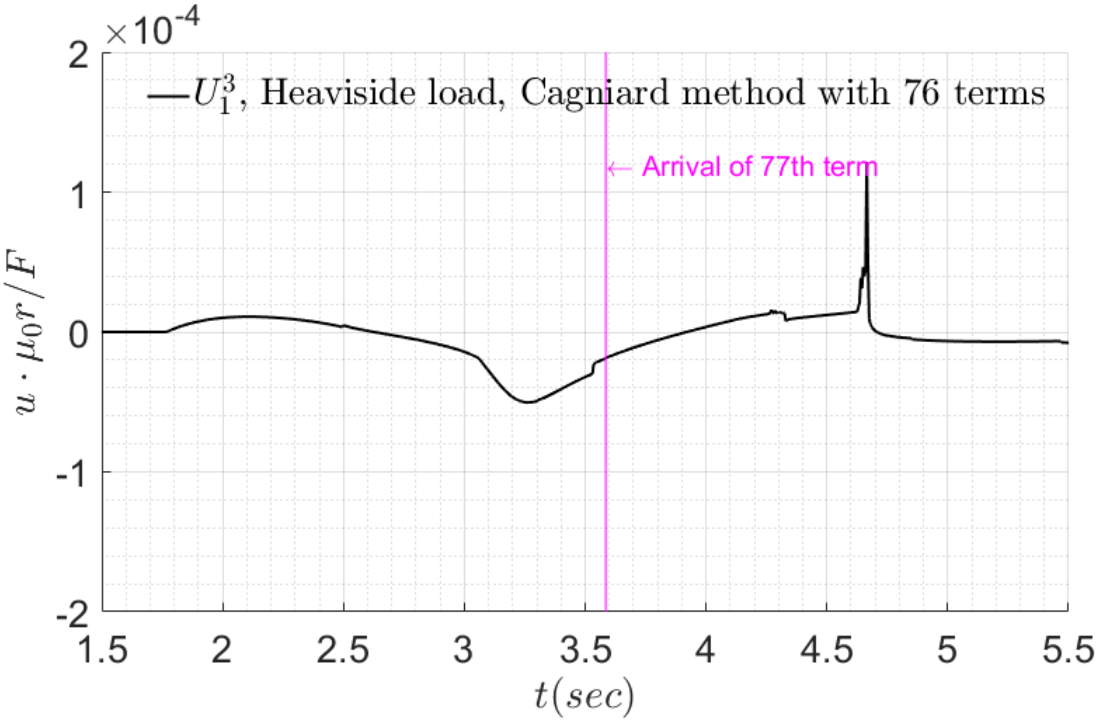
$\times 10^{-4}$
2
1
0
-1
-2
$u \cdot \mu_0 r / F$
1.5
2
2.5
3
3.5
4
4.5
5
5.5
$t(sec)$
U_1^3, Heaviside load, Cagniard method with 76 terms
← Arrival of 77th term

(b)

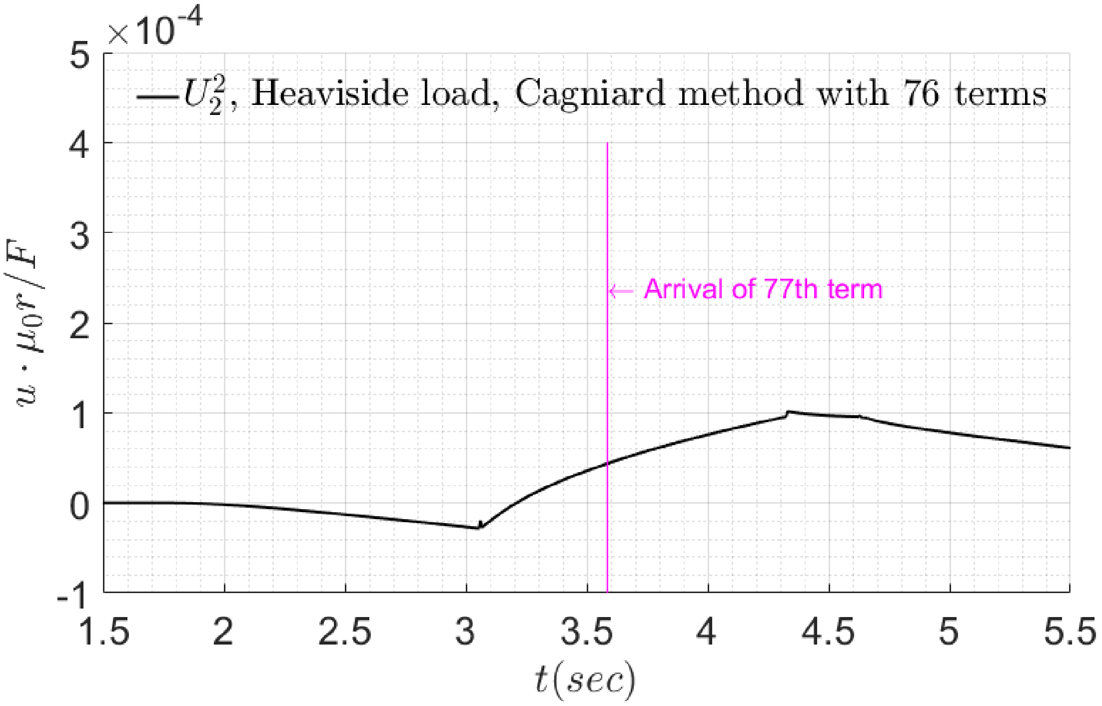
×10^-4
U_2^2, Heaviside load, Cagniard method with 76 terms
← Arrival of 77th term
$u \cdot \mu_0 r/F$
5
4
3
2
1
0
-1
1.5
2
2.5
3
3.5
4
4.5
5
5.5
$t(sec)$

(c)

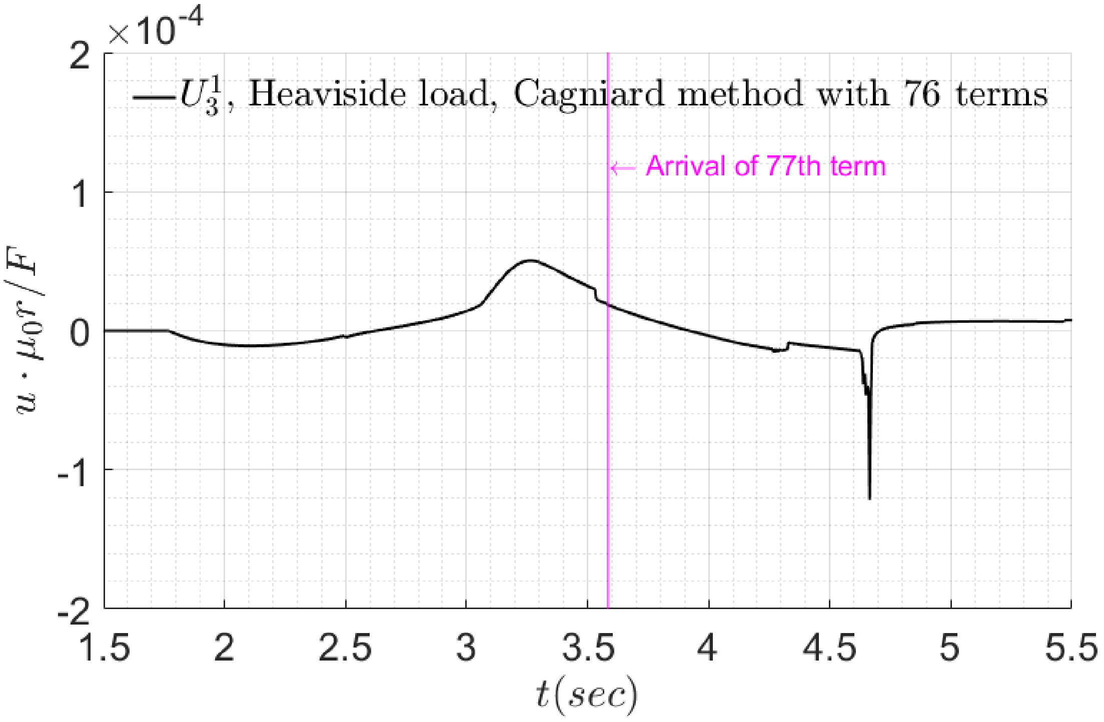
×10^-4
U_3^1, Heaviside load, Cagniard method with 76 terms
← Arrival of 77th term
$u \cdot \mu_0 r/F$
2
1
0
-1
-2
1.5
2
2.5
3
3.5
4
4.5
5
5.5
$t(sec)$

(d)

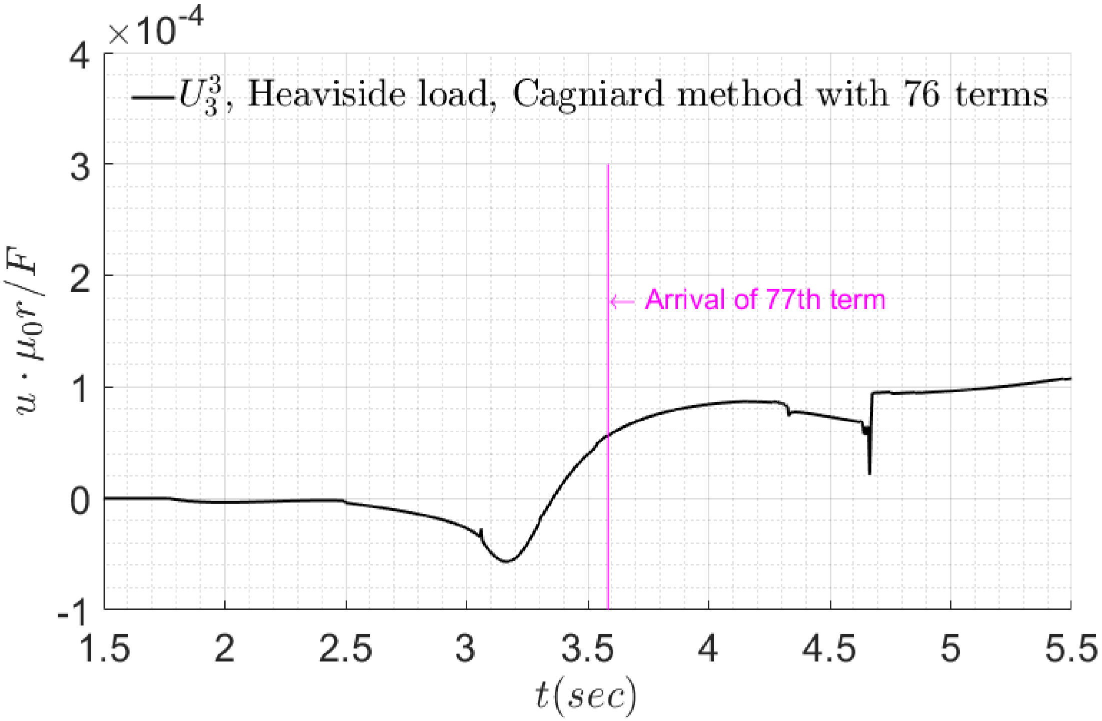

(e)

Figure 7.15: Time history of displacement components with Heaviside load for Example 4

7.9 Summary

In this chapter, a rigorous and systematic method to investigate the wave propagation in three-dimensional multi-layer media is presented. The method is performed under cylindrical coordinate system with displacement potentials and integral transforms. The solution in the transformed domain is expanded with Newmann series, each term of which describes a particular generalized wave group. Time domain solution is then obtained via the proposed method, and the arrival time of each wave group is derived through branch cut analysis. Using the numerical result from Fourier synthesis in Chapter 5 as references, examples shows that the proposed method is valid and accurate.

Chapter 8

BEM-FEM coupling for time-domain soil-structure interaction analysis

8.1 Introduction

The effect of dynamic soil-structure interaction is well recognized to be important in seismic analysis of structures. Among the most promising methods for time-domain soil-structure interaction analysis, one is the coupled BEM-FEM (Boundary Element Method-Finite Element Method) approach. FEM is versatile at modeling structures with complex geometries and nonlinear materials, while BEM is an effective approach for representing infinite and semi-infinite space since the radiation condition are taken care of by the Green's function automatically. The concept of FEM-BEM coupling was firstly developed for elastostatic analysis (Zienkiewicz and Bettess 1977), and then applied to dynamic problem in the frequency-domain (Mita and Luco 1987) as well as the time-domain (Spyrakos and Beskos 1986). The coupling formulations generally fall into two main categories: the direct coupling and the staggered coupling.

The direct coupling formulation combines the FEM and BEM matrices system through equilibrium as well as compatibility conditions at the interface, and form a global matrix system. Using the BEM to relate the interfacial nodal displacement to contact stress, Spyrakos and Beskos (1986) investigated a 2-D flexible surface strip-footing subjected either to a point, uniform pressure and moment loadings or to seismic waves, while the solution for 3-D is presented in Karabalis and Beskos (1985). With similar ideas, Von Estorff (1991) developed a coupling approach, and performed a quantitative assessment of the effects of various system parameters on the dynamic response of a block embedded into the soil.

As an alternative to a direct coupling approach, staggered schemes solve the equations for both subdomains separately, while the boundary conditions at the soil–structure interface are updated until convergence is achieved. Using B-Spline characteristic responses in place of the BE equations, Rizos and Wang (2002) proposed a staggered BE–FE coupled scheme that yields an efficient implementation with matrices that are extremely sparse, and the scheme is demonstrated by the soil-structure interaction between flexible structures and the supporting soil. The methodology is then applied for the analysis of vibrations in a railroad track system, induced by the passage of conventional and high-speed trains Brien and Rizos (2005). Rizos and Wang (2002)'s scheme solved the equations of each subdomain once for each time step, which requires a sufficiently small time step in order to achieve convergence as noted in François et al. (2015). To circumvent such a difficulty and to take into account nonlinearities within the FEM subdomains, iterations for each step was introduced into the staggered scheme in Soares et al. (2004) and the response of a nonlinear half-space to an impulse load was modeled by the scheme. In terms of how the Neumann or Dirichlet boundary conditions on the interface are imposed, the staggered schemes can be cast into 4 algorithms, namely, sequential Neumann-Dirichlet, sequential Dirichlet-Neumann, parallel Neumann-Neumann and parallel Dirichlet-Dirichlet algorithm. François et al. (2015) investigated the effect of these algorithms and the relaxation parameter on the convergence of the coupling iteration.

The direct coupling is conceptually simpler and easy to implement, while it yields non-symmetric and non-positive definite system matrix that requires the development of special solution strategies (Rizos and Wang 2002). The staggered scheme avoids the assembly and solution of a global system of coupled equations and enable the possibility to model large structural systems, and it allows the use of different time step sizes for the two subdomains. The downside of the staggered schemes is that they incorporate iterations within each step to achieve convergence which make the computation much less efficient. To enable and speed up the convergence, a relaxation operator is applied to the interfacial conditions, the choice of which are unfortunately rather empirical (Liu et al. 2011).

Although time domain BEMs and its coupling with FEMs has been extensively studied in the last few decades, most of them incorporate full-space green's function, i.e. the Stokes' solution, while the number of researches on BEM with half-space Green's functions remains limited. The reason is mostly attributed to the complexity of half-space Green's function in aspect of theoretic derivation, numerical implementation as well as the computation. Comparing with the full-space Green's functions, the half-space Green's functions satisfy the free-surface condition and hence the BEMs with half-space Green's functions bypass the need of discretizing the free-surface in soil-structure interaction problems. It reduces the errors related to the discretization, leads to a smaller matrix system for BEMs and eliminates the limitation of the duration of valdiity of the computed solution.

Using Johnson (1974)'s solution on Lamb's problem as the Green's function for a homogenous half-space, Triantafyllidis (1991) presented a direct time-domain boundary element method and investigated its applications to various dynamic soil-structure interaction problems. Based on half-space Green's functions for displacements elicited by Heaviside time-dependent surface point loads, Bodes et al. (2002) proposed time-domain FEM-BEM direct coupling formulation and applied it to analyses the dynamic response of a railway track due to moving wheel set. The Green's functions in C. Bode et al. (2002) restrict that both source and receiver points to be located on the free surface and thus the FEM-BEM formulation cannot deal with the cases where structures are embedded into the soil. Again, by virtue of Johnson (1974)'s fundamental solutions and some effective treatment on the singularities at the arrival time of the Rayleigh waves, Galvín and Romero (2014) implemented a direct FEM-BEM coupling toolbox for soil-structure interaction analysis. Furthermore, to consider the influence of soil stratification, Romero and Galvín (2015) presented a coupled FEM-BEM formulation in time domain, where layered half-space Green's functions developed by Park and Kausel (2006) was adopted for the BEM.

In this chapter the regularized time-domain BEM formulation that established in chapter 2 is enhanced with the homogeneous and multi-layered half-space Green's functions. A direct coupling of BEM with FEM is presented then to proceed transient soil-structure interaction analysis.

8.2 Time-domain BEM for half-space

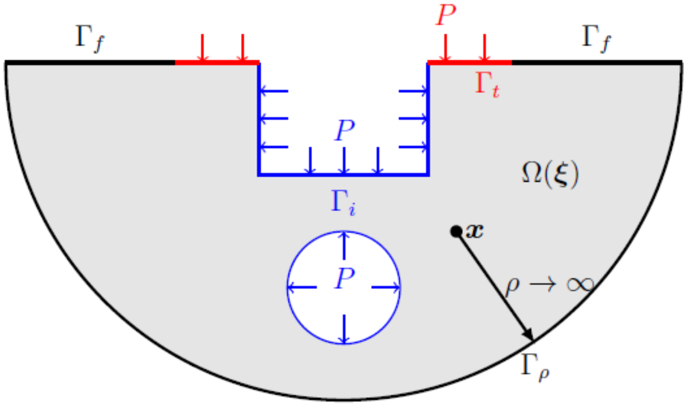

Figure 8.1: 3-D half-space problem

As shown in Figure 8.1 is a half-space body $\Omega(\xi)$ with several excavations, which may be in shape of foundations, cavities, rocks, underground structures, etc. It is recalled here that, with the aid of Graffi's reciprocal theorem and time-domain Green's function pertaining to the half-space, the displacement of a point $\boldsymbol{x}$ inside $\Omega(\xi)$ can be represented by a boundary integral, i.e.,

$$u_k(\mathbf{x},t)*g(t)=\int_\Gamma t_i(\xi,t)*\hat{U}_i^k(\xi,t;\mathbf{x}\,|\,g)\mathrm{d}\Gamma_\xi-\int_\Gamma \hat{T}_i^k(\xi,t;\mathbf{n},\mathbf{x}\,|\,g)*u_i(\xi,t)\mathrm{d}\Gamma_\xi. \quad \mathbf{x}\in\Omega \quad (8.1)$$

where $\boldsymbol{u}$ and $\mathbf{t}$ respectively identifies the displacement and traction, $*$ stands for the Riemann convolution, $\hat{U}$ and $\hat{T}$ designates the Green's function of displacements and tractions, and $g(t)$ denotes time variation of the point load associated with the Green's function.

To take the advantages of several properties of Green's function, the close boundary $\Gamma(\xi)$ of $\Omega(\xi)$ is partitioned into four parts here, i.e.,

$\boldsymbol{\Gamma}_i$ **:** Boundaries of the inside excavations;

$\boldsymbol{\Gamma}_t$ **:** Part of the surface of the half-space that is bearing external tractions;

Γ_f : Free surface of the excavated half-space;

Γ_ρ : Outer surface of the half-space with an infinity radius.

Consider firstly Γ_ρ. The general regularity condition requires that

$$\lim_{\rho\to\infty}\int_{\Gamma_\rho}\left(t_i(\xi,t)*\hat{U}_i^k(\xi,t;\mathbf{x}\,|\,g)-\hat{T}_i^k(\xi,t;\mathbf{n},\mathbf{x}\,|\,g)*u_i(\xi,t)\right)\mathrm{d}\Gamma_\xi=0,\quad\forall\mathbf{x}\in\Omega. \tag{8.2}$$

Noting that the traction $\mathbf{t}$ vanishes on the surface Γ_f, while $\hat{T}$ vanishes on both Γ_f and Γ_t, one can obtain from Eqn. (8.1) that

$$u_k(\mathbf{x},t)*g(t)=\int_{\Gamma_t+\Gamma_i}t_i(\xi,t)*\hat{U}_i^k(\xi,t;\mathbf{x}\,|\,g)\mathrm{d}\Gamma_\xi-\int_{\Gamma_i}\hat{T}_i^k(\xi,t;\mathbf{n},\mathbf{x}\,|\,g)*u_i(\xi,t)\mathrm{d}\Gamma_\xi,\quad\mathbf{x}\in\Omega. \tag{8.3}$$

Making use of the decomposition of the Green function as in Chapter 2, a regularized boundary integral equation can be established from Eqn. (8.3) as

$$\begin{aligned}u_k(\mathbf{x},t)*g(t)=&\int_{\Gamma_t+\Gamma_i}t_i(\xi,t)*\hat{U}_i^k(\xi,t;\mathbf{x}\,|\,g)\mathrm{d}\Gamma_\xi-\int_{\Gamma_i}[\hat{T}_i^k(\xi,t;\mathbf{n},\mathbf{x}\,|\,g)]_2*u_i(\xi,t)\mathrm{d}\Gamma_\xi\\&-\int_{\Gamma_i}[\hat{T}_i^k(\xi,t;\mathbf{n},\mathbf{x}\,|\,g)]_1*\left(u_i(\xi,t)-u_i(\mathbf{x},t)\right)\mathrm{d}\Gamma_\xi,\quad\mathbf{x}\in\Omega,\end{aligned} \tag{8.4}$$

where the singular part of the Green's function $[\hat{T}_i^k(\xi,t;\mathbf{n},\mathbf{x}\,|\,g)]_1$ and the regular part $[\hat{T}_i^k(\xi,t;\mathbf{n},\mathbf{x}\,|\,g)]_2$ are defined through

$$\begin{aligned}&[\hat{T}_i^k(\xi,t;\mathbf{n},\mathbf{x}\,|\,g)]_1=\hat{\hat{T}}_i^k(\xi;\mathbf{n},\mathbf{x})g(t)\\&[\hat{T}_i^k(\xi,t;\mathbf{n},\mathbf{x}\,|\,g)]_2=\hat{T}_i^k(\xi,t;\mathbf{n},\mathbf{x}\,|\,g)-[\hat{T}_i^k(\xi,t;\mathbf{n},\mathbf{x}\,|\,g)]_1\end{aligned}. \tag{8.5}$$

Here, $\hat{\hat{T}}_i^k(\xi;\mathbf{n},\mathbf{x})$ is usually taken to be static Green's functions that can capture the singularity of the time-domain Green's functions. For a homogeneous half-space, $\hat{\hat{T}}_i^k(\xi;\mathbf{n},\mathbf{x})$ can be

Mindlin (1936)'s solution while for a multi-layered half-space, $\hat{\hat{T}}_i^k\left(\boldsymbol{\xi};\mathbf{n},\mathbf{x}\right)$ is the static Green's function of a bi-material full-space (Guzina and Pak 1999). It should be pointed out that, after the regularization by singularity extraction, the boundary integral equation (8.4) contains integrands that are at most weakly singular as the need to evaluate the Cauchy principal value of integrals in the classical boundary element formulations is eliminated.

From a temporal and spatial discretization of Eqn. (8.4), a recurrence relationship for step $n+1$

$$\left[\mathbf{H}\right]\{\mathbf{u}\}_{n+1}=\left[\mathbf{G}\right]\{\mathbf{t}\}_{n+1}+\{\mathbf{R}\}_{n+1}, \tag{8.6}$$

supposing everything is known till step n as discussed in Chapter 2.

8.3 Finite element formulation

In the context of FEM, the semi-discrete equation of motion is usually written as

$$\left[\mathbf{M}\right]\left\{\ddot{\mathbf{u}}\right\}+\left[\mathbf{C}\right]\left\{\dot{\mathbf{u}}\right\}+\left[\mathbf{k}\right]\left\{\mathbf{u}\right\}=\left[\mathbf{f}\right] \tag{8.7}$$

where $\left[\mathbf{M}\right]$ stands for the mass matrix, $\left[\mathbf{C}\right]$ designates the viscous damping matrix, and $\left[\mathbf{K}\right]$ denotes the stiffness matrix, $\left\{\mathbf{F}\right\}$ is the vector of external forces, and $\left\{\mathbf{u}\right\},\left\{\dot{\mathbf{u}}\right\},\left\{\ddot{\mathbf{u}}\right\}$ are the displacement, velocity and acceleration vectors respectively.

One of the most widely used time integration algorithm for Eqn. (8.7) is the Newmark method, which consists of the following equations:

$$\begin{aligned}\{\mathbf{u}\}_{n+1}&=\{\mathbf{u}\}_n+\Delta t\{\dot{\mathbf{u}}\}_n+\frac{\Delta t^2}{2}\left[\left(1-2\beta\right)\{\ddot{\mathbf{u}}\}_n+2\beta\{\ddot{\mathbf{u}}\}_{n+1}\right],\\ \{\dot{\mathbf{u}}\}_{n+1}&=\{\dot{\mathbf{u}}\}_n+\Delta t\left[\left(1-\gamma\right)\{\ddot{\mathbf{u}}\}_n+\gamma\{\ddot{\mathbf{u}}\}_{n+1}\right],\end{aligned} \tag{8.8}$$

where the subscript n denotes the time step, Δt stands for the time step size, β and γ are two parameters that determine the stability and accuracy characteristics of the algorithm.

Recall that the fundamental unknowns in BEM formulation are nodal traction and displacement. In preparation for the coupling with BEM formulation, it is useful to represent all unknowns in Eqn. (8.7) in terms of displacement by virtue of Eqn. (8.8). To this end, one may establish Newmark's integration algorithm in the form of

$$\left[\tilde{\mathbf{K}}\right]\{\mathbf{u}\}_{n+1} = \{\tilde{\mathbf{f}}\}_{n+1}, \tag{8.9}$$

with

$$\left[\tilde{\mathbf{K}}\right] = \frac{1}{\beta \Delta t^2}[\mathbf{M}] + \frac{\gamma}{\beta \Delta t}[\mathbf{C}] + [\mathbf{K}], \tag{8.10}$$

and

$$\begin{aligned} \{\tilde{\mathbf{f}}\}_{n+1} = \{\mathbf{f}\}_{n+1} + \left(\frac{1}{\Delta t^2}[\mathbf{M}] + \frac{\gamma}{\beta \Delta t}[\mathbf{C}]\right)\left(\{\mathbf{u}\}_n + \Delta t\{\dot{\mathbf{u}}\}_n + \frac{\Delta t^2}{2}(1-2\beta)\{\ddot{\mathbf{u}}\}_n\right). \\ -[\mathbf{C}]\left(\{\dot{\mathbf{u}}_n\} + \Delta t(1-\gamma)\{\ddot{\mathbf{u}}\}_n\right) \end{aligned} \tag{8.11}$$

Depending on the choice of the 2 paramaters, Newmark algorithm can be implicit or explicit. A special case of Newmark's family is the commonly used method of *central difference* with

$$\begin{aligned} \{\dot{\mathbf{u}}\}_n &= \frac{1}{2\Delta t}\left(\{\mathbf{u}\}_{n+1} - \{\mathbf{u}\}_{n-1}\right) \\ \{\ddot{\mathbf{u}}\}_n &= \frac{1}{\Delta t^2}\left(\{\mathbf{u}\}_{n+1} - 2\{\mathbf{u}\}_n + \{\mathbf{u}\}_{n-1}\right) \end{aligned}. \tag{8.12}$$

Invoking the central difference Eqn. (8.12), the finite element equation of motion (8.7) can be rewritten in the form of Eqn. (8.9) with

$$\left[\tilde{\mathbf{K}}\right] = \frac{1}{\Delta t^2}[\mathbf{M}] + \frac{1}{2\Delta t}[\mathbf{C}], \tag{8.13}$$

and

$$\{\tilde{\mathbf{f}}\}_{n+1} = \{\tilde{\mathbf{f}}\}_n + \left(\frac{2}{\Delta t^2}[\mathbf{M}] - [\mathbf{K}]\right)\{\mathbf{u}\}_n + \left(\frac{1}{2\Delta t}[\mathbf{C}] - \frac{1}{\Delta t^2}[\mathbf{M}]\right)\{\mathbf{u}\}_{n-1}. \tag{8.14}$$

8.4 BEM-FEM coupling

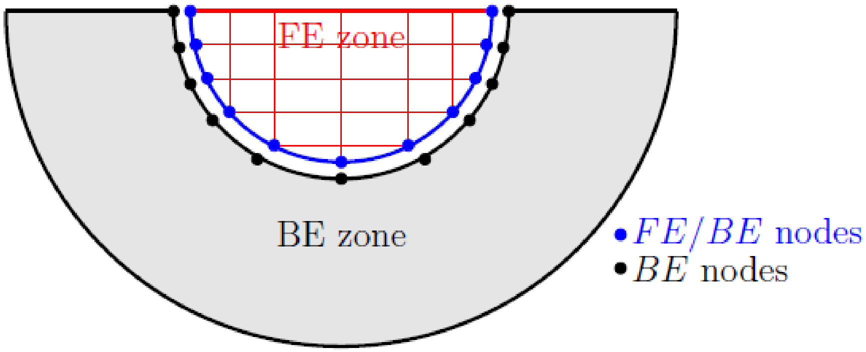

Figure 8.2: BE-FE coupling

The compatibility and equilibrium condition across the FE-BE interface imply that

$$\begin{aligned} \mathbf{u}^{FE/BE} &= \mathbf{u}^{BE} \\ \mathbf{t}^{FE/BE} &= -\mathbf{t}^{BE} \end{aligned}. \tag{8.15}$$

Note that the relationship between nodal forces and tractions is

$$\{\mathbf{f}\}^{FE/BE} = [\mathbf{T}]\{\mathbf{t}\}^{FE/BE} = -[\mathbf{T}]\{\mathbf{t}\}^{BE}. \tag{8.16}$$

Here the force-traction transformation matrix $[\mathbf{T}]$ can be computed through

$$[\mathbf{T}] = \int_{\Gamma_{FE/BE}} [\mathbf{N}]^T [\mathbf{N}] d\Gamma, \tag{8.17}$$

where $[\mathbf{N}]$ stands for the matrix of shape functions.

In the coupling of a finite element zone with a boundary element interface, the unknown displacements in Eqn. (8.9) are partitioned into two sets. One contains the DOFs related to interior FE nodes, while the other contains the DOFs associated with the interfaces. Consequently, Eqn. (8.9) becomes

$$\begin{bmatrix} \tilde{\mathbf{K}}^{FE} & \tilde{\mathbf{K}}^{FE/BE} \\ \tilde{\mathbf{K}}^{FE/BE^T} & \tilde{\mathbf{K}}^{BE/BE} \end{bmatrix} \begin{Bmatrix} \mathbf{u}^{FE}_{n+1} \\ \mathbf{u}^{FE/BE}_{n+1} \end{Bmatrix} = \begin{Bmatrix} \tilde{\mathbf{f}}^{FE}_{n+1} \\ \tilde{\mathbf{f}}^{FE/BE}_{n+1} \end{Bmatrix}. \tag{8.18}$$

Next, the nodal forces exerted upon the interfacial nodes by the BEM is superimposed to yield

$$\begin{bmatrix} \tilde{\mathbf{K}}^{FE} & \tilde{\mathbf{K}}^{FE/BE} \\ \tilde{\mathbf{K}}^{FE/BE^T} & \tilde{\mathbf{K}}^{BE/BE} \end{bmatrix} \begin{Bmatrix} \mathbf{u}_{n+1}^{FE} \\ \mathbf{u}_{n+1}^{FE/BE} \end{Bmatrix} = \begin{Bmatrix} \tilde{\mathbf{f}}_{n+1}^{FE} \\ \tilde{\mathbf{f}}_{n+1}^{FE/BE} - [\mathbf{T}]\{\mathbf{t}\}_{n+1}^{BE} \end{Bmatrix}. \tag{8.19}$$

Invoking the BEM Eqn. (8.6) to represent the traction on the interface in terms of displacements, one finds that

$$\begin{bmatrix} \tilde{\mathbf{K}}^{FE} & \tilde{\mathbf{K}}^{FE/BE} \\ \tilde{\mathbf{K}}^{FE/BE^T} & \tilde{\mathbf{K}}^{BE/BE} \end{bmatrix} \begin{Bmatrix} \mathbf{u}_{n+1}^{FE} \\ \mathbf{u}_{n+1}^{FE/BE} \end{Bmatrix} = \begin{Bmatrix} \tilde{\mathbf{f}}_{n+1}^{FE} \\ \tilde{\mathbf{f}}_{n+1}^{FE/BE} - [\mathbf{T}][\mathbf{G}]^{-1}[\mathbf{H}]\{\mathbf{u}\}_{n+1}^{BE} + [\mathbf{T}][\mathbf{G}]^{-1}\mathbf{R}_{n+1}^{BE} \end{Bmatrix}. \tag{8.20}$$

Appealing to the compatibility condition described in Eqn. (8.15), Eqn. (8.20) can be assembled yielding the final equation system of

$$\begin{bmatrix} \tilde{\mathbf{K}}^{FE} & \tilde{\mathbf{K}}^{FE/BE} \\ \tilde{\mathbf{K}}^{FE/BE^T} & \tilde{\mathbf{K}}^{BE/BE} + [\mathbf{T}][\mathbf{G}]^{-1}[\mathbf{H}] \end{bmatrix} \begin{Bmatrix} \mathbf{u}_{n+1}^{FE} \\ \mathbf{u}_{n+1}^{FE/BE} \end{Bmatrix} = \begin{Bmatrix} \tilde{\mathbf{f}}_{n+1}^{FE} \\ \tilde{\mathbf{f}}_{n+1}^{FE/BE} + [\mathbf{T}][\mathbf{G}]^{-1}\{\mathbf{R}\}_{n+1}^{BE} \end{Bmatrix}. \tag{8.21}$$

8.5 Numerical examples

8.5.1 Buried cavity

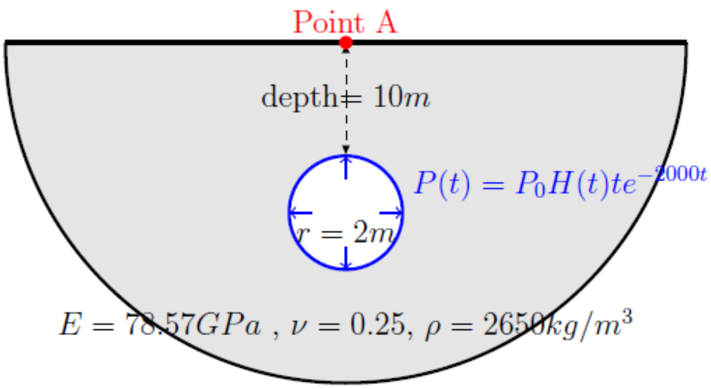

Figure 8.3: 3-D buried cavity under internal pressure

Considered a spherical cavity of radius $r = 1m$ buried in a homogenous half-space as illustrated in Figure 8.3. The cavity is subjected to an internal blast loading, pressure of which is specified to be

$$P(t) = 5436.56H(t)te^{-2000t}\,(Pa). \tag{8.22}$$

The BEM formulation with half-space Green's function as stated in Eqn. (8.4) is employed to do the analysis, and thus only the surface of the spherical cavity is needed to be discretized. In this example, the cavity surface is meshed with 272 linear elements.

A short-time analytical solution for the displacement history of point A in Figure 8.3 has been investigated by (Jiang, Baird, & Blair, 1994). The analytical solution is only valid before the reflection waves hit the free-surface, while specifically in this example, the analytical solution is valid between time interval $[0, t_{valid}]$, where $t_{valid} = 5e^{-3}s$.

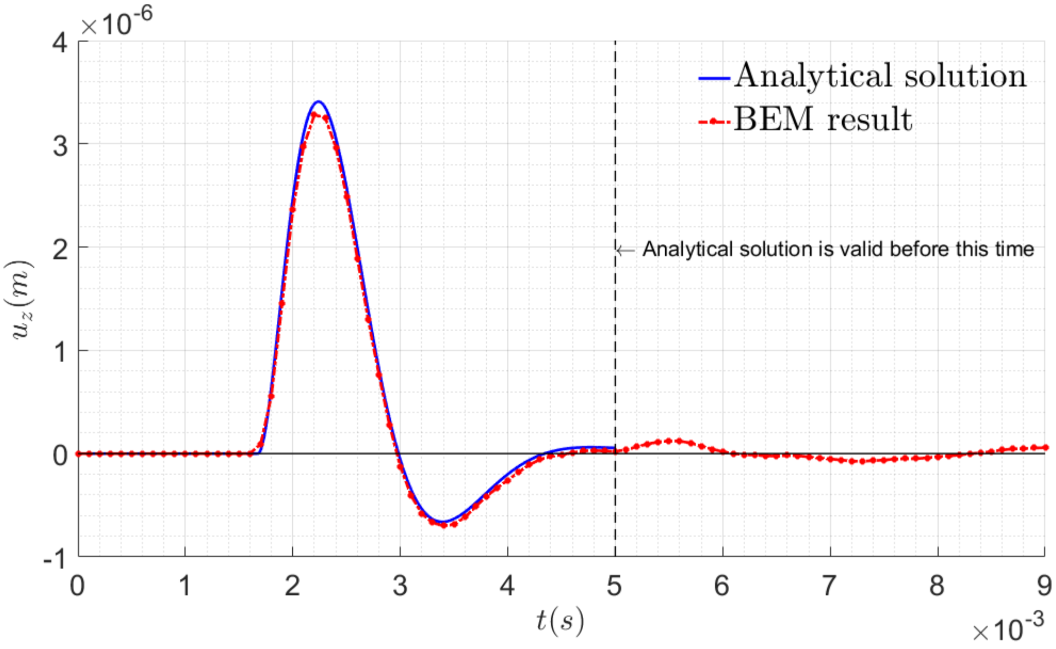

Figure 8.4: Vertical displacement history of point A.

For comparison, the time history of the point A's vertical displacement obtained from BEM solutions are plotted together with the analytical solution in Figure 8.4. As can be seen from the display, the numerical result matches very well with the analytical solution between $\left[0, t_{valid}\right]$. Beyond time t_{valid}, the displacement fluctuates due to the waves reflected back and forth between the free surface and the cavity surface, and eventually decays to 0 because of the radiation damping.

This problem has also been investigated by BEM based on Convolution Quadrature Method in Kager (2015). Full-space Green's function was utilized in Kager (2015)'s treatment, and a patch of the free-surface with dimension of 30m×30m centered at the origin of the coordinate system was discretized with several thousand triangular elements. On contrast, the BEM formulation employing half-space Green's function proposed here avoids such a discretization and yields better solution.

8.5.2 Soil-structure interaction

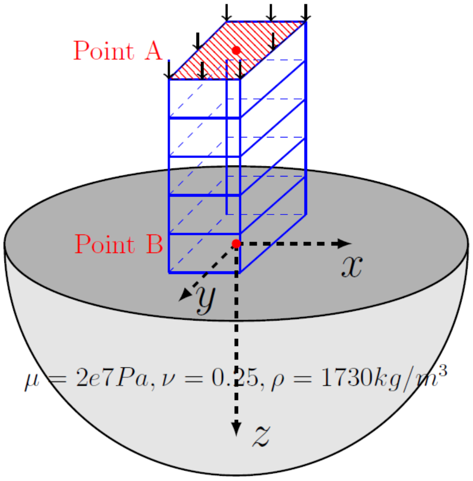

Figure 8.5: Soil-structure interaction model

As shown in Figure 8.5 is a building structure bonded on the free-surface of a half-space. The cuboid structure has dimensions of (0.4, 0.4, 2) meters in (x, y, z) −directions respectively. The structure and the soil are made up of the same linear isotropic material with parameters of

$\mu = 2e7Pa$, $\rho = 1730Kg/m^3$ and $\nu = 0.25$. Uniform vertical traction is applied on top of the building, which can be expressed as

$$P(t) = 2500H(t). \tag{8.23}$$

The structure is modeled by FEM, while the soil is by BEM, which are then coupled in the manner of Eqn. (8.21). For the boundary element zone, 4-node quadratic surface elements are used. For the finite element zone, 3-D 8-node cubic solid elements are employed. For time integration of FEM, the Newmark method is employed with $\beta = \frac{1}{4}$ and $\gamma = \frac{1}{2}$. Time step size Δt is chosen such that $\beta = \Delta t \cdot \frac{c_d}{l_e} = 1$, where l_e is the dimension of the elements and c_d is the longitudinal wave speed.

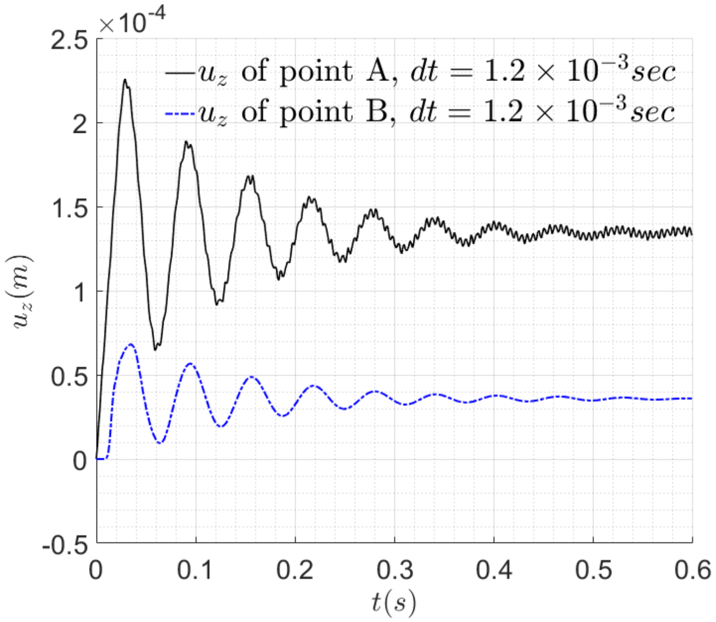

Figure 8.6: Time history of vertical displacement of points A and B

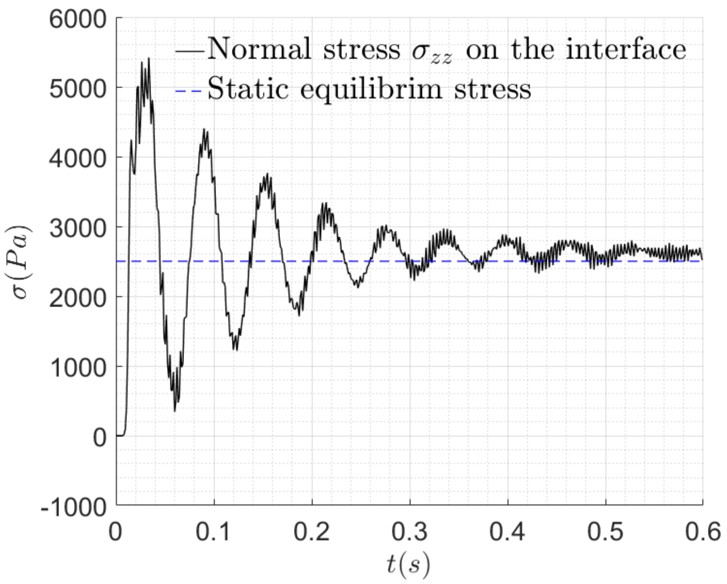

Figure 8.7: Time history of σ_{zz} at point B

Figure 8.6 displays time history of the vertical displacement of both point A and B, which oscillates with a decaying amplitude and dies eventually due to the radiation damping. The same phenomenon of decaying oscillation can be observed from the time history of traction at point B. The traction at point B approaches the static equilibrium stress as time goes on.

8.5.3 Two-zone soil-structure interaction

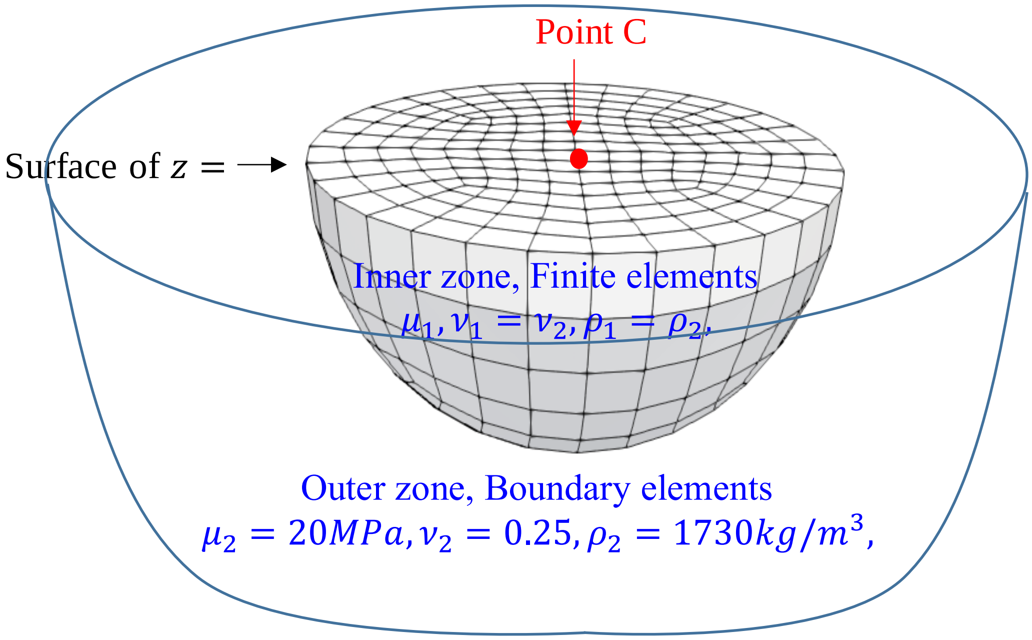

Figure 8.8: A two-zone FE-BE model

Considered in this example is a hemisphere buried in a homogeneous half-space as shown in Figure 8.8. The radius of the hemisphere is 1meter, and its top surface aligns parallelly with the free-surface of the half-space. The hemisphere is denoted as inner zone while the excavated half-space is denoted as outer zone in Figure 8.8. Geometrically, the inner and outer zone form a half-space. For the boundary element zone, 8-node quadratic surface elements are used. For the finite element zone, 20-node cubic solid elements are employed.

To study the dynamic response of the two-zone model under the uniform pressure on the top surface of the hemisphere, the inner zone is discretized with solid finite elements while the outer zone is discretized by boundary elements. In this example, the finite element mesh conforms with the boundary element mesh on the interface. For the sake of accuracy as well as numerical stability, the time step size Δt is chosen such that $\beta = \Delta t \cdot \frac{c_d}{l_e} = 1$, where l_e is the dimension of the elements and c_d is the longitudinal wave speed. The uniform pressure on the top surface is specified to be a sinusoidal pulse, i.e.,

$$p(t) = \begin{cases} \sin\left(2\pi t/0.03\right), & t \le 0.03\text{sec} \\ 0, & t > 0.03\text{sec} \end{cases}. \tag{8.24}$$

To verify the FEM-BEM coupling algorithm described in this section, the elastic material parameters are set to the same as the half-space, which are $\mu_1 = \mu_2 = 20MPa,\ \nu_1 = \nu_2 = 0.25,\ \rho_1 = \rho_2 = 1730kg/m^3$. In this case, the two-zone forms a single homogeneous half-space, and time history of vertical displacement of point C can be obtained analytically through the integration of Green's function proposed in Chapter 5. The numerical result of point C's vertical displacement is compared against the analytical solution in Figure 8.9. From Figure 8.9(a), one can see that the numerical solution is close to the analytical solution with residue oscillations at the early stage, while Figure 8.9(b) shows that the numerical results become unstable after a long-time run.

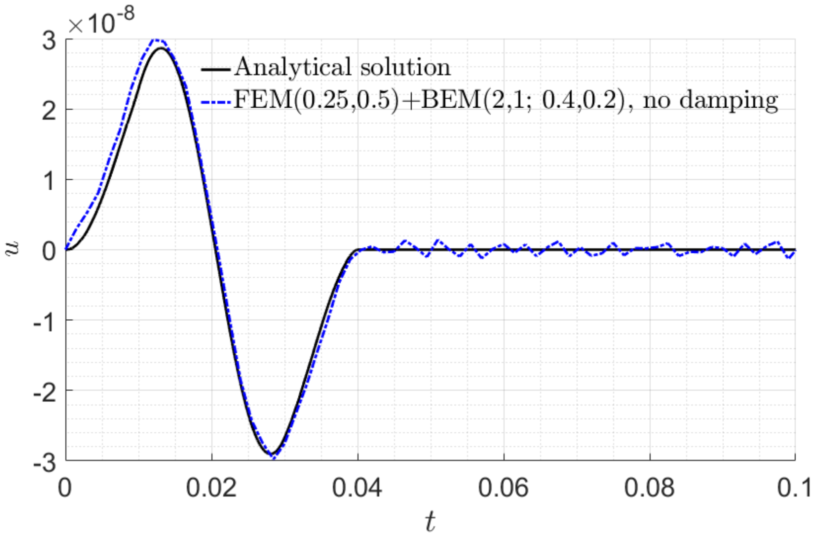

(a) Response at the early stage

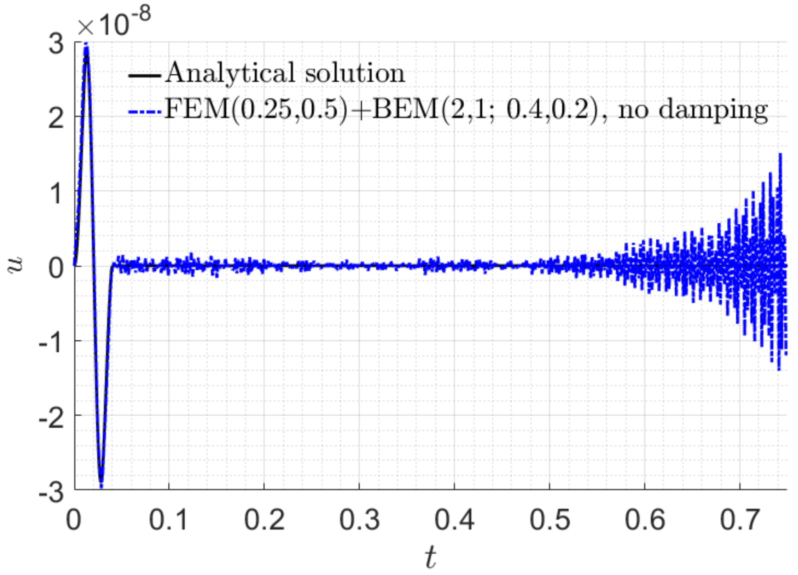

(b) Response over a long time

Figure 8.9: Time history of vertical displacement of point C.

To reduce the numerical oscillations and avoid the instability, a Rayleigh damping is introduced as

$$\mathbf{C} = \beta_d \mathbf{K} . \tag{8.25}$$

As shown in Figure 8.10, the Rayleigh damping with $\beta_d = 5e^{-4}$ improves the response's smoothness and its stability over a long-time run, although the damping also brings about some phase shift/delay as in step-by-step time integration in finite eelement methods. To explore the issue further, the effect of damping is examined with the comparison among the cases of $\beta_d = 5e^{-4},\ 5e^{-3},\ 1e^{-2}$, and the results are shown in Figure 8.11. One can see that a larger damping ratio for the finite element zone reduces the amplitude of the response and brings in more phase delay as expected.

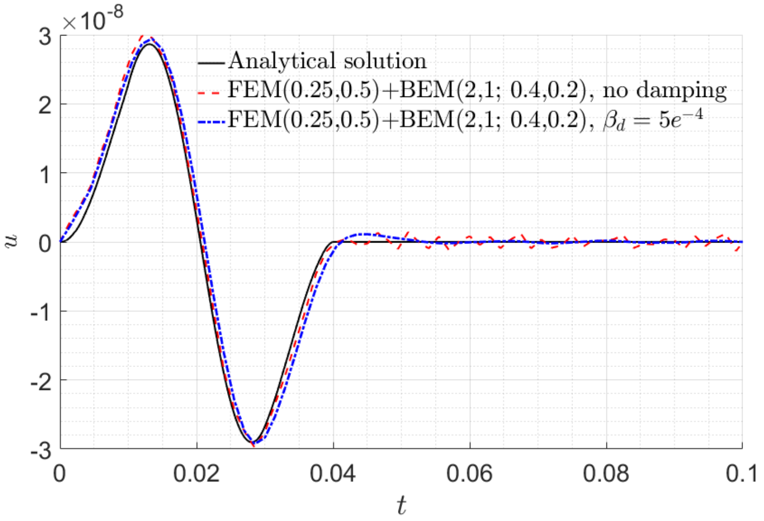

(a) Response at the early stage

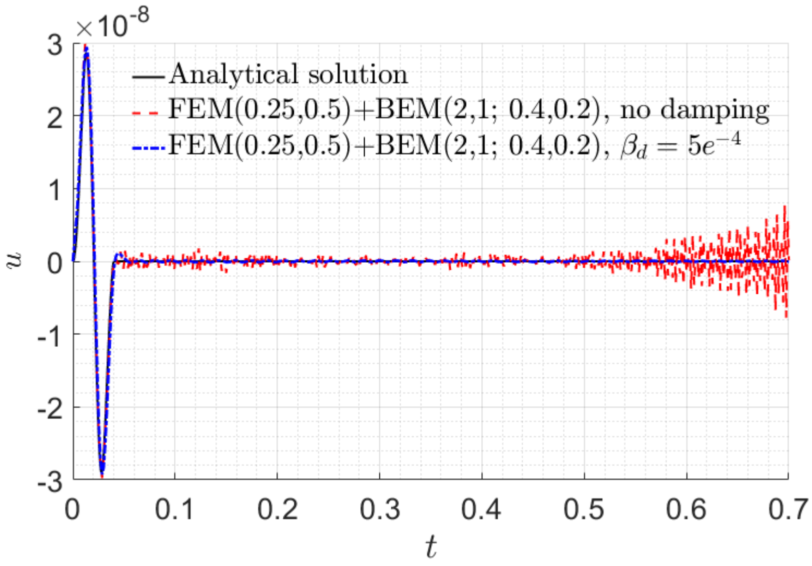

(b) Response over a long time

Figure 8.10: Time history of vertical displacement of point C in case of damping

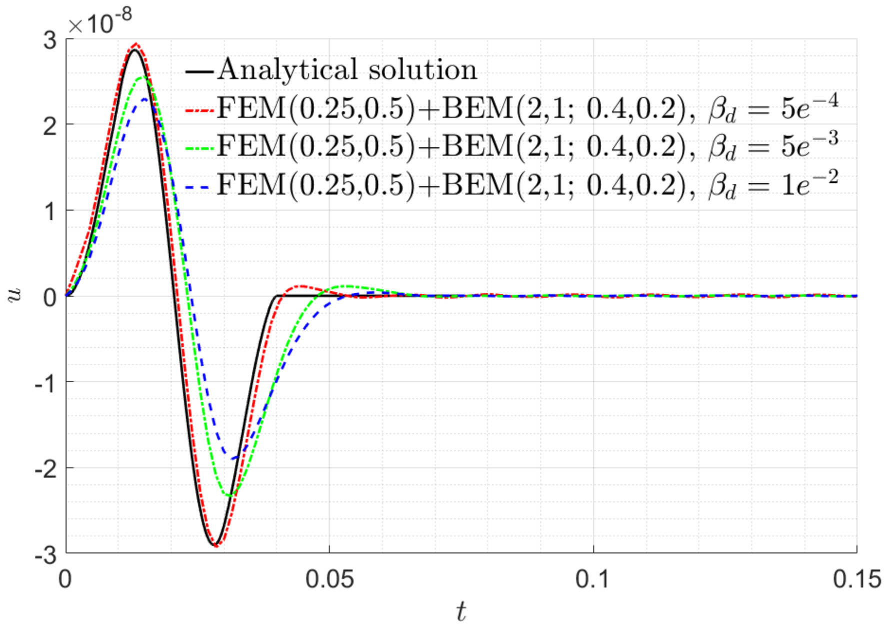

Figure 8.11: Effect of damping ratio

Another way to introduce some numerical damping is by adjusting the values of β, γ in the Newmark-β integration scheme, e.g., see Hughes (2012). For example, three combinations, namely, $(\beta,\gamma)=(0.25,0.5)$, $(0.3.0.6)$, $(0.35,0.7)$ are tested, and the results are plotted in Figure 8.12. Among the three, one can see that the larger β leads to smoother results.

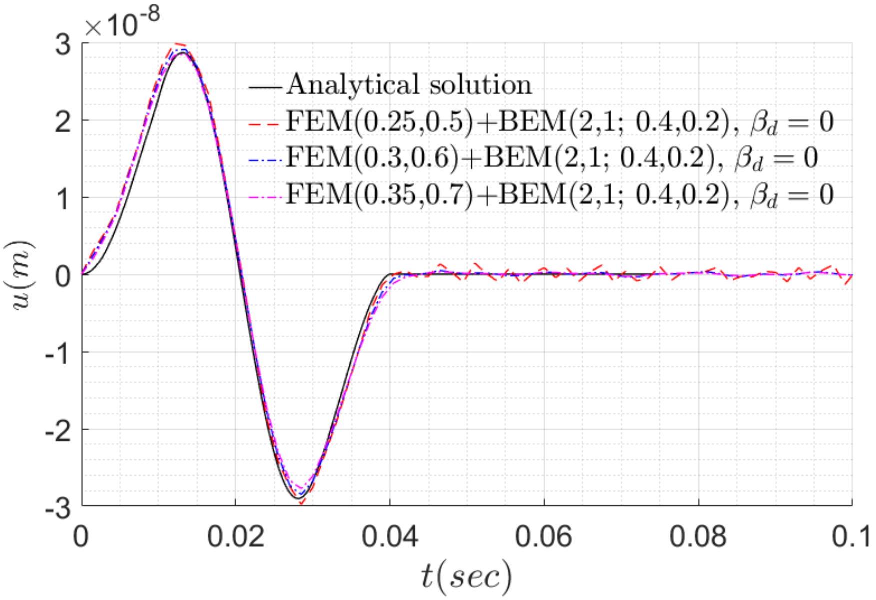

Figure 8.12: Effect of Newmark-β parameters

Similar to using the Newmark-β parameters, the parameters of $(\mathcal{O}^u,\mathcal{O}^t;\alpha_a,\alpha_b)$ in the proposed generalized boundary element time-marching scheme can also be used to control the numerical performance as described in Chapter 2 and 3. As depicted in Figure 8.13, the result corresponding the choice of $(\mathcal{O}^u,\mathcal{O}^t;\alpha_a,\alpha_b)=(2,1;\ 0.2,0.2)$ is found to be unstable, while a slight increase in α_a helps to stabilize the result. For completeness, the approximate stability zone of the $(\mathcal{O}^u,\mathcal{O}^t)=(2,1)$ -scheme with respect to collocation weights $\left(\alpha_a,\alpha_b\right)$ is shown in Figure 8.14.

To check the influence of $(\mathcal{O}^u,\mathcal{O}^t;\alpha_a,\alpha_b)$ on accuracy, three different combinations are examined in Figure 8.15. One can observe that all three combinations leads to results that are close to the analytical solution. As the difference between them is not noticeable, this indicates that the choice of $(\mathcal{O}^u,\mathcal{O}^t;\alpha_a,\alpha_b)$ is not too influential to the accuracy at least in this example.

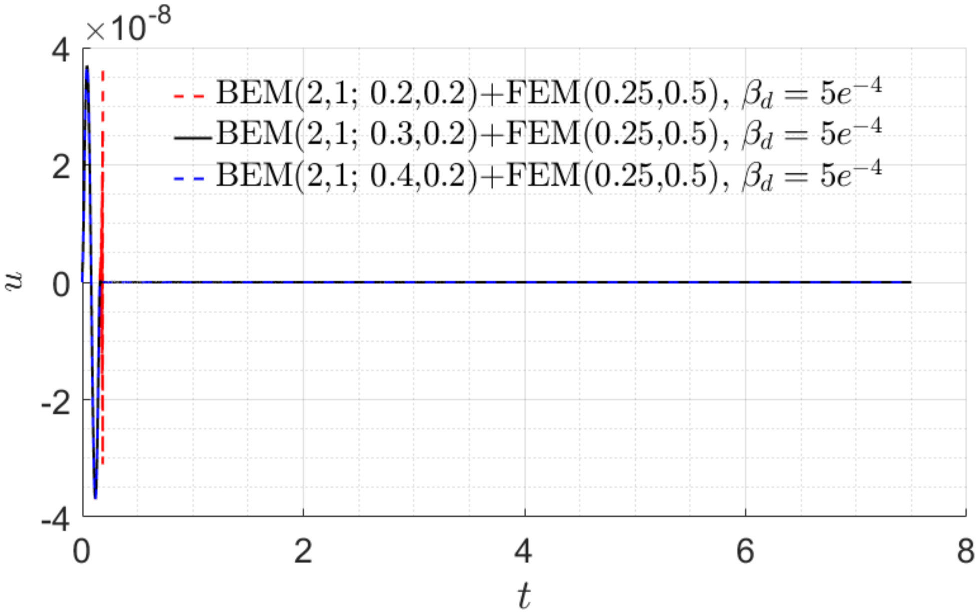

Figure 8.13: Effect of (α_a, α_b) on the stability. $\Delta t = l_e/c_d$.

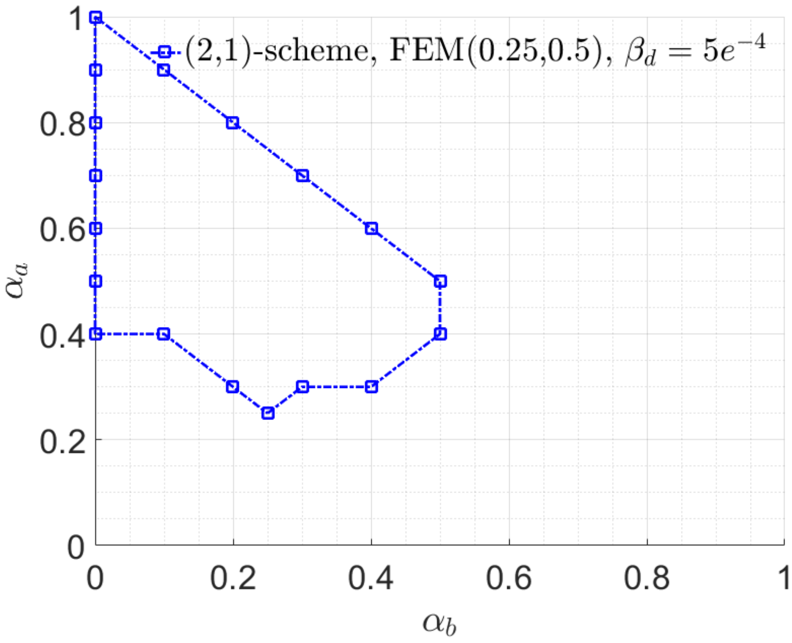

Figure 8.14: Stability zone of the $(\mathcal{O}^u,\mathcal{O}^t)=(2,1)$ -scheme with respect to collocation weights (α_a, α_b). $\Delta t = l_e/c_d$

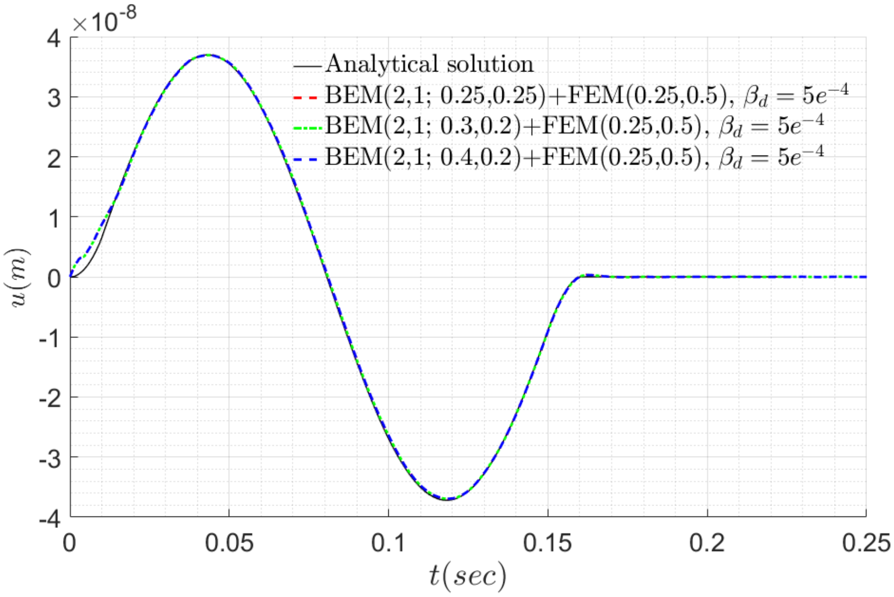

Figure 8.15: Effect of (α_a, α_b) on accuracy. $\Delta t = l_e/c_d$.

For the two-zone model with identical homogenous elastic properties, it is demonstrated that the FEM-BEM coupling algorithm presented in this chapter can achieve accurate and stable results via a suitable choic of algorithmic parameters and mesh configuration**.** Using $\beta = 0.25$, $\gamma = 0.5$ for FEM's Newmark-β time integration for the finite inner zone and (2,1; 0.4,0.2; 1,1) in the proposed generalized-BEM scheme for the exterior half-space, the two-zone model with different properties (and the same mesh configuration) are investigated by the coupled FEM-BEM algorithm. To examine further the physics of the problem, the interior and exterior zone's parameters are also set to have three different shear modulus ratios of $\frac{\mu_1}{\mu_2} = 0.4, 1, 2$ with the same mass density ρ, Poisson's ratio of 0.25, and a common reference $\mu_2 = 20$MPa. Two interior zones, one of which is much more softer and the other is much stiffer than exterior zone, are considered and the results are compared with the homogeneous case as shown in Figure 8.16. From the comparison, one can see, as expected, that the amplitude of the displacement at point C is larger in the case where the interior zone is softer. For all cases, the displacements go back to zero eventually because the wave-transmitting effect offered by BEM representation of the half-space.

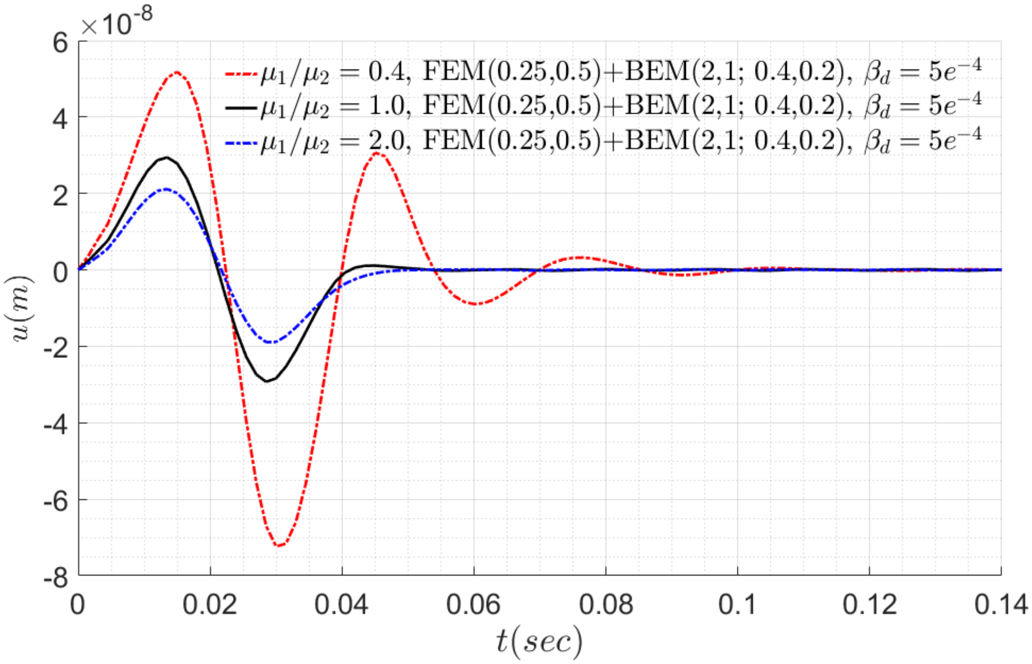

Figure 8.16: Effect of shear modulus

8.5.4 Soil-foundation-structure interaction by FE-BE coupling

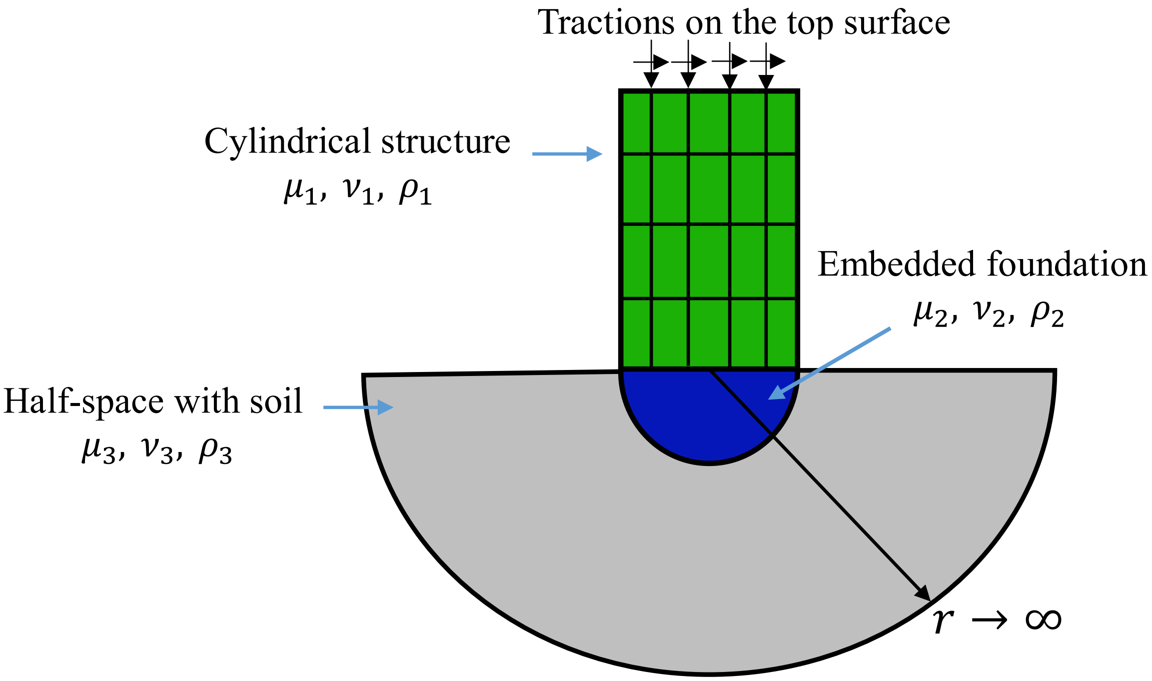

Figure 8.17: Three-dimensional soil-foundation-structure interaction model

Going beyond testing the BEM-FEM coupling method for the test case of a two-zone representation of the halfspace, the performance of the formulation to a more general structure-foundation-soil configurations is of interest. One such soil-structure interaction problem is depicted in Figure 8.17. In this case, the scenarios of an applied uniform vertical traction (a load with x-y plane symmetry) and a uniform horizontal traction (an asymmetric load) at the top surface of the cylindrical structure are both considered. As before, both the cylindrical structure and its foundation underneath are discretized with finite elements while the excavated half-space is modeled by boundary elements as shown in Figure 8.18. For the BE zone, 4-node quadrilateral elements are used, while for the FE zone, 8-node cubic elements are used in this example.

For the configuration where $\mu_1 = 1e7\text{Pa}$, $\mu_2 = \mu_3 = 2e7\text{Pa}$, $\nu_1 = \nu_2 = \nu_3 = 0.25$, and $\rho_1 = 1000\text{kg/m}^3, \rho_2 = \rho_3 = 1730\text{kg/m}^3$, the vertical displacement history of point A corresponding to a vertical traction is plotted in Figure 8.19, where time function of the vertical traction is

$$p(t) = \begin{cases} \sin\left(2\pi t/0.03\right), & t \le 0.03\text{sec} \\ 0, & t > 0.03\text{sec} \end{cases}. \tag{8.25}$$

The computed time histories of the horizontal displacement of point A and B corresponding to a horizontal traction are plotted in Figure 8.20 and Figure 8.21 respectively. From the results, one can see that the magnitude of the structure motion decays as time goes on, which reflects the energy radiation transmitted into the half-space. One may also note that the decay of motion under vertical load is considerably faster than under horizontal loading, a well-known difference in the characteristics of radiation damping bertween the two cases.

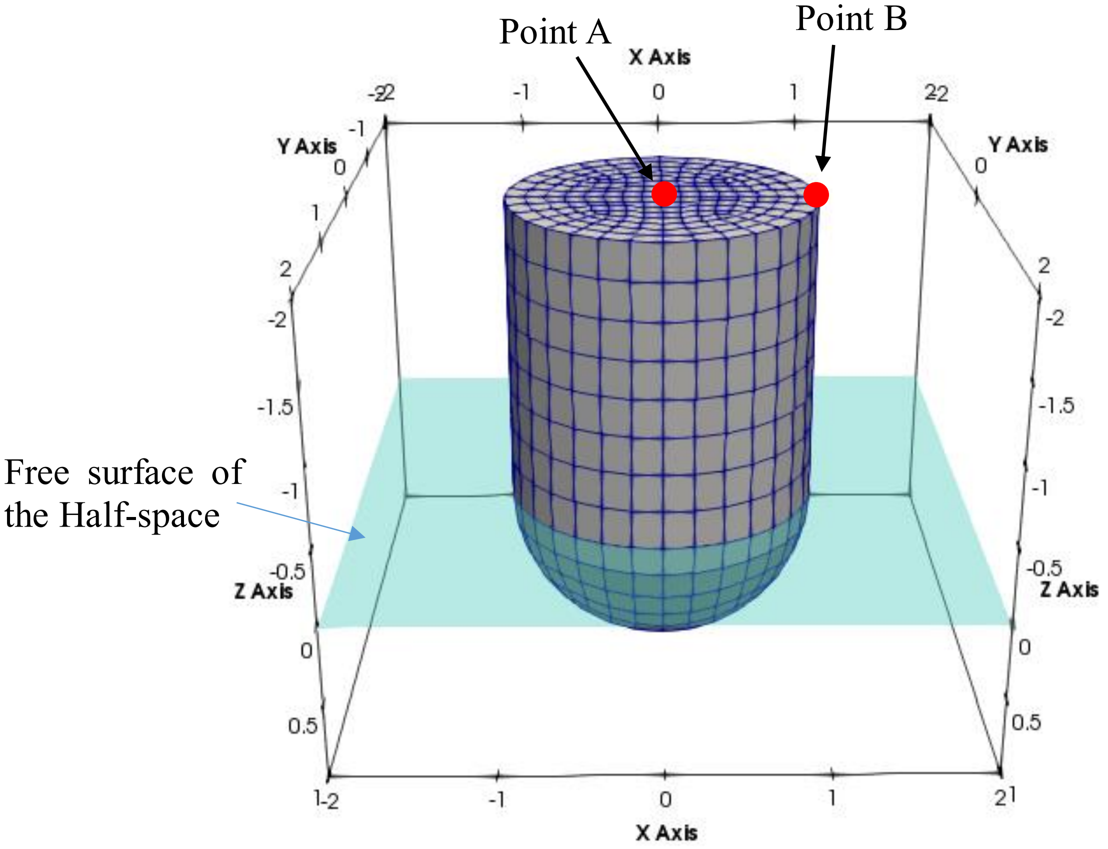

Figure 8.18: FEM+BEM mesh for the soil-foundation-structure interaction model

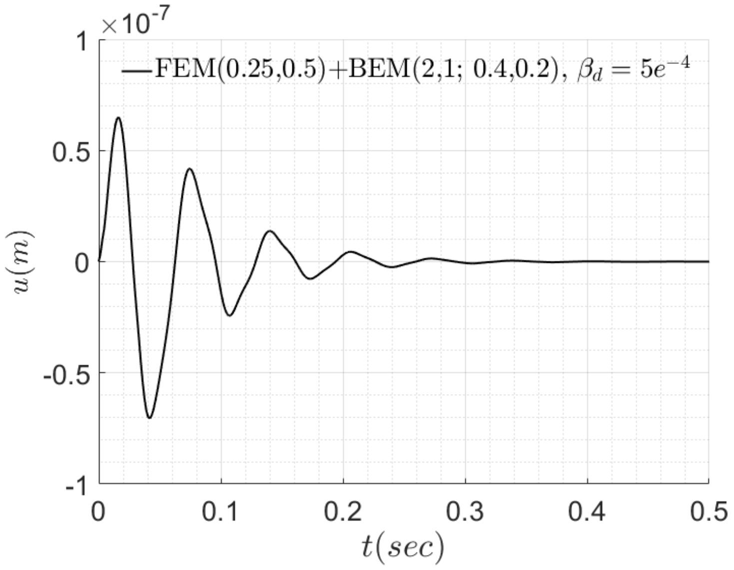

Figure 8.19: Time history of vertical displacement of Point A to a vertical pressure

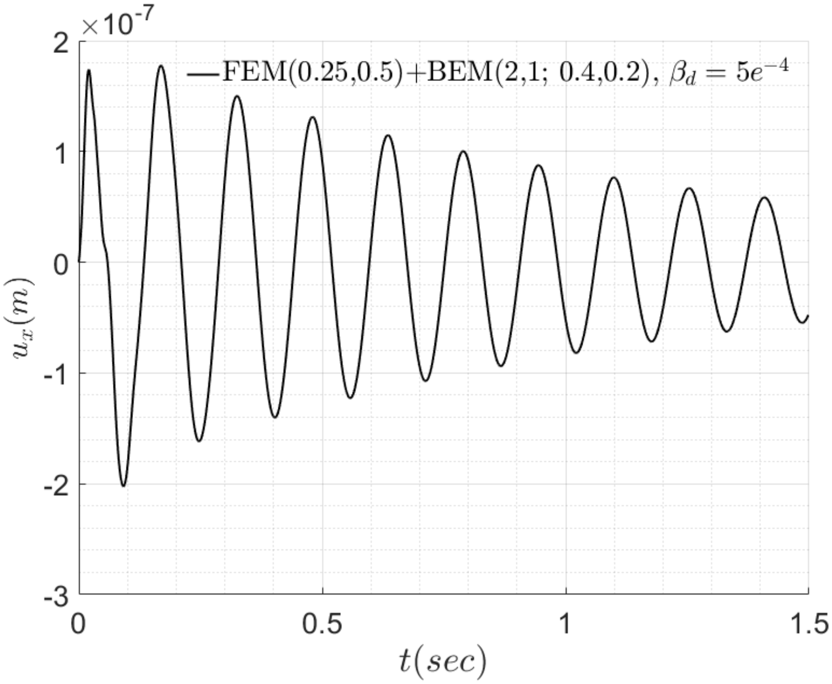

Figure 8.20: Time history of lateral displacement of Point A to a horizontal traction

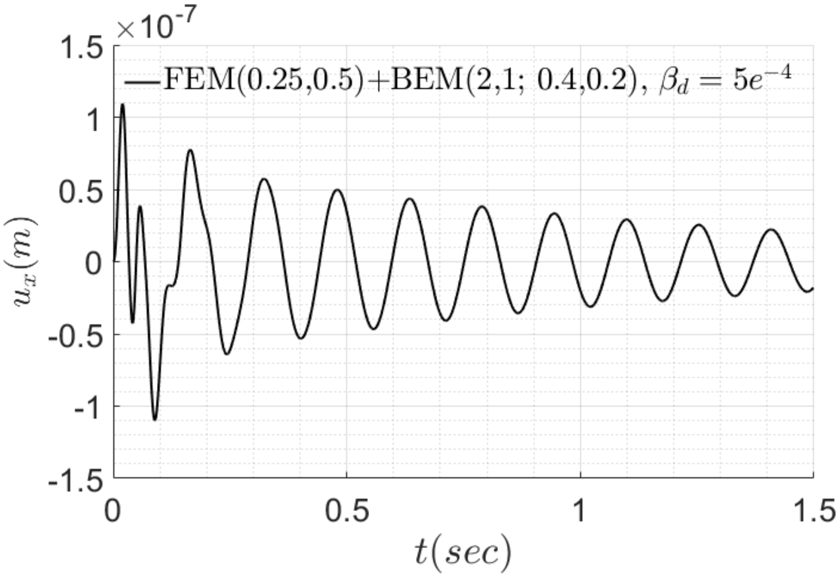

Figure 8.21: Time history of lateral displacement of point B to a horizontal traction

Chapter 9

Conclusions

Intended to establish a framework for the analysis of transient dynamic soil-structure interaction, several analytical and computational techniques for time-domain BEMs for transient problems especially for unbounded multi-layered media have been developed in this investigation. The developments include a regularization of the TD-BEM formulation, a generalized time-marching solution scheme, time-domain multi-layer half-space Green's functions and the coupling of BEM with FEM. The key achievements can be summarized as follows.

- Owing to the strong singularity of traction Green's functions in elastodynamics, one common feature among various classical time-domain BEM formulation is the presence of Cauchy principal value of integrals, the evaluation of which is sensitive and mathematical demanding. To resolve this challenge, the time-dependent point-load Green's functions are decomposed into a singular and regular part, with the former being the static bi-material full-space Green's function (Pak & Guzina, 1999) whose integration can be done analytically with the aid of static equilibrium and the latter being amenable to ordinary numerical quadrature. On basis of such a decomposition, a regularized boundary integral equation involving at most weakly singular kernels is derived for a simpler analytical framework and numerical implementation.

- As noted in many past studies and observed in the present study, the elementary single-step time-marching scheme for TD-BEM often suffers from numerical instability. To achieve a higher degree of control of both the stability and accuracy aspects, a generalized multi-step collocation scheme with variable weights and time projections to advance the solution in time is developed in this investigation. The numerical performance of the proposed TD-BEM formulation and time-marching scheme is illustrated via the benchmark problems of a finite 1D-bar and a spherical cavity wave-propagation problem. It is shown that using the proposed formulation with suitable combinations of displacement and traction projection orders as well as collocation weights can improve the accuracy as well as the stability of the solution.

- As the numerical stability of direct time-domain boundary element methods (TD-BEM) has been a major challenge without a rigorous evaluation method, a compact but formal analytical framework for the stability evaluation of TD-BEM schemes is formulated in this study. This is achieved by showing that a direct TD-BEM time-marching algorithm can, with appropriate arrangements, be framed as a linear multi-step time integration procedure with a hybrid amplification matrix whose spectral radius is directly related to the stability of the algorithm. Through a systematic variation of the key parameters of the proposed TD-BEM scheme which encompasses a number of past TD-BEM algorithms as degenerate cases, a definitive identification of the parametric space associated with a set of stable TD-BEM schemes is achieved With minor adaptations, the proposed approach to evaluate TD-BEM's stability is apt to be also usable to evaluate or guide the development of better time-domain boundary integral-element methods.

- For the usage in the BEMs for half-space problems, a synthesis of the time-domain Green's function of multilayer half-space subjected to a general interior point load with a cubic B-spline time function is developed using a Fourier synthesis of existing frequency-domain multilayer half-space Green's functions. As the Fourier transform of cubic B-Spline function decays strongly with increasing frequency, the kernel of the inverse Fourier transform representation for the time-domain Green's function also has greatly reduced effective frequency spectrum, allowing the integration to be truncated at a finite value with minimal error while avoiding the difficult task of computing the frequency-domain Greens function at very high frequency.

- To improve the efficacy of TD-BEMs for problems involving unbounded domains with depth wise material variation, a new set of time-domain dynamic Green's functions for a multilayer half-space are developed by integral transform methods whose inversion to the time domain is developed through an analytical extension of Cagniard's basic idea in wave propagation theory and seismology. By the proposed method, past needs and complications of computing variable branch line integrals, Cauchy principal values as well as residues in time-domina Green's function methods are particularly alleviated. Such reduction in complexities is apt to be helpful in many fields of applied sciences.

- Incorporating the proposed half-space Green's functions for both the homogeneous and multilayer half-space into the regularized time-domain boundary integral equation, a TD-BEM for dynamic analysis of half-space problems is established. With the use of a half-space Green's function, the BEM is free from the need to discretize the free-surface over a finite region, the action of which introduces extra approximation error while limiting the validity of the solution.

- Using the theoretical and computational methodologies developed, the possibility of a more effective time-domain finite element-boundary element coupling formulation with attention to both accuracy and stability aspects is developed for dynamic soil-structure interaction problems. Promising results have been obtained for a number of fundamental test cases.

Apart from its direct application to geotechnical earthquake engineering and dynamic soil-structure interaction problems, it is believed that the fundamental ideas explored and substantiated in this study are apt to be relevant to theoretical and computational modeling of not only transient elastodynamics but also acoustics, electromagnetics and seismology.

References

(1) Ablowitz, M. J., & Fokas., A. S. (2003). Complex variables: introduction and applications. Cambridge University Press.

(2) Ahlfors, L. V. (1953). Complex analysis: an introduction to the theory of analytic functions of one complex variable. New York, London.

(3) Aimi, A. e. (2012). A stable 3D energetic Galerkin BEM approach for wave propagation interior problems. Engineering Analysis with Boundary Elements 36(12), 1756-1765.

(4) Aimi, A., Diligenti, M., & Guardasoni, C. (2011). On the energetic Galerkin boundary element method applied to interior wave propagation problems. Journal of Computational and Applied Mathematics 235(7) , 1746-1754.

(5) Aki, K., & Richards, P. G. (2002). Quantitative seismology. Vol. 1.

(6) Antes, H. (1985). A boundary element procedure for transient wave propagations in two-dimensional isotropic elastic media. Finite Elements in Analysis and Design 1(4), 313-322.

(7) Apsel, R. J., & Luco, J. E. (1983). On the Green's functions for a layered half-space. Part II. Bulletin of the Seismological Society of America, 73(4), 931-951.

(8) Araujo, F. C., Mansur, W. J., & Nishikava, L. K. (1999). A linear time-marching algorithm in 3D BEM formulation for elastodynamics. Engineering analysis with boundary elements 23(10), 825-833.

(9) Ashlock, J. C. (2006). Computational and experimental modeling of dynamic foundation interactions with sand, doctoral dissertation, University of Colorado at Boulder.

(10) Banerjee, P. K., Ahmad, S., & Manolis, G. D. (1986). Transient elastodynamic analysis of threedimensional problems by boundary element method. Earthquake engineering & structural dynamics 14(6), 933-949.

(11) Banjai, L., Messner, M., & Schanz, M. (2012). Runge–Kutta convolution quadrature for the boundary element method . Computer Methods in Applied Mechanics and Engineering, 245, 90-101.

(12) Bathe, K. J., & Wilson, E. L. (1976). Numerical methods in finite element analysis.

Ben-Menahem, A., & Vered, M. (1973). Extension and interpretation of the Cagniard-Pekeris method for dislocation sources. Bulletin of the Seismological Society of America, 1611-1636.

(13) Bode C., Hirschauer R., Savidis S.A. (2002). Soil-structure interaction in the time domain using half-space Green's functions. Soil Dynamics and Earthquake Engineering 22, 183-195.

(14) Brebbia, C. A., J. C. F. Telles, L. O. Wrobel. (1984). Boundary element techniques: theory and applications in engineering. Springer.

(15) Brekhovskikh, L. (2012). Waves in layered media. Vol. 16. Elsevier.

(16) Cagniard, L. (1962). Reflection and refraction of progressive seismic waves. McGraw-Hill.

(17) Carrer, J. A., Pereira, W. L., & Mansur, W. J. (2012). Two-dimensional elastodynamics by the time-domain boundary element method: Lagrange interpolation strategy in time integration. Engineering Analysis with Boundary Elements, 36(7), 1164-1172.

(18) Cerveny, V. (2005). Seismic ray theory. Cambridge University Press.

(19) Chao, C. C. (1960). Dynamical response of an elastic half-space to tangential surface loadings. Journal of Applied Mechanics 27(3), 559-567.

(20) Chopra, A. K. (2001). Dynamics of structures: Theory and applications. Pearson Education.

(21) Christensen, R. (2012). Theory of viscoelasticity: an introduction. Elsevier.

(22) Churchill, R. V. (1958). Operational mathematics. McGraw-Hill.

(23) Coda, H. B.; Venturini, W. S. (1995). Three-dimensional transient BEM analysis. Computers & structures 56(5), 751-768.

(24) Cole, D. M., Koslo, D. D., & Minster, J. B. (1978). A numerical boundary integral equation method for elastodynamics. I. Bulletin of the Seismological Society of America 68(5), 1331-1357.

(25) Das, B. M. (2016). Principles of soil dynamics. Cengage Learning.

(26) de Hoop, A. T. (1960). A modification of Cagniard's method for solving seismic pulse problems. Applied Scientific Research, Section B, 8(1), 349-356.

(27) de Hoop, A. T. (1988). Application of the modified Cagniard technique to transient electromagnetic diffusion problems. Geophysical Journal International 94(3), 387-397.

(28) Dehestani, M. (2013). Computation of the stresses in a moving reference system in a half-space due to a traversing time-varing concentrated load. Computers & mathematics with Applications 65(11), 1849-1862.

(29) Desceliers, C. (2008). A time-domain method to solve transient elastic wave propagation in a multilayer medium with a hybrid spectral-finite element space approximation. Wave Motion 45(4), 383-399.

(30) Dix, C. H. (1954). The method of Cagniard in seismic pulse problems. Geophysics 19(4), 722-738.

(31) Doménech, A., Martínez-Rodrigo, M. D., Romero, A., & Galvín, P. (2016). On the basic phenomenon of soil-structure interaction on the free vibration response of beams: Application to railway bridges. Engineering Structures, 125 , 254-265.

(32) Dominguez, J. (1993). Boundary elements in dynamics. Wit Press.

(33) Domínguez, J., & Abascal, R. (1984). On fundamental solutions for the boundary integral equations method in static and dynamic elasticity . Engineering Analysis, 1(3), 128-134.

(34) Dominguez, J., & Gallego, R. (1991). The time domain boundary element method for elastodynamic problems. Mathematical and Computer Modelling, 15(3-5), 119-129.

(35) Eatwell, G. P., Simmons, J. A., & Willis., J. R. (1982). A new representation for the dynamic Green's tensor of an elastic half-space or layered medium. Wave motion 4(1), 53-73.

(36) Eduardo, K. (2012). lamb's problem at its simplest. Proc. R. Soc. A. The Royal Society.

(37) Enrique Luco, J. (1998). A simple model for structural control including soil–structure interaction effects. Earthquake engineering & structural dynamics 27(3) , 225-242.

(38) François, S., Coulier, P., & Degrande., G. (2015). Finite element–boundary element coupling algorithms for transient elastodynamics. Engineering Analysis with Boundary Elements 55 , 104-121.

(39) Frangi, A ; Novati, G. (1999). On the numerical stability of time-domain elastodynamic analyses by BEM. Computer Methods in Applied Mechanics and Engineering, 173(3-4), 403-417.

(40) Frangi, A. (2000). “Causal” shape functions in the time domain boundary element method. . Computational mechanics, 25(6), 533-541.

(41) Galvín, P., & Romero, A. (2014). A 3D time domain numerical model based on half-space Green's function for soil–structure interaction analysis. Computational Mechanics, 53(5), 1073-1085.

(42) Garvin, W. W. (1956). Exact transient solution of the buried line source problem. Proceedings of the Royal Society of London a: Mathematical, Physical and Engineering Sciences, Vol. 234.

(43) Gilbert, F., & Backus, G. E. (1966). Propagator matrices in elastic wave and vibration problems. Geophysics, 31(2), 326-332.

(44) Gilbert, F., & Helmberger, D. V. (1972). Generalized ray theory for a layered sphere. Geophysical Journal International 27(1), 57-80.

(45) Graff, K. F. (1975). Wave motion in elastic solids. Oxford University Press.

(46) Gurtin, M. E., & Sternberg., E. (1962). On the linear theory of viscoelasticity. Archive for Rational Mechanics and Analysis 11(1), 291-356.

(47) Gustafsson, B., Kreiss, H.-O., & Sundström., A. (1972). Stability theory of difference approximations for mixed initial boundary value problems. II. Mathematics of Computation , 649-686.

(48) Guzina, B. B. & Pak, R. Y. S. (1999). Static fundamental solutions for a bi-material full-space. International journal of solids and structures, 36(4), 493-516.

(49) Guzina, B. B (1996). Seismic response of foundations and structures in multilayered media (Doctoral dissertation, University of Colorado).

(50) Guzina, B. B., & Pak, R. Y. S. (2001). On the analysis of wave motions in a multi-layered solid. Quarterly Journal of Mechanics and Applied Mathematics, 54(1), 13-38.

(51) Ha-Duong, T., B. L., & Terrasse, I. (2003). A Galerkin BEM for transient acoustic scattering by an absorbing obstacle. International Journal for Numerical Methods in Engineering 57(13), 1845-1882.

(52) Haskell, N. A. (1953). The dispersion of surface waves on multilayered media. Bulletin of the seismological Society of America 43(1), 17-34.

(53) Hayami, K. (2005). Variable transformations for nearly singular integrals in the boundary element method. Publications of the Research Institute for Mathematical Sciences 41(4) , 821-842.

(54) Helmberger, D. V. (1968). The crust-mantle transition in the Bering Sea. Bulletin of the Seismological Society of America 58(1) , 179-214.

(55) Hernandez, V., Roman, J. E., & Vidal, V. (2005). SLEPc: A scalable and flexible toolkit for the solution of eigenvalue problems. .ACM Transactions on Mathematical Software (TOMS), 31(3), 351-362.

(56) Hilderbrand, F. (1965). Methods of Applied Mathematics. 2nd ed., Prentice Hall.

(57) Hisada, Y. (1994). An efficient method for computing Green's functions for a layered half-space with sources and receivers at close depths. Bulletin of the Seismological Society of America 84(5), 1456-1472.

(58) Hisada, Y. (1995). An efficient method for computing Green's functions for a layered half-space with sources and receivers at close depths (Part 2). Bulletin of the Seismological Society of America 85(4), 1080-1093.

(59) Horn, R. A., & Johnson, C. R. (2012). Matrix analysis. Cambridge university press.

(60) Hughes, T. J. R. (2012). The finite element method: linear static and dynamic finite element analysis. Courier Corporation.

(61) Jiang, J., Baird, G. R., & Blair, d. P. (1994). Dynamic response of a half-space to a buried spherical source. Geophysical Journal International 119(3), 753-765.

(62) Johnson, L. R. (1974). Green's function for Lamb's problem. Geophysical Journal International, 37(1), 99-131.

(63) Kager, B. (2015). Efficient Convolution Quadrature Based Boundary Element Formulation for Time-domain Elastodynamics. Verlag der Techn. Univ.

(64) Karabalis, D. L. (1984). Dynamic response of 3-D rigid surface foundations by time domain boundary element method. Earthquake engineering & structural dynamics 12(1), 73-93.

(65) Karabalis, D. L. (1987). Three-dimensional soil-structure interaction by boundary element methods. Applications in Geomechanics. Springer, Berlin, Heidelberg, 1-26.

(66) Karabalis, D. L., & Beskos, D. E. (1985). Dynamic response of 3-D flexible foundations by time domain BEM and FEM. International Journal of Soil Dynamics and Earthquake Engineering 4(2), 91-101.

(67) Kausel, E. (2012). Lamb's problem at its simplest. In Proc. R. Soc. A (p. rspa20120462). The Royal Society.

(68) Kennett, B. L. N. (2013). Seismic wave propagation in stratified media. ANU Press.

(69) Kennett, B. L. N. (1974). Reflections, rays, and reverberations. Bulletin of the Seismological Society of America 64(6), 1685-1696.

(70) Kennett, B. L. N., & Kerry, N. J. (1979). Seismic waves in a stratified half space. Geophysical Journal International, 57(3), 557-583.

(71) Knopoff, L. (1964). A matrix method for elastic wave problems. Bulletin of the Seismological Society of America 54(1), 431-438.

(72) Kramer, S. L. (1996). Geotechnical earthquake engineering . Prentice Hall.

(73) Kutt, H. R. (1975). Quadrature formulae for finite-part integrals. Special Report WISK 178, National Research Institute for Mathematical Sciences, Pretoria, South Africa.

(74) Lachat, J. C., & Watson, J. O. (1976). Effective numerical treatment of boundary integral equations: A formulation for three-dimensional elastostatics. International Journal for Numerical Methods in Engineering 10(5), 991-1005.

(75) Lamb, H. (1904). On the propagation of tremors over the surface of an elastic solid. Philosophical Transactions of the Royal Society of London. Series A, Containing papers of a mathematical or physical character, 203, 1-42.

(76) Lee, G. S., & Ma, C. C. (2000). Transient elastic waves propagating in a multi–layered medium subjected to in–plane dynamic loadings. I. Theory. In Proceedings of Royal Society of London A: Mathematical, Physical and Engineering Sciences, 456(1998), 1355-1374.

(77) Liu, Y. J. (1970). Nearly singular and hypersingular integrals in the boundary element method. WIT Transactions on Modelling and Simulation 1.

(78) Liu, Y. J., Mukherjee, S., Nishimura, N., Schanz, M., & Ye, W. S. (2011). Recent advances and emerging applications of the boundary element method. Applied Mechanics Reviews, 64(3), 030802.

(79) Luchi, M. L. (1987). Boundary elements for three-dimensional elastic crack analysis. International journal for numerical methods in engineering 24(12) , 2253-2271.

(80) Luco, J. E., & Apsel, R. J. (1983). On the Green's functions for a layered half-space. Part I. Bulletin of the Seismological Society of America, 73(4), 909-929.

(81) M.Marrero, & J.Dominguez. (2003). Numerical behavior of time domain BEM for three-dimensional transient elastodynamics problems. Engineering Analysis with Boundary Elements 27, 39-48.

(82) Ma, C. C., & Lee., G. S. (2000). Transient elastic waves propagating in a multi–layered medium subjected to in–plane dynamic loadings II. Numerical calculation and experimental measurement. Proceedings of Royal Society of London A: Mathematical, Physical and Engineering Sciences. 456(1998), 1375-1396.

(83) Ma, C. C., & Lee, G. S. (2006). General three-dimensional analysis of transient elastic waves in a multilayered medium. Journal of applied mechanics, 73(3), 490-504.

(84) Ma, C. C., Liu, S. W., & Lee, G. S. (2001). Dynamic responses of a layered medium subjected to anti-plane loadings. International journal of solids and structures, 38(50), 9295-9312.

(85) Mansur, W. J. (1983). A time-stepping technique to solve wave propagation problems using the boundary element method. University of Southampton.

(86) Miklowitz, J. (1978). The theory of elastic waves and waveguides. North-Holland.

(87) Mindlin, R. D. (1936). Force at a point in the interior of a semi-infinite solid. Physics, 7(5), 195-202.

(88) Mita, A., & Luco, J. E. (1987). Dynamic response of embedded foundations: a hybrid approach. Computer methods in applied mechanics and engineering 63(3) , 233-259.

(89) Mitra, A. K. (1987). Resolving difficulties in the BIEM caused by geometric corners and discontinuous boundary conditions. Mathematical and Computational Aspects. Springer, Berlin, Heidelberg, 519-532.

(90) Mooney, H. M. (1974). Some numerical solutions for Lamb's problem. Bulletin of the Seismological Society of America 64(2), 473-491.

(91) Ngo, K. T., & Erickson., K. T. (1997). Stability of discrete-time matrix polynomials. IEEE transactions on automatic control 42(4), 538-542.

(92) O'Brien, J., & Rizos, D. C. (2005). A 3D BEM-FEM methodology for simulation of high speed train induced vibrations. Soil Dynamics and Earthquake Engineering 25(4) , 289-301.

(93) Padrón, L. A., Aznárez, J. J., & Maeso., O. (2011). 3-D boundary element–finite element method for the dynamic analysis of piled buildings. Engineering analysis with boundary elements 35(3) , 465-477.

(94) Pak, R. Y. S. (1987). Asymmetric wave propagation in an elastic half-space by a method of potentials. J. Appl. Mech 54 (1), 121-126.

(95) Pak, R. Y. S., & Guzina, B. B. (1999). Seismic soil-structure interaction analysis by direct boundary element methods. International Journal of Solids and Structures, 36(31), 4743-4766.

(96) Pak, R. Y. S., & Guzina, B. B. (2002). Three-dimensional Green’s functions for a multilayered half-space in displacement potentials. Journal of Engineering Mechanics, 128(4), 449-461.

(97) Pak, R. Y. S. & Morteza, E. G. (2007). On the completeness of a method of potentials in elastodynamics. Quartely of applied Mathematics, 65(4), 789-797.

(98) Pak, R. Y. S., & Bai, X. (2018). A regularized direct time-domain boundary element formlation for 3D Transient Elastodynamics. Engineering analysis with Boundary Elements, 93, 135-142.

(99) Panagiotopoulos, C. G., & Manolis, G. D. (2011). Stability issues in 3D BEM formulations for transient elastodynamics. Boundary Elements and Other Mesh Reduction Methods XXXIII, 143.

(100) PAO, Y. H., Su X. Y., and Tian J. Y. (2000). "Reverberation matrix method for propagation of sound in a multilayered liquid." Journal of Sound and Vibration 230(4): 743-760.

(101) Park, J., & Kausel, E. (2006). Response of layered half-space obtained directly in the time domain, part I: SH sources. Bulletin of the Seismological Society of America, 96(5), 1795-1809.

(102) Peirce, A., and E. Siebrits. (1997). Stability analysis and design of time-stepping schemes for general elastodynamic boundary element models. International Journal for Numerical Methods in Engineering 40(2), 319-342.

(103) Pekeris, C. L. (1955a). The seismic surface pulse. Proceedings of the National Academy of Sciences 41(7), 469-639.

(104) Pekeris, C. L. (1955b). The sismic buried pulse. Proceedings of the National Academy of Sciences 41(9), 629-639.

(105) Pekeris, C. L., & Lifson, H. (1957). Motion of the Surface of a Uniform Elastic Half-Space Produced by a Buried Pulse. The Journal of the Acoustical Society of America, 29(11), 1233-1238.

(106) Regueiro, R. A. (2014). ONR MURI project on soil blast modeling and simulation. Dynamic Behavior of Materials, Volume 1. Springer, Cham, 341-353.

(107) Reshef, M. (1988). Three dimensional elastic modeling by the Fourier method. Geophysics 53(9), 1184-1193.

(108) Richtmyer, R. D., & Morton, K. W. (1994). Difference methods for initial-value problems. 2nd ed., Malabar, Fla: Krieger Publishing Co, .

(109) Rizos, D. C., & Wang, Z. (2002). Coupled BEM–FEM solutions for direct time domain soil–structure interaction analysis. Engineering Analysis with Boundary Elements 26(10), 877-888.

(110) Rizos, D. C., & Zhou, S. (2006). An advanced direct time domain BEM for 3-D wave propagation in acoustic media. Journal of sound and vibration, 293(1), 196-212.

(111) Rizos, D. C., Karabalis,D. L. (1994). An advanced direct time domain BEM formulation for general 3-D elastodynamic problems. Computational Mechanics 15(3), 249-269.

(112) Rizzo, F. J. (1985). A boundary integral equation method for radiation and scattering of elastic waves in three dimensions. International journal for numerical methods in engineering 21(1) , 115-129.

(113) Roever, W. L., Vining, T. F., & Strick, E. (1959). Propagation of elastic wave motion from an impulsive source along a fluid/solid interface. Philosophical Transactions of the Royal Society of London A: mathematical, Physical and Engineering Sciences 251(1000), 455-523.

(114) Romero, A., & Galvín, P. (2015). A BEM–FEM using layered half-space Green′ s function in time domain for SSI analyses. Engineering Analysis with Boundary Elements, 55, 93-103.

(115) Schanz, M. ; Antes, H. (1997). A new visco-and elastodynamic time domain boundary element formulation. Computational Mechanics, 20(5), 452-459.

(116) Schanz, M., & Antes, H. (1997). Application of ‘operational quadrature methods’ in time domain boundary element methods. Meccanica 32(3) , 179-186.

(117) Schanz, M., Ye, W., & Xiao, J. (2016). Comparison of the convolution quadrature method and enhanced inverse FFT with application in elastodynamic boundary element method. Computational Mechanics, 57(4), 523-536.

(118) Shearer, P. M. (2009). Introduction to seismology. Cambridge University Press.

(119) Sladek, J. &. (1991). Regularized integral representation of thermoelastic stresses. Engineering analysis with boundary elements 8(5) , 224-230.

(120) Soares Jr, D., Estorff, O. V., & Mansur., W. J. (2004). Iterative coupling of BEM and FEM for nonlinear dynamic analyses. Computational Mechanics 34(1), 67-73.

(121) Soares, D., & Mansur, W. J. (2007). An efficient stabilized boundary element formulation for 2D time-domain acoustics and elastodynamics. Computational Mechanics, 40(2), 355-365.

(122) Spencer, T. W. (1960). The method of generalized reflection and transmission coefficients. Geophysics 25(3), 625-641.

(123) Spyrakos, C. C., & Beskos, D. E. (1986). Dynamic response of flexible strip-foundations by boundary and finite elements. Soil dynamics and earthquake engineering, 5(2), 84-96.

(124) Stewart, J. E. (2012). Soil-structure interaction for building structures. No. Grant/Contract Reports (NISTGCR)-12-917-21.

(125) Stokes, G. G. (1849). On the dynamical theory of diffraction. Transactions of the Cambridge Philosophical Society, 9, 1-48.

(126) Strikwerda, J. C. (2004). Finite difference schemes and partial differential equations. Society for Industrial and Applied Mathematics.

(127) Su, X. Y., Tian, J. Y., & Pao, Y. H. (2002). Application of the reverberation-ray matrix to the propagation of elastic waves in a layered solid. International Journal of Solids and Structures, 39(21), 5447-5463.

(128) Thomson, W. T. (1950). Tansmission of Elastic Waves thorugh a Stratified Solid Medium. Journal of Applied Physics 21, 89, 89-93.

(129) Tian, J., & Xie, Z. (2009). A hybrid method for transient wave propagation in a multilayered solid. Journal of Sound and Vibration, 325(1), 161-173.

(130) Triantafyllidis, T. (1991). 3-D time domain BEM using half-space Green's functions. . Engineering Analysis with Boundary Elements, 8(3), 115-124.

(131) Verweij, M., & de Hoop, A. T. (1990). Determination of seismic wavefields in arbitrariy continuously layered media using modified Cagniard method. Geophysical Journal Internatinal 103(3), 731-754.

(132) Von Estorff, O. (1991). Dynamic response of elastic blocks by time domain BEM and FEM. Computers & Structures 38(3), 289-300.

(133) Von Estorff, O., & Hagen., C. (2006). Iterative coupling of FEM and BEM in 3D transient elastodynamics. Engineering Analysis with Boundary Elements 30(7) , 611-622.

(134) Wheeler, L. T., & Sternberg, E. (1968). Some theorems in classical elastodynamics. Archive for Rational Mechanics and Analysis 31(1), 51-90.

(135) Wigginst, R. A., & Helmberger, D. V. (1974). Synthetic seismogram computation by expansion in generalized rays. Geophysical Journal International, 37(1), 73-90.

(136) Wolf, J. (1985). Dynamic soil-structure interaction (No. LCH-BOOK-2008-039). Prentice Hall, Inc.

(137) Yazdi, A. K., Omidvar, B., & Rahimian, M. (2011). Improving the stability of time domain dual boundary element method for three dimensional fracture problems: A time weighting approach. Engineering Analysis with Boundary Elements, 35(10), 1142-1148.

(138) Yu, G. (1998). A linear method applied to 2D timedomain BEM. Communications in Numerical Methods in Engineering, 14(12), 1171-1179.

(139) Yu, G. M., W. J., C., M., J. A., & Gong, L. (2000). Stability of Galerkin and collocation time domain boundary element methods as applied to the scalar wave equation. Computers & Structures, 74(4), 495-506.

(140) Yu, G., Mansur, W. J., & Carrer, J. A. (1998). Time weighting in time domain BEM. Engineering analysis with boundary elements 22(3), 175-181.

(141) Zienkiewicz, O. C., & Bettess, D. W. (1977). The coupling of the finite element method and boundary solution procedures. International journal for numerical methods in engineering 11(2), 355-375.